Special Issue Reprint

Multifunctional Application of Biopolymers and Biomaterials

Edited by
Swarup Roy and Valentina Siracusa

MDPI

Multifunctional Application of Biopolymers and Biomaterials

Multifunctional Application of Biopolymers and Biomaterials

Editors

Swarup Roy
Valentina Siracusa

MDPI

Editors

Swarup Roy
Food Technology and Nutrition
Lovely Professional University
Phagwara
India

Valentina Siracusa
Chemical Science
University of Catania
Catania
Italy

This is a reprint of articles from the Special Issue published online in the open access journal *International Journal of Molecular Sciences* (ISSN 1422-0067) (available at: www.mdpi.com/journal/ijms/special_issues/mul_biopoly_biomat).

For citation purposes, cite each article independently as indicated on the article page online and as indicated below:

LastName, A.A.; LastName, B.B.; LastName, C.C. Article Title. *Journal Name* **Year**, *Volume Number*, Page Range.

Contents

About the Editors

Swarup Roy

Dr. Swarup Roy is currently working as an Assistant Professor in the Department of Food Technlogy and Nutrition, Lovely Professional University. He previously worked as an Assistant Professor at the School of Bioengineering and Food Technology, Faculty of Applied Sciences and Biotechnology, Shoolini University, Solan, India. He has completed his Ph.D. in Biochemistry (2016) from the University of Kalyani, West Bengal. He holds more than five years of postdoctoral research experience from various institutes Kyung Hee University (3 years) and Inha University (1 year), Republic of Korea, and Indian Institute of Technology Indore (1.5 years). His academic contributions include several international scientific papers, reviews, book chapters, published by ACS, Elsevier, Springer, Taylor & Francis, RSC, Wiley, etc. He has published a total of 111 SCI publications, 2 book chapters, filed 2 patents, and 30 other papers with 4700 citations, 40 h-index, and 83 i10-index (Google Scholar). At present, Dr. Roy is involved in research work based on the fabrication of blend biopolymers-based food packaging films/coatings. His research work is focused on the preparation and application of biopolymer-based functional active and smart food packaging film and coatings for food preservation applications.

Valentina Siracusa

Siracusa Valentina received her degree in Industrial Chemistry from the University of Catania (Italy) at 23 years old. She completed her PhD and post-PhD study working on the synthesis and characterization of innovative polyesters used in the engineering field. After a period as a lecturer for "Chemistry and Materials" for Engineering, from 2006, she has been an Associate Professor in Chemistry for Engineering at University of Catania (Italy) and Invited Professor on "Life Cycle Assessment Study (LCA)" courses at University of Bologna (Italy). She collaborates on several research projects, both for academic than industrial interest, on topic such as recycle, ambient, food packaging, graphene for packaging application, nanoparticles, and polymer drug delivery. She collaborates with national and international research groups on biopolymers used in the field of food packaging, for modified atmosphere packaging of fresh foods, with also Life Cycle Assessment study (with SimaPro software). She is author of more than 110 papers in high-impact-factor scientific journals, she is author of several book chapters for Wiley, Springer, Elsevier, she is author of articles for special Module of Elsevier Encyclopedia and she is Editorial Board Member and Lead Guest Editor of several International Journals. Her research interest includes: synthesis and full characterization of biodegradable and bio-based polymers; gas barrier behavior in standard as well as in moisture condition, at different temperature; Life Cycle Assessment (LCA) study of polymers; thermal and photo degradation behavior of packaging materials analyzed during food shelf-life study.

Editorial

Multifunctional Application of Biopolymers and Biomaterials

Swarup Roy [1,*] **and Valentina Siracusa** [2]

[1] Department of Food Technology and Nutrition, School of Agriculture, Lovely Professional University, Phagwara 144411, India
[2] Department of Chemical Sciences, University of Catania, Viale Andrea Doria 6, 95125 Catania, Italy; vsiracus@dmfci.unict.it
[*] Correspondence: swaruproy2013@gmail.com

Biopolymers and biomaterials are two interconnected key topics, which have recently drawn significant attention from researchers across all fields, owing to the emerging potential in multifunctional use. Biopolymers are commonly used to fabricate many biomaterials and, moreover, the combination of biomaterials and biopolymers can produce a new generation of materials for versatile applications. Biopolymers are a topic of interest nowadays, not only due to their potential applications in food, pharmaceuticals, textiles, medicals and other sectors but also to address the challenges of upward environmental pollution [1]. The unorganized use of readily available and cost-effective synthetic plastic has already caused severe damage to the environment and, now, these plastics are becoming a serious threat to all living beings on the planet [2,3]. The tremendous use of synthetic plastic in all daily used items is becoming a serious threat to us and, thus, there is a need for an instant alternative, and, in this context, bio-based sustainable and degradable polymers have high potential to replace the petrochemical-derived synthetic polymers. There are various biopolymers, such as protein, polysaccharides or their combinations, that are commonly used to develop bioplastics. Biopolymer-based polymers have comparable properties like their synthetic counterparts [4,5]. The addition of functional materials, such as nanomaterials, essential oils, phytochemicals, bioactive components, etc., helps in further improvements in both physical and functional properties of the biopolymer-based materials [6–8]. Recent research has shown that biopolymer-based functional packaging (active and intelligent packaging) film and coatings have good potential to improve the life span of packed food items [9,10]. Moreover, biopolymers have also been used as hydrogel and dressing materials to treat wounds in the biomedical sector [11,12]. Even biomaterials are commonly used to fabricate medical devices [13].

Biomaterials include, but are not limited to, synthetic or natural polymers, ceramics and composites, which can interact with biological matter. Recently, biomaterials have been increasingly used and, day by day, they are substituting the conventional polymeric materials in agriculture, textile, medical, food, cosmetics and pharmaceutical sectors [14–17]. The medical sector is the most used market for biomaterials [18]. Nowadays, in the pharmaceutical and textile sectors, biomaterials are also readily available. Many biopolymer-based biomaterials are used as micro- and nanofibers in the textile sector [19]. Biomaterials are frequently used in drug delivery systems in the pharmaceutical industry. Moreover, there is growing public concern for the environment and health; indeed, many folds replicate the use of biomaterials in various sectors. Even though biomaterials and biopolymers are emerging very rapidly, as already discussed, more research is still needed for further development in this field. Nevertheless, the complete conversion of conventional materials to biomaterials is expected to take more time.

Biomaterials and biopolymers are promising for making sustainable materials, but there are many concerns, which need more attention before further progress. The cost of these materials is higher than the traditionally used ones, which restricts the use in many sectors. More in-depth knowledge about biopolymers and biomaterials is required to

produce futuristic materials. Furthermore, there is a need for improvements in the physical properties of the biomaterials to meet the requirement in industrial-level applications. The ongoing and future research on this topic is anticipated to help in developing more sustainable materials.

Conflicts of Interest: The authors declare no conflict of interest.

References

1. Baranwal, J.; Barse, B.; Fais, A.; Delogu, G.L.; Kumar, A. Biopolymer: A Sustainable Material for Food and Medical Applications. *Polymers* **2022**, *14*, 983. [CrossRef] [PubMed]
2. Prata, J.C. Airborne Microplastics: Consequences to Human Health? *Environ. Pollut.* **2018**, *234*, 115–126. [CrossRef] [PubMed]
3. Lau, W.W.Y.; Shiran, Y.; Bailey, R.M.; Cook, E.; Stuchtey, M.R.; Koskella, J.; Velis, C.A.; Godfrey, L.; Boucher, J.; Murphy, M.B.; et al. Evaluating Scenarios toward Zero Plastic Pollution. *Science* **2020**, *369*, eaba9475. [CrossRef] [PubMed]
4. Bose, I.; Roy, S.; Pandey, V.K.; Singh, R. A Comprehensive Review on Significance and Advancements of Antimicrobial Agents in Biodegradable Food Packaging. *Antibiotics* **2023**, *12*, 968. [CrossRef]
5. Zhang, W.; Roy, S.; Rhim, J.-W. Copper-Based Nanoparticles for Biopolymer-Based Functional Films in Food Packaging Applications. *Compr. Rev. Food Sci. Food Saf.* **2023**, *22*, 1933–1952. [CrossRef] [PubMed]
6. Ebrahimzadeh, S.; Biswas, D.; Roy, S.; McClements, D.J. Incorporation of Essential Oils in Edible Seaweed-Based Films: A Comprehensive Review. *Trends Food Sci. Technol.* **2023**, *135*, 43–56. [CrossRef]
7. Gupta, V.; Biswas, D.; Roy, S. A Comprehensive Review of Biodegradable Polymer-Based Films and Coatings and Their Food Packaging Applications. *Materials* **2022**, *15*, 5899. [CrossRef] [PubMed]
8. Priyadarshi, R.; Roy, S.; Ghosh, T.; Biswas, D.; Rhim, J.W. Antimicrobial Nanofillers Reinforced Biopolymer Composite Films for Active Food Packaging Applications—A Review. *Sustain. Mater. Technol.* **2022**, *32*, e00353. [CrossRef]
9. Roy, S.; Priyadarshi, R.; Ezati, P.; Rhim, J.W. Curcumin and Its Uses in Active and Smart Food Packaging Applications—A Comprehensive Review. *Food Chem.* **2022**, *375*, 131885. [CrossRef] [PubMed]
10. Domínguez, R.; Barba, F.J.; Gómez, B.; Putnik, P.; Bursać Kovačević, D.; Pateiro, M.; Santos, E.M.; Lorenzo, J.M. Active Packaging Films with Natural Antioxidants to Be Used in Meat Industry: A Review. *Food Res. Int.* **2018**, *113*, 93–101. [CrossRef] [PubMed]
11. Tan, C.; Wang, J.; Sun, B. Biopolymer-Liposome Hybrid Systems for Controlled Delivery of Bioactive Compounds: Recent Advances. *Biotechnol. Adv.* **2021**, *48*, 107727. [CrossRef] [PubMed]
12. Yegappan, R.; Selvaprithiviraj, V.; Amirthalingam, S.; Jayakumar, R. Carrageenan Based Hydrogels for Drug Delivery, Tissue Engineering and Wound Healing. *Carbohydr. Polym.* **2018**, *198*, 385–400. [CrossRef] [PubMed]
13. Kouhi, M.; Prabhakaran, M.P.; Ramakrishna, S. Edible Polymers: An Insight into Its Application in Food, Biomedicine and Cosmetics. *Trends Food Sci. Technol.* **2020**, *103*, 248–263. [CrossRef]
14. Dziuba, R.; Kucharska, M.; Madej-Kiełbik, L.; Sulak, K.; Wiśniewska-Wrona, M. Biopolymers and Biomaterials for Special Applications within the Context of the Circular Economy. *Materials* **2021**, *14*, 7704. [CrossRef] [PubMed]
15. Sharma, N.; Allardyce, B.; Rajkhowa, R.; Adholeya, A.; Agrawal, R. A Substantial Role of Agro-Textiles in Agricultural Applications. *Front. Plant Sci.* **2022**, *13*, 895740. [CrossRef] [PubMed]
16. Wusigale; Liang, L.; Luo, Y. Casein and Pectin: Structures, Interactions, and Applications. *Trends Food Sci. Technol.* **2020**, *97*, 391–403. [CrossRef]
17. Nehra, A.; Biswas, D.; Roy, S. Fabrication of Brewer's Spent Grain Fortified Bio-Based Edible Bowls: A Promising Alternative to Plastic Containers. *Biomass Convers. Biorefinery* **2022**, 1–10. [CrossRef]
18. Valle, K.Z.M.; Saucedo Acuña, R.A.; Ríos Arana, J.V.; Lobo, N.; Rodriguez, C.; Cuevas-Gonzalez, J.C.; Tovar-Carrillo, K.L. Natural Film Based on Pectin and Allantoin for Wound Healing: Obtaining, Characterization, and Rat Model. *Biomed Res. Int.* **2020**, *2020*, 6897497. [CrossRef] [PubMed]
19. Deng, Z.; Wang, T.; Chen, X.; Liu, Y. Applications of Chitosan-Based Biomaterials: A Focus on Dependent Antimicrobial Properties. *Mar. Life Sci. Technol.* **2020**, *2*, 398–413. [CrossRef]

Article

Oxygen Nanocarriers for Improving Cardioplegic Solution Performance: Physico-Chemical Characterization

Maria Tannous [1,2,3] , Gjylije Hoti [1] , Francesco Trotta [1,*], Roberta Cavalli [2], Takanobu Higashiyama [4], Pasquale Pagliaro [3] and Claudia Penna [3]

[1] Department of Chemistry, University of Turin, 10125 Turin, Italy; maria.tannous@unito.it (M.T.); gjylije.hoti@unito.it (G.H.)
[2] Department of Drug Science and Technology, University of Turin, 10125 Turin, Italy; roberta.cavalli@unito.it
[3] Department of Clinical and Biological Sciences, University of Turin, 10043 Orbassano, Italy; pasquale.pagliaro@unito.it (P.P.); claudia.penna@unito.it (C.P.)
[4] Hayashibara Co., Ltd., 675-1 Fujisaki, Naka-ku, Okayama 702-8006, Japan; takanobu.higashiyama@hb.nagase.co.jp
*   Correspondence: francesco.trotta@unito.it

Abstract: Nanocarriers for oxygen delivery have been the focus of extensive research to ameliorate the therapeutic effects of current anti-cancer treatments and in the organ transplant field. In the latter application, the use of oxygenated cardioplegic solution (CS) during cardiac arrest is certainly beneficial, and fully oxygenated crystalloid solutions may be excellent means of myocardial protection, albeit for a limited time. Therefore, to overcome this drawback, oxygenated nanosponges (NSs) that can store and slowly release oxygen over a controlled period have been chosen as nanocarriers to enhance the functionality of cardioplegic solutions. Different components can be used to prepare nanocarrier formulations for saturated oxygen delivery, and these include native α-cyclodextrin (αCD), αcyclodextrin-based nanosponges (αCD-NSs), native cyclic nigerosyl-nigerose (CNN), and cyclic nigerosyl-nigerose-based nanosponges (CNN-NSs). Oxygen release kinetics varied depending on the nanocarrier used, demonstrating higher oxygen release after 24 h for NSs than the native αCD and CNN. CNN-NSs presented the highest oxygen concentration (8.57 mg/L) in the National Institutes of Health (NIH) CS recorded at 37 °C for 12 h. The NSs retained more oxygen at 1.30 g/L than 0.13 g/L. These nanocarriers have considerable versatility and the ability to store oxygen and prolong the amount of time that the heart remains in hypothermic CS. The physicochemical characterization presents a promising oxygen-carrier formulation that can prolong the release of oxygen at low temperatures. This can make the nanocarriers suitable for the storage of hearts during the explant and transport procedure.

Keywords: oxygen delivery; cardioplegic solution; α-cyclodextrin; cyclic nigerosyl-nigerose; nanosponges; prolonged release; hypothermia; organ transplantation; organ explantation

1. Introduction

The safe capture, storage, and adsorption of large quantities of gas are some of the major technological and scientific challenges facing scientists today. Gas storage is a topic that affects several research fields, as well as climate change, energy production, and medical applications. In particular, oxygen assumes a great therapeutic value in the treatment of solid tumors. The latter is characterized by a highly hypoxic environment that greatly limits current therapies such as chemotherapy, radiotherapy, photodynamic therapy, and even immunotherapy. Different approaches are used to increase the oxygen concentration in tumor tissues. In particular, perfluorocarbons capable of solubilizing large quantities of oxygen are used. However, they cause severe inflammation, release oxygen in an uncontrolled manner, and, above all, are immiscible in both hydrophilic and hydrophobic environments. For these reasons, it is essential to find materials capable of transporting

oxygen and releasing it in a controlled way that is biocompatible, non-toxic, and easily synthesized and therefore easily transferable to industrial production [1–4]. Cyclodextrins (CDs) are natural cyclic oligosaccharides with a lipophilic central cavity and a hydrophilic outer surface consisting of (α-1,4-)-linked α-D-glucopyranose units. They contain six (αCD), seven (βCD), and eight (γCD) D-glucose units. The presence of numerous reactive hydroxyl groups on CDs enables their chemical modification, using a wide variety of bi- or polyfunctional chemicals and thus tailoring their structure. Consequently, water-soluble and insoluble cyclodextrin-based polymers are produced. The insoluble cyclodextrin-based polymers or cyclodextrin-based nanosponges (CD-based NSs) are chemically cross-linked polymers obtained by reacting the parent CDs with an appropriate cross-linking agent such as dianhydrides, active carbonyl compounds, carboxylic acids, epoxides, diisocyanates, etc. CD-based NSs are three-dimensional polymer networks with remarkable adsorption properties due to their extensive nanometer-sized porosity. The most outstanding feature of CD-based NSs is their capability to form inclusion complexes with a wide range of liquid, solid, and gaseous compounds through a molecular complexation. CD-based NSs have shown more benefits than CDs to improve the stability, release, and bioavailability of complex guest molecules. This is because the CDs' cross-linking agent molar ratio affects the nanochannels produced [5–11].

Various parameters, such as chemical composition, pore size, and thus surface area and pore volume, can be effectively modulated, even in theoretical simulation models, to optimize the gas adsorption capacity of nanosponges (NSs).

The ability of CD-based NSs to bind compounds reversibly, even in the gas phase, does not require high pressures and low temperatures and thus avoids the hazards of handling high-pressure compressed gases and the technological constraints associated with the low temperatures of liquefied gas. This is possible via physical absorption mechanisms, which may lead to the development of a new technology for the efficient storage of significant amounts of gas in strikingly small volumes [12,13].

CD-based NSs, particularly those prepared based on alpha cyclodextrins (αCD), have proven themselves to be highly suitable for the storage of gases. The ring that makes up αCD resembles a conical cylinder, or truncated cone, in the shape of a crown and includes six glucopyranose units that form a cavity, which is lined by hydrogen atoms that form glycosidic oxygen bridges. The non-bonding electron pairs of these oxygen glycosidic bridges point towards the internal part of the cavity, yielding high electron density and providing it with some basic Lewis properties. Its internally hydrophobic and externally hydrophilic nature means that αCD is principally used for stabilizing reactive intermediates and trapping small molecules (Figure 1) [14,15].
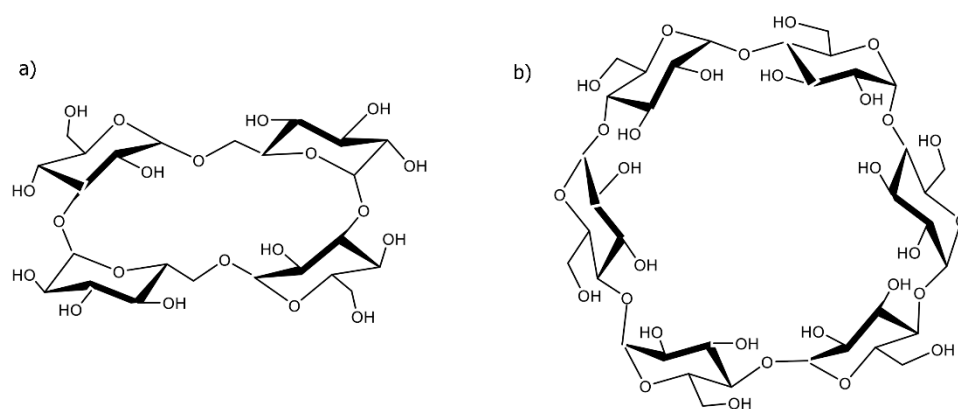
Figure 1. Chemical structures of (**a**) cyclic nigerosyl-1,6-nigerose (CNN) and (**b**) α-cyclodextrin (αCD).

On the other hand, cyclic nigerosyl-1,6-nigerose (CNN), also known as cyclo tetra glucose, is also worth considering for gas storage. It is naturally found in sake (the sediment formed during rice-wine production) and *Saccharomyces cerevisiae* cells. Indeed, CNN is a

natural, novel, non-reducing carbohydrate in which four glucopyranose units are bound by alternating α-1,6 and α-1,3 glycosidic linkages.

Numerous potential applications for sugar-based NSs have been investigated in several technological fields, including pharmaceuticals, cosmetics, catalysis, gas storage, agriculture, and polymer additives. One of the most promising areas of investigation is the application of sugar-based NSs as novel drug-delivery systems. The use of oxygenated cardioplegic solution (CS) during cardiac arrest may be beneficial. Indeed, cold, fully oxygenated crystalloid solutions can be an excellent means of myocardial protection [16]. However, the forced oxygenation of a cardioplegic solution, while maximizing its oxygen content, may result in it becoming highly alkaline. The equilibration of a bicarbonate-containing solution with 100 percent oxygen decreases the amount of dissolved carbon dioxide and consequently that of carbonic acid [17].

Altering the pH of a CS can undoubtedly affect the functional recovery of an explanted organ. Furthermore, the concentration of hydrogen ions alters with cooling, as the dissociation constant of any salt solution is a function of temperature. Therefore, when introducing a gas into a cardioplegic solution, it is necessary to control both the temperature of the gas and the temperature at which the solution is delivered, as they interact to determine the final pH and concentration of the gas [18,19].

Oxygenated nanosponges that can store and slowly release oxygen over a controlled time have been chosen as nanocarriers to enhance the functionality of cardioplegic solutions for this purpose. Different formulations are used to prepare nanocarriers for oxygen delivery, and these include native αCD, α-cyclodextrin nanosponges (αCD-NSs), native CNN, and cyclic nigerosyl-nigerose nanosponges (CNN-NSs), among others, which have proven to be innovative tools for controlled and prolonged oxygen delivery.

The addition of nanocarriers with desirable versatility to cold (4 °C) cardioplegic solution, which can be sterilized to reduce the risk of infections, can be naturally decomposed to release more oxygen, thereby improving the functional recovery and/or prolong the amount of time that the heart stays in static hypothermic cardioplegic solution (so-called "static cold storage", SCS). Thus, it can be theoretically possible to extend the time in hypothermia and to use organs explanted in facilities far away from the recipient's location, thus exceeding the 4–5 h that have canonically been tolerated so far [20].

Because temperature greatly influences the solubility of a gas in a liquid, the ability of oxygen-loaded formulations to store and slowly release oxygen over time was evaluated at 4 °C, at room temperature (RT, 23 °C), and 37 °C. The chosen temperatures were the ones utilized in laboratory and clinical practice. Specifically, 4 °C mimics the hypothermic situation in which organ metabolism is low (i.e., SCS), while room temperature can be considered the sub-normothermic state [21].

This investigation aimed to compare two diverse biocompatible nanodevices (CNN-NSs and αCD-NSs) as oxygen reservoirs. This study displays for the first time the ability of synthesized nanosponges (CNN-NSs and αCD-NSs) to encapsulate, store, and release oxygen into the cardioplegic solution for a more prolonged period.

These naturally proposed nanocarriers can be sterilized, infused into the organ before explantation, and added to the cardioplegic solution. CNN-NSs presented as a more controlled oxygen release than CD-NSs. These findings will serve such a perspective for the further investigation of indicated nanodevices with pre-clinical studies and thereafter clinically as cardioprotective agents.

2. Results

The oxygenation of a cardioplegic solution (CS) can likely improve explanted heart vitality and functions.

Several strategies have been studied to increase the concentration of CS oxygen from red blood cells to artificial oxygen carriers, such as hemoglobin-based oxygen carriers, extracellular vesicles, per-fluorocarbon emulsions, and nanoparticulate systems.

In the present work, two glucose derivatives, αCD and CNN, and two cross-linked polymers between them that form nanoparticles called nanosponges (NS) have been investigated in an assessment of their oxygen-carrier capacity in the National Institutes of Health (NIH) CS. Both αCD and CNN are cyclic oligosaccharides with a central cavity (see Figure 1) that can encapsulate molecules, including gases, which can be entrapped and stored in the α-CD and CNN cavities and the nanoporous matrices of αCD and CNN nanosponges, as previously demonstrated. Oxygen-loaded αCD- and CNN-based nanosponges have recently been demonstrated to protect against hypoxia/reperfusion (H/R)-induced cell death in cell experiments [22,23].

In this work, the effect of the addition of oxygenated αCD, CNN, αCD-NS, and CNN-NS on the oxygenation of NIH CS (National Institutes of Health Cardioplegic Solution) was evaluated at different temperatures and concentrations to increase and prolong the oxygen content over time.

First, the αCD- and CNN-based nanosponges were successfully synthesized according to a previously tuned procedure, and their stability in NIH CS was evaluated.

Four oxygenated formulations were then prepared with the addition of αCD, CNN, αCD-NS, and CNN-NS to NIH CS and loaded with oxygen. The formulations were characterized, and their physicochemical parameters (Table 1) were determined.

Table 1. Physicochemical characterization of NIH CS with αCD and CNN loaded with oxygen.

Sample	NIH CS	NIH CS + CNN	NIH CS + αCD
pH	8.68	8.40	8.21
Viscosity (mPa)	1.20	1.60	1.20

The basic pH value of the cardioplegic solution is due to the presence of bicarbonate in its composition. The presence of the two compounds slightly decreased the pH of NIH CS. Interestingly, the addition of O_2 maintained the basic pH value. The viscosity increased only in the presence of CNN oligosaccharide, but the solution is still suitable for organ perfusion.

Table 2 reports the physicochemical characteristics of NIH CS in the presence of the two types of oxygen-loaded nanosponges. The two formulations are nanosuspensions, which, from the physical point of view, are αCD- and CNN-based nanosponges and consequently solid water-insoluble nanoparticles.

Table 2. Physicochemical characteristics of NIH CS with the two types of oxygen-loaded NSs.

Sample	NIH CS + CNN NS	NIH CS + αCD NS
pH	8.50	8.30
Average Diameter ± SD (nm)	485.80 ± 44.10	560.70 ± 35.60
PDI ± SD	0.38 ± 0.01	0.31 ± 0.03
Viscosity (mPa)	1.56	1.26
Zeta Potential ± SD (mV)	−25.58 ± 2.60	−19.30 ± 1.13

Both the oxygen-loaded CNN-NSs and αCD-NSs were around 500 nm in size and had a negative surface charge, with zeta potential values high enough to avoid aggregation phenomena in NIH CS.

The sizes and surface charges of the two NSs formulations in NIH CS are similar to those measured in water. Only the PDI showed a slight increase, and this can be correlated to the salts present in the solution.

The addition of oxygen-loaded NSs did not increase the pH value, as the oxygen is stored in the nanocarriers and not immediately available in the solution. This behavior can

overcome the limitations of the formation of more alkaline solutions because of the low buffering capacity of the bicarbonate concentration present.

The viscosity-value increase in NIH CS was negligible in the presence of αCD-NSs, while it reached a value of 1.56 mPAs with the addition of CNN-NSs. Nevertheless, the two values are suitable for the potential clinical application of the formulations.

The production of Reactive Oxygen Species (ROS), which can induce cell damage and apoptosis, is a limitation in oxygen delivery. The amount of ROS in oxygenated NIH CS formulations was determined and compared with formulations that are not saturated with oxygen. The results are reported in Table 3. Interestingly, the addition of αCD and αCD-NSs did not significantly increase the ROS concentration compared to the value of NIH CS.

Table 3. Reactive Oxygen Species (ROS) concentration in the oxygenated NIH CS formulations.

Sample	Concentration (μM)
Water	0.05
PBS	0.01
NIH CS	0.01
CS + O$_2$	0.03
αCD in CS	0.04
αCD NS in CS	0.02
αCD in CS + O$_2$	0.01
αCD NS in CS + O$_2$	0.02
CNN in CS	0.08
CNN NS in CS	0.04
CNN in CS + O$_2$	0.01
CNN NS in CS + O$_2$	0.03

Because temperature remarkably influences the solubility of a gas in a liquid, the capability of the oxygen-loaded formulations to store and slowly release oxygen over time was evaluated at 4 °C, at room temperature (RT, 23 °C), and 37 °C.

Figure 2 reports the oxygen profiles of gas diffusion from the oxygenated NIH CS at three different temperatures for up to 24 h.
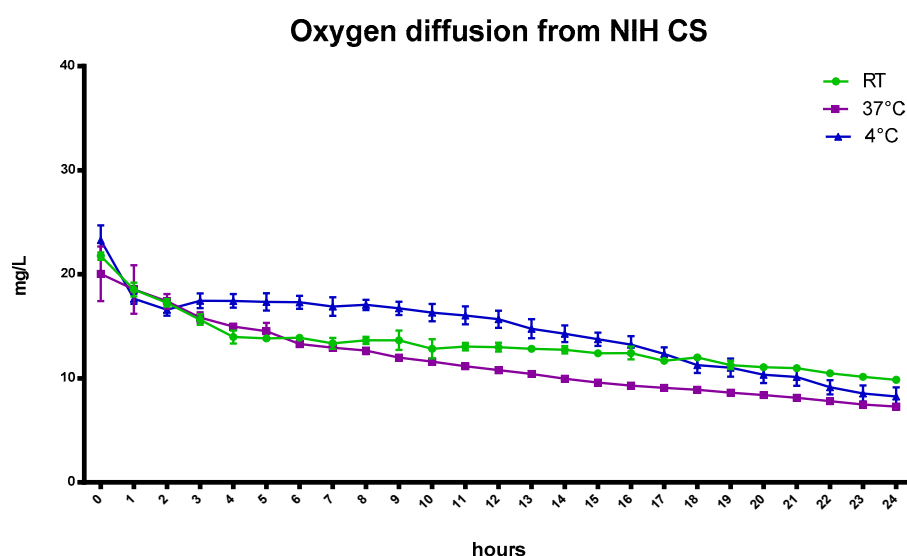
Figure 2. Oxygen diffusion from NIH-oxygen-saturated cardioplegic solutions at different temperatures.

Slight differences in oxygen content were observed between room temperature and 37 °C (Table 4) after the first hours.

Table 4. The concentration of oxygen in oxygenated NIH CS was recorded after 30 min at different temperatures.

Oxygen Concentration in NIH Cardioplegic Solution	4 °C	RT	37 °C
(mg/L)	29.60 ± 3.01	20.38 ± 2.50	18.64 ± 2.42

Indeed, as the temperature increases (4 °C, room temperature (RT), and 37 °C), the solubility of a gas decreases from 29.60 mg/L to 18.64 mg/L because of the tendency of a gas to expand [24,25]. Moreover, the presence of salts in the NIH CS can play a crucial role in favoring the liberation of gas from solution.

Henry's law states that "at a constant temperature, the amount of a given gas that dissolves in a given type and volume of liquid is directly proportional to the partial pressure of that gas in equilibrium with that liquid".

The oxygen concentration in NIH CS depends on Henry's law and, after 24 h, the amount of oxygen reaches equilibrium with the atmospheric content.

The oxygen-saturated NIH CS was considered as a reference in testing the ability of the oxygen-carrier-containing formulations to store and prolong the release kinetics of oxygen over time.

Figure 3 reports the kinetics of oxygen release from oxygenated NIH CS that contained CNN, which was added at a concentration of 1.3 g/L, at different temperatures. The graph also confirms the effect of temperature on the amount of dissolved oxygen in this NIH CS formulation, although the presence of CNN markedly affects the amount of dissolved oxygen in the CS solution and produced sustained release over time. Specifically, the oxygen-carrier capability of CNN is evident at 4 °C.
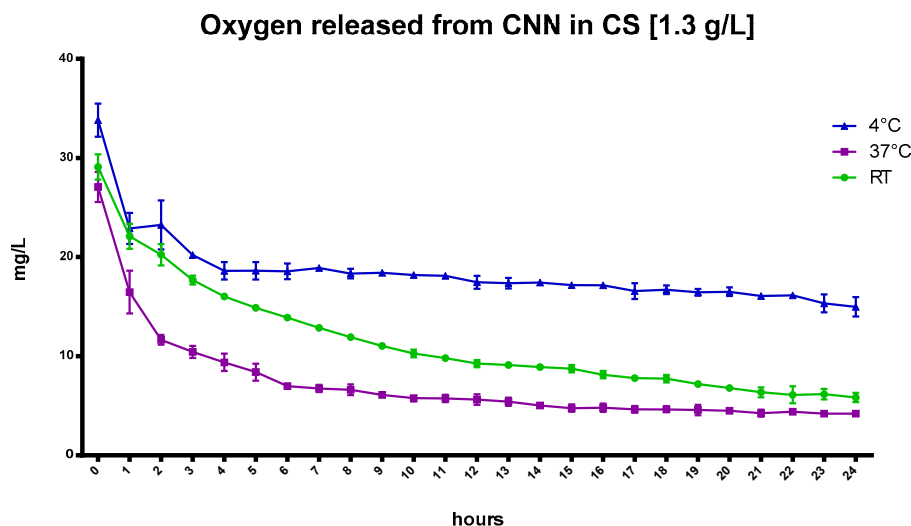
Figure 3. In-vitro release kinetics of oxygen from CNN in cardioplegic solution CS at a concentration of 1.3 g/L at different temperatures.

The addition of CNN played an important role in sustaining oxygen release for a longer time in the NIH CS solution, as it can encapsulate oxygen in the inner cavity of the molecule.

The prolonged oxygen release is demonstrated by the greater O_2 concentration at 4 °C, which can be compared to the marked gas-concentration drop in NIH CS after 6 h. Moreover, the oxygen concentration is still higher after 24 h. This behavior may be promising for the enhancement of heart storage before transplant in static cold storage [17].

Interestingly, the capability of CNN to sustain oxygen release was enhanced with the addition of CNN-NSs in NIH CS.

The benefits that the CNN-NSs display over the CNN oligosaccharide in the NIH CS are underlined by a slower and more controlled release achieved using the nanosponges, at least over the first 6 h of the recorded oxygen release. This is in contrast to the quick decrease in oxygen concentration in the CNN-containing cardioplegic solution. The entrapment of oxygen is also evident at 37 °C (Figure 4), and this behavior underscores the crucial role played by the polymer network in the matrix and by the CNN cavities, as reported in Figure 5.
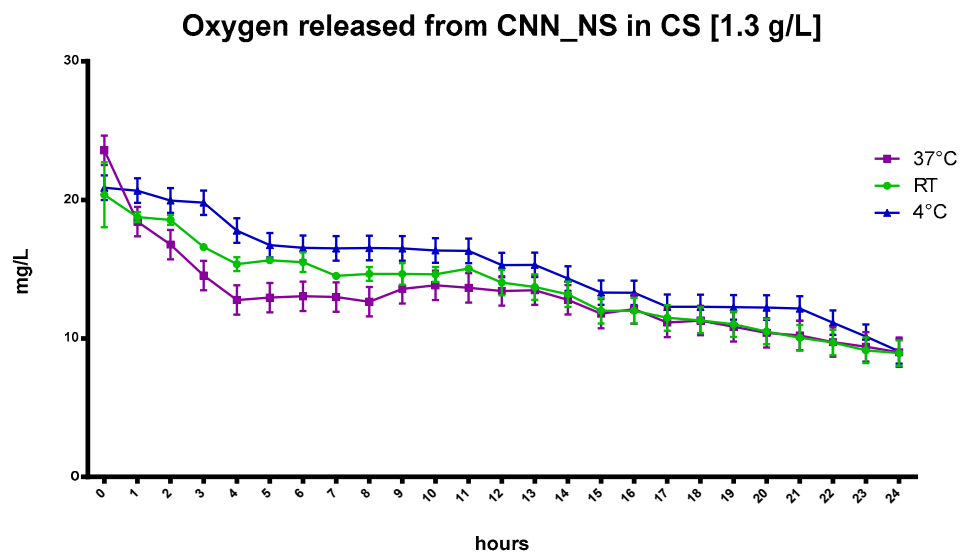
Figure 4. The kinetics of in-vitro oxygen release from saturated cardioplegic solution with CNN-NSs at a concentration of 1.3 g/L at different temperatures.
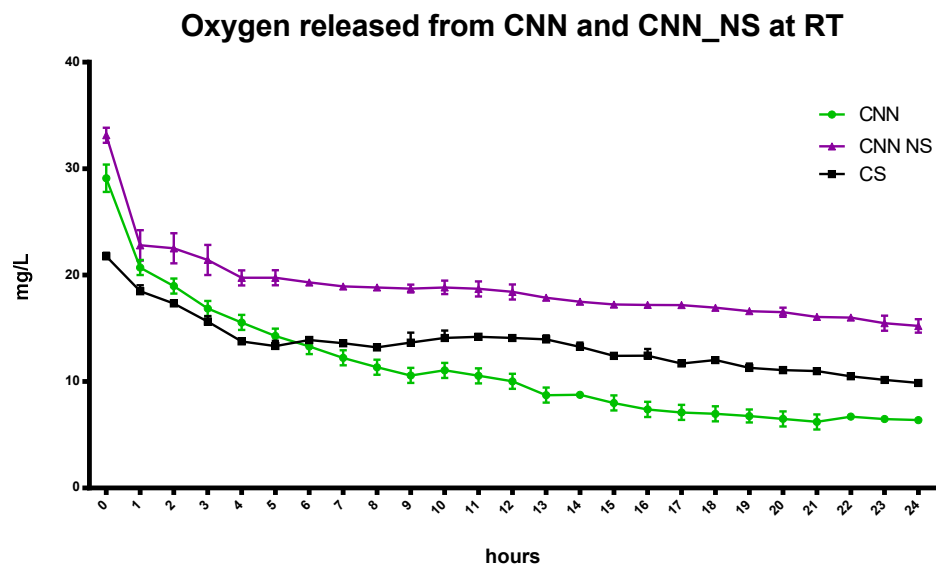
Figure 5. Comparison of the kinetics of the in-vitro release of oxygen from CNN and CNN-NSs in CS at the same concentration at room temperature.

The capability of αCD to act as an oxygen nano reservoir is also demonstrated.

The kinetics of oxygen release from αCD in CS at different temperatures is shown in Figure 6.

Oxygen released from αCD in CS [1.3 g/L]
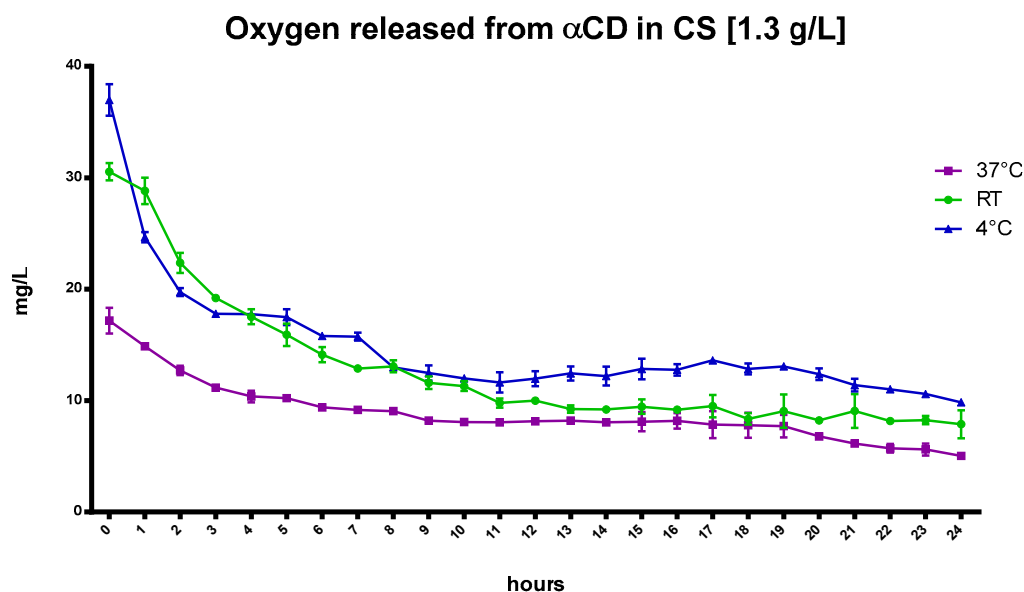
Figure 6. The kinetics of in-vitro oxygen release from saturated CS with αCD oligosaccharide at a concentration of 1.3 g/L at different temperatures.

Similar to the CNN results, the αCD, dissolved at a concentration of 1.3 g/L in NIH CS and loaded with oxygen, increased oxygen concentration in the solution. Moreover, αCD displayed faster release at higher temperatures compared to the αCD-NSs nanoformulations, as presented in Figure 7.

Oxygen released from αCD_NS in CS [1.3 g/L]
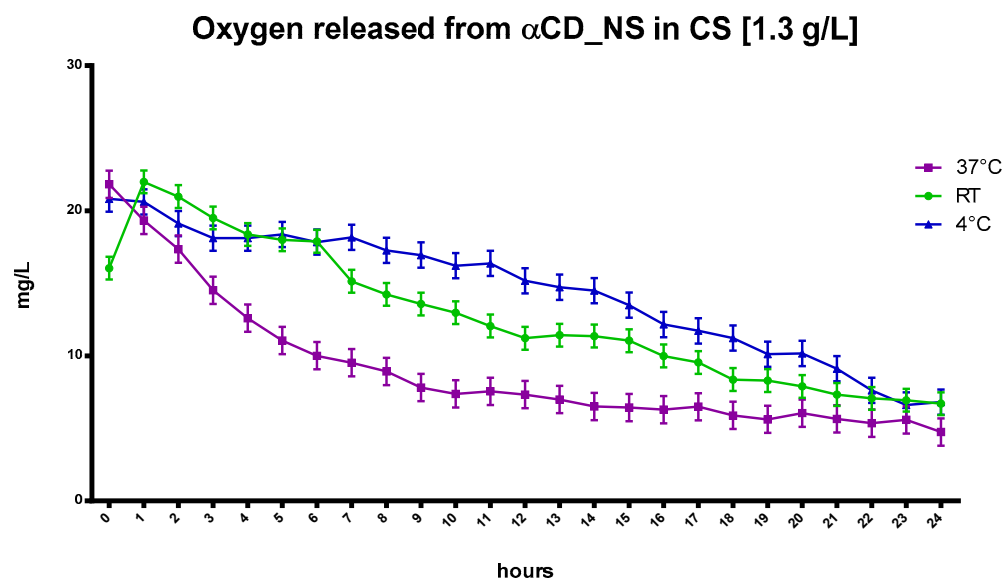
Figure 7. The kinetics of in-vitro oxygen release from saturated CS with αCD-NS at a concentration of 1.3 g/L at different temperatures.

The kinetics of oxygen release from the oxygen-loaded αCD-NSs displays a marked difference compared to results with αCD oligosaccharide. Oxygen encapsulation was greater in the nanosponges due to the presence of the polymer network caused by the presence of a cross-linking agent in the NSs matrix and the cooperation of the αCD cavities (Figure 8), as previously observed with CNN-NSs.

Oxygen released from αCD and αCD_NS at RT
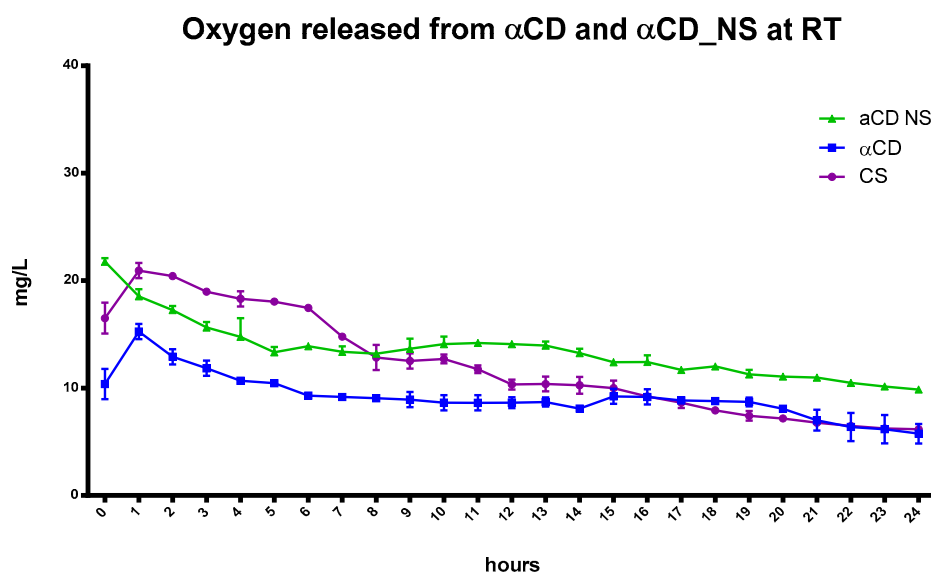
Figure 8. Comparison of the in-vitro release kinetics of oxygen from αCD, αCD-NSs, and CS at room temperature.

CS released a higher concentration of oxygen over the first six hours (Figure 8). However, 24 h later, the αCD-NSs had a higher oxygen concentration than that of αCD alone or CS.

The results showed that oxygen-release kinetics were slower for CNN in CS than that for αCD since CNN is a tetraglucose that has a smaller cavity and is more polar than αCD, which consists of six glucose units; the smaller cavity of CNN favors oxygen encapsulation.

The effect of oxygen-loaded nanosponge concentration on the gas storage and delivery capability was then investigated (Table 5). The NSs retained more oxygen at 1.3 g/L than when diluted to 0.13 g/L and showed no significant increase at a concentration of 13.0 g/L, with this effect being more marked at 37 °C.

Table 5. Oxygen concentration in NIH CS with increasing nanocarrier concentration, was recorded at 37 °C for 12 h.

The Concentration of Prepared Nanosuspension (g/L)	The Concentration of Oxygen (mg/L)		
	0.13	**1.30**	**13.0**
αCD	5.39 ± 0.31	6.01 ± 0.50	6.12 ± 1.50
CNN	5.63 ± 0.25	5.25 ± 0.32	6.81 ± 1.02
αCD-NSs	6.02 ± 1.03	8.63 ± 1.23	7.38 ± 0.43
CNN-NSs	8.57 ± 1.51	14.52 ± 2.43	11.33 ± 1.73

This behavior suggests that small amounts of nanosponge can be used to obtain a suitable oxygen concentration.

The histograms (Figures 9–13) highlight the oxygen percentages recorded at a certain time over the 24 h release study. CNN-NSs and αCD-NSs are more adequate nanocarriers than the parent CNN and αCD, thus validating the concept of storing oxygen in the cardioplegic solution for at least 12 h after the loading procedure. The tuning of the flux time, concentration, storage conditions, and controlled environment are areas for further study and can strengthen the rationale and support the results.

NIH CS
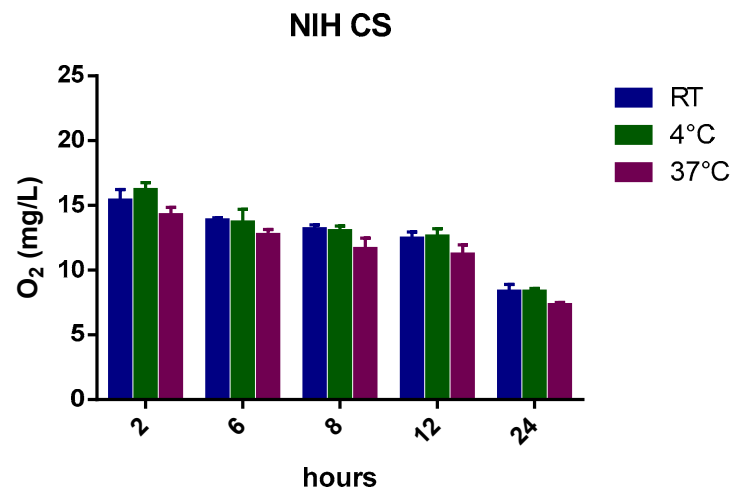
Figure 9. Histogram showing the variation of oxygen concentration in cardioplegic solution at different temperatures.

CS + CNN
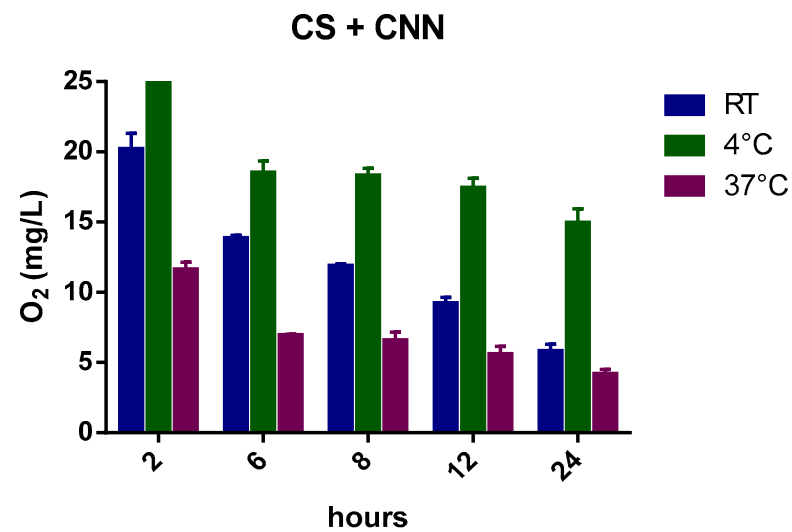
Figure 10. Histogram showing the variation of oxygen concentration in cardioplegic solution + CNN monomer (at a concentration of 1.3 g/L) at different temperatures.

CS + CNN_NS
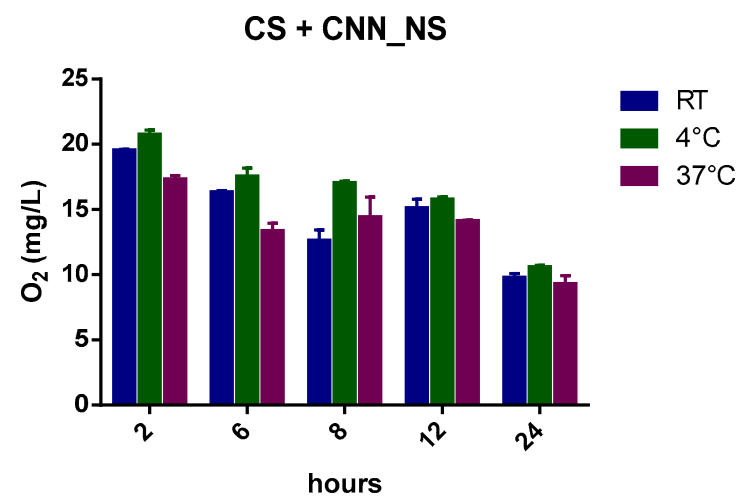
Figure 11. Histogram showing the variation of oxygen concentration in cardioplegic solution + CNN-NSs (at a concentration of 1.3 g/L) at different temperatures.

CS + αCD
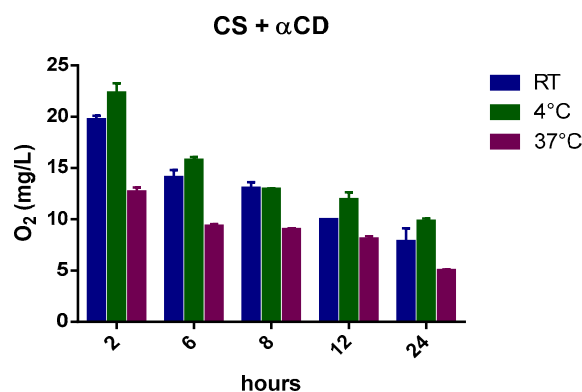
Figure 12. Histogram showing the variation of oxygen concentration in cardioplegic solution + αCD monomer (at a concentration of 1.3 g/L) at different temperatures.

CS + αCD_NS
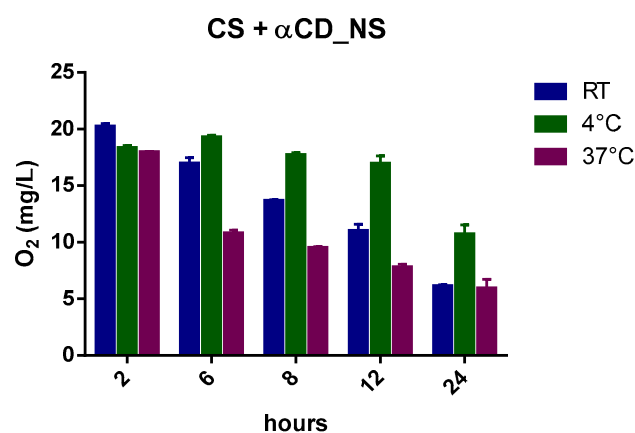
Figure 13. Histogram showing the variation of oxygen concentration in cardioplegic solution + αCD-NSs (at a concentration of 1.3 g/L) at different temperatures.

3. Discussion

Nanocarriers as a tool to improve the delivery and storage of oxygen have been the focus of extensive research in the field of organ transplants. The static cold storage (SCS) of the donor's heart after brain death remains the clinical standard. The main advantage of hypothermia is to "prevent" ischemic damage when the cardioplegic flow is interrupted. This advantage is achieved by a reduction in the temperature-dependent rate of myocardial metabolism, which results in a slowing of the rate of ischemic damage. However, even when drastically reduced by cold cardioplegia, the heart continues to have a minimally oxygen-demanding metabolism [26,27].

The automated machine perfusion (MP) of a donor's heart is being evaluated as an alternative approach to donor-organ management and as a means to expand the donor pool and/or increase the utilization rate. However, technical and biological issues (e.g., machine malfunction, user error, infections, and costs) limit its large-scale use, and further well-designed studies are needed to draw clear conclusions.

Previous studies have demonstrated the ability of αCD-NSs and CNN-NSs to accommodate and convey oxygen, thus addressing growth problems in several diseases, from inflammation to cancer, and improving tumor treatment. The αCD-based formulations can be used for the treatment of cardiovascular diseases as oxygen nanocarriers that can limit ischemic reperfusion injury (IRI) via direct injection into the myocardial wall before starting full-blood reperfusion. Similarly, the proposed CNN-based nanocarriers have shown marked efficacy in controlled oxygenation and have effectively protected cellular models (e.g., cardiomyocytes and endothelial cells) from simulated IRI, thus reducing cell mortality [13,22,23,28,29]. The polymerization reactions lead to a successful synthesis of carbonate NSs. The resulting products were further investigated to understand the

difference between CNN and α-CD as building blocks. When the CNN and α-CD react with CDI, two OH groups are completely esterified, and the reaction results in imidazole formation. The cross-linking process is confirmed via carbonate formation. The formed product is more resistant to hydrolysis than, for example, the synthesized-based NSs based on carboxylic acid esters [8].

In this novel study, two different biocompatible low-temperature oxygen-releasing nanodevices (CNN-NSs and αCD-NSs) that can be easily sterilized, infused into the organ before explantation and added to the cardioplegic solution under SCS conditions, where they release oxygen over a long period, are evaluated. Under these conditions, the organs to be transplanted can be theoretically kept under oxygenated conditions in SCS for a longer time, with the belief that these nanodevices can be first verified experimentally with pre-clinical studies and later clinically as cardioprotective agents.

The two kinds of nanocarriers were capable of playing the relevant roles of oxygen reservoirs in this evaluation of their oxygen-encapsulation capability. The two NSs were compared with their building units, i.e., αCD and CNN. Interestingly, the NSs nanostructure can affect oxygen storage and release, and CNN-NSs have been demonstrated to be a better oxygen reservoir than CD-NSs.

This behavior may be related to the different nanostructures of the two nanocarriers. Compared with CNN, αCD has a much larger and more hydrophobic cavity. CNN has two inward-oriented hydroxyl moieties, so only small molecules can be included within them. Nevertheless, similarly to CD, CNN-NSs have two types of nanopores: the interstitial spaces between the CD units and the internal hydrophobic CD cavities. The spaces between the CD can be more or less hydrophilic, depending on cross-link density and cross-linking agent polarity. Due to a large number of reactive hydroxyl groups, starch derivatives can act as polyfunctional monomers and be cross-linked using a wide array of chemicals (e.g., active carbonyl compounds, diisocyanates, dianhydrides, epoxides, carboxylic acids with two or more functionalities, etc.), thus yielding three-dimensional, insoluble polymers [8], with specific characteristics and capability for molecule encapsulation.

As it is known, the formation of an inclusion complex involves partial or complete coverage of the host molecule. This provides, on the one hand, protection from evaporative degradation and oxidation and allows for the stabilization of the host, while on the other, it alters many of the physicochemical properties of the molecule. These modifications facilitate the use of characterization techniques to verify that the host is indeed contained in the cavity. αCD and CNN may maintain some of their ability to form hydrogen bonds with other molecules, allowing them to stay, at least partially, soluble in water in the form of an inclusion complex [30]. Furthermore, αCD and CNN cross-linking insoluble nanodevices are obtained with increased oxygen encapsulation capacity.

In addition, the storage of oxygen in nanodevices and the subsequent slow and constant delivery avoid the formation of high ROS species that can damage heart cells in the NIH CS. It is a key point to the limitation of free radical species in transplantation to maintain organ function.

Oxygen-release kinetics at low temperatures varied according to the nanocarrier used, suggesting that they may be appropriate and tuned for typical SCS temperatures (4 °C). Nevertheless, this aspect requires verification via the use of a transplanted heart and clinical applications.

Unquestionably, either a slight or severe oxygen deficiency can lead to cell death, but a wealth of research suggests that fluctuating oxygen levels rather than persistently low pO2 are the most harmful aspects [31]. The most intriguing aspect of oxygen consumption by the heart is that it can switch from low to high consumption levels in response to metabolic demand. As a result, we can suggest that the intracellular compartment experiences a range of oxygen tensions, from high to low, depending on the balance between supply and demand. A pro-oxidative environment is created by a positive balance. In this context, the changes in oxygen levels (dysoxia) switching from hypothermia to normothermia can be crucial. Indeed, interactions of oxygen with other gases, such as nitric oxide, can either

aggravate or protect ischemic organs, depending on several circumstances and including the relative level of the two gases. Additionally, the effects of dysoxia are crucial for iron metabolism. Therefore, only future studies can reveal the real effects of controlled oxygen delivery by nanodevices into transplanted organs that are first stored at low temperatures and then transplanted into a warm body.

4. Materials and Methods

4.1. Chemicals

α-Cyclodextrin (α-CD, M_w = 972.846 g/mol) was a gift from Roquette Frères SA (Lestrem, France). Cyclic nigerosyl-1-6-nigerose (CNN, M_w = 648.564 g/mol) was obtained from Hayashibara (Tokyo, Japan). CNN and α-CD were desiccated in an oven at 80 °C up to constant weight before their usage to remove any traces of absorbed moisture. Additionally, 1,1′-Carbonyldiimidazole (CDI, ≥97.0%), 2′,7′-dichlorodihydrofluorescein diacetate (H2DCFDA fluorescent probe), and 2′,7′-dichlorofluorescein (DCF), N,N-dimethylformamide (DMF, ≥99.8%), acetone (≥99% (GC)), and ethanol (96.0–97.2%) were purchased from Sigma-Aldrich (Munich, Germany). Deionized and MilliQ® water was obtained using a Millipore Direct-QTM 5 production system. All other chemicals used to prepare the cardioplegic solution (CS) were commercially available as analytical-grade products.

4.2. CNN-Based Nanosponge Synthesis

CNN-based nanosponges (CNN-NSs) were successfully synthesized following an existing procedure in literature with minor modifications [22]. The synthesis was performed by dissolving 5.00 g (7.70 mmol) of anhydrous CNN (Figure 1) powder in 30 mL DMF at room temperature in a round bottom flask, using a hotplate stirrer equipped with thermoregulation and heat-on block. Subsequently, 4.99 g (30.70 mmol) of CDI as a cross-linking agent was added, and to observe a clear solution, the temperature was increased up to 80 °C until the gel formation. Additionally, the formed gel was kept at 90 °C for around 5 h until a solid product was obtained. The stoichiometric molar ratio between CNN and CDI was 1:4. The acquired monolithic block was then broken up and manually ground in a mortar. The product was further purified with an excess of deionized water and recovered using a Buchner filtration system using filter paper (Whatman No. 1, Whatman, Maidstone, UK). The by-products were completely removed through Soxhlet extraction using ethanol for around 24 h. Finally, the CNN-NSs were air-dried, milled, and exploited for characterization as a white homogeneous powder.

4.3. αCD-Based Nanosponge Synthesis

The same synthesis, purification, and recovery procedures, as previously described for CNN-NSs, were utilized to obtain αCD-based nanosponges (αCD-NSs). Briefly, 5.00 g (5.14 mmol) of αCD and 3.33 g (20.54 mmol) of CDI were dissolved in 30 mL DMF. The stoichiometric molar ratio between α-CD and CDI was 1:4. A schematic representation of the synthesis of αCD-NSs is shown in Figure 14.
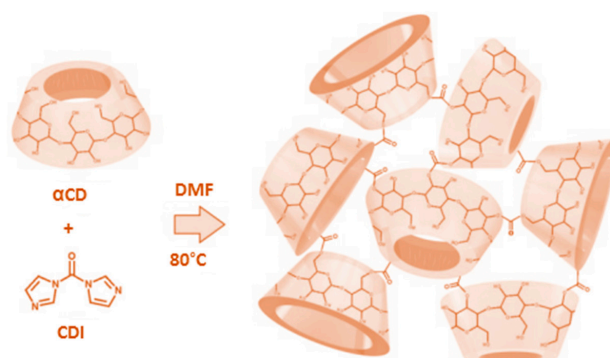
Figure 14. The schematic representation of the reaction of αCD with CDI at certain conditions.

4.4. Preparation of Cardioplegic Solution

The National Institutes of Health (NIH) cardioplegic solution (CS) used throughout our experiments was freshly prepared according to the National Institute of Health for Cardioplegic Protection protocol. The formulation is reported in Table 6 with a slight modification [32].

Table 6. Composition of NIH cardioplegic solution.

NIH CS Components	mmol/L
Na	98.9
Cl	107.8
K	30.0
Ca	1.0
HCO_3	22.0
Glucose	152.6
Mannitol	68.6
Lidocaine, mg/L *	20.0

*—Lidocaine is reported in mg/L.

4.5. Preparation of Nanoformulations

The defined amounts of CNN and αCD powders were weighed and dissolved in the prepared NIH cardioplegic solution to obtain solutions with different concentrations. A weighed amount of finely milled NSs powder was first added to the cardioplegic solution and then homogenized with a high-shear mixer (Ultra-Turrax®, Konigswinter, Germany) at 24,000 rpm for 10 min to reduce the size and obtain well-distributed suspensions with a uniform particle size. The aqueous suspension was later subjected to an ultrasonic sonicator for 20 min to achieve homogenization. The obtained nanosuspensions were then purified and stored in the fridge. All nanoformulations were stable after one week at 4 °C.

4.6. Characterization of Nanoformulations

The different NSs formulations were further characterized in vitro to evaluate their size and surface charge. The average diameter and polydispersity index of the formulations were measured using photon correlation spectroscopy (PCS) with a 90 Plus instrument (Brookhaven, NY, USA) at a fixed angle of 90 and a temperature of 25 °C after dilution with filtered water. The zeta potential was determined using a 90 Plus instrument (Brookhaven, NY, USA). For zeta-potential determination, diluted samples of nanoformulations were placed in an electrophoretic cell, to which a rounded 15 V/cm electric field was applied. The pH was recorded at room temperature using an Orion 420A pH meter.

4.7. Oxygen-Loading Procedure

To prepare oxygen-loaded nanoformulations, different quantities of αCD, CNN, αCD-NSs, and CNN-NSs were weighed and placed into a vial with the prepared NIH cardio-plegic solution. After shear homogenization and ultrasound sonication, NSs dispersions were transferred into a three-neck round-bottom flask and saturated with an oxygen purge at a flux of 4 L/min under stirring, while the gas concentration was monitored up to 35 mg/L in the external aqueous phase. The stability of the oxygen-encapsulating NSs was evaluated over time at different temperatures by measuring the oxygen concentration inside sealed falcon tubes using the oximeter electrode mounted inside.

4.8. Oxygen-Release Profile

The dissolved oxygen (DO) concentration was recorded using an oxygen bench meter (HI5421, Hanna Instruments Inc., Woonsocket, RI, USA). The bench meter is supplied with a probe for laboratory use and a built-in temperature sensor (HI76483 Hanna Instruments Inc. Woonsocket, RI, USA) was inserted inside a sealed falcon tube. This allowed the

measurements of DO to be carried out in a closed system and thus avoided the interferences from the oxygen in the environment. A fixed volume of 45 mL of oxygen-loaded NIH CS solution/nanosuspension was purged with oxygen flux for 30 min. After a predetermined incubation and equilibration time, the cap of the falcon tube was removed and replaced with the electrode for DO measurement. The oxygen concentration was logged every 30 min for 24 h. To minimize fluctuations in the readings caused by environmental and instrumentation factors, both a thermostat and a cryo-compact circulator (JULABO GmbH, Seelbach, Germany) were used to regulate the temperature (4–37 °C) of the medium in the falcon containing the solution and the probe. All measurements were carried out in triplicate under determined conditions.

4.9. Determination of Reactive Oxygen Species (ROS)

The fluorescence method was used, based on the oxidation of the H2DCFDA fluorescent probe (2′,7′-dichlorodihydrofluorescein diacetate), for the determination of the oxygen free radicals present in the cardioplegic-solution samples.

For this purpose, a 2 mL ethanolic solution of H2DCFDA (10 mM) was added to 0.5 mL of 0.01 M NaOH to hydrolyze H2DCFDA into DCFH (non-fluorescent compound). The hydrolysis product was maintained at room temperature for 30 min and neutralized by adding 10 mL of PBS (50 mM, pH 7.2). The presence of ROS in the DCFH compound is rapidly oxidized to 2′,7′-dichlorofluorescein (DCF).

The green fluorescence color of DCF was measured using a fluorimeter (EnSightTM automated multimode plate reader, PerkinElmer, Inc., Waltham, MA 02451, USA) with the excitation wavelength set at 485 nm and emission at 530 nm. The concentration of ROS was determined using a calibration curve built by analyzing a series of standard solutions of DCF in the 0.001–0.500 μM concentration range. Standard solutions were prepared by diluting a stock solution of DCF (500 μM) with phosphate buffer saline solution (PBS).

A linear calibration curve was obtained in the concentration range between 0.001 and 0.500 μM, with an R^2 value of 0.998.

4.10. Quantitative Determination of ROS in Blank/Oxygen-Loaded Samples

The safety profiles of the αCD-NSs and CNN-NSs have been thoroughly investigated as candidates for several pharmaceutical applications [33–36]. Their cytotoxicity on anaplastic thyroid cancer cells and internalized in the A2780 cell line have been evaluated in previous studies [28,37].

For the determination of ROS, the blank cardioplegic solution CS, the prepared solutions, and the nanosuspensions with the αCD, CNN, αCD-NSs, and CNN-NSs (concentration 10 mg/mL) were loaded with oxygen for 30 min before being tested. In separate vials, 2 mL of each sample was pipetted, and 25 μL of the prepared DCFH was added to reach a final concentration of 5 μM. The samples were left at room temperature and protected from light for 20 min to achieve reaction completion. The fluorescence intensity was then measured with a fluorimeter (excitation 485 nm, emission 530 nm) for 60 min. The analyses were performed in triplicate on each sample.

5. Conclusions

In this study, two oligosaccharides, i.e., CNN and αCD, and their cross-linked polymers, namely CNN-NSs, and αCD-NSs were extensively studied as artificial oxygen nanocarriers. Oxygen-release kinetics were slower for CNN than for αCD, and the results showed that the polymer network can play a key role in oxygen storage and release. CNN-NSs and αCD-NSs display the ability to encapsulate, store, and release oxygen into the cardioplegic solution for a more prolonged period.

The proposed nanocarriers have considerable versatility; they can be sterilized by their addition to the cardioplegic solution which reduces the risk of infections, and they can be naturally decomposed so that they release oxygen. This leads to potentially prolonging the amount of time that the heart stays in the hypothermic cardioplegic solution.

Furthermore, the nanocarriers can be used for distant organ transport, thus exceeding the current canonically tolerated time (around 6 h). These findings are promising for the tuning of an oxygen-carrier formulation that can prolong the storage of the heart during the explantation and transport procedures.

References

1. Zhang, Y.; Liu, X.; Geng, C.; Shen, H.; Zhang, Q.; Miao, Y.; Wu, J.; Ouyang, R.; Zhou, S. Two Hawks with One Arrow: A Review on Bifunctional Scaffolds for Photothermal Therapy and Bone Regeneration. *Nanomaterials* **2023**, *13*, 551. [CrossRef] [PubMed]
2. Qi, Q.; Wang, Q.; Li, Y.; Silva, D.Z.; Ruiz, M.E.L.; Ouyang, R.; Liu, B.; Miao, Y. Recent Development of Rhenium-Based Materials in the Application of Diagnosis and Tumor Therapy. *Molecules* **2023**, *28*, 2733. [CrossRef]
3. Zhou, J.; Wang, P.; Yu, D.-G.; Zhu, Y. Biphasic drug release from electrospun structures. *Expert Opin. Drug Deliv.* **2023**, *14*, 1–20. [CrossRef] [PubMed]
4. Zhang, J.; Tang, K.; Fang, R.; Liu, J.; Liu, M.; Ma, J.; Wang, H.; Ding, M.; Wang, X.; Song, Y.; et al. Nanotechnological strategies to increase the oxygen content of the tumor. *Front. Pharmacol.* **2023**, *14*, 1140362. [CrossRef] [PubMed]
5. Loftsson, T.; Jarho, P.; Másson, M.; Järvinen, T. Cyclodextrins in drug delivery. *Expert Opin. Drug Deliv.* **2005**, *2*, 335–351. [CrossRef]
6. Kurkov, S.V.; Loftsson, T. Cyclodextrins. *Int. J. Pharm.* **2013**, *453*, 167–180. [CrossRef]
7. Del Valle, E.M.M. Cyclodextrins and Their Uses: A Review. *Process Biochem.* **2004**, *39*, 1033–1046. [CrossRef]
8. Caldera, F.; Tannous, M.; Cavalli, R.; Zanetti, M.; Trotta, F. Evolution of Cyclodextrin Nanosponges. *Int. J. Pharm.* **2017**, *531*, 470–479. [CrossRef]
9. Trotta, F. Cyclodextrin Nanosponges and their Applications. In *Cyclodextrins in Pharmaceutics, Cosmetics, and Biomedicine*; John Wiley & Sons: Hoboken, NJ, USA, 2011; pp. 323–342.
10. Trotta, F.; Zanetti, M.; Cavalli, R. Cyclodextrin-based nanosponges as drug carriers. *Beilstein J. Org. Chem.* **2012**, *8*, 2091–2099. [CrossRef]
11. Hoti, G.; Caldera, F.; Cecone, C.; Pedrazzo, A.R.; Anceschi, A.; Appleton, S.L.; Monfared, Y.K.; Trotta, F. Effect of the Cross-Linking Density on the Swelling and Rheological Behavior of Ester-Bridged β-Cyclodextrin Nanosponges. *Materials* **2021**, *14*, 478. [CrossRef]
12. Caldera, F.; Tannous, M. Nanosponges for Gas Storage. In *Nanosponges*; Trotta, F., Mele, A., Eds.; John Wiley & Sons: Hoboken, NJ, USA, 2019. [CrossRef]
13. Cavalli, R.; Akhter, A.K.; Bisazza, A.; Giustetto, P.; Trotta, F.; Vavia, P. Nanosponge formulations as oxygen delivery systems. *Int. J. Pharm.* **2010**, *402*, 254–257. [CrossRef]
14. Trotta, F.; Cavalli, R.; Martina, K.; Biasizzo, M.; Vitillo, J.G.; Bordiga, S.; Vavia, P.; Ansari, K. Cyclodextrin nanosponges as effective gas carriers. *J. Incl. Phenom. Macrocycl. Chem.* **2011**, *71*, 189–194. [CrossRef]
15. Deluzio, T.G.B. Tissue Engineering Scaffolds with Enhanced Oxygen Delivery Using a Cyclodextrin Inclusion Complex. Electronic Thesis and Dissertation Repository, 2244. 2014. Available online: https://ir.lib.uwo.ca/etd/2244 (accessed on 31 March 2023).
16. Bøtker, H.E.; Hausenloy, D.; Andreadou, I.; Antonucci, S.; Boengler, K.; Davidson, S.M.; Deshwal, S.; Devaux, Y.; Di Lisa, F.; Di Sante, M.; et al. Practical guidelines for rigor and reproducibility in preclinical and clinical studies on cardioprotection. *Basic Res. Cardiol.* **2018**, *113*, 39. [CrossRef] [PubMed]
17. Hendren, W.G.; Geffin, G.A.; Love, T.R.; Titus, J.S.; Redonnett, B.E.; O'keefe, D.D.; Daggett, W.M. Oxygenation of cardioplegic solutions: Potential for the calcium paradox. *J. Thorac. Cardiovasc. Surg.* **1987**, *94*, 614–625. [CrossRef] [PubMed]

18. Von Oppell, U.O.; King, L.M.; Du Toit, E.F.; Owen, P.; Reichart, B.; Opie, L.H. Effect of oxygenation and consequent pH changes on the efficacy of St. Thomas' Hospital cardioplegic solution. *J. Thorac. Cardiovasc. Surg.* **1991**, *102*, 396–404. [CrossRef] [PubMed]

19. Von Oppell, U.; King, L.; Du Toit, E.; Owen, P.; Reichart, B.; Opie, L. Effect of pH shifts induced by oxygenating crystalloid cardioplegic solutions. *Ann. Thorac. Surg.* **1991**, *52*, 903–907. [CrossRef] [PubMed]

20. Penna, C.; Trotta, F.; Cavalli, R.; Pagliaro, P. Nanocarriers Loaded with Oxygen to Improve the Protection of the Heart to be Transplanted. *Curr. Pharm. Des.* **2021**, *28*, 468–470. [CrossRef]

21. Karangwa, S.A.; Dutkowski, P.; Fontes, P.; Friend, P.J.; Guarrera, J.V.; Markmann, J.F.; Mergental, H.; Minor, T.; Quintini, C.; Selzner, M.; et al. Machine Perfusion of Donor Livers for Transplantation: A Proposal for Standardized Nomenclature and Reporting Guidelines. *Am. J. Transplant.* **2016**, *16*, 2932–2942. [CrossRef]

22. Femminò, S.; Penna, C.; Bessone, F.; Caldera, F.; Dhakar, N.; Cau, D.; Pagliaro, P.; Cavalli, R.; Trotta, F. α-Cyclodextrin and α-Cyclodextrin Polymers as Oxygen Nanocarriers to Limit Hypoxia/Reoxygenation Injury: Implications from an In Vitro Model. *Polymers* **2018**, *10*, 211. [CrossRef]

23. Penna, C.; Femminò, S.; Caldera, F.; Pedrazzo, A.R.; Cecone, C.; Alfì, E.; Comità, S.; Higashiyama, T.; Trotta, F.; Pagliaro, P.; et al. Cyclic Nigerosyl-Nigerose as Oxygen Nanocarrier to Protect Cellular Models from Hypoxia/Reoxygenation Injury: Implications from an In Vitro Model. *Int. J. Mol. Sci.* **2021**, *22*, 4208. [CrossRef]

24. Laing, R.W.; Bhogal, R.H.; Wallace, L.; Boteon, Y.; Neil, D.A.H.; Smith, A.; Stephenson, B.T.F.; Schlegel, A.; Hübscher, S.G.; Mirza, D.F.; et al. The Use of an Acellular Oxygen Carrier in a Human Liver Model of Normothermic Machine Perfusion. *Transplantation* **2017**, *101*, 2746. [CrossRef] [PubMed]

25. Bodewes, S.B.; van Leeuwen, O.B.; Thorne, A.M.; Lascaris, B.; Ubbink, R.; Lisman, T.; Monbaliu, D.; De Meijer, V.E.; Nijsten, M.W.N.; Porte, R.J. Oxygen Transport during Ex Situ Machine Perfusion of Donor Livers Using Red Blood Cells or Artificial Oxygen Carriers. *Int. J. Mol. Sci.* **2021**, *22*, 235. [CrossRef] [PubMed]

26. Buckberg, G.D. Myocardial protection: An overview. *Semin. Thorac. Cardiovasc. Surg.* **1993**, *5*, 98–106. [PubMed]

27. Ledingham, S.; Braimbridge, M.; Hearse, D. Improved myocardial protection by oxygenation of the St. Thomas' Hospital cardioplegic solutions: Studies in the rat. *J. Thorac. Cardiovasc. Surg.* **1988**, *95*, 103–111. [CrossRef] [PubMed]

28. Caldera, F.; Argenziano, M.; Trotta, F.; Dianzani, C.; Gigliotti, C.L.; Tannous, M.; Pastero, L.; Aquilano, D.; Nishimoto, T.; Higashiyama, T.; et al. Cyclic nigerosyl-1,6-nigerose-based nanosponges: An innovative pH and time-controlled nanocarrier for improving cancer treatment. *Carbohydr. Polym.* **2018**, *194*, 111–121. [CrossRef]

29. Yang, F.; Xue, J.; Wang, G.; Diao, Q. Nanoparticle-based drug delivery systems for the treatment of cardiovascular diseases. *Front. Pharmacol.* **2022**, *13*, 999404. [CrossRef]

30. Neoh, T.-L.; Yoshii, H.; Furuta, T. Encapsulation and Release Characteristics of Carbon Dioxide in α-Cyclodextrin. *J. Incl. Phenom. Macrocycl. Chem.* **2006**, *56*, 125–133. [CrossRef]

31. Mancardi, D.; Ottolenghi, S.; Attanasio, U.; Tocchetti, C.G.; Paroni, R.; Pagliaro, P.; Samaja, M. Janus, or the Inevitable Battle Between Too Much and Too Little Oxygen. *Antioxidants Redox Signal.* **2022**, *37*, 972–989. [CrossRef]

32. Kober, I.M.; Obermayr, R.; Brüll, T.; Ehsani, N.; Schneider, B.; Spieckermann, P. Comparison of the Solutions of Bretschneider, St. Thomas' Hospital and the National Institutes of Health for Cardioplegic Protection during Moderate Hypothermic Arrest. *Eur. Surg. Res.* **1998**, *30*, 243–251. [CrossRef]

33. Monfared, Y.K.; Mahmoudian, M.; Caldera, F.; Pedrazzo, A.R.; Zakeri-Milani, P.; Matencio, A.; Trotta, F. Nisin delivery by nanosponges increases its anticancer activity against in-vivo melanoma model. *J. Drug Deliv. Sci. Technol.* **2023**, *79*, 104065. [CrossRef]

34. Monfared, Y.K.; Mahmoudian, M.; Cecone, C.; Caldera, F.; Zakeri-Milani, P.; Matencio, A.; Trotta, F. Stabilization and Anti-cancer Enhancing Activity of the Peptide Nisin by Cyclodextrin-Based Nanosponges against Colon and Breast Cancer Cells. *Polymers* **2022**, *14*, 594. [CrossRef] [PubMed]

35. Monfared, Y.K.; Mahmoudian, M.; Hoti, G.; Caldera, F.; Nicolás, J.M.L.; Zakeri-Milani, P.; Matencio, A.; Trotta, F. Cyclodextrin-Based Nanosponges as Perse Antimicrobial Agents Increase the Activity of Natural Antimicrobial Peptide Nisin. *Pharmaceutics* **2022**, *14*, 685. [CrossRef] [PubMed]

36. Dhakar, N.K.; Matencio, A.; Caldera, F.; Argenziano, M.; Cavalli, R.; Dianzani, C.; Zanetti, M.; López-Nicolás, J.M.; Trotta, F. Comparative Evaluation of Solubility, Cytotoxicity and Photostability Studies of Resveratrol and Oxyresveratrol Loaded Nanosponges. *Pharmaceutics* **2019**, *11*, 545. [CrossRef] [PubMed]

37. Gigliotti, C.L.; Ferrara, B.; Occhipinti, S.; Boggio, E.; Barrera, G.; Pizzimenti, S.; Giovarelli, M.; Fantozzi, R.; Chiocchetti, A.; Argenziano, M.; et al. Enhanced cytotoxic effect of camptothecin nanosponges in anaplastic thyroid cancer cells in vitro and in vivo on orthotopic xenograft tumors. *Drug Deliv.* **2017**, *24*, 670–680. [CrossRef]

Article

Application of Box–Behnken Design to Optimize Phosphate Adsorption Conditions from Water onto Novel Adsorbent CS-ZL/ZrO/Fe$_3$O$_4$: Characterization, Equilibrium, Isotherm, Kinetic, and Desorption Studies

Endar Hidayat [1,2] ![ORCID]**, Nur Maisarah Binti Mohamad Sarbani** [1,2]**, Seiichiro Yonemura** [1,2]**, Yoshiharu Mitoma** [1,2]
and Hiroyuki Harada [1,2,*] ![ORCID]

---

[1] Graduate School of Comprehensive and Scientific Research, Prefectural University of Hiroshima, Shobara 727-0023, Japan; hidayatendar1@gmail.com (E.H.)
[2] Department of Life and Environmental Science, Faculty of Bioresources Science, Prefectural University of Hiroshima, Shobara 727-0023, Japan
[*] Correspondence: ho-harada@pu-hiroshima.ac.jp

Abstract: Phosphate (PO_4^{3-}) is an essential nutrient in agriculture; however, it is hazardous to the environment if discharged in excess as in wastewater discharge and runoff from agriculture. Moreover, the stability of chitosan under acidic conditions remains a concern. To address these problems, CS-ZL/ZrO/Fe$_3$O$_4$ was synthesized using a crosslinking method as a novel adsorbent for the removal of phosphate (PO_4^{3-}) from water and to increase the stability of chitosan. The response surface methodology (RSM) with a Box–Behnken design (BBD)-based analysis of variance (ANOVA) was implemented. The ANOVA results clearly showed that the adsorption of PO_4^{3-} onto CS-ZL/ZrO/Fe$_3$O$_4$ was significant ($p \leq 0.05$), with good mechanical stability. pH, dosage, and time were the three most important factors for the removal of PO_4^{3-}. Freundlich isotherm and pseudo-second-order kinetic models generated the best equivalents for PO_4^{3-} adsorption. The presence of coexisting ions for PO_4^{3-} removal was also studied. The results indicated no significant effect on PO_4^{3-} removal ($p \leq 0.05$). After adsorption, PO_4^{3-} was easily released by 1 M NaOH, reaching 95.77% and exhibiting a good capability over three cycles. Thus, this concept is effective for increasing the stability of chitosan and is an alternative adsorbent for the removal of PO_4^{3-} from water.

Keywords: phosphate adsorption; zeolite; chitosan; ZrO; Fe$_3$O$_4$; Box–Behnken design; mechanical stability

1. Introduction

Phosphate (PO_4^{3-}) is a macronutrient needed for plant growth and is frequently applied as a fertilizer on agricultural lands. The increasing demands of food supply nowadays have led to the excessive application of fertilizer. However, excessive fertilizer use can cause PO_4^{3-} to leach into waterways, leading to eutrophication and harmful algal bloom. These blooms diminish oxygen levels [1–3], interfere with aquatic life, and adversely affect the quality of drinking water (taste and odor) [4]. According to [5], PO_4^{3-} decontamination must be performed efficiently while having a minimal impact on the surrounding ecosystem. Many methods have been reported to be effective in removing PO_4^{3-} from water, including biological [6] methods, electrochemical [7,8] methods, precipitation [9], ion exchange [10], and adsorption [11,12]. Each strategy has advantages and disadvantages. Biological techniques are more economical; however, the residue of dead bacteria left behind after the process is inconvenient [13]. Electrochemical techniques are expensive but have a lower effectivity toward PO_4^{3-} removal [14]. The precipitation process is simple

21

and effective for chemical treatment but is inefficient for sewage sludge and waste disposal [15]. Ion exchange may also be used to remove anions by exchanging sulfates (SO_4^{2-}) for PO_4^{3-} ions; however, this would make the solution more corrosive, and it requires a costly clean-up (Blaney et al. [16]). Adsorption is the best option and is the most widely used method for water contaminants including PO_4^{3-} ions [17,18]. This is because the technique is environmentally safe, the operation is easy and fast, and the technology is highly efficient.

Chitosan is currently gaining popularity as a potential adsorbent for water contaminants because it contains hydroxyl (–OH) and amino (–NH_2) functional groups, which can easily react with other materials and are environmentally friendly [19]. This material, which cannot be accessed readily from nature, is synthesized through the chemical deacetylation of chitin. However, because of its low tensile strength and dissolution under acidic conditions, the use of chitosan directly in wastewater treatment technologies is not recommended. Therefore, chitosan must be modified to increase its chemical stability and adsorption capability [20]. The selection of an appropriate modification method and modifying agent is crucial for assessing the quality and functionality of the product created during the modification process. Crosslinking is one of the most frequently used procedures to enhance the physicochemical characteristics of chitosan [21,22]. Crosslinking is the process of combining two or more molecules via covalent bonds.

Zeolites are crystalline aluminum silicate ($Al_2O_3 \cdot 2SiO_2$) minerals with a porous and highly stable structure, and they could enhance the adsorption of chitosan onto their surface, leading to the improved stability of chitosan. These materials can be obtained from natural sources, such as shrimp, or can be synthesized using various methods [23]. Several reports have proven the use of chitosan and zeolite to remove dyes [24,25], pharmaceuticals [26], nitrate [27], and humic acid [28]. On the other hand, the fabrication of chitosan–metal oxides has attracted the attention of a lot of scientists owing to their numerous beneficial characteristics, such as chemical stability, a large surface area, and favorable adsorptive characteristics [29]. Magnesium oxide (MgO) [30], titanium oxide (TiO) [31], zinc oxide (ZnO) [32,33], zirconium oxide (ZrO) [34], and copper oxide (CuO) [35] are examples of metal oxides. ZrO was selected for this study owing to its strong affinity for anions [36].

The separation of the adsorbents is another issue of concern since the usual separation procedures result in the loss of the adsorbents as well as possible dangers to the environment [37,38]. Magnetite (Fe_3O_4) is one of the most magnetic particles that can be used in the manufacture of magnetic adsorbents for water purification because of its biodegradability, thermal stability, and large surface area [39,40]. The use of the crosslinking method to combine magnetite, zeolite, ZrO, and chitosan is a viable strategy. This is because the magnetic particles allow for easy separation when subjected to an external magnetic field, while the chitosan, zeolite, and ZrO provide many adsorption sites [41]. Therefore, the amalgamation of chitosan/zeolite/ZrO, and Fe_3O (CS-ZL/ZrO/Fe_3O_4) may result in the development of novel composite materials with multifunctional constituents.

This study synthesized CS-ZL/ZrO/Fe_3O_4 with the target of using it as a novel adsorbent for PO_4^{3-} removal from water. The response surface methodology (RSM) with the Box–Behnken design (BBD) optimization strategy was used to acquire insight into the effect of process factors such as pH, adsorbent dosage, temperature, and time to achieve the maximal adsorptive removal of PO_4^{3-}. This process was performed to obtain the highest PO_4^{3-} adsorptive removal. The adsorption isotherms and kinetic models were also calculated to figure out the adsorption mechanism.

2. Results and Discussion

2.1. Characterization of CS-ZL/ZrO/Fe₃O₄

The experimental results of BBD are listed in Table 1. It can be concluded that a pH of 2 offers the best conditions for PO_4^{3-} removal. The pH_{ZPC} findings revealed that, at a pH of 2, the surface of CS-ZL/ZrO/Fe_3O_4 had a positive charge (pH < pH_{zpc}) (Figure 1a). This might indicate the protonation of the -NH_2 groups to -NH_3^+ groups on the surface. These

attract negatively charged $H_2PO_4^-$ ions to CS-ZL/ZrO/Fe$_3$O$_4$, resulting in the construction of a surface complex between PO_4^{3-} ions and CS-ZL/ZrO/Fe$_3$O$_4$. This study was similar to that reported by [42,43], which used SCBC-La and leftover coal, respectively, for PO_4^{3-} removal under acidic conditions. The other possible reaction that could occur is shown in Equation (1).

$$Fe_3O_4 + 4Zr(OH)_4 + 6H_2PO_4- \rightarrow FeZr(PO_4)_3 + 12H_2O \tag{1}$$

Table 1. Experimental data results from 4 factors of BBD for PO_4^{3-} removal onto CS-ZL/ZrO/Fe$_3$O$_4$.

Run	pH	Dosage	Temperature	Time	% Removal
1	2	0.02	45	35	58.95
2	10	0.02	45	35	51.75
3	2	0.10	45	35	72.77
4	10	0.10	45	35	54.54
5	7	0.06	30	10	61.83
6	7	0.06	60	10	56.68
7	7	0.06	30	60	64.95
8	7	0.06	60	60	64.94
9	2	0.06	45	10	59.09
10	10	0.06	45	10	54.34
11	2	0.06	45	60	72.75
12	10	0.06	45	60	59.57
13	7	0.02	30	35	56.02
14	7	0.10	30	35	61.46
15	7	0.02	60	35	56.69
16	7	0.10	60	35	59.69
17	2	0.06	30	35	66.84
18	10	0.06	30	35	60.16
19	2	0.06	60	35	64.70
20	10	0.06	60	35	55.08
21	7	0.02	45	10	54.40
22	7	0.10	45	10	58.87
23	7	0.02	45	60	56.72
24	7	0.10	45	60	69.58
25	7	0.06	45	35	53.48
26	7	0.06	45	35	55.47
27	7	0.06	45	35	53.47
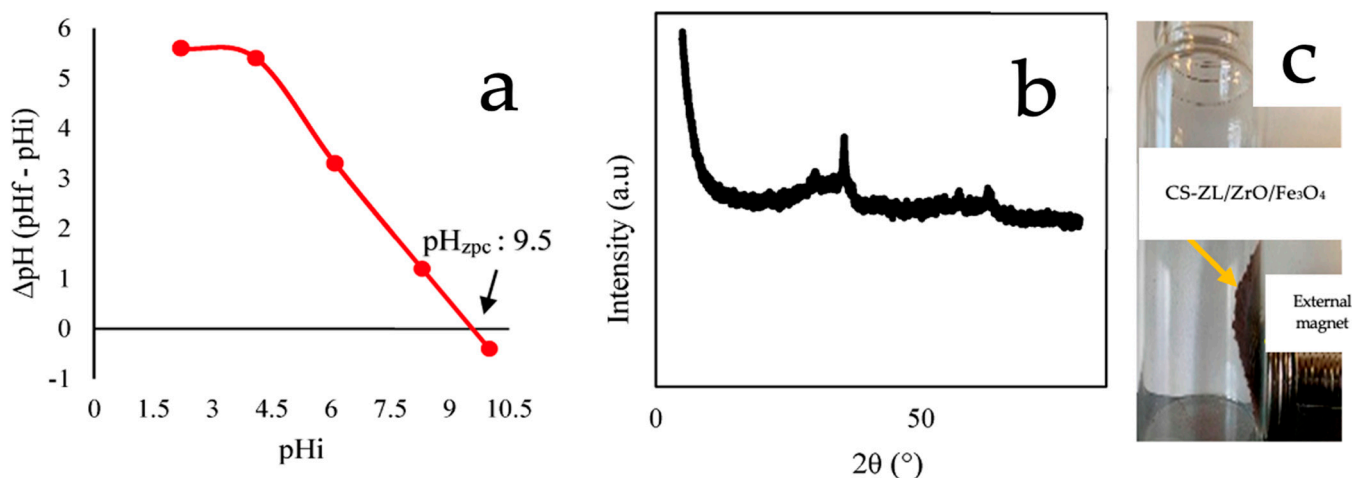
Figure 1. (**a**) pH$_{zpc}$ of CS-ZL/ZrO/Fe$_3$O$_4$, (**b**) XRD spectra of CS-ZL/ZrO/Fe$_3$O$_4$, and (**c**) photograph of CS-ZL/ZrO/Fe$_3$O$_4$ (taken by phone).

Table 2 summarizes the physical characteristics of these adsorbents. The results show that the BET-specific surface area was 88.1 m^2/g, with a pore volume of 0.572 mL/g, an

average diameter of 43.9 μm, and a porosity of 59%. These parameters show that the adsorbent had a substantial surface area for the adsorption of PO_4^{3-} ions.

Table 2. Physical properties of the adsorbent.

Specific Surface Area	Value
BET-specific surface area (m^2/g)	88.1
Pore volume (mL/g)	0.572
Average diameter (μm)	43.9
Porosity (%)	59

Figure 1b shows the XRD data used to verify the crystalline structure of the composite material. The XRD pattern shows a huge hump around 2θ = 21.22, which is a chitosan-specific peak [20]. Furthermore, the sharp peaks at 30.11, 35.49, 43.21 are mostly composed of crystalline phases, such as quartz, hematite, and alumina, which are all formed from zeolite- and zirconium-based materials. Magnetite corresponds to the peaks at 53.52, 57.08, and 62.78 [44]. Figure 1c shows a photograph of CS-ZL/ZrO/Fe_3O_4. It can be seen that the adsorbent is attached to the external magnet.

The SEM-EDS characterization of CS-ZL/ZrO/Fe_3O_4 was carried out to explore the surface properties and chemical components of the material. Figure 2 and Table 3 compare the SEM images and EDS data before and after PO_4^{3-} adsorption. Before adsorption, the surface morphology of the adsorbent was sticky, rough, and porous. The surface became smooth and compact after PO_4^{3-} adsorption, and this indicates that PO_4^{3-} ions were trapped on the adsorbent surface. The primary objective of the EDS data analysis was to identify the components of the adsorbent materials. The weight percentages of Zr and Fe were the highest at 50.68 and 38.92%, respectively. The N value was derived from the chitosan materials [45–47]. Al, Si, and Fe were derived from zeolite and magnetite, respectively. Furthermore, the presence of P after the adsorption process indicates that PO_4^{3-} was successfully adsorbed.
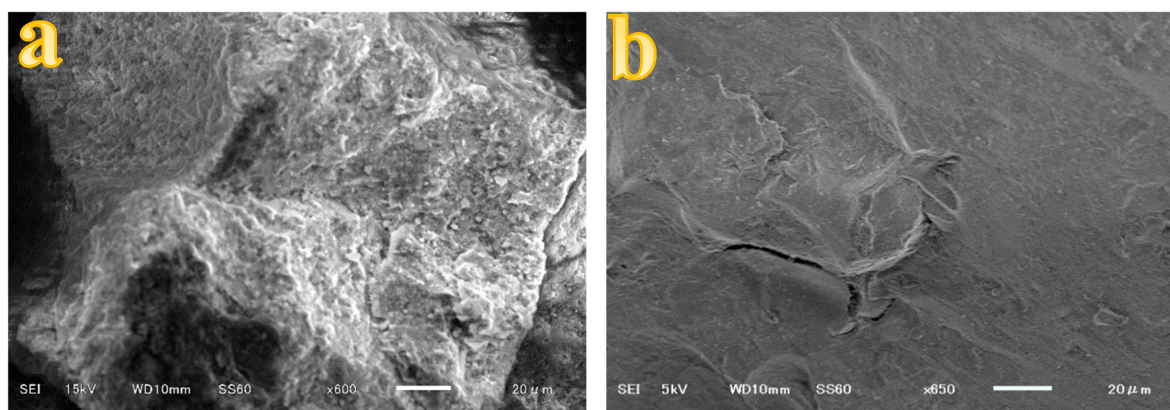
Figure 2. SEM images before (**a**), and after (**b**) PO_4^{3-} adsorption.

Table 3. EDS data before and after PO_4^{3-} adsorption.

Element	Weight %		Atomic %	
	Before	After	Before	After
N	3.27	2.06	13.43	7.66
Al	0.78	0.93	1.65	1.79
Si	6.35	1.70	12.98	3.15
Fe	38.92	56.39	40.03	52.69
Zr	50.68	27.76	31.91	15.88
P		11.17		18.82

Figure 3 shows the functional groups in CS-ZL/ZrO/Fe$_3$O$_4$ before and after PO$_4{}^{3-}$ adsorption through an FTIR-ATR analysis. A CS-ZL/ZrO/Fe$_3$O$_4$ band was detected following PO$_4{}^{3-}$ adsorption from 3326 cm^{-1} to 3320 cm^{-1}. This shows that PO$_4{}^{3-}$ ions interact with the stretching vibrations of hydrogen and amine in chitosan [48]. After PO$_4{}^{3-}$ adsorption, a decrease in the peak from 1634 to 1627 cm^{-1} was observed, which is associated with carboxyl groups (–COOCH$_3$) [49]. An increased peak and a more curved and newer peak appeared after PO$_4{}^{3-}$ adsorption from 951 to 1006 cm^{-1} and at 2161 cm^{-1}, which were assigned to Si-O-Al, Fe-O-Si, or Zr-O-Fe and CN stretching, respectively. This indicated a strong interaction with PO$_4{}^{3-}$ ions.
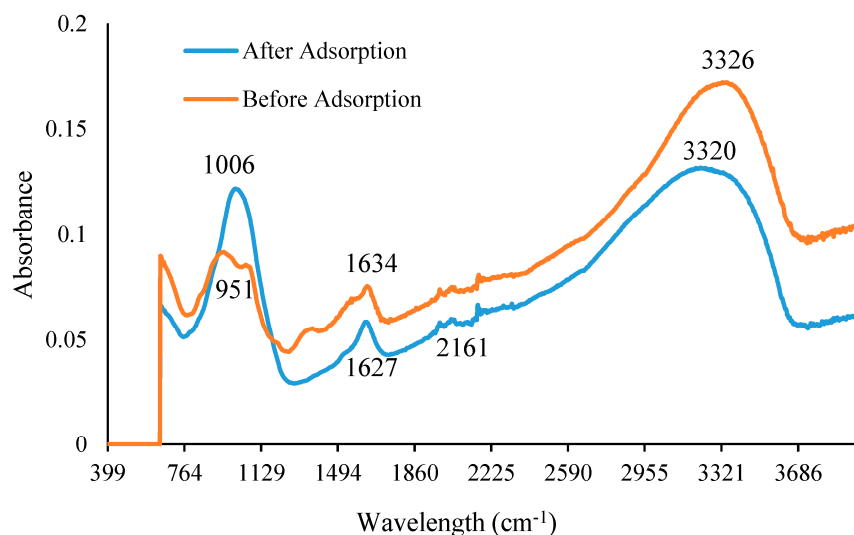
Figure 3. FTIR-ATR before, and after PO$_4{}^{3-}$ adsorption.

2.2. Mechanical Stability

The mechanical stability of the CS-ZL/ZrO/Fe$_3$O$_4$ composite was determined through the percentage of the initial mass that was preserved after drying. Figure 4a shows that increasing the concentration of the solution led to a higher WR%. Compared to the HCl-containing solution, the H$_2$SO$_4$-containing solution exhibited a higher WR%. Consequently, the crystalline structure of CS-ZL/ZrO/Fe$_3$O$_4$ was deformed, indicating that H$_2$SO$_4$ had significant contact with the chitosan group. Figure 4b shows the IR spectra after treatment. The positions of the peaks were consistent for all the samples. According to [50], the broad band visible at 3176–3345 cm^{-1} is assigned to the -NH$_2$ groups changing to –NH$_3{}^+$ groups. The peaks between 1611 and 1630 cm^{-1}, which were ascribed to the carboxyl (–COOCH$_3$) and –NH$_2$ groups, were generated through H$^+$ generation by HCl and H$_2$SO$_4$. The peak shifted to 1068 cm^{-1}, and expansion occurred when treated with 0.1 M H$_2$SO$_4$. SO$_4{}^{2-}$ ions have been shown to be associated with Si, Al, Fe, and Zr [51]. According to these results, the physical and chemical characteristics of the CS-ZL/ZrO/Fe$_3$O$_4$ composites did not change significantly.
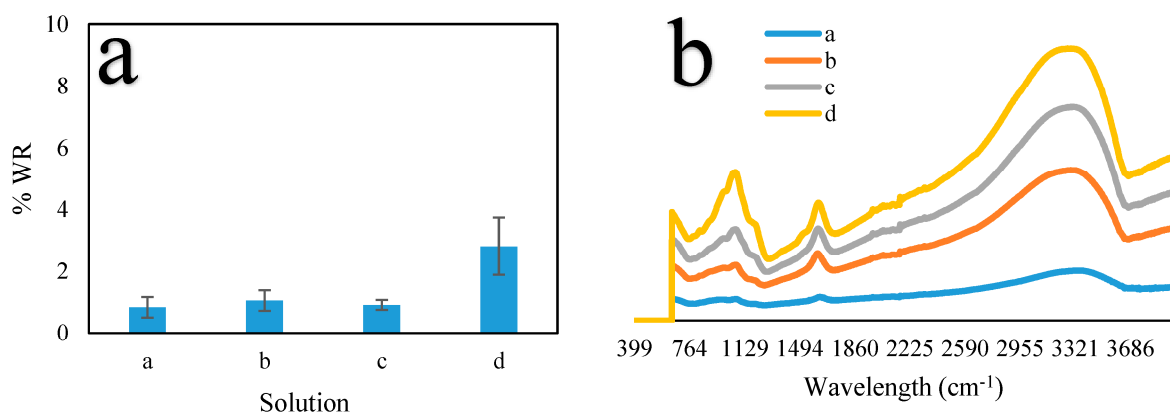
Figure 4. WR of CS-ZL/ZrO/Fe₃O₄. (**a**) Percentage WR, and (**b**) FTIR-ATR of CS-ZL/ZrO/Fe₃O₄ after treatment. Solution a (0.01 M HCl), b (0.1 M HCl), c (0.01 M H₂SO₄), and d (0.1 M H₂SO₄). Standard deviation (error bars).

2.3. ANOVA and Equations for Fitting Empirical Models

Table 4 shows the results of the statistical analysis, using the ANOVA test to evaluate the relationship between the input effective variables (A, B, C, and D) and their responses (Y). Table 4 shows that the F-value of the quadratic model was 16.68 and that the *p*-value was <0.0001, indicating that this model was significant. Models A, B, D, A^2, C^2, D^2, A × B, A × D, and C × D, marked with an asterisk (*), were found to be significant parameters of the model. The statistical variables obtained from the ANOVA test (Equation (2)) provide a full quadratic regression model for PO_4^{3-} removal (%).

$$PO_4^{3-} \text{ removal (\%)} = 99.2 - 1.72 \, A + 63 \, B - 1.478 \, C - 0.472 \, D + 0.2333 \, A^2 + 840 \, B^2 + 0.01575 \, C^2 + 0.00661 \, D^2 - 17.23 \, A*B - 0.0123A*C - 0.02107 \, A*D - 1.02 \, B*C + 2.098 \, B*D + 0.00343 \, C*D$$

(2)

Table 4. ANOVA results for PO_4^{3-} removal.

Source	DF	Sum of Squares	Mean of Squares	F-Value	*p*-Value	Remarks
Model	14	839.751	59.982	16.68	<0.0001 *	Significant
A	1	296.610	296.610	51.8093	<0.0001 *	
B	1	149.672	149.672	12.5582	<0.0001 *	
C	1	15.143	15.143	1.2835	0.063	
D	1	156.241	156.241	0.6342	<0.0001 *	
A^2	1	74.285	74.285	12.8151	0.001 *	
B^2	1	9.642	9.642	1.4722	0.127	
C^2	1	67.008	67.008	7.1279	0.001 *	
D^2	1	90.952	90.952	1.9374	<0.0001 *	
A × B	1	30.415	30.415	4.2734	0.013 *	
A × C	1	2.161	2.161	0.3036	0.453	
A × D	1	17.766	17.766	8.2118	0.046 *	
B × C	1	1.488	1.488	0.2091	0.532	
B × D	1	17.598	17.598	0.0540	0.047 *	
C × D	1	6.605	6.605	1.84	0.200	
Error	12	43.157	3.596			
Lack-of-Fit	10	40.504	4.050	3.05	0.272	
Pure Error	2	2.653	1.3267			
Total	26	882.908				
R^2		95.11				
R^2 adj		89.41				

* Significant.

The coefficients in the equation with positive and negative signs describe the additive and multiplicative effects of the variables on the response. The "Lack of Fit" was determined by comparing the residual error to the pure error in close proximity to the repeatedly

designed points. F = 3.05 and *p* = 0.272 for the "Lack of Fit" revealed that it was not significant for the model (*p* < 0.05). It can be assumed that the model was adequately fitted and that there was no lack of fit.

The R^2 value of the calculated second-order response model was 95.11, which is also known as the coefficient of determination. Consequently, it can be applied to reliably calculate the response at any given parameter level regardless of their values. In addition, a regression model was used to calculate the standardized influence of the independent factors on PO$_4^{3-}$ removal. A response surface plot was generated to investigate the influence of two components at initial the PO$_4^{3-}$ concentration of 20 mg/L (Figure 5). This plot was used to determine the standardized effects of all the independent variables. A surface plot is an easier way to display the response behavior that occurs when two parameters are simultaneously altered at the same time. It is more beneficial to select the quantity of various ingredients to obtain the desired response. Figure 5a displays a Pareto chart that compares the relative magnitude and the corresponding main, square, and interaction effects of the selected variables. The square effects of all four factors were found to be very significant (*p* ≤ 0.05) in addition to the main effects of the factors, which were also found to be highly significant (*p* ≤ 0.05). The ANOVA results reported in Table 4 led to the same conclusions. PO$_4^{3-}$ removal continuously increased in response to the pH, adsorbent dosage, and time. Figure 5b,c show that pH is a key factor in the removal of PO$_4^{3-}$, and Figure 5d shows that increasing the contact time increases the percentage removal.
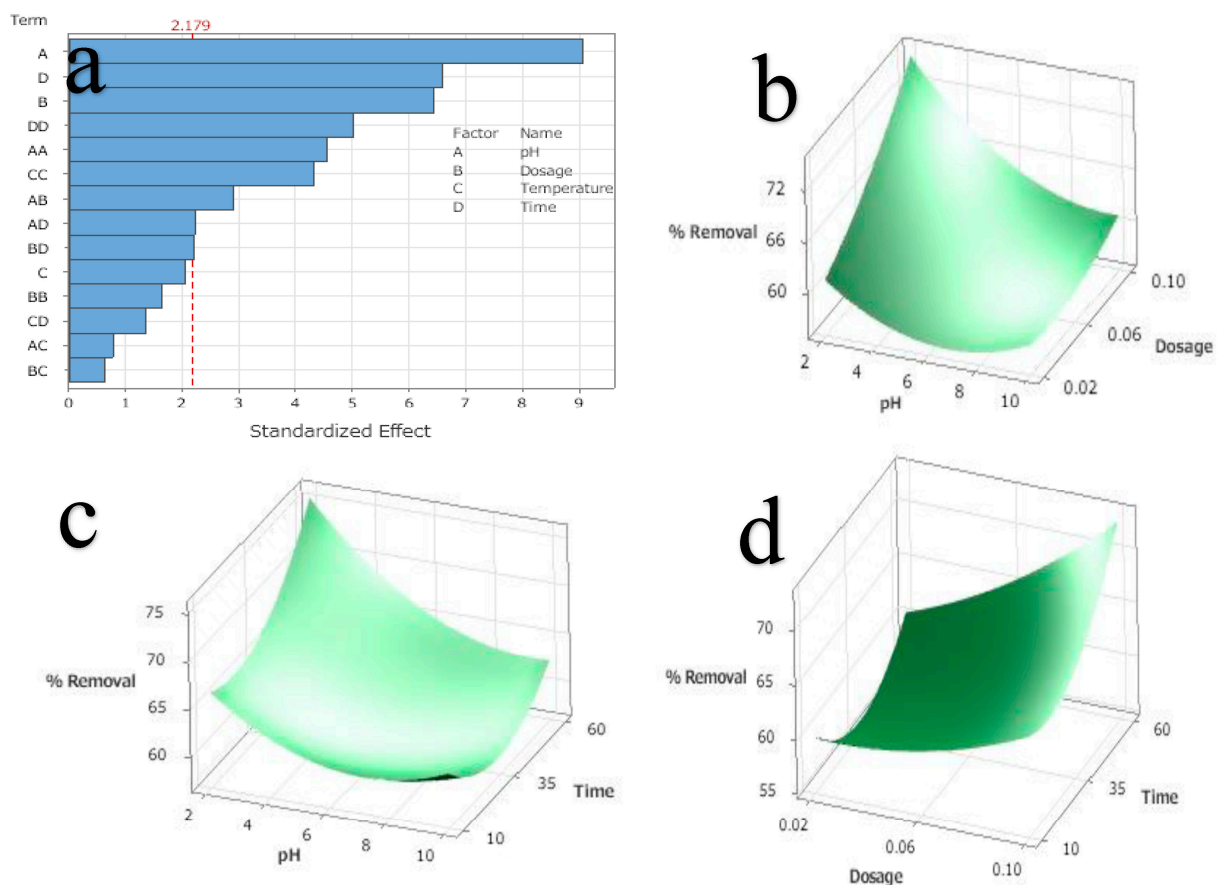
Figure 5. (**a**) Pareto chart for the standardized effect of various factors on PO$_4^{3-}$ removal by adsorbent, (**b**) pH and dosage of adsorbent response surface's effect on PO$_4^{3-}$ removal (%), (**c**) pH and time response surface's effect on PO$_4^{3-}$ removal (%), and (**d**) pH and dosage of adsorbent and time response surface's effect on PO$_4^{3-}$ removal (%).

2.4. Initial Concentration and Isotherm Studies

The effects of the initial PO_4^{3-} concentrations ranging from 20 to 500 mg/L, 0.06 g of adsorbent (CS-ZL/ZrO/Fe_3O_4), and pH (2.0) were investigated. Figure 6 shows that the PO_4^{3-} adsorption capacity rose from 30.64 to 682.31 mg/g; however, the percentage of PO_4^{3-} removal decreased from 91.91% to 81.88%. The adsorption capacity increased with the concentration because the total number of molecules increased. Consequently, the mass transfer resistance of adsorbate decreased. As a result, the percentage of removal decreased [52].
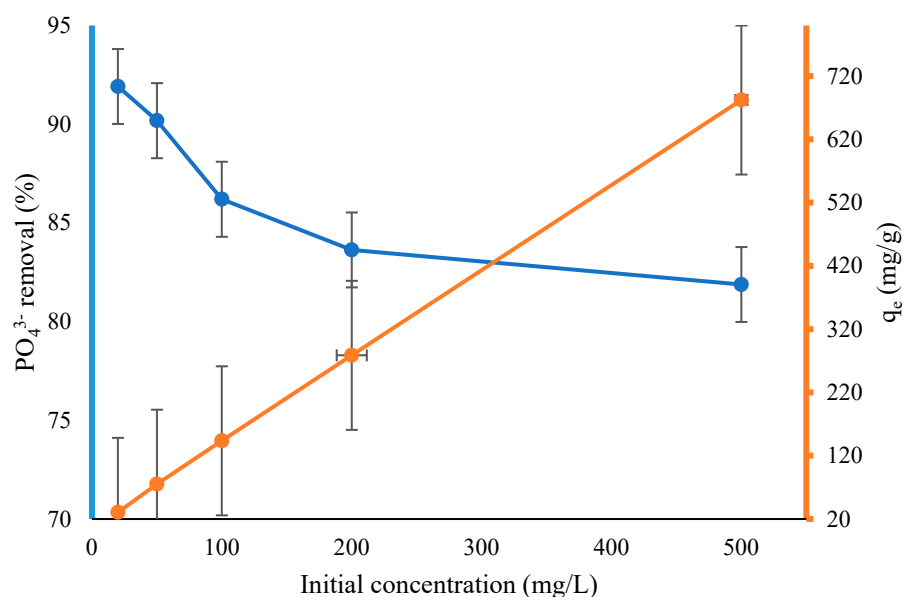
Figure 6. Effect of initial concentration on PO_4^{3-} removal onto CS-ZL/ZrO/Fe_3O_4. Standard deviation (error bars).

Adsorption isotherms are necessary to assess the capabilities of an adsorbent and the interactions between an adsorbate (a solution containing PO_4^{3-} ions) and an adsorbent (CS-ZL/ZrO/Fe_3O_4). The acquired isotherm parameters can be used to conduct an accurate analysis while constructing an effective adsorption system. Both the equilibrium concentration and the adsorption capacity were estimated. The Langmuir model describes the monolayer adsorption processes at the designated homogenous surfaces on the adsorbent (Equation (3)). The essential property of the Langmuir model can be described as a dimensionless constant also known as the separation factor (R_L), which is shown in Equation (4). By contrast, the Freundlich model is based on heterogeneous surfaces and multilayer sorption (Equation (5)). This is a linear equation, which is shown as follows:

$$C_e/q_e = (\frac{C_e}{q_{max}}) + 1/(K_1 q_{max}) \tag{3}$$

$$R_L = (\frac{1}{1 + bC_o}) \tag{4}$$

$$Ln\ q = lnK_f + \frac{1}{n}x\ lnC_e \tag{5}$$

q_e (mg/g) is the adsorption capacity; K_1 (L/mg) is the equilibrium constant of adsorption; q_{max} (mg/g) is the maximal adsorption capacity; C_e (mg/L) is the equilibrium concentration; C_o (mg/L) is the initial concentration; R_L is the separation factor; $0 < R_L$ is favorable; $R_L > 1$ is unfavorable; $R_L = 1$ is linear; and K_f (mg/g) and $1/n$ are the adsorption capacity and the intensity of adsorption, respectively.

Figure 7 shows the isotherm model curves, and Table 5 shows the fitting results corresponding to these curves. The Freundlich model's linear correlation coefficient (R^2) was 0.9970, indicating that it provided the best fit compared to the other models. More importantly, the Langmuir and Freundlich parameters, known as R_L and $1/n$, indicate that the PO_4^{3-} ion has a type of <1. According to these data, the PO_4^{3-} adsorption method is favorable.
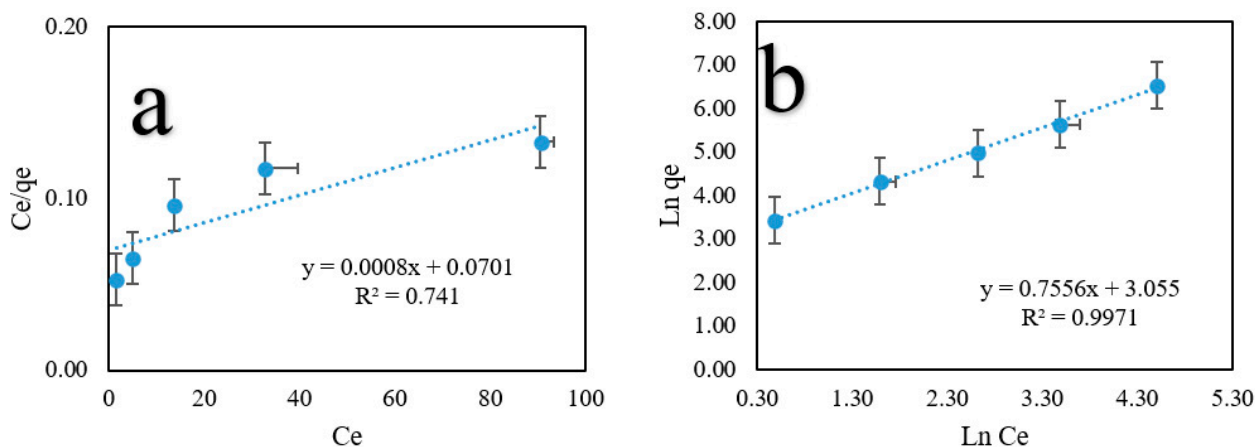
Figure 7. Linear curves of PO_4^{3-} adsorption isotherm models. (**a**) Langmuir, and (**b**) Freundlich models. Standard deviation (error bars).

Table 5. Isotherm model parameters for PO_4^{3-} removal onto CS-ZL/ZrO/Fe_3O_4.

Isotherms	Parameters	Value
Langmuir	q_{max}	1259.79
	K_L	14.27
	R^2	0.7409
	R_L	0.0007
Freundlich	K_f	1135.07
	$1/n$	0.7555
	R^2	0.9970

2.5. Adsorption Kinetic Studies

This study investigated the influence of the contact time (35–2880 min) on PO_4^{3-} adsorption at 30 °C. Figure 8 shows that the percentage of PO_4^{3-} removal and the capacity for adsorption increased rapidly from 35 to 60 min and then gradually increased up to 90 min. This is because the adsorbent includes carboxyl, amine, hydrogen, and magnetite groups, all of which cause the adsorbent surface to become active and trap PO_4^{3-} ions. Subsequently, the adsorption capacity decreased and increased, resulting in fast/slow PO_4^{3-} adsorption, and it finally reached equilibrium at 1440 min, with an adsorption capacity and percent removal of 732.56 mg/g and 87.91%, respectively.

Adsorption kinetic studies are important because they deliver information on the adsorption mechanism, which is necessary to assess the effectiveness of the process [53]. Two kinetic models were used in this study: pseudo-first-order (PFO) (Equation (6)) and pseudo-second-order (PSO) (Equation (7)) models were investigated. The linear form can be obtained by calculating the following equation.

$$Log(q_e - q_t) = \log q_e - K_1 t \tag{6}$$

$$t/q_t = 1/\left(K_2 q_e^2\right) + t/q_e \tag{7}$$

where k_1 (min^{-1}) is the rate constant of the PFO model, t (min) is the time, and a linear plot of log t against log ($q_e - q_t$) and t against t/q_t was used to determine K_1 and K_2 from the slope of the linear plots, respectively.
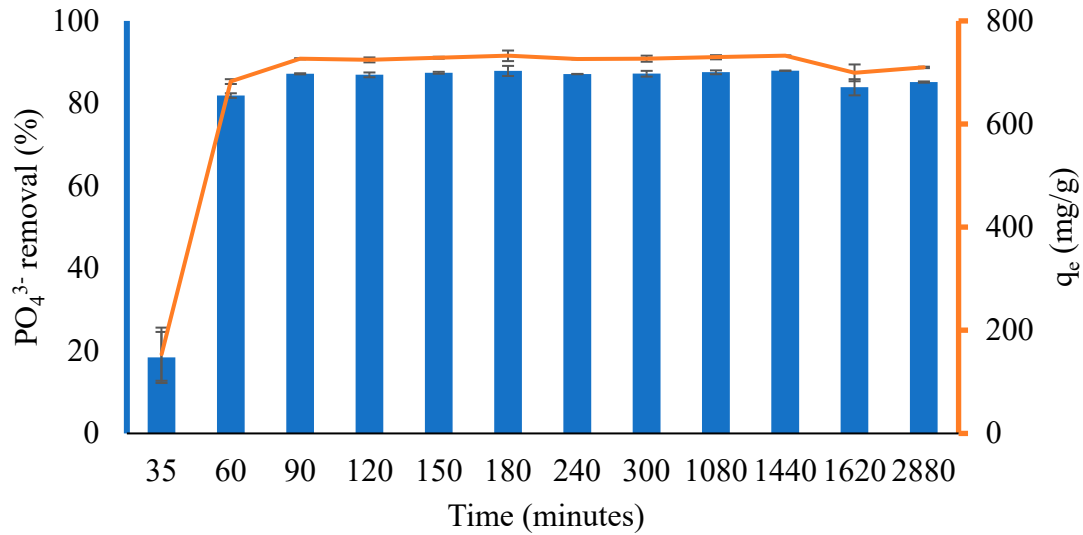
Figure 8. The effect of contact time on PO_4^{3-} removal onto CS-ZL/ZrO/Fe$_3$O$_4$. Standard deviation (error bars).

Figure 9 shows the fitting curves for the kinetic models, and Table 6 lists the fitting results corresponding to those curves. The findings confirm that the PSO model provided better results than the PFO model in terms of the linear correlation coefficient R^2 value (0.9979). These findings imply that chemical processes control the adsorption rate.
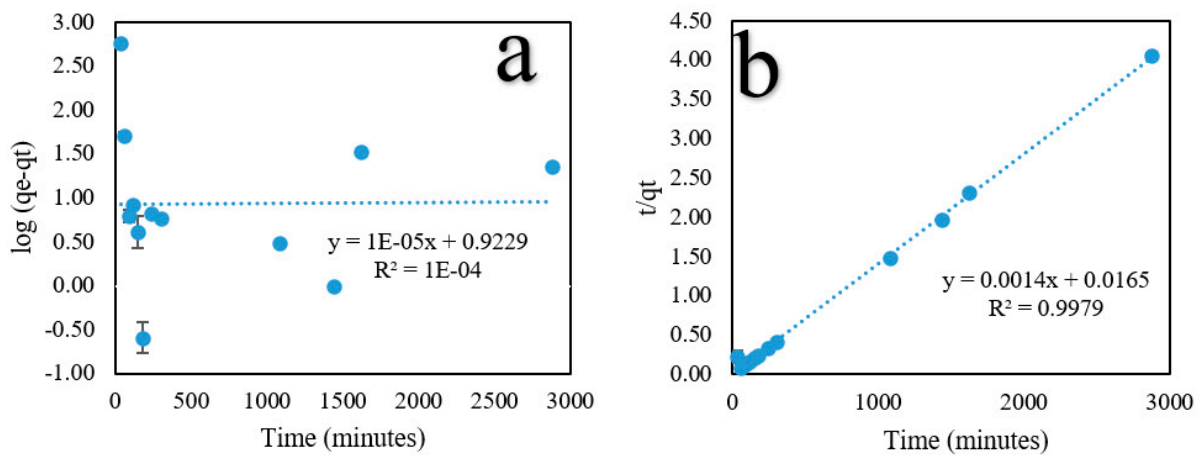
Figure 9. Linear curves of PO_4^{3-} adsorption kinetic studies. (**a**) Pseudo-first-order (PFO) and (**b**) pseudo-second-order (PSO) models. Standard deviation (error bars).

Table 6. Kinetic model parameters for PO_4^{3-} removal onto CS-ZL/ZrO/Fe$_3$O$_4$.

Kinetics	Parameters	Value
PFO	q_e	2.5165
	K_1	1.42857×10^{-6}
	R^2	1.00×10^{-4}
PSO	q_e	510,204.1
	K_2	0.000119
	R^2	0.9979

2.6. Effect of Anions and Cations on PO_4^{3-} Removal onto CS-$ZL/ZrO/Fe_3O_4$

Wastewater contains various substances, including anions and cations, which can affect the adsorption process [54]; it is essential to investigate the effect of ionic strength in an aqueous solution. This is because wastewater is made up of numerous components that might be found together. Figure 10 depicts the effect of different anions and cations on the PO_4^{3-} adsorption capacity of CS-ZL/ZrO/Fe$_3$O$_4$. The experimental data indicate that there was no significant influence on PO_4^{3-} removal. It revealed that the fabrication of CS-ZL/ZrO/Fe$_3$O$_4$ was effective in eliminating PO_4^{3-} from water.
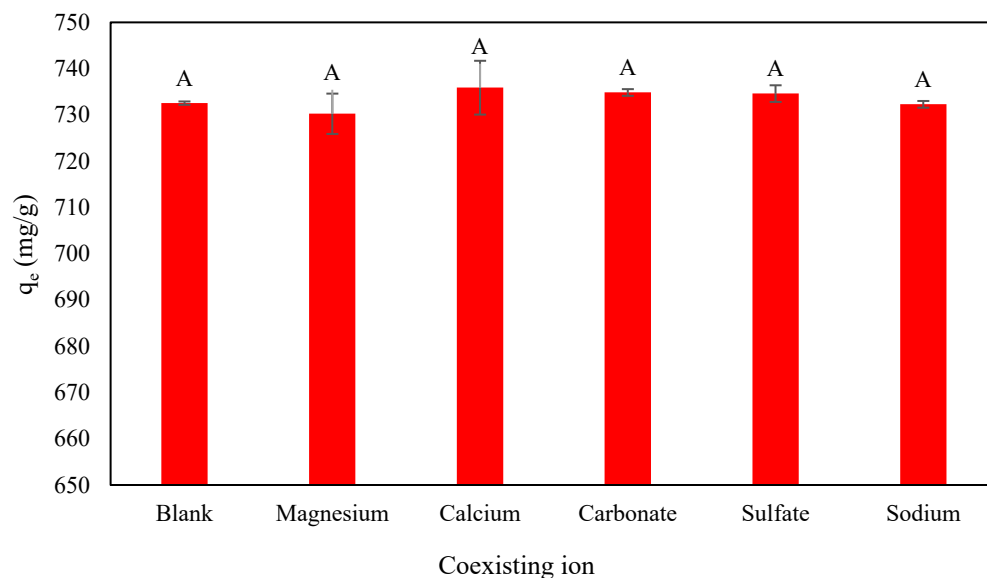
Figure 10. The effect of coexisting ions on PO_4^{3-} removal onto CS-ZL/ZrO/Fe$_3$O$_4$. Standard deviation (error bars). A: no significant effect ($p \leq 0.05$).

2.7. Desorption Studies

Figure 11a shows the desorption percentage of PO_4^{3-} at different NaOH concentrations from 0.01 M to 1 M for 30 min at 30 °C. The results indicate that increasing the concentration increased the desorption percentage to 95.77%. Then, subsequent experiment at different contact times, from 30 to 150 min, using 1 M NaOH (Figure 11b). The desorption percentage increased and then decreased up to 150 min, which is similar to the results of the adsorption studies. The highest desorption percentage was observed after 30 min. The desorption mechanism may cause the hydroxide ions (OH-) in the sodium hydroxide solution to react with the CS-ZL/ZrO/Fe$_3$O$_4$-P surface and replace the PO_4^{3-} groups, resulting in the release of PO_4^{3-} into the liquid solution (Equation (8)). The reusability studies of PO_4^{3-} adsorption onto CS-ZL/ZrO/Fe$_3$O$_4$ showed good performance for three cycles (Figure 11c).

$$H_2PO_4^- + OH^- \rightarrow HPO_4^{2-} + H_2O \tag{8}$$
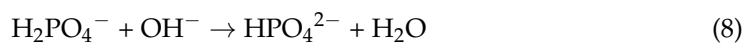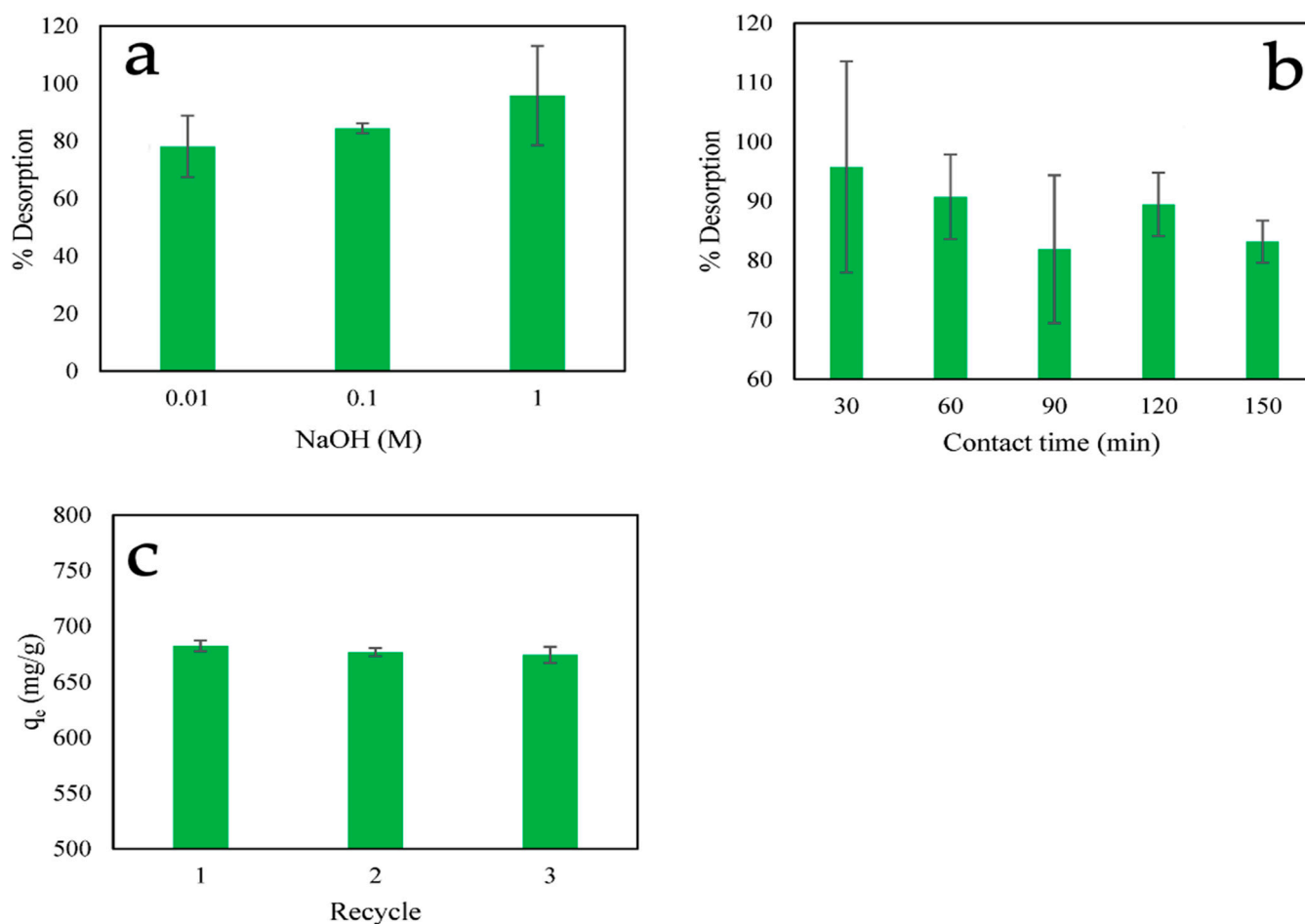
Figure 11. The percentage of desorption. (**a**) Different NaOH concentrations and (**b**) different contact times using 1 M NaOH, and (**c**) in recycle studies on PO_4^{3-} adsorption capacity. Standard deviation (error bars).

2.8. Adsorption Performance Comparison

Table 7 compares the equilibrium and maximum adsorption capacity of CS-ZL/ZrO/ Fe_3O_4 with those of various adsorbents. It can be seen that the pH is one of the main factors for PO_4^{3-} removal onto the adsorbent, and the surface charge can become either positive or negative over a wide pH range, which influences the interaction between the adsorbent and PO_4^{3-} ions. It is clear that the CS-ZL/ZrO/Fe_3O_4 adsorbent has a higher capacity than the other adsorbents. It is feasible to conclude that these adsorbents are viable alternatives for removing PO_4^{3-} from water.

Table 7. List comparing PO_4^{3-} adsorption amounts.

Adsorbent	pH	q_e (mg/g)	References
Magnetic iron oxide nanoparticles	11	5.03	[1]
Fe-HNT	4	5.46	[18]
Halloysite	4	3.56	[18]
20MMSB	4	121.25	[55]
Amine-functionalized nano magnetic Fe_3O_4 polymer	3.0	102.04	[56]
MFB-MCs	3.0	487.99	[57]
Fe_3O_4@SiO_2 core/shell magnetic nanoparticles	-	27.8	[58]
AgNPs-TAC	3	13.62	[59]

Table 7. *Cont.*

Adsorbent	pH	q_e (mg/g)	References
$Ce_{0.8}Zr_{0.2}O_2$	6.2	112.23	[60]
Zr/Al-Mt	5.0	17.2	[61]
PZC 7.3	11	2.41	[62]
Zeolite	11	0.69	[62]
Biochar	11	3.60	[62]
$CS-ZL/ZrO/Fe_3O_4$	2	732.56	Present study

3. Materials and Methods

3.1. Materials

Chitosan (CH) ($C_6H_{11}NO_4$) with molecular weight of 100,000–300,000 Da was bought from Acros Organics, Belgium. Zeolite (ZL) ($Al_2O_3 \cdot 2SiO_2$) was obtained from Tosoh Co. Ltd., Japan. Sodium hydroxide (NaOH), acetic acid (CH_3COOH), disodium hydrogen phosphate (Na_2HPO_4), ferric chloride ($FeCl_3$), ferrous sulfate (Fe_2SO_4), ammonium molybdate (($(NH_4)_6Mo_7O_{24} \cdot 4H_2O$)), antimony potassium tartrate ($K_2Sb_2(C_4H_2O_6)_2$), ascorbic acid ($C_6H_8O_6$), hydrochloric acid (HCl), and sulfuric acid (H_2SO_4) were bought from Kanto Chemical Co., Inc., Tokyo, Japan. ZrClO was purchased from Fujifilm Wako Chemical, Tokyo, Japan.

3.2. Synthesis of CS-ZL/ZrO/Fe₃O₄

$CS-ZL/ZrO/Fe_3O_4$ was synthesized through crosslinking method; chitosan (1 g) was dissolved in 100 mL of acetic acid (1%), and the resulting viscous solution was maintained at ambient temperature (25–30 °C) with magnetic stirring for 24 h (Equation (9)). Subsequently, 25 mL of the resulting chitosan solution was mixed with 0.5 g of zeolite and 20 mL of 1 M $FeCl_3$ + 0.5 M Fe_2SO_4 + 0.5 M ZrClO. The mixture solution was then heated to 60 °C and was stirred for 1 h. The pH of the solution was adjusted to 10 using 3 M NaOH over 24 h with magnetic stirring at ambient temperature (25–30 °C), and the solution was filtered and washed multiple times with acetone and distilled water (DW) to remove any remaining NaOH. Subsequently, the materials were dried for 48 h in an oven at 60 °C (Equation (13)). The adsorbents are referred to as $CS-ZL/ZrO/Fe_3O_4$.

$$(CH_3COOH)n + (C_6H_{11}NO_4)m \rightarrow (CH_3COO^-)n(C_6H_{11}NO_4H^+)m \tag{9}$$

$$(C_6H_{11}NO_4H^+)n + Al_2O_3 \cdot 2SiO_2 \rightarrow (C_6H_{11}NO_4 - Al_2O_3 \cdot 2SiO_2)n + 2H_2O \tag{10}$$

$$5FeCl_3 + 15Fe_2(SO_4)_3 + 12NaOH \rightarrow 5Fe_3O_4 + 15Na_2SO_4 + 6H_2O + 36NaCl \tag{11}$$

$$FeCl_3 + 3Fe_2(SO_4)_3 + ZrClO + 14NaOH \rightarrow 5Fe_3O_4 + Zr(OH)_4 + 2Na_2SO_4 + 6NaCl + 7H_2O \tag{12}$$

$$2(CH_3COO^-)n(C_6H_{11}NO_4H^+)m + 3Al_2O_3 \cdot 2SiO_2 + 3FeCl_3 + Fe_2SO_4 + ZrClO_4 + 14NaOH \rightarrow [3Al_2O_3 \cdot 2SiO_2 - (C_6H_{11}NO_4)]2m/3 \cdot Fe_3O_4 \cdot xH_2O + 3Fe(OH)_3 + 2Zr(OH)_4 + 6NaCl + (2n + 2m)CH_3COONa + (2n + m)H_2O \tag{13}$$

Following this reaction, the negatively charged surface of the zeolite ($Al_2O_3.2SiO_2$) may interact with the positively charged chitosan to produce chitosan–aluminosilicate complex. Electrostatic interactions between Fe^{3+} and Zr^{4+} ions and chitosan are another mechanism by which chitosan combines with metal ions to form chitosan–metal complexes. $Fe(OH)_3$ and Fe_3O_4 are formed when Fe^{2+} and Fe^{3+} ions react with hydroxide ions (OH^-) from NaOH.

3.3. The Design of the Experiment

Experiments were conducted using response surface methodology (RSM) in combination with Box–Behnken design (BBD), and statistical analysis was performed using Minitab 21.3.1 software. (A) The pH (2–10), (B) dosage (0.02–0.1 g), (C) temperature (30–60 °C),

and (D) contact time (10–60 min) were the independent variables examined in the BBD, with three levels and four parameters (Table 8). In total, 27 different sets of experiments were performed to determine the optimal conditions for PO_4^{3-} removal. The data obtained were assessed using an equation for a quadratic polynomial response surface, which was calculated using Equation (14), to identify the relationships between independent variables and response.

$$Y = E_0 + E_1 A + E_2 B + E_3 C + E_4 D + E_{11}A^2 + E_{22}B^2 + E_{33}C^2 + E_{12}AB + E_{13}AC + E_{23}BC + \varepsilon \qquad (14)$$

Table 8. Variables and levels.

Symbol	Factor	Level 1 (− 1)	Level 2 (0)	Level 3 (+ 1)
A	pH	2	7	10
B	Dosage (g)	0.02	0.06	0.10
C	Temperature (°C)	30	45	60
D	Time (min)	10	35	60

The coefficients of the polynomial model are represented as follows: E0 is constant expression, E1–E3 are linear effects, E11–E33 are second-order effects, E12–E23 are interactive effects, and ε is error term. An analysis of variance (ANOVA) was performed to calculate the F- and *p*-values of the model to measure its statistical significance and appropriateness. The statistical significance of the model is shown through the model's F-value and *p*-value, and a lack-of-fit study of the proposed model was executed using Minitab 21.3.1 software. In addition, a 3D response surface plot and Pareto chart of standardized effects were developed to figure out the cooperative quantitative impact of the independent variables on the response and overall value of the model [63].

3.4. Batch Adsorption Study and Response Determination (PO_4^{3-} Removal %)

To evaluate the efficiency of PO_4^{3-} removal, batch adsorption approach was used in this study. In total, 100 mL of PO_4^{3-} (20 mg/L) was placed in a 300 mL conical flask. After the adsorption procedure was completed, external magnetite was placed in the conical flask to separate the adsorbent and adsorbate. PO_4^{3-} removal was calculated using Equation (15).

$$PO_4^{3-} \text{ removal } \% = \frac{C_o - C_e}{C_o} \times 100 \qquad (15)$$

where C_o and C_e are the initial and equilibrium PO_4^{3-} concentrations (mg/L), respectively.

The data from run 17 of the BBD were used for subsequent experiments (isotherm and kinetic models). However, 30 min was not used because the results were far from equilibrium. The amount of PO_4^{3-} adsorbed was determined using Equation (16).

$$q_e = \frac{C_o - C_e}{W} \times V \qquad (16)$$

where q_e (mg/g) is the adsorption capacity, W (g) is the amount of CS-ZL/ZrO/Fe$_3$O$_4$, and V (L) is the volume of adsorbate (PO_4^{3-} solution).

3.5. Adsorption Isotherm Studies

The isotherm model was studied with PO_4^{3-} solutions ranging from 20 mg/L to 500 mg/L with pH of 2. These examinations were performed for 60 min at 30 °C, and adsorbent dosage of 0.06 g was placed in the flask. In this work, Langmuir and Freundlich models were used to assess PO_4^{3-} adsorption onto CS-ZL/ZrO/Fe$_3$O$_4$ [64].

3.6. Adsorption Kinetic Studies

Pseudo-first-order (PFO) and pseudo-second-order (PSO) models were used to investigate the model of adsorption kinetics. The following parameters were used in the

experiment: an adsorption temperature of 30 °C, an initial PO_4^{3-} concentration of 500 mg/L at pH of 2, an adsorbent dosage of 0.06 g, and contact time ranging from 35 to 2880 min.

3.7. Influence of Coexisting Ionic Strength

The experiment was conducted under optimum conditions with a dosage of 0.06 g, an initial PO_4^{3-} concentration of 500 mg/L, and a contact time of 1440 min at 30 °C. The coexisting ion was prepared with cationic and anionic ions at a concentration of 20 mg/L (Mg^{2+}, Ca^{2+}, CO_3^{2-}, SO_4^{-}, and Na^{+}).

3.8. Desorption and Reusability Studies

In most practical applications, it is essential to employ adsorbents with high level of reusability. NaOH was chosen as desorbing agent to release PO_4^{3-} ion from CS-ZL/ZrO/Fe$_3$O$_4$. Firstly, 0.06 g of CS-ZL/ZrO/Fe$_3$O$_4$ was loaded with 500 mg/L of PO_4^{3-} ion at pH of 2.0, which was called CS-ZL/ZrO/Fe$_3$O$_4$-P. Then, 0.01 g of CS-ZL/ZrO/Fe$_3$O$_4$-P was dispersed in 60 mL of NaOH at 30 °C. The desorption capacity and desorption percentage are shown in Equations (17) and (18), respectively. Reusability was assessed using the same treatment as described above.

$$q_{des} = \frac{C}{W} \times V \tag{17}$$

$$\% \text{ Desorption} = \frac{q_{des}}{q_e} \times 100 \tag{18}$$

where q_{des} (mg/g) is the desorption capacity; C (mg/L) is the PO_4^{3-} concentration of desorption; % Desorption (%) is the percentage desorption; and W, V, and q_e are the same as above.

3.9. PO_4^{3-} Measurements

PO_4^{3-} ions were measured using the molybdate blue method. A total of 12 g of $(NH_4)_6Mo_7O_{24}\cdot 4H_2O$ was mixed with 100 mL of DW. $K_2Sb_2(C_4H_2O_6)_2$ (0.277 g) was added followed by 140 mL of 18 M H_2SO_4. Afterward, it was adjusted to 1 L with distilled water (solution A). A total of 1.06 g of $C_6H_8O_6$ was added to and mixed with 100 mL of solution A, 25 mL of 4 N H_2SO_4 was added, and the solution was adjusted to 1 L with DW (solution B). Note: This solution must be prepared in every experiment. The procedure for the mixed solution was as follows: 2 mL of liquid sample/standard was mixed with 10 mL of solution B. Afterwards, we waited for 30 min and then analyzed the solution using a UV-Vis spectrophotometer (Jasco V-530) at a wavelength of 693 nm. A standard curve for PO_4^{3-} was constructed using Na_2HPO_4.

3.10. Mechanical Stability

The mechanical stability of the CS-ZL/ZrO/Fe$_3$O$_4$ composite was evaluated based on the responses of the samples to a water bath shaker at 80 °C. For one hour, dried CS-ZL/ZrO/Fe$_3$O$_4$ was soaked in HCl and H_2SO_4 concentrations ranging from 0.01 to 0.1 M. Following that, the sample was dried in an oven at 60 °C for twenty-four hours. The calculation of the dry weight retention (WR) was performed using Equation (19).

$$\text{WR } (\%) = \frac{w_i}{w_a} \times 100 \tag{19}$$

where w_i and w_a are the dry weights of CS-ZL/ZrO/Fe$_3$O$_4$ before and after treatment, respectively.

3.11. Characterization of CS-ZL/ZrO/Fe$_3$O$_4$

The crystalline structure of CS-ZL/ZrO/Fe$_3$O$_4$ was analyzed using a powder X-ray diffractometer (XRD) equipped with Cu/Kα radiation (Hypix-3000). Fourier transform

infrared spectra (FTIR) of CS-ZL/ZrO/Fe$_3$O$_4$ were measured before and after PO$_4^{3-}$ adsorption using a Thermo Scientific Nicolet iS10 instrument (Thermo Fisher Scientific Inc., Waltham, MA, USA). The ATR-FTIR approach was used to analyze samples with a resolution of 4 cm^{-1} throughout the wavenumber spectrum spanning 400–4000 cm^{-1}. To determine the specific surface area (SSA), the BET approach was combined with a surface area analyzer (MicroActive AutoPore V 9600 2.03.00, Micromeritics, Norcross, GA, USA). SEM-EDS (JIED-2300, Shimadzu, Kyoto, Japan) was used to examine the SEM images and the elemental distributions of CS-ZL/ZrO/Fe$_3$O$_4$. The initial (pHi) and final (pHf) pH values of the solutions were measured to determine the surface charge over a range of pH values (pH$_{zpc}$). The pHi was adjusted from 2.0 to 10.0 in 0.01 M NaCl solution. Following that, 0.1 g of CS-ZL/ZrO/Fe$_3$O$_4$ was added and stirred for 24 h at 30 °C, and pHf was measured. A plot of ΔpH = pHf − pHi vs. pHi was used to determine pH$_{pzc}$, which corresponds to the neutral surface charge.

3.12. Data Analysis

All results were noted and edited using Microsoft Excel. The effects of coexisting ions on PO$_4^{3-}$ removal were examined using a completely randomized design (CRD). Data were analyzed using ANOVA with Tukey's test ($p \leq 0.05$) using Minitab 21.3.1.

4. Conclusions

In this study, a novel adsorbent, CS-ZL/ZrO/Fe$_3$O$_4$, was prepared from chitosan (CS), zeolite (ZL), ZrO, and magnetite (Fe$_3$O$_4$) via a crosslinking approach. The Box–Behnken design (BBD) and the response surface methodology (RSM), with their corresponding four separate factors (pH, dosage, temperature, and time), were used to develop the best experimental conditions for PO$_4^{3-}$ removal. Weight retention (WR) was measured in a batch reactor under acidic conditions (HCl and H$_2$SO$_4$) at 80 °C for 1 h to determine the mechanical stability. The results indicate that CS-ZL/ZrO/Fe$_3$O$_4$ was stable and did not change in the functional group peak area after treatment. The best conditions were at a pH of 2.0, with an adsorption capacity and percentage removal of 732.56 mg/g and 87.91%, respectively. The Freundlich isotherm and pseudo-second-order (PSO) kinetic models were fitted to PO$_4^{3-}$ removal, indicating heterogeneous and chemical sorption. In addition, the results suggest that PO$_4^{3-}$ adsorption occurred via the electrostatic interactions between the positive charge of CS-ZL/ZrO/Fe$_3$O$_4$ and the negative charge of H$_2$PO^{4-} as well as ion exchange and hydrogen bonding. The presence of coexisting ions (Mg^{2+}, Ca^{2+}, CO$_3^{2-}$, SO$_4^{2-}$, and Na$^+$) had no effect on the removal of PO$_4^{3-}$ ($p \leq 0.05$). The desorption studies revealed that 1 M NaOH was better at releasing PO$_4^{3-}$, reaching 95.77% after 30 min of treatment at 30 °C. The reusability of CS-ZL/ZrO/Fe$_3$O$_4$ showed good performance over three cycles. These findings imply that CS-ZL/ZrO/Fe$_3$O$_4$ is the best way to improve the stability of chitosan under acidic conditions, and it is a good adsorbent for removing PO$_4^{3-}$ and other potential water pollutants from water.

References

1. Yoon, S.-Y.; Lee, C.-G.; Park, J.-A.; Kim, J.-H.; Kim, S.-B.; Lee, S.-H.; Choi, J.-W. Kinetic, equilibrium and thermodynamic studies for phosphate adsorption to magnetic iron oxide nanoparticles. *Chem. Eng. J.* **2014**, *236*, 341–347. [CrossRef]

2. Chen, M.; Ding, S.; Chen, X.; Sun, Q.; Fan, X.; Lin, J.; Ren, M.; Yang, L.; Zhang, C. Mechanisms driving phosphorus release during algal blooms based on hourly changes in iron and phosphorus concentrations in sediments. *Water Res.* **2018**, *133*, 153–164. [CrossRef] [PubMed]

3. Schindler, D.W.; Carpenter, S.R.; Chapra, S.C.; Hecky, R.E.; Orihel, D.M. Reducing phosphorus to curb lake eutrophication is a success. *Environ. Sci. Technol.* **2016**, *50*, 8923–8929. [CrossRef]

4. Pawar, R.R.; Gupta, P.; Lalhmunsiama; Bajaj, H.C.; Lee, S.-M. Al-intercalated acid activated bentonite beads for the removal of aqueous phosphate. *Sci. Total Environ.* **2016**, *572*, 1222–1230. [CrossRef]

5. Xie, Q.; Li, Y.; Lv, Z.; Zhou, H.; Yang, X.; Chen, J.; Guo, H. Effective Adsorption and Removal of Phosphate from Aqueous Solutions and Eutrophic Water by Fe-based MOFs of MIL-101. *Sci. Rep.* **2017**, *7*, 3316. [CrossRef] [PubMed]

6. Wei, W.; Du, J.; Li, J.; Yan, M.; Zhu, Q.; Jin, X.; Zhu, X.; Hu, Z.; Tang, Y.; Lu, Y. Construction of Robust Enzyme Nanocapsules for Effective Organophosphate Decontamination, Detoxification, and Protection. *Adv. Mater.* **2013**, *25*, 2212–2218. [CrossRef]

7. Wang, F.; Wei, J.; Zou, X.; Fu, R.; Li, J.; Wu, D.; Lv, H.; Zhu, G.; Wu, X.; Chen, H. Enhanced electrochemical phosphate recovery from livestock wastewater by adjusting pH with plant ash. *J. Environ. Manag.* **2019**, *250*, 109473. [CrossRef]

8. Ren, Y.; Zheng, W.; Duan, X.; Goswami, N.; Liu, Y. Recent advances in electrochemical removal and recovery of phosphorus from water: A review. *Environ. Funct. Mater.* **2022**, *1*, 10–20. [CrossRef]

9. Hidayat, E.; Harada, H. Simultaneously Recovery of Phosphorus and Potassium Using Bubble Column Reactor as Struvite-K and Implementation on Crop Growth. In *Crystallization and Applications*; IntechOpen: London, UK, 2022. [CrossRef]

10. Guida, S.; Rubertelli, G.; Jefferson, B.; Soares, A. Demonstration of ion exchange technology for phosphorus removal and recovery from municipal wastewater. *Chem. Eng. J.* **2021**, *420*, 129913. [CrossRef]

11. Hidayat, E.; Yoshino, T.; Yonemura, S.; Mitoma, Y.; Harada, H. A Carbonized Zeolite/Chitosan Composite as an Adsorbent for Copper (II) and Chromium (VI) Removal from Water. *Materials* **2023**, *16*, 2532. [CrossRef]

12. Zahari, K.F.A.; Sahu, U.K.; Khadiran, T.; Surip, S.N.; Alothman, Z.A.; Jawad, A.H. Mesoporous Activated Carbon from Bamboo Waste via Microwave-Assisted K_2CO_3 Activation: Adsorption Optimization and Mechanism for Methylene Blue Dye. *Separations* **2022**, *9*, 390. [CrossRef]

13. Matei, A.; Racoviteanu, G. Review of the technologies for nitrates removal from water intended for human consumption. In *IOP Conference Series: Earth and Environmental Science*; IOP Publishing Ltd.: Bristol, UK, 2021. [CrossRef]

14. Rodrigues, L.A.; da Silva, M.L.C.P. An investigation of phosphate adsorption from aqueous solution onto hydrous niobium oxide prepared by co-precipitation method. *Colloids Surf. A Physicochem. Eng. Asp.* **2009**, *334*, 191–196. [CrossRef]

15. Huang, W.; Zhang, Y.; Li, D. Adsorptive removal of phosphate from water using mesoporous materials: A review. In *Journal of Environmental Management*; Academic Press: Cambridge, MA, USA, 2017; Volume 193, pp. 470–482.

16. Blaney, L.; Cinar, S.; Sengupta, A.K. Hybrid anion exchanger for trace phosphate removal from water and wastewater. *Water Res.* **2007**, *41*, 1603–1613. [CrossRef] [PubMed]

17. Hidayat, E.; Yoshino, T.; Yonemura, S.; Mitoma, Y.; Harada, H. Synthesis, Adsorption Isotherm and Kinetic Study of Alkaline-Treated Zeolite/Chitosan/Fe^{3+} Composites for Nitrate Removal from Aqueous Solution—Anion and Dye Effects. *Gels* **2022**, *8*, 782. [CrossRef] [PubMed]

18. Almasri, D.A.; Saleh, N.B.; Atieh, M.A.; McKay, G.; Ahzi, S. Adsorption of phosphate on iron oxide doped halloysite nanotubes. *Sci. Rep.* **2019**, *9*, 3232. [CrossRef] [PubMed]

19. Ladeira, N.M.B.; Donnici, C.L.; de Mesquita, J.P.; Pereira, F.V. Preparation and characterization of hydrogels obtained from chitosan and carboxymethyl chitosan. *J. Polym. Res.* **2021**, *28*, 335. [CrossRef]

20. Mohammed, I.A.; Malek, N.N.A.; Jawad, A.H.; Mastuli, M.S.; Alothman, Z.A. Box–Behnken Design for Optimizing Synthesis and Adsorption Conditions of Covalently Crosslinked Chitosan/Coal Fly Ash Composite for Reactive Red 120 Dye Removal. *J. Polym. Environ.* **2022**, *30*, 3447–3462. [CrossRef]

21. Jawad, A.H.; Hameed, B.H.; Abdulhameed, A.S. Synthesis of biohybrid magnetic chitosan-polyvinyl alcohol/MgO nanocomposite blend for remazol brilliant blue R dye adsorption: Solo and collective parametric optimization. *Polym. Bull.* **2022**, *80*, 4927–4947. [CrossRef]

22. Aramesh, N.; Bagheri, A.R.; Bilal, M. Chitosan-based hybrid materials for adsorptive removal of dyes and underlying interaction mechanisms. In *International Journal of Biological Macromolecules*; Elsevier B.V.: Amsterdam, The Netherlands, 2021; Volume 183, pp. 399–422. [CrossRef]

23. Salehi, S.; Anbia, M. Adsorption Selectivity of CO_2 and CH_4 on Novel PANI/Alkali-Exchanged FAU Zeolite Nanocomposites. *J. Inorg. Organomet. Polym. Mater.* **2017**, *27*, 1281–1291. [CrossRef]

24. Hidayat, E.; Yonemura, S.; Mitoma, Y.; Harada, H. Methylene Blue Removal by Chitosan Cross-Linked Zeolite from Aqueous Solution and Other Ion Effects: Isotherm, Kinetic, and Desorption Studies. *Adsorpt. Sci. Technol.* **2022**, *2022*, 1853758. [CrossRef]

25. Hidayat, E.; Harada, H.; Mitoma, Y.; Yonemura, S.; A Halem, H.I. Rapid Removal of Acid Red 88 by Zeolite/Chitosan Hydrogel in Aqueous Solution. *Polymers* **2022**, *14*, 893. [CrossRef]

26. Vakili, M.; Qiu, W.; Cagnetta, G.; Huang, J.; Yu, G. Mechanochemically oxidized chitosan-based adsorbents with outstanding Penicillin G adsorption capacity. *J. Environ. Chem. Eng.* **2021**, *9*, 105454. [CrossRef]

27. Gao, Y.; Bao, S.; Zhang, L.; Zhang, L. Nitrate removal by using chitosan/zeolite molecular sieves composite at low temperature: Characterization, mechanism, and regeneration studies. *Desalination Water Treat* **2020**, *203*, 160–171. [CrossRef]
28. Lin, J.; Zhan, Y. Adsorption of humic acid from aqueous solution onto unmodified and surfactant-modified chitosan/zeolite composites. *Chem. Eng. J.* **2012**, *200–202*, 202–213. [CrossRef]
29. Mohammad, A.K.T.; Abdulhameed, A.S.; Jawad, A.H. Box-Behnken design to optimize the synthesis of new crosslinked chitosan-glyoxal/TiO₂ nanocomposite: Methyl orange adsorption and mechanism studies. *Int. J. Biol. Macromol.* **2019**, *129*, 98–109. [CrossRef] [PubMed]
30. Nga, N.K.; Chau, N.T.T.; Viet, P.H. Preparation and characterization of a chitosan/MgO composite for the effective removal of reactive blue 19 dye from aqueous solution. *J. Sci. Adv. Mater. Devices* **2020**, *5*, 65–72. [CrossRef]
31. Spoială, A.; Ilie, C.-I.; Dolete, G.; Croitoru, A.-M.; Surdu, V.-A.; Trușcă, R.-D.; Motelica, L.; Oprea, O.-C.; Ficai, D.; Ficai, A.; et al. Preparation and Characterization of Chitosan/TiO₂ Composite Membranes as Adsorbent Materials for Water Purification. *Membranes* **2022**, *12*, 804. [CrossRef]
32. Reghioua, A.; Barkat, D.; Jawad, A.H.; Abdulhameed, A.S.; Rangabhashiyam, S.; Khan, M.R.; Alothman, Z.A. Magnetic Chitosan-Glutaraldehyde/Zinc Oxide/Fe₃O₄ Nanocomposite: Optimization and Adsorptive Mechanism of Remazol Brilliant Blue R Dye Removal. *J. Polym. Environ.* **2021**, *29*, 3932–3947. [CrossRef]
33. Reghioua, A.; Barkat, D.; Jawad, A.H.; Abdulhameed, A.S.; Khan, M.R. Synthesis of Schiff's base magnetic crosslinked chitosan-glyoxal/ZnO/Fe₃O₄ nanoparticles for enhanced adsorption of organic dye: Modeling and mechanism study. *Sustain. Chem. Pharm.* **2021**, *20*, 100379. [CrossRef]
34. Cho, D.-W.; Jeon, B.-H.; Jeong, Y.; Nam, I.-H.; Choi, U.-K.; Kumar, R.; Song, H. Synthesis of hydrous zirconium oxide-impregnated chitosan beads and their application for removal of fluoride and lead. *Appl. Surf. Sci.* **2016**, *372*, 13–19. [CrossRef]
35. Sathiyavimal, S.; Vasantharaj, S.; Kaliannan, T.; Pugazhendhi, A. Eco-biocompatibility of chitosan coated biosynthesized copper oxide nanocomposite for enhanced industrial (Azo) dye removal from aqueous solution and antibacterial properties. *Carbohydr. Polym.* **2020**, *241*, 116243. [CrossRef]
36. Salehi, S.; Alijani, S.; Anbia, M. Enhanced adsorption properties of zirconium modified chitosan-zeolite nanocomposites for vanadium ion removal. *Int. J. Biol. Macromol.* **2020**, *164*, 105–120. [CrossRef] [PubMed]
37. Rosales, E.; Anasie, D.; Pazos, M.; Lazar, I.; Sanromán, M.A. Kaolinite adsorption-regeneration system for dyestuff treatment by Fenton based processes. *Sci. Total Environ.* **2018**, *622–623*, 556–562. [CrossRef] [PubMed]
38. Ghobadi, M.; Gharabaghi, M.; Abdollahi, H.; Boroumand, Z.; Moradian, M. MnFe₂O₄-graphene oxide magnetic nanoparticles as a high-performance adsorbent for rare earth elements: Synthesis, isotherms, kinetics, thermodynamics and desorption. *J. Hazard. Mater.* **2018**, *351*, 308–316. [CrossRef]
39. Maksoud, M.I.A.A.; Elgarahy, A.M.; Farrell, C.; Al-Muhtaseb, A.H.; Rooney, D.W.; Osman, A.I. Insight on water remediation application using magnetic nanomaterials and biosorbents. In *Coordination Chemistry Reviews*; Elsevier B.V.: Amsterdam, The Netherlands, 2020; Volume 403.
40. Fu, Z.; Li, H.; Yang, L.; Yuan, H.; Jiao, Z.; Chen, L.; Huang, J.; Liu, Y.-N. Magnetic polar post-cross-linked resin and its adsorption towards salicylic acid from aqueous solution. *Chem. Eng. J.* **2015**, *273*, 240–246. [CrossRef]
41. Al-Harahsheh, M.; AlJarrah, M.; Mayyas, M.; Alrebaki, M. High-stability polyamine/amide-functionalized magnetic nanoparticles for enhanced extraction of uranium from aqueous solutions. *J. Taiwan Inst. Chem. Eng.* **2018**, *86*, 148–157. [CrossRef]
42. Zong, E.; Shen, Y.; Yang, J.; Liu, X.; Song, P. Preparation and Characterization of an Invasive Plant-Derived Biochar-Supported Nano-Sized Lanthanum Composite and Its Application in Phosphate Capture from Aqueous Media. *ACS Omega* **2023**, *8*, 14177–14189. [CrossRef]
43. Mekonnen, D.T.; Alemayehu, E.; Lennartz, B. Removal of Phosphate Ions from Aqueous Solutions by Adsorption onto Leftover Coal. *Water* **2020**, *12*, 1381. [CrossRef]
44. Zhang, M.; Zhang, Z.; Peng, Y.; Feng, L.; Li, X.; Zhao, C.; Sarfaraz, K. Novel cationic polymer modified magnetic chitosan beads for efficient adsorption of heavy metals and dyes over a wide pH range. *Int. J. Biol. Macromol.* **2020**, *156*, 289–301. [CrossRef]
45. Safaei-Ghomi, J.; Tavazo, M.; Shahbazi-Alavi, H. Chitosan-attached nano-Fe₃O₄ as a superior and retrievable heterogeneous catalyst for the synthesis of benzopyranophenazines using chitosan-attached nano-Fe₃O₄. *Z. Fur Nat.—Sect. B J. Chem. Sci.* **2019**, *74*, 733–738. [CrossRef]
46. Annaduzzaman, M.; Bhattacharya, P.; Ersoz, M.; Lazarova, Z. Characterization of a chitosan biopolymer and arsenate removal for drinking water treatment. In *One Century of the Discovery of Arsenicosis in Latin America (1914–2014): As 2014—Proceedings of the 5th International Congress on Arsenic in the Environment*; CRC Press/Balkema: Boca Raton, FL, USA, 2014; pp. 745–747.
47. Yang, T.; Zhang, W.; Liu, H.; Guo, Y. Enhanced removal of U(VI) from aqueous solution by chitosan-modified zeolite. *J. Radioanal. Nucl. Chem.* **2020**, *323*, 1003–1012. [CrossRef]
48. Fajardo, A.R.; Lopes, L.C.; Pereira, A.G.; Rubira, A.F.; Muniz, E.C. Polyelectrolyte complexes based on pectin–NH₂ and chondroitin sulfate. *Carbohydr. Polym.* **2012**, *87*, 1950–1955. [CrossRef]
49. Zhang, S.; Zhang, Y.; Fu, L.; Jing, M. A chitosan fiber as green material for removing Cr(VI) ions and Cu(II) ions pollutants. *Sci. Rep.* **2021**, *11*, 22942. [CrossRef] [PubMed]
50. Cui, Z.; Xiang, Y.; Si, J.; Yang, M.; Zhang, Q.; Zhang, T. Ionic interactions between sulfuric acid and chitosan membranes. *Carbohydr. Polym.* **2008**, *73*, 111–116. [CrossRef]
51. Bouchet, R.; Siebert, E. Proton conduction in acid doped polybenzimidazole. *Solid State Ion.* **1999**, *118*, 287–299. [CrossRef]

52. Miraboutalebi, S.M.; Nikouzad, S.K.; Peydayesh, M.; Allahgholi, N.; Vafajoo, L.; McKay, G. Methylene blue adsorption via maize silk powder: Kinetic, equilibrium, thermodynamic studies and residual error analysis. *Process. Saf. Environ. Prot.* **2017**, *106*, 191–202. [CrossRef]

53. Jembere, A.L.; Genet, M.B. Comparative adsorptive performance of adsorbents developed from sugar industrial wastes for the removal of melanoidin pigment from molasses distillery spent wash. *Water Resour. Ind.* **2021**, *26*, 100165. [CrossRef]

54. Lin, B.; Hua, M.; Zhang, Y.; Zhang, W.; Lv, L.; Pan, B. Effects of organic acids of different molecular size on phosphate removal by HZO-201 nanocomposite. *Chemosphere* **2017**, *166*, 422–430. [CrossRef]

55. Li, R.; Wang, J.J.; Zhou, B.; Awasthi, M.K.; Ali, A.; Zhang, Z.; Lahori, A.H.; Mahar, A. Recovery of phosphate from aqueous solution by magnesium oxide decorated magnetic biochar and its potential as phosphate-based fertilizer substitute. *Bioresour. Technol.* **2016**, *215*, 209–214. [CrossRef]

56. Shen, H.; Wang, Z.; Zhou, A.; Chen, J.; Hu, M.; Dong, X.; Xia, Q. Adsorption of phosphate onto amine functionalized nano-sized magnetic polymer adsorbents: Mechanism and magnetic effects. *RSC Adv.* **2015**, *5*, 22080–22090. [CrossRef]

57. Jung, K.W.; Lee, S.; Lee, Y.J. Synthesis of novel magnesium ferrite ($MgFe_2O_4$)/biochar magnetic composites and its adsorption behavior for phosphate in aqueous solutions. *Bioresour. Technol.* **2017**, *245*, 751–759. [CrossRef] [PubMed]

58. Lai, L.; Xie, Q.; Chi, L.; Gu, W.; Wu, D. Adsorption of phosphate from water by easily separable Fe_3O_4@SiO_2 core/shell magnetic nanoparticles functionalized with hydrous lanthanum oxide. *J. Colloid Interface Sci.* **2016**, *465*, 76–82. [CrossRef] [PubMed]

59. Trinh, V.T.; Nguyen, T.M.P.; Van, H.T.; Hoang, L.P.; Nguyen, T.V.; Ha, L.T.; Vu, X.H.; Pham, T.T.; Quang, N.V.; Nguyen, X.C. Phosphate Adsorption by Silver Nanoparticles-Loaded Activated Carbon derived from Tea Residue. *Sci. Rep.* **2020**, *10*, 3634. [CrossRef]

60. Su, Y.; Yang, W.; Sun, W.; Li, Q.; Shang, J.K. Synthesis of mesoporous cerium–zirconium binary oxide nanoadsorbents by a solvothermal process and their effective adsorption of phosphate from water. *Chem. Eng. J.* **2015**, *268*, 270–279. [CrossRef]

61. Huang, W.; Chen, J.; He, F.; Tang, J.; Li, D.; Zhu, Y.; Zhang, Y. Effective phosphate adsorption by Zr/Al-pillared montmorillonite: Insight into equilibrium, kinetics and thermodynamics. *Appl. Clay Sci.* **2014**, *104*, 252–260. [CrossRef]

62. Deng, Z.; Gu, S.; Cheng, H.; Xing, D.; Twagirayezu, G.; Wang, X.; Ning, W.; Mao, M. Removal of Phosphate from Aqueous Solution by Zeolite-Biochar Composite: Adsorption Performance and Regulation Mechanism. *Appl. Sci.* **2022**, *12*, 5334. [CrossRef]

63. Shukla, S.K.; Pandey, S.; Saha, S.; Singh, H.R.; Mishra, P.K.; Kumar, S.; Jha, S.K. Removal of crystal violet by Cu-chitosan nano-biocomposite particles using Box–Behnken design. *J. Environ. Chem. Eng.* **2021**, *9*, 105847. [CrossRef]

64. Hidayat, E.; Khaekhum, S.; Yonemura, S.; Mitoma, Y.; Harada, H. Biosorption of Eriochrome Black T Using Exserohilum rostratum NMS1.5 Mycelia Biomass. *J* **2022**, *5*, 427–434. [CrossRef]

Review

The Osteogenic Properties of Calcium Phosphate Cement Doped with Synthetic Materials: A Structured Narrative Review of Preclinical Evidence

Siti Sarah Md Dali [1], Sok Kuan Wong [1,*], Kok-Yong Chin [1] and Fairus Ahmad [2]

1   Department of Pharmacology, Faculty of Medicine, Universiti Kebangsaan Malaysia, Jalan Yaacob Latif,
    Bandar Tun Razak, Cheras, Kuala Lumpur 56000, Malaysia; aramddali96@gmail.com (S.S.M.D.);
    chinkokyong@ppukm.ukm.edu.my (K.-Y.C.)
2   Department of Anatomy, Faculty of Medicine, Universiti Kebangsaan Malaysia, Jalan Yaacob Latif,
    Bandar Tun Razak, Cheras, Kuala Lumpur 56000, Malaysia; fairusahmad@ukm.edu.my
*   Correspondence: sokkuan@ukm.edu.my; Tel.: +60-3-9145-9566

Abstract: Bone grafting is commonly used as a treatment to repair bone defects. However, its use is challenged by the presence of medical conditions that weaken the bone, like osteoporosis. Calcium phosphate cement (CPC) is used to restore bone defects, and it is commonly available as a bioabsorbable cement paste. However, its use in clinical settings is limited by inadequate mechanical strength, inferior anti-washout characteristics, and poor osteogenic activity. There have been attempts to overcome these shortcomings by adding various natural or synthetic materials as enhancers to CPC. This review summarises the current evidence on the physical, mechanical, and biological properties of CPC after doping with synthetic materials. The incorporation of CPC with polymers, biomimetic materials, chemical elements/compounds, and combination with two or more synthetic materials showed improvement in biocompatibility, bioactivity, anti-washout properties, and mechanical strength. However, the mechanical property of CPC doped with trimethyl chitosan or strontium was decreased. In conclusion, doping of synthetic materials enhances the osteogenic features of pure CPC. The positive findings from in vitro and in vivo studies await further validation on the efficacy of these reinforced CPC composites in clinical settings.

Keywords: biomimetic materials; bone defect; chemical elements; polymers

1. Introduction

Bone grafts are used to fill missing bone segments, improve skeletal projection, and provide mechanical support in bone defects by promoting osseous ingrowth, providing a structural substrate, and acting as a vehicle for controlled drug delivery in bone healing [1,2]. Although bone grafting is a widely utilised treatment to rebuild bone, the management of bone defects remains a great challenge, especially in individuals with medical conditions which compromise the bone healing process, such as osteoporosis, diabetes, and hypothyroidism [3]. An excellent bone graft should meet the characteristics of bioactive, biocompatible, osteoinductive, osteoconductive, resorbable, and high mechanical strength [4].

Autogenous bone graft represents the gold standard for treating bone defects because it does not cause immunoreaction and has osteoconductive properties. However, the use of autogenous bone grafts in clinical practice is restricted by limited bone grafts that are readily available, as well as the high incidence of complications at the donor and recipient sites [5]. Other alternatives used to optimise treatment include allografts and xenografts. Donor site morbidity issues are avoided by using these alternatives. However, they require sterilisation and purification, do not produce osteoconductive signals, and lack living cells. Additionally, they have the potential to cause bacterial or viral infections as well as a host

tissue immunological reaction after implantation [6]. Herein, artificially produced bone grafts have been considered for the reasons of unlimited supply, minimal risk of disease transmission or immunoreaction, easy sterilisation and storage, as well as the availability of different shapes and sizes for surgical applications [7].

Calcium phosphate cement (CPC) is a synthetic self-setting material serving as an alternative to treat bone defects. CPC comprises a liquid phase and a calcium phosphate-solid phase in which they react chemically to form hydroxyapatite when combined. CPC offers the advantages of biocompatibility, injectability, mouldability, and hardening in situ, allowing optimal bone tissue-implant contact even in irregular defect dimensions and minimally invasive surgery, thus making it a highly appealing bone substitute in surgical applications [8]. However, the major drawbacks of CPC are brittleness, low mechanical strength, inferior anti-washout, and the lack of osteogenic ability, which decreases the implant stability that limits its application to non-stress bearing locations. To overcome these shortcomings, many studies have been conducted to design and fabricate CPCs enhanced by biological and synthetic materials with superior mechanical strength and osteogenic properties.

A recent review has been published to summarise the incorporation of CPC with materials derived from living organisms (including bone-related transcription factors, proteins, polysaccharides, and blood components) in treating bone defects [9]. Herein, the current review confers a comprehensive overview of the CPC reinforced by synthetic materials on their physical, mechanical, and biological properties (Figure 1). The available evidence indicates the strategies are reinforcement with synthetic polymers, biomimetic materials, chemical elements or compounds, and the combination of several synthetic materials.
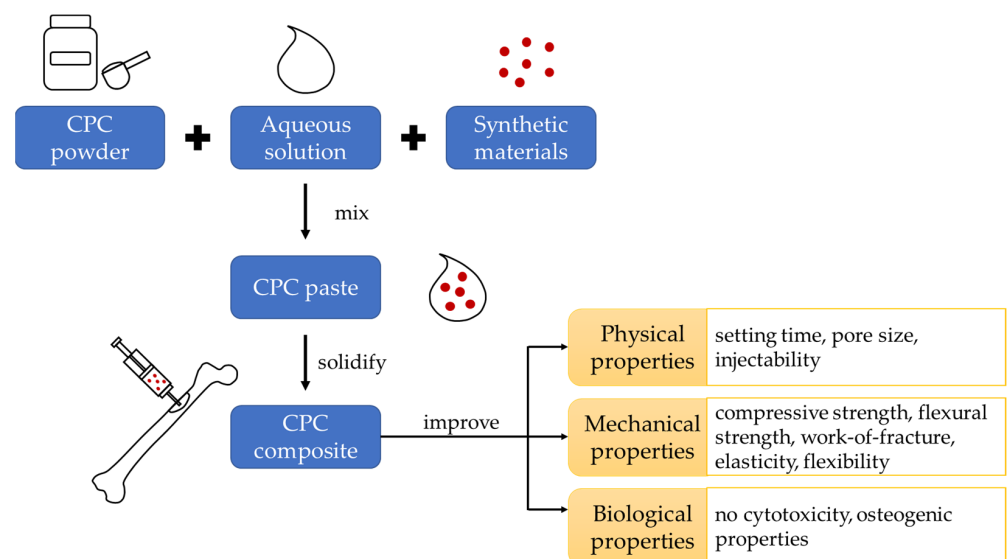
Figure 1. Conceptual framework of the review.

2. Literature Search

Literature acquisition was performed using the PubMed and Scopus databases with the search string: (enhancement OR improvement OR reinforcement) AND (calcium phosphate cement) AND (bone OR osteoporosis OR fracture OR osteoblast OR osteoclast OR osteocyte). From the search, we obtained 815 and 348 records from inception until 15 January 2023 from PubMed and Scopus, respectively. Duplicate articles ($n = 222$) were excluded. The titles and abstracts were initially screened to exclude reviews, non-English, articles, books, book chapters, commentaries, conference papers, letters to the editor, meta-analyses, and irrelevant articles. Subsequently, the full-text articles were screened based on the inclusion and exclusion criteria. The main objective of this review is to summarise the characteristics of CPC enhanced with synthetic materials, defined as materials made by humans through chemical synthesis. The exclusion criteria of this review are (a) the

reinforcement of CPC with biological materials derived from living organisms; (b) original research articles not reporting bone parameters as the primary outcomes; and (c) original research articles with the absence of in vitro and in vivo experimental methods. A total of 30 relevant original research articles were included in this review. The evidence collection framework is summarised in Figure 2.
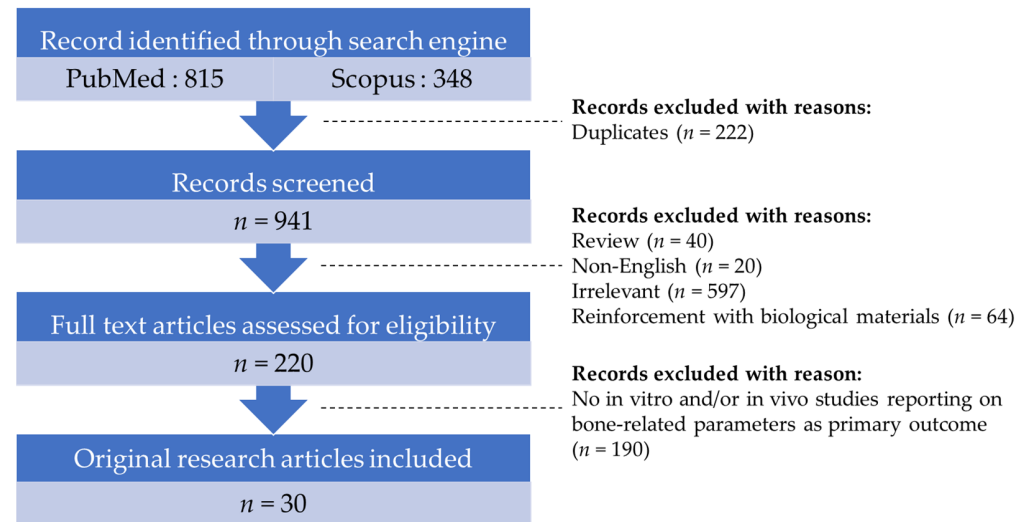
Figure 2. Evidence collection framework.

3. The Enhancement of CPC Using Synthetic Materials

3.1. Synthetic Polymers

Synthetic polymers refer to macromolecules artificially produced in laboratories through repetitive bonding of multiple monomers [10,11]. Several polymers, including poly(lactic-co-glycolic acid) (PLGA), PEGylated poly(glycerol sebacate) (PEGS), and sodium polyacrylate (PAAS), have been incorporated into CPC to enhance its properties (Table 1).

PLGA is produced by the co-polymerisation of glycolic acid and lactic acid. It was commonly used as an enhancer for CPC as it has excellent biocompatibility, and the degradation time can be controlled. A study by Lu et al. showed that the addition of PLGA with different particle morphologies influenced the characteristics of CPC. Their findings indicated that CPC incorporated with dense spherical and irregularly shaped PLGA had proper setting time and improved compressive strength, whereas porous PLGA prolonged final setting time and decreased compressive strength of CPC. However, PLGA favoured cell proliferation of mouse bone mesenchymal stem cells regardless of their morphologies [12]. In another study, the addition of PLGA fibres electrospun on CPC exhibited higher flexural strength and work-of-fracture as compared to the CPC without PLGA fibres. The seeding of human umbilical cord mesenchymal stem cells (hUCMSCs) on CPC incorporated with PLGA fibres showed rapid cell proliferation and mineralisation. The expressions of alkaline phosphatase (ALP), osteocalcin (OCN), and collagen type I (COL1) were higher in hUCMSCs cultured on CPC containing PLGA [13]. Likewise, good cell proliferation and growing ALP activity were detected using rat bone marrow mesenchymal stem cells (rMSCs) seeded on PLGA/CPC scaffolds [14]. In the same study, the implantation of CPC with PLGA on bone defects at the femora of New Zealand white rabbits showed that the implant was gradually replaced by the host's new bones and numerous osteoblasts after 16 weeks [14]. A study done by Maenz et al. also showed improved bone microstructure, bone mineral density (BMD), bone biomechanical compression strength, and static bone histomorphometry in ageing osteopenic female sheep with lumbar vertebrae bone defects and subjected to implantation using CPC incorporated with PLGA after 3 and 9 months [15].

PEGS is a biodegradable elastomer formed from the polycondensation of glycerol and sebacic acid. It has been developed to address the drawbacks of CPC in enhancing mechanical robustness, biocompatibility, bioactivity, and osteogenic activity for bone re-

generation [16,17]. Ma et al. conducted in vitro and in vivo experiments to investigate the effects of PEGS-modified CPC scaffold for bone regeneration using rMSCs and rat calvarial defect model. The results indicated an increase in cell viability, cell proliferation, cell attachment, and osteogenic differentiation of rMSCs on PEGS/CPC scaffolds. New bone formation, greater mineralisation rate, higher bone volume/total volume (BV/TV), and promoted osteogenesis were also detected in rats subjected to two critical-sized (5 mm) calvarial defects and implanted with PEGS/CPC scaffold [16].

PAAS is a cross-linked polymer containing sodium with a super-absorbing ability. It is non-toxic and biocompatible, suggesting that it is frequently used as a food additive and has a potential application in drug delivery. When dissolved in aqueous solutions, PAAS has a high viscosity, strong hydrophilicity, and shape retention properties, thus rendering it a potential enhancer to enhance the anti-washout property of CPC [18]. A previous study demonstrated that the incorporation of PAAS into CPC enhanced the anti-washout, injectability, and compressive strength of the cement paste while retaining the setting time and material microstructure. The mouse mesenchymal stem cells were well-adhered, spread, and proliferated when incubated on PAAS/CPC in vitro [18].

Table 1. Bone-sparing properties of CPC enhanced by polymers.

Enhancer	Type of Study	Cell Culture/Animal Model	Findings	References
Dense & irregularly shaped PLGA	In vitro	Mouse bone mesenchymal stem cell	Cell proliferation: ↑, setting time: ↔, degradation rate: ↑, compressive strength: ↑, good biocompatibility	[12]
Porous PLGA			Cell proliferation: ↑, final setting time: ↑, compressive strength: ↓, good biocompatibility	
PLGA	In vitro	hUCMSCs	Flexural strength: ↑, work-of-fracture: ↑, cell proliferation: ↑, ALP: ↑, OCN: ↑, COL1: ↑, mineralisation: ↑	[13]
PLGA	In vitro	rMSCs	Bone regeneration: ↑	[14]
	In vivo	Defect in the femora of New Zealand white rabbits	Cell proliferation: ↑, ALP activity: ↑	
PLGA	In vivo	Bone defect at L4 lumbar vertebral body in aged osteopenicfemale sheep	BV/TV: ↑, BMD: ↑, biomechanical compression strength: ↑, bone erosion: ↓, osteoid volume: ↑, osteoid surface: ↑	[15]
PEGS	In vitro	rMSCs	Cell viability: ↑, cell proliferation: ↑, cell attachment: ↑, COL1: ↑, Runx-2: ↑, OCN: ↑	[16]
	In vivo	Calvarial defect model of male Sprague-Dawley rats	BV/TV: ↑, Tb.Th: ↑, mineralisation: ↑	
PAAS	In vitro	Mouse bone marrow stromal cells	Setting time: ↑, compressive strength: ↑, cell proliferation: ↑	[18]

Abbreviations: ALP, alkaline phosphatase; BV/TV, bone volume/total volume; COL1, collagen type I; hUCMSC, human umbilical cord mesenchymal stem cell; PAAS, sodium polyacrylate; PEGS, PEGylated poly (glycerol sebacate); PLGA, poly(lactic-co-glycolic acid); rMSCs, rat bone marrow mesenchymal stem cells; Tb.Th, trabecular thickness; OCN, osteocalcin; ↑, increase; ↓, decrease; ↔, no change.

3.2. Biomimetic Materials

Biomimetic materials are known as artificial synthetic materials which imitate biological substances of living organisms [19]. A variety of biological signalling cues are

required to provide an optimal environment for the physiological bone healing process. Thus, biomimetic materials can be alternatives to replicate the configuration of the microenvironment in natural bone tissue. Synthetic collagen I mimetic P-15, trimethyl chitosan, and chondroitin sulphate are examples of biomimetic materials incorporated into CPC (Table 2).

Synthetic collagen I mimetic P-15 is a synthetic 15-amino-acid sequence that is identical to the alpha I chain of COL1. It can bind with an inorganic bone matrix (hydroxyapatite), creating ideal conditions of biocompatibility, biodegradability and osteoconduction [20]. Since both CPC and P-15 have similar beneficial properties of osteoinductivity, osteoconductivity, and resorbability, their combination offers synergistic features in maintaining the stability of composite compared to the primary material [21]. A study using human mesenchymal stem cells seeded on chamber slides coated with CPC containing synthetic collagen I mimetic P-15 showed that the osteogenic differentiation was increased, evidenced by higher ALP, osteopontin (OPN), Runt-related transcription factor 2 (Runx-2), COL1, osteonectin, and OCN [21]. In addition, calcium deposits were detected in cells cultured on CPC with synthetic collagen I mimetic P-15 as an enhancer. Using the vertebrae of non-osteoporotic and osteoporotic sheep, the same group of researchers found that the bone augmented with CPC containing synthetic collagen I mimetic P-15 exhibited greater pull-out strength after pedicle screw insertion [21].

Trimethyl chitosan is a quarternised hydrophilic derivative of chitosan, which outperformed the parent molecule by its superior water solubility, biodegradable, biocompatible, and bioadhesive [22]. As it solves the well-known solubility drawback of chitosan, trimethyl chitosan is used as a reinforcing agent added to liquid CPC. The trimethyl chitosan-modified CPC had a longer setting time, improved wettability, and increased load-bearing capacity while maintaining the elasticity and bending strength compared to CPC without trimethyl chitosan additive. In vitro, the osteoblastic-like (MG-63) cells showed increased cell viability on CPC added with trimethyl chitosan, indicating good biocompatibility of the materials [23].

Chondroitin sulphate is a predominant glycosaminoglycan made up of alternating glucuronic acid and N-acetylgalactosamine disaccharide units [24]. It is an important structural component of the extracellular matrix network in bone and cartilage, incorporating fibronectin and growth factors to facilitate cell adhesion, migration, proliferation, and differentiation. Chondroitin sulphate can be animal-derived or manufactured synthetically. It has been introduced into CPC to enhance its osteogenic and integration abilities. Shi et al. (2019) reported that the setting time was prolonged, injectability was improved, and the fibronectin adsorption amount favouring cell adhesion was increased in the CPC paste reinforced with chondroitin sulphate relative to CPC per se. The bone mesenchymal stem cells also showed higher cell proliferation, cell differentiation, as well as osteogenic expression of ALP and OPN when cultured on the chondroitin sulphate-added CPC [25].

Table 2. Bone-sparing properties of CPC enhanced by biomimetic materials.

Enhancer	Type of Study	Cell Culture/Animal Model	Findings	References
Synthetic collagen I mimetic P-15	In vitro	Human mesenchymal stem cell	ALP: ↑, OPN: ↑, Runx-2: ↑, COL1: ↑, osteonectin: ↑, OCN: ↑, calcium deposit: ↑	[21]
	In vivo	Sheep vertebra of non-osteoporotic and osteoporotic model	Pull-out strength: ↑	

Table 2. *Cont.*

Enhancer	Type of Study	Cell Culture/Animal Model	Findings	References
Trimethyl chitosan	In vitro	MG-63 cells	Setting time: ↑, specific surface area: ↓, wettability: ↑, compressive strength: ↔, elastic modulus: ↑, bending strength: ↑, cell viability: ↑, biocompatibility: ↑, load-bearing capacity: ↑	[23]
Chondroitin sulphate	In vitro	Bone mesenchymal stem cells	Setting time: ↑, injectability: ↑, fibronectin adsorption: ↑, cell proliferation: ↑, Runx-2: ↑, COL1: ↑, OCN: ↑, ALP: ↑, OPN: ↑	[25]

Abbreviations: ALP, alkaline phosphatase; BMD, bone mineral density; BV/TV, bone volume/total volume; COL1, collagen type I; OCN, osteocalcin; OPN, osteopontin; Runx-2, Runt-related transcription factor 2; ↑, increase; ↓, decrease; ↔, no change.

3.3. Chemical Elements and Compounds

Chemical elements are defined as substances that cannot be decomposed into simpler materials by the normal chemical process. On the other hand, chemical compounds refer to substances that contain two or more chemical elements held together by chemical bonds. Both chemical elements and compounds, such as strontium, selenium, iron, zinc, copper, magnesium, lithium, silicon, and calcium silicate, have been incorporated into CPC as enhancers (Table 3).

Similar to calcium, strontium is located in group 2 of the periodic table, indicating the comparable chemical properties and biological functions between these elements. Strontium exists as a trace element in the human body, and it concentrates in the bones [26]. With the distinct ability to intensify osteoblastogenesis and suppress osteoclastogenesis, strontium-releasing CPC might be a promising material for the regeneration of bone defects. The reinforcement of CPC by strontium resulted in no significant difference in the setting time but greater compressive modulus in comparison to CPC alone [27,28]. Two in vitro studies demonstrated higher cell proliferation and ALP activity in MG-63 cells [28] and primary human mesenchymal stromal cells seeded on strontium-doped CPC [27]. The performance of strontium-loaded CPC on defect at the non-load bearing (distal femoral condyle) and load-bearing sites (proximal tibia metaphysis) of female merino sheep were evaluated. After 26 weeks of implantation, the bone area and proportion of materials covered with bone were increased, but material degradation and osteoclast formation were not affected [29]. The clinical applicability of strontium-modified CPC in balloon kyphoplasty was tested in an 80-year-old male cadaver via vertebral body reconstruction, in which the sample was injected into the vertebral bodies of a human cadaver. The findings revealed that the strontium-containing CPC had higher viscosity, thus a lower tendency to leak out into the surrounding tissue during treatment compared to the control, PMMA cement [27]. In another study, male Sprague-Dawley rats with calvarial defect and implanted with nanostrontium-loaded CPC had increased bone formation, as well as higher expressions of bone morphogenetic protein-2 (BMP-2), OCN, and osteoprotegerin (OPG) in comparison to those implanted with CPC without nanostrontium [30]. Strontium ranelate is one of the anti-osteoporosis medications in postmenopausal women. The addition of strontium ranelate into CPC caused an increase in cell spreading area, cell proliferation, and expression of COLI, ALP, OCN, and Runx-2 after the culture of mouse bone marrow mesenchymal stem cells [31]. The expression of osteoclastogenesis-related genes coding for tartrate-resistant acid phosphatase (TRAP), cathepsin K (CTSK), matrix metalloproteinase 9 (MMP-9), and carbonic anhydrase II (Car2) was downregulated in the murine macrophage (RAW264.7) cells cultured on strontium ranelate-containing CPC [31]. Although the combination of strontium ranelate and CPC is a promising formula to stimulate

osteogenesis and new bone formation, the potential cardiovascular risks of strontium ranelate should not be neglected.

Selenium is an essential trace mineral required for the synthesis of selenoproteins. The skeletal-promoting effects of selenium have been widely established in vivo, whereby selenium deficiency was associated with impaired bone health which can be reversed through selenium supplementation [32]. Given the potential beneficial effects of selenium on bone, selenium-based biomaterials have been developed to promote bone tissue regeneration. An ovariectomised rat model with bone defect at the femoral epiphysis was utilised to study the effects of selenium in enhancing the efficacy of CPC in the treatment of osteoporotic bone defect for 12 weeks. Micro-computed tomography analysis pointed out that the animals treated with selenium-added CPC exhibited higher BMD, BV/TV, trabecular number (Tb.N), connectivity density (Conn.D), trabecular thickness (Tb.Th), but lower trabecular separation (Tb.Sp). The implantation of selenium-added CPC also resulted in greater new bone formation, mineral apposition rate (MAR), and biomaterial biodegradation at the defect site. The levels of superoxide dismutase (SOD), glutathione peroxidase (GPX), and OPG were raised, whereas the expression of catalase (CAT) and receptor activator of nuclear factor-kappa B ligand (RANKL) were decreased. These findings indicated that the rapid bone-repairing ability of this material might be in part achieved through suppression of oxidative stress and receptor activator of nuclear factor-kappa B (RANK)/RANKL/OPG pathway [33].

Iron is a mineral naturally present in many types of foods and available as a dietary supplement. It is a necessary component of haemoglobins, enzymes, and cytochromes. Accumulating evidence suggested that iron deficiency exerted a negative impact on bone. Female rats fed on an iron-restricted diet had compromised trabecular bone microstructure at lumbar vertebrae [34,35]. Hence, iron sufficiency plays an important role in bone regeneration. Zhang et al. reported that the setting time was shortened, but the injectability and compressive strength were increased in the iron-doped CPC relative to CPC alone. The effects of these materials on osteogenesis and angiogenesis were tested using two different cells, mouse bone marrow stromal cells and human umbilical vein endothelial cells (HUVECs). The cell proliferation of mouse bone marrow stromal cells and expression of ALP, COL1, OPN, and Runx-2 were elevated when incubated with iron-modified CPC. Higher levels of vascular endothelial growth factor (VEGF) and endothelial nitric oxide synthase (eNOS) were also detected in HUVECs when cultured on CPC containing iron [36]. Moreover, iron-incorporated CPC demonstrated good biocompatibility with new bone formation as well as no sign of inflammation and necrosis at the defect site in female sheep after implantation [37].

Zinc is a crucial mineral for the growth, development, and maintenance of healthy bones [38]. A meta-analysis conducted by Ceylan et al. pinpointed that serum zinc concentration was lower in osteoporotic patients than in healthy subjects, and zinc supplementation was effective in increasing bone formation markers and BMD [39]. Based on the beneficial role of zinc in maintaining normal physiological bone growth, the use of zinc as an additive to reinforce CPC for bone tissue regeneration is hypothesised. Two in vitro studies found higher cell viability, cell proliferation, ALP activity, and osteogenic gene expression in murine mesenchymal stem cells and MC3T3-E1 cells seeded on zinc-modified CPC as compared to the cement without zinc [40,41].

Magnesium is the second most abundant intracellular cation in the human body after potassium. Approximately 60% of magnesium is present in bone. Magnesium deficiency negatively impacts bone health in different ways: (a) it directly increases osteoclastic activity and decreases osteoblastic activity; (b) it indirectly induces hormonal changes (such as parathyroid hormone and vitamin D) as well as promotes inflammatory response and oxidative stress, leading to bone loss [42]. Apart from its physiological role in maintaining musculoskeletal health, magnesium is a degradable metal with potential use as an alternative for non-resorbable materials in the fabrication of implantable medical devices [43]. The bone cell response to CPC doped with magnesium has been investigated in vitro and

in vivo by two groups of investigators. Zhang et al. revealed higher fibronectin adsorption, cell attachment, integrin α5β1, ALP activity, COL1 and OCN expression in bone marrow stromal cells cultured on CPC reinforced with magnesium than pure CPC [44]. Another study also showed higher cell proliferation of MG-63 cells cultured on CPC mixed with magnesium [45]. Besides, both studies showed increased osteogenesis and new bone formation in in vivo studies using the calvarial bone defect model in rats and rabbits.

Copper is a vital trace element in the human body for the proper functioning of organs and metabolic processes. Adequate serum copper level is important in maintaining good bone health, whereby lower concentration was associated with decreased BMD, and higher concentration was associated with increased fracture risk [46]. Considering the potential bone-protecting effects of copper, its application can be broadened to the repairing of bone defects. With the addition of copper, there were increases in setting time, compressive strength, and injectability of the CPC. However, there was no significant difference in the porosity of the CPC after the addition of copper. Mouse bone marrow mesenchymal stem cells seeded on CPC containing copper displayed higher adhesion activity, cell proliferation, and osteogenic expression of COL1, OCN, and ALP. HUVECs cultured on the combination of CPC and copper ions showed higher expression of angiogenesis-related genes [including eNOS, VEGF, basic fibroblast growth factor (bFGF), and nitric oxide] compared to pure CPC [47].

Apart from its use in the treatment of bipolar disorder, lithium has received much attention for its osteoprotective properties [48]. Lithium is a well-known inhibitor of glycogen synthase kinase-3 beta (GSK3β), a protein kinase that modulates the canonical Wingless (Wnt)/beta (β)-catenin pathways via phosphorylation of β-catenin as the downstream target [49]. Hence, lithium can be an excellent candidate to be incorporated into CPC to enhance bone regeneration. A lithium chloride-doped CPC was developed and tested for bone regenerative effects in MC3T3-E1 cells and ovariectomised rats with bone defects. The in vitro experiment showed higher cell proliferation, cell differentiation, mineralisation, and osteogenic differentiation after the incubation of MC3T3-E1 cells on a lithium/CPC scaffold. Mechanistically, the osteogenic properties of lithium-modified CPC were mediated through activation of the Wnt/β-catenin pathway, indicated by a higher level of phosphorylated GSK3β and a lower level of phosphorylated β-catenin. In in vivo study, lithium-modified CPC was implanted on bone defect created at the medial tibial shaft of female Sprague-Dawley rats. The findings showed higher BV/TV and increased new bone formation around the defect site implanted with lithium and CPC [50].

Silicon carbide whiskers are fibre-like materials produced by mixing and sintering silicon carbide fibres and alumina powder. It has excellent elasticity, strength, hardness, and chemical stability (such as wear, corrosion, and temperature resistance), thus, is commonly used as a reinforcement material for ceramics, metals, and plastics for a wide range of industrial applications [51]. With these features, silicon carbide whiskers were fused into CPC to overcome its brittleness, resulting in superior strength and toughness for weight-bearing applications. An early study found that the compressive strength, flexural strength, and elastic modulus of CPC were elevated after the addition of silicon carbide whiskers. However, the MC3T3-E1 cells cultured on pure CPC and silicon carbide whiskers/CPC composite showed similar live cell density, cell adhesion, cell viability, and cell proliferation [52].

Calcium silicate is a compound synthesised by reacting calcium oxide and silica at different ratios [53]. Both calcium and silica have a wide application for bone tissue engineering, mainly attributed to their role in promoting osteogenic differentiation and bone calcification, respectively [54]. The outstanding bioactivity and biocompatibility of calcium silicate make it a promising bioceramic in the field of dentistry and orthopaedics [53]. Zhao and colleagues proved that the MC3T3-E1 cells and HUVECs cultured on CPC incorporated with calcium silicate had higher cell proliferation and ALP activity [55].

Table 3. Bone-sparing properties of CPC enhanced by chemical elements/compounds.

Enhancer	Type of Study	Cell Culture/Animal Model	Findings	References
Strontium	In vitro	MG-63 cells	Setting time: ↓, compressive strength: ↔, cell proliferation: ↑, ALP activity: ↑	[28]
Strontium	In vitro	Primary human mesenchymal stromal cells	Setting time: ↔, compressive strength: ↑, cell proliferation: ↑, ALP activity: ↑,	[27]
	In vivo	Vertebral body reconstruction in an 80-year-old male cadaver	Viscosity: ↑, tendency to leak out: ↓	
Strontium	In vivo	Calvarial bone defect in male Sprague-Dawley rats	Bone formation: ↑, BMP-2: ↑, OCN: ↑, OPG: ↑	[30]
Strontium	In vivo	Two bone defects, one at distal femoral condyle and one at proximal tibial metaphysis of adult female merino sheep	B.Ar/T.Ar: ↑, material resorption: ↔, osteoclast number: ↔	[29]
Strontium ranelate	In vitro	Mouse bone marrow mesenchymal stem cells	Cell spreading area: ↑, cell proliferation: ↑, COL1: ↑, ALP: ↑, OCN: ↑, Runx-2: ↑	[31]
	In vitro	RAW264.7 cells	TRAP: ↓, CTSK: ↓, MMP-9: ↓, Car2: ↓	
Selenium	In vivo	Bone defect at femoral epiphysis ofovariectomised rats	BMD: ↑, BV/TV: ↑, Tb.N: ↑, Conn.D: ↑, Tb.Th: ↑, Tb.Sp: ↓, bone regeneration: ↑, biomaterial degradation: ↑, MAR: ↑, SOD: ↑, CAT: ↓, GPX: ↑, OPG: ↑, RANKL: ↓	[33]
Iron	In vitro	Mouse bone marrow stromal cells	Setting time: ↓, injectability: ↑, compressive strength: ↑, cell proliferation: ↑, ALP: ↑, COL1: ↑, OPN: ↑, Runx-2: ↑	[36]
		Human umbilical vein endothelial cells	VEGF: ↑, eNOS: ↑	
Iron	In vivo	Four bone defects created at the proximal and distal extremities of the humerus and femur in female Romanian alpine sheep	New bone and blood vessel formation: ↑, cells at resorption zone: ↑, osteoid formation: ↑, no inflammation & necrosis	[37]
Zinc	In vitro	Mouse bone mesenchymal stem cells	Cell proliferation: ↑, ALP activity: ↑, COL1: ↑, Runx-2: ↑	[40]
Zinc	In vitro	MC3T3-E1 cells	Setting time: ↓, tensile strength: ↑, cell viability: ↑, cell proliferation: ↑, ALP activity: ↑	[41]
Magnesium	In vitro	Rat bone marrow stromal cells	Fibronectin adsorption: ↑, cell attachment: ↑, integrin α5β1 expression: ↑, ALP: ↑, COL1: ↑, OCN: ↑	[44]
	In vivo	Calvarial defect of 4-month-old Sprague Dawley rats	New bone formation: ↑, material residue: ↓	
Magnesium	In vitro	MG-63 cells	Cell proliferation: ↑	[45]
	In vivo	Calvarial defect in New Zealand rabbits	New bone formation: ↑	

Table 3. *Cont.*

Enhancer	Type of Study	Cell Culture/Animal Model	Findings	References
Copper	In vitro	Mouse bone marrow mesenchymal stem cells	Setting time: ↑, compressive strength: ↑, porosity: ↔, injectability: ↑, adhesion activity: ↑, cell proliferation: ↑, COL1: ↑, OCN: ↑, ALP: ↑	[47]
		Human umbilical vein endothelial cells	eNOS: ↑, VEGF: ↑, bFGF: ↑, nitric oxide: ↑	
Lithium chloride	In vitro	MC3T3-E1 cells	Cell proliferation: ↑, ALP activity: ↑, mineralisation: ↑, COL1: ↑, OCN: ↑, OPG: ↑, Runx-2: ↑, p-β-catenin: ↓, p-GSK3β: ↑	[50]
	In vivo	Bone defect at the medial tibial shaft of female ovariectomised Sprague-Dawley rats	BMD: ↑, new bone formation: ↑, the gap was occupied by new bone.	
Silicon carbide whiskers	In vitro	MC3T3-E1 cells	Flexural strength: ↑, work-of-fracture: ↑, elastic modulus: ↑, hardness: ↑, cell adhesion: ↔, cell viability: ↔, cell proliferation: ↔	[52]
Calcium silicate	In vitro	MC3T3-E1 cells	Cell proliferation: ↑, ALP activity: ↑	[55]
		Human umbilical vein endothelial cell		

Abbreviations: ALP, alkaline phosphatase; B.Ar/T.Ar, bone area/total area; BMD, bone mineral density; BMP-2, bone morphogenetic protein-2; BV/TV, bone volume/total volume; Car2, carbonic anhydrase II; CAT, catalase; COL1, collagen type I; Conn.D, connectivity density; CTSK, cathepsin K; eNOS, endothelial nitric oxide synthase; GPX, glutathione peroxidase; MAR, mineral apposition rate; MMP-9, matrix metalloproteinase 9; OCN, osteocalcin; OPG, osteoprotegerin; OPN, osteopontin; p-GSK3β, phosphorylated glycogen synthase kinase-3 beta; RANKL: receptor activator of nuclear factor-kappa B ligand; Runx-2, Runt-related transcription factor 2; SOD, superoxide dismutase; Tb.N, trabecular number; Tb.Sp, trabecular separation; Tb.Th, trabecular thickness; TRAP, tartrate-resistant acid phosphatase; VEGF, vascular endothelial growth factor; ↑, increase; ↓, decrease; ↔, no change.

3.4. Combination between Two or More Synthetic Materials

Two or more synthetic materials can be combined/mixed to enhance CPC (Table 4). PLGA has been incorporated into the CPC as an individual enhancer or in combination with other synthetic materials, such as wollastonite, perfluorocarbon, silicon/zinc, simvastatin/strontium, and alendronate.

Wollastonite is a naturally occurring mineral composed of calcium, silicon, and oxygen. It possesses outstanding performance in apatite mineralisation, biocompatibility, biodegradability, non-toxicity, mechanical properties, osteogenesis, vascularisation, and the ability to release bioactive silicon ions, suggesting its significant application in bone tissue regeneration [56]. Wollastonite has a rapid rate of decomposition, causing a rise in the pH level in the local environment and, subsequently, the release of excessive silicon ions, which can be harmful to cells. For this reason, wollastonite is not typically employed as a bone graft individually [57]. Qian et al. revealed that the flexibility was increased when wollastonite was mixed with PLGA as the enhancer for CPC. The cell attachment, cell proliferation, and expression of Runx-2, COL1, and BSP of mouse bone mesenchymal stem cells on wollastonite/PLGA/CPC composite were improved. Implanted material with wollastonite/PLGA/CPC on bone defect at the femoral condyle of New Zealand rabbits also showed increases in new bone formation, bone matrix, new blood vessels, and a decrease in material residual [57].

Perfluorocarbons are synthetic colourless, odourless, non-flammable, and unreactive compounds consisting of fluorine and carbon. It can dissolve oxygen, thus playing a crucial role in the delivery of oxygen for organ preservation [58]. Recent evidence reported the bone fracture healing properties of nanoscale perfluorocarbon in a rabbit model with radial fractures, as shown by the elevations in soft callus formation, collagen synthesis,

as well as the expression of VEGF, MMP-9, and OCN [59]. Perfluoro-15-crown-5-ether (PFCE) is a commonly used perfluorocarbon, which is chemically and biologically inert, temperature and storage stable, as well as posing no infectious risk. In a study conducted by Mastrogiacomo et al., a novel composite was created by combining PFCE, PLGA, and gold nanoparticles, followed by incorporation into CPC. This composite was tested in vivo using a rat femoral condyle defect model and the increase in new bone formation was seen [60].

Various trace elements are present in the natural physiological extracellular environment to facilitate osteogenesis. Therefore, mimicking the bone microenvironment would require more than one trace element as the doping material. Silicon stimulates collagen synthesis and vascularisation, whereas zinc promotes bone growth and mineralisation. A study by Liang et al. showed increases in initial and final setting time, injectability, and compressive strength when PLGA microsphere and silicon/zinc dual elements were presented in CPC. The osteoimmunomodulatory effects of PLGA/silicon/zinc/CPC scaffold were proven to be superior to either one of the materials mixed with CPC, indicated by higher production of BMP-2 in the rMSCs. The immunomodulatory effects of the composites were tested using the RAW 264.7 macrophages. Better cell adhesion and spreading, lower pro-inflammatory cytokines [tumour necrosis factor-alpha (TNF-α) and interleukin-6 (IL-6)], higher anti-inflammatory mediators [interleukin-10 (IL-10) and transforming growth factor-1 beta (TGF-1β)], as well as raised vascular genes [VEGF and platelet-derived growth factor-BB (PDGF-BB)] were detected in the RAW 264.7 cells seeded on PLGA/silicon/zinc/CPC composite. The implantation of PLGA/silicon/zinc/CPC scaffold on bone defect at the femur of male Sprague-Dawley rats also resulted in higher new bone formation, bone ingrowth, and BV/TV with a lower residual material area as early as week 4 [61].

Simvastatin is a hypolipidemic medication that can promote bone regeneration. Statin exerts pleiotropic effects, which include hypocholesterolemic and bone protective actions via the inhibition of the mevalonate pathway by blocking 3-hydroxy-3-methylglutaryl coenzyme A (HMG-CoA) reductase, an enzyme catalysing the conversion of HMG-CoA to mevalonic acid. Subsequently, the downstream synthesis of cholesterol is suppressed, whereas the expression of bone morphogenetic protein-2 is promoted via inhibition of protein prenylation using isoprenoid intermediates as substrates, such as farnesyl pyrophosphate (FPP) and geranylgeranyl pyrophosphate (GGPP) [62]. The combination of PLGA microsphere, simvastatin, and strontium improved CPC features. For instance, (a) PLGA microsphere provides a good delivery system due to its biodegradation potential; (b) statin enhances the stability of PLGA microspheres; and (c) strontium affects the reactivity of CPC by inducing osteoblastic activity and suppressing osteoclastic activity [30]. The implantation of PLGA/simvastatin/strontium/CPC scaffold for 8 weeks into parietal bone defects in rabbits showed superior osteogenic activities and biocompatibility [30].

Alendronate is a bisphosphonate medication to treat osteoporosis. The anti-resorptive effects of alendronate are mediated through several mechanisms: (a) it directly prevents the development and recruitment of osteoclast progenitors and promotes apoptosis of osteoclasts [63]; (b) it interferes with the mevalonate pathway by inhibiting farnesyl pyrophosphate synthase enzyme and reduced prenylated protein, thus inducing osteoclast apoptosis [64]. A study by van Houdt et al. incorporated alendronate and PLGA into CPC. The findings showed that the increase in alendronate content gradually increased the initial and final setting time but decreased the compressive strength of the composite. The biological performance of the composite was evaluated in vivo using ovariectomised female Wistar rats subjected to femoral condyle bone defect. Micro-computed tomography analysis showed the implanted material was in contact with surrounding bone tissue. In addition, the animals implanted with alendronate and PLGA-loaded CPC displayed stimulated bone formation and raised bone density along with the reduction of material remnants from week 4 to week 12 [3].

Laponite® is a synthetic nanoclay which has been described as a biocompatible disk-shaped silicate [65]. The particle size on Laponite® is 1 nm in thickness and 25–30 nm in

diameter, with a negative charge on the surface and a positive charge at the edge. Laponite® displays non-cytotoxic and osteogenic effects on human bone marrow stromal cells. It also has wide application in the fabrication of composites to enhance mechanical properties [66]. On the other hand, dexamethasone is an anti-inflammatory and immunosuppressive medication used to treat inflammatory conditions. Utilising an in vivo ectopic bone formation model, the muscle of rats implanted with scaffolds containing dexamethasone and BMP-2 had higher bone formation than those implanted with scaffolds containing BMP-2 only, reiterating that the presence of dexamethasone enhanced the osteogenic capability of BMP-2, thus potentially reducing the required dosage of BMP-2 for clinical application [67]. Both Laponite® and dexamethasone were used in combination and added into CPC to enhance its properties. Higher compressive strength and modulus but shorter setting time were noted in CPC encapsulated with dexamethasone-loaded Laponite® nanoplates. When tested in vitro, the proliferation of MG-63 cells was improved after being cultured on dexamethasone/Laponite® nanoplates/CPC composite [68]. Although the osteogenic capability of dexamethasone has been reported, the adverse effects of glucocorticoid in inducing bone loss should be under careful consideration for its suitability to be used as an enhancer for bone tissue engineering.

Table 4. Bone-sparing properties of CPC enhanced by the combination of two or more synthetic materials.

Enhancer	Type of Study	Cell Culture/Animal Model	Findings	References
PLGA + wollastonite	In vitro	Mouse bone mesenchymal stem cells	Flexibility: ↑, cell attachment: ↑, cell proliferation: ↑, Runx-2: ↑, COL1: ↑, BSP: ↑	[57]
	In vivo	Bone defect at femoral condyle of New Zealand rabbits	New bone formation: ↑, material residual: ↓, bone matrix: ↑, new blood vessel: ↑	
PLGA + PFCE + gold nanoparticles	In vivo	Bone defect at femoral condyle of male Wistar rats	New bone formation: ↑	[60]
PLGA + silicon/zinc	In vitro	rMSCs	Setting time: ↑, injectability: ↑, compressive strength: ↑, BMP-2: ↑	[61]
		RAW 264.7 cells	cell adhesion & spreading: ↑, TNF-α: ↓, IL-6: ↓, IL-10: ↑, TGF-1β: ↑, VEGF, PDGF-BB: ↑	
	In vivo	Bone defect at femur of male Sprague-Dawley rats	New bone formation: ↑, BV/TV: ↑, residual material: ↓	
PLGA microspheres + simvastatin + nanostrontium	In vivo	Parietal bone defect in male New Zealand white rabbits	New bone area: ↑, good biocompatibility	[30]
PLGA + alendronate	In vivo	Bone defect at both femoral condyles of ovariectomised female Wistar rats	Setting time: ↑, compressive strength: ↓, bone formation: ↑, BMD: ↑	[3]
Dexamethasone + Laponite® nanoplates	In vitro	MG63 cells	Compressive strength: ↑, setting time: ↓, cell proliferation: ↑	[68]

Abbreviations: BMD, bone mineral density; BMP-2, bone morphogenetic protein-2; BSP, bone sialoprotein; BV/TV, bone volume/total volume; COL1, collagen type I; IL-6, interleukin-6; IL-10, interleukin-10; PDGF-BB, platelet-derived growth factor-BB; PFCE, perfluoro-15-crown-5-ether: PLGA, poly(lactic-co-glycolic acid); rMSCs, rat bone marrow mesenchymal stem cells; Runx-2, Runt-related transcription factor 2; TGF-1β, transforming growth factor-1 beta; TNF-α, tumour necrosis factor-alpha; VEGF, vascular endothelial growth factor; ↑, increase; ↓, decrease.

4. Perspectives

The current review presented evidence on CPC enhancement by several synthetic materials in bone defect healing. The incorporation of various synthetic materials in CPC has been scientifically proven to resolve the limitations of CPC and/or influence the characteristics of CPC in terms of physical, mechanical, and biological properties. The addition of synthetic polymers (such as PLGA and PAAS) resulted in increased setting time, biomechanical strength, and osteogenic properties of CPC. For PLGA, the setting time and compressive strength of the composite were highly dependent on its particle morphology, whereby incorporating dense PLGA leads to proper setting time and increased compressive strength, whereas introducing porous PLGA into CPC prolonged the setting time and decreased compressive strength. Based on the previous evidence, biomimetic materials (such as synthetic collagen and chondroitin sulfate) have been proven to be a potential enhancer for CPC as the reinforced CPC exhibited more superior characteristics of injectability, raised mechanical strength, osteoconductivity, and osteogenic properties than pure CPC, satisfying the requirements for a good bone graft. However, trimethyl chitosan did not improve the compressive strength of the CPC after their combination. Strontium, iron, and zinc reduced, but copper increased the setting time of the incorporated CPC. Most chemical elements and compounds increased biomechanical properties and promoted osteogenic differentiation after addition into CPC. For strontium, both the setting time and compressive strength decreased with increasing content of strontium in the composite. The combination of PLGA with wollastonite or silicon/zinc as an enhancer seemed to increase the flexibility and injectability, which was not observed in the PLGA/CPC composite. The setting time of the composites was also increased when CPC was enhanced by the combination of PLGA and silicon/zinc or alendronate. In addition, alendronate was found to compromise the increased compressive strength conferred by PLGA. The overall characteristics of CPC after the addition of synthetic polymers, biomimetic materials, chemical elements/compounds, or in combination have been summarised (Table 5).

Table 5. The characteristics of CPC upon enhancement by different types of synthetic enhancers.

	Polymers	Biomimetic Materials	Chemical Elements/ Compound	Combination of Synthetic Materials
Physical properties	↑ setting time ↓ pore size	↑ injectability ↑ setting time	↑ injectability (iron and copper) ↓ setting time (except copper increased in setting time)	↑ injectability ↑ setting time (except dexamethasone + Laponite® decreased in setting time)
Mechanical properties	↑ compressive strength ↑ flexural strength ↑ work-of-fracture	↑ compressive strength (except trimethyl chitosan, no improvement in compressive strength) ↑ elasticity	↑ compressive strength (except strontium decreased in compressive strength with an increasing percentage of strontium) ↑ flexural strength	↑ compressive strength (except PLGA + alendronate decreased in compressive strength) ↑ flexibility
Biological properties	No cytotoxicity ↑ osteogenesis ↑ bone density ↓ bone erosion ↑ mineralisation ↑ osteogenic differentiation	No cytotoxicity ↑ osteogenesis ↑ bone density (except synthetic collagen I mimetic P-15, no change in bone density) ↑ osteogenic differentiation	No cytotoxicity ↑ osteogenesis ↑ bone density ↑ osteogenic differentiation	No cytotoxicity ↑ osteogenesis ↑ bone density ↑ osteogenic differentiation

Abbreviations: PLGA, poly(lactic-co-glycolic acid); ↑, increase; ↓, decrease.

Several limitations of current evidence need to be acknowledged. Young osteoporotic animals have been widely used as a model in most of these studies. The presence of other medical conditions may inhibit bone regeneration and thus should be tested in research using a bone defect model in animals with various types of diseases. In addition, small animals (such as rats, mice, and rabbits) were used as research models for bone defects, which may have different prognoses than large animals such as sheep and bovine. It may take a longer time to exert similar outcomes, understand the mechanisms involved, and validate the mechanisms of the components involved to be translated into clinical settings. The synthetic materials used to enhance CPC summarised in the current review were heterogenous, indicating the lack of original evidence to allow the direct comparison between pure CPC and those enhanced by single or multiple synthetic materials in the same experimental setting.

5. Conclusions

In summary, the incorporation of synthetic materials into CPC can help to overcome the drawbacks of the conventional powder-liquid type of cement. The composites displayed enhanced properties in the aspects of mechanical strength and osteogenic activities while retaining CPC's injectability, mouldability, osteoconductivity, biocompatibility and biodegradability; the various composites possess great potential to be used as materials for implantation in bone defect via minimally invasive surgical techniques. It is recommended to validate the effectiveness of synthetically-enhanced cement in human trials and investigate its effects in more challenging conditions such as the coexistence of infection or disease, poor blood supply, and critical bone defects.

Author Contributions: Conceptualisation, S.K.W.; methodology, S.S.M.D. and S.K.W.; validation, S.K.W. and K.-Y.C.; writing—original draft preparation, S.S.M.D. and S.K.W.; writing—review and editing, S.K.W., K.-Y.C. and F.A.; visualisation, S.K.W. and K.-Y.C.; supervision, S.K.W., K.-Y.C. and F.A.; project administration, S.K.W.; funding acquisition, S.K.W. All authors have read and agreed to the published version of the manuscript.

Institutional Review Board Statement: Not applicable.

Informed Consent Statement: Not applicable.

Data Availability Statement: Not applicable.

Conflicts of Interest: The authors declare no conflict of interest.

References

1. Wang, W.; Yeung, K.W.K. Bone grafts and biomaterials substitutes for bone defect repair: A review. *Bioact. Mater.* **2017**, *2*, 224–247. [CrossRef] [PubMed]
2. Zhao, R.; Yang, R.; Cooper, P.R.; Khurshid, Z.; Shavandi, A.; Ratnayake, J. Bone Grafts and Substitutes in Dentistry: A Review of Current Trends and Developments. *Molecules* **2021**, *26*, 3007. [CrossRef] [PubMed]
3. van Houdt, C.I.; Gabbai-Armelin, P.R.; Lopez-Perez, P.M.; Ulrich, D.J.; Jansen, J.A.; Renno, A.C.M.; van den Beucken, J.J. Alendronate release from calcium phosphate cement for bone regeneration in osteoporotic conditions. *Sci. Rep.* **2018**, *8*, 15398. [CrossRef] [PubMed]
4. Canillas, M.; Pena, P.; Antonio, H.; Rodríguez, M.A. Calcium phosphates for biomedical applications. *Boletín De La Soc. Española De Cerámica Y Vidr.* **2017**, *56*, 91–112. [CrossRef]
5. Kloss, F.R.; Offermanns, V.; Kloss-Brandstätter, A. Comparison of allogeneic and autogenous bone grafts for augmentation of alveolar ridge defects-A 12-month retrospective radiographic evaluation. *Clin. Oral Implant. Res.* **2018**, *29*, 1163–1175. [CrossRef]
6. Schroeder, J.E.; Mosheiff, R. Tissue engineering approaches for bone repair: Concepts and evidence. *Injury* **2011**, *42*, 609–613. [CrossRef]
7. Parchi, P.D.; Simonetti, M.; Bonicoli, E.; Piolanti, N.; Scaglione, M. Synthetic Bone Grafting in Aseptic Loosening of Acetabular Cup: Good Clinical and Radiological Outcomes in Contained Bone Defects at Medium-Term Follow Up. *Int. J. Environ. Res. Public Health* **2020**, *17*, 5624. [CrossRef]
8. Lodoso-Torrecilla, I.; van den Beucken, J.J.J.P.; Jansen, J.A. Calcium phosphate cements: Optimization toward biodegradability. *Acta Biomater.* **2021**, *119*, 1–12. [CrossRef]

9. Wong, S.K.; Wong, Y.H.; Chin, K.Y.; Ima-Nirwana, S. A Review on the Enhancement of Calcium Phosphate Cement with Biological Materials in Bone Defect Healing. *Polymers* **2021**, *13*, 3075. [CrossRef]

10. Lim, J.V.; Bee, S.T.; Tin Sin, L.; Ratnam, C.T.; Abdul Hamid, Z.A. A Review on the Synthesis, Properties, and Utilities of Functionalized Carbon Nanoparticles for Polymer Nanocomposites. *Polymers* **2021**, *13*, 3547. [CrossRef]

11. Namazi, H. Polymers in our daily life. *BioImpacts BI* **2017**, *7*, 73–74. [CrossRef] [PubMed]

12. Lu, T.; He, F.; Ye, J. Physicochemical Properties, In Vitro Degradation, and Biocompatibility of Calcium Phosphate Cement Incorporating Poly(lactic-co-glycolic acid) Particles with Different Morphologies: A Comparative Study. *ACS Omega* **2021**, *6*, 8322–8331. [CrossRef] [PubMed]

13. Bao, C.; Chen, W.; Weir, M.D.; Thein-Han, W.; Xu, H.H. Effects of electrospun submicron fibers in calcium phosphate cement scaffold on mechanical properties and osteogenic differentiation of umbilical cord stem cells. *Acta Biomater.* **2011**, *7*, 4037–4044. [CrossRef]

14. He, F.; Ye, J. In vitro degradation, biocompatibility, and in vivo osteogenesis of poly(lactic-co-glycolic acid)/calcium phosphate cement scaffold with unidirectional lamellar pore structure. *J. Biomed. Mater. Res. Part A* **2012**, *100*, 3239–3250. [CrossRef] [PubMed]

15. Maenz, S.; Brinkmann, O.; Kunisch, E.; Horbert, V.; Gunnella, F.; Bischoff, S.; Schubert, H.; Sachse, A.; Xin, L.; Günster, J.; et al. Enhanced bone formation in sheep vertebral bodies after minimally invasive treatment with a novel, PLGA fiber-reinforced brushite cement. *Spine J. Off. J. N. Am. Spine Soc.* **2017**, *17*, 709–719. [CrossRef]

16. Ma, Y.; Zhang, W.; Wang, Z.; Wang, Z.; Xie, Q.; Niu, H.; Guo, H.; Yuan, Y.; Liu, C. PEGylated poly(glycerol sebacate)-modified calcium phosphate scaffolds with desirable mechanical behavior and enhanced osteogenic capacity. *Acta Biomater.* **2016**, *44*, 110–124. [CrossRef]

17. Wang, Y.; Wu, H.; Wang, Z.; Zhang, J.; Zhu, J.; Ma, Y.; Yang, Z.; Yuan, Y. Optimized Synthesis of Biodegradable Elastomer PEGylated Poly(glycerol sebacate) and Their Biomedical Application. *Polymers* **2019**, *11*, 965. [CrossRef]

18. Li, X.; He, F.; Ye, J. Preparation, characterization and in vitro cell performance of anti-washout calcium phosphate cement modified by sodium polyacrylate. *RSC Adv.* **2017**, *7*, 32842–32849. [CrossRef]

19. Glaser, D.E.; Viney, C. Biomimetic materials. In *Biomaterials science*; Elsevier: Amsterdam, The Netherlands, 2013; pp. 349–360.

20. Gomar, F.; Orozco, R.; Villar, J.L.; Arrizabalaga, F. P-15 small peptide bone graft substitute in the treatment of non-unions and delayed union. A pilot clinical trial. *Int. Orthop.* **2007**, *31*, 93–99. [CrossRef]

21. Krenzlin, H.; Foelger, A.; Mailänder, V.; Blase, C.; Brockmann, M.; Düber, C.; Ringel, F.; Keric, N. Novel Biodegradable Composite of Calcium Phosphate Cement and the Collagen I Mimetic P-15 for Pedicle Screw Augmentation in Osteoporotic Bone. *Biomedicines* **2021**, *9*, 1392. [CrossRef]

22. Kulkarni, A.D.; Patel, H.M.; Surana, S.J.; Vanjari, Y.H.; Belgamwar, V.S.; Pardeshi, C.V. *N,N,N*-Trimethyl chitosan: An advanced polymer with myriad of opportunities in nanomedicine. *Carbohydr. Polym.* **2017**, *157*, 875–902. [CrossRef] [PubMed]

23. Gallinetti, S.; Mestres, G.; Canal, C.; Persson, C.; Ginebra, M.P. A novel strategy to enhance interfacial adhesion in fiber-reinforced calcium phosphate cement. *J. Mech. Behav. Biomed. Mater.* **2017**, *75*, 495–503. [CrossRef] [PubMed]

24. Awofiranye, A.E.; Hudson, J.; Tithi, A.D.; Linhardt, R.J.; Vongsangnak, W.; Koffas, M.A. Chondroitin sulfate and its derivatives: A review of microbial and other production methods. *Fermentation* **2022**, *8*, 323. [CrossRef]

25. Shi, H.; Ye, X.; Zhang, J.; Ye, J. Enhanced Osteogenesis of Injectable Calcium Phosphate Bone Cement Mediated by Loading Chondroitin Sulfate. *ACS Biomater. Sci. Eng.* **2019**, *5*, 262–271. [CrossRef] [PubMed]

26. Kołodziejska, B.; Stępień, N.; Kolmas, J. The Influence of Strontium on Bone Tissue Metabolism and Its Application in Osteoporosis Treatment. *Int. J. Mol. Sci.* **2021**, *22*, 6564. [CrossRef] [PubMed]

27. Lode, A.; Heiss, C.; Knapp, G.; Thomas, J.; Nies, B.; Gelinsky, M.; Schumacher, M. Strontium-modified premixed calcium phosphate cements for the therapy of osteoporotic bone defects. *Acta Biomater.* **2018**, *65*, 475–485. [CrossRef]

28. Kuang, G.M.; Yau, W.P.; Lam, W.M.; Wu, J.; Chiu, K.Y.; Lu, W.W.; Pan, H. An effective approach by a chelate reaction in optimizing the setting process of strontium-incorporated calcium phosphate bone cement. *J. Biomed. Mater. Res. Part B Appl. Biomater.* **2012**, *100*, 778–787. [CrossRef]

29. Reitmaier, S.; Kovtun, A.; Schuelke, J.; Kanter, B.; Lemm, M.; Hoess, A.; Heinemann, S.; Nies, B.; Ignatius, A. Strontium(II) and mechanical loading additively augment bone formation in calcium phosphate scaffolds. *J. Orthop. Res. Off. Publ. Orthop. Res. Soc.* **2018**, *36*, 106–117. [CrossRef]

30. Masaeli, R.; Kashi, T.S.J.; Dinarvand, R.; Tahriri, M.; Rakhshan, V.; Esfandyari-Manesh, M. Preparation, characterization and evaluation of drug release properties of simvastatin-loaded PLGA microspheres. *Iran. J. Pharm. Res. IJPR* **2016**, *15*, 205.

31. Wu, T.; Yang, S.; Lu, T.; He, F.; Zhang, J.; Shi, H.; Lin, Z.; Ye, J. Strontium ranelate simultaneously improves the radiopacity and osteogenesis of calcium phosphate cement. *Biomed. Mater.* **2019**, *14*, 035005. [CrossRef]

32. Yang, T.; Lee, S.Y.; Park, K.C.; Park, S.H.; Chung, J.; Lee, S. The Effects of Selenium on Bone Health: From Element to Therapeutics. *Molecules* **2022**, *27*, 392. [CrossRef] [PubMed]

33. Li, T.L.; Tao, Z.S.; Wu, X.J.; Yang, M.; Xu, H.G. Selenium-modified calcium phosphate cement can accelerate bone regeneration of osteoporotic bone defect. *J. Bone Miner. Metab.* **2021**, *39*, 934–943. [CrossRef] [PubMed]

34. Parelman, M.; Stoecker, B.; Baker, A.; Medeiros, D. Iron restriction negatively affects bone in female rats and mineralization of hFOB osteoblast cells. *Exp. Biol. Med.* **2006**, *231*, 378–386. [CrossRef] [PubMed]

35. Medeiros, D.M.; Stoecker, B.; Plattner, A.; Jennings, D.; Haub, M. Iron deficiency negatively affects vertebrae and femurs of rats independently of energy intake and body weight. *J. Nutr.* **2004**, *134*, 3061–3067. [CrossRef]

36. Zhang, J.; Shi, H.; Liu, J.; Yu, T.; Shen, Z.; Ye, J. Good hydration and cell-biological performances of superparamagnetic calcium phosphate cement with concentration-dependent osteogenesis and angiogenesis induced by ferric iron. *J. Mater. Chem. B* **2015**, *3*, 8782–8795. [CrossRef]

37. Vlad, M.D.; Șindilar, E.V.; Mariñoso, M.L.; Poeată, I.; Torres, R.; López, J.; Barracó, M.; Fernández, E. Osteogenic biphasic calcium sulphate dihydrate/iron-modified α-tricalcium phosphate bone cement for spinal applications: In vivo study. *Acta Biomater.* **2010**, *6*, 607–616. [CrossRef]

38. Yamaguchi, M. Role of nutritional zinc in the prevention of osteoporosis. *Mol. Cell. Biochem.* **2010**, *338*, 241–254. [CrossRef]

39. Ceylan, M.N.; Akdas, S.; Yazihan, N. Is Zinc an Important Trace Element on Bone-Related Diseases and Complications? A Meta-analysis and Systematic Review from Serum Level, Dietary Intake, and Supplementation Aspects. *Biol. Trace Elem. Res.* **2021**, *199*, 535–549. [CrossRef]

40. Xiong, K.; Zhang, J.; Zhu, Y.; Chen, L.; Ye, J. Zinc doping induced differences in the surface composition, surface morphology and osteogenesis performance of the calcium phosphate cement hydration products. *Mater. Sci. Eng. C Mater. Biol. Appl.* **2019**, *105*, 110065. [CrossRef]

41. Horiuchi, S.; Hiasa, M.; Yasue, A.; Sekine, K.; Hamada, K.; Asaoka, K.; Tanaka, E. Fabrications of zinc-releasing biocement combining zinc calcium phosphate to calcium phosphate cement. *J. Mech. Behav. Biomed. Mater.* **2014**, *29*, 151–160. [CrossRef]

42. Rondanelli, M.; Faliva, M.A.; Tartara, A.; Gasparri, C.; Perna, S.; Infantino, V.; Riva, A.; Petrangolini, G.; Peroni, G. An update on magnesium and bone health. *Biometals Int. J. Role Met. Ions Biol. Biochem. Med.* **2021**, *34*, 715–736. [CrossRef] [PubMed]

43. Hung, C.C.; Chaya, A.; Liu, K.; Verdelis, K.; Sfeir, C. The role of magnesium ions in bone regeneration involves the canonical Wnt signaling pathway. *Acta Biomater.* **2019**, *98*, 246–255. [CrossRef] [PubMed]

44. Zhang, J.; Ma, X.; Lin, D.; Shi, H.; Yuan, Y.; Tang, W.; Zhou, H.; Guo, H.; Qian, J.; Liu, C. Magnesium modification of a calcium phosphate cement alters bone marrow stromal cell behavior via an integrin-mediated mechanism. *Biomaterials* **2015**, *53*, 251–264. [CrossRef] [PubMed]

45. Cabrejos-Azama, J.; Alkhraisat, M.H.; Rueda, C.; Torres, J.; Blanco, L.; López-Cabarcos, E. Magnesium substitution in brushite cements for enhanced bone tissue regeneration. *Mater. Sci. Eng. C Mater. Biol. Appl.* **2014**, *43*, 403–410. [CrossRef]

46. Qu, X.; He, Z.; Qiao, H.; Zhai, Z.; Mao, Z.; Yu, Z.; Dai, K. Serum copper levels are associated with bone mineral density and total fracture. *J. Orthop. Transl.* **2018**, *14*, 34–44. [CrossRef]

47. Lin, Z.; Cao, Y.; Zou, J.; Zhu, F.; Gao, Y.; Zheng, X.; Wang, H.; Zhang, T.; Wu, T. Improved osteogenesis and angiogenesis of a novel copper ions doped calcium phosphate cement. *Mater. Sci. Eng. C* **2020**, *114*, 111032. [CrossRef]

48. Wong, S.K.; Chin, K.Y.; Ima-Nirwana, S. The Skeletal-Protecting Action and Mechanisms of Action for Mood-Stabilizing Drug Lithium Chloride: Current Evidence and Future Potential Research Areas. *Front. Pharmacol.* **2020**, *11*, 430. [CrossRef]

49. Snitow, M.E.; Bhansali, R.S.; Klein, P.S. Lithium and Therapeutic Targeting of GSK-3. *Cells* **2021**, *10*, 255. [CrossRef]

50. Li, L.; Peng, X.; Qin, Y.; Wang, R.; Tang, J.; Cui, X.; Wang, T.; Liu, W.; Pan, H.; Li, B. Acceleration of bone regeneration by activating Wnt/β-catenin signalling pathway via lithium released from lithium chloride/calcium phosphate cement in osteoporosis. *Sci. Rep.* **2017**, *7*, 45204. [CrossRef]

51. Qian, M.; Xu, X.; Qin, Z.; Yan, S. Silicon carbide whiskers enhance mechanical and anti-wear properties of PA6 towards potential applications in aerospace and automobile fields. *Compos. Part B Eng.* **2019**, *175*, 107096. [CrossRef]

52. Xu, H.H.; Smith, D.T.; Simon, C.G. Strong and bioactive composites containing nano-silica-fused whiskers for bone repair. *Biomaterials* **2004**, *25*, 4615–4626. [CrossRef] [PubMed]

53. Youness, R.A.; Tag El-deen, D.M.; Taha, M.A. A Review on Calcium Silicate Ceramics: Properties, Limitations, and Solutions for Their Use in Biomedical Applications. *Silicon* **2022**, 1–13. [CrossRef]

54. Srinath, P.; Abdul Azeem, P.; Venugopal Reddy, K. Review on calcium silicate-based bioceramics in bone tissue engineering. *Int. J. Appl. Ceram. Technol.* **2020**, *17*, 2450–2464. [CrossRef]

55. Zhao, Q.; Qian, J.; Zhou, H.; Yuan, Y.; Mao, Y.; Liu, C. In vitro osteoblast-like and endothelial cells' response to calcium silicate/calcium phosphate cement. *Biomed. Mater.* **2010**, *5*, 35004. [CrossRef]

56. Zenebe, C.G. A Review on the Role of Wollastonite Biomaterial in Bone Tissue Engineering. *BioMed Res. Int.* **2022**, *2022*, 4996530. [CrossRef] [PubMed]

57. Qian, G.; Fan, P.; He, F.; Ye, J. Novel Strategy to Accelerate Bone Regeneration of Calcium Phosphate Cement by Incorporating 3D Plotted Poly(lactic-co-glycolic acid) Network and Bioactive Wollastonite. *Adv. Healthc. Mater.* **2019**, *8*, e1801325. [CrossRef]

58. Hosgood, S.A.; Nicholson, M.L. The role of perfluorocarbon in organ preservation. *Transplantation* **2010**, *89*, 1169–1175. [CrossRef]

59. Wang, S.; Qiu, J.; Guo, A.; Ren, R.; He, W.; Liu, S.; Liu, Y. Nanoscale perfluorocarbon expedites bone fracture healing through selectively activating osteoblastic differentiation and functions. *J. Nanobiotechnol.* **2020**, *18*, 84. [CrossRef]

60. Mastrogiacomo, S.; Dou, W.; Koshkina, O.; Boerman, O.C.; Jansen, J.A.; Heerschap, A.; Srinivas, M.; Walboomers, X.F. Perfluorocarbon/Gold Loading for Noninvasive in Vivo Assessment of Bone Fillers Using (19)F Magnetic Resonance Imaging and Computed Tomography. *ACS Appl. Mater. Interfaces* **2017**, *9*, 22149–22159. [CrossRef]

61. Liang, W.; Gao, M.; Lou, J.; Bai, Y.; Zhang, J.; Lu, T.; Sun, X.; Ye, J.; Li, B.; Sun, L. Integrating silicon/zinc dual elements with PLGA microspheres in calcium phosphate cement scaffolds synergistically enhances bone regeneration. *J. Mater. Chem. B* **2020**, *8*, 3038–3049. [CrossRef]

62. Hasan, W.N.W.; Chin, K.Y.; Jolly, J.J.; Ghafar, N.A.; Soelaiman, I.N. Identifying Potential Therapeutics for Osteoporosis by Exploiting the Relationship between Mevalonate Pathway and Bone Metabolism. *Endocr. Metab. Immune Disord. Drug Targets* **2018**, *18*, 450–457. [CrossRef] [PubMed]

63. Hughes, D.E.; Wright, K.R.; Uy, H.L.; Sasaki, A.; Yoneda, T.; Roodman, G.D.; Mundy, G.R.; Boyce, B.F. Bisphosphonates promote apoptosis in murine osteoclasts in vitro and in vivo. *J. Bone Miner. Res. Off. J. Am. Soc. Bone Miner. Res.* **1995**, *10*, 1478–1487. [CrossRef] [PubMed]

64. Tricarico, P.M.; Girardelli, M.; Kleiner, G.; Knowles, A.; Valencic, E.; Crovella, S.; Marcuzzi, A. Alendronate, a double-edged sword acting in the mevalonate pathway. *Mol. Med. Rep.* **2015**, *12*, 4238–4242. [CrossRef]

65. Ruzicka, B.; Zaccarelli, E. A fresh look at the Laponite phase diagram. *Soft Matter* **2011**, *7*, 1268–1286. [CrossRef]

66. Choi, D.; Heo, J.; Aviles Milan, J.; Oreffo, R.O.C.; Dawson, J.I.; Hong, J.; Kim, Y.-H. Structured nanofilms comprising Laponite® and bone extracellular matrix for osteogenic differentiation of skeletal progenitor cells. *Mater. Sci. Eng. C* **2021**, *118*, 111440. [CrossRef] [PubMed]

67. Yuasa, M.; Yamada, T.; Taniyama, T.; Masaoka, T.; Xuetao, W.; Yoshii, T.; Horie, M.; Yasuda, H.; Uemura, T.; Okawa, A.; et al. Dexamethasone enhances osteogenic differentiation of bone marrow- and muscle-derived stromal cells and augments ectopic bone formation induced by bone morphogenetic protein-2. *PLoS ONE* **2015**, *10*, e0116462. [CrossRef]

68. Roozbahani, M.; Kharaziha, M. Dexamethasone loaded Laponite(®)/porous calcium phosphate cement for treatment of bone defects. *Biomed. Mater.* **2019**, *14*, 055008. [CrossRef]

Article

Prospect of Bioactive Curcumin Nanoemulsion as Effective Agency to Improve Milk Based Soft Cheese by Using Ultrasound Encapsulation Approach

Uday Bagale [1],* , Ammar Kadi [1] , Mostafa Abotaleb [2] , Irina Potoroko [1] and Shirish Hari Sonawane [3]

1   Department of Food and Biotechnology, South Ural State University, Chelyabinsk 454080, Russia
2   Department of System Programming, South Ural State University, Chelyabinsk 454080, Russia
3   Department of Chemical Engineering, National Institute of Technology Warangal, Telangana 506004, India
*   Correspondence: bagaleu@susu.ru; Tel.: +7-(351)-267-93-80

Abstract: The aim of this paper was to determine the effect of stabilized curcumin nanoemulsions (CUNE) as a food additive capable of directionally acting to inhibit molecules involved in dairy products' quality and digestibility, especially cheese. The objects were cheeses made from the milk of higher grades with addition of a CUNE and a control sample. The cheeses were studied using a scanning electron microscope (SEM) in terms of organoleptic properties, such as appearance, taste, and aroma. The results show that the addition of CUNEs improved the organoleptic properties compared to the control cheese by 150% and improved its shelf life. The SEM study shows that formulation with CUNE promotes the uniform distribution of porosity. The CUNE-based cheese shows a better sensory evaluation compared to the emulsion without curcumin. CUNE-processed cheese provided better antioxidant and antimicrobial analysis than the control sample and offers added value to the dairy sector.

Keywords: curcumin nanoemulsion; cheese; ultrasound; SEM; self-life and sensory analysis

1. Introduction

Dairy products are an important sector of the food industry. Daily dairy consumption varies from 150 to 500 g per capita in different countries and is steadily increasing [1]. Processed cheese has gained more success, owing to a combination of economical available ingredients and better functional properties than other cheese [2,3]. However, processed cheeses have a problem with storage and shelf life. This problem can be minimized by the fortification of cheese with bio-active compounds. Bioactive compounds, such as essential oils, medical plants, and fruit extracts, have resulted in better versions of cheese [4–7]. The addition of bioactive compounds in processed cheese also affects the taste and the consistency [7].

A common antioxidant is curcumin, extracted from turmeric root [7–11]. Curcumin is a polyphenol, characterized by more than one phenolic group per molecule. Turmeric contains a wide variety of vitamins and other substances essential for the human organism. In addition, curcumin has antioxidant, anticarcinogenic, immunomodulatory, antifungal, and anti-inflammatory properties, which make it suitable in the medical and food industries [9–15]. However, the poor water solubility of curcumin limits its direct use. This poor solubility also leads to low absorption, fast metabolism, and quick systematic elimination [16,17]. To enhance the bioavailability and biological activity of curcumin, structural modifications are required [18].

Most research reported that stability can be improved by scaling to nanosize particles using high or low energy methods, such as ultrasound, high speed homogenization, or solvent evaporation [9,10,17,19]. Curcumin nanoparticles have a higher surface charge and surface area, are more hydrophobic, and have greater antioxidant activity than untreated

curcumin. Curcumin nanoparticles have higher water solubility and suspension, which improves their antimicrobial activity [20–22].

The use of nanoemulsions is a promising technique for incorporating these bioactive complexes into foods [23–25]. Nanoscale curcumin provides superior properties in comparison to micron-scale curcumin, allowing it to mix effectively with other food ingredients to reduce the biological and enzymatic reactions, and allowing innovative products to be fabricated [26]. Nanoemulsions can be exploited in the food industry, since there are different approaches for their preparation, and they are stable systems for the encapsulation of bioactive substances [24–26]. Ultrasound techniques produce bioactive nanoemulsions with a higher yield and encapsulation efficiency [9,15,17,26,27].

The present study investigated the incorporation of curcumin in cheese in order to improve its dietary value. In this work, with the aid of ultrasound technology and polysorbate 20 as an emulsifier, a stable curcumin nanoemulsion (CUNE) was created. Data on particle size, encapsulation effectiveness, and stability were used to characterize the nanoemulsions. These were incorporated into the cheese which was checked, using a scanning electron microscope, against a control sample for sensory evaluation, antimicrobial activity.

2. Results and Discussion

Initially, we stabilized the CUNE containing edible oil and Tween 20 by using a sonochemical approach. To obtain stable CUNE, we optimized the oil and emulsifier concentration along with curcumin concentration. In the nanoemulsion, the curcumin concentration was encapsulated in the oil phase from 0.15 g to 0.75 g. We tried different inner and outer phase combinations to make a stable nanoemulsion, but only a few were found to be stable on centrifuge and heating at 80 °C for 30 min.

2.1. Characterization of Nanoemulsion

In the current study, we first used a sonochemical method to stabilize the curcumin nanoemulsion made up of edible oil and Tween 20. The curcumin concentration ranged from 0.75 g to 0.15 g in the oil phase of the current o/w nanoemulsion technology. Only a few of the inner and outer phase combinations we explored to create a stable nanoemulsion were discovered to be stable after centrifugation and 30 min of heating at 80 °C.

Particle Size Distribution, Polydispersity Index (PDI), and Optical Microscope for Stable Nanoemulsion

Nanotrac software was used to analyze the diameter size of the nanoemulsion and its polydispersity index (PDI) based on dynamic light scattering. Stable nanoemulsion results for the particle size and PDI are shown in Table 1, while stable particle size distribution is shown in Figure 1. With a PDI smaller than 0.4, stable nanoemulsions have a limited particle size distribution. According to Ahmed et al. (2012), an emulsion will not be stable if the PDI is higher than 0.5. In terms of their release phenomena, they also proposed that medium chain triglyceride-based nanoemulsions offer superior stability and improve curcumin's bio-availability. According to Bagale et al., stable nanoemulsion with 50:50 (long-chain triglyceride: short-chain triglyceride) oil ratio has polydispersity less than 0.4 and an average droplet size of 200 nm. CUNE with medium-chain triglyceride palm oil has less water solubility than short-chain triglyceride oil, which shows a polydispersity index in the range of 0.3–0.357.

Figure 2a,b show the optical microscope image of CUNE with concentrations of 0.15 and 0.75 g curcumin. We can observe the encapsulation of curcumin in the oil in water morphology. The dark spots present in micelles are curcumin particles, which are surrounded by a layer of oil droplets in a stable form without any aggregation. There are some micelles without curcumin. The optical microscope images show the particle size distribution of the oil–water droplets. The droplet sizes are approximately 10–20 nm, calculated by using TEM and confirmed through light scattering. These oil droplets are tiny and disperse thoroughly in the nanoemulsion. The total phenolic content method used

the normal correction curve of gallic acid at variance with an R^2 value of 0.9894 to calculate encapsulation efficiency. CUNE has a higher encapsulation efficiency because of the small surface tension among droplets; flocculation, and accumulation are eluded, cultivating curcumin solubility. According to Bagale et al. (2022), who optimized the sonication period, polydispersity gives insight into the homogeneity of the size distribution and was low (0.3) for all samples, indicating the creation of monodisperse systems. This suggests that sonication would increase the effectiveness of encapsulation. Tween 20 concentrations that promote curcumin stability also increase the effectiveness of encapsulation [28].

Table 1. pH and gravitational stability of nanoemulsions data.

Exp No	pH	Gravitational Stability at Room Temperature(Days)	Particle Size for Fresh Sample (nm)	Particle Size after 60 Days (nm)	PDI	Zeta Potential mV	Encapsulation Efficiency
CUNE 1	5.68	15	180 ± 0.5	820 ± 5	0.63	−15	
CUNE 2	5.62	70	13.35 ± 0.5	14.05 ± 0.5	0.27	−25	
CUNE 3	5.69	75	11.05 ± 0.5	12 ± 05	0.35	−27	94%
CUNE 4	5.55	15	135 ± 3	625 ± 10	0.43	−18	
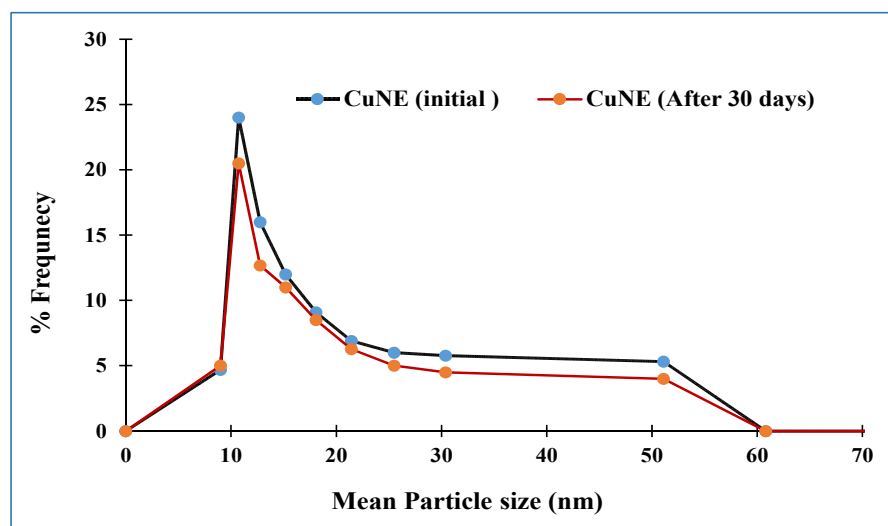
Figure 1. Stability data of curcumin nanoemulsion sample in term of PSD.
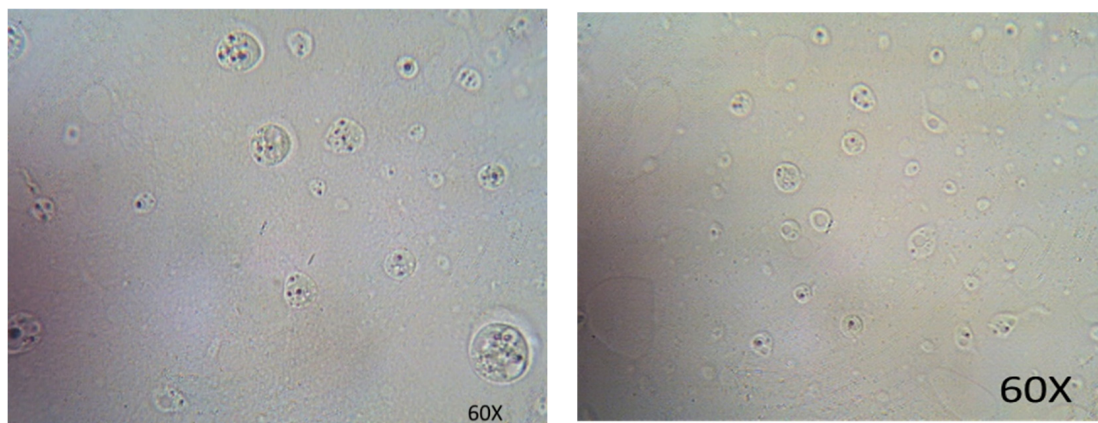
(**a**) CuNE2 (**b**) CuNE3

Figure 2. Optical image for curcumin encapsulation in different nanoemulsion sample.

Figure 3 shows the FTIR spectra of free curcumin and CUNE. The spectra of CUNE resembled that of pure curcumin, which contained all the normal absorption peaks. The two most significant functional groups were C=O stretching (1741.72 cm^{-1}) and O-H bending (1348.24 cm^{-1}). Due to the presence of O-C=O (2953.03 cm^{-1}), O-H (2852.72 cm^{-1}), and C-H (2922.16 cm^{-1}) groups in the curcumin-loaded nanoemulsion, the other bands in the area of 2965–2855 cm^{-1} were provided by the C-H stretching vibration.
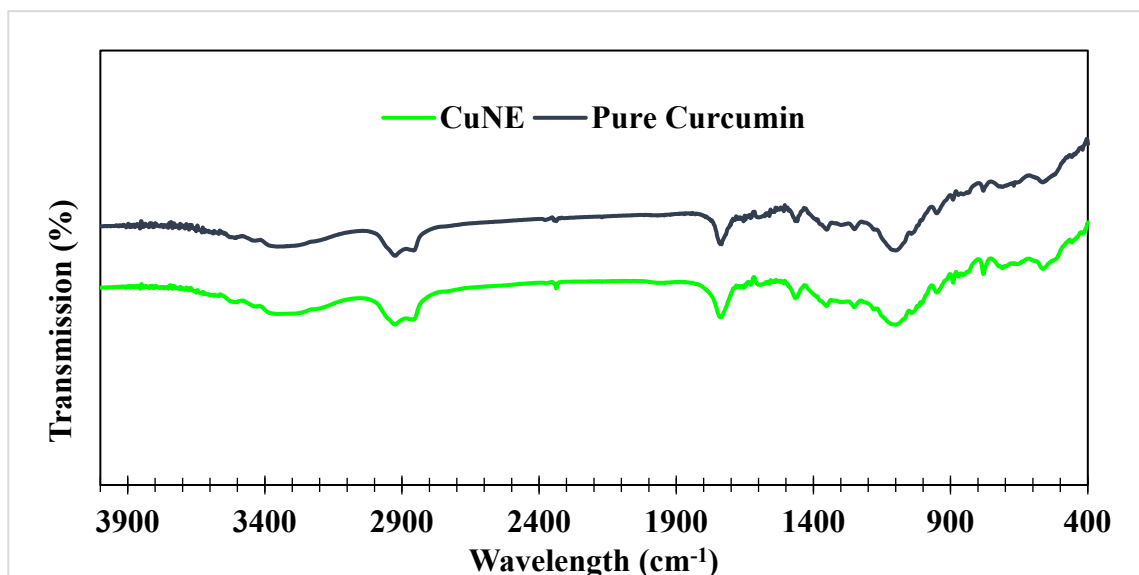
Figure 3. FTIR spectra Free curcumin and Curcumin nanoemulsion.

2.2. Transmission Electron Microscope Analysis of Nanoemulsion

Figure 4 shows that the nanoemulsion has a particle size of 14 nm and is spherical in shape. According to Biswas et al. [20], the noble assets and functionality of the nanoparticles are owing to his higher ratio surface area/volume and nanoscale size and hydrophobicity. They also reported that CUNE with a particle size of approximately 5–50 nm shows higher antimicrobial potential than its natural form.
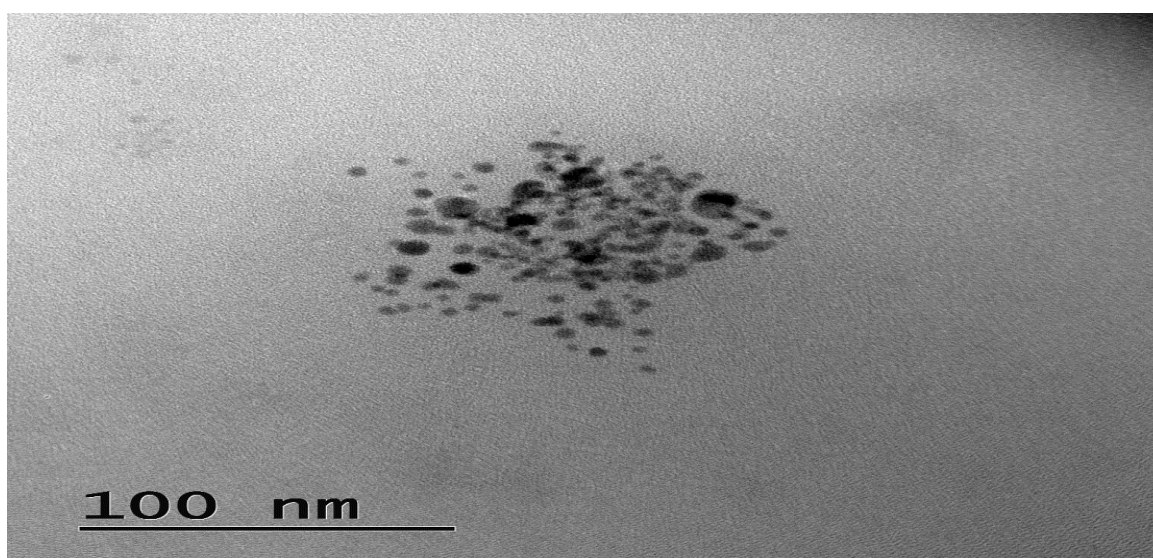
Figure 4. *Cont.*
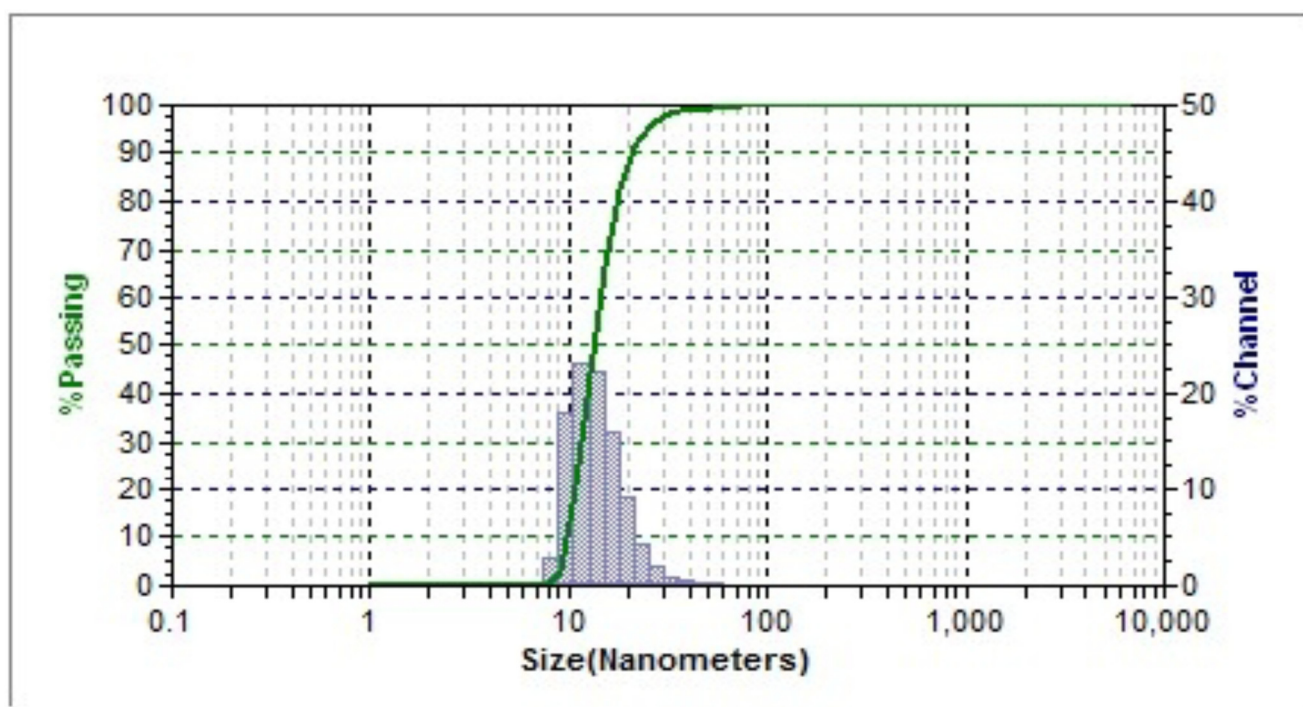
Figure 4. Transmission electron microscope analysis of CUNE sample.

2.3. Antimicrobial Activity Nanoemulsion

The outcomes of the antibacterial potential of CUNE are revealed in Table 2 (Figure 5). CUNE with a concentration of 100 and 50 μg/mL showed the highest antibacterial activity against S. aureus and E. coli. At a concentration of 25 μg/mL, the nanoemulsion showed reasonable antibacterial activity for both strains; however, the lowest antimicrobial inhibition level was at a diameter of 5 mm. An earlier study found that CUNE had better aqueous-phase solubility and dispersibility than pure curcumin and hence had antibacterial activity. Any nanoscale particle's antibacterial potential will depend on its physicochemical characteristics (size, shape, and surface qualities), as well as the quantity used. According to Naghadri et al. [29] and Wang et al. [30], nanoparticles smaller than 100 nm have a higher adhesion to the surface of cell membranes than larger nanoparticles, which can cause disruptions in the functions of the cell membrane.

2.4. Curcumin Nanoemulsion in Cheese Formulation and Its Analysis

Based on the above result, we took the curcumin nanoemulsion (CUNE 2) for further study in terms of its addition in cheese formulation.

Table 2. Antimicrobial activity of CUNE.

Microorganism	Zone Inhibition Diameter (mm)			
	100 *	50 *	25 *	12.5 *
E. Coli	18	15	13	8.2
S. Aureus	12	9	6	3

Concentration of CUNE are in percent as follows 100 * = 100 μg NC/mL, 50 * = 50 μg NC/mL, 25 * = 25 μg NC/mL, and 12.5 * = 12.5 μg NC/mL. Note: All analysis measurement was conducted in triplets and have ± SEM ($p < 0.05$).

(**a**)   (**b**)
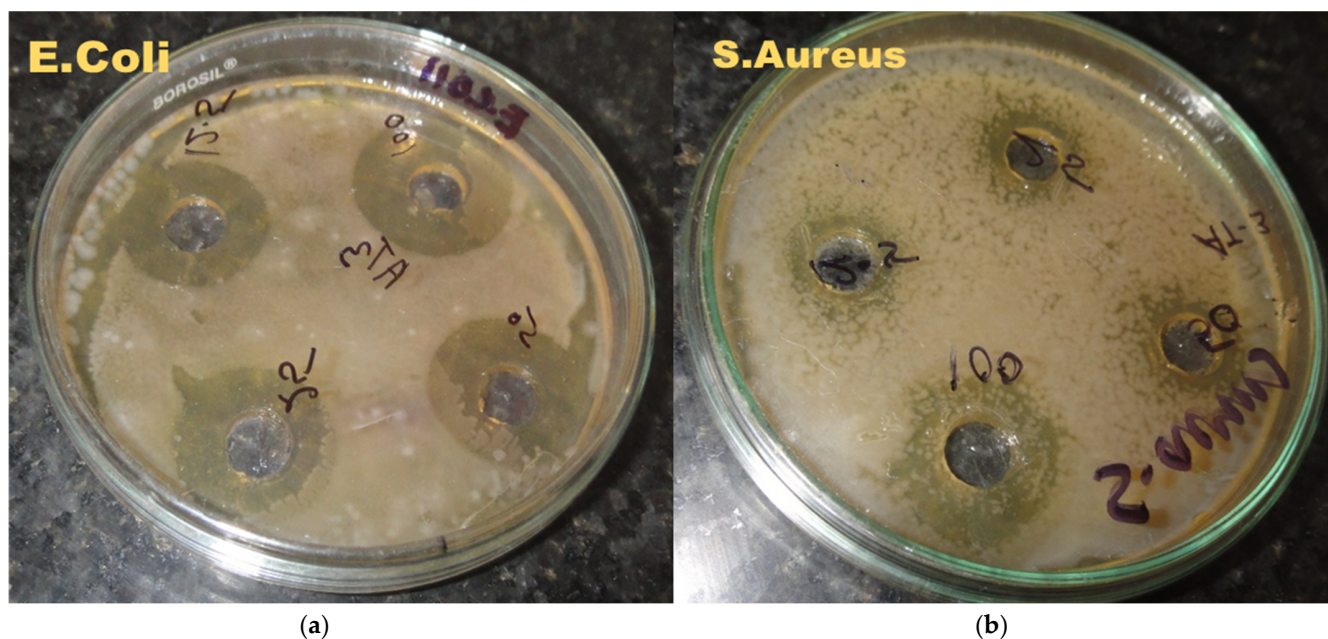
Figure 5. Antimicrobial activity of curcumin nanoemulsion for (**a**) *E. coli* and (**b**) *S. aureus*.

2.4.1. Sensory Analysis of Cheese

The number of foods enriched with bioactive compounds are increasing in the dairy and food industries. As bioactive compounds show better antioxidant activity, these food products promote health and wellness. Figure 6 provides an evaluation of the CUNE-enriched effect on the organoleptic properties of cheese compared to the control and emulsion cheeses during a 60-day period (at 4 °C).

With a decrease in the particle size, there is an increase in the surface-to-volume ratio, and a reduction of the concentration at which compounds are added to food products. This does not hamper its sensory analysis compared to the control sample. The data show that lower concentrations can have more strength than otherwise [31], such as a droplet delivering the identical sensory profile [32] or an increase in sensory perception [33]. It is suggested that a larger particle surface causes an increase in the saliva dissolution rate and, possibly, a stronger taste perception. Figure 6 shows that there were no significant differences ($p > 0.05$) in color, smell, appearance, acceptability, or taste between the control and CUNE-enriched samples. However, when compared to the control and CUNE samples, the emulsion without curcumin samples had the lowest ($p < 0.05$) sensory values. This is owing to the structural change in the cheese matrix caused by the larger particle size of the emulsion affecting the organoleptic values. While the outer layer of a nanoemulsion can be designed to be resistant to the environment during the first stages of ingestion, preventing consumers from experiencing any unpleasant tastes or odors, nanoencapsulation may offer a potential mechanism to physically trap the compounds that cause these unpleasant tastes and odors. The product's quality and acceptability are directly tied to the raw material and production quality. Consumers are showing a preference for minimally processed foods with the highest natural constituents, additives with health benefits such as antimicrobials, and naturally occurring antioxidants. In order to meet this demand, nanotechnology allows for the development of many ingredients' functionality by lowering the concentration of substances, altering their solubility, and enhancing or controlling their effectiveness [31,32].
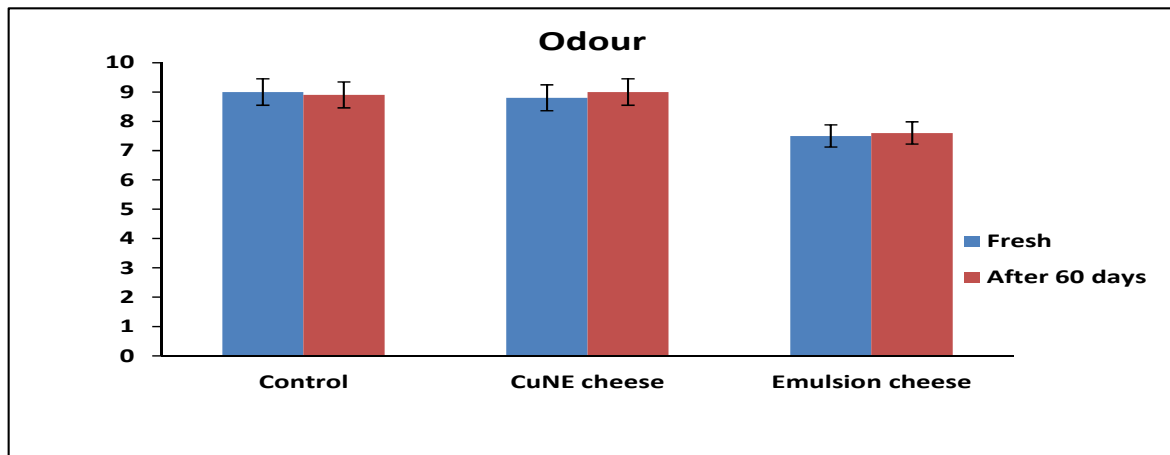
(**a**)
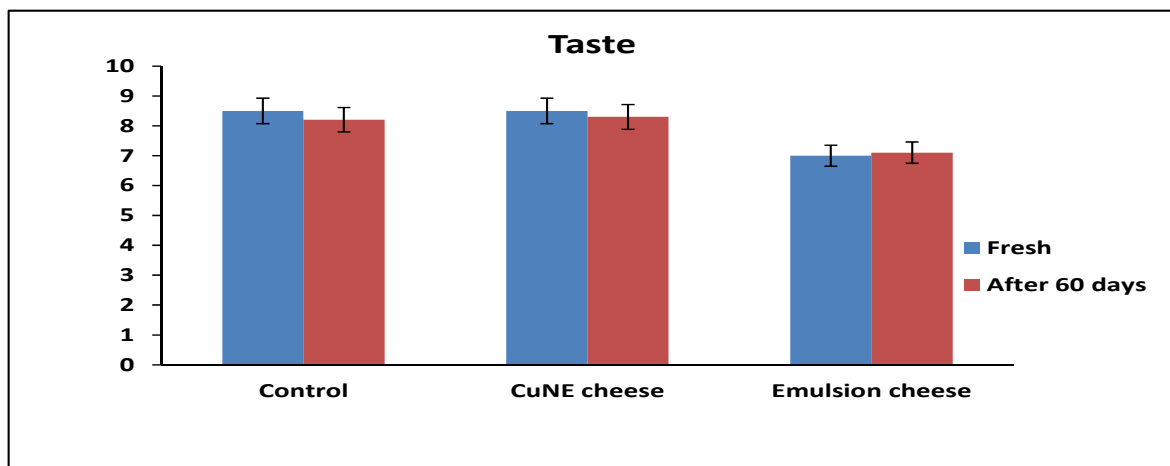
(**b**)
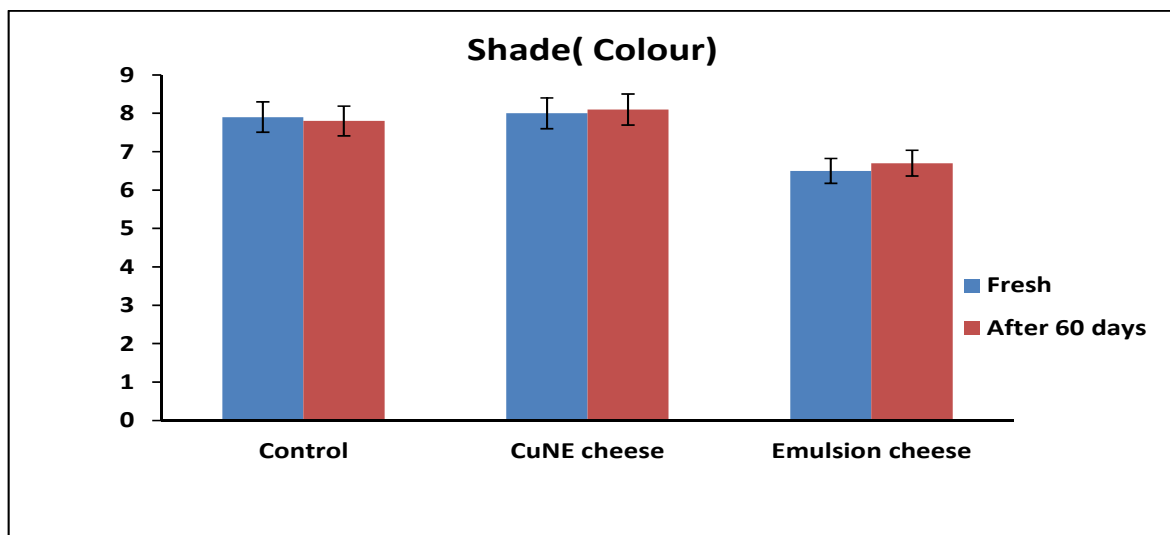
(**c**)

Figure 6. *Cont.*
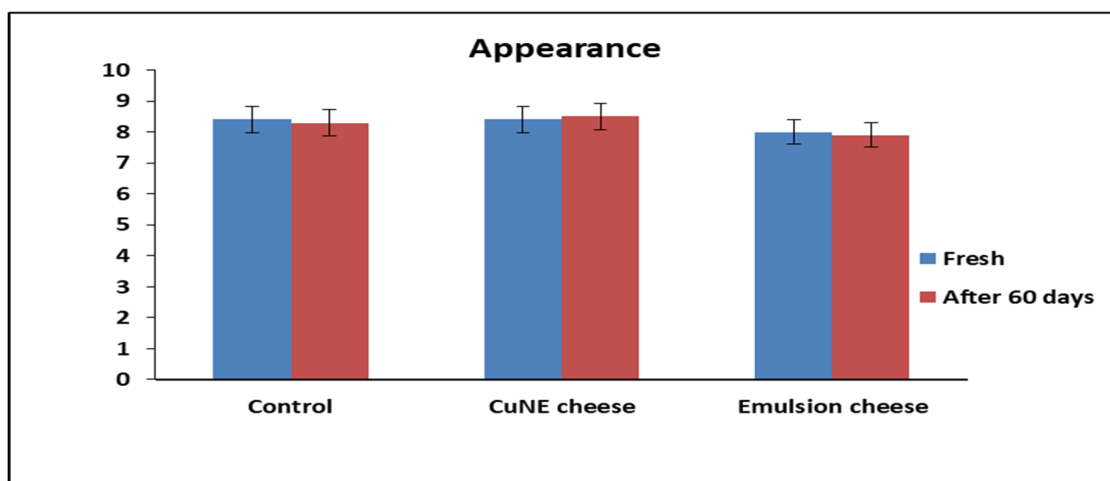
(**d**)
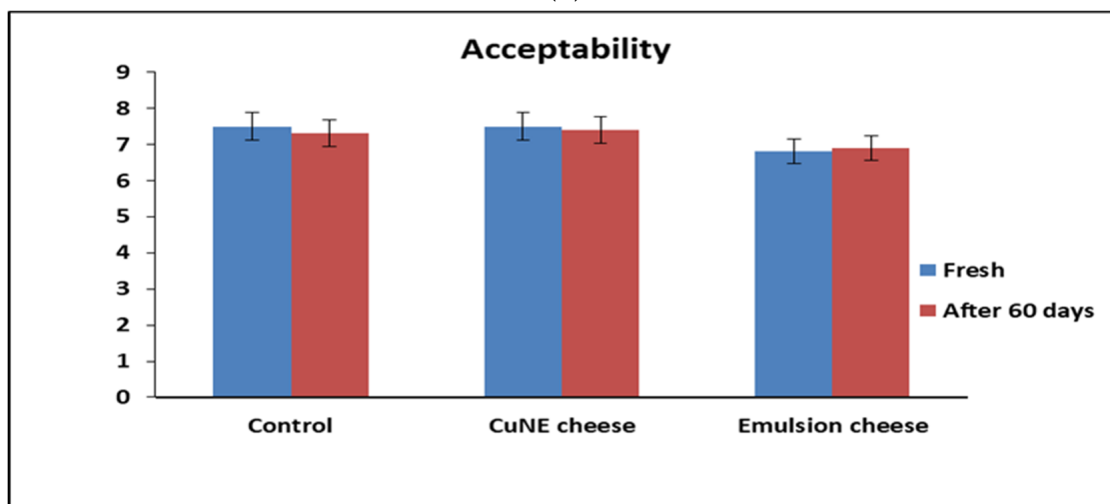
(**e**)

Figure 6. Sensory analysis of cheese sample with addition of curcumin nanoemulsion and emulsion: (**a**) Odor, (**b**) Taste, (**c**) Shade, (**d**) Appearance, and (**e**) Acceptability.

2.4.2. Physicochemical Parameters for Cheese

The physicochemical features of nutriments play a part in defining their effectiveness and shelf life. Table 3 shows that the physicochemical properties of the cheese treated with two types of emulsifiers (CUNE and emulsion) compared to the control sample stored at 4 °C and kept for 30 and 60 days. With the fresh sample as a control, the CUNE- and emulsion-based cheeses do not have significant differences ($p > 0.05$) for dry matter, ash, and protein content. However, after 30 days, there are significant difference ($p < 0.05$) observed in the percentage of dry matter for CUNE and emulsion compared to the control, which increased in dry matter content. As dry matter content increases, the total phenolic content decreases and shows less antioxidant activity. Whereas the CUNE sample has less dry matter content over time, which maintains its integrity in the cheese matrix, as the nanoemulsion, with a smaller particle size, is better distributed within the cheese matrix. Fresh samples from each group did not differ significantly from one another in the content of ash, fat, or protein ($p > 0.05$), while the control samples showed significant differences ($p < 0.05$) after 30 and 60 days of storage. The percentage of fat, protein, and ash increased in the control sample, while the CUNE and emulsion samples showed no significant differences [34,35]. The presence of emulsifiers in the treated samples reduced the increase of dry matter and thus reduced moisture loss compared to the control sample.

Thus, the nanoemulsion is recommended for fortifying cheese. For the pH, there was no noticeable change in the pH values with a storage period of 30 or 60 days.

Table 3. Physicochemical analysis of cheese.

	Storage Time	Ash,%	Dry Matter,%	pH	Protein,%	Fat,%
Control	Fresh	5.53 ± 0.13	39.46 ± 0.34	6.2 ± 0.08	12.12 ± 0.08	18.85 ± 0.27
	30 days	5.98 ± 0.14	42.34 ± 0.11	6.04 ± 0.04	12.66 ± 0.09	19.65 ± 0.2
	60 days	6.01 ± 0.1	43.24 ± 0.15	6.01 ± 0.06	12.91 ± 0.12	20.71 ± 0.13
E1 (Cur)	Fresh	5.66 ± 0.11	39.28 ± 0.33	6.19 ± 0.08	12.63 ± 0.36	18.68 ± 0.23
	30 days	5.71 ± 0.14	40.53 ± 0.11	6.05 ± 0.04	12.6 ± 0.09	18.93 ± 0.38
	60 days	5.75 ± 0.08	41.72 ± 0.22	6.03 ± 0.03	12.68 ± 0.09	19.14 ± 0.12
E2	Fresh	5.61 ± 0.38	39.14 ± 0.57	6.21 ± 0.08	11.72 ± 0.15	18.97 ± 0.27
	30 days	5.64 ± 0.07	41.41 ± 0.48	6.1 ± 0.01	11.7 ± 0.17	19.23 ± 0.21
	60 days	5.69 ± 0.09	41.84 ± 0.22	6.04 ± 0.05	11.74 ± 0.14	19.41 ± 0.12

2.5. Scanning Electron Microscope Analysis of Cheese

SEM was used to study the structural morphology of the cheese matrix with the addition of CUNE and the emulsion in comparison to the control. Three-dimensional images were obtained to facilitate the identification of substances. The photograph of the sample (control samples 1, 2) is shown in Figure 7. There are fewer variances in the protein structure between the CUNE samples compared to the control. There is some free fat present, and the cheese fat and protein clusters are tightly packed. The control sample's protein and fat clusters look smaller than those in the CUNE sample. The control sample has substantially more free fat globules than those seen in the other samples. The fat-free globules in the control sample are smaller than those in the emulsion sample. The hardness was reduced, and the casein network structure softened when CUNE was added, showing that the incorporation of CUNE transformed the structure of the protein–fat network. CUNE was added together with emulsifying salts, which increased the dispersion of fat globules. It is possible to infer that the cheese produced with the CUNE supplement has particle-filled gel networks, where fat globules serve as filler molecules in the protein network. According to [31], foods containing nanoemulsions enhance the functionality of the formulations' constituents. Nanoemulsions can also be utilized to modify texture. Depending on the internal-phase percentage, oil composition, stabilizer (type and concentration), and droplet size, nanoemulsions may exhibit rheological characteristics that are different from those of viscous liquids in viscoelastic solids.
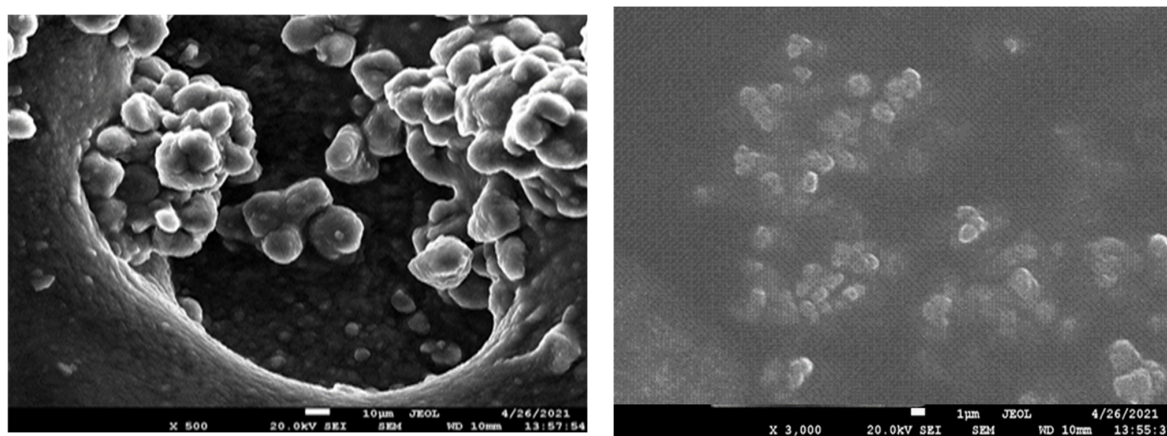
(**A**) **Control Cheese**   (**B**) **CUNE cheese**

Figure 7. *Cont.*
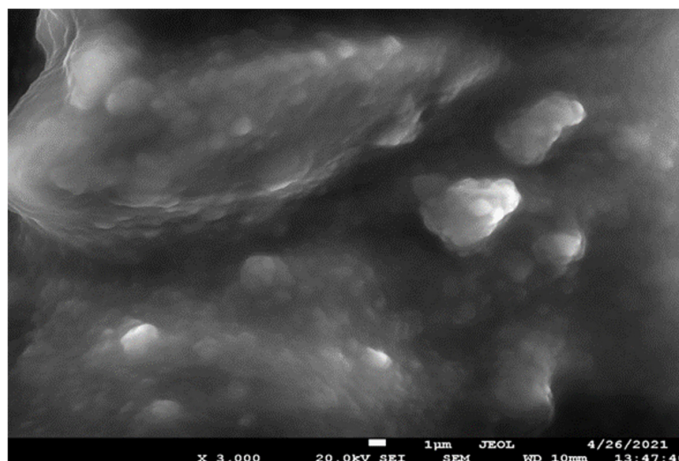
(**C**) **Normal Emulsion**

Figure 7. Photo study experienced samples prepared using scanning electron microscopy (total magnification of ×5000) Cheese matrix: (**A**) Control, (**B**) CUNE (**C**) Normal emulsion.

2.6. Antioxidant Activity of Curcumin Nanoemulsion

As shown in Table 4, the antioxidant capacity of the control sample and samples 1 and 2 is expressed as μg of Trolox equivalents (TE) per g of nanoemulsion. Regardless of surfactant content, the antioxidant capacity of the nanoemulsion as determined by the ferric reducing antioxidant power (FRAP) assay did not show any significant changes. The antioxidant capacity values reported by the FRAP assay, however, were considerably lower than those obtained by DPPH. In this respect, it follows that if one species is reduced, another must be oxidized. Curcumin's three active sites can be oxidized through hydrogen abstraction and electron transfer. Test samples differed in antioxidant activity depending on the additives introduced into the formulation. Samples 1 and 2, compared with the control sample, had a higher antioxidant activity. The CUNE cheese (sample 2) showed the most significant antioxidant activity (2.3 times the control sample). CUNE contributes to maintaining and enhancing BAS (curcumin) encapsulated in the nanoemulsion with sonication. This is due to the fact that the antioxidant capabilities of the nanoemulsions containing Tween 20 differed depending on the surfactant concentration and the assay for curcumin measurement utilized. Although based on our findings that high Tween 20 concentrations resulted in a slow release of curcumin, it has been reported that an excess of this surfactant can form micelles capable of encasing the bioactive compound, which enhances the protection of encapsulated curcumin and thereby boosts the system's antioxidant capacity. The sonication method, which compactly embeds curcumin in the nanoemulsion and controls its solubility, is one of the main reasons for the increase in antioxidant activity.

Table 4. AOA prototypes cheese.

Specimen	AOA Prototypes Crumb mg
The control	0.1059 ± 0.05
Sample 1 (CUNE)	0.3164 ± 0.015
Sample 2 (Emulsion)	0.0829 ± 0.02

3. Materials and Methods

Native lab grade curcumin (Magiya vostoka), Safflower oil (FAO Code: 0281), Tween 20 (DIY ECO Cosmetic, 3.2 fat% milk (Prostokvashino) and NaCl were procured from a local market in Chelyabinsk, Russian Federation. In all experiments, a 440 W U-sonic ultrasound at 80% power, 22 ± 1.65 kHz, and with a tip diameter of 22 mm. Distilled water was used for the experiment.

3.1. Ultrasound Assisted Curcumin Encapsualtion

Initially, to prepare a lipid phase of the emulsion, curcumin powder (0.05 g/mL) was dissolved in Safflower oil at 50 °C [15]. The aqueous phase was created by dissolving Tween 20 in distilled water at concentrations of 0.2 and 0.3 g/mL oil. The oil phase was added slowly to the water phase and stirred to make a coarse emulsion (15 min at 2000 rpm), then sonochemically at 80% amplitude of the total power (400 W). A digital thermometer was used to track the temperature during the emulsification and to keep it below 50 °C. A cool water jacket encircled the reactor, and the sonication time was divided into four cycles of 3 min each to reduce hot spot creation during sonication. Once the sample was prepared under vacuum, the emulsion was freeze dried (Figure 8).
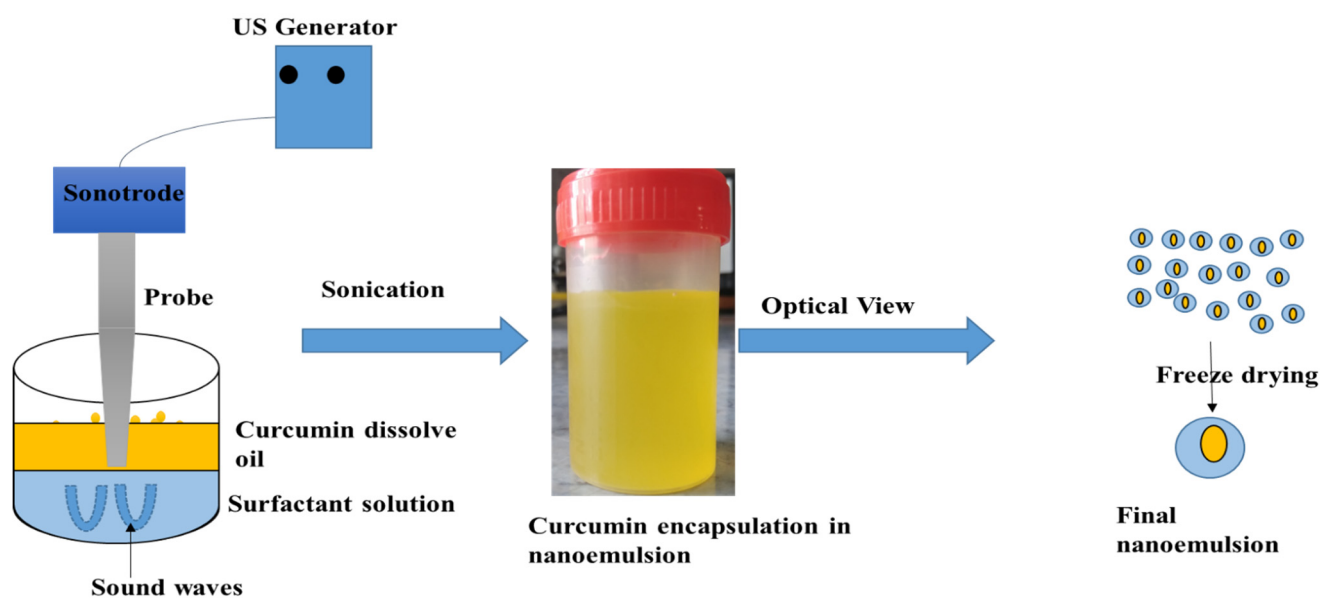
Figure 8. Schematic diagram for preparation of curcumin nanoemulsion using ultrasound.

3.2. Physicochemical Analysis of Nanoemulsions
Nanoemulsion Stability

Nanoemulsion stability was confirm using a technique defined in Kumar et al. 2016 [28]. The 10 mL of nanoemulsions samples were kept in a hot water bath at 80 °C for 30 min, then moved to a freeze for 15 min, and monitored by centrifugation (Hettich Zentrifugen, Mikro 22R) at 5000 rpm for 30 min. The whole volume (WV) and emulsion phase volume (EPV) of the nanoemulsion in the centrifuge tube were measured. The nanoemulsion stability was calculated using the formula below (ES):

$$\text{Nanomulsion stability } (\%) = \frac{\text{Volume of nanoemulsion phase}}{\text{Total volume of nanoemulsion}} \times 100 \tag{1}$$

Using Nanotrac FLEX, the average particle size of the fresh nanoemulsion was evaluated. For analysis, the nanoemulsion sample was diluted in water to measure the particle size through dynamic light scattering. The total phenolic content of the nanoemulsion was used to calculate encapsulation efficiency. The Folin–Ciocalteu reagent was used to determine the total phenolic content of the nanoemulsion. The percentage oxidation inhibition and encapsulation effectiveness of the CUNE were measured before and 30 min after the centrifugation at 5000 rpm. Encapsulation efficiency was determined using the method in [36] with some modifications. For instance, 15 mL of the nanoemulsion was centrifuged at 5000 rpm at 5 °C for 30 min after being passed through a filter membrane. Following the collection of centrifuged permeate, the UV (Shimadzu UV-2700, Japan) absorbance at 520 nm wavelength was measured. Triplets were performed for all the measurements. For optical imaging of the nanoemulsion, a sample on a slide was dried and checked at magni-

fications of 40× to 60×. CUNE and free curcumin scanned in the range of 400–4000 cm^{-1} wavelength using a Fourier-transform infrared (FTIR) spectrometer.

3.3. Transmission Electron Microscope (TEM) of Nanoemulsion Samples

The magnitude and nature of the CUNE were resolute by TEM (JEOL-100 CX). An aqueous solution of nanoemulsion sample (1:4 ratio) was sonicated for 10 min. A droplet of the sample was placed on a 200-mesh carbon-coated copper grid at room temperature and dried, before 2% uranyl acetate was added at 37 °C and grid mounted for TEM inspection.

3.4. Antimicrobial Activity of CuNE

For the antimicrobial potential of CUNE, we used two different strains: one positive strain, *Staphylococcus aureus*, and one negative strain, *Escherichia coli*. To check antimicrobial activity, we performed a zone inhibition test. The bacteria culture was added to a Petri dish that contained nutrient agar. On the nutrient agar, was a sample that had been antimicrobially treated. The Petri dish was then kept at 36 °C for 18 to 24 h.

3.5. Preparation of Cheese with Nanoemulsion

The ultrafiltrate (UF) milk retentate was pasteurized (72 °C, 15 s) and then a 5% nanoemulsion with and without curcumin were enriched for cheese production at 32 °C. A standard white cheese was produced and used as a reference. The schematic formation of the cheese is shown in Figure 9.
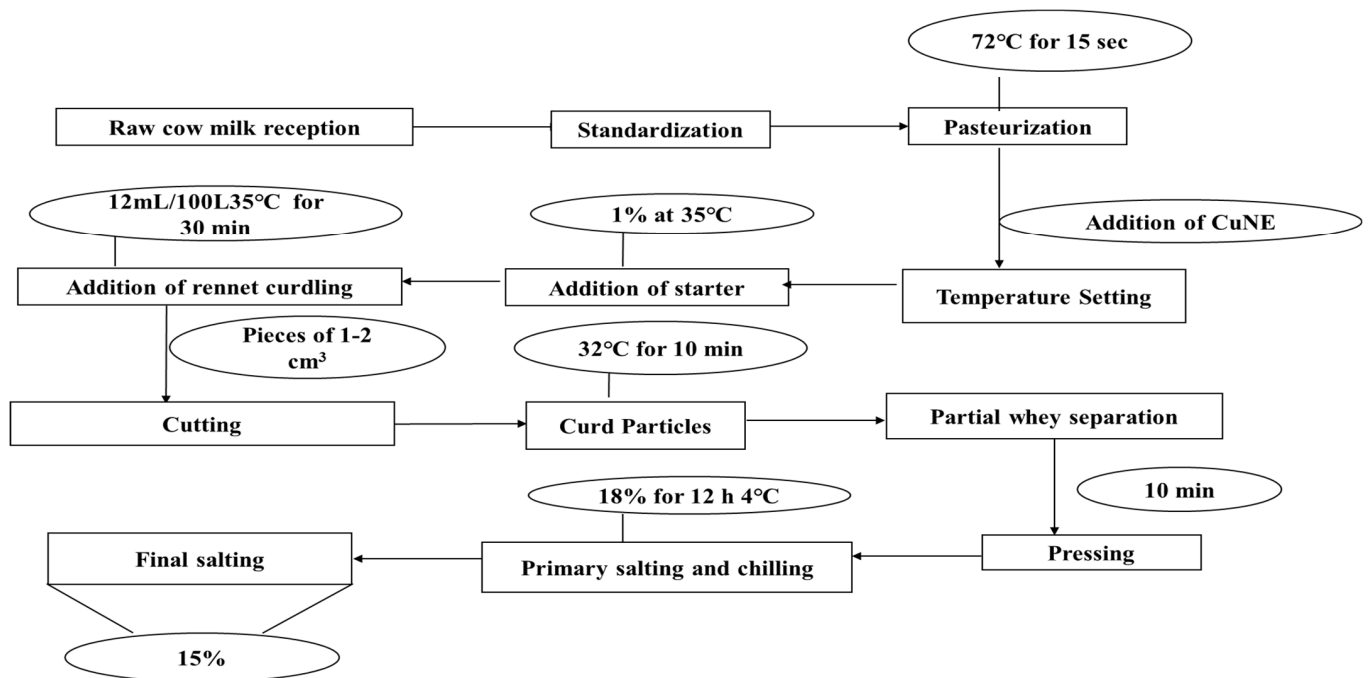
Figure 9. Schematic diagram for addition of curcumin nanoemulsion during cheese making.

Physical and Chemical Analysis of Nanoemulsion-Enriched Cheese

The pH of the nanoemulsion-based cheese was restrained through an electrode (model HI98103, Hanna Instruments, Romania) inserted into grated cheese after calibration with the standard buffers pH 4 and 7 from 22 to 31 °C. Titratable acidity was measured (g/100 g of lactic acid) using the technique in [37]. Dry matter (DM) content of cheese samples was analyzed using the oven drying method at 102 ± 2 °C. The Kjeldahl method determined total nitrogen (TN), WSN, and NPN (Jalilzadeh et al. 2020). The cheese was cut into cylinders at a height of 20 mm and a diameter of 20 mm, using a stainless-steel cylinder knife, and kept at room temperature (20 °C). The ash content of the cheese samples was determined using the method described in [38].

3.6. Field Emission Scanning Electron Microscope of Cheese

Cheese samples of 5 mm^2 had their exterior microstructure and morphology determined by FE-SEM. The cheese was immersed into liquid nitrogen to remove any moisture content and then ruptured. Using an ion sputter, gold was sucked into the punctured cheese. Finally, the sample was imaged using FE-SEM at 5 kV (Jeol JSM-7001F, Moscow).

3.7. Organoleptic Analysis of Cheese

We invited 15 students (aged 25–40) from the food and biotechnology department of South Ural State University, Chelyabinsk for the organoleptic analysis of the cheeses. Each evaluator received the three kinds of cheese simultaneously, each with a different number assigned to it. The panel consisted of 15 experts who rated the smell, color, appearance, mouth feel, and taste in two consecutive sessions using shapeless scales with anchors at the split ends. A nine-point system was used (1 = extremely dislike, 3 = moderately dislike, 5 = neither like nor dislike, 7 = moderately like, and 9 = extremely like).

3.8. Antioxidant of Processed Cheese

A 0.1 mm DPPH radical solution was made to test the antioxidant activity of the cheese samples with CUNE. Using a UV spectrophotometer, the solution's absorbance was measured at 515 nm. Cheese samples were prepared by soaking 10 g in 90% ethanol for 45 min at 150 rpm in a LOIP LS-120 laboratory shaker. The mixture was then centrifuged for 10 min, and the supernatant was collected for testing. Each sample received 280 μL of DPPH radical solution and 20 μL of supernatant in a microplate. After 30 min of incubation, the samples were examined, and the absorbance was calculated using a 517 nm reference wavelength.

3.9. Statistical Analysis

For each group, the data are shown as the standard error of mean (SEM). GraphPad Prism software version 8.0 was used for statistical analysis (GraphPad software, 2019). The column values in Tables 1–4 were with significance of difference ($p < 0.05$).

4. Conclusions

The current work demonstrates the successful formation of stable curcumin encapsulation in a nanoemulsion with a high percent of loading (0.05 g/mL) containing Tween 20 surfactant using the ultrasound approach and its incorporation in cheese. CUNE shows good antimicrobial activity for *S. aureus* and *E. coli* (12- and 18-mm zone inhibition diameters). Based on the data, we can conclude that there is no negative impact of CUNE on cheese, as it maintain its overall sensory analysis and physicochemical properties in comparison with a control sample. A normal emulsion without curcumin shows reasonable sensory analysis compared to control emulsion.

Author Contributions: U.B. was responsible for conceptualization, methodology, validation, formal analysis, investigation, resources, data curation, writing—original draft preparation, and writing—review, and editing; A.K. and M.A. were responsible for formal analysis and validation; I.P. and S.H.S. were responsible for supervision project administration.. All authors have read and agreed to the published version of the manuscript.

Institutional Review Board Statement: There are no competing interests and there is no study on animals conducted for this manuscript. However, on human studies we have taken approval from the Ethics Committee of the Federal State Autonomous Educational Institution of Higher Education South Ural State University (NRU) with MU 28-1/2406.

References

1. Mateos-Aparicio, I.; Matias, A. *Food Industry Processing by-Products in Foods*; Elsevier Inc.: Amsterdam, The Netherlands, 2019. [CrossRef]
2. Talbot-Walsh, G.; Kannar, D.; Selomulya, C. A review on technological parameters and recent advances in the fortification of processed cheese. *Trends Food Sci. Technol.* **2018**, *81*, 193–202. [CrossRef]
3. El-sayed, M.; Awad, S.; Ahmed, A.; El-sayed, I. The Effect of Storage Conditions on Physicochemical, Microbial and Textural Properties of UHT-Processed Cheese. *Acta Sci. Nutr. Health* **2020**, *4*, 76–85.
4. Mohamed, A.; Shalaby, S. Texture, chemical properties and sensory evaluation of a spreadable processed cheese analogue made with apricot pulp (*Prunus armeniaca* L.). *Int. J. Dairy Sci.* **2016**, *11*, 61–68. [CrossRef]
5. Mohamed, A.; Shalaby, S.; Gafour, W. Quality characteristics and acceptability of an analogue processed spreadable cheese made with carrot paste (*Daucus carota* L.). *Int. J. Dairy Sci.* **2016**, *11*, 91–99. [CrossRef]
6. Mehanna, N.; Hassan, F.; El-Messery, T.; Mohamed, A. Production of functional processed cheese by using tomato juice. *Int. J. Dairy Sci.* **2017**, *12*, 155–160. [CrossRef]
7. Přikryl, J.; Hájek, T.; Švecová, B.; Salek, R.; Černíková, M.; Červenka, L.; Buňka, F. Antioxidant properties and textural characteristics of processed cheese spreads enriched with rutin or quercetin: The effect of processing conditions. *LWT* **2018**, *87*, 266–271. [CrossRef]
8. Aguilera-Garrido, A.; del Castillo-Santaella, T.; Galisteo-González, F.; Gálvez-Ruiz, M.J.; Maldonado-Valderrama, J. Investigating the role of hyaluronic acid in improving curcumin bioaccessibility from nanoemulsions. *Food Chem.* **2021**, *351*, 129301. [CrossRef]
9. Páez-Hernández, G.; Mondragón-Cortez, P.; Espinosa-Andrews, H. Developing curcumin nanoemulsions by high-intensity methods: Impact of ultrasonication and microfluidization parameters. *Lwt* **2019**, *111*, 291–300. [CrossRef]
10. Artiga-Artigas, M.; Lanjari-Pérez, Y.; Martín-Belloso, O. Curcumin-loaded nanoemulsions stability as affected by the nature and concentration of surfactant. *Food Chem.* **2018**, *266*, 466–474. [CrossRef]
11. Jiang, T.; Liao, W.; Charcosset, C. Recent advances in encapsulation of curcumin in nanoemulsions: A review of encapsulation technologies, bioaccessibility and applications. *Food Res. Int.* **2020**, *132*, 109035. [CrossRef]
12. Xu, W.; Huang, L.; Jin, W.; Ge, P.; Shah, B.; Zhu, D.; Jing, J. Encapsulation and release behavior of curcumin based on nanoemulsions-filled alginate hydrogel beads. *Int. J. Biol. Macromol.* **2019**, *134*, 210–215. [CrossRef] [PubMed]
13. Hong, S.; Garcia, C.V.; Park, S.; Shin, G.; Kim, J. Retardation of curcumin degradation under various storage conditions via turmeric extract-loaded nanoemulsion system. *Lwt* **2019**, *100*, 175–182. [CrossRef]
14. Qazi, H.; Ye, A.; Acevedo-Fani, A.; Singh, H. In vitro digestion of curcumin-nanoemulsion-enriched dairy protein matrices: Impact of the type of gel structure on the bioaccessibility of curcumin. *Food Hydrocoll.* **2021**, *117*, 106692. [CrossRef]
15. Bagale, U.; Tsaturov, A.; Potoroko, I.; Potdar, S.; Sonawane, S. In-vitro evaluation of high dosage of curcumin encapsulation in palm-oil-in-water, nanoemulsion stabilized with a sonochemical approach. *Karbala Int. J. Mod. Sci.* **2022**, *8*, 83–95. [CrossRef]
16. Schneider, C.; Gordon, O.; Edwards, R.; Luis, P. Degradation of Curcumin: From Mechanism to Biological Implications. *J. Agric. Food Chem.* **2015**, *63*, 7606–7614. [CrossRef]
17. Moghaddasi, F.; Housaindokht, M.; Darroudi, M.; Bozorgmehr, M.; Sadeghi, A. Soybean oil-based nanoemulsion systems in absence and presence of curcumin: Molecular dynamics simulation approach. *J. Mol. Liq.* **2018**, *264*, 242–252. [CrossRef]
18. Mošovská, S.; Petáková, P.; Kaliňák, M.; Mikulajová, A. Antioxidant properties of curcuminoids isolated from *Curcuma longa* L. *Acta Chim. Slovaca.* **2016**, *9*, 130–135. [CrossRef]
19. Luo, X.; Zhou, Y.; Bai, L.; Liu, F.; Deng, Y.; McClements, D. Fabrication of β-carotene nanoemulsion-based delivery systems using dual-channel microfluidization: Physical and chemical stability. *J. Colloid Interface Sci.* **2017**, *490*, 328–335. [CrossRef]
20. Biswas, A.; Islam, M.; Choudhury, Z.; Mostafa, A.; Kadir, M. Nanotechnology based approaches in cancer therapeutics. *Adv. Nat. Sci. Nanosci. Nanotechnol.* **2014**, *5*, 043001. [CrossRef]
21. Rajasekar, A.; Devasena, T. Facile synthesis of Curcumin nanocrystals and validation of its antioxidant activity against circulatory toxicity in wistar rats. *J. Nanosci. Nanotechnol.* **2015**, *15*, 4119–4125. [CrossRef]

22. Moghaddasi, F.; Housaindokht, M.; Darroudi, M.; Bozorgmehr, M.; Sadeghi, A. Synthesis of nano curcumin using black pepper oil by O/W Nanoemulsion Technique and investigation of their biological activities. *LWT* **2018**, *92*, 92–100. [CrossRef]

23. Robles-García, M.; Rodríguez-Félix, F.; Márquez-Ríos, E.; Aguilar, J.; Barrera-Rodríguez, A.; Aguilar, J.; Ruiz-Cruz, S.; Del-Toro-Sánchez, C. Applications of nanotechnology in the agriculture, food, and pharmaceuticals. *J. Nanosci. Nanotechnol.* **2016**, *16*, 8188–8207. [CrossRef]

24. Lu, W.; Huang, D.; Wang, C.; Yeh, C.; Tsai, J.; Huang, Y.; Li, P. Preparation, characterization, and antimicrobial activity of nanoemulsions incorporating citral essential oil. *J. Food Drug Anal.* **2018**, *26*, 82–89. [CrossRef] [PubMed]

25. de Cenobio-Galindo, A.J.; Campos-Montiel, R.; Jiménez-Alvarado, R.; Almaraz-Buendía, I.; Medina-Pérez, G.; Fernández-Luqueno, F. Development and incorporation of nanoemulsions in food. *Int. J. Food Stud.* **2019**, *8*, 105–124. [CrossRef]

26. Rezaei, A.; Fathi, M.; Jafari, S. Nanoencapsulation of hydrophobic and low-soluble food bioactive compounds within different nanocarriers. *Food Hydrocoll.* **2019**, *88*, 146–162. [CrossRef]

27. Solans, C.; Solé, I. Nano-emulsions: Formation by low-energy methods. *Curr. Opin. Colloid Interface Sci.* **2012**, *17*, 246–254. [CrossRef]

28. Kumar, D.; Mann, B.; Pothuraju, R.; Sharma, R.; Bajaj, R. Minaxi, Formulation and characterization of nanoencapsulated curcumin using sodium caseinate and its incorporation in ice cream. *Food Funct.* **2016**, *7*, 417–424. [CrossRef] [PubMed]

29. Negahdari, R.; Ghavimi, M.A.; Barzegar, A.; Memar, M.Y.; Balazadeh, L.; Bohlouli, S.; Maleki Dizaj, S. Antibacterial effect of nanocurcumin inside the implant fixture: An in vitro study. *Clin. Exp. Dent. Res.* **2020**, *7*, 163–169. [CrossRef] [PubMed]

30. Wang, L.; Hu, C.; Shao, L. The antimicrobial activity of nanoparticles: Present situation and prospects for the future. *Int. J. Nanomed.* **2017**, *12*, 1227. [CrossRef]

31. Moncada, M.; Astete, C.; Sabliov, C.; Olson, D.; Boeneke, C.; Aryana, K. Nano spray-dried sodium chloride and its effects on the microbiological and sensory characteristics of surface-salted cheese crackers. *J. Dairy Sci.* **2015**, *98*, 5946–5954. [CrossRef]

32. Salminen, H.; Ankenbrand, J.; Zeeb, B.; Bönisch, G.B.; Schäfer, C.; Kohlus, R.; Weiss, J. Influence of spray drying on the stability of food-grade solid lipid nanoparticles. *Food Res. Int.* **2019**, *119*, 741–750. [CrossRef] [PubMed]

33. Yusop, S.; O'Sullivan, M.; Preuß, M.; Weber, H.; Kerry, J.; Kerry, J. Assessment of nanoparticle paprika oleoresin on marinating performance and sensory acceptance of poultry meat. *LWT—Food Sci. Technol.* **2012**, *46*, 349–355. [CrossRef]

34. El-Sayed, M.I.; Shalaby, T.I. Production of Processed Cheese Supplemented with Curcumin Nanoemulsion. *Am. J. Food Nutr.* **2021**, *9*, 96–105. [CrossRef]

35. Kadi, A.; Bagale, U.; Potoroko, I. The effect of ultrasonic processing on physical and chemical properties of milk-based soft, brine cheese. *Indones. J. Biotechnol.* **2022**, *27*, 219–226. [CrossRef]

36. Surassmo, S.; Min, S.; Bejrapha, P.; Choi, M. Effects of surfactants on the physical properties of capsicum oleoresin-loaded nanocapsules formulated through the emulsion-diffusion method. *Food Res. Int.* **2010**, *43*, 8–17. [CrossRef]

37. Sahingil, D.; Hayaloglu, A.; Simsek, O.; Ozer, B. Changes in volatile composition, proteolysis and textural and sensory properties of white-brined cheese: Effects of ripening temperature and adjunct culture. *Dairy Sci. Technol.* **2014**, *94*, 603–623. [CrossRef]

38. Shabbir, M.; Ahmed, H.; Maan, A.; Rehman, A.; Afraz, M.; Iqbal, M.; Khan, I.; Amir, R.; Ashraf, W.; Khan, M.; et al. Effect of non-thermal processing techniques on pathogenic and spoilage microorganisms of milk and milk products. *Food Sci. Technol.* **2021**, *41*, 279–294. [CrossRef]

Review

Natural Gum-Based Functional Bioactive Films and Coatings: A Review

Arushri Nehra [1], Deblina Biswas [1], Valentina Siracusa [2,*] and Swarup Roy [1,*]

[1] School of Bioengineering and Food Technology, Shoolini University, Solan 173229, India
[2] Department of Chemical Sciences, University of Catania, Viale Andrea Doria 6, 95125 Catania, Italy
*   Correspondence: vsiracus@dmfci.unict.it (V.S.); swaruproy2013@gmail.com (S.R.)

Abstract: Edible films and coatings are a current and future food packaging trend. In the food and envi-ronmental sectors, there is a growing need to understand the role of edible packaging and sus-tainability. Gums are polysaccharides of natural origin that are frequently utilized as thickeners, clarifying agents, gelling agents, emulsifiers, and stabilizers in the food sector. Gums come in a variety of forms, including seed gums, mucilage gums, exudate gums, and so on. As a biodegradable and sustainable alternative to petrochemical-based film and coatings, gums could be a promising option. Natural plant gum-based edible packaging helps to ensure extension of shelf-life of fresh and processed foods while also reducing microbiological alteration and/or oxidation processes. In this review, the possible applications of gum-based polymers and their functional properties in development of edible films and coatings, were comprehensively dis-cussed. In the future, technology for developing natural gum-based edible films and coatings might be applied commercially to improve shelf life and preserve the quality of foods.

Keywords: natural gums; polysaccharides; edible polymers; coating and film; active packaging

1. Introduction

Balanced nutrition is essential to maintaining optimal health in an individual, and can be obtained through food. Hence, food plays an important role in everyone's lives. In this current era of globalization, food packaging has emerged as a most exciting and pro-ductive aspect of the food industry [1,2]. Food waste is currently a key concern, as it con-tributes to a high amount of food loss and has a negative influence on national resources and economic progress. Furthermore, food oxidation plays a significant role in degrading food quality due to its deteriorating effects. It reduces the nutritional quality and flavor of food, raises toxicity, and alters textural qualities. Thus, a primary focus of the food indus-try is to preserve food quality and wholesomeness, thus gaining in consumer acceptability. One viable alternative to dealing with food waste and plastic packaging problems would be through incorporating edible film- and coating-based food packaging [3–6].

The global production of packaging materials rises by roughly 8% every year. Over 90% of used plastics are accumulating in landfills, while <5% are recycled, resulting in a huge environmental threat [7,8]. Inventors have focused on the development of appropri-ate tools to resolve these concerns. Attempts have involved various tactics, such as in-creased safety, preservation quality, and recycling [9,10]. Biodegradable packaging is an attractive alternative to traditional plastics due to its sustainability, renewability, and nontoxicity. Thus, a variety of biopolymers have been used to produce materials for envi-ronmentally friendly food packaging [11–15]. Recently, demands have increased for food packaging that does not contribute to pollution, that is produced using environmentally friendly methods, and that remains affordable. Coatings and edible films are key packag-ing types for edible materials [4,16–19].

Food packaging extends shelf life by reducing unwanted variations in food and safe-guarding food from microbiological infection, moisture loss, and exterior damage. In this

context, active food packaging (AP) technology is a promising approach [20–23]. Edible films and coatings can be used as postharvest treatments to protect the quality of foods while lowering the amount of nonbiodegradable packaging materials used. As a result, edible films and coatings fabricated from hydrocolloids (e.g., chitosan, carrageenan, pullulan, hydroxyl propyl methyl cellulose, alginate, etc.) are commonly used to maintain the quality of foods [6,24–28]. To make edible films, natural gums could be a promising alter-native, as they are biocompatible, inexpensive, nontoxic, and readily available [29,30]. Natural gums have attracted considerable interest recently due to their unusual rheologi-cal qualities and structural variety. Gum hydrocolloids, often called gum polysaccharides, are common and adaptable polymers utilized to collect materials with varying structural and functional characteristics [29]. Several novel gums have been reported in the litera-ture in recent years from various sources [31,32].

Gum-based edible packaging is already known to preserve the quality of fruits and vegetables after harvest [33]. Plants, microbes, and animal tissues are all sources of gums. However, plant-derived gums are the most popular [34]. Plant-derived gums are readily available. Furthermore, two or more gums can be mixed together to offer synergistic benefits [29]. In gums, plant seed gums like guar, locust bean, tara, and tamarind were used to extract or isolate polysaccharides [35]. Polysaccharides-based gums are generated from the endosperm of many plant seeds (mostly leguminosae). The majority of polysaccharides gums are galactomanans. These are polysaccharides that are primarily made up of the monosaccharides mannose and galactose. Depending on the plant origin, mannose components from linear chains are coupled with galactopyranosyl residues as sidechains [36].

Gums can bind water and produce gels. Mucilage gums, seed gums, exudate gums, and other types of gums exist [32,37]. Gums come from a variety of plant parts, e.g., seed epidermis, leaves, and bark [37]. Some plant gum exudates, such as karaya, Ghatti, and tragacanth, have been well documented in recent decades. Gum Arabic has been used for over 5000 years [4,38]. Natural gums have generated interest in fruit and vegetable coat-ing applications [39].

There have been few literature reviews on gum, gum extraction methods, or methods of dealing with gum structural modification. There have been studies on gum-based film and coatings and their application in food systems, however [35]. Previously, Khezerlou et al. reviewed fabrication of edible films and coatings using plant gums [35]. The use of gum coating on food products has been reviewed [29]. Recently, gums have been used in active and intelligent food packaging, i.e., film and coating [32,37,40,41]. Although some review articles have been published on natural plant gum-based films and coatings, there were, as of this review, no up-to-date reports available regarding the use of gums in food packaging. Therefore, in this review, we introduced various types of gums, their sources and properties, and finally, their utilization in food packaging film and coatings. Consequent-ly, the application of various gum-based bioactive functional composite film and coating in fruits, vegetables, and animal food product packaging was discussed comprehensively.

2. Types of Plant Gums

There are various types of plant-based gums. Gums and mucilage are mainly poly-saccharides. Gums are known as polyuronides and contain various salts of potassium, magnesium, calcium, and so on [35]. Mucilages are mainly sulfuric acid esters of polysac-charides. Galactose and arabinose are commonly found sugars in gums and mucilage [29]. The details of various types of gums will be briefly discussed below.

2.1. Seed Gum and Mucilage

Gums are derived from a variety of plant components. Some gums come from the seed epidermis, whereas others are derived from plant leaves. Gums are pathogenic con-stituents that are produced by plant impairment or unfavorable situations. Mucilage is a naturally metabolic product generated in the cell. Mucilage is insoluble in water. Almost all plants and certain microbes create mucilage, a thick, sticky material. Both gums and

mucilage are plant hydrocolloids; hence, they have certain similarities. They are likewise made up of a combination of transparent amorphous polymers and monosaccharide polymers, as well as uronic acid [37]. Mucilage is widely used in the food industry, owing to its exceptional functional properties (e.g., antimicrobial, antioxidant, water-holding, oil holding, etc.) which are beneficial for food packaging film and coatings [35,37]. However, the films formed from mucilage films are fragile and have poor mechanical properties [35].

2.1.1. Guar Gum

Guar gum is a galactomannan originating from the seed of the plant Cyamopsis tetragonolobus [42,43]. Guar gum is made by separating the endosperm from the hull and germ [44]. It is a high molecular weight, odorless polysaccharide attained from the guar plant that has a white to yellowish-white color. The guar plant grows to a height of 0.6 m, with pods ranging in length from 5 to 12.5 cm [31]. This plant is a largely sun-loving plant that can withstand high temperatures, but it is vulnerable to cold. Guar gum powder is the most common form used as a food ingredient. Guar gum is similar to locust bean gum in that it is made up mostly of the complex carbohydrate polymer galactose and mannose. However, the amounts of these two sugars differ in these gums. India produces 80% of the world's guar, with Rajasthan accounting for 70% of the crop. Guar is cultivated in north-ern provinces of India, including Rajasthan, Gujrat, Haryana, and Punjab, and India is the global leader in guar production [45]. Guar gum-based films are known for their great mechanical strength, good barrier qualities, and antibacterial or germ resistance [31]. Because of its long polymeric chain and high molecular weight relative to other forms of gums, guar gum is an excellent choice for making edible coatings. It is a galactomannan with a mannose backbone ((14)-linked -D-mannopyranose) and galactose side groups ((16)-linked -D-galactopyranose).

2.1.2. Locust Bean Gum

Locust bean gum (LBG) is made from the seed endosperm of the carob tree's fruit pods. These are botanically known as *Ceratonia siliqua* L. and are found in Mediterranean countries. As a result, locust bean gum is often referred to as carob gum. The husk, endosperm, and germ are the three sections of the carob seed. LBG is used in food, paper, textiles, oil well drilling, and in the cosmetics sector [45]. It is a neutral polysaccharide comprised of mannose and galactose. The seeds are primarily made of galactomannan, which accounts for around 80% of the total weight. The remaining 20% is proteins and impurities. The protein concentration of LBG is roughly 32% albumin and globulin, and the rest is glutelin and impurities (ash and acid-insoluble materials) [46]. Among natural polysaccharides, LBG is a promising alternative for food packaging. LBG is only weakly soluble in cold water. In order to attain full hydration and maximal viscosity, an LBG solution must be heated up to a certain temperature. It can produce films and coatings with high mechanical and water vapor barrier characteristics. LBG has been explored for its potential applications in film production and coating applications [47]. It can also be used to stabilize dispersion and emulsion in the food sector as a fat replacement in several dairy products [34].

2.1.3. Tara Gum

Tara gum, commonly known as Peruvian carob, is obtained from the seed endosperm of the *Caesalpinia spinosa* tree [48]. The primary constituent of this gum is galactomannan polysaccharides [49]. Tara gum is a commonly used food additive [50]. It is also used as a thickener and binding agent. The water-binding ability of Tara gum makes it perfect for rapid hydration-forming thick colloidal solutions. It can be used as a thickening agent or viscosity modifier. Additionally, it is used as a polymer matrix for food packaging applications.

2.1.4. Basil Gum

Basil (*Ocimum basilicum* L.) is widely grown in India's Himalayan states of Jammu and Kashmir. In aqueous conditions, the seeds of this plant create mucilage. Mucilage is produced and is closely linked to the seed core, providing a large amount of polysaccharides and soluble fiber [51]. Basil is an aromatic plant that is commonly used to give food a distinct aroma and taste. To use as a spice, the leaves can be used fresh or dried. Food additives can be made from essential oils taken from fresh plants and flowers. Basil seed gum (BSG) has great potential in the food sector as a gelling, foaming, thickening, binding, fat replacement, and reducing agent [52].

2.1.5. Fenugreek Gum

Natural fenugreek gum is produced by the *Trigonellafoenum graecum* plant (Family Leguminosae). Northern Africa, Canada, Western Asia, and India are among the countries that grow it. It can be used as a spice, a vegetable, or a medicinal herb, among other things [53]. The leaves, seeds (whole and gum), chemical components (such as hydroxy isoleucine), and immature shoots are known to possess antioxidant activities [54]. It is also applied as a food binder, glue, and emulsifier in food products [53]. More significantly, it has been used to create healthy, nutritious extruded and baked products. Because of its dietary fiber, protein, and gum content, it is utilized as a food stabilizer, glue, and emulsifying agent. Fenugreek is made up of 23–26% fenugreek, protein, 6–7% fat, and 58% carbohydrates (approximately 25% of which is nutritional fiber) [55]. Dietary fiber, particularly soluble fiber, may be found in a variety of foods and beverages, including cereal bars, yogurts, and nutritious beverages. Soluble fiber powder or total dietary fiber powder can be mixed with fruit juices, spices, and other spice blends [56].

2.2. Exudate Gum

Plant exudate-based gums originate from the bark and branches of trees to protect them from environmental and microbiological harm. The earliest forms include exudates gums, which are regularly utilized as thickeners, stabilizers, rheology modifiers, soluble fiber, and fat replacers [44].

2.2.1. Gum Ghatti

The extruded gum from the *Anogeissus latifolia* tree, commonly known as India Gum, is known as gum ghatti (GG). Gotifilia is the term given to a newly produced GG, a spray-dried powder made from specially selected high-grade GG. It has a uniform color and is extremely soluble. The high emulsification characteristics of GG is a key attribute. GG's capacity to emulsify is superior to that of gum Arabic or any other natural gum. It may form stable emulsions at concentrations as low as 25% of those of gum Arabic [57]. Due to its component glycoprotein, GG could potentially be useful in manufacture of films. It is commonly used in the food industry as a thickener, stabilizer, and emulsifier [58]. It has been used in India since ancient times due to medicinal and related characteristics that make it beneficial for use in food items. It is found in numerous writings such as Indian (Ayurveda) and Greek (Unani) medical systems. It is used as a wellness product in some parts of India, or as a mark of status and richness [32].

2.2.2. Persian Gum

Persian gum (PG) is derived from the *Amygdalus scoparia*. Since PG is less expensive than other natural hydrocolloids, it is a possible alternative to other gums. It is comprised of approximately 90% polysaccharides, mostly galactopyranosyl and arabinofuranosyl, based on the dry weight. PG can normally be dissolved in water at 25–30% which makes it a good chemical for the production of film-forming solutions [59]. Currently, it has the potential to be used as a suspending or emulsifying agent in foods, medicines, and other sectors [44].

2.2.3. Tragacanth Gum

Tragacanth gum (TG) is produced by wounds in some plants. *Astragalus gummifer* and other *Asiatic Astragalus* species generate the gum as a dry exudate from their stems and branches [40]. It is commonly utilized as a natural thickening agent and emulsifier. Additionally, it possesses outstanding thermal stability, great solubility, and good rheological behavior [60]. It is an excellent emulsifier which enhances aqueous phase viscosity [61]. TG is known to be used as a thickening agent in a variety of foods, including sauce, ice cream, jelly, salad dressing, syrup, confectionery, and mayonnaise [40]. In the presence of water, TG expands and forms a polymeric molecular network. This eventually stabilizes the aqueous and serum phases of food items and increases their viscosity. TG is also utilized as a binder in a variety of confectionary products (i.e., candies). Subsequently, it is used in ice cream to achieve a smooth texture as well as to hinder ice crystal development during storage [32]. In Table 1, types of gums used in fabrication of bio-based edible film are presented.

Table 1. Types of natural gums used in fabrication solution casting films.

Types of Gums	Additives	Conditions	References
Guar Gum	Chitosan	To make the films, 150 mL of film-forming solutions were put into Teflon plates that were leveled. After that, the plates were dried at 50 °C in ventilated oven with relative humidity of 50%.	[62]
Locus Bean Gum		Before casting into the plate, the temperature was kept at 80 °C for 1 h.	[47]
Tara Gum	Glycerol	TG was suspended in distilled water while being agitated for a period of 3 h at 45 °C. After that, the solution was centrifuged for 3 min at 4000 rpm.	[63]
Basil Seed Gum	Glycerol	At 60 °C, the solution was stirred continuously for 45 min. BSG was cast by pouring the mixture onto a polypropylene plate and drying it for 10 h at 40 °C in a hot-air oven.	[64]
Fenugreek Gum	Glycerol	FG solution (aq.) was prepared. A magnetic stirrer was used to mix the solution at 65 °C for 3 h at 1000 rpm. The nano clay was gently added to the mixture, and it was mixed for another 3 h under the same circumstances.	[55]
Ghatti Gum	Glycerol and Sorbitol	Aqueous solution was prepared at 25 ± 2 °C for 15 min with continuing stirring, then heated at 40 °C.	[58]
Tragacanth and Persian Gum	Glycerol	Centrifugation was used to separate water-insoluble part after being heated to 70 °C and agitated for 10 min.	[65]

3. Preparation of Natural Gum-Based Films and Coatings

The fabrication of natural gum-based films is primarily performed by relatively simple solution casting techniques. Various stages of film casting processes are schematically represented in Figure 1, while an overview of preparation process of films or coatings for active food packaging application is illustrated in Figure 2. Furthermore, the preparation of various natural gum-based films is briefly described herein, and some of the results are tabulated in Table 2.
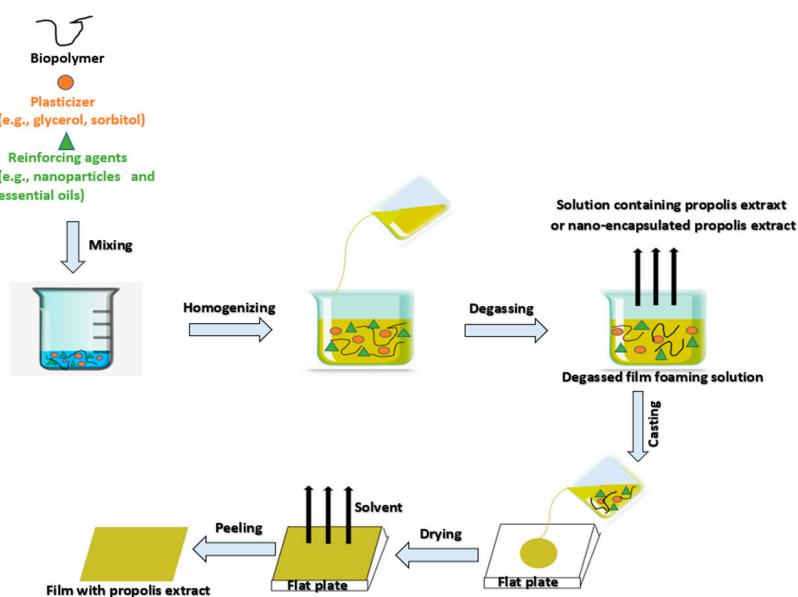
Figure 1. Schematic representation of various stages in a film casting process (Modified from Yong & Liu et al., 2021 [66]).
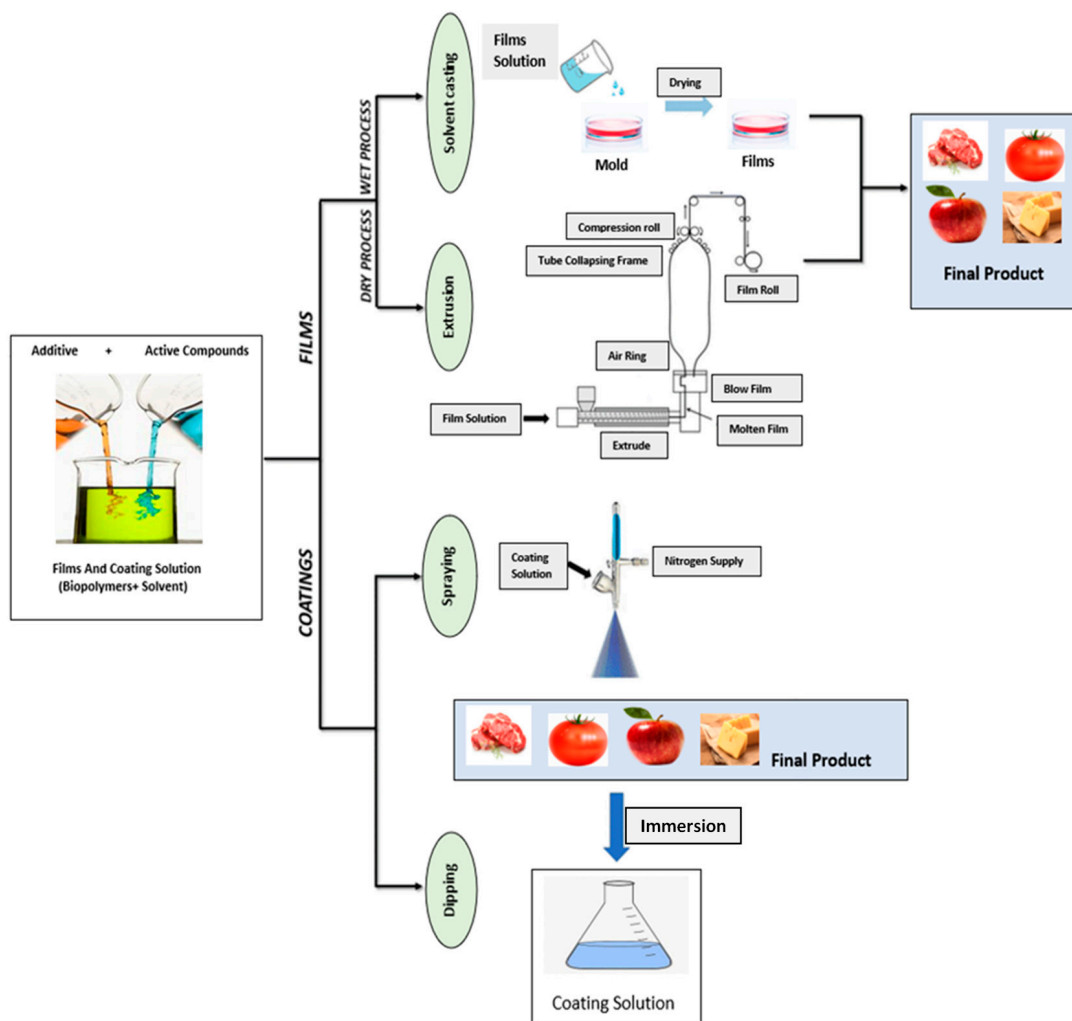
Figure 2. Preparation process of films or coatings for active food packaging application (Modified from Ribeiro et al. (2021) [67]).

Table 2. Various plant originated gum based functional films and coatings.

Types of Gums	Added Fillers	Key Result	References
Guar Gum	Curcumin/orange oil	The curcumin addition or cross-linking did not significantly change the thickness of the film. The density of the film was increased while the dissolution of the film in water greatly improved (~50%). The water vapor permeability of the film was reduced and the water contact angle slightly improved (15%). The opacity of the film increased meaningfully without significantly altering the moisture percentage in the film. The antimicrobial action of orange oil and curcumin were retained in films toward *E. coli* and *B. subtills*.	[68]
Locust Bean Gum	Carrageenan/Clay	When the clay concentration was raised, the films' strength and flexibility values were also improved significantly. The gas permeability ability was also highly influenced by the different content of clay. The thermal degradation of the film was also delayed in presence of clay minerals. The film showed increased antimicrobial activity toward *L. monocytogenes*.	[69]
Locust Bean Gum	Carrageenan	The mixing of κ-carrageenan into LBG increased the films' barrier characteristics, resulting in a reduction in water vapor permeability (WVP). Moreover, the tensile strength of the k-carrageenan/LBG mix films meaningfully increased (20%) when k-carrageenan/LBG was mixed in 40:60. Actually, the hydrogen bonds interactions among κ-carrageenan and LBG exerted a strong influence on film properties. The moisture content of the film also varied significantly.	[70]
Basil Seed Gum	Oregano essential oil	The thickness of the film was unaltered after adding the essential oil. The WVP was reduced pointedly (~10%) by the inclusion of Oregano essential oil, whereas the moisture content remained unchanged. Contact angle improved pointedly from 48.5 °C to 82 °C, transparency and swelling indexes of edible films were also increased. The film showed strong antioxidant activity in DPPH, ABTS, and FRAP assay. Antimicrobial property of the film was expressively increased against *S. Typhimurium*, *E. coliO157:H7*, *P. aeruginosa*, *S. aureus*, and *B. cereus* in presence of the Oregano essential oil and it was found to be maximum in *B. cereus*.	[71]
Basil Seed Gum	*Zataria* multiflora essential oil	The *Zataria* multiflora essential oil nanoemulsion-incorporated film showed better physical and functional performance. The thickness of the film was slightly increased, while the water solubility was decreased by 20%. The density of the film increased slightly, whereas the mechanical strength of the bioactive film was significantly improved from 20 mPa to 35 mPa in presence of 3 wt% of nanoemulsion. Antimicrobial property of the film was increased in presence of essential oil. The film showed bacteristaric effects on both *E. coli* and *B. cereus*.	[72]
Fenugreek Gum	Nano clays	The incorporation of nanoclays reduced the moisture content of the film and increased tensile strength 4-fold; there was a slight reduction in elongation at break (EB) of the film. The water vapor barrier properties and thermal stability were not greatly altered in presence of nanoclays. Moreover, the composite film showed excellent antimicrobial activity towards food-borne pathogens (*S. aureus*, *L. monocytogenes*, *E. coli O157:H7*, *B. cereus*). The highest zone of inhibition was detected for *L. monocytogenes*.	[55]
Ghatti Gum	Sodium alginate	The mixing of sodium alginate in ghatti gum produced a compatible film. The opacity and WVP of the film were increased after mixing with sodium alginate. The blending of sodium alginate in ghatti gum also improved the mechanical strength of films by 10%. The blend film showed enhanced light barrier properties (65.17%).	[73]

Table 2. *Cont.*

Types of Gums	Added Fillers	Key Result	References
Persian Gum	Sodium caseinate/ *Zingiber officinale* extract	The Persian gum/sodium caseinate-based bioactive films tensile strength and EB were significantly improved after mixing *Zingiber officinale* extract. Moreover, the transparency of the film was reduced while the hydrodynamic properties (water resistance, WVP, and water solubility) of the film pointedly improved.	[74]
Tragacanth Gum	Whey protein	The gum tragacanth-added whey protein film was more flexible and less brittle, while the tensile strength of the film was slightly reduced. The thickness and density of the film were decreased, whereas the opacity increased. The total soluble matter of the film was decreased by 20%. The 1.5% gum-included whey protein film showed almost 50% improvement in water vapor barrier properties.	[75]
Carrageenan Gum	Plantago seeds mucilage and red beet extract	The film developed with mucilage (0–20%) and red beet extract (0–10%) showed a decrease in the tensile strength and transparency. The mixing of mucilage enhanced the crystalline property of the film while the extract reduced the crystallinity. The antioxidant performance of the mucilage and extract included film was pointedly improved.	[76]

3.1. Guar Gum

A total of 150 mL of film-forming solutions were put onto Teflon plates (15 cm × 15 cm) lying on a flat surface to make the films. The dried films were peeled away from the surface of the casting. In a controlled temperature and humidity chamber, films were equilibrated at 23 °C and relative humidity (RH) of 50% to measure barrier and mechanical characteristics [62].

3.2. Locust Bean Gum

For complete solubilization of LBG in an aqueous solution, it was heated for 1 h at 80 °C using a magnetic stirrer. The gum solutions were left to stand overnight at 4 °C after dissolution. Before casting into plates, film-forming solutions were centrifuged to eliminate air bubbles. Each gum solution was poured into Teflon plates and dried in an air oven. They were then carefully peeled off the plates and stored with saturated Mg $(NO_3)_2$ at 23 °C until they reached a constant weight at RH of 52.80 ± 0.20% [47].

3.3. Tara Gum

TG (0.75%) solution was made in distilled water using agitation at 45 °C. The plasticizer (a 1:1 combination of sorbitol and glycerol) was then added. After that, ultrasonic treatment was used to eliminate any remaining air bubbles in the solution and it was cast in petri plates [63].

3.4. Basil Seed Gum

A total of 70 g of mucilage was mixed with 30 g kg^{-1} (based on BSM weight) glycerol as a plasticizer to make basil seed mucilage (BSM) film. Then, depending on the original weight of BSM, 30 g kg^{-1} of TA, MA, and SA were added. At 60 °C, the solution was agitated continuously for 45 min. BSM was made by putting the mixture onto a polypropylene plate and drying it for 10 h at 40 °C in a hot air oven. To complete crosslinking, the BSM film was baked in the oven at 150 °C for 10 min. Before characterization, the dry BSM film was peeled off and stored [64].

3.5. Fenugreek Gum

FSG was dissolved in distilled water containing glycerol for 3 h at 1000 rpm at 65 °C. Nano clay (2.5, 5, and 7.5%) was then gently mixed into the FSG solution. The nanocomposite films were made by pouring the film forming solutions onto Teflon plates and drying them for 24 h at 45 °C [55].

3.6. Ghatti Gum

GG films were made by mixing 0.75 and 1.0% GG in water for 15 min at 25 ± 2 °C with steady stirring. In a thermostatic bath water, they were heated at 40 °C for 1 h. After cooling to room temperature, plasticizer was mixed, and then cast on Petri dishes [58]. Finally, dried films were immersed in crosslinking solutions (1.5% $CaCl_2$ + 1% citric acid) for 5 min to yield crosslinked films.

3.7. Tragacanth and Persian Gum

Tragacanth and Persian gum granules were mixed in water and heated to 60 °C for 30 min until the particles were completely dissolved. Following that, glycerol was added and agitated for an additional 15 min and then cast to make film [65].

3.8. Mucilage

Various types of mucilage were already used for the fabrication of film [77–80]. Recently biodegradable film was developed based on *Pereskia aculeata* Miller mucilage [81]. The film-forming solution was made by dissolving 1.5, 1.8, and 2.0% of the mucilage in water and kept for 12 h for hydration. Thereafter homogenization was used at 12,000 rpm for half an hour and then varying content of glycerol (20–25% (w/w)) was mixed and again stirred for 10 min. The film forming solution was casted in Teflon coated surface to fabricate the film.

4. Various Film Forming Properties of Natural Gums

Primarily, there are two key types of packaging: edible films & coatings. The films are mainly utilized for edible packaging, wrapping over the food surface whereas the coating is directly used on the food surfaces [11]. Casting and extrusion are the most commonly used tools to fabricate film. On the other hand, there are many methods, such as dipping, panning, spraying, etc., for coatings [13].

The film casting process uses a wet chemical method for developing film. It is the most commonly used method for making film at lab scale. In this method, the biopolymers are solubilized in a solvent, and in this regard, water and ethyl alcohol are most commonly used. The completely soluble biopolymer solution is poured into the mold and dried until all the solvent is removed to make a film [22]. The primary advantage of this method is easy handling without any equipment and cost effectiveness. However, it has many limitations, including a long processing time, limited forms, etc. On the other hand, the extrusion technique is a commercially-applicable dry method for making film. In this method, generally, no solvent is used. It includes melting of biopolymers and mixing with other ingredients to produce film of the prescribed thickness and shape. The extrusion process in temperature sensitive and as a result, biopolymers which are highly sensitive to temperature cannot be used in the extruder [13]. Extrusion is an efficient and high-performance method for commercial purposes but in this process, only temperature-tolerant polymers can be used. Additionally, the cost of equipment is high, another major drawback of this method.

In coating, dipping is the most commonly-used method in lab scale. It includes immersion of the food system in the coating formulation and generation of a thin layer on the food product [28]. A thick coating is sometimes disadvantageous for respiration of food. Another widely-applied technique is spraying, in which liquid solution is sprayed in the form of small droplets on the surface of the food items. There are different types of spraying methods, such as air spray atomization, pressure atomization, etc. [28]. This method produces uniformly thick coating on the food surface but the highly viscous coating

formulation is difficult to spray. Panning is another suitable and efficient method for coating of foods, where in a large pan of food is coated while spinning. Using this method, large quantities of food items can be coated easily [28].

While edible films and coatings lack in several essential packaging characteristics (e.g., mechanical strength and water barrier capabilities, lack of functionalities), they provide certain unique features (e.g., biodegradability, sustainability) to food packaging. There are solutions to extant problems. Mixing of bioactive components like essential oils (EOs) in the gum-based edible film can be useful to improve physical and functional properties (e.g., antibacterial and antioxidant activities). The release of oil-soluble compounds from the edible film into the mobile lipid phase of fatty meals might provide extra nutritional advantages while also preventing oxidative rancidity and microbiological deterioration. A decrease in film hydrophilicity was predicted with the addition of essential oil, crosslinking, or bioactive compounds. The addition of orange oil, along with curcumin, induced antibacterial properties in GG films [68].

In a study, Martins et al. developed LBG- and kappa-carrageenan (k-car)-based edible films with specific qualities [70]. The mixing of k-car to LBG increased the films' barrier characteristics, resulting in a reduction in WVP. Furthermore, as compared to carrageenan and LBG films, the carrageenan/LBG blend films had a higher tensile strength (TS). The same authors studied the effects of organically modified clay Cloisite 30B (C30B) on the same composition of film [69]. The authors reported that, with the increase in clay content, strength and flexibility were improved remarkably. Moreover, the authors reported that, as quantity of C30B in the film formulation was increased, the antibacterial activity toward *L. monocytogenes* improved. Carrageenan/LBG–C30B showed antibacterial action.

Gahruie et al., observed that, in the presence of *Z. multiflora* essential oils nanoemulsion, the mechanical characteristics of the film improved and they showed increased antibacterial activity by reducing the particle size of the nanoemulsion [72]. *Z. multiflora* essential oils (ZMEO) were effectively added to basil seed gum films in order to fabricate next-generation active packaging materials with enhanced antimicrobial properties. In another study, when oregano essential oil was added to basil seed gum edible film, it resulted in a film with potential antibacterial and antioxidant properties [71]. Memis et al. used a nano clay to fabricate FSG films [55]. The nano clay improved the barrier properties of the films. FSG-based nanocomposite films have good mechanical characteristics and antibacterial activities, which could be promising for use in food packaging.

A combination of sodium alginate and GG was investigated in order to enhance the performance of biodegradable SA film [73]. The film had improved mechanical and barrier properties. In addition, the mix film's light barrier qualities were increased by 65.17%. Khezerlou et al. reported a film made from sodium caseinate (SC), *Zingiber officinale* extract (ZOE), and PG [74]. The addition of ZOE resulted in a considerable improvement in tensile strength. However, the presence of ZOE and the PG reduced elongation at break (EB). Furthermore, the addition of ZOE improved hydrodynamic properties, but the presence of PG increased opacity. Tonyali et al., studied the effects of whey protein isolate (WPI) on tragacanth gum-based film [75]. The results showed that combining WPI and TG in film formulation resulted in elastic, less soluble films with reduced water permeability and less transparency. The addition of Plantago seed mucilage in carrageenan gum led to reduction in mechanical strength and increase in flexibility of the film. The antioxidant activity and crystallinity of the carrageenan-based film was improved [76]. The blending of chia seed mucilage (2.5%) on levan-based film was studied [82]. The author reported that the presence of mucilage had a good impact on the mechanical and barrier properties of the levan-based film. The transparency of the film was reduced, but the antioxidant activity and antimicrobial performance of the film were significantly enhanced.

The biodegradable film fabricated using *Pereskia aculeata* Miller mucilage was opaque and the films mechanical properties was low (TS = ~1–5 Mpa) [81]. The moisture barrier properties of the films based on mucilage were higher compared to synthetic film and the water solubility is low. The film also showed good thermal stability. The authors

inferred that both mucilage and glycerol content affected the physical properties such as mechanical, barrier, and thermal properties of the film. In another work, quince seed mucilage (1%) based functional packaging film was developed adding thyme essential oil [83]. The film exhibited good mechanical and barrier characteristics excellent antioxidant activity and inhibited the growth of *Shewanella putrefaciens, Listeria monocytogenes* and *Staphylococcus aureus*.

Dick et al., 2015 studied the fabrication of Chia seed mucilage edible film [84]. 1% mucilage and varying content of glycerol (25, 50, 75% (*w/w*)) was used to produce the film. The fabricated films presented high solubility, transparency, and strong UV-light barrier properties. With increasing glycerol content, the mechanical strength of the film was reduced while the elongation at break and water vaper permeability increased. The blend film of chia seed mucilage in whey protein isolate (WPI) was studied by Muñoz et al., 2012 [85]. The authors used chia mucilage in blend (1:3 or 1:4) with WPI for the development of film. They reported the formed film showed good mechanical properties and high water vapor barrier properties. In another work edible and biodegradable film was developed using mucilage from *Opuntia ficus-indica* [86]. The mucilage-based films' physical properties were reported to improve by adding pectin. Araújo et al., studied the Okra mucilage based edible packaging film and reported the characteristics of the film was analogous to the other polysaccharide-based film [87]. The physical properties of the film such as water vapor permeability, solubility, thermal and mechanical properties, etc. were improved by mixing with starch. Very recently the cactus (*Cylindropuntia fulgida*) mucilage has also been used to fabricate biopolymer based antimicrobial packaging film [88]. The authors used Cactus mucilage and gelatine as biopolymers while *Euphorbia caducifolia* extract as an antimicrobial agent. The various physical properties such as water solubility, the water vapor barrier properties, flexibility as well as antimicrobial activity of the films were meaningfully improved in presence of 20% extract.

5. Application in Food Preservation

Various gum-based edible coating and films are effective to delay aging and extend the storage life of various foods. Natural hydrocolloid-based edible coatings and films provide extra protection to foods.

Dipping, coacervation, and spraying are a few of the available methods for applying edible coatings on food [89]. Each method has a number of reported benefits and drawbacks, and the success of each method is greatly determined by the traits and qualities of the items to be coated, as well as the coating's physical characteristics (viscosity, surface tension, density) [90]. For instance, in a study, while using the dipping approach, the outer layer of the meal was seen to be diluted by coating suspensions. Consequently, functional properties of the coating are reduced by fruits and vegetables. Edible finishes are often applied in single layer coatings on food using the dipping technique [91]. Natural gum edible coatings provide a promising way to expand the quality of foods while also extending their shelf life [29]. The use of natural gum-based films and coating on food preservation is briefly presented in Table 3.

GG was used to delay the ripening of Roma tomatoes by reducing their respiration rate [92]. The results indicated that GG coating not only preserved firmness but also enhanced postharvest quality when stored at room temperature. The GG coating was transparent and stuck effectively to the surface of the Roma tomato. During the 20-day storage period, all tomato fruits shrunk, but the coated ones shrunk more slowly than the uncoated ones. The GG coating was biodegradable, easy to apply, and less costly than other hydrocolloids and commercial waxes. Therefore, it could be applied large-scale to extend the shelf-life of Roma tomatoes (Figure 3).

Table 3. Application of gum-based film films and coatings on food preservation.

Types of Gums	Source	Application on Food Product	Observation	References
Guar Gum	*Cyamopsis tetragonolobus*	Roma tomato	Delaying the ripening process at 22 ± 2 °C. The quality of the Roma tomato was better preserved and, most importantly, the bacterial counts found to be lowered.	[92]
Guar Gum	*Cyamopsis tetragonolobus*	Unripe green mangoes	The quality of the green mangoes was better preserved and, most notably, the microbial counts were lowered. As a result, the ripening process of green mangoes was delayed.	[93]
Locust Bean Gum	*Caesalpinia spinosa*	Sausages	The packaging reduced oil content and increased shelf life of the sausage.	[94]
Tara Gum	*Anogeissus latifolia*	Peaches	The gum-based functional packaging lowered growth of yeast and molds on peaches.	[95]
Basil Seed Gum	*Ocinum basilicum*	Strawberries	The basil seed gum-based film helped to extend shelf life, reduce mass losses, and maintain the nutritional value of the strawberries.	[96]
Fenugreek Gum	*Trigonella foenum-groecum*	Guava	The packaging reduced weight loss and enhanced shelf life of guava.	[97]
Ghatti Gum	*Anogeissus latifolia*	Grapes	The antioxidant activity of the film helped to improve the preharvest quality of the grapes.	[57]
Persian Gum	Wild almond tree	Banana	The persian gum-based film effectively reduced microbial growth on bananas during storage.	[98]
Tragacanth Gum	Astragalus	Apple slices	The packaging decreased respiration, dehydration, and enzymatic browning of apple slices, which was effective to improve the shelf life.	[60]
Xanthan Gum and Flaxseed Mucilage	Sugar and *Xanthomonas campestris* bacteria	Cheddar cheese	Coating the cheddar cheese with xanthan gum and flaxseed mucilage exhibited noteworthy effects on chemical properties such as acidity, pH, fats, dry matters, and moisture of cheese during storage for 3 months.	[99]
Arabic Gum and plantago Seeds Mucilage	Acacia senegal and Acacia seyal	Chicken breast	The coating improved the shelf life of chicken breast by delaying the spoilage during storage at 4 °C.	[100]
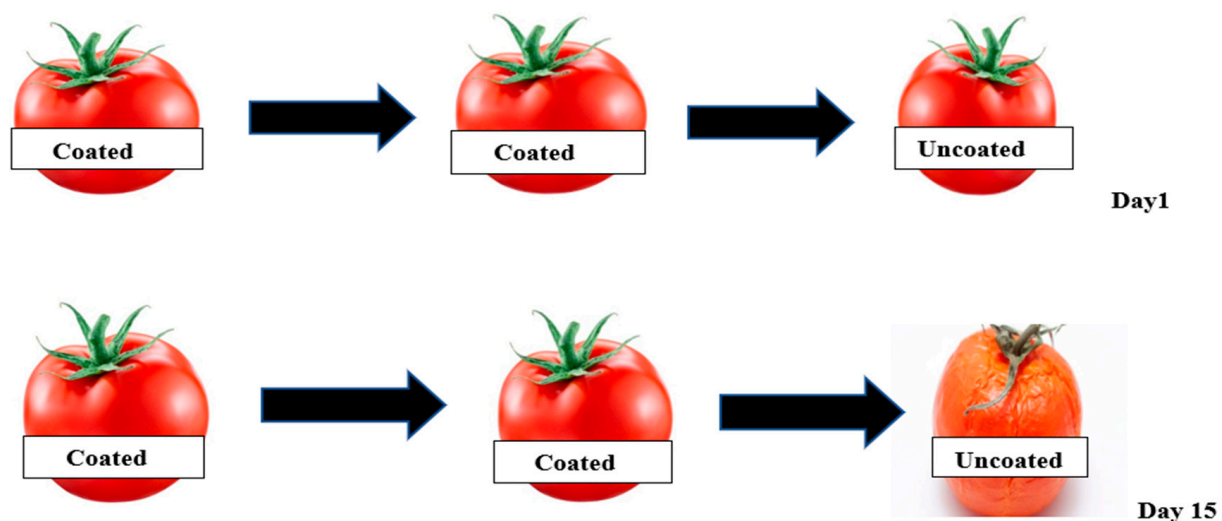
Figure 3. Effect of storage time (day 1 and day 15) on Roma tomatoes coated with guar gum (C) and uncoated (UC) at room temperature (22± 2 °C) (Modified from Ruelas-Chacon et al., 2017 [92]).

Mangoes are seasonal fruits with a short post-harvest life. Their storage life is mostly determined by the mango fruit variety chosen and the storage conditions. When kept at 13 °C, the shelf life might be as long as a week. Mango fruit losses of 20–30% are recorded

annually, amounting to 3000 tons (~28 million USD), owing to incorrect handling, insufficient storage and poor strategies after harvest [93]. Various techniques have been used to increase the life span of mangoes in normal and cold storage environments. Mangoes coated with GG infused with EOs had a 24-day shelf life. The hardness of the mangoes diminished as the storage period progressed. However, the delicious scent of the raw mangoes remained. The fruits' skin color altered from greenish to yellowish, indicating that they were fully ripe.

The use of LBG coating on sausages led to a prominent reduction in moisture loss [94]. Coating lowered the rate of respiration, reduced the oil content, and prolonged the life span of the meat. The coated samples could be stored for up to two weeks during cold storage at 5 °C. TG reduced mass loss, maintained firmness, reduced color change, and inhibited mold and yeast development in peaches [95]. The best results were obtained using Tara gum in combination with citric and ascorbic acids, as well as sodium chloride. Tara gum reduced mass loss, maintained firmness, reduced color change, and inhibited mold and yeast development. As a result, this gum showed great potential an edible coating substance.

The use of BSG coating as a polysaccharide-based coating on fresh strawberries improved their physicochemical, sensory, and microbiological qualities during cold storage [96]. Furthermore, adding echinacea extract to the BSG coating composition improved the quality of fresh strawberries in a synergetic manner. Microbial counts (yeast and molds) decreased as the content of Echinacea extract increased.

Recently it was reported that the optimal coating composition was able to increase the postharvest quality of guava fruit [97]. The response surface approach was shown to be a useful statistical tool for separating the interacting effects of independent variables. Weight loss and TSS were considerably decreased when edible coatings based on FG and Guar galactomannan were used. Furthermore, during storage, the covered fruit was fresher, firmer, and lower in TA. Weight loss was found to be 1.71% and 2.11%, firmness to be 0.72% and 2.14%, TSS to be 1.02% and 1.44%, pH to be 0.83 and 1.36, and acidity to be 1.03% and 1.44% in edible coatings, respectively. Coated guava showed a significant reduction in weight loss and maximal firmness retention. TSS enhanced in all treatments up to a specific storage duration and then declined as the storage period extended. However, pH increased while acidity decreased significantly. The edible coating of guava may be enhanced significantly by integrating Guar galactomannan and FG.

Grapes were coated with chitosan-based formulas with and without GG to increase postharvest quality [57]. Weight loss, acidity, pH, etc., of grapes were all improved when gum-ghatti was added to the chitosan solution. During two months of cold storage, coatings slowed down variations in ascorbic acid and enhanced polyphenol oxidase antioxidant enzyme activity. The chitosan-gum-ghatti-based coatings retained the bioactive components in grapes. The appropriate sort of chitosan-GG coating on grapes could help to improve its life span during transportation.

In comparison to untreated controls, the use of Kurdi Gum (KG) and PG solutions considerably enhanced the sensory features of bananas, and the addition of 0.25 and 0.5% *Prosopis farcta* extract enhanced the sensory features even more [98]. As a result, using KG and FG coatings supplemented with *P. farcta* extract should help boost banana commercialization during long-term storage. Tragacanth gum is commonly utilized in the food sector as a polysaccharide food covering. Reduced respiration, dehydration, and enzymatic browning are achieved by using TG as a food coating. Because fruits like bananas deteriorate quickly, TG has also been used as an edible covering material. In comparison to uncoated samples, coated dried banana slices showed reduced shrinkage, higher quality, low water loss, and improved rehydration [60].

The flaxseed mucilage (0.75%, 1% and 1.25%) and xanthan gum (0.5%) was used as a coating material for preservation of Cheddar cheese and it was reported that the coating showed substantial effect on the storage shelf-life of Cheddar cheese [99]. In another work, the effect of varying content of plantego mucilage (15, 20 and 25%) was added to the Arabic

gum solution and used as a coating material for chicken breast storage [100]. The meat specimen coated with 25% Plantago showed the lowest value of lipid peroxidation and total bacterial count. The coating significantly improved the life span of chicken breast during storage for 3 weeks.

Taghinia et al. 2021, recently developed intelligent packaging film using *lallemantia iberica* seed mucilage and curcumin for Shrimp freshness indicator [101]. They found that mechanical strength of the film was meaningfully improved while the flexibility reduced in presence of curcumin. The functional film also showed good antioxidant activity as well as antibacterial/mold activity. Moreover, the film showed good pH dependent color indicator properties which used to detect the freshness of Shrimp. It was reported that good correlation between TVBN content of shrimp and color change of the film during storage. The quince seed mucilage-based edible films functionalized with essential oil (oregano or thyme) was used for preservation of rainbow trout fillets [102]. It was reported that the thyme oil incorporated film effectively reduced the microbiological count in the fish fillets during refrigerated storage. Kang et al. 2020, developed okra mucilage and polyvinyl alcohol-based smart color indicator packaging label using anthocyanin [103]. The film showed distinctive color change in pH 2–12 range. The color indicator film was efficiently screen shrimp freshness in real time and the changes in color of the film were clearly identified.

Edible coatings and films on the surface of food act as a semipermeable membrane barrier which in turn restricts the exchange of gas and moisture [104,105]. The gas and moisture adjust the internal atmosphere of the food, affecting food qualities such as color, sensory quality, firmness, antioxidant activity, etc. Apparently, the different food quality parameters greatly influence food shelf-life [105]. Employing coating and film on food surfaces can effectively reduce the gas and moisture exchange of the food. The inclusion of antioxidant and antimicrobial agents into the food packaging matrix (coating or film) also help improve food shelf life by restricting the growth of unwanted foodborne pathogens, as well as by lowering the oxidation of food [28,104]. The mechanism of an active packaging system is schematically presented in Figure 4. The gas and moisture scavengers are absorbed by the functional active packaging system. The gas scavenger is used to restrict the browning reaction of foods.
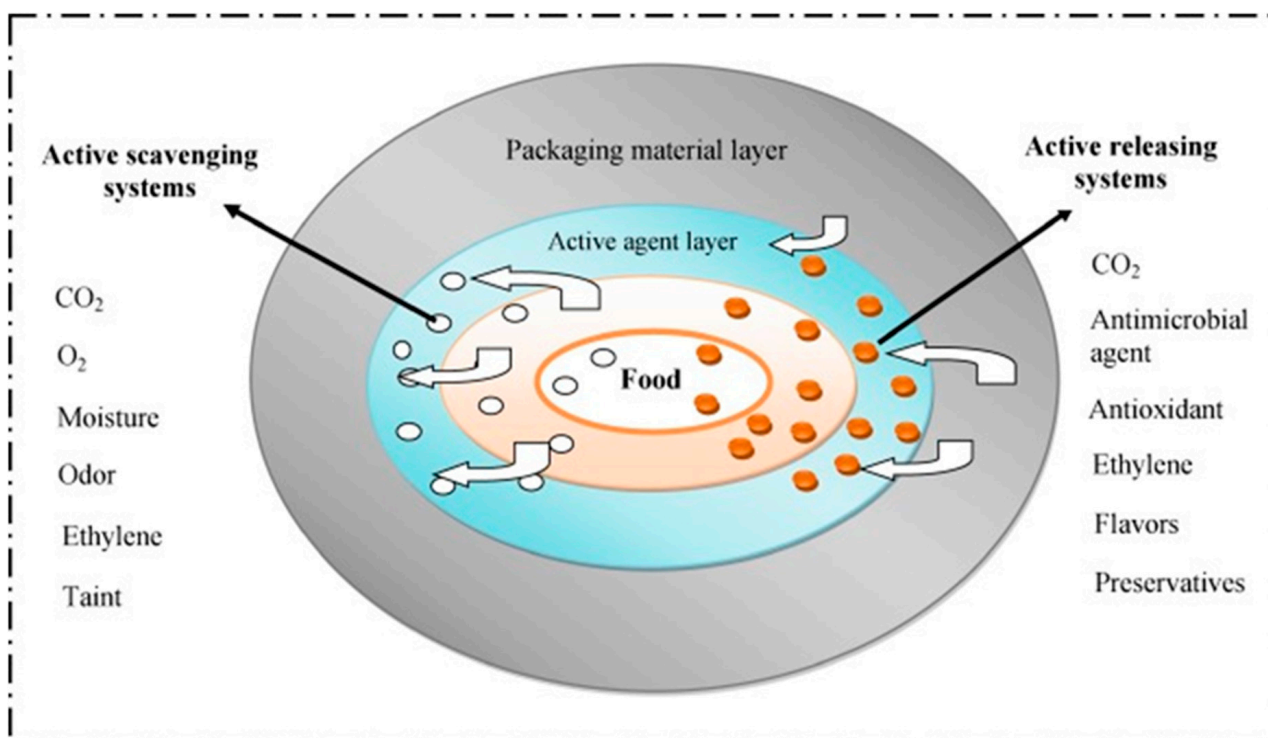
Figure 4. Mechanism of active packaging (Reproduced from Ahmed et al., 2017 [106]).

The food sector has struggled to preserve and extend the life span of chopped fresh fruits and vegetables. Thus, various food preservation methods have been investigated. Foodborne pathogens have been identified as one of the leading causes of human illness. Therefore, attempts to reduce microbial contamination in fresh fruits and vegetables are inevitable. In this context, applying various coatings on chopped fruits and vegetables could effectively reduce the spread of microbial illnesses. Edible gum-based coatings provide a reductive packaging approach to enhance the life span of foods and prevent postharvest illnesses [107].

6. Conclusions and Future Prospective

The manufacturing of bio-based edible coatings and films based on plant-derived natural gums has received enormous attention in recent years. Several researchers have studied and evaluated the potential of plant gums as a possible replacement for synthetic packaging. By altering the proportion of plasticizers and bioactive compounds, edible films with preferred physical characteristics and antioxidant/antimicrobial activities may be developed. Plant-derived, gum-based functional films and coatings are effective in food preservation as they delay ripening, lower respiration, reduce oxidation, hinder microbial development, and carry antioxidants and antimicrobial chemicals that eventually improve the foods' life span.

Natural gum-based bioactive films and coatings could be beneficial for active packaging purposes, but neat gum-based film exhibited very low mechanical properties and high water affinity compared to synthetic plastic film—which is a primary concern in making active packaging film. Moreover, these gum-based films are not effective for all types of food products owing to their permeable acid, base and water—which can be addressed by mixing with other additives and biopolymers. The mechanical properties of neat natural gum-based films are lower compared to conventional packaging. However, these mechanical (and other physical) properties could be improved by incorporating other biopolymers, bioactive materials, or additives. One of the major tasks facing researchers is to find an appropriate recipe for plant gum biopolymers and additives to achieve optimum parameters for the packaging of food products. Moreover, in most cases, wet methods are produced to develop packaging, which makes commercialization troublesome. Even though natural gum-based materials are promising, further research should emphasize the use of optimum combinations of edible covering materials to improve the nutritional value of foods. Since gum-based edible coatings and films are in the developmental stage, future research should focus on development of prototypes. It is anticipated that researchers will soon be able to address key challenges and advance appropriate skills that will aid industries in upscaling the fabrication of edible films and coatings for food products.

References

1. Souza, E.; Gottschalk, L.; Freitas-Silva, O. Overview of Nanocellulose in Food Packaging. *Recent Pat. Food. Nutr. Agric.* **2020**, *11*, 154–167. [CrossRef] [PubMed]

2. Priyadarshi, R.; Roy, S.; Ghosh, T.; Biswas, D.; Rhim, J.W. Antimicrobial Nanofillers Reinforced Biopolymer Composite Films for Active Food Packaging Applications—A Review. *Sustain. Mater. Technol.* **2022**, *32*, e00353. [CrossRef]

3. Hoffmann, T.; Peters, D.A.; Angioletti, B.; Bertoli, S.; Vieira, L.P.; Reiter, M.G.R.; Souza, C.K. De Potentials Nanocomposites in Food Packaging. *Chem. Eng. Trans.* **2019**, *75*, 253–258. [CrossRef]

4. Galus, S.; Kibar, E.A.A.; Gniewosz, M.; Kraśniewska, K. Novel Materials in the Preparation of Edible Films and Coatings—A Review. *Coatings* **2020**, *10*, 674. [CrossRef]

5. Otoni, C.G.; Avena-Bustillos, R.J.; Azeredo, H.M.C.; Lorevice, M.V.; Moura, M.R.; Mattoso, L.H.C.; McHugh, T.H. Recent Advances on Edible Films Based on Fruits and Vegetables—A Review. *Compr. Rev. Food Sci. Food Saf.* **2017**, *16*, 1151–1169. [CrossRef] [PubMed]

6. Ezati, P.; Roy, S.; Rhim, J.-W. Effect of Saffron on the Functional Property of Edible Films for Active Packaging Applications. *ACS Food Sci. Technol.* **2022**, *2*, 1318–1325. [CrossRef]

7. Schmaltz, E.; Melvin, E.C.; Diana, Z.; Gunady, E.F.; Rittschof, D.; Somarelli, J.A.; Virdin, J.; Dunphy-Daly, M.M. Plastic Pollution Solutions: Emerging Technologies to Prevent and Collect Marine Plastic Pollution. *Environ. Int.* **2020**, *144*, 106067. [CrossRef]

8. Roy, S.; Priyadarshi, R.; Rhim, J.-W. Gelatin/Agar-Based Multifunctional Film Integrated with Copper-Doped Zinc Oxide Nanoparticles and Clove Essential Oil Pickering Emulsion for Enhancing the Shelf Life of Pork Meat. *Food Res. Int.* **2022**, *160*, 111690. [CrossRef]

9. Dehghani, S.; Hosseini, S.V.; Regenstein, J.M. Edible Films and Coatings in Seafood Preservation: A Review. *Food Chem.* **2018**, *240*, 505–513. [CrossRef]

10. Kim, H.-J.; Roy, S.; Rhim, J.-W. Gelatin/Agar-Based Color-Indicator Film Integrated with Clitoria Ternatea Flower Anthocyanin and Zinc Oxide Nanoparticles for Monitoring Freshness of Shrimp. *Food Hydrocoll.* **2022**, *124*, 107294. [CrossRef]

11. Atarés, L.; Chiralt, A. Essential Oils as Additives in Biodegradable Films and Coatings for Active Food Packaging. *Trends Food Sci. Technol.* **2016**, *48*, 51–62. [CrossRef]

12. Parente, A.G.; de Oliveira, H.P.; Cabrera, M.P.; de Morais Neri, D.F. Bio-Based Polymer Films with Potential for Packaging Applications: A Systematic Review of the Main Types Tested on Food. *Polym. Bull.* **2022**, 1–29. [CrossRef]

13. Roy, S.; Rhim, J.W. New Insight into Melanin for Food Packaging and Biotechnology Applications. *Crit. Rev. Food Sci. Nutr.* **2022**, *62*, 4629–4655. [CrossRef] [PubMed]

14. Roy, S.; Rhim, J.-W. Starch/Agar-Based Functional Films Integrated with Enoki Mushroom-Mediated Silver Nanoparticles for Active Packaging Applications. *Food Biosci.* **2022**, *49*, 101867. [CrossRef]

15. Siracusa, V.; Rocculi, P.; Romani, S.; Rosa, M.D. Biodegradable Polymers for Food Packaging: A Review. *Trends Food Sci. Technol.* **2008**, *19*, 634–643. [CrossRef]

16. Hoque, M.; Gupta, S.; Santhosh, R.; Syed, I.; Sarkar, P. Biopolymer-Based Edible Films and Coatings for Food Applications. In *Food, Medical, and Environmental Applications of Polysaccharides*; Elsevier: Amsterdam, The Netherlands, 2021; pp. 81–107. [CrossRef]

17. Siracusa, V.; Romani, S.; Gigli, M.; Mannozzi, C.; Cecchini, J.P.; Tylewicz, U.; Lotti, N. Characterization of Active Edible Films Based on Citral Essential Oil, Alginate and Pectin. *Materials* **2018**, *11*, 1980. [CrossRef]

18. Chakravartula, S.S.N.; Soccio, M.; Lotti, N.; Balestra, F.; Dalla Rosa, M.; Siracusa, V. Characterization of Composite Edible Films Based on Pectin/Alginate/Whey Protein Concentrate. *Materials* **2019**, *12*, 2454. [CrossRef]

19. Roy, S.; Ezati, P.; Priyadarshi, R.; Biswas, D.; Rhim, J.-W. Recent Advances in Metal Sulfide Nanoparticle-Added Bionanocomposite Films for Food Packaging Applications. *Crit. Rev. Food Sci. Nutr.* **2022**, 1–14. [CrossRef]

20. Qian, M.; Liu, D.; Zhang, X.; Yin, Z.; Ismail, B.B.; Ye, X.; Guo, M. A Review of Active Packaging in Bakery Products: Applications and Future Trends. *Trends Food Sci. Technol.* **2021**, *114*, 459–471. [CrossRef]

21. Yildirim, S.; Röcker, B.; Pettersen, M.K.; Nilsen-Nygaard, J.; Ayhan, Z.; Rutkaite, R.; Radusin, T.; Suminska, P.; Marcos, B.; Coma, V. Active Packaging Applications for Food. *Compr. Rev. Food Sci. Food Saf.* **2018**, *17*, 165–199. [CrossRef]

22. Roy, S.; Priyadarshi, R.; Ezati, P.; Rhim, J.W. Curcumin and Its Uses in Active and Smart Food Packaging Applications—A Comprehensive Review. *Food Chem.* **2022**, *375*, 131885. [CrossRef]

23. Chandel, V.; Biswas, D.; Roy, S.; Vaidya, D.; Verma, A.; Gupta, A. Current Advancements in Pectin: Extraction, Properties and Multifunctional Applications. *Foods* **2022**, *11*, 2683. [CrossRef]

24. Roy, S.; Rhim, J.-W. Fabrication of Chitosan-Based Functional Nanocomposite Films: Effect of Quercetin-Loaded Chitosan Nanoparticles. *Food Hydrocoll.* **2021**, *121*, 107065. [CrossRef]

25. Roy, S.; Shankar, S.; Rhim, J.W. Melanin-Mediated Synthesis of Silver Nanoparticle and Its Use for the Preparation of Carrageenan-Based Antibacterial Films. *Food Hydrocoll.* **2019**, *88*, 237–246. [CrossRef]

26. Roy, S.; Kim, H.C.; Panicker, P.S.; Rhim, J.-W.; Kim, J. Cellulose Nanofiber-Based Nanocomposite Films Reinforced with Zinc Oxide Nanorods and Grapefruit Seed Extract. *Nanomaterials* **2021**, *11*, 877. [CrossRef]

27. Łopusiewicz, Ł.; Macieja, S.; Śliwiński, M.; Bartkowiak, A.; Roy, S.; Sobolewski, P. Alginate Biofunctional Films Modified with Melanin from Watermelon Seeds and Zinc Oxide/Silver Nanoparticles. *Materials* **2022**, *15*, 2381. [CrossRef]

28. Gupta, V.; Biswas, D.; Roy, S. A Comprehensive Review of Biodegradable Polymer-Based Films and Coatings and Their Food Packaging Applications. *Materials* **2022**, *15*, 5899. [CrossRef]
29. Salehi, F. Edible Coating of Fruits and Vegetables Using Natural Gums: A Review. *Int. J. Fruit Sci.* **2020**, *20*, S570–S589. [CrossRef]
30. Yun, D.; He, Y.; Zhu, H.; Hui, Y.; Li, C.; Chen, D.; Liu, J. Smart Packaging Films Based on Locust Bean Gum, Polyvinyl Alcohol, the Crude Extract of *Loropetalum Chinense* Var. Rubrum Petals and Its Purified Fractions. *Int. J. Biol. Macromol.* **2022**, *205*, 141–153. [CrossRef]
31. Sharma, G.; Sharma, S.; Kumar, A.; Al-Muhtaseb, A.H.; Naushad, M.; Ghfar, A.A.; Mola, G.T.; Stadler, F.J. Guar Gum and Its Composites as Potential Materials for Diverse Applications: A Review. *Carbohydr. Polym.* **2018**, *199*, 534–545. [CrossRef]
32. Barak, S.; Mudgil, D.; Taneja, S. Exudate Gums: Chemistry, Properties and Food Applications—A Review. *J. Sci. Food Agric.* **2020**, *100*, 2828–2835. [CrossRef] [PubMed]
33. Mahfoudhi, N.; Hamdi, S. Use of Almond Gum and Gum Arabic as Novel Edible Coating to Delay Postharvest Ripening and to Maintain Sweet Cherry (*Prunus avium*) Quality during Storage. *J. Food Process. Preserv.* **2015**, *39*, 1499–1508. [CrossRef]
34. Tahir, H.E.; Xiaobo, Z.; Mahunu, G.K.; Arslan, M.; Abdalhai, M.; Zhihua, L. Recent Developments in Gum Edible Coating Applications for Fruits and Vegetables Preservation: A Review. *Carbohydr. Polym.* **2019**, *224*, 115141. [CrossRef]
35. Khezerlou, A.; Zolfaghari, H.; Banihashemi, S.A.; Forghani, S.; Ehsani, A. Plant Gums as the Functional Compounds for Edible Films and Coatings in the Food Industry: A Review. *Polym. Adv. Technol.* **2021**, *32*, 2306–2326. [CrossRef]
36. Prajapati, V.D.; Jani, G.K.; Moradiya, N.G.; Randeria, N.P.; Nagar, B.J. Locust Bean Gum: A Versatile Biopolymer. *Carbohydr. Polym.* **2013**, *94*, 814–821. [CrossRef] [PubMed]
37. Amiri, M.S.; Mohammadzadeh, V.; Yazdi, M.E.T.; Barani, M.; Rahdar, A.; Kyzas, G.Z. Plant-Based Gums and Mucilages Applications in Pharmacology and Nanomedicine: A Review. *Molecules* **2021**, *26*, 1770. [CrossRef] [PubMed]
38. Prasad, N.; Thombare, N.; Sharma, S.C.; Kumar, S. Gum Arabic—A Versatile Natural Gum: A Review on Production, Processing, Properties and Applications. *Ind. Crops Prod.* **2022**, *187*, 115304. [CrossRef]
39. Ahmad, S.; Ahmad, M.; Manzoor, K.; Purwar, R.; Ikram, S. A Review on Latest Innovations in Natural Gums Based Hydrogels: Preparations & Applications. *Int. J. Biol. Macromol.* **2019**, *136*, 870–890. [CrossRef] [PubMed]
40. Mallakpour, S.; Tabesh, F.; Hussain, C.M. Potential of Tragacanth Gum in the Industries: A Short Journey from Past to the Future. *Polym. Bull.* **2022**, 1–20. [CrossRef]
41. Abu Elella, M.H.; Goda, E.S.; Gab-Allah, M.A.; Hong, S.E.; Pandit, B.; Lee, S.; Gamal, H.; Rehman, A.U.; Yoon, K.R. Xanthan Gum-Derived Materials for Applications in Environment and Eco-Friendly Materials: A Review. *J. Environ. Chem. Eng.* **2021**, *9*, 104702. [CrossRef]
42. Jussen, D.; Sharma, S.; Carson, J.K.; Pickering, K.L. Preparation and Tensile Properties of Guar Gum Hydrogel Films. *Polym. Polym. Compos.* **2019**, *28*, 180–186. [CrossRef]
43. Verma, D.; Sharma, S.K. Recent Advances in Guar Gum Based Drug Delivery Systems and Their Administrative Routes. *Int. J. Biol. Macromol.* **2021**, *181*, 653–671. [CrossRef] [PubMed]
44. Saha, A.; Tyagi, S.; Gupta, R.K.; Tyagi, Y.K. Natural Gums of Plant Origin as Edible Coatings for Food Industry Applications. *Crit. Rev. Biotechnol.* **2017**, *37*, 959–973. [CrossRef]
45. Barak, S.; Mudgil, D. Locust Bean Gum: Processing, Properties and Food Applications—A Review. *Int. J. Biol. Macromol.* **2014**, *66*, 74–80. [CrossRef]
46. Dionísio, M.; Grenha, A. Locust Bean Gum: Exploring Its Potential for Biopharmaceutical Applications. *J. Pharm. Bioallied Sci.* **2012**, *4*, 175. [CrossRef]
47. Mostafavi, F.S.; Kadkhodaee, R.; Emadzadeh, B.; Koocheki, A. Preparation and Characterization of Tragacanth–Locust Bean Gum Edible Blend Films. *Carbohydr. Polym.* **2016**, *139*, 20–27. [CrossRef]
48. Nuvoli, L.; Conte, P.; Fadda, C.; Reglero Ruiz, J.A.; García, J.M.; Baldino, S.; Mannu, A. Structural, Thermal, and Mechanical Properties of Gelatin-Based Films Integrated with Tara Gum. *Polymer* **2021**, *214*, 123244. [CrossRef]
49. Ma, Q.; Ren, Y.; Gu, Z.; Wang, L. Developing an Intelligent Film Containing *Vitis amurensis* Husk Extracts: The Effects of pH Value of the Film-Forming Solution. *J. Clean. Prod.* **2017**, *166*, 851–859. [CrossRef]
50. Wu, Y.; Ding, W.; Jia, L.; He, Q. The Rheological Properties of Tara Gum (*Caesalpinia spinosa*). *Food Chem.* **2015**, *168*, 366–371. [CrossRef]
51. Nazir, S.; Wani, I.A. Functional Characterization of Basil (*Ocimum basilicum* L.) Seed Mucilage. *Bioact. Carbohydrates Diet. Fibre* **2021**, *25*, 100261. [CrossRef]
52. Naji-Tabasi, S.; Razavi, S.M.A. Functional Properties and Applications of Basil Seed Gum: An Overview. *Food Hydrocoll.* **2017**, *73*, 313–325. [CrossRef]
53. Senarathna, S.; Navaratne, S.; Wickramasinghe, I.; Coorey, R. Use of Fenugreek Seed Gum in Edible Film Formation: Major Drawbacks and Applicable Methods to Overcome. *J. Food Sci. Technol.* **2022**, 1–10. [CrossRef]
54. Roberts, K.T.; Cui, S.W.; Chang, Y.H.; Ng, P.K.W.; Graham, T. The Influence of Fenugreek Gum and Extrusion Modified Fenugreek Gum on Bread. *Food Hydrocoll.* **2012**, *26*, 350–358. [CrossRef]
55. Memiş, S.; Tornuk, F.; Bozkurt, F.; Durak, M.Z. Production and Characterization of a New Biodegradable Fenugreek Seed Gum Based Active Nanocomposite Film Reinforced with Nanoclays. *Int. J. Biol. Macromol.* **2017**, *103*, 669–675. [CrossRef]
56. Wani, S.A.; Kumar, P. Fenugreek: A Review on Its Nutraceutical Properties and Utilization in Various Food Products. *J. Saudi Soc. Agric. Sci.* **2018**, *17*, 97–106. [CrossRef]

57. Eshghi, S.; Karimi, R.; Shiri, A.; Karami, M.; Moradi, M. Effects of Polysaccharide-Based Coatings on Postharvest Storage Life of Grape: Measuring the Changes in Nutritional, Antioxidant and Phenolic Compounds. *J. Food Meas. Charact.* **2022**, *16*, 1159–1170. [CrossRef]

58. Zhang, P.; Zhao, Y.; Shi, Q. Characterization of a Novel Edible Film Based on Gum Ghatti: Effect of Plasticizer Type and Concentration. *Carbohydr. Polym.* **2016**, *153*, 345–355. [CrossRef]

59. Pak, E.S.; Ghaghelestani, S.N.; Najafi, M.A. Preparation and Characterization of a New Edible Film Based on Persian Gum with Glycerol Plasticizer. *J. Food Sci. Technol.* **2020**, *57*, 3284. [CrossRef]

60. Nazarzadeh Zare, E.; Makvandi, P.; Tay, F.R. Recent Progress in the Industrial and Biomedical Applications of Tragacanth Gum: A Review. *Carbohydr. Polym.* **2019**, *212*, 450–467. [CrossRef]

61. Taghavizadeh Yazdi, M.E.; Nazarnezhad, S.; Mousavi, S.H.; Sadegh Amiri, M.; Darroudi, M.; Baino, F.; Kargozar, S. Gum Tragacanth (GT): A Versatile Biocompatible Material beyond Borders. *Molecules* **2021**, *26*, 1510. [CrossRef]

62. Rao, M.S.; Kanatt, S.R.; Chawla, S.P.; Sharma, A. Chitosan and Guar Gum Composite Films: Preparation, Physical, Mechanical and Antimicrobial Properties. *Carbohydr. Polym.* **2010**, *82*, 1243–1247. [CrossRef]

63. Ma, Q.; Hu, D.; Wang, H.; Wang, L. Tara Gum Edible Film Incorporated with Oleic Acid. *Food Hydrocoll.* **2016**, *56*, 127–133. [CrossRef]

64. Thessrimuang, N.; Prachayawarakorn, J. Development, Modification and Characterization of New Biodegradable Film from Basil Seed (*Ocimum basilicum* L.) Mucilage. *J. Sci. Food Agric.* **2019**, *99*, 5508–5515. [CrossRef] [PubMed]

65. Khodaei, D.; Oltrogge, K.; Hamidi-Esfahani, Z. Preparation and Characterization of Blended Edible Films Manufactured Using Gelatin, Tragacanth Gum and, Persian Gum. *LWT* **2020**, *117*, 108617. [CrossRef]

66. Yong, H.; Liu, J. Active packaging films and edible coatings based on polyphenol-rich propolis extract: A review. *Compr. Rev. Food Sci. Food Saf.* **2021**, *20*, 2106–2145. [CrossRef]

67. Ribeiro, A.M.; Estevinho, B.N.; Rocha, F. Preparation and incorporation of functional ingredients in edible films and coatings. *Food Bioprocess Technol.* **2021**, *14*, 209–231. [CrossRef]

68. Aydogdu, A.; Radke, C.J.; Bezci, S.; Kirtil, E. Characterization of Curcumin Incorporated Guar Gum/Orange Oil Antimicrobial Emulsion Films. *Int. J. Biol. Macromol.* **2020**, *148*, 110–120. [CrossRef]

69. Martins, J.T.; Bourbon, A.I.; Pinheiro, A.C.; Souza, B.W.S.; Cerqueira, M.A.; Vicente, A.A. Biocomposite Films Based on κ-Carrageenan/Locust Bean Gum Blends and Clays: Physical and Antimicrobial Properties. *Food Bioprocess Technol.* **2013**, *6*, 2081–2092. [CrossRef]

70. Martins, J.T.; Cerqueira, M.A.; Bourbon, A.I.; Pinheiro, A.C.; Souza, B.W.S.; Vicente, A.A. Synergistic Effects between κ-Carrageenan and Locust Bean Gum on Physicochemical Properties of Edible Films Made Thereof. *Food Hydrocoll.* **2012**, *29*, 280–289. [CrossRef]

71. Hashemi, S.M.B.; Mousavi Khaneghah, A. Characterization of Novel Basil-Seed Gum Active Edible Films and Coatings Containing Oregano Essential Oil. *Prog. Org. Coat.* **2017**, *110*, 35–41. [CrossRef]

72. Hashemi Gahruie, H.; Ziaee, E.; Eskandari, M.H.; Hosseini, S.M.H. Characterization of Basil Seed Gum-Based Edible Films Incorporated with Zataria Multiflora Essential Oil Nanoemulsion. *Carbohydr. Polym.* **2017**, *166*, 93–103. [CrossRef] [PubMed]

73. Cheng, T.; Xu, J.; Li, Y.; Zhao, Y.; Bai, Y.; Fu, X.; Gao, X.; Mao, X. Effect of Gum Ghatti on Physicochemical and Microstructural Properties of Biodegradable Sodium Alginate Edible Films. *J. Food Meas. Charact.* **2021**, *15*, 107–118. [CrossRef]

74. Khezerlou, A.; Ehsani, A.; Tabibiazar, M.; Moghaddas Kia, E. Development and Characterization of a Persian Gum–Sodium Caseinate Biocomposite Film Accompanied by Zingiber Officinale Extract. *J. Appl. Polym. Sci.* **2019**, *136*, 47215. [CrossRef]

75. Tonyali, B.; Cikrikci, S.; Oztop, M.H. Physicochemical and Microstructural Characterization of Gum Tragacanth Added Whey Protein Based Films. *Food Res. Int.* **2018**, *105*, 1–9. [CrossRef]

76. Daei, S.; Mohtarami, F.; Pirsa, S. A biodegradable film based on carrageenan gum/Plantago psyllium mucilage/red beet extract: Physicochemical properties, biodegradability and water absorption kinetic. *Polym. Bull.* **2022**, *79*, 11317–11338. [CrossRef]

77. López-Díaz, A.S.; Méndez-Lagunas, L.L. Mucilage-Based Films for Food Applications. *Food Rev. Int.* **2022**, 1–30. [CrossRef]

78. Soukoulis, C.; Gaiani, C.; Hoffmann, L. Plant seed mucilage as emerging biopolymer in food industry applications. *Curr. Opin. Food Sci.* **2018**, *22*, 28–42. [CrossRef]

79. Tosif, M.; Najda, A.; Bains, A.; Kaushik, R.; Dhull, S.; Chawla, P.; Walasek-Janusz, M. A Comprehensive Review on Plant-Derived Mucilage: Characterization, Functional Properties, Applications, and Its Utilization for Nanocarrier Fabrica-tion. *Polymers* **2021**, *13*, 1066. [CrossRef]

80. Beikzadeh, S.; Khezerlou, A.; Jafari, S.M.; Pilevar, Z.; Mortazavian, A.M. Seed mucilages as the functional ingredients for biodegradable films and edible coatings in the food industry. *Adv. Colloid Interface Sci.* **2020**, *280*, 102164. [CrossRef]

81. Oliveira, N.L.; Rodrigues, A.A.; Neves, I.; Lago, A.M.T.; Borges, S.; de Resende, J.V. Development and characterization of biodegradable films based on Pereskia aculeata Miller mucilage. *Ind. Crop. Prod.* **2019**, *130*, 499–510. [CrossRef]

82. Ağçeli, G.K. A new approach to nanocomposite carbohydrate polymer films: Levan and chia seed mucilage. *Int. J. Biol. Macromol.* **2022**, *218*, 751–759. [CrossRef] [PubMed]

83. Jouki, M.; Mortazavi, S.A.; Yazdi, F.T.; Koocheki, A. Characterization of antioxidant–antibacterial quince seed mucilage films containing thyme essential oil. *Carbohydr. Polym.* **2014**, *99*, 537–546. [CrossRef] [PubMed]

84. Dick, M.; Costa, T.M.H.; Gomaa, A.; Subirade, M.; de Oliveira Rios, A.; Flôres, S.H. Edible film production from chia seed mucilage: Effect of glycerol concentration on its physicochemical and mechanical properties. *Carbohydr. Polym.* **2015**, *130*, 198–205. [CrossRef] [PubMed]

85. Muñoz, L.; Aguilera, J.; Rodriguez-Turienzo, L.; Cobos, A.; Diaz, O. Characterization and microstructure of films made from mucilage of Salvia hispanica and whey protein concentrate. *J. Food Eng.* **2012**, *111*, 511–518. [CrossRef]

86. Sandoval, D.C.G.; Sosa, B.L.; Martínez-Ávila, G.C.G.; Fuentes, H.R.; Abarca, V.H.A.; Rojas, R. Formulation and Characteri-zation of Edible Films Based on Organic Mucilage from Mexican Opuntia ficus-indica. *Coatings* **2019**, *9*, 506. [CrossRef]

87. Araújo, A.; Galvao, A.; Filho, C.J.A.D.S.; Mendes, F.; Oliveira, M.; Barbosa, F.; Filho, M.S.; Bastos, M. Okra mucilage and corn starch bio-based film to be applied in food. *Polym. Test.* **2018**, *71*, 352–361. [CrossRef]

88. Kumar, L.; Deshmukh, R.K.; Gaikwad, K.K. Antimicrobial packaging film from cactus (Cylindropuntia fulgida) mucilage and gelatine. *Int. J. Biol. Macromol.* **2022**, *215*, 596–605. [CrossRef]

89. Al-Tayyar, N.A.; Youssef, A.M.; Al-Hindi, R.R. Edible Coatings and Antimicrobial Nanoemulsions for Enhancing Shelf Life and Reducing Foodborne Pathogens of Fruits and Vegetables: A Review. *Sustain. Mater. Technol.* **2020**, *26*, e00215. [CrossRef]

90. Suhag, R.; Kumar, N.; Petkoska, A.T.; Upadhyay, A. Film formation and deposition methods of edible coating on food products: A review. *Food Res. Int.* **2020**, *136*, 109582. [CrossRef]

91. Lara, G.; Yakoubi, S.; Villacorta, C.M.; Uemura, K.; Kobayashi, I.; Takahashi, C.; Nakajima, M.; Neves, M.A. Spray technology applications of xanthan gum-based edible coatings for fresh-cut lotus root (Nelumbo nucifera). *Food Res. Int.* **2020**, *137*, 109723. [CrossRef]

92. Ruelas-Chacon, X.; Contreras-Esquivel, J.C.; Montañez, J.; Aguilera-Carbo, A.F.; Reyes-Vega, M.L.; Peralta-Rodriguez, R.D.; Sanchéz-Brambila, G. Guar Gum as an Edible Coating for Enhancing Shelf-Life and Improving Postharvest Quality of Roma Tomato (Solanum lycopersicum L.). *J. Food Qual.* **2017**, *2017*, 8608304. [CrossRef]

93. Naeem, A.; Abbas, T.; Ali, T.M.; Hasnain, A. Effect of guar gum coatings containing essential oils on shelf life and nutritional quality of green-unripe mangoes during low temperature storage. *Int. J. Biol. Macromol.* **2018**, *113*, 403–410. [CrossRef] [PubMed]

94. Dilek, M.; Polat, H.; Kezer, F.; Korcan, E. APPLICATION OF LOCUST BEAN GUM EDIBLE COATING TO EXTEND SHELF LIFE OF SAUSAGES AND GARLIC-FLAVORED SAUSAGE. *J. Food Process. Preserv.* **2010**, *35*, 410–416. [CrossRef]

95. Pizato, S.; Cortez-Vega, W.R.; de Souza, J.T.A.; Prentice-Hernández, C.; Borges, C.D. Effects of Different Edible Coatings in Physical, Chemical and Microbiological Characteristics of Minimally Processed Peaches (*Prunus persica* L. Batsch). *J. Food Saf.* **2013**, *33*, 30–39. [CrossRef]

96. Moradi, F.; Emamifar, A.; Ghaderi, N. Effect of basil seed gum based edible coating enriched with echinacea extract on the postharvest shelf life of fresh strawberries. *J. Food Meas. Charact.* **2019**, *13*, 1852–1863. [CrossRef]

97. Ainee, A.; Hussain, S.; Nadeem, M.; Al-Hilphy, A.R.; Siddeeg, A. Extraction, Purification, Optimization, and Application of Galactomannan-Based Edible Coating Formulations for Guava Using Response Surface Methodology. *J. Food Qual.* **2022**, *2022*, 1–10. [CrossRef]

98. Shahbazi, Y.; Shavisi, N. Application of active Kurdi gum and Farsi gum-based coatings in banana fruits. *J. Food Sci. Technol.* **2020**, *57*, 4236–4246. [CrossRef]

99. Soleimani-Rambod, A.; Zomorodi, S.; Raeisi, S.N.; Asl, A.K.; Shahidi, S.-A. The Effect of Xanthan Gum and Flaxseed Muci-lage as Edible Coatings in Cheddar Cheese during Ripening. *Coatings* **2018**, *8*, 80. [CrossRef]

100. El-Sheikh, D.M. Efficiency of using Arabic Gum and Plantago Seeds Mucilage as Edible Coating for Chicken Boneless Breast. *Food Sci. Qual. Mgmt.* **2014**, *32*, 28–33.

101. Taghinia, P.; Abdolshahi, A.; Sedaghati, S.; Shokrollahi, B. Smart edible films based on mucilage of lallemantia iberica seed incorporated with curcumin for freshness monitoring. *Food Sci. Nutr.* **2021**, *9*, 1222–1231. [CrossRef]

102. Jouki, M.; Yazdi, F.T.; Mortazavi, S.A.; Koocheki, A.; Khazaei, N. Effect of quince seed mucilage edible films incorporated with oregano or thyme essential oil on shelf life extension of refrigerated rainbow trout fillets. *Int. J. Food Microbiol.* **2014**, *174*, 88–97. [CrossRef] [PubMed]

103. Kang, S.; Wang, H.; Xia, L.; Chen, M.; Li, L.; Cheng, J.; Li, X.; Jiang, S. Colorimetric film based on polyvinyl alcohol/okra mucilage polysaccharide incorporated with rose anthocyanins for shrimp freshness monitoring. *Carbohydr. Polym.* **2019**, *229*, 115402. [CrossRef] [PubMed]

104. Anis, A.; Pal, K.; Al-Zahrani, S.M. Essential Oil-Containing Polysaccharide-Based Edible Films and Coatings for Food Security Applications. *Polymers* **2021**, *13*, 575. [CrossRef]

105. Ramakrishnan, R.; Kulandhaivelu, S.V.; Roy, S.; Viswanathan, V.P. Characterisation of ternary blend film of alginate/carboxymethyl cellulose/starch for packaging applications. *Ind Crops Prod.* **2023**, *193*, 116114. [CrossRef]

106. Ahmed, I.; Lin, H.; Zou, L.; Brody, A.L.; Li, Z.; Qazi, I.M.; Pavase, T.R.; Lv, L. A comprehensive review on the application of active packaging technologies to muscle foods. *Food Control.* **2017**, *82*, 163–178. [CrossRef]

107. Jiang, H.; Zhang, W.; Chen, L.; Liu, J.; Cao, J.; Jiang, W. Recent advances in guar gum-based films or coatings: Diverse property enhancement strategies and applications in foods. *Food Hydrocoll.* **2023**, *136*, 108278. [CrossRef]

Article

Silver Nanoparticles and *Glycyrrhiza glabra* (Licorice) Root Extract as Modifying Agents of Hydrogels Designed as Innovative Dressings

Magdalena Kędzierska [1], Magdalena Bańkosz [2], Anna Drabczyk [2],*, Sonia Kudłacik-Kramarczyk [2], Mateusz Jamroży [3],* and Piotr Potemski [1]

[1] Department of Chemotherapy, Medical University of Lodz, Copernicus Memorial Hospital of Lodz, 93-513 Lodz, Poland

[2] Department of Materials Engineering, Faculty of Materials Engineering and Physics, Cracow University of Technology, 37 Jana Pawła II Av., 31-864 Krakow, Poland

[3] Faculty of Materials Engineering and Physics, Cracow University of Technology, 37 Jana Pawła II Av., 31-864 Krakow, Poland

* Correspondence: anna.drabczyk2@pk.edu.pl (A.D.); mateusz.jamrozy@student.pk.edu.pl (M.J.)

Abstract: The interest in the application of plant extracts as modifiers of polymers intended for biomedical purposes is constantly increasing. The therapeutic properties of the licorice root, including its anti-inflammatory and antibacterial activity, make this plant particularly promising. The same applies to silver nanoparticles showing antibacterial properties. Thus the main purpose of the research was to design hydrogel dressings containing both licorice root extract and nanosilver so as to obtain a system promoting wound regeneration processes by preventing infection and inflammation within the wound. The first step included the preparation of the plant extract via the solid-liquid extraction using the Soxhlet extractor and the synthesis of silver nanoparticles by the chemical reduction of silver ions using a sodium borohydride as a reducing agent. Subsequently, hydrogels were synthesized via photopolymerization and subjected to studies aiming at characterizing their sorption properties, surface morphology via scanning electron microscopy, and their impact on simulated physiological liquids supported by defining these liquids' influence on hydrogels' structures by FT-IR spectroscopy. Next, the tensile strength of hydrogels and their percentage elongation were determined. Performed studies also allowed for determining the hydrogels' wettability and free surface energies. Finally, the cytotoxicity of hydrogels towards L929 murine fibroblasts via the MTT reduction assay was also verified. It was demonstrated that developed materials showed stability in simulated physiological liquids. Moreover, hydrogels were characterized by high elasticity (percentage elongation within the range of 24–29%), and their surfaces were hydrophilic (wetting angles below 90°). Hydrogels containing both licorice extract and nanosilver showed smooth and homogeneous surfaces. Importantly, cytotoxic properties towards L929 murine fibroblasts were excluded; thus, developed materials seem to have great potential for application as innovative dressings.

Keywords: hydrogel dressings; licorice root extract; silver nanoparticles; wettability; cytotoxicity; tensile strength; sorption ability

1. Introduction

Glycyrrhiza glabra (licorice) root is widely applied as a sweetener and flavoring agent in candies, sweets, and other food products. The sweet taste of licorice root results from the presence of glycyrrhizin [1,2]. However, despite its use in the food industry, this plant is also applied as a medicinal herb [3]. Licorice root has been used in Chinese medicine for over 1000 years. Its pharmacological properties result from the fact that it consists of a huge amount of active chemical compounds, including isoflavonoids, chalcones, amino acids, lignins, amines, gums, and volatile oils. It was demonstrated that the composition of licorice

root contains over 20 triterpenoids and 300 flavonoids [4,5]. Such an extensive chemical composition makes this plant an extremely interesting research material in terms of the possibilities of its pharmaceutical applications. Biologically active licorice compounds are used in many diseases due to their anti-inflammatory, antibacterial, and antiviral properties [6–8]. Furthermore, licorice also shows anti-carcinogenic and neuroprotective activity (it may prevent or delay the degradation of neurons) [9]. It has also been proven that licorice may be applied as an effective therapeutic agent in the treatment of diabetes [10]. As has been demonstrated by Yang et al., licorice extracts show excellent anti-diabetic activity both in vitro and in vivo. They affect the mechanisms of insulin receptor site sensitivity, increase the use of glucose in various tissues and organs, and correct metabolic disorders improving microcirculation in the body simultaneously [11]. Subsequently, it has also been reported that glabrydin occurring in the licorice root may be an alternative therapeutic agent in thrombogenic disorders due to the impact of this compound on the prevention of platelet aggregation [12]. *Glycyrrhiza* L. root may also be successfully used in the treatment of infectious hepatitis and bronchitis [13]. Feng Yeh et al. proved the effective activity of licorice extract against HRSV infection on airway epithelial cells. Bioactive compounds present in this plant extract prevented virus transfer and internalization. Moreover, it has been demonstrated that under the influence of *Glycyrrhiza* L., mucosal cells are stimulated to release IFN-β, counteracting the same viral infection [14]. It has also been stated that the flavonoids extracted from licorice root reduced the inflammation of acute pneumonia induced in vivo in mice by lipopolysaccharide [15]. Studies on the application of licorice extracts in the treatment of respiratory diseases, including COVID-19, were also presented by Gomaa et al. [16] and li Ng et al. [17]. Additionally, the possibility of the application of licorice extracts in the treatment of alcoholic liver injury was described in [18]. Furthermore, the attention of scientists was focused not only on the therapeutic effect of the bioactive compounds included in licorice but also on their ability to enhance the action of the other medicinal compounds by forming supermolecular complexes with them [19]. Due to its antioxidant, anti-inflammatory, and antibacterial properties, many studies have been on the use of licorice in the treatment of inflammation accompanying certain skin diseases [20]. It has been shown that the preparations based on licorice extract may be successfully applied in the treatment of erythema [21], vitiligo [22,23], atopic dermatitis [24,25], as well as baldness [26].

The wide spectrum of the activity of the compounds included in the licorice root corresponds to the great application potential of this plant. Thus considering its properties desirable in terms of skin inflammation treatment, the main purpose of the presented research was to develop hydrogel dressing material modified with licorice root extract. Many commercially available preparations occur in the form of a gel of an ointment wherein such forms may cause some of the active substance to rub into clothing; thus, the introduction of such a substance into the hydrogel dressing may prevent this phenomenon. In this work, the results of the research aimed at developing hydrogel dressing materials containing bioactive substances extracted from licorice root. Furthermore, developed materials were additionally incorporated with silver nanoparticles showing antibacterial properties. The main hypothesis of the research was to develop a multifunctional dressing material that could simultaneously fulfill protective functions, absorb wound exudate, and show anti-inflammatory and antibacterial properties due to the presence of the modifiers: licorice root extract and nanosilver. To our knowledge, such a combination is innovative and has not yet been presented. The base forming the hydrogel matrix consisted of natural polymers such as gelatin and chitosan, demonstrating high biocompatibility. In the first step of the research, the synthesis of silver nanoparticles was performed, while for this purpose, the chemical reduction was employed. Next, licorice extract was prepared via the Soxhlet extraction. Both these materials were subsequently used as modifiers of chitosan/gelatin-based hydrogel dressings. The hydrogels were obtained by means of UV radiation and next subjected to the detailed physicochemical characteristic. In the course of the research, sorption properties of hydrogels important in terms of potential sorption

of the wound exudate were determined. Next, incubation of hydrogels in simulated physiological liquids supported by determining their impact on hydrogels' structure via FT-IR spectroscopy was also performed. Hydrogels' surface morphology, wettability as well as mechanical properties, including the tensile strength and the percentage elongation, were also characterized. Finally, the cytotoxicity of hydrogels towards L929 murine fibroblasts via the MTT reduction assay was also verified.

2. Results and Discussion

2.1. Characteristic of Nanosilver Suspension

2.1.1. The Particle Size Analysis via DLS Technique

Below in Figure 1, the results of the DLS analysis are presented.
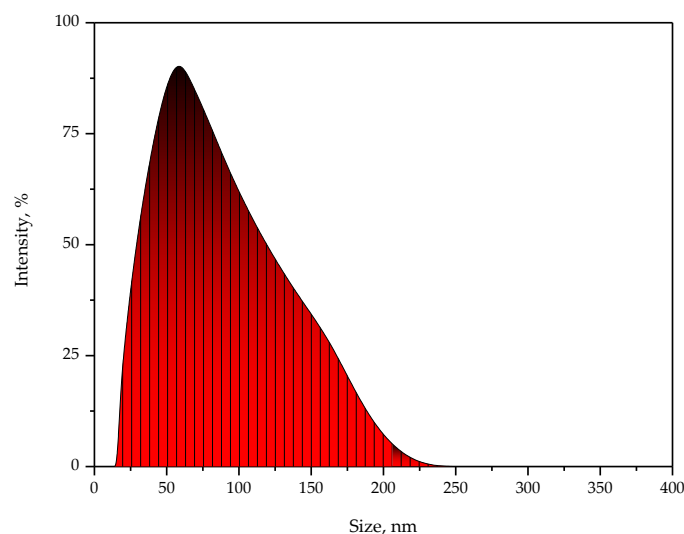
Figure 1. The particle size distribution in obtained silver nanoparticles suspension.

Based on the performed analysis, it may be reported that in the tested suspension, the particles with sizes within the range of 20–200 nm occurred, wherein the most common population of the particles showed the size with an average hydrodynamic diameter within the range of 40–80 nm. Thus the results of the DLS analysis clearly indicated the presence of nanoparticles in the suspension.

2.1.2. Characterization of Optical Properties of Nanosilver Suspension

UV–Vis spectrum of the suspension obtained as a result of the chemical reduction of silver ions is presented below in Figure 2. The analysis allowed us to verify whether silver nanoparticles were obtained as a result of the method applied.

In order to confirm the presence of the silver nanoparticles, the suspension obtained as a result of the procedure described in Section 3.2. of the paper was subjected to UV–Vis spectroscopy. Noble metal nanoparticles, including silver ones, are characterized by specific optical properties as well as the ability to absorb radiation within the range of visible and ultraviolet. Thus, UV–Vis spectroscopy is one of the most frequently used methods aimed at confirming the presence of silver nanoparticles [27,28]. On the UV–Vis spectrum visible in Figure 3, the absorption band with a maximum at a wavelength of approximately 432 nm, typical exactly for silver nanoparticles, was observed. The absorption band at a similar wavelength demonstrating the presence of nanosilver was also presented by Agustina et al. [29] and Alim-Al-Razy et al. [30]. This, in turn, indicates the consistency of the results of the performed analysis with previously reported studies.
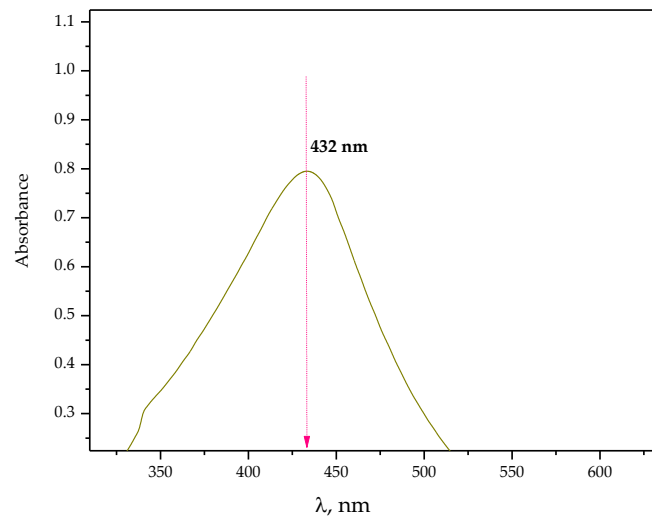
Figure 2. UV–Vis spectrum of the particle suspension obtained as a result of the chemical reduction of silver ions.
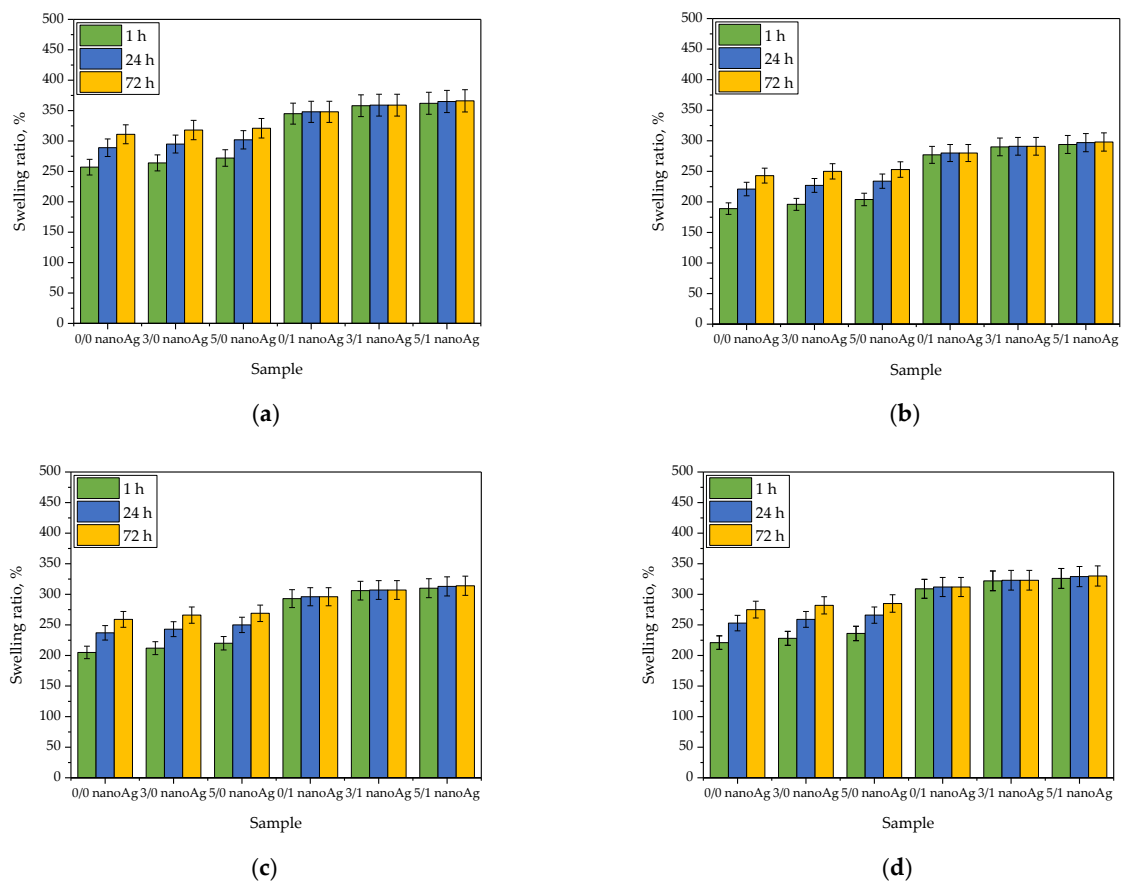
Figure 3. Results of investigations on sorption properties of hydrogels in distilled water (**a**), SBF (**b**), Ringer liquid (**c**), and artificial saliva (**d**) (n = 3, n—number of repetitions).

2.2. Results of Hydrogels' Swelling Ability Measurements

Swelling ratios of tested hydrogels are presented below in Figure 3, wherein the results are compiled separately for each liquid. The study was conducted in triplicates, and the results are shown as average values with corresponding standard deviations (SD, presented as error bars).

Studies on the swelling properties of the materials are aimed at determining the ability of the material to interact with aqueous solutions, which means its ability to their absorption. Such ability may be expressed as the swelling ratio (with unit %) after the appropriate calculation, including the mass of a dry hydrogel and a mass of hydrogel after swelling at a specific time. So based on such calculations for performed experiments, it may be concluded that tested hydrogels showed a sorption capability of about 200–300%. Importantly, the highest values of this parameter were reported for hydrogels swelling in distilled water, wherein the lowest ones were in the case of materials tested in SBF. High values of swelling ratio in selected liquid mean that the samples absorbed this liquid to the greatest extent. Distilled water, contrary to the rest of the tested media, does not contain any ions which could negatively affect the sorption process of the tested material. For example, divalent ions such as calcium ions may interact with the polymer network, resulting in an increase in the crosslinking density of polymer chains. This, in turn, may result in a decrease in the swelling properties of such polymer. This dependence is clearly visible in the case of the results presented in Figure 3b–d, where the calculated swelling ratios are lower than the ones presented in Figure 3a.

Results of performed studies also allow for determining the impact of the modifiers—licorice root extract and nanosilver suspension—on the sorption properties of hydrogels. Thus, referring to the first mentioned modifier, it may be reported that the presence of the plant extract in the hydrogel matrix did not affect the swelling properties of tested materials. Due to the fact that hydrogels showing high swelling properties are considered beneficial in terms of their biomedical application as dressings, the lack of the negative impact of the licorice root extract on this property is determined as a positive aspect. Thus it may be concluded that the mentioned extract does not affect the swelling ability and, importantly, does not reduce this ability compared to the swelling properties of hydrogel without this additive. Another situation was observed in the case of the modification of hydrogels with nanosilver. A clear increase in the swelling ratios of hydrogels containing this modifier was reported. Probably this resulted from the interactions between the aqueous suspension of silver nanoparticles and the hydroxyl groups included in the medium in which the swelling samples were placed. These interactions cause the attraction of the water molecules and thus contribute to the higher values of the swelling ratios observed on the y-axis. From the application viewpoint, such a phenomenon is most desirable. Nonetheless, it should be emphasized that the appropriate selection of the components of the hydrogel matrix allows for controlling the sorption properties of the tested materials.

2.3. Results of Incubation Studies

Results of the measurements of the pH and the temperature of incubation media in the presence of the hydrogel samples are presented in Figures 4–7. The study was performed in triplicates wherein the results are given as average values with corresponding standard deviations (SD, shown as error bars).

The occurrence of rapid changes in pH may indicate the degradation of hydrogel materials or the release of unreacted reagents, such as a crosslinking agent or photoinitiator from the matrix, which is an undesirable phenomenon. In the case of all tested materials, such rapid and significant changes in the values of tested parameters have not been observed. This, in turn, indicates the stability of the hydrogels in tested environments. However, some slight changes of various natures—i.e., decreases or increases—in measured pH values of the incubation media were noticed. Nonetheless, these changes were very slight, i.e., by a maximum of one pH unit. The hydrogel swells under the influence of the incubation medium; this phenomenon has been described in more detail in Section 2.2. As a result of liquid sorption, the loosening of the polymer network may take place. This, in turn, may lead to the occurrence of various interactions between the components of the polymer and the incubation medium. As a result, numerous compounds (both acidic and alkaline in nature) included in the licorice root extract acting as a modifier of the hydrogel may release from the polymer matrix. Finally, slight changes in pH of the incubation

media in which such a release takes place may be observed. Alternating changes in pH values (i.e., their slight decreases or increases) may be caused by constant interactions of the incubation material with the liquid. Such a phenomenon indicating the gradual release of active compounds present in licorice root extract is beneficial due to the fact that it gives information on the development of the materials with active substance delivery function.
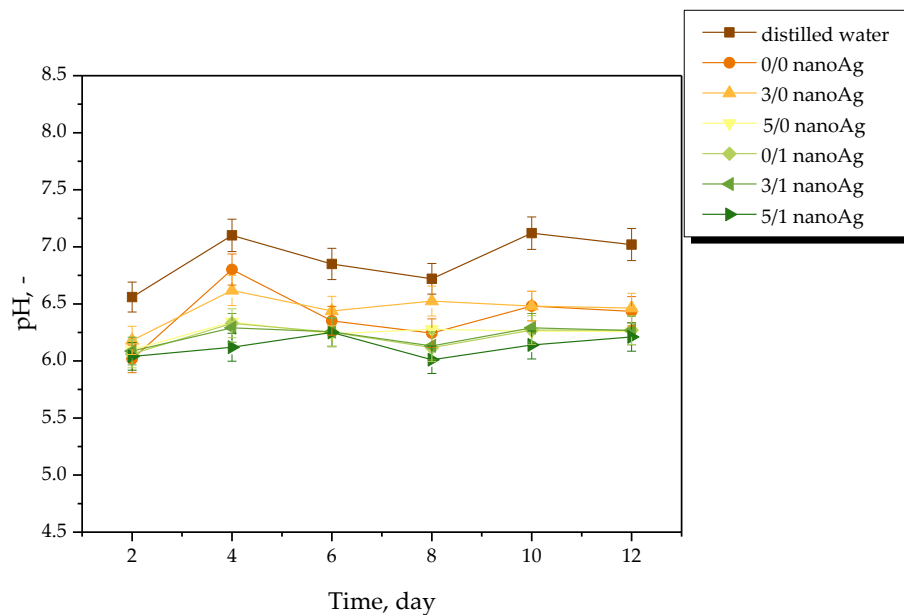
(**a**)
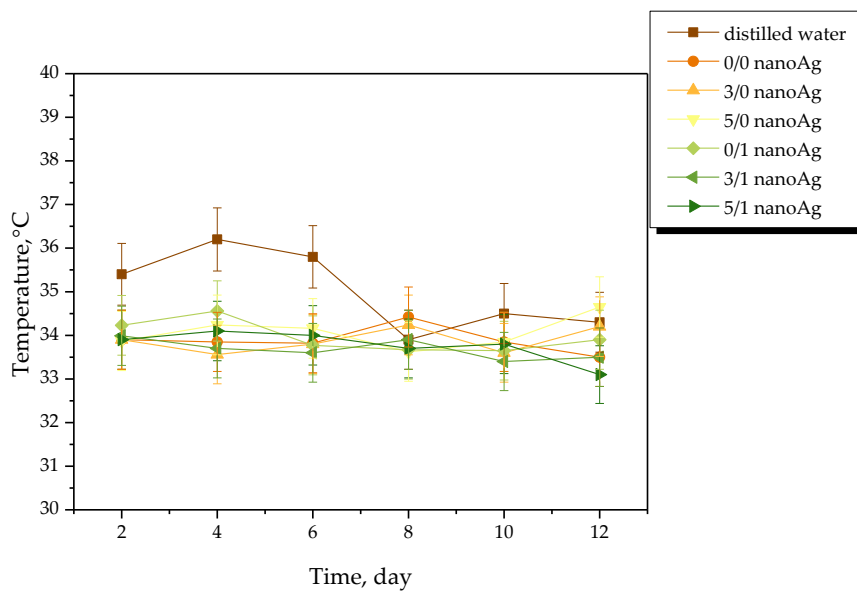
(**b**)

Figure 4. pH (**a**) and temperature (**b**) measurements of distilled water during hydrogels' incubation (n = 3, n—number of repetitions).

(**a**)

(**b**)
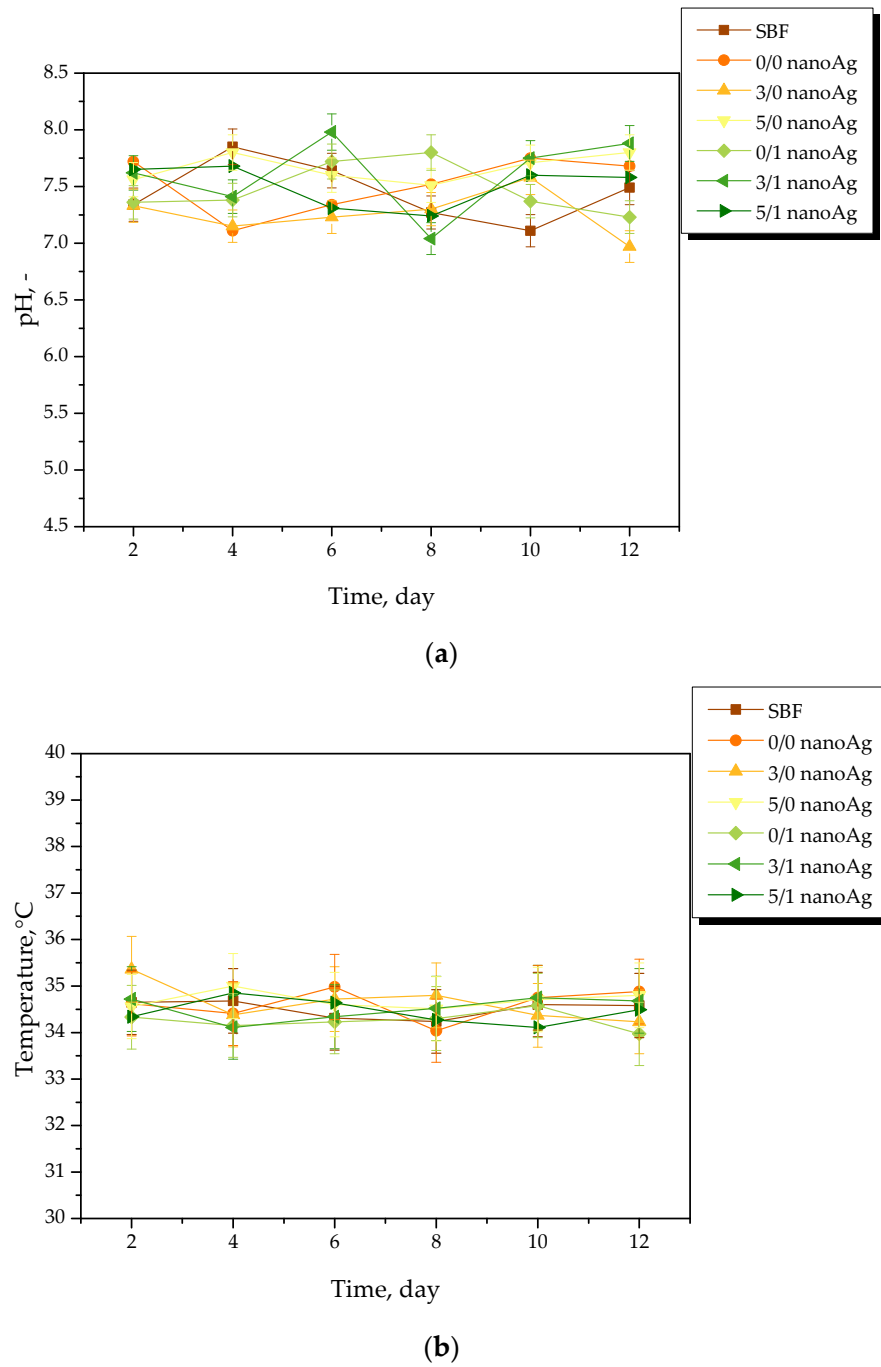
Figure 5. pH (**a**) and temperature (**b**) measurements of SBF during hydrogels' incubation (n = 3, n—number of repetitions).

(**a**)

(**b**)
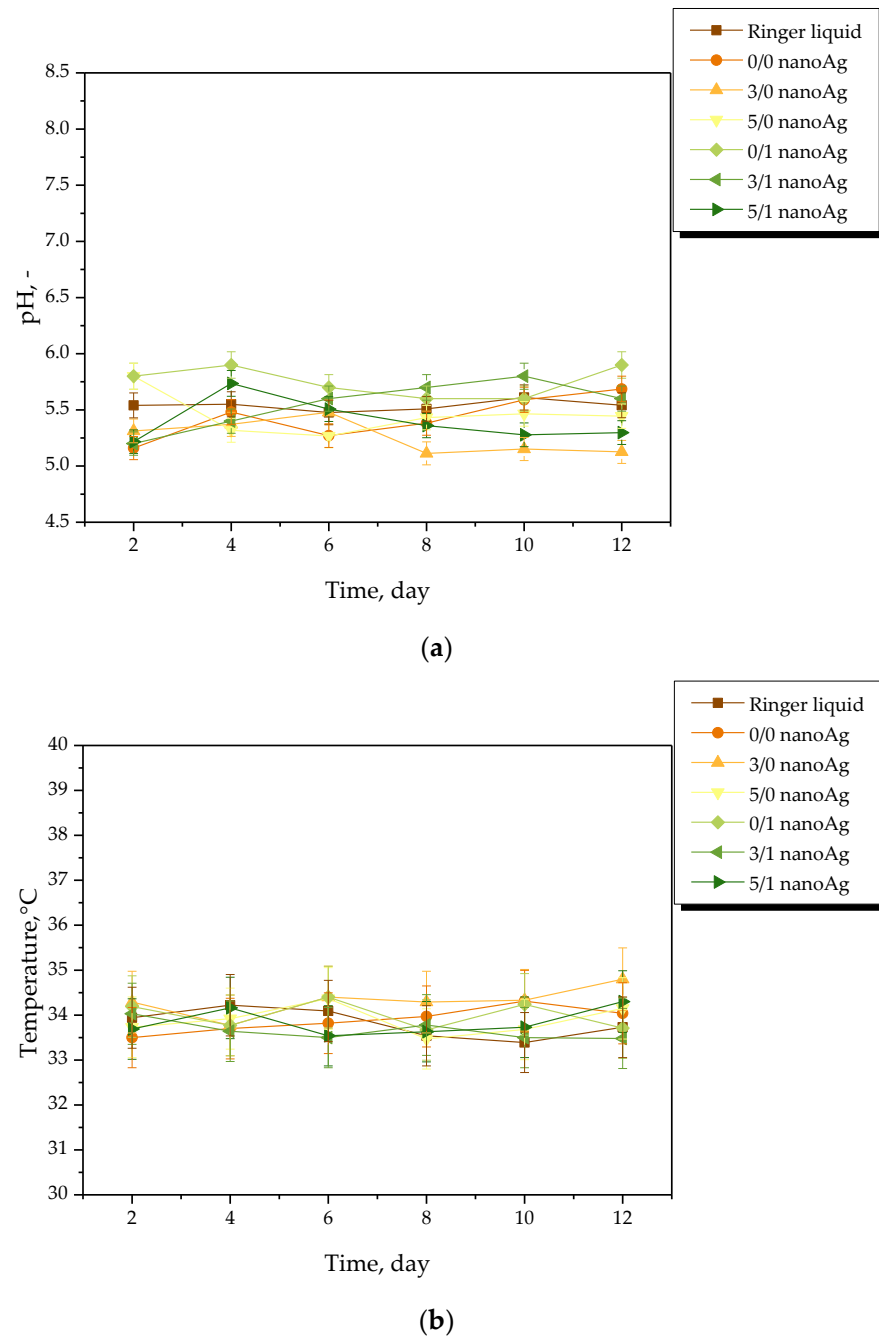
Figure 6. pH (**a**) and temperature (**b**) measurements of Ringer liquid during hydrogels' incubation (n = 3, n—number of repetitions).

(**a**)

(**b**)
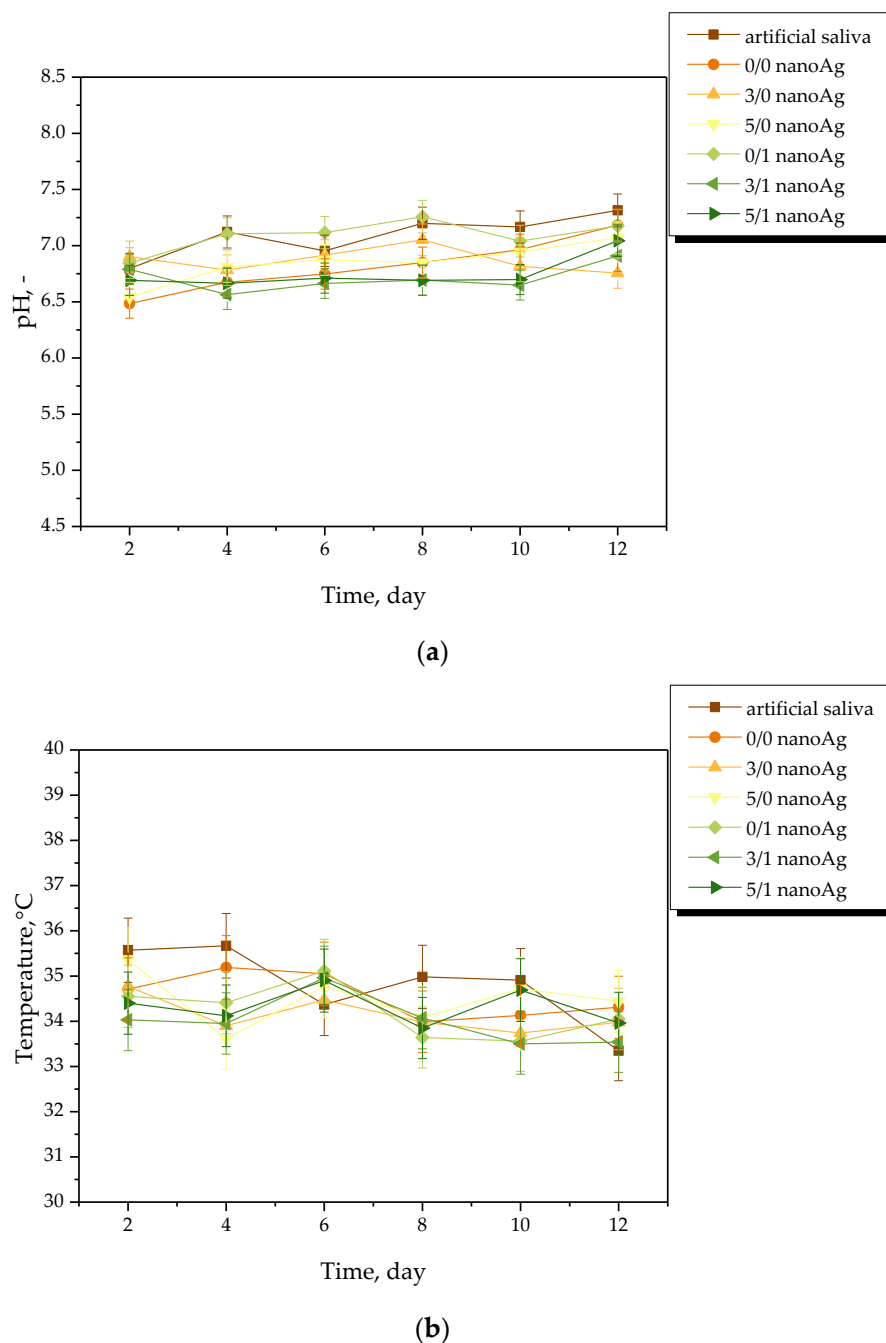
Figure 7. pH (**a**) and temperature (**b**) measurements of artificial saliva during hydrogels' incubation (n = 3, n—number of repetitions).

2.4. The Impact of the Incubation Studies on Hydrogels' Chemical Structure Verified via FT-IR Spectroscopy

FT-IR spectra of hydrogels are presented in Figure 8. The spectra were compiled in such a way as to compare the structure of particular samples before and after the incubation in tested media.

The performed spectroscopic analysis allowed for verifying the presence of characteristic groups for compounds included in developed polymer matrices. The study was performed both for samples before and after the incubation in simulated physiological liquids. On the one hand, the disappearance of characteristic absorption bands may suggest the degradation of the tested material. On the other hand, it may be reported that such a degradation did not occur because this process would be reflected in significant pH changes

of incubation media, and such ones have not been observed. Thus such disappearance or decrease in the intensity of some absorption bands may also indicate the release of the modifiers—i.e., licorice root extract or silver nanoparticles—which, located within the polymer network, may obscure some characteristic groups (as a result, the signal deriving from them is limited).
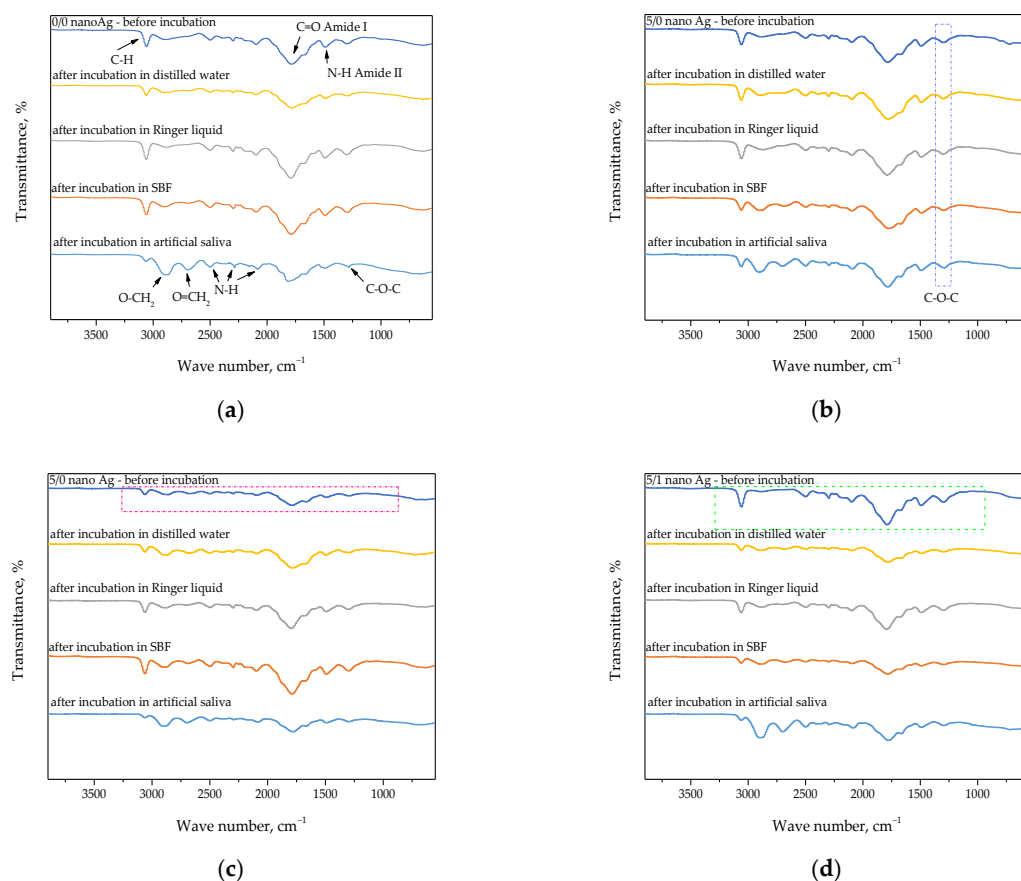
Figure 8. FT-IR spectra showing the impact of the incubation on the structure of sample 0/0 nanoAg (**a**), 5/0 nanoAg (**b**), 0/1 nanoAg (**c**), and 5/1 nanoAg (**d**).

In Figure 8a, it is possible to observe the absorption bands characteristic of the structure of two polymers used for the synthesis of hydrogel matrix, i.e., chitosan and gelatin [31–33]. Additionally, on FT-IR spectra of the sample after incubation in artificial saliva, an occurrence of more absorption bands characteristic for these polymers—invisible on the spectrum of the material prior to incubation—was observed (Figure 8a). This may suggest that the polymer chains in the tested material after the drying process were arranged in a way that allowed the disclosure and detection of more groups characteristic for components forming the polymer matrix. Such a dependence was also observed for other tested materials, i.e., in Figure 8b–d). This probably results from the chemical composition of the artificial saliva and the interactions occurring between the functional groups of the polymers and ions included in this incubation liquid.

An interesting dependence was also observed in the case of the hydrogel modified with licorice root extract. In Figure 8b), an increase in the intensity of the absorption band characteristic for the –C–O–C– group deriving from polysaccharides included in this extract may be observed (this has been marked via the blue frame in Figure 8b). Thus, this demonstrates that the presence of the additive in the form of the plant extract is indicated by the increase in the intensity of the selected absorption band in the FT-IR spectra.

Another equally interesting dependence observable during the performed study may be noticed in the FT-IR spectra of hydrogels incorporated with silver nanoparticles. In

Figure 8c,d, the spectra of materials before incubation may be observed (the absorption bands have been marked via the frames—pink one in Figure 8c and green one in Figure 8d), wherein in the case of the material without the licorice root extract (Figure 8c), the spectrum is very blurry and differs significantly in the intensity from the spectrum visible in Figure 8d. In the case of the hydrogel with nanosilver, these nanoparticles are probably located between the polymer chains (in free spaces between them), which makes it difficult to identify groups deriving from polymers. However, a release of nanosilver or its elution probably takes place as a result of the incubation, which in turn results in exposing the characteristic groups giving the same appropriate absorption bands on FT-IR spectra. In the case of the hydrogels modified both with licorice root extract and nanosilver, such a phenomenon was not observed. This is probably caused by the different placement of metallic nanoparticles within the polymer structure. Additionally, some absorption bands derive also from the polysaccharides included in the plant extract.

2.5. Results of SEM Imaging of Hydrogels

The surface morphology of hydrogels was characterized by means of scanning electron microscopy. Obtained SEM images are presented in Figure 9.
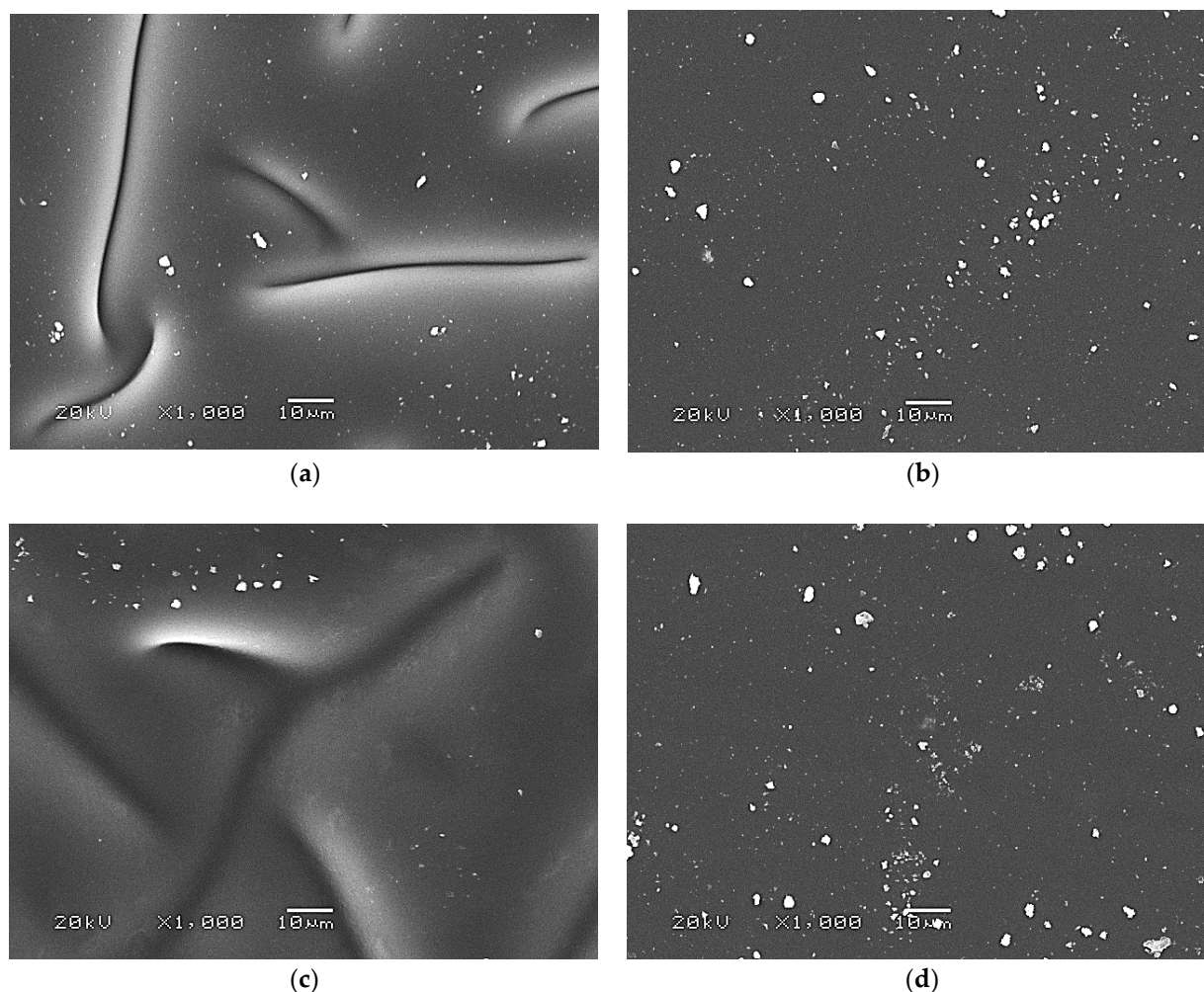
Figure 9. SEM images of hydrogel materials: sample: 0/0 nanoAg (**a**); 5/0 nanoAg (**b**); 0/1 nanoAg (**c**); 5/1 nanoAg (**d**).

Based on the presented SEM images, it may be reported that the highest impact on the surface morphology of the hydrogels has the presence of the plant extract. The samples without this additive (whose images are presented in Figure 9a,b) are characterized

by heterogeneous and undulating surfaces. In the case of hydrogels modified with the mentioned extract, their surface is homogeneous and smooth (Figure 9b,d). The plant extract introduced into the polymer matrix probably fills the cavities on the polymer surface, thus making it smoother. On the other hand, any significant impact of nanosilver on the developed materials' surface morphology was not observed.

2.6. Wettability of Hydrogels Supported by Determining Their Surface Free Energy

Next, in order to verify the hydrophilicity or hydrophobicity of the surfaces of developed hydrogels, their wetting angles were determined. The results of performed investigations supported by the images showing the first contact of the liquid of distilled water with the hydrogel sample are presented in Table 1, wherein the results of the statistical analysis are shown in Table 2.

Table 1. Results of hydrogels' wettability analysis.

Sample Name	Total Surface Free Energy, mJ/m^2	Contact Angle, °	Image of Hydrogel during Its First Contact with Water
0/0 nanoAg	55.22	42.85 ± 0.68	
3/0 nanoAg	60.58	35.15 ± 1.15	
5/0 nanoAg	67.67	29.17 ± 0.93	
0/1 nanoAg	55.88	41.45 ± 0.97	
3/1 nanoAg	62.28	33.85 ± 1.02	
5/1 nanoAg	72.08	26.58 ± 1.18	

Table 2. Results of the statistical analysis of contact angle measurements performed via the two-way analysis of variance (ANOVA) (*p* indicates the statistical significance).

Analysis of Variance	*p*
Source of Variation	
Licorice root extract	0.02275
Nanosilver suspension	0.002
Interaction	0.99443

Based on the performed analysis, it was reported that as the content of the modifiers in the polymer matrices increased, the values of their wetting angles decreased. In the

case of the unmodified hydrogel sample, its wetting angle was 42°, wherein the value of this parameter determined for the sample containing both these additives (i.e., 5 mL of the plant extract and 1 mL of nanosilver suspension) was 26°. Hydrophilic surfaces are defined as the ones for which the value of their wetting angle is lower than 90° [34]. Thus it may be concluded that all analyzed materials showed a hydrophilic surface wherein the larger the amount of the modifiers, the higher hydrophilicity. Due to the presence of the chemical compounds included in licorice root extract in the modified materials, interactions in the form of hydrogen bonds between functional groups from these compounds and the water molecules may occur, thus increasing the wettability of such materials' surface. Moreover, in the case of the presence of nanosilver, which was introduced into the polymer matrix in the form of an aqueous suspension, such interactions between modified hydrogels and the drop of liquid may occur, which also translates into the decrease of the wetting angle. The surface wettability is strictly correlated with the value of its surface free energy. Along with the decreasing values of the contact angle, the increase in the value of the surface free energy, which may be defined as a measure of the attractive force of the tested substrate, is observed. The highest value of the total surface free energy was reported in the case of the samples characterized by the lowest wetting angle and thus the most hydrophilic surface, i.e., sample 5/1 nanoAg (modified with the highest amounts of licorice root extract and nanosilver).

The material's surface, its roughness, wettability, topography, as well as surface free energy constitute the very important parameters characterizing the biomaterial. The initial cell adhesion, which depends to a large extent on the aforementioned parameters, is of key importance for further cell proliferation and their regenerative processes [35]. As it was reported by Majhy et al., a moderate surface free energy of 70 mJ/m^2 is the most favorable for effective cell adhesion, growth, and proliferation [36]. This is consistent with other works where it was demonstrated that cells show better adhesion to hydrophilic surfaces [37]. Considering the obtained results, it may be concluded that developed materials, due to the surfaces' hydrophilic nature and the high surface free energy values, show the desired features in terms of supporting regeneration processes.

2.7. Results of Mechanical Investigations including Determining the Hydrogels' Tensile Strength and Percentage Elongation

Results of studies on the tensile strength of hydrogels are presented in Figure 10, the values of their percentage elongation are shown in Figure 11, and the results of the statistical analysis are shown in Tables 3 and 4.

Materials, which are considered for applications for biomedical purposes, should meet a number of requirements. Apart from biocompatibility and relatively simple and quick synthesis methodology, their mechanical properties are extremely important [38]. One of the most popular tools for characterizing the mechanical properties of hydrogels is the static tensile test which provides information about the hydrogels' tensile strength and the possibility of their elongation [39]. Tensile strength may be defined as the maximum stress that a material is able to withstand before its breakage [40].

Based on the results presented in Figure 11, it may be observed that the highest tensile strength—i.e., 0.112 MPa—was reported for unmodified hydrogel. Next, as the amount of the licorice root extract increased, the hydrogel tensile strength decreased, wherein the lowest value of this parameter—i.e., 0.072 MPa—was calculated for the sample containing 5 mL of the plant extract and 1 mL of nanosilver suspension (sample 5/1 nanoAg). The decrease in the value of the tensile strength results from the introduction into the material of additional modifying substances while simultaneously maintaining the same amount of crosslinking agent. The introduction of the plant extract and nanosilver suspension results in the dilution of the reaction mixture, while the use of the same amount of the crosslinker may result in the preparation of the material with a lower crosslinking density. However, it should be emphasized that in the case of the percentage elongation, which indicates the hydrogels' elasticity, such changes in its values were not so visible. The elasticity of modified

hydrogels compared to the elasticity of unmodified materials decreased slightly. The sample containing the highest amounts of the modifying substances—sample 5/1 nanoAg—is characterized by a percentage elongation of approximately 24.5%, which in the case of the application of such a material as dressing, is beneficial and consistent with previously presented research [41–43].
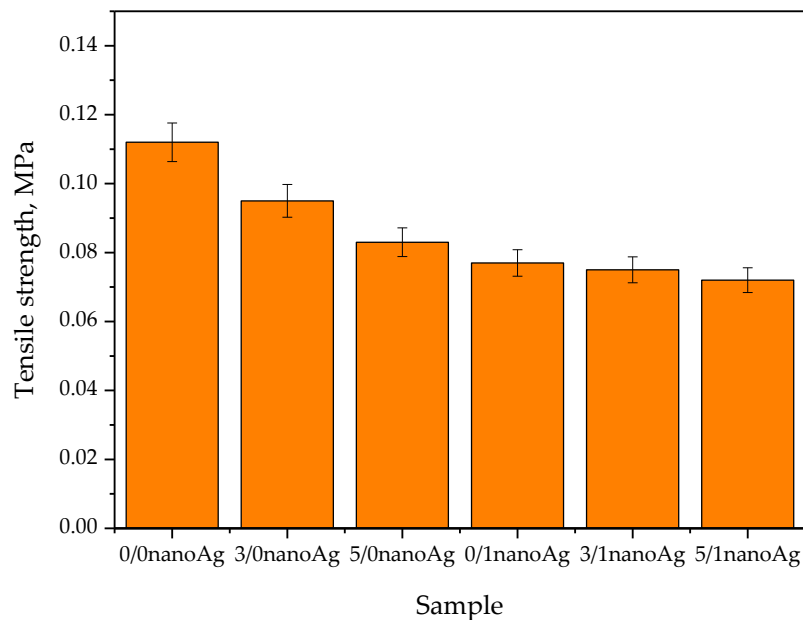
Figure 10. Results of tensile strength measurements of hydrogels (number of repetitions n = 3).
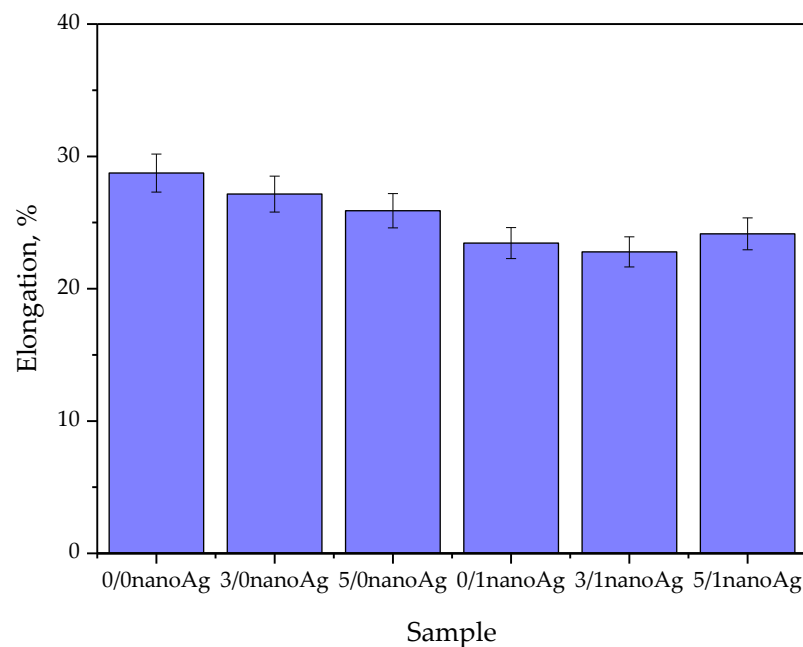
Figure 11. Results of percentage elongation measurements of hydrogels (number of repetitions n = 3).

Table 3. Results of the statistical analysis of hydrogels' tensile strength measurements performed via the two-way analysis of variance (ANOVA) (*p* indicates the statistical significance).

Analysis of Variance	*p*
Source of Variation	
Licorice root extract	0.01991
Nanosilver suspension	3.8525×10^{-4}
Interaction	0.01991

Table 4. Results of the statistical analysis of hydrogels' percentage elongation measurements performed via the two-way analysis of variance (ANOVA) (*p* indicates the statistical significance).

Analysis of Variance	*p*
Source of Variation	
Licorice root extract	0.02092
Nanosilver suspension	0.00634
Interaction	0.02094

2.8. In Vitro Biological Analysis of Hydrogels via MTT Reduction Assay

In vitro cytotoxicity analysis was performed in line with EN ISO 10993-5:2009 standard [44]. Results of the MTT assay performed using L929 murine fibroblasts are presented in Figure 12, wherein the results of the statistical analysis are shown in Table 5. The study was performed in triplication, wherein the results are presented as average values with corresponding standard deviations (SD, given as error bars).
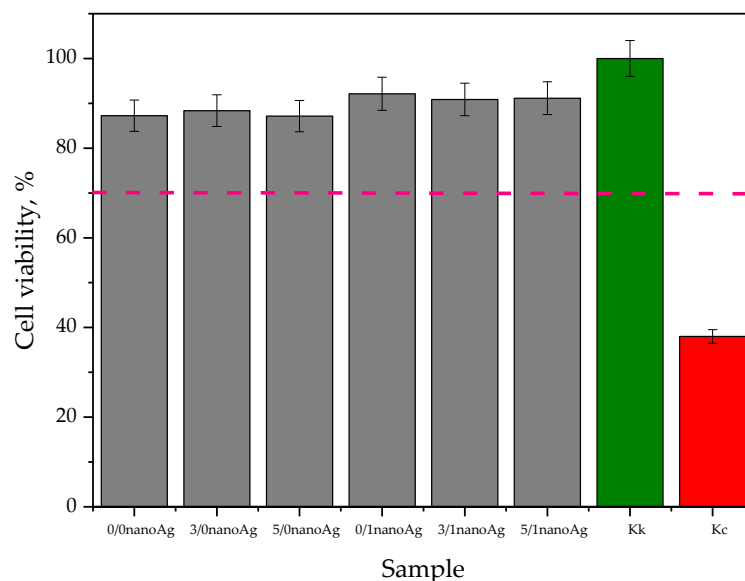
Figure 12. Results of in vitro cytotoxicity analysis of hydrogels via the MTT reduction assay.

Table 5. Results of the statistical analysis of MTT reduction assay conducted via the two-way analysis of variance (ANOVA) (*p* indicates the statistical significance).

Analysis of Variance	*p*
Source of Variation	
Licorice root extract	0.03264
Nanosilver suspension	5.32907×10^{-4}
Interaction	0.03264

In accordance with the guidelines of the previously indicated standard, the material is defined as non-cytotoxic in the case when the viability of the selected cell line is incubated for 24 h in its presence above 70% (this cell viability has been marked in Figure 12 via the pink dotted line). Thus, in the case of all tested materials, this requirement was met, which confirms the lack of cytotoxic activity of developed hydrogels against the L929 murine fibroblasts. As it was demonstrated in Figure 12, in the case of samples containing silver nanoparticles, the cell viability slightly increased. This effect may be attributed to the antibacterial activity of nanosilver [45,46]. Developed materials that are applicable for biomedical uses were obtained in strictly controlled conditions, ensuring the highest possible sterility. However, during the synthesis, transport, or investigations, their slight contamination will occur; then, the presence of silver nanoparticles showing antibacterial properties may result in a slight increase in cell survival. This, in turn, constitutes an additional advantage of developed materials.

3. Materials and Methods

3.1. Materials

Chitosan (high molecular weight, deacetylation degree 75–85%), gelatin (obtained from porcine skin, Type A, gel strength 300), 2-hydroxy-2-methylpropiophenone (photoinitiator, d = 1.077 g/mL, 97%), diacrylate poly(ethylene glycol (crosslinking agent, d = 1.120 g/mL, average molecular weight M_n = 700 g/mol), and polyvinylpyrrolidone (average molecular weight 10,000 g/mol) were bought in Merck (Darmstadt, Germany). Silver nitrate (99.9%, pure p.a.) and sodium borohydride ($NaBH_4$, 98%, pure p.a.) were purchased from Avantor Performance Materials Poland S.A. (Gliwice, Poland). *Glycyrrhiza glabra* (Licorice) root was bought in Natur-Sklep (Wrocław, Poland).

3.2. Preparation of Glycyrrhiza glabra (Licorice) Root Extract

In order to obtain bioactive components of licorice, the solid–liquid extraction using the Soxhlet extractor was performed. This is the first-choice type of extraction in the case of isolating organic compounds from plant materials. The scheme of this process is presented below in Figure 13.

Licorice root
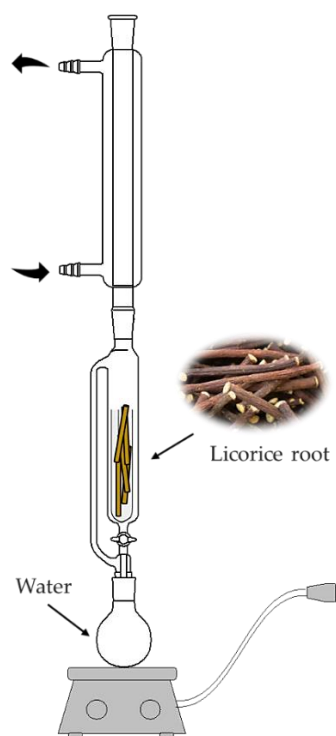
Water

Figure 13. Licorice root extraction scheme.

The procedure of the extraction was as follows: firstly, the licorice root was placed in a thimble while the distilled water was placed in the round bottom flask. Then, the solvent was heated to the boiling point. Such a process was performed for 4 h while maintaining a mild boiling state. Obtained aqueous extract of licorice root was subsequently used as a modifying agent of hydrogels.

3.3. Synthesis of Silver Nanoparticles via the Chemical Reduction Process

Silver nanoparticles were prepared via chemical reduction in which a silver nitrate was used as a source of silver while sodium borohydride was used as a reducing agent. Firstly, 0.039 g $AgNO_3$ (so 250 ppm Ag) was dissolved in a 3% aqueous PVP solution (mixture I). Next, a solution of $NaBH_4$ in 3% PVP solution was prepared and introduced dropwise to mixture I. Such process was performed at constant stirring and at ambient temperature. After dropping, obtained mixture was maintained at constant stirring for 15 min. Next, it was centrifuged (13,000 rpm) for 20 min. The supernatant was decanted, wherein the residue was suspended in distilled water.

3.4. Characterization of Silver Nanoparticle Suspension

3.4.1. The Particle Size Analysis via DLS Technique

The size of the particles obtained via the chemical reduction was verified using dynamic light scattering (DLS technique). For this purpose, a Zetasizer Nano ZS Malvern apparatus (Malvern Panalytical Ltd., Malvern, UK) was employed, wherein the measurements were performed at ambient temperature.

3.4.2. Analysis of the Optical Properties of Nanosilver Suspension

Suspension of silver nanoparticles was also subjected to UV–Vis spectroscopy. The study aimed to determine the ability of nanoparticles to absorb light within the UV–Vis range. The analysis was conducted using a ThermoScientific Evolution 220 UV–Vis spectrometer (Thermo Fisher Scientific, Waltham, MA, USA) at room temperature.

3.5. Synthesis of Hydrogel Polymers via the Photopolymerization Process

In order to prepare hydrogel materials, the UV-induced photopolymerization process was employed. This method allows for obtaining hydrogels in a quick, waste-free, and low energy-demand manner. As a source of UV radiation, an EMITA VP-60 lamp (power 180 W, $\lambda = 320$ nm) was applied. Firstly, a 3% chitosan solution in 0.05% acetic acid solution and 2% gelatin solution was prepared. Next, adequate amounts of these solutions were mixed with adequate amounts of Glycyrrhiza glabra (licorice) root extract, nanosilver suspension, crosslinking agent, and photoinitiator. The mixtures obtained were thoroughly mixed, poured into the Petri dishes, and treated with UV radiation for 120 s. Detailed compositions of all prepared hydrogels are given below in Table 6.

Table 6. Compositions of prepared hydrogels.

No.	3% Chitosan Solution, mL	2% Gelatin Solution, mL	Crosslinking Agent, mL	Photoinitiator, mL	Licorice Root Extract, mL	Nanosilver Suspension, mL	Sample
1.					-	-	0/0 nanoAg
2.					3	-	3/0 nanoAg
3.	30	20	8	0.25	5	-	5/0 nanoAg
4.					-	1	0/1 nanoAg
5.					3	1	3/1 nanoAg
6.					5	1	5/1 nanoAg

After the synthesis, hydrogels were dried at 37 °C for 24 h and investigated to characterize their physicochemical and biological properties. The main attention was focused on determining the impact of the modifiers—licorice root extract and nanosilver suspension—on

hydrogels' properties. Moreover, the discussion over the results of performed experiments also included their evaluation in terms of their application as dressing materials.

3.6. Assessment of the Swelling Properties of Hydrogels

High swelling properties are one of the most characteristic features of hydrogels. Swelling ability of these materials is particularly important in terms of their potential use as dressings with wound exudate sorption function. Thus the hydrogels' swelling capacity was verified in the artificial saliva, SBF, Ringer liquid, and distilled water. The procedure was as follows: dry hydrogel samples (with a diameter of 2 cm) were firstly accurately weighed and then placed in tested liquids (50 mL) for 1 h. Next, the materials were separated from the liquids, the excess liquid (unbound with the sample) was removed via the paper towel, and samples were weighed again. Subsequently, the hydrogels were placed again in the same liquids, and the procedure was repeated after 24 h and 72 h. The swelling ability of hydrogels was defined in each tested liquid and after each swelling period via the swelling ratio (Q) calculated by means of the following Equation (1):

$$Q = \frac{m_s - m_d}{m_d} \times 100\% \tag{1}$$

where: Q—swelling ratio, %; m_s—weight of hydrogel after swelling for a specific time period (i.e., after 1 h, 24 h, or 72 h), g; m_d—weight of dry sample (before swelling), g.

The swelling studies were performed at ambient temperature and in triplicates for each sample.

3.7. Analysis of the Influence of Hydrogels on Simulated Physiological Fluids (Incubation Studies)

The incubation studies consisted of introduction of dry hydrogel samples (weighing approximately 1.0 g and with a diameter of 2.0 cm) into selected liquids for 12 days and measurement every two days of the pH and the temperature of the incubation medium. In terms of the potential application of tested materials for biomedical purposes (as dressing materials), the following liquids were selected for incubation: artificial saliva solution, Ringer liquid (infusion liquid used to restore the body's water-electrolyte balance), simulated body fluid (SBF, isotonic to human blood plasma) and distilled water (as a reference liquid). The study aimed to verify whether hydrogel affects the parameters of the liquids. The measurements were performed using the multifunctional ELMETRON CX-701 (Elmetron, Zabrze, Poland) meter. In order to simulate conditions occurring in the human body to a greater extent, the incubation was performed at 37 °C. The study was conducted in triplicates for each sample.

3.8. Evaluation of the Impact of Hydrogels' Incubation on Their Chemical Structure via FT-IR Spectroscopy

Hydrogel samples, after incubation in simulated physiological liquids, were subjected to FT-IR spectroscopy to verify potential changes in their structures resulting from the incubation. Such changes could indicate, e.g., the degradation of the hydrogels. The spectroscopic analysis was carried out using the Nicolet iS5 Thermo Scientific (Thermo Fischer Scientific, Waltham, MA, USA) spectrometer, wherein the spectra were recorded within the range 4500–500 cm^{-1} and at a resolution of 4.0 cm^{-1}.

3.9. Analysis of the Surface Morphology Using SEM Technique

The next step in the research involved characterization of hydrogels' surface morphology. For this purpose, dry hydrogel samples (with dimensions 1 cm × 1 cm) were sputtered with gold and subjected to the analysis using scanning electron microscopy, wherein the study was conducted by means of a Jeol 5510 LV (Jeol Ltd., Tokyo, Japan) microscope. The imaging was conducted at ambient temperature.

3.10. Studies on the Wettability of Hydrogels Supported by Determining the Surface Free Energy

The hydrogels were also subjected to the analysis of their wettability. For this purpose, hydrogel samples were treated with a drop of double distilled water dispensed from a syringe. The procedure was conducted with simultaneous recording of the behavior of the drop of the wetting liquid during its first contact with the tested material. Therefore, as a result of the study, the wetting angle for each sample, as well as the images showing the placement of the drop on its surface, were obtained. The measurements were performed at ambient temperature using the Drop Shape Analyzer Kruss DSA100 M measuring instrument (Gmbh, Hamburg, Germany). The whole procedure of the analysis was described in more detail in our previous paper [47]. Importantly, the analysis also enabled the calculation of the surface free energy via the Owens-Wendt method [48].

3.11. Characteristics of the Mechanical Properties of Hydrogels

Hydrogels were also subjected to the analysis of their mechanical properties, including determining their percentage elongation and tensile strength. The study was performed according to the ISO 37 type 2 and ISO 527-2 type 5A standards, wherein the universal testing machine (Shimadzu, Kyoto, Japan) was applied for the measurements. Firstly, after the synthesis, the paddle-shaped hydrogel samples were prepared using the ZCP020 manual blanking press, and they were next dried under pressure (to keep the shape) at 37 °C for 24 h. Then, the measurements were performed, during which hydrogel samples were placed between the jaws of the machine. During the analysis, the jaws moved apart, proceeding with simultaneous sample stretching. The procedure was carried on until the sample breakage. The measurements were performed at ambient temperature. Such an analysis allowed to determine the hydrogels' tensile strength (R_m) using Equation (2) and the percentage elongation (A) using Equation (3). Both equations are presented below:

$$R_m = \frac{Fm}{S_0} \tag{2}$$

$$A = \frac{(l_u - l_0)}{l_0} \times 100\% \tag{3}$$

where: F_m—maximum hydrogel's strength; S_0—cross-sectional area of sample in its initial state (before the analysis); I_u—measuring length after sample breakage; I_0—measuring length of sample in its initial state (before the analysis).

3.12. In Vitro MTT Reduction Assay Using L929 Murine Fibroblasts

In addition to characterizing the physicochemical properties of hydrogels, the key aspect was to verify their cytotoxicity towards selected cell lines. For this purpose, in vitro MTT reduction assay was employed, wherein, as tested cell lines, L929 murine fibroblasts were selected. Conducting this type of preliminary biological investigation provides information on whether the chosen synthesis methodology, as well as the composition of the developed materials, leads to the preparation of materials that could be considered for more advanced biological experiments. When such an assay indicates cytotoxicity of the hydrogels, then the synthesis methodology or the amounts of individual reagents applied during the synthesis needs to be modified. The principle of MTT reduction assay is to check the cell viability by determining their metabolic activity. For this purpose, the MTT reagent (i.e., 3-(4,5-dimethylthiazol-2-yl)-2,5-diphenyltetrazolium bromide; tetrazolium salt) is added to the medium with tested cell lines (here: L929 murine fibroblasts). Metabolically active cells secrete into the culture medium mitochondrial dehydrogenase, and this enzyme converts the MTT reagent into formazan. The blue crystals of formazan are next dissolved in the organic solvent (e.g., in dimethyl sulfoxide (DMSO)), and obtained solution may be next analyzed via UV–Vis spectroscopy. The absorbance of the solution corresponds to its concentration and, thus, to the amount of the enzyme present in the tested medium. In turn, the amount of the enzyme provides information on the number of viable cells.

The procedure of MTT reduction assay, as well as L929 murine fibroblast culture, were described more precisely in our previous publication [49].

3.13. Statistical Analysis

The results of the research were subjected to statistical analysis wherein the statistical importance was determined by means of the two-way analysis of variance (ANOVA) ($\alpha = 5\%$). The calculations were performed in the case of the results of the mechanical studies, contact angle measurements, and biological studies (MTT reduction assay). The statistical analysis was carried out to verify the importance of the modifying factors—i.e., licorice root extract and nanosilver suspension. All experiments were performed in triplicates, and their results are provided, including the average value and the standard deviation (SD).

4. Conclusions

- All developed materials showed swelling ability. The modification of hydrogels with licorice root extract did not significantly affect this property. However, the incorporation of hydrogels with nanosilver resulted in an increase in this ability, which was probably caused by the interactions between aqueous nanosilver suspension and the liquid penetrating the polymer matrix.
- Incubation studies in simulated physiological liquids supported by the analysis of the structure of incubated hydrogels via FT-IR spectroscopy excluded the degradation of tested materials in these environments. The only slight changes (by a maximum of one pH unit) in the pH of incubation media reported in the course of the incubation probably resulted from the interactions between the components of the polymer matrix and the incubation media.
- Based on the SEM imaging, it was reported that licorice root extract may fill the outer cavities of the hydrogels, which results in the smoothing of its surface.
- The surface wettability of modified hydrogels indicated their hydrophilicity. The wetting angles of all tested samples were lower than 90°. The lowest wetting angles and the highest surface free energies were determined for hydrogels modified with the highest amounts of the additives (i.e., 5 mL of licorice root extract and 1 mL of nanosilver suspension).
- The introduction of the modifying agents into the hydrogels reduced their tensile strength from 0.112 MPa (for unmodified hydrogels) to 0.072 MPa (for the materials with the highest amounts of additives). However, the changes in the percentage elongations between unmodified materials and modified ones were not as significant. The hydrogel containing the highest amounts of additives showed approximately 24% elongation.
- In vitro biological analysis with L929 murine fibroblasts excluded the cytotoxic activity of the hydrogels; the viability of tested cells was within the range of 87.0–92.5%. Nanosilver present in hydrogel matrices positively affected this property and increased the cell viability.
- The results of the physicochemical analysis confirming the stability of the tested hydrogels in simulated physiological liquids, the possibility of their modification, and the lack of cytotoxic activity proved the correctness of the synthesis methodology applied. Moreover, the sorption properties of hydrogels indicated the possibility of absorbing wound exudate by these materials, while their hydrophilic surfaces demonstrated that they constitute a suitable substrate for cell adhesion and proliferation. Furthermore, their elasticity of approximately 30% flexibility indicated the possibility of their easy application. Thus, in summary, the above-mentioned features confirm the possibility of the use of developed hydrogels as dressing materials supporting regenerative processes.

Abbreviations

FT-IR spectroscopy, Fourier transform infrared spectroscopy; MTT, 3-(4,5-dimethylthiazol-2-yl)-2,5-diphenyltetrazolium bromide; HRSV, human respiratory syncytial virus; UV, ultraviolet; DLS, dynamic light scattering; UV–Vis, ultraviolet–visible, SD, standard deviation; SEM, scanning electron microscopy; EN ISO, English International Organization for Standardization; PVP, polyvinylpyrrolidone; SBF, simulated body fluid; DMSO, dimethyl sulfoxide.

References

1. Khaitov, B.; Karimov, A.; Khaitbaeva, J.; Sindarov, O.; Karimov, A.; Li, Y. Perspectives of Licorice Production in Harsh Environments of the Aral Sea Regions. *Int. J. Environ. Res. Public Health* **2022**, *19*, 11770. [CrossRef] [PubMed]
2. Noreen, S.; Mubarik, F.; Farooq, F.; Khan, M.; Khan, A.U.; Pane, Y.S. Medicinal Uses of Licorice (*Glycyrrhiza glabra* L.): A Comprehensive Review. *Maced. J. Med. Sci.* **2021**, *9*, 668–675.
3. Kao, T.C.; Wu, C.H.; Yen, G.C. Bioactivity and Potential Health Benefits of Licorice. *J. Agric. Food Chem.* **2014**, *62*, 542–553. [CrossRef] [PubMed]
4. Jiang, M.; Zhao, S.; Yang, S.; Lin, X.; He, X.; Wie, X.; Song, Q.; Li, R.; Fu, C.; Zhang, J.; et al. An "essential herbal medicine"—Licorice: A review of phytochemicals and its effects in combination preparations. *J. Ethnopharmacol.* **2020**, *249*, 112439. [CrossRef] [PubMed]
5. Markina, Y.V.; Kirichenko, T.V.; Markin, A.M.; Yudina, I.Y.; Starodubova, A.V.; Sobenin, I.A.; Orekhov, A.N. Atheroprotective Effects of *Glycyrrhiza glabra* L. *Molecules* **2022**, *27*, 4697. [CrossRef]
6. Tamura, Y. The History of Licorice Applications in Maruzen Pharmaceuticals Co., Ltd. In *Biological Activities and Action Mechanisms of Licorice Ingredients*; Sakagami, H., Ed.; IntechOpen: London, UK, 2017.
7. Cherry, R.N.; Blanchard, S.S.; Chogle, A.; Santucci, N.R.; Mehta, K.; Russell, A.C. Herbal Approaches to Pediatric Functional Abdominal Pain. *Children* **2022**, *9*, 1266. [CrossRef]
8. Dogan, S.C.; Baylan, M.; Erdoğan, Z.; Küçükgül, A.; Bulancak, A. The effects of Licorice (Glycyrrhiza glabra) root on performance, some serum parameters and antioxidant capacity of laying hens. *Braz. J. Poult. Sci.* **2018**, *20*, 699–706. [CrossRef]
9. Kim, K.J.; Choi, J.S.; Kim, K.W.; Jeong, J.W. The anti-angiogenic activities of glycyrrhizic acid in tumor progression. *Phytother. Res.* **2013**, *27*, 841–846. [CrossRef]
10. Tanideh, N.; Rokhsari, P.; Mehrabani, D.; Mohammandi Samani, S.; Sarvestani, S.F.; Ashraf, M.J.; Hosseinabadi, K.O.; Shamsian, S.; Ahmadi, N. The Healing Effect of Licorice on Pseudomonas aeruginosa Infected Burn Wounds in Experimental Rat Model. *World J. Plast. Surg.* **2014**, *3*, 99–106.
11. Yang, L.; Jiang, Y.; Zhang, Z.; Hou, J.; Tian, S.; Liu, Y. The anti-diabetic activity of licorice, a widely used Chinese herb. *J. Ethnopharmacol.* **2020**, *263*, 113216. [CrossRef]
12. Chung, C.-L.; Chen, J.-H.; Huang, W.-C.; Sheu, J.-R.; Hsia, C.-W.; Jayakumar, T.; Hsia, C.-H.; Chiou, K.-R.; Hou, S.-M. Glabridin, a Bioactive Flavonoid from Licorice, Effectively Inhibits Platelet Activation in Humans and Mice. *Int. J. Mol. Sci.* **2022**, *23*, 11372. [CrossRef]
13. Fan, R.; Gao, Y. Maillard and Hydrolytic Reactions in Subcritical Water Extraction of Bioactive Compounds from Licorice. *Molecules* **2022**, *27*, 6851. [CrossRef]
14. Yeh, C.F; Wang, K.C; Chiang, L.C.; Shieh, D.; Yen, M.H.; Chang, J.S. Water extract of licorice had anti-viral activity against human respiratory syncytial virus in human respiratory tract cell lines. *J. Ethnopharmacol.* **2013**, *148*, 466–473.
15. Xie, Y.C.; Dong, X.E.; Wu, X.M.; Yan, X.F.; Xie, Q.M. Inhibitory effects of flavonoids extracted from licorice on lipopolysaccharide-induced acute pulmonary inflammation in mice. *Int. Immunopharmacol.* **2009**, *9*, 194–200. [CrossRef]

16. Gomaa, A.A.; Abdel-Wadood, Y.A. The potential of glycyrrhizin and licorice extract in combating COVID-19 and associated conditions. *Phytomedicine Plus* **2021**, *1*, 100043. [CrossRef]

17. Li Ng, S.; Khaw, K.Y.; Goh, B.H. Licorice: A Potential Herb in Overcoming SARS-CoV-2 Infections. *J. Evid.-Based Integr. Med.* **2021**, *26*, 2515690X21996662.

18. Hu, L.; Xie, S.; Geng, Z.; Yang, X.; Zhang, Q. Evaluating the Potential of *Glycyrrhiza uralensis* (Licorice) in Treating Alcoholic Liver Injury: A Network Pharmacology and Molecular Docking Analysis Approach. *Processes* **2022**, *10*, 1808.

19. Ageeva, A.A.; Kruppa, A.I.; Magin, I.M.; Babenko, S.V.; Leshina, T.V.; Polyakov, N.E. New Aspects of the Antioxidant Activity of Glycyrrhizin Revealed by the CIDNP Technique. *Antioxidants* **2022**, *11*, 1591. [CrossRef]

20. Wahab, S.; Annadurai, S.; Abullais, S.S.; Das, G.; Ahmad, W.; Ahmad, M.F.; Kandasamy, G.; Vasudevan, R.; Ali, M.S.; Amir, M. *Glycyrrhiza glabra* (Licorice): A Comprehensive Review on Its Phytochemistry, Biological Activities, Clinical Evidence and Toxicology. *Plants* **2021**, *10*, 2751. [CrossRef]

21. Kwon, Y.J.; Son, D.H.; Chung, T.H.; Lee, Y.J. A Review of the Pharmacological Efficacy and Safety of Licorice Root from Corroborative Clinical Trial Findings. *J. Med. Food* **2020**, *2*, 1–9. [CrossRef]

22. Mou, K.H.; Han, D.; Liu, W.L.; Li, P. Combination therapy of orally administered glycyrrhizin and UVB improved active-stage generalized vitiligo. *Braz. J. Med. Biol. Res.* **2016**, *49*, e5354. [CrossRef] [PubMed]

23. Allam, M.; Riad, H. Concise review of recent studies in vitiligo. *Qatar Med. J.* **2013**, *2013*, 1–19. [CrossRef] [PubMed]

24. Hoffmann, J.; Gendrisch, F.; Schempp, C.M.; Wölfle, U. New Herbal Biomedicines for the Topical Treatment of Dermatological Disorders. *Biomedicines* **2020**, *8*, 27. [CrossRef] [PubMed]

25. Saeedi, M.; Morteza-Semnani, K.; Ghoreishi, M.R. The treatment of atopic dermatitis with licorice gel. *J. Dermatolog. Treat.* **2003**, *14*, 153–157. [CrossRef] [PubMed]

26. Xue, X. Effects of compound glycyrrhizin on serum IFN-γ, IL-10 and immunological index in patients with alopecia areata. *Pharm. Bioprocess.* **2018**, *6*, 15–20.

27. Vinci, G.; Rapa, M. Noble Metal Nanoparticles Applications: Recent Trends in Food Control. *Bioengineering* **2019**, *6*, 10. [CrossRef]

28. Klębowski, B.; Depciuch, J.; Parlińska-Wojtan, M.; Baran, J. Applications of Noble Metal-Based Nanoparticles in Medicine. *Int. J. Mol. Sci.* **2018**, *19*, 4031. [CrossRef]

29. Agustina, T.E.; Handayani, W.; Imawan, C. The UV-VIS Spectrum Analysis from Silver Nanoparticles Synthesized Using Diospyros maritima Blume. Leaves Extract. *Adv. Biol. Res.* **2020**, *14*, 411–419.

30. Alim-Al-Razy, M.; Bayazid, G.M.A.; Rahman, R.; Bosu, R.; Shamma, S.S. Silver nanoparticle synthesis, UV-Vis spectroscopy to find particle size and measure resistance of colloidal solution. *J. Phys. Conf. Ser.* **2020**, *1706*, 012020. [CrossRef]

31. Mohonta, S.K.; Maria, K.H.; Rahman, S.; Das, H.; Hoque, S.M. Synthesis of hydroxyapatite nanoparticle and role of its size in hydroxyapatite/chitosan-gelatin biocomposite for bone grafting. *Int. Nano Lett.* **2021**, *11*, 381–393. [CrossRef]

32. Nawaz, A.; Ullah, S.; Alnuwaiser, M.A.; Rehman, F.U.; Selim, S.; Al Jaouni, S.K.; Farid, A. Formulation and Evaluation of Chitosan-Gelatin Thermosensitive Hydrogels Containing 5FU-Alginate Nanoparticles for Skin Delivery. *Gels* **2022**, *8*, 537. [CrossRef]

33. Magli, S.; Rossi, G.B.; Risi, G.; Bertini, S.; Cosentino, C.; Crippa, L.; Ballarini, E.; Cavaletti, G.; Piazza, L.; Masseroni, E.; et al. Design and Synthesis of Chitosan—Gelatin Hybrid Hydrogels for 3D Printable in vitro Models. *Front. Chem.* **2020**, *8*, 524. [CrossRef]

34. Latthe, S.S.; Terashima, C.; Nakata, K.; Fujishima, A. Superhydrophobic Surfaces Developed by Mimicking Hierarchical Surface Morphology of Lotus Leaf. *Molecules* **2014**, *19*, 4256–4283. [CrossRef]

35. Nakamura, M.; Hori, N.; Ando, H.; Namba, S.; Toyama, T.; Nishimiya, N.; Yamashita, K. Surface free energy predominates in cell adhesion to hydroxyapatite through wettability. *Mater. Sci. Eng. C* **2016**, *62*, 283–292. [CrossRef]

36. Majhy, B.; Priyadarshini, P.; Sen, A.K. Effect of surface energy and roughness on cell adhesion and growth-facile surface modification for enhanced cell culture. *RSC Adv.* **2021**, *11*, 15467–15476. [CrossRef]

37. Cai, S.; Wu, C.; Yang, W.; Liang, W.; Yu, H.; Liu, L. Recent advance in surface modification for regulating cell adhesion and behaviors. *Nanotechnol. Rev.* **2020**, *9*, 971–989. [CrossRef]

38. Li, X.; Sun, Q.; Li, Q.; Kawazoe, N.; Chen, G. Functional Hydrogels With Tunable Structures and Properties for Tissue Engineering Applications. *Front. Chem.* **2018**, *6*, 499. [CrossRef]

39. Oyen, M. Mechanical characterisation of hydrogel materials. *Int. Mater. Rev.* **2013**, *59*, 44–59. [CrossRef]

40. Pal, T.; Pramanik, S.; Verma, K.D.; Naqvi, S.Z.; Manna, P.K.; Kar, K.K. Fly ash-reinforced polypropylene composites. In *Handbook of Fly Ash*; Butterworth-Heinemann: Oxford, UK, 2022; pp. 243–270.

41. Macha, I.J.; Sufi, S. Novel slow drug release bioceramic composite materials for wound dressing applications: Potential of natural materials. *SN Appl. Sci.* **2020**, *2*, 176. [CrossRef]

42. Nam, S.Y.; Nho, Y.C.; Hong, S.H.; Chae, G.T.; Jang, H.S.; Suh, T.S.; Ahn, W.S.; Ryu, K.E.; Chun, H.J. Evaluations of poly (vinyl alcohol)/alginate hydrogels cross-linked by γ-ray irradiation technique. *Macromol. Res.* **2004**, *12*, 219–224. [CrossRef]

43. Sirousazar, M.; Kokabi, M.; Hassan, Z.M. In Vivo and Cytotoxic Assays of a Poly (vinyl alcohol)/Clay Nanocomposite Hydrogel Wound Dressing. *J. Biomater. Sci.* **2011**, *22*, 1023–1033. [CrossRef] [PubMed]

44. *ISO-10993-5-2009*; Biological Evaluation of Medical Devices—Part 5: Tests for In Vitro Cytotoxicity. Technical Committee: Geneva, Switzerland, 2009.

45. Yin, I.X.; Zhang, J.; Zhao, I.S.; Mei, M.L.; Li, Q.; Chu, C.H. The Antibacterial Mechanism of Silver Nanoparticles and Its Application in Dentistry. *Int. J. Nanomed.* **2020**, *15*, 2555–2562. [CrossRef] [PubMed]
46. Bruna, T.; Maldonado-Bravo, F.; Jara, P.; Caro, N. Silver Nanoparticles and Their Antibacterial Applications. *Int. J. Mol. Sci.* **2021**, *22*, 7202. [CrossRef] [PubMed]
47. Kudłacik-Kramarczyk, S.; Głąb, M.; Drabczyk, A.; Kordyka, A.; Godzierz, M.; Wróbel, P.S.; Krzan, M.; Uthayakumar, M.; Kędzierska, M.; Tyliszczak, B. Physicochemical Characteristics of Chitosan-Based Hydrogels Containing Albumin Particles and Aloe vera Juice as Transdermal Systems Functionalized in the Viewpoint of Potential Biomedical Applications. *Materials* **2021**, *14*, 5832. [CrossRef]
48. Owens, D.K.; Wendt, R.C. Estimation of the surface free energy of polymers. *J. Appl. Polym. Sci.* **1969**, *13*, 1741–1747. [CrossRef]
49. Drabczyk, A.; Kudłacik-Kramarczyk, S.; Głąb, M.; Kędzierska, M.; Jaromin, A.; Mierzwiński, D.; Tyliszczak, B. Physicochemical Investigations of Chitosan-Based Hydrogels Containing Aloe Vera Designed for Biomedical Use. *Materials* **2020**, *13*, 3073. [CrossRef]

Article

Colourimetric Plate Assays Based on Functionalized Gelatine Hydrogel Useful for Various Screening Purposes in Enzymology

Karolina Labus * and Halina Maniak

Department of Micro, Nano and Bioprocess Engineering, Faculty of Chemistry, Wroclaw University of Science and Technology, Wybrzeże Wyspiańskiego 27, 50-370 Wrocław, Poland
* Correspondence: karolina.labus@pwr.edu.pl; Tel.: +48-71-320-3314

Abstract: Hydrogels are intensively investigated biomaterials due to their useful physicochemical and biological properties in bioengineering. In particular, naturally occurring hydrogels are being deployed as carriers for bio-compounds. We used two approaches to develop a plate colourimetric test by immobilising (1) ABTS or (2) laccase from *Trametes versicolor* in the gelatine-based hydrogel. The first system (1) was applied to detect laccase in aqueous samples. We investigated the detection level of the enzyme between 0.05 and 100 μg/mL and pH ranging between 3 and 9; the stability of ABTS in the solution and the immobilised form, as well as the retention functional property of the hydrogel in 4 °C for 30 days. The test can detect laccase within 20 min in the concentration range of 2.5–100 μg/mL; is effective at pH 3–6; preserves high stability and functionality under storage and can be also successfully applied for testing samples from a microbial culture. The second system with the immobilised laccase (2) was tested in terms of substrate specificity (ABTS, syringaldazine, guaiacol) and inhibitor (NaN$_3$) screening. ABTS appeared the most proper substrate for laccase with detection sensitivity $C_{ABTS} > 0.5$ mg/mL. The NaN$_3$ tested in the range of 0.5–100 μg/mL showed a distinct inhibition effect in 20 min for 0.5 μg/mL and total inhibition for ≥ 75 μg/mL.

Keywords: gelatine hydrogel; laccase detection; inhibitor screening; substrate specificity screening; storage stability; microbial cultivation

1. Introduction

Currently, a progressive degeneration of the natural environment is being observed due to expansive human activity [1–4]. In addition to large-scale mining and refining processes, as well as the daily consumption of material goods by humankind, the manufacturing industry has the largest share in the global generation of waste and pollution of all types. In particular, the food, pharmaceutical, and chemical sectors produce millions of tons of by-products, and waste effluents contributing to the high carbon footprint [4–9]. Intensive multi-directional research is constantly being carried out to minimise these adverse environmental effects [5,6,10,11]. In this respect, one of the most promising trends is the replacement of classical chemical processes with sustainable biocatalytic transformations [12–15]. The leading benefit of enzyme use is the possibility of carrying out chemical reactions under mild processing conditions with high selectivity. Moreover, biocatalysts are used not only at the stage of synthesis/conversion of various compounds, but they are also efficient tools for the detection and neutralisation of harmful substances [16–19]. Hence, it seems reasonable to undertake research in the development of more effective functional biocatalytic systems for various industrial applications. Due to great diversity and relatively easy handling of cultivation, microorganisms are most often used as a rich source of enzymes with valuable catalytic activities, high selectivity, and process stability [20–22]. The displacement of polymers and plastics from industrial trade in favour of biomaterials has also a very significant impact on reducing the global formation of nuisance post-production and post-consumer wastes [23–27]. In this case, the main advantage

of biomaterials is their easy degradability to environmentally harmless, low-molecular-weight compounds, which can be used as ready-to-use products [27–29]. Different types of biopolymers such as polysaccharides or proteins are not only renewable source of valuable mono- and oligomers, but also serve as carriers of bioactive molecules, e.g., drugs, enzymes, agrochemicals, nanoparticles, stem cells, and antibodies [30–36]. To this extent, more and more attention is being paid to hydrogels. These materials are being intensively researched due to their favourable functional properties, such as biodegradability, biocompatibility, swelling capacity, porosity, semi-permeability, and the ability to create stable multilayer structures [37–39]. In particular, they found applications in bioengineering sectors including medicine, pharmacy, tissue engineering, food processing, agriculture, wastewater treatment, environmental protection, biocatalytic processes, and many others [38–45]. Specifically, over the past few years, interest in hydrogels has increased in the context of their use as chemosensors in colourimetric assays. These systems contain an immobilised enzyme or chromogenic/fluorogenic substrate or functional groups in a hydrogel matrix, which react with a target analyte in the sample to give a coloured product. They have been developed mainly as potential diagnostic tools with applications for the detection of molecules, such as ions, low-molecular-weight compounds, and macromolecules. For instance, colourimetric assays were applied for sensing hydrogen [46], nitrite [47,48], nitrate, phosphate [47], and heavy metal ions [49]. In the group of low-molecular-weight compounds, we found cholesterol [50], melanin [51], urea [52], dopamine [53], and bisphenol A [54]. The tests for detecting macromolecules concerned RNA [55] and proteins of specific activity such as streptavidin alkaline phosphatase [56], galactosidase, and glucuronidase [57] or horseradish peroxidase [58]. Both synthetic and natural-originated hydrogel matrices were used in the examples discussed, which are polyalcohols [47,52,54–56], polysaccharides [46,49,53,57], and gelatine [44,59,60]. The cited reports do not exhaust the already published colourimetric assays for the detection of specific analytes; however, it should be noted, that only individual examples of the colourimetric research with immobilised laccase in hydrogels were described in the literature so far. In such studies, laccase was used for the reduction of persistent compounds such as bisphenol A [46,47] and synthetic dye [48], but not strictly for detection purposes. Laccase was immobilised on cellulose/alginate composite hydrogel [46], in poly(ethylene glycol) [47], or alginate/gelatine hydrogel [48]. The other usage of the colourimetric test was the entrapment of a substrate in the solid agar medium and used for identifying the microbes producing laccase [49,50]. Apart from immobilisation in hydrogel matrices, another example was the application of the ABTS-impregnated paper discs for the determination of laccase activity. Such a non-hydrogel assay was applied during the purification of this enzyme on chromatographic columns [51], but practical application, possibilities, and limitations have not been presented in detail.

The system we propose is also based on the use of a substrate that in the presence of a particular enzyme undergoes visible conversion to a coloured product. However, we show the broader applicability of such a system in two opposite modes. In our approach, one of the bioactive compounds (depending on the application: substrate or enzyme) was immobilised within the naturally originated hydrogel matrix to obtain the stable testing kit. For this purpose, we used gelatine, which is a readily available, cheap compound obtained as a side product of commercial animal and fish processing [27,52,53]. Importantly, it is certified by U.S. Food and Drug Administration as a GRAS compound (Generally Recognised As Safe) [54] and is commonly used as a gelling agent for food [27,52,55,56], cosmetics [57,58], medicines [39,56,58,59], pharmaceuticals [54,56,58], and in other branches [39,60]. Furthermore, gelatine has favourable physicochemical properties as a hydrogel matrix. It provides suitable reaction conditions for enzyme activity and is easily biodegradable to non-toxic, low-molecular-weight compounds [36,39,43,44,61]. The selection of gelatine was additionally supported by the results obtained in our previous work, where the properties of alginate and gelatine hydrogel as enzyme carriers were compared [62]. In this case, the gelatine-based hydrogel enzymatically cross-linked with microbial transglutaminase

(mTGase) was a more efficient support for the permanent immobilisation of the given enzyme.

We would like to underline that our concept of a colourimetric detection test based on hydrogel matrices enriched with bioactive ingredients can be applied to enzymes with various catalytic activities. We have already started considering the development of such a solution for selected enzymes in previous research for β-galactosidase [63,64], and tyrosinase [65]. However, it was only applied in the case of detecting their presence in the tested samples, whereas in the current study, we would like to present the multifunctionality of using gelatine hydrogel matrices containing targeted active compounds in enzymological screening studies. To precisely analyse the possibilities of the practical application of the provided test, we used the laccase (EC 1.10.3.2) as a model enzyme, and its substrate, 2,2'-azino-bis(3-ethylbenzothiazoline-6- sulfonate) sodium salt (ABTS).

2. Results and Discussion

For convenience and readability of the experiments undertaken, we have schematically presented the particular stages of the research considered (Figure 1). Briefly, the first stage, highlighted in blue, involves the preparation of the hydrogel matrices enriched with (1) ABTS (left side) and (2) laccase (right side). The second step, marked in red, includes the example tests and applications of both types of hydrogel matrices developed in the current study.
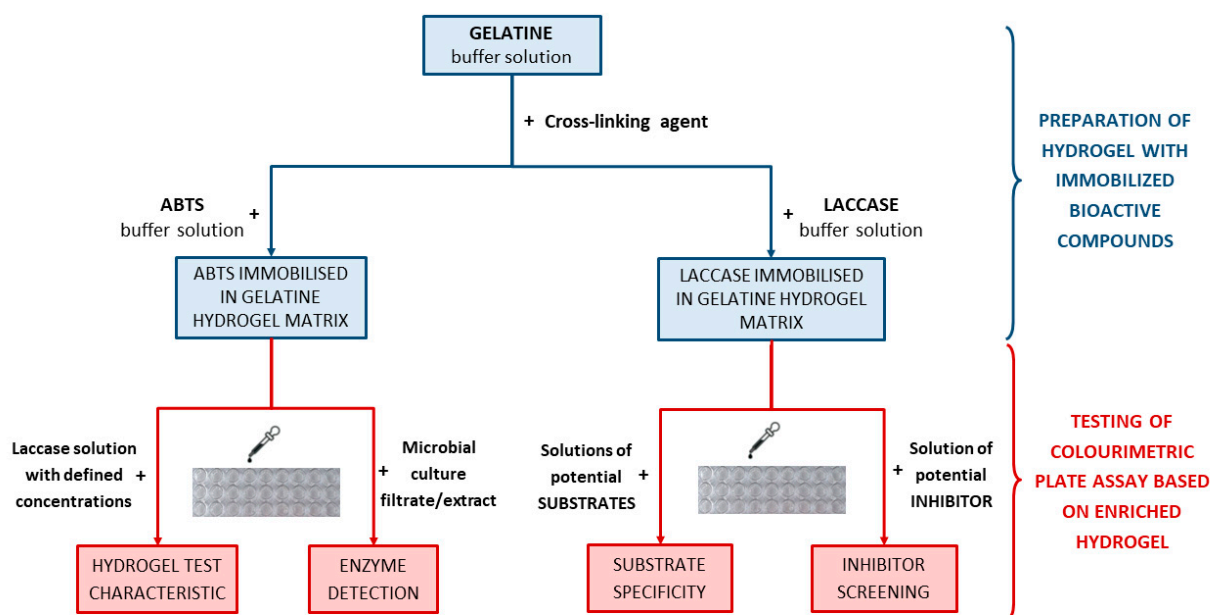
Figure 1. Scheme of research on the development of hydrogel-based colourimetric tests for various screening purposes in enzymology using laccase as the model biocatalyst.

2.1. Hydrogel-Based Test for Colourimetric Detection of Laccase

A quick and simple test that allows the effective detection of a biocatalyst with a specific activity is a desirable analytical tool to improve the preliminary enzymatic screening in both microbiological cultures and other multicomponent mixtures.

In our research, we focused on preparing a diagnostic test which was based on gelatine hydrogel matrices enriched with a substrate (2,2'-azino-bis(3-ethylbenzothiazoline-6-sulfonate) sodium salt, ABTS) of laccase for the detection of its activity in a sample. The following functional parameters for detection sensitivity, operating pH range, and storage stability were determined. Validation of the proposed solution was performed using a commercial laccase preparation from *Trametes versicolor*. In the next stage, the suitability of the developed assay for screening laccase in culture fluids during the cultivation of *Cerrena unicolor* was tested.

2.1.1. Development of the Test for the Detection of Laccase in Aqueous Solutions

The typical substrates used for measurements of laccase activity were presented in Figure 2. The colourimetric test for laccase detection proposed in this study was based on gelatine hydrogel matrices enriched with 2,2′-azino-bis(3-ethylbenzothiazoline-6-sulfonate) sodium salt (ABTS)—one of the well-known synthetic substrate of this enzyme [49,51,66–69]. Syringaldazine (SNG) [70–75] and guaiacol [49,50,67,76] are other substrates frequently used in the determination of laccase activity. Unfortunately, their application in hydrogel-based tests has some limitations which were discussed in Section 2.2.1. In the assay with ABTS, the presence of laccase was indicated by the appearance of a green-blue product resulting from the biocatalytic oxidation of ABTS to its radical cation (Figure 2b).
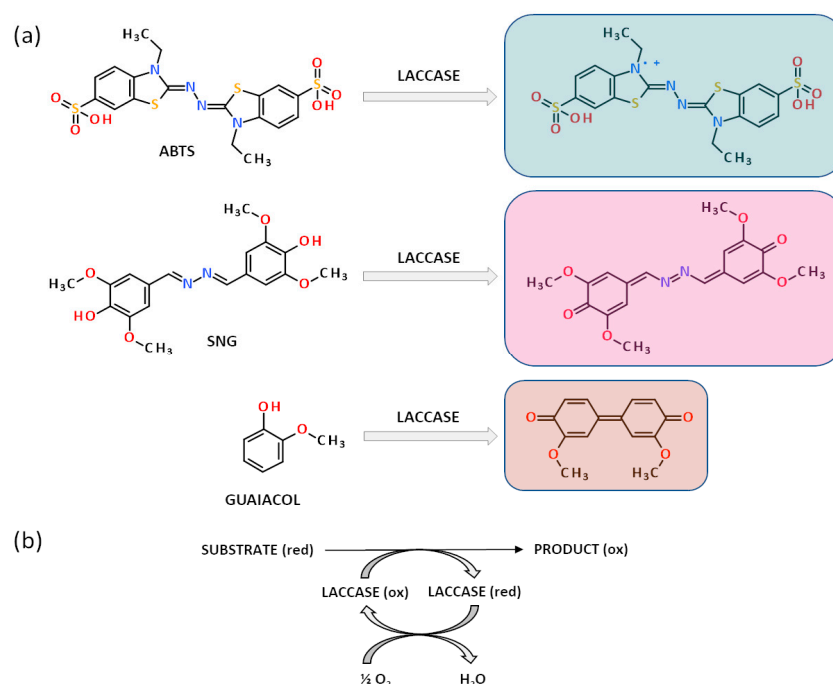
Figure 2. Laccase catalysed reactions with typical synthetic substrates. (**a**). The oxidation of ABTS (upper), syringaldazine (SNG, middle), and guaiacol (lower) to colourful products: green-blue, pink-violet, and orange-brown, respectively. (**b**). The scheme of substrate oxidation by laccase is part of the red-ox reaction where the enzyme undergoes reduction by substrate oxidation and in turn, it returns to its native oxidised form by transferring the electrons to the oxygen molecule which is a final electron acceptor.

The proposed colourimetric assay for visual detection of laccase is based on the use of ABTS entrapped in gelatine-based hydrogel introduced into a 96-well plate. The methodology proceeds as follows: a small amount of aqueous solution potentially containing this enzyme was applied to the surface of the ABTS-enriched hydrogel matrix and the colour change from transparent to green-blue was monitored over time. The appearance of colour indicated the presence of laccase in the test solution. Whereas, the intensity of the colour that appeared after a defined time allowed us to estimate the approximate enzyme concentration. Applying this procedure, we performed detailed studies to determine the functional properties of the proposed diagnostic test. Firstly, we have taken into consideration its detection sensitivity. For this purpose, the laccase solutions of different concentrations (0.05–100 µg/mL) were prepared and added on the surface of gelatine hydrogel matrices, as shown in Figure 3.

Figure 3. The visual response obtained after a different time (0–1440 min) of hydrogel-based test with immobilised 1.5 mg/mL ABTS performed for laccase from *Trametes versicolor* solutions with a concentration range of 0.05–100 µg/mL, left—top view, right—side view.

As early as 5 min after the samples were applied, a distinct change in the gel colour was observed for laccase in the concentration between 10 and 100 µg/mL (Figure 3, side view). Prolonging the assay time to at least 20 min increased the sensitivity of the test which enabled the detection of the laccase concentration even at 2.5 µg/mL. Further extension of the time to 120 min resulted in a colour response in the ABTS test for two successively lower concentrations of this enzyme (1.0 and 0.5 µg/mL). Moreover, the results after 24 h (Figure 3, last row), revealed the presence of laccase activity as low as 0.25 µg/mL. Concluding this part of the research, the satisfactory results of visual laccase detection in the test are obtained for enzyme concentrations between 2.5 and 100 µg/mL and higher. In this case, the required duration of the analysis is at least 20 min. Nevertheless, it is also possible to detect lower concentrations of laccase (starting from 0.25 µg/mL), but then the test time should be extended to 24 h.

Based on the literature review, laccases of different origins may have a varying range of preferential pH [77,78]. Therefore, in the next step, we verified the possibility of detecting this enzyme under different pH conditions. For that purpose, we used the hydrogel with immobilised ABTS and laccase solutions in one fixed concentration, prepared in buffers at pH ranging from 3.0 to 9.0. Such samples were subjected to colourimetric detection according to the developed procedure. The results of the experiment are shown in Figure 4.

As could be observed after just 2 min, the change in gel colour became rapidly visible for enzyme solutions at a pH from 3.0 to 6.0. Prolongation of the analysis time resulted in a deepening blue-green colour in this pH range, and 60 min was required to visualise the presence of the laccase activity at pH 7.0. Based on these results, it was concluded that the activity of commercial laccase from *Trametes versicolor* in the proposed assay conditions certainly could not be determined at pH 8.0 and above; however, one should take into account that the test results reflected the pH range at which the enzyme exhibited activity. In fact, the pH range at which the laccase from *T. versicolor* preserves the ability to oxidise ABTS is between 3 and 6 [79,80] with the optimum falling at around pH 5 [69,80,81]. Thus, this colourimetric test is also a suitable tool for qualitative diagnosis of the spectrum of enzyme activity, depending on the pH applied.

Figure 4. Visual response of the assays in a hydrogel matrix with immobilised ABTS (1.5 mg/mL) obtained after exposure time between 0 and 60 min for laccase solution (100 µg/mL) prepared in the citrate-phosphate buffer with pH ranging from 3.0 to 9.0.

The next step in the development of the hydrogel test with immobilised ABTS was to determine the sensibility of laccase detection at different pH values. The enzyme was prepared in the concentration range of 1–100 µg/mL and fixed pH values between 3 and 9. As shown in Figure 5, regardless of the concentration used, the presence of the colour was observed in the pH between 4.0 and 5.2. At the lowest enzyme concentration (1 µg/mL), the effect of ABTS oxidation was also detected at pH 3.0 and 6.0, but the colour of the product was visible at the perceptual border. As mentioned above, these pH values overlapped the pH range at which laccase from *T. versicolor* preserves the ABTS oxidation activity [79,80].

Figure 5. The results of the colourimetric test for the different concentrations of laccase in phosphate-citrate buffer with fixed pH values. The comparison of the detection level of enzymatic activity was examined for laccase concentrations of 100, 10, and 1 µg/mL and in the pH range of 3.0–9.0. Test conditions: hydrogel gelatine matrices containing ABTS at a concentration of 1.5 mg/mL; test time: 60 min.

To summarise this part of the research, it may be concluded that the proposed colourimetric assay based on immobilised ABTS in a gelatine matrix was effective in detecting laccase at its relatively low concentrations. A key aspect was the pH of the tested solutions. The values of pH should coincide with the pH range of the enzyme's catalytic activity. In the case of the commercial enzyme used here, the level of detection of laccase activity was observed even at its lowest concentration, i.e., 1 µg/mL, in the pH range of 3–6.

A very important functional parameter that determines the commercial applicability of any type of chemical or enzymatic test is its storage stability. An economically desirable characteristic is the longest possible shelf life of the proposed product. Therefore, our next experiments were concerned with the determination of the storage stability of both the substrate (ABTS) chosen to measure enzymatic activity as well as the ABTS-containing gelatine hydrogel matrix. The ABTS was examined in the form of a buffer solution and

immobilised in a hydrogel matrix. The results of ABTS storage in particular form was shown in Figure 6a. The buffer solution of ABTS underwent slow but visible auto-oxidation after only 5 days of storage at 4 °C. While the ABTS entrapped in the gelatine hydrogel was stable for 20 days of storage under similar conditions.

ABTS form	Storage period at 4°C [days]		
	0	5	20
buffer solution			
immobilized in gelatine-based hydrogel			

(**a**)

The time of laccase detection test [min]	Storage period at 4°C [days]		
	0	10	30
0			
30			

(**b**)
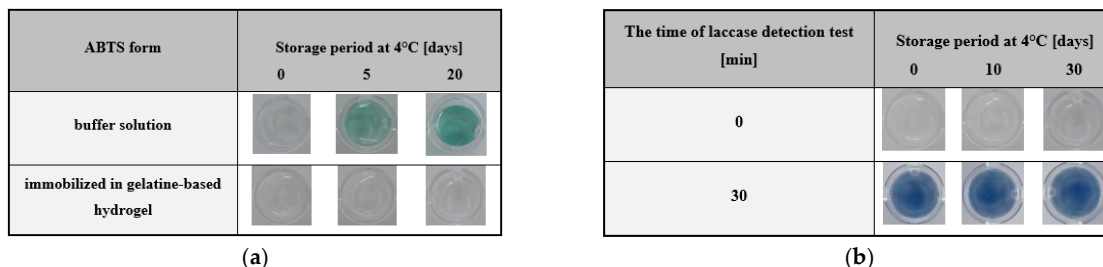
Figure 6. Evaluation of storage stability for ABTS—a substrate used for determination of laccase activity in a gelatine hydrogel-based colourimetric test. ABTS was tested in its native form in a phosphate-citrate buffer solution at pH 5.2 (**a**), and as immobilised in a hydrogel matrix after 0–20 days (**b**). Storage stability of gelatine hydrogel test with immobilised ABTS was performed after 30 days. Laccase detection assays were compared after 30 min of colourimetric test applying enzyme concentration of 100 µg/mL. Experimental conditions: 4 °C, and with 1.5 mg/mL of ABTS.

When considering the storage stability of the entire system tested, a similar procedure was applied. The gelatine matrices containing ABTS were left in closed well plates at 4 °C for 30 days. During this time, the determination of storage stability was performed for the hydrogel matrix at days 10 and 30 and for the matrix at the start of the test (control). The results of the colourimetric response of the test for time t = 0 min and after 30 min for the storage period considered were presented in Figure 6b. A visual comparison of the results of the laccase detection test indicated that there were no differences in the response of the system, and the colour intensity for the storage times (day 0, 10, and 30) was comparable. In conclusion, the experimental results justified that immobilisation of the substrate in the hydrogel matrix as a key step in the development of a colourimetric test. Furthermore, the developed hydrogel-based assay was stable throughout the storage period, which confirms the validity of the approach considered in the current study. This approach provided suitable conditions for the determination of laccase activity and ensured the long-term stability of the developed test.

Another important parameter defining the reliability of the proposed colourimetric assay is the repeatability of the detection response obtained for a given concentration of the enzyme. As shown in Figure 7, the colour intensity is visually comparable in all 8 replicates performed for each of the tested solutions.

Concentration of laccase from *Trametes versicolor* [µg/mL]	COLOUR TEST FOR LACCASE DETECTION TOP VIEW							
	Repetition number [-]							
	1	2	3	4	5	6	7	8
100								
50								
10								
5								
1								
0								
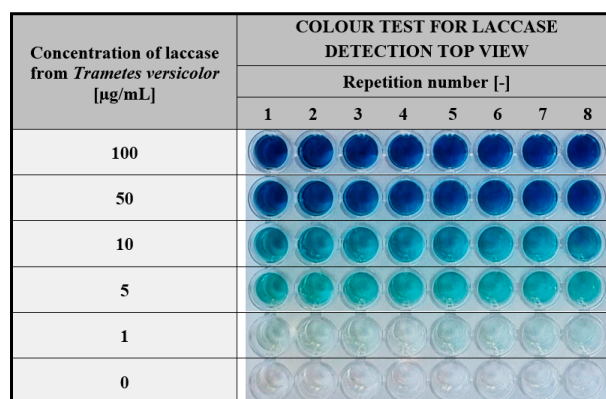
Figure 7. Repeatability of the visual responses of the hydrogel-based test performed for the different concentrations of laccase in phosphate-citrate buffer pH 5.2. Test conditions: hydrogel gelatine matrices containing ABTS at a concentration of 1.5 mg/mL; test time: 60 min.

These results demonstrate that the test developed in our study is reliable over the entire range of laccase concentrations used (1–100 µg/mL) and can be applied effectively for various screening research in enzymology.

2.1.2. Application of the Hydrogel-Based Colourimetric Assay in Microbiological Cultures

Microbiological cultures are long-term processes usually occupying several to dozens of days. During this time, studies are conducted on the growth of the microorganism, the products released and the substrate consumed. Analytical methods used in monitoring changes in microbial cultures require special equipment, reagents, and specific physico-chemical conditions. Samples for these analyses often require dilution to contain a specific concentration of an analyte. Some analyses take several hours (determination of dry weight), while others require elevated temperatures or specialised reagents and developed standard curves. Therefore, any opportunity to reduce the duration of sample preparation and analysis is highly desirable.

To verify the applicability of a quick test based on the colour reaction of the investigated sample with the substrate entrapped in the hydrogel matrix, a microbial cultivation experiment was planned. We employed a fungus *Cerrena unicolor* that produces an extracellular laccase secreted into the culture medium. The detailed characteristics and process parameters that resulted from microbiological culture may be found in Supporting Materials Table S1. The general assumption of the experiment was to quantitatively analyse laccase activity by spectrophotometric measurement of the ABTS oxidation rate expressed in U/mg units and compare it with the analytical results obtained in hydrogel assays. *Cerrena unicolor* cultivation results were presented in Figure 8. Briefly, the monitoring of changes in biomass (X), glucose (S), specific laccase activity (U/mg of protein), and pH was conducted for 16 days.
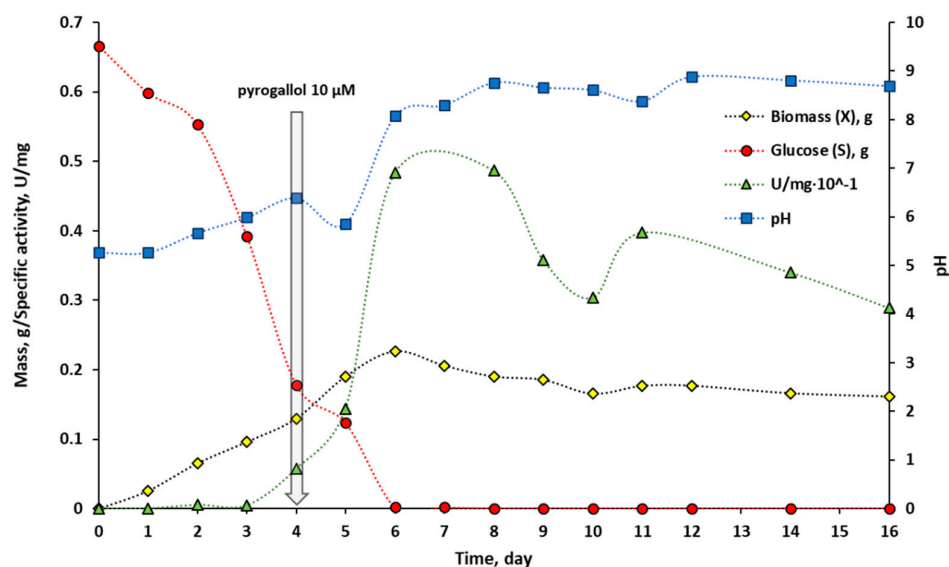
Figure 8. The course of *Cerrena unicolor* cultivation. The legend: yellow diamond—fungal dry mass [g], red circle—glucose (substrate) mass [g], green triangle—specific laccase activity [U/mg], blue square—pH in culture medium. The set of similar points was linked with a dotted line for clarity. The starting glucose mass was 0.63 g, on the 4th day the culture was induced with 10 µM of pyrogallol.

Spectroscopic measurements reflecting the course of laccase activity (green triangles) showed that the production of the enzyme appeared on day 4 of culture and increased rapidly reaching a maximum on days between 6 and 8. The analysis of the course for the specific laccase activity revealed another peak of maximum activity recorded on day 11. This phenomenon is known and typical for the white-rot fungi cultures and could be attributed to the production of laccase isoforms at different stages of growth [82–84]. After day 11, a decrease in specific laccase activity was observed, associated with substrate

depletion and culture collapse. Figure 9 showed the results of a colourimetric hydrogel-based test performed for analogous samples measured spectrophotometrically.

Figure 9. The visual response of colourimetric assay measurements performed for *Cerrena unicolor* culture samples (day 1–16) measured at different times (0–1440 min) using a hydrogel-based assay with immobilised ABTS (1.5 mg/mL); left—top view, right—side view.

Determination of laccase activity with a colourimetric test allowed detection of the enzyme activity as early as 5 min after the sample was applied on the hydrogel surface. At this time, it was possible to determine the samples with the most concentrated active protein that was for samples corresponding to days 6–16 (Figure 9, side view). At the 20 min of the test, the substantial effect was visible on days 6–8 and 11. These visual response corresponded to the maxima of laccase activity determined spectrophotometrically (Figure 8) and were reflected by the more intense colour of the oxidised ABTS in the hydrogel matrix. After 2 and 3 h, it was possible to detect even the smallest amount of laccase in samples corresponding to the initial days of culture—days 2 and 3. Such determinations were not observed in the spectrophotometric measurement of enzyme activity. Based on the results, it appeared that laccase from *Cerrena unicolor* could be detected with the hydrogel test even in a culture solution having a slightly alkaline pH, such as pH 8.1–8.8 (Figure 8, blue square). A comparison of the above results with a commercial preparation, for which detection was possible up to pH 6 (Figure 5), showed that pH is an important factor for determining enzyme activity in samples of different origins. Laccases from *C. unicolor* show higher pH tolerance [82,83], when compared to laccase from *T. versicolor*, since *C. unicolor* production medium, reaches the alkaline pH [85] and therefore laccase activity could be detected by the colourimetric test.

To sum up the results of the experiment, it should be claimed that assays based on the determination of laccase activity in a gelatin hydrogel matrix enriched with ABTS are tests ready to use since they do not require the preparation of any additional reagents and specific reaction conditions. An important advantage of the test is the size of the sample introduced on the surface of the matrix, which is in the range of 50–250 μL, this preserves a significant amount of material for testing and performing other additional analyses. Furthermore, a distinctive feature of this assay is the rapid response in the hydrogel matrix, which becomes visible in the form of a coloured stripe, ensuring ease of reading. The

intensity of this colour increases over time and enables one to conclude which sample contains significant amounts of the enzyme in a relatively short time (in 5 min). Finally, the analyses are performed at room temperature so they do not require the application of any additional equipment.

2.2. Gelatine Hydrogels Containing Immobilised Laccase for Various Purposes in Enzymology

Following the success achieved in the case of developing a detection test for laccase using ABTS-enriched gelatine matrices, it was decided to use the potential of such enzyme/substrate/support system in a reversed mode. In this approach, the main functional element of the test was laccase immobilised by entrapment in a gelatine-based hydrogel. In this approach, such type of assay was examined in terms of suitability for screening potential substrates and inhibitors of the tested enzyme.

2.2.1. Hydrogel-Based Assay for Colourimetric Screening a Substrate Specificity of Laccase

Laccase-enriched gelatine matrices served as a colourimetric assay to determine the substrate specificity of this enzyme. To demonstrate the application potential of laccase-enriched gelatine matrices for substrate testing, we used three compounds most commonly used to determine the activity of this enzyme—ABTS, syringalazine (SNG) and guaiacol. As mentioned earlier, their common feature is that they are all oxidised into coloured products by laccase (Figure 2a,b), which is essential for an effective visual response in the assay. The tests were conducted for different concentrations of each compound. For ABTS and guaiacol, the range was 0.5–10 mg/mL. Whereas, due to the low solubility of syringaldazine, the concentrations were one order lower (0.05–1.0 mg/mL). Colourimetric results obtained after different test times for ABTS, guaiacol, and SNG were depicted in Figures 10–12 respectively.

Figure 10. The visual response obtained after a different time of hydrogel-based test with immobilised laccase from *Trametes versicolor* (final concentration 200 µg/mL) was performed for ABTS solutions with a concentration in the range of 0.5–10 mg/mL.

One can notice that in all cases, a positive response was visible in the form of a colour stripe after only 10 min for all the solutions used; however, in the case of ABTS, the colour change for each concentration was the most apparent (Figure 10). This was one of the main reasons for using ABTS as a reference substrate in all the studies presented in this paper. The obtained results indicate the high potential of laccase-enriched gelatine hydrogel matrices as the screening test for substrates of a given enzyme. We would like to emphasise that also other enzyme-substrate systems can be analysed using this concept of the detection assay. There are only two restrictions: (i) the enzyme should retain its

properties after immobilisation in the hydrogel matrix and (ii) the analysed compounds should be converted into coloured products upon contact with the biocatalyst.

Figure 11. The visual response obtained after a different time of hydrogel-based test with immobilised laccase from *Trametes versicolor* (final concentration 200 μg/mL) performed for guaiacol solutions with a concentration in the range of 0.5–10 mg/mL.

Figure 12. The visual response obtained after a different time of hydrogel-based test with immobilised laccase from *Trametes versicolor* (final concentration 200 μg/mL) performed for syringaldazine solutions with a concentration in the range of 0.05–1.0 mg/mL.

2.2.2. Hydrogel-Based Assay for Colourimetric Screening Potential Inhibitors of Laccase

The next possible application of gelatine matrices containing immobilised laccase as a bioactive agent is screening potential inhibitors of this enzyme. Studies on the identification of effective enzyme inhibitors are particularly time-consuming and require a considerable number of experiments and analyses [74,75]. Preliminary studies require the testing of a large group of compounds in different concentrations. Therefore the use of a rapid colourimetric assay with immobilised enzyme significantly reduces the time of prescreening and allows the selection of potentially active inhibitors for further kinetic studies in a short time. In order to demonstrate the feasibility of such test in practice, sodium azide (NaN$_3$) was

used as a well-known laccase inorganic inhibitor. In the study, a colourimetric assay was performed using a fixed concentration ABTS mixture (1.5 mg/mL) and various concentrations of sodium azide (0.5–100 µg/mL). The potency of this inhibitor was investigated by observing the colour change of individual samples over time with relation to a reference sample containing only the substrate solution (ABTS). As expected, as the concentration of NaN_3 increased, the intensity of the green-blue colour decreased (Figure 13). This means that by applying the colourimetric assay presented here, it is possible not only to effectively screen potential laccase inhibitors, but also to preliminarily estimate the concentration of this compound that rapidly inhibits catalytic activity.

Figure 13. The visual response obtained after a different time of hydrogel-based test with immobilised laccase from *Trametes versicolor* (final concentration 200 µg/mL) performed for a fixed concentration of ABTS (1.5 mg/mL) containing different concentrations of sodium azide (0.5–100 µg/mL).

2.3. Results Discussion

Current research has resulted in the development of multifunctional colorimetric assays based on ABTS or laccase immobilised in gelatine hydrogel matrices. Through the use of this biopolymer support enriched with bioactive compounds, long-lasting, sensitive test kits for various enzymological screening studies were provided. In our study, we proposed two approaches for this enzyme/substrate/hydrogel system. The first one uses hydrogel matrix containing ABTS, which enables the sensitive detection of laccase in a relatively short time (20 min) in a wide range of concentrations (2.5–100 µg/mL) and pH (3.0–6.0). While the second is based on the reverse mode (laccase immobilised in a gelatine support) and enables effective screening for substrates already within 10 min (ABTS and guaiacol in the range of 0.5–10 mg/mL; syringaldazyne 0.05–1.0 mg/mL) and potential inhibitors within 30 min (sodium azide 0.5–100 µg/mL). To the best of our knowledge, the solutions demonstrating the versatility of using the hydrogel/laccase/ABTS system for the development of rapid visual screening tests proposed in our study are novel and not described in detail in the available literature. In previous reports, one can only find examples of using hydrogel-immobilised laccase for the removal of various compounds from aquous solutions (e.g., bisphenol A [46,47], synthetic dye [48]). In turn, the use of ABTS retained on some support for the detection of laccase has been described only for

paper discs impregnated with this compound [51], and due to incomplete data in the source article (laccase concentration in the tested samples was not given), the results cannot be directly compared with each other.

3. Materials and Methods

3.1. Materials

Potato dextrose agar was purchased from Merck (Warsaw, Poland), glucose test was from Biomaxima (Lublin, Poland), 2,2′-azino-bis(3-ethylbenzothiazoline-6-sulfonate) sodium salt (ABTS), laccase from *Trametes versicolor* (EC 1.10.3.2), bovine serum albumin, porcine skin gelatine, sodium azide (NaN_3) and Lowry reagent were from Sigma-Aldrich (Poznan, Poland). Other chemicals were purchased from POCh (Gliwice, Poland). Transglutaminase (mTGase) Activa®WM was kindly donated by Ajinomoto (Tokyo, Japan). All the chemicals used were of analytical grade.

3.2. Methods

3.2.1. Preparation of Gelatine Hydrogel Matrices Containing Reactive Compounds

Gelatine hydrogel matrices with immobilised 2,2′-azino-bis(3-ethylbenzothiazoline-6- sulfonate) sodium salt (ABTS) or a commercial preparation of laccase from *Trametes versicolor* were prepared according to a modified procedure described in the previous study [86]. Briefly, a weighted portion of gelatine (15% *w/v*) was dissolved in 0.1 M citrate-phosphate buffer (pH 5.2) in a glass beaker thermostated at 80 °C for approximately 30 min. Next, the solution was cooled to 45 °C and incubated at this temperature for a few minutes. In parallel, a buffer solution of ABTS or laccase with given concentration was prepared. Then, after total dissolution, a weighted portion of cross-linking agent (microbial transglutaminase, mTGase) was added to obtain its concentration of 3% *w/v*. The cross-linking step began by mixing the ABTS/mTGase or laccase/mTGase solution with gelatine at the volume ratio of 1:2. The blend thus obtained was pipetted into the 96-well plate (85.4 × 127.6 × 14.4 mm) with 200 μL for each hole (diameter: 6.5 mm; height: 10.8 mm) and stored until use at 4 °C. The gelatine hydrogel and the 96-well plate used are shown in Figure S1. In our study, concentrations of 4.5 mg/mL ABTS and 600 μg/mL commercial preparation of laccase were used for immobilisation purposes.

3.2.2. Hydrogel-Based Assay for Colourimetric Detection of Laccase

The test for laccase detection was based on the monitoring of the colour change of the gelatin matrix containing the immobilised ABTS from transparent to green-blue. The appearance of the colour indicates the presence of laccase in the tested sample, and the intensity of the green-blue colour enables us to estimate the concentration of laccase.

The test was performed by applying 100 μL of an aqueous solution potentially containing laccase to the surface of a hydrogel containing ABTS placed on a microlitre well plate with a volume of 200 μL and monitoring the appearance of the colour in time from transparent to green-blue, or lack thereof.

3.2.3. Determination of Laccase Concentration Range Effectively Detected by the Hydrogel-Based Assay

First, solutions of laccase from *Trametes versicolor* with various concentrations (0.05–100 μg/mL) were prepared in 0.1 M citrate-phosphate buffer (pH 5.2). The protein concentrations in the enzyme solutions were determined by using the Lowry method [87]. Then, a 100 μL of each laccase preparation was applied to the gelatine-based hydrogel matrix containing ABTS, and the progress of the change in gel colour from transparent to green-blue was monitored in time.

3.2.4. Determination of the pH Range in which Laccase Is Effectively Detected by the Hydrogel-Based Assay

First, solutions of laccase from *Trametes versicolor* in a given concentration (200 μg/mL) were prepared in 0.1 M citrate-phosphate buffer with different pH (range of 3.0–9.0) Then, a 100 μL of each laccase preparation was applied to the gelatine-based hydrogel matrix containing ABTS (1.5 mg/mL), and the progress of the change in gel colour from transparent to green-blue was monitored in time.

3.2.5. Determination of Storage Stability of 2,2′-Azino-bis(3-ethylbenzothiazoline-6-sulfonate) Sodium Salt

The ABTS is known to auto-oxidise, therefore its stability in native and immobilised form was verified after storage of the samples on the well plate at 4 °C for a specified time (0–20 days). The result for each ABTS formulation (solution or entrapped in hydrogel) stored for a particular time was compared with the results determined on day 0 (control sample).

3.2.6. Determination of Storage Stability of the Hydrogel-Based Test

The stability of gelatine hydrogel matrices containing ABTS was verified by performing a detection test for a given concentration of laccase from *Trametes versicolor* by using matrices that were previously stored at 4 °C for a specified time (0–30 days) in closed well plates. The result for each hydrogel matrix stored for a particular time was compared with the results determined on day 0 (control sample). For this purpose, the intensity of the colour change after 30 min was compared with that at the start of the laccase detection test. The hydrogel assay was classified as stable under storage conditions if the effect of the change in gel colour from transparent to green-blue determined 30 min after the application of the enzyme solution at the same concentration (100 μg/mL) was similar to that obtained for the control test performed on day 0.

3.2.7. Hydrogel-Based Assay for Colourimetric Screening a Substrate Specificity of Laccase

The test for screening the substrate specificity of laccase was based on the monitoring of the colour change of the solution potentially containing a substrate that was dropped on the gelatine matrix containing immobilised laccase (200 μg/mL). The appearance of the colour indicates that laccase effectively converts the given substrate to the colourful product. The intensity of the colour enables us to estimate the affinity strength of the laccase for the given substrate. It should be noted that this test is limited to substrates converted by the enzyme to colourful products. In our study, ABTS, guaiacol, and syringaldazine (SNG) were used as substrates that give green-blue, red-brown, and pink products, respectively. The ABTS and guaiacol were used as buffer solutions in the concentration range of 0.5–10 mg/mL. Syringaldazine was used as a methanolic solution in a lower concentration range (0.05–1.0 mg/mL) due to the poor solubility in water. The test was performed in a microlitre well plate filled with 200 μL hydrogel containing immobilised laccase by applying 100 μL of the tested solution potentially containing the substrate on the hydrogel surface and monitoring the appearance of the colour or lack thereof.

3.2.8. Hydrogel-Based Assay for Colourimetric Screening Potential Inhibitors of Laccase

The test for screening potential inhibitors of laccase was based on the monitoring of the colour change of the ABTS solution potentially containing an inhibitor that was dropped on the gelatine matrix containing immobilised laccase. In the presented studies, sodium azide (NaN_3) was used as a model inhibitor. The appearance of the deep green-blue colour indicated that laccase effectively converted the ABTS (1.5 mg/mL); however, the lower intensity of the colour or lack thereof was observed for solutions consisting of ABTS (1.5 mg/mL) and sodium azide at different concentrations (range of indicate the presence of inhibitor) in the analysed samples. The test was performed on a microlitre well plate. One hundred microliters of ABTS solution potentially containing the inhibitor was applied

on the surface of a hydrogel with the immobilised laccase (200 μL). The differences in colour appearance between the solution potentially containing laccase inhibitor and control solution of ABTS itself were observed.

3.2.9. Microorganism and Cultivation Conditions

A white-rot fungus *Cerrena unicolor* (Bull.ex.Fr.) Murr, strain no. 139 originated from the culture collection of the Department of Biochemistry, University of Lublin (Poland). The stock culture was maintained on potato dextrose agar at 4 °C and periodically transferred to a fresh medium. The fungus cultivation and laccase production were monitored for 16 days according to [2,88] with changes. On the fourth day, the culture was induced with pyrogallol dissolved in methanol to a final concentration of 10 μM [89]. The changes in pH, substrate, biomass, protein concentration, and laccase activity were determined by analysing the cultivation medium in a single flask corresponding to one day of cultivation. A detailed description of the culture cultivation can be found in Supporting Materials.

3.2.10. Analytical Procedures

The mass of mycelium was determined by its separation from the cultivation medium through a paper filter, washing with distilled water, and drying at 85 °C to a constant mass. In the filtrate, pH, glucose, protein content, and laccase activity were determined. The pH measurements were performed with Crison Basic 20 pH-meter and a Crison 52 09 pH electrode at room temperature. The glucose amount was determined using the enzymatic test kit according to the procedure provided by a supplier (Biomaxima) and glucose as a standard. Protein content was determined with Lowry's method [87] and albumin serum bovine as a standard. The analytical measurements were performed in triplicate with a standard deviation (SD) of less than 5%.

3.2.11. Determination of Laccase Catalytic Activity

Laccase activity was determined based on the spectrophotometric measurements (λ = 420 nm, Shimadzu UV-1800) of the oxidation reaction rate using 1.5 mg/mL ABTS as a substrate in 0.1 M citrate-phosphate buffer (pH 5.2, 25 °C). The proportion of the enzyme to the substrate was 1:2 (*v/v*). The specific activity unit (U/mg) was defined as the amount of the enzyme (1 mg) that oxidises ABTS to the 1 μmole of the product (ε_{420} = 36 000 $M^{-1}cm^{-1}$) per minute at 25 °C.

4. Conclusions

In this article, we have reported the preparation and application of a quick and effective colourimetric test based on a hydrogel matrix for the determination of enzyme catalytic properties. The assay components were the laccase from *Trametes versicolor*, its substrate ABTS, and a gelatine hydrogel. We presented two approaches for using this test. The first concept concerned a hydrogel matrix with an immobilised substrate (ABTS) for application in the monitoring of laccase production in microbiological culture by detecting its oxidation activity. The second approach used immobilised laccase in the hydrogel for the determination of its substrate specificity for ABTS, syringaldazine, and guaiacol as well as evaluation of the inhibitor influence on enzyme activity with NaN_3 as an example. The work was additionally supported by giving the characteristic parameters for the test, namely the detection sensitivity of the enzyme amount and pH range of examined samples, storage stability, and repeatability of the visual response. Despite the numerous advantages of this colourimetric test, there are some key requirements for its application: (i) the enzyme should retain its catalytic properties after immobilisation in the hydrogel matrix, (ii) the reaction product should be visually detectable, and (iii) the hydrogel matrix-substrate system should maintain a high level of enzyme detection for several weeks during storage at 4 °C.

We would like to emphasise that the examples given in this paper do not exhaust the application potential of the colourimetric test considered in the case of laccase. Other

possible usages are studies of decolourisation processes, detoxification of wastewater from the textile industry, and detection of polyphenols or amines. The proposed well plate assay can be also prepared in such a way that it enables the simultaneous detection of enzymes with different biocatalytic properties. In particular, this property can be very useful for the selective screening of given biocatalysts in complex mixtures of microbial culture fluids. These examples offer a further research challenge for the development of new effective colourimetric tests based on different enzymes, substrates, and hydrogel matrices.

Supplementary Materials: The supporting information can be downloaded at: https://www.mdpi.com/article/10.3390/ijms24010033/s1.

Author Contributions: Conceptualisation, K.L.; methodology, K.L. and H.M.; validation, K.L. and H.M.; formal analysis, K.L. and H.M.; investigation, K.L. and H.M.; resources, K.L. and H.M.; data curation, K.L. and H.M.; writing—original draft preparation, K.L. and H.M.; writing—review and editing, K.L. and H.M.; visualisation, K.L. and H.M.; project administration, K.L.; funding acquisition, K.L. and H.M. All authors have read and agreed to the published version of the manuscript.

Institutional Review Board Statement: Not applicable.

Informed Consent Statement: Not applicable.

Data Availability Statement: Not applicable.

Conflicts of Interest: The authors declare no conflict of interest.

References

1. Akhtar, N.; Syakir Ishak, M.I.; Bhawani, S.A.; Umar, K. Various natural and anthropogenic factors responsible for water quality degradation: A review. *Water* **2021**, *13*, 2660. [CrossRef]
2. Scanes, C.G. Human activity and habitat loss: Destruction, fragmentation, and degradation. In *Animals and Human Society*; Elsevier: Amsterdam, The Netherlands, 2018; pp. 451–482, ISBN 9780128052471.
3. Karak, T.; Bhagat, R.M.; Bhattacharyya, P. Municipal solid waste generation, composition, and management: The world scenario. *Crit. Rev. Environ. Sci. Technol.* **2012**, *42*, 1509–1630. [CrossRef]
4. Naidu, R.; Biswas, B.; Willett, I.R.; Cribb, J.; Kumar Singh, B.; Paul Nathanail, C.; Coulon, F.; Semple, K.T.; Jones, K.C.; Barclay, A.; et al. Chemical pollution: A growing peril and potential catastrophic risk to humanity. *Environ. Int.* **2021**, *156*, 106616. [CrossRef] [PubMed]
5. Sharma, J.; Joshi, M.; Bhatnagar, A.; Chaurasia, A.K.; Nigam, S. Pharmaceutical residues: One of the significant problems in achieving 'clean water for all' and its solution. *Environ. Res.* **2022**, *215*, 114219. [CrossRef] [PubMed]
6. Papagiannaki, D.; Belay, M.H.; Gonçalves, N.P.F.; Robotti, E.; Bianco-Prevot, A.; Binetti, R.; Calza, P. From monitoring to treatment, how to improve water quality: The pharmaceuticals case. *Chem. Eng. J. Adv.* **2022**, *10*, 100245. [CrossRef]
7. Kayode-Afolayan, S.D.; Ahuekwe, E.F.; Nwinyi, O.C. Impacts of pharmaceutical effluents on aquatic ecosystems. *Sci. Afr.* **2022**, *17*, e01288. [CrossRef]
8. Pandey, A. Food wastage: Causes, impacts and solutions. *Sci. Herit. J.* **2021**, *5*, 17–20. [CrossRef]
9. Scholz, K.; Eriksson, M.; Strid, I. Carbon footprint of supermarket food waste. *Resour. Conserv. Recycl.* **2015**, *94*, 56–65. [CrossRef]
10. Conti, I.; Simioni, C.; Varano, G.; Brenna, C.; Costanzi, E.; Neri, L.M. Legislation to limit the environmental plastic and microplastic pollution and their influence on human exposure. *Environ. Pollut.* **2021**, *288*, 117708. [CrossRef]
11. Kumar, V.; Sharma, N.; Umesh, M.; Selvaraj, M.; Al-Shehri, B.M.; Chakraborty, P.; Duhan, L.; Sharma, S.; Pasrija, R.; Awasthi, M.K.; et al. Emerging challenges for the agro-industrial food waste utilization: A review on food waste biorefinery. *Bioresour. Technol.* **2022**, *362*, 127790. [CrossRef]
12. Sheldon, R.A.; Woodley, J.M. Role of biocatalysis in sustainable chemistry. *Chem. Rev.* **2018**, *118*, 801–838. [CrossRef]
13. Kate, A.; Sahu, L.K.; Pandey, J.; Mishra, M.; Sharma, P.K. Green catalysis for chemical transformation: The need for the sustainable development. *Curr. Res. Green Sustain. Chem.* **2022**, *5*, 100248. [CrossRef]
14. Woodley, J.M. New frontiers in biocatalysis for sustainable synthesis. *Curr. Opin. Green Sustain. Chem.* **2020**, *21*, 22–26. [CrossRef]
15. Alcántara, A.R.; Domínguez de María, P.; Littlechild, J.A.; Schürmann, M.; Sheldon, R.A.; Wohlgemuth, R. Biocatalysis as Key to Sustainable Industrial Chemistry. *ChemSusChem* **2022**, *15*, e202102709. [CrossRef]

16. Alcalde, M.; Ferrer, M.; Plou, F.J.; Ballesteros, A. Environmental biocatalysis: From remediation with enzymes to novel green processes. *Trends Biotechnol.* **2006**, *24*, 281–287. [CrossRef]

17. Alshabib, M.; Onaizi, S.A. A review on phenolic wastewater remediation using homogeneous and heterogeneous enzymatic processes: Current status and potential challenges. *Sep. Purif. Technol.* **2019**, *219*, 186–207. [CrossRef]

18. Kumaran, A.; Vashishth, R.; Singh, S.; Surendran, U.; James, A.; Velayudhaperumal Chellam, P. Biosensors for detection of organophosphate pesticides: Current technologies and future directives. *Microchem. J.* **2022**, *178*, 107420. [CrossRef]

19. Sarkar, A.; Sarkar, K.D.; Amrutha, V.; Dutta, K. An overview of enzyme-based biosensors for environmental monitoring. In *Tools, Techniques and Protocols for Monitoring Environmental Contaminants*; Elsevier: Amsterdam, The Netherlands, 2019; pp. 307–329, ISBN 9780128146798.

20. Farias, T.C.; Kawaguti, H.Y.; Bello Koblitz, M.G. Microbial amylolytic enzymes in foods: Technological importance of the Bacillus genus. *Biocatal. Agric. Biotechnol.* **2021**, *35*, 102054. [CrossRef]

21. Deckers, M.; Deforce, D.; Fraiture, M.A.; Roosens, N.H.C. Genetically modified micro-organisms for industrial food enzyme production: An overview. *Foods* **2020**, *9*, 326. [CrossRef]

22. Singh, R.; Kumar, M.; Mittal, A.; Mehta, P.K. Microbial enzymes: Industrial progress in 21st century. *3 Biotech* **2016**, *6*, 174. [CrossRef]

23. Lebreton, L.; Andrady, A. Future scenarios of global plastic waste generation and disposal. *Palgrave Commun.* **2019**, *5*, 6. [CrossRef]

24. Dziuba, R.; Kucharska, M.; Madej-Kiełbik, L.; Sulak, K.; Wiśniewska-Wrona, M. Biopolymers and biomaterials for special applications within the context of the circular economy. *Materials* **2021**, *14*, 7704. [CrossRef] [PubMed]

25. Samir, A.; Ashour, F.H.; Hakim, A.A.A.; Bassyouni, M. Recent advances in biodegradable polymers for sustainable applications. *npj Mater. Degrad.* **2022**, *6*, 68. [CrossRef]

26. Acquavia, M.A.; Pascale, R.; Martelli, G.; Bondoni, M.; Bianco, G. Natural polymeric materials: A solution to plastic pollution from the agro-food sector. *Polymers* **2021**, *13*, 158. [CrossRef] [PubMed]

27. Das, A.; Ringu, T.; Ghosh, S.; Pramanik, N. *A Comprehensive Review on Recent Advances in Preparation, Physicochemical Characterization, and Bioengineering Applications of Biopolymers*; Springer: Berlin/Heidelberg, Germany, 2022; ISBN 0123456789.

28. Folino, A.; Karageorgiou, A.; Calabrò, P.S.; Komilis, D. Biodegradación de bioplásticos desechados en entornos naturales e industriales. *Sustainability* **2020**, *12*, 6030. [CrossRef]

29. Polman, E.M.N.; Gruter, G.J.M.; Parsons, J.R.; Tietema, A. Comparison of the aerobic biodegradation of biopolymers and the corresponding bioplastics: A review. *Sci. Total Environ.* **2021**, *753*, 141953. [CrossRef]

30. Silva, M.P.; Fabi, J.P. Food biopolymers-derived nanogels for encapsulation and delivery of biologically active compounds: A perspective review. *Food Hydrocoll. Health* **2022**, *2*, 100079. [CrossRef]

31. Udayakumar, G.P.; Muthusamy, S.; Selvaganesh, B.; Sivarajasekar, N.; Rambabu, K.; Banat, F.; Sivamani, S.; Sivakumar, N.; Hosseini-Bandegharaei, A.; Show, P.L. Biopolymers and composites: Properties, characterization and their applications in food, medical and pharmaceutical industries. *J. Environ. Chem. Eng.* **2021**, *9*, 105322. [CrossRef]

32. Machado, T.O.; Grabow, J.; Sayer, C.; de Araújo, P.H.H.; Ehrenhard, M.L.; Wurm, F.R. Biopolymer-based nanocarriers for sustained release of agrochemicals: A review on materials and social science perspectives for a sustainable future of agri- and horticulture. *Adv. Colloid Interface Sci.* **2022**, *303*, 102645. [CrossRef]

33. Rivero Berti, I.; Islan, G.A.; Castro, G.R. Enzymes and biopolymers. The opportunity for the smart design of molecular delivery systems. *Bioresour. Technol.* **2021**, *322*, 124546. [CrossRef]

34. Bilal, M.; Iqbal, H.M.N. Naturally-derived biopolymers: Potential platforms for enzyme immobilization. *Int. J. Biol. Macromol.* **2019**, *130*, 462–482. [CrossRef]

35. Abdul Khalil, H.P.S.; Bashir Yahya, E.; Jummaat, F.; Adnan, A.S.; Olaiya, N.G.; Rizal, S.; Abdullah, C.K.; Pasquini, D.; Thomas, S. Biopolymers based aerogels: A review on revolutionary solutions for smart therapeutics delivery. *Prog. Mater. Sci.* **2023**, *131*, 101014. [CrossRef]

36. Czyzewska, K.; Trusek, A. Encapsulated nola™ fit 5500 lactase—An economically beneficial way to obtain lactose-free milk at low temperature. *Catalysts* **2021**, *11*, 527. [CrossRef]

37. Raghuwanshi, V.S.; Garnier, G. Characterisation of hydrogels: Linking the nano to the microscale. *Adv. Colloid Interface Sci.* **2019**, *274*, 102044. [CrossRef]

38. Chauhan, N.; Saxena, K.; Jain, U. Hydrogel based materials: A progressive approach towards advancement in biomedical applications. *Mater. Today Commun.* **2022**, *33*, 104369. [CrossRef]

39. Mushtaq, F.; Raza, Z.A.; Batool, S.R.; Zahid, M.; Onder, O.C.; Rafique, A.; Nazeer, M.A. Preparation, properties, and applications of gelatin-based hydrogels (GHs) in the environmental, technological, and biomedical sectors. *Int. J. Biol. Macromol.* **2022**, *218*, 601–633. [CrossRef]

40. Elkhoury, K.; Morsink, M.; Sanchez-Gonzalez, L.; Kahn, C.; Tamayol, A.; Arab-Tehrany, E. Biofabrication of natural hydrogels for cardiac, neural, and bone Tissue engineering Applications. *Bioact. Mater.* **2021**, *6*, 3904–3923. [CrossRef]

41. Saqib, M.N.; Khaled, B.M.; Liu, F.; Zhong, F. Hydrogel beads for designing future foods: Structures, mechanisms, applications, and challenges. *Food Hydrocoll. Health* **2022**, *2*, 100073. [CrossRef]

42. ALSamman, M.T.; Sánchez, J. Recent advances on hydrogels based on chitosan and alginate for the adsorption of dyes and metal ions from water. *Arab. J. Chem.* **2021**, *14*, 103455. [CrossRef]

43. Meyer, J.; Meyer, L.E.; Kara, S. Enzyme immobilization in hydrogels: A perfect liaison for efficient and sustainable biocatalysis. *Eng. Life Sci.* **2022**, *22*, 165–177. [CrossRef]

44. Tan, Z.; Bilal, M.; Raza, A.; Cui, J.; Ashraf, S.S.; Iqbal, H.M.N. Expanding the biocatalytic scope of enzyme-loaded polymeric hydrogels. *Gels* **2021**, *7*, 194. [CrossRef] [PubMed]

45. Yang, Y.; Ren, Y.; Song, W.; Yu, B.; Liu, H. Rational design in functional hydrogels towards biotherapeutics. *Mater. Des.* **2022**, *223*, 111086. [CrossRef]

46. Zhang, F.; Lian, M.; Alhadhrami, A.; Huang, M.; Li, B.; Mersal, G.A.M.; Ibrahim, M.M.; Xu, M. Laccase immobilized on functionalized cellulose nanofiber/alginate composite hydrogel for efficient bisphenol A degradation from polluted water. *Adv. Compos. Hybrid Mater.* **2022**, *5*, 1852–1864. [CrossRef]

47. Piao, M.; Zou, D.; Yang, Y.; Ren, X.; Qin, C.; Piao, Y. Multi-functional laccase immobilized hydrogel microparticles for efficient removal of Bisphenol A. *Materials* **2019**, *12*, 704. [CrossRef] [PubMed]

48. Mogharabi, M.; Nassiri-Koopaei, N.; Bozorgi-Koushalshahi, M.; Nafissi-Varcheh, N.; Bagherzadeh, G.; Faramarzi, M.A. Immobilization of laccase in alginate-gelatin mixed gel and decolorization of synthetic dyes. *Bioinorg. Chem. Appl.* **2012**, *2012*, 823830. [CrossRef]

49. Kiiskinen, L.L.; Rättö, M.; Kruus, K. Screening for novel laccase-producing microbes. *J. Appl. Microbiol.* **2004**, *97*, 640–646. [CrossRef]

50. Fu, K.; Fu, S.; Zhan, H.; Zhou, P.; Liu, M.; Liu, H. A newly isolated wood-rot fungus for laccase production in submerged cultures. *BioResources* **2013**, *8*, 1385–1397. [CrossRef]

51. Dias, A.A.; Matos, A.J.S.; Fraga, I.; Sampaio, A.; Bezerra, R.M.F. An easy method for screening and detection of laccase activity. *Open Biotechnol. J.* **2017**, *11*, 89–93. [CrossRef]

52. Mariod, A.A.; Adam, H.F. Review: Gelatin, source, extraction and industrial applications. *Acta Sci. Pol. Technol. Aliment.* **2013**, *12*, 135–147.

53. Alipal, J.; Mohd Pu'ad, N.A.S.; Lee, T.C.; Nayan, N.H.M.; Sahari, N.; Basri, H.; Idris, M.I.; Abdullah, H.Z. A review of gelatin: Properties, sources, process, applications, and commercialisation. *Mater. Today Proc.* **2021**, *42*, 240–250. [CrossRef]

54. Elzoghby, A.O. Gelatin-based nanoparticles as drug and gene delivery systems: Reviewing three decades of research. *J. Control. Release* **2013**, *172*, 1075–1091. [CrossRef]

55. Lu, Y.; Luo, Q.; Chu, Y.; Tao, N.; Deng, S.; Wang, L.; Li, L. Application of Gelatin in Food Packaging: A Review. *Polymers* **2022**, *14*, 436. [CrossRef]

56. Lv, L.C.; Huang, Q.Y.; Ding, W.; Xiao, X.H.; Zhang, H.Y.; Xiong, L.X. Fish gelatin: The novel potential applications. *J. Funct. Foods* **2019**, *63*, 103581. [CrossRef]

57. Sun, G.; Huang, Z.; Zhang, Z.; Liu, Y.; Li, J.; Du, G.; Lv, X.; Liu, L. A two-step cross-linked hydrogel immobilization strategy for diacetylchitobiose deacetylase. *Catalysts* **2022**, *12*, 932. [CrossRef]

58. Al-Nimry, S.; Dayah, A.A.; Hasan, I.; Daghmash, R. Cosmetic, biomedical and pharmaceutical applications of fish gelatin/hydrolysates. *Mar. Drugs* **2021**, *19*, 145. [CrossRef]

59. Irfan, N.I.; Mohd Zubir, A.Z.; Suwandi, A.; Haris, M.S.; Jaswir, I.; Lestari, W. Gelatin-based hemostatic agents for medical and dental application at a glance: A narrative literature review. *Saudi Dent. J.* **2022**, *34*, 699–707. [CrossRef]

60. Wang, X.; Bai, Z.; Zheng, M.; Yue, O.; Hou, M.; Cui, B.; Su, R.; Wei, C.; Liu, X. Engineered gelatin-based conductive hydrogels for flexible wearable electronic devices: Fundamentals and recent advances. *J. Sci. Adv. Mater. Devices* **2022**, *7*, 100451. [CrossRef]

61. Tang, Y.; Wang, H.; Liu, S.; Pu, L.; Hu, X.; Ding, J.; Xu, G.; Xu, W.; Xiang, S.; Yuan, Z. A review of protein hydrogels: Protein assembly mechanisms, properties, and biological applications. *Colloids Surf. B Biointerfaces* **2022**, *220*, 112973. [CrossRef]

62. Labus, K.; Wolanin, K.; Radosiński, Ł. Comparative study on enzyme immobilization using natural hydrogel matrices—Experimental studies supported by molecular models analysis. *Catalysts* **2020**, *10*, 489. [CrossRef]

63. Labus, K. Effective detection of biocatalysts with specified activity by using a hydrogel-based colourimetric assay - β-galactosidase case study. *PLoS ONE* **2018**, *13*, e0205532. [CrossRef]

64. Labus, K. Żelatynowe Matryce Hydrożelowe, Sposób ich Wytwarzania Oraz ich Zastosowanie. 2019; pp. 1–10. Available online: https://ewyszukiwarka.pue.uprp.gov.pl/search/pwp-details/P.421412?lng=en (accessed on 18 December 2022).

65. Labus, K.; Krystek, K. Zastosowanie L-3,4-dihydroksyfenyloalaniny Immobilizowanej w Żelatynowych Matrycach Hydrożelowych. 2021; pp. 1–11. Available online: https://ewyszukiwarka.pue.uprp.gov.pl/search/pwp-details/P.422983 (accessed on 18 December 2022).

66. Lonergan, G.; Mew, E.; Schliephake, K.; Baker, W.L. Phenolic substrates for fluorometric detection of laccase activity. *FEMS Microbiol. Lett.* **1997**, *153*, 485–490. [CrossRef] [PubMed]

67. Senthivelan, T.; Kanagaraj, J.; Panda, R.C.; Narayani, T. Screening and production of a potential extracellular fungal laccase from Penicillium chrysogenum: Media optimization by response surface methodology (RSM) and central composite rotatable design (CCRD). *Biotechnol. Rep.* **2019**, *23*, e00344. [CrossRef] [PubMed]

68. Lisov, A.V.; Trubitsina, L.I.; Lisova, Z.A.; Trubitsin, I.V.; Zavarzina, A.G.; Leontievsky, A.A. Transformation of humic acids by two-domain laccase from Streptomyces anulatus. *Process Biochem.* **2019**, *76*, 128–135. [CrossRef]

69. Mishra, A.; Kumar, S. Kinetic studies of laccase enzyme of Coriolus versicolor MTCC 138 in an inexpensive culture medium. *Biochem. Eng. J.* **2009**, *46*, 252–256. [CrossRef]

70. Grassin, C.; Dubourdieu, D. Quantitative determination of Botrytis laccase in musts and wines by the syringaldazine test. *J. Sci. Food Agric.* **1989**, *48*, 369–376. [CrossRef]

71. Leonowicz, A.; Grzywnowicz, K. Quantitative estimation of laccase forms in some white-rot fungi using syringaldazine as a substrate. *Enzyme Microb. Technol.* **1981**, *3*, 55–58. [CrossRef]

72. Harkin, J.M.; Obst, J.R. Syringaldazine, an effective reagent for detecting laccase and peroxidase in fungi. *Experientia* **1973**, *29*, 381–387. [CrossRef]

73. Tetianec, L.; Chaleckaja, A.; Vidziunaite, R.; Kulys, J.; Bachmatova, I.; Marcinkeviciene, L.; Meskys, R. Development of a laccase/syringaldazine system for NAD(P)H oxidation. *J. Mol. Catal. B Enzym.* **2014**, *101*, 28–34. [CrossRef]

74. Maniak, H.; Talma, M.; Matyja, K.; Trusek, A.; Giurg, M. Synthesis and structure-activity relationship studies of hydrazide-hydrazones as inhibitors of laccase from *Trametes versicolor*. *Molecules* **2020**, *25*, 1255. [CrossRef]

75. Maniak, H.; Talma, M.; Giurg, M. Inhibitory potential of new phenolic hydrazide-hydrazones with a decoy substrate fragment towards laccase from a phytopathogenic fungus: SAR and molecular docking studies. *Int. J. Mol. Sci.* **2021**, *22*, 12307. [CrossRef]

76. Abd El Monssef, R.A.; Hassan, E.A.; Ramadan, E.M. Production of laccase enzyme for their potential application to decolorize fungal pigments on aging paper and parchment. *Ann. Agric. Sci.* **2016**, *61*, 145–154. [CrossRef]

77. Singh, G.; Bhalla, A.; Kaur, P.; Capalash, N.; Sharma, P. Laccase from prokaryotes: A new source for an old enzyme. *Rev. Environ. Sci. Biotechnol.* **2011**, *10*, 309–326. [CrossRef]

78. Mandic, M.; Djokic, L.; Nikolaivits, E.; Prodanovic, R.; O'connor, K.; Jeremic, S.; Topakas, E.; Nikodinovic-Runic, J. Identification and characterization of new laccase biocatalysts from Pseudomonas species suitable for degradation of synthetic textile dyes. *Catalysts* **2019**, *9*, 629. [CrossRef]

79. Han, M.-J.; Choi, H.-T.; Song, H.-G. Purification and characterization of laccase from white rot fungi *Trametes versicolor*. *J. Microbiol.* **2005**, *43*, 555–560.

80. Stoilova, I.; Krastanov, A.; Stanchev, V. Properties of crude laccase from *Trametes versicolor* produced by solid-substrate fermentation. *Adv. Biosci. Biotechnol.* **2010**, *1*, 208–215. [CrossRef]

81. Asgher, M.; Nasir Iqbal, H.M.; Asad, M.J. Kinetic characterization of purified laccase produced from *Trametes versicolor* IBL-04 in solid state bio-processing of corncobs. *BioResources* **2012**, *7*, 1171–1188.

82. Lisova, Z.A.; Lisov, A.V.; Leontievsky, A.A. Two laccase isoforms of the basidiomycete Cerrena unicolor VKMF-3196. Induction, isolation and properties. *J. Basic Microbiol.* **2010**, *50*, 72–82. [CrossRef]

83. Rogalski, J.; Janusz, G. Purification of extracellular laccase from Cerrena unicolor. *Prep. Biochem. Biotechnol.* **2010**, *40*, 242–255. [CrossRef]

84. Rola, B.; Karaśkiewicz, M.; Majdecka, D.; Mazur, I.; Bilewicz, R.; Rogalski, J.; Ohga, S. Scale up of Cerrena unicolor laccase production. *J. Fac. Agric. Kyushu Univ.* **2013**, *58*, 231–238. [CrossRef]

85. Antecka, A.; Blatkiewicz, M.; Głuszcz, P.; Ledakowicz, S. Improvement of laccase biosynthesis by various feeding strategies and in situ integration of biomass separation. *Chem. Eng. Process. Process Intensif.* **2021**, *159*. [CrossRef]

86. Labus, K.; Drozd, A.; Trusek-Holownia, A. Preparation and characterisation of gelatine hydrogels predisposed to use as matrices for effective immobilisation of biocatalystst. *Chem. Pap.* **2016**, *70*, 523–530. [CrossRef]

87. Lowry, O.H.; Rosebrough, N.J.; Farr, A.L.; Randall, R.J. Protein measurement with the Folin phenol reagent. *J. Biol. Chem.* **1951**, *193*, 265–275. [CrossRef] [PubMed]

88. Fahraeus, G.; Reinhammar, B. Large scale production and purification of laccase from cultures of the fungus Polyporus versicolor and some properties of laccase A. *Acta Chem. Scand.* **1967**, *21*, 2367–2378. [CrossRef] [PubMed]

89. Al-adhami, A.J.H.; Bryjak, J.; Greb-Markiewicz, B.; Peczynska-Czoch, W. Immobilization of wood-rotting fungi laccases on modified cellulose and acrylic carriers. *Process Biochem.* **2002**, *37*, 1387–1394. [CrossRef]

Review

Recent Advances of Chitosan Formulations in Biomedical Applications

Mohammed A. S. Abourehab [1,2,*], Sheersha Pramanik [3], Mohamed A. Abdelgawad [4],
Bassam M. Abualsoud [5], Ammar Kadi [6], Mohammad Javed Ansari [7] and A. Deepak [8,*]

[1] Department of Pharmaceutics, College of Pharmacy, Umm Al Qura University, Makkah 21955, Saudi Arabia
[2] Department of Pharmaceutics and Industrial Pharmacy, Faculty of Pharmacy, Minia University, Minia 11566, Egypt
[3] Department of Biotechnology, Bhupat and Jyoti Mehta School of Biosciences, Indian Institute of Technology Madras, Chennai 600036, India
[4] Department of Pharmaceutical Chemistry, College of Pharmacy, Jouf University, Sakaka 72341, Saudi Arabia
[5] Department of Pharmaceutics and Pharmaceutical Technology, College of Pharmacy, Al-Ahliyya Amman University, Amman 19328, Jordan
[6] Department of Food and Biotechnology, South Ural State University, 454080 Chelyabinsk, Russia
[7] Department of Pharmaceutics, College of Pharmacy, Prince Sattam Bin Abdulaziz University, Al-Kharj 11942, Saudi Arabia
[8] Saveetha School of Engineering, Saveetha Institute of Medical and Technical Sciences, Chennai 600128, India
* Correspondence: maabourehab@uqu.edu.sa (M.A.S.A.); deepakarun@saveetha.com (A.D.)

Abstract: Chitosan, a naturally abundant cationic polymer, is chemically composed of cellulose-based biopolymers derived by deacetylating chitin. It offers several attractive characteristics such as renewability, hydrophilicity, biodegradability, biocompatibility, non-toxicity, and a broad spectrum of antimicrobial activity towards gram-positive and gram-negative bacteria as well as fungi, etc., because of which it is receiving immense attention as a biopolymer for a plethora of applications including drug delivery, protective coating materials, food packaging films, wastewater treatment, and so on. Additionally, its structure carries reactive functional groups that enable several reactions and electrochemical interactions at the biomolecular level and improves the chitosan's physicochemical properties and functionality. This review article highlights the extensive research about the properties, extraction techniques, and recent developments of chitosan-based composites for drug, gene, protein, and vaccine delivery applications. Its versatile applications in tissue engineering and wound healing are also discussed. Finally, the challenges and future perspectives for chitosan in biomedical applications are elucidated.

Keywords: chitosan; natural polymer; biomedical applications; drug delivery; tissue engineering; wound healing

1. Introduction

Carbohydrates, the most common natural polymers, join their monomeric units through glycosidic linkages. Some of the beneficial polysaccharides in the biomedical field include starch, cellulose, chitin, pectin, and so on [1]. Scientists in the polymeric field have regarded chitin and chitosan as important biopolymers in the biomedical, electronic, and pharmaceutical fields [2]. Representing one of the most abundant natural polymers, the polycationic biopolymer, chitosan, has several applications such as sewage purification [3], cell entrapment coacervation [4], and seed coating for higher crop yields [5], and also as a food packaging material [6].

Chitosan is a straight-chain polymer of a (1→4)-linked 2-amino-2-deoxy-D-glucopyranose with some residual D-glucosamine units, that can be readily obtained by N-deacetylation of the highly crystalline heteropolymer, chitin [7]. It is naturally found in the cell walls of filamentous fungi, particularly the *Zygomycetes* class [8]. It refers to a heterogenous

139

collection of oligomers and polymers which are distinct in the various degrees of polymer-ization, portions of acetylation, and the arrangements of acetylation [9]. It is industrially manufactured by hydrolysis of the amino acetyl functional groups of chitins. Chitosan is more relevant industrially than chitin because of its reactive amino and hydroxyl groups, its low crystallinity which makes it more receptive to reagents, and its solubility in most organic acidic solutions below its pKa of 6.5 [10].

Chitosan is used in a variety of industries, including treating effluents (removal of metallic ions, dyes, and as a membrane in contaminant expulsion), the food manufacturing sector (fat binding and cholesterol-lowering, food additives, packaging, and preservatives, farming (seed and fertilizer coatings, controlled agrochemical discharge), paper manu-facturing (surface treatment, adhesive paper), cosmetic products (skincare products, face creams, etc.), tissue regeneration, and wound repair [11]. Gels, nanofibers, membranes, beads, microparticles, nanoparticles, sponges, and scaffolds could all be manufactured readily from chitin and chitosan [12].

Among the different biopolymers available in nature, chitosan especially has garnered attention because of its unique properties, such as inherent antimicrobial properties, natural abundance, versatility, non-toxicity, and biodegradability. Its degradation product consists of an innocuous amino sugar that could be absorbed by human tissues. The availability of reactive functional groups on the chitosan backbone makes it convenient to tailor it using physical or chemical means to fabricate desirable scaffolds for biological purposes [13,14]. For example, chitosan exhibits functional properties such as mucoadhesion, colon targeting, efflux pump inhibition, permeation improvement, in situ gelation, transfection, and other properties owing to its amino functionality in the chitosan structure [15].

There has been a rise in the number of publications reviewing the various facets of the extraction, preparation, properties, and applications of chitosan in recent years [14,16–19]. This review highlights the most current and significant advances in utilizing chitosan and its nanocarriers as drug delivery systems, tissue engineering scaffolds, wound dressings, and vaccine delivery carriers. The scope of the present work is to highlight the various aspects of chitosan and its derivatives, sometimes in combination with other biomaterials, in biomedical research areas. The Section 1 gives a general overview of chitosan, and its structural, physical, and chemical properties detailing the extraction, properties, and various methods for its modification and the implications in the desired biomedical ap-plications. The Section 2 focuses on the current trends in chitosan applications in each biomedical domain. The Section 13 delves into the limitations and future potentialities of chitosan as a versatile biopolymer.

2. Properties of Chitosan

2.1. Physical Properties

Hydrophilic polymeric scaffolds derived from chitosan have a three-dimensional cross-linked structure. Due to their physicochemical and biochemical properties, chitosan hydrogels are manufactured via chemical or physical cross-linking amongst the polymer backbone. They are used in therapeutic applications. Because of their capacity to regulate drug release using pH-responsive and temperature-responsive release techniques, as well as the networks that can carry active pharmaceutical compounds, chitosan hydrogels are helpful in drug delivery. Chitosan hydrogels are also a good alternative for wound healing due to their strong antibacterial properties, ability to provide humidity and heat to the wound, cytocompatibility, etc. Additionally, the swelling ratio, porosity, and mechanical behavior of these hydrogels make them an excellent choice for use as a tissue regeneration scaffold [20].

2.1.1. Solubility

Chitosan is perhaps the most significant chitin derivative and the inclusion of numer-ous functional units on the polysaccharide backbone of this material, such as the hydroxyl and amine groups, allows for the creation of molecularly imprinted polymers and mor-

phological changes [21]. Each D-glucosamine monomer has a free amino position, which could also become positively charged and provide essential features to chitosan, including solubility and antibacterial activity [22,23]. These moieties form excellent chelating ligands that can bind to several metal ions and electrostatically precipitate the dye anions. Furthermore, these amino units may be protonated, resulting in chitosan's solubility in a dilute acid medium [24,25].

Chitosan is water-insoluble and insoluble in most liquid organic media; nevertheless, it is soluble in various aqueous acidic media below its pKa (pH = 6.5), including lactic acids, acetic acid, formic acid, and citric acid, as well as 10-camphor sulfonic acid, p-toluene sulfonic acid, and dimethyl sulfoxide. Carboxymethylation, quaternization, and phosphorylation of chitosan are structural modifications that enhance the polymer's solubility in various solvent systems at atmospheric temperatures [26].

Chitosan's solubility may be improved by lowering its molecular mass. The concentration of N-acetylglucosamine chains in chitosan is affected by molecular weight, which has intramolecular and intermolecular effects, leading to diverse chitosan morphologies. Nevertheless, regulating the deacetylation improves solubility at the expense of yield [27]. Breaking down the chitosan crystalline structure expands the spectrum of chitosan solubility. The researchers looked at both the physical as well as chemical ways of increasing chitosan solubility. Re-acetylation enhanced chitosan's solubility until pH = 7.4 in their chemical method. The physical strategy included the utilization of admixtures with the ability to disturb the intra- and intermolecular hydrogen bond interactions, including urea and guanidine hydrochloride [28]. Chitosan's solubility can be dramatically increased by adding smaller reactive groups to its structure, including alkyl (hydroxypropyl chitosan or carboxymethyl groups) [29]. Implementing a series of low MW chitosan compounds, a quick and efficient method of manufacturing solubilized chitosan (half N-acetylated chitosan) was devised [30].

2.1.2. Viscosity

According to Kramer $[\eta]_{Kra}$ and Huggins $[\eta]_{Hug}$, the intrinsic viscosity of chitosan in a buffered aqueous solution (0.3/0.3 M CH_3COOH/CH_3COONa) was 646 and 637, respectively [12]. Kasaai et al. studied the relationship between intrinsic viscosity and the molecular weight of shrimp shell-derived chitosan in 0.25 M acetic acid/0.25 M sodium acetate solution. The Mark–Houwink–Sakurada equation (MHS) was suggested for chitosan between molecular weight ranges of 35–2220 kDa. The exponent α in the MHS indicated that chitosan behaved as a flexible chain in the solvent composition. The α and K are inversely proportional and depend upon the degree of deacetylation, pH, and ionic strength of the solvents [31].

2.2. Chemical Properties

The degradation products of chitosan called chito-oligosaccharides are water-soluble, have no cytotoxicity to organisms, are easily absorbable through the intestines, and are eliminated through the kidneys. Chito-oligosaccharides (COS) offer a plethora of biological properties, such as cholesterol-reducing activity, anticancer activity, and immunomodulatory activity [32].

2.3. Biodegradability

Many studies have looked at the biodegradability of chitosan. Under certain conditions, lysozyme [33], proteases [34], and porcine pancreatic enzymes were discovered to be capable of degrading chitosan [35]. The *Aspergillus niger* pectinase isozyme was further demonstrated to degrade chitosan at low pH, leading to lower MW chitosan [36,37]. Connell et al. employed human feces to show that chitosan-based films, glutaraldehyde polymerized films, and tripolyphosphate crosslinked films degraded significantly [38]. According to Brenner et al., many of the enzymatic catalysts appear to have an effect against chitosan, particularly in vitro; however, variants could result in indigestible compounds.

To be therapeutically effective, these chemical particles must be sufficiently tiny to be eliminated by the kidneys (< 42 Å for neutral compounds). The bio-distribution is controlled by the mode of delivery, dose form, and chitosan properties, i.e., due to the physical qualities, the film/dense matrices will exist at the location of the application. The deterioration of the matrix can be controlled by changing the amine units' crosslinking. Particle size (less than 100 nm) can affect intravenous diffusion, while molecular mass can dictate particle lifespan [39].

2.4. Toxicity

Chitosans' toxicity was studied in several ways, such as in guinea pigs, frogs, human nasal palate tissues, and the nasal mucosa of rats. Toxicity was minimal in each experiment [40–42]. Ribeiro et al. investigated the in vitro cytotoxic effects of chitosan-based hydrogels using rat-skin dermal fibroblasts. The hydrogel, as well as its breakdown byproducts, were shown to be non-cytotoxic in a cell viability assay. The total absence of a reactive or granuloma-forming inflammatory reaction in skin infections treated with chitosan biomaterials and no pathological irregularities in the organs corroborated the hydrogel's systemic and local histocompatibility [43].

The intravenous injection of chitosan (4.5 mg/kg/day for 11 days) to rabbits resulted in no aberrant alterations, according to in vivo chronic toxicological tests. Data are generally scarce on chitosan's toxic effects from human research [44]. According to Gades et al., the human participants who consumed more than 4.5 g of chitosan per day did not experience any harmful consequences. Even greater oral doses of up to 6.75 g were found to be safe [45]. Brief human testing lasting up to 12 weeks has revealed no clinically substantial effects, such as no signs of an allergic reaction [46]. The safety of chitosan mouthwash was determined using the Ames, MTT, and V79 chromosomal abnormality studies. The chitosan-based mouthwash was less toxic and had more decisive antibacterial action than the conventional mouthwash. Moreover, unlike commercialized mouthwash, this was found to suppress two pathogenicity indicators (streptococcus and enterococcus) while causing no significant changes in the survival of the typical oral microbiota [47].

Ravindranathan et al. examined pure, mild endotoxin chitosan and found that the viscosity/molecular weight and deacetylation degree within the limits of 20–600 CP and 80–97 percent, correspondingly, have not affected the immunogenicity of chitosan. Endotoxin exposure was expected to have a significant impact on immunogenicity. Only endotoxin concentration, deacetylation degree, or viscosity impacted on the chitosan-induced immune reactions, according to their findings. Their findings also showed that lower endotoxin chitosan (0.01 EU/mg) with viscosities of 20–600 cP and deacetylation levels of 80–97% is largely innocuous. This work emphasized the importance of more thorough identification and purification of chitosan in laboratory development before being employed in clinical trials [48].

According to Baldrick, chitosan could be employed as a non-parenteral and non-blood constitutive medicinal excipient. The appropriate use of chitosan as an injectable excipient is not apparent depending on the existing data. The material's hemostatic physiological nature allows it to be used as a medical device to stop hemorrhaging, and investigations have shown local findings, such as blood clotting, thrombosis development, and platelet adhesion [49]. Despite some cytotoxicity observations in vitro, there are still instances of non-toxic chitosan used in medicines, such as to halt blood loss [50–52].

3. Methods of Preparation

Chitosan is naturally derived from the polysaccharide chitin, which is the second most abundant bio polysaccharide, generally seen in the shells of lobsters, shrimps, crabs, tortoises, and even insects [53]. Chitosan is produced by the physical or chemical deacetylation of chitin, and even though an established definition of chitosan does not exist, it is generally accepted that 70% deacetylated chitin is chitosan [54]. However, in commercial applications, a degree of deacetylation (DD) of 70–90% or even higher may be desirable by

undergoing subsequent deacetylation steps [55]. However, this process may also lead to polymer degradation and increased chances of reacetylation. Hence, chitosan's molecular weight is generally dependent on its DD. The lower the DD, the higher the MW, which imparts more significant chemical and mechanical stability but also decreases its solubility in most solvents in regular use. This deacetylation reaction is ideally carried out in a nitrogen-rich environment or by adding it to a mixture of NaOH and sodium borohydride to avoid any side reactions from taking place. In this way, the chitosan produced has an average molecular weight of 1.2×10^5 gmol^{-1} [55].

Throughout the past decades, scientists have explored and implemented several ways of extracting chitosan from the shells of various crustaceans, insects, and fungi [56]. Chitosan biopolymers can also be produced from *Labeo rohita's* discarded scales [57]. To produce chitosan from chitin, two techniques with differing degrees of acetylation had proved to be widely employed. The first is the heterogeneous deacetylation of dry chitin, while the second is the uniform deacetylation of pre-swollen chitin in an aqueous solution in a vacuum [58]. The deacetylation procedure requires strong alkali treatments and extended operating durations in both of the circumstances. The production time is determined by whether the circumstances are heterogeneous or homogeneous and can range from 1 to over 80 h. Alternative manufacturing procedures have been devised to lessen the relatively long processing time and significant volume of alkali. Employing thiophenol in DMSO for sequential alkali processes [59]; thermo-mechanical methods employing a cascade reactor maintained at a low alkali percentage [60]; flash procedures under saturated steam [61]; microwave dielectric heating [62]; and periodic water washing [63,64] are other instances of alternative manufacturing procedures. Previous studies have revealed various sophisticated chitosan recovery strategies involving high-energy bombardment. Microwave radiation is a common alternative energy source that can transmit power directly and fast into the substrates, enhancing reaction efficiency [65]. Furthermore, microwave treatment can minimize the number of chemical compounds employed in the chitosan extraction method; nevertheless, the DD of chitosan obtained is not convincing. Rashid et al. described a –irradiation methodology for making chitosan from prawn shells that substantially increased chitin's DD while using a low alkali quantity [56].

4. Extraction

4.1. Deproteinization

Desiccated crustacean shells will be initially washed with an alkaline solution (e.g., NaOH, KOH, etc.) to eliminate the proteins. The alkali-insoluble portion is then separated by centrifugation, accompanied by repeated washings with distilled water till the pH reaches neutrality [53].

4.2. Desulfurization

Next, the mineral contaminants are removed from deproteinized shells using a dilute mineral acid (e.g., HCl). The acid-insoluble portion is then separated using centrifugation. The acid is rinsed out of the isolated fraction using distilled water. The chitin, which is somewhat pink in color, evaporates to dryness overnight [53].

4.3. Decolorization

The chitin is decolorized by reacting with an oxidizing agent such as potassium permanganate, hydrogen peroxide, or other oxidizing agents, then washed with an oxalic acid solution. Purified chitin is the name given to the end product [53].

4.4. Deacetylation

The decolorized chitin would then be treated with highly alkaline solutions over many hours to deacetylate it and transform it into chitosan. Centrifugation separates the alkaline fraction of the combination, and excessive alkali is discharged with a rinse of distilled water till the pH becomes neutral. The chitosan portion recovered is then dried

and kept at ambient temperature. Raw chitosan is diluted with aqueous 2 percent (*w/v*) acetic acid to get the optimum product. The insoluble substance is then filtered, yielding a precise supernatant mixture neutralized with NaOH solution, yielding a pure chitosan specimen as a colorless precipitate. The chitosan appears in flakes that range in color from white to yellow and can be made into beads or powder form. To create medicinal and pharmaceutical-grade chitosan, more purification may be necessary [53].

5. Modifications of Chitosan

In recent years, chitosan has been increasingly utilized in the pharmaceutical and biomedical fields because of its many advantages, such as low immunoreactions, good biocompatibility, easy biological degradability, excellent mucoadhesion, and its natural abundance [66]. The versatile biological and physicochemical characteristics of chitosan are possible because of the availability of different functional groups. These groups can be functionalized by a variety of processes, such as the Schiff's base chemical reaction of aldehydes or ketones with the -NH$_2$ functional group, carboxymethylation, acetylation, quaternization, chelation with metals, alkylation, and sulfonation, etc. [2,67].

In its native form, chitosan has three terminal functional groups at distinct places: the C6-OH group, C3-OH group, and the C2-NH2 group, of which the C2-NH2 and the C6-OH groups could be easily modified, but the modification at the C3-OH site is not favorable because of the higher steric hindrance [68]. Naturally, the amino groups are the most common modifications made because of the feasible reactivity of the C2-NH2 group, making the grafting reactions much simpler. These amino groups are slightly more reactive with nucleophiles; nonetheless, both the hydroxyl and amino groups can readily react in electrophilic reactions with reagents such as acyl chlorides, acids, and alkanes, which can lead to the functionalization of the OH and NH2 groups in a non-selective manner [68]. Several reactive functional groups allow chitosan to interact with proteins and gain a cationic character, enhancing the adherence and differentiation of cells. Apart from this, the poor aqueous solubility of chitosan is an issue, which limits chitosan's biomedical utility, especially in physiological conditions, wherein it is poorly soluble and thus becomes a poor absorption promoter [69]. In addition, chitosan's efficiency of transfection is relatively low, and many beneficial functionalities are absent in chitosan, severely limiting its applications. Hence, it becomes imperative to modify the chemical characteristics of chitosan or to add some desirable functionalities, which will increase the water solubility for various therapeutic applications and offer a potential resource for endorsing novel biochemical actions while enhancing its material properties [70]. Astonishingly, it has been seen that modifying the structural features alone did not cause any significant change in chitosan's basic properties, but it does give them new properties. Chitosan has a unique structure that allows it to undergo various reactions, such as halogenation, oxidation, reduction, cross-linking, complexation, phosphorylation, and acylation, which impart new properties to these derivatives [68]. Thus, chitosan, along with its derivatives, has been famous for its tunable biological and chemical characteristics. Compared to native chitosan, their functionalized analogs have quicker gel-formation properties, greater aqueous solubility, and the capability of forming self-assembling nanostructures. Additionally, the design of hydrophobic equivalents with amphiphilic properties and chemical groups with a wide range of medicinal and active compounds; improved DNA complexing characteristics; and improved bioactivity [71].

Quaternized chitosan-modified black phosphorus nanosheets (BP-QCS) were prepared by Zhang et al. by electrostatic adsorption, wherein BP-QCS had more chemical stability and dispersiveness than plain BP in an aqueous medium. BP-QCS also had good biocompatibility, and photothermal/pharmacologic combination antibacterial action under NIR radiation (98% *S. aureus* inactivation in vivo) [72].

6. Antimicrobial Properties of Chitosan

Researchers have been quite interested in the antibacterial properties of chitosan as well as its analogs. Chitosan was shown to have antimicrobial inhibitory activity against bacteria, filamentous fungus, and yeast strains. Chitosan has also been identified as an antibacterial agent, although its ability to work in this manner is still unknown, as various distinct processes have been ascribed to its character. According to one theory, chitosan stimulates the migration of Ca++ from anionic locations of the membranes when subjected to the bacterial cell walls, leading to cell damage. It additionally has antiplaque efficacy against *Porphyromonomas gingivalis, Prevotella intermedia*, and *Actinobacillus actinomycetemcomitans*, among other oral infections [73–75].

Chitosan has a broad spectrum of action and high mortality towards gram-positive and gram-negative microorganisms, while being relatively nontoxic to mammals. Chitosan's bactericidal properties are said to be based on its molecular size. No et al. tested the antimicrobial property of six chitosan oligomers with wildly differing molecular masses against gram-positive and gram-negative bacteria to verify this theory. They discovered that chitosan significantly slowed the development of most bacteria examined, albeit the inhibitory effects varied depending on molecular size and strain. For gram-positive bacteria, chitosan had a more significant bactericidal impact than gram-negative bacteria. The explanation for this disparity is unknown; however, Y. J. Jeon et al. discovered that oligosaccharides and chitosan had stronger inhibitory activity against gram-positive microorganisms than gram-negative ones. As a result, it is understandable that chitosan has a strong inhibitory effect on gram-positive lactobacilli [28,76].

7. Applications in Drug Delivery

In recent years, nanocarrier-based drug delivery systems have become increasingly popular for the administration of active compounds to the desired site of action [77–84]. Numerous pieces of research have been conducted to determine chitosan's effectiveness as an orally administered vehicle [75,85]. The use of such medication carriers reduces the risks of systemic delivery [86]. Chitosan-based composite materials can be used to create reliable local drug carriers with the necessary mechanical behavior, retention time, and extended-release pattern [87]. Chitosan microspheres were designed to actively deliver therapeutics in disease areas [88,89]. Chitosan is non-toxic when taken orally and approved as a food additive by the Food and Drug Administration (FDA). It has also been investigated as a drug carrier for various macromolecules, including DNA, siRNA, growth regulators, and a variety of therapeutics [90,91].

Over the years, chitosan has been utilized in nanotechnology-based formulations, such as nanoparticles for drug, protein, and gene delivery through various routes of administration such as oral, topical, and parenteral routes [11]. To enhance the stability of chitosan nanoparticles (NPs), Saeed et al. used polyphosphoric acid or hexametaphosphate for concurrent ionotropic/covalent crosslinking with chitosan NPs. The resultant NPs showed considerable stability under $CaCl_2$, 10% fetal bovine serum, and harsh pH conditions [92]. Similarly, Yu et al. synthesized octenyl succinic anhydride-modified chitosan nanoparticles to improve the anti-inflammatory and antioxidant properties of two model drugs: quercetin and curcumin. The as-prepared NPs exhibited pH-dependent release with faster drug release achieved at around pH 6.0 [93]. Thus, the versatile physicochemical properties and the tunable nature of chitosan renders it as a great candidate for nanotherapeutic drug delivery.

In a study by Barbosa et al. quercetin was delivered using novel polymeric nanoparticles derived from fucoidan and chitosan. Fucoidan/chitosan (F/C) nanoparticles, having three distinct weight fractions (1/1, 3/1, and 5/1), were produced by Barbosa et al. using the polyelectrolyte self-assembly approach. On increasing the mass ratio of fucoidan to chitosan inside the nanoparticles, the amount of quercetin in the fucoidan/chitosan nanoparticles ranged from 110 ± 3 to 335 ± 4 mgmL-1. With the size of the nanoparticles in the 300–400 nm region and membrane potential of more than +30 mV for the 1F/1C

145

proportion nanoparticles and about 30 mV for the 3F/1C and 5F/1C ratio nanoparticles, the physicochemical characteristics of stable nanoparticles were developed. As the pH rose from 2.5 to 7.4, the 1F/1C ratio nanoparticles grew larger and much more unstable, but the 3F/1C and 5F/1C nanoparticles remained unchanged. This showed that the latter nanoparticles remained stable throughout the digestive tract. Within simulated gastrointestinal conditions (particularly for the 3F/1C and 5F/1C combinations), the quercetin-loaded fucoidan/chitosan nanoparticles demonstrated significant antioxidant potential and controlled delivery, limiting quercetin deterioration and improving its oral absorption [94].

The fabrication of a film containing chitosan, sodium alginate (SA), and ethyl cellulose (EC) for buccal mucosa delivery was described in a study by Wang et al. (as depicted in Figure 1a). Utilizing self-made equipment, an interfacial reactive solvent-drying process was used to create a film of CS-SA unilateral releasing drug-loaded water-repellent layer EC. When matched to CS-EC and SA-EC films, the CS-SA-EC film had excellent tensile qualities. FT-IR acknowledged the formation of the amide linkage. DSC revealed that the active ingredient was distributed in an amorphous state inside the carrier system. The model compounds from the CS-SA-EC films had superior release qualities, according to the in vitro drug release study. All of the combinations of the drug release pathways are best described by the Ritger–Peppas theory. The films' permeation properties were tested using the TR146 cells culture and rabbit buccal mucosae through immunofluorescence and Western blotting. The prototype drugs' aggregate permeation levels were dramatically boosted. The film suppressed the translation of ZO-1 protein, and the ZO-1 protein expression pattern agreed with the results of the in vitro penetration tests. In rat models, the bioavailability of the drug-loaded films was assessed and compared to oral delivery. Compared to oral delivery, the relative absorption of the model medicines was 246.00 percent (Zolmitriptan) and 142.12 percent (Etodolac). The findings of this investigation show that the CS-SA-EC carrier has the capacity to transport drugs to the mucosal layer [95].

Chemotherapy is presently employed for most cancer therapies, but one of the substantial drawbacks of this approach is that it harms the body's normal tissues [96]. As a result, a few of the globe's most significant problems are developing new mechanisms for the smart and targeted delivery of these medications in tumor tissue. As a result, substantial money is now being spent on developing innovative drug delivery systems (DDS) featuring targeted delivery (as shown in Figure 1b). In a study by Kheiri et al., glutaraldehyde was employed to produce chitosan-polyacrylic acid-encapsulated Fe_3O_4 magnetic nanogelic core-shell (Fe_3O_4@CS-PAA) for carrying anticancer 5-fluorouracil (5-FU) medication. Then, the drug carrier assays were performed in an in vitro setting that mimicked a physiologic microenvironment and tumor tissue parameters. The Fe_3O_4@CS-PAA improved the rates of 5-FU release from nanogelic core-shell under tumor tissue settings (pH 4.5) compared to physiological fluids (pH 7.4). A variety of models were also employed to examine the drug release process. The process of 5-FU release from Fe_3O_4@CS-PAA was governed by Fickian diffusion [97].

Classic chemotherapy medicines for lung carcinoma have several drawbacks, including harsh side-effects, unpredictable drug release, low absorption, and resistant strains [98–102]. To overcome the constraints of unloaded drugs and enhance treatment outcomes, Zhu et al. created novel T7 peptide-based nanoparticles (T7-CMCS-BAPE, CBT) premised on carboxymethyl chitosan (CMCS), which were also likely to bind to the transferrin receptor (TfR) presented on lung carcinoma cells and accurately control the drug release depending on the pH and reactive oxygen species (ROS) levels. The drug-load content of docetaxel (DTX) and curcumin (CUR) was nearly 7.82 percent and 6.48 percent, respectively. Substantial biosafety was achieved even at concentrations as high as 500 g/mL. Notably, the T7-CMCS-BAPE-DTX/CUR (CBT-DC) combinations outperformed DTX solo therapy and other nanostructures loaded with DTX and CUR alone in vitro and in vivo studies. Additionally, they discovered that CBT-DC could improve the immunosuppressive surroundings, promoting tumor inhibitory activity (as illustrated in Figure 1c). These findings help set the groundwork for multimodal anticancer therapy [103].

p-mercaptobenzoic acid-embedded N, N, N-trimethyl chitosan nanoparticles (MT NPs) were effectively synthesized by Zhang et al. to carry anticancer medicines, genes, and immunological agents in a homogeneous nanoparticulate platform. Paclitaxel (PTX) was entrapped in the hydrophobic cavity of the MT NPs, while the hydrophilic exterior of the MT NPs had been loaded with survivin shRNA-expressing plasmids (iSur-pDNA) and recombinant human interleukin-2 (rhIL-2). The large quantity of glutathione induced a fast release of PTX due to the redox sensitivity of MT NPs. The MT/PTX/pDNA/rhIL-2 NPs were provided with higher anticancer therapeutic efficacy and enhanced tumor-induced immune responses resulting from the combined effects of PTX (1.5 mg/kg), iSur-pDNA (1.875 mg/kg), and rhIL-2 (6×10^5 IU/kg) at low dosages. The co-delivery of PTX, iSur-pDNA, and rhIL-2 by amphipathic chitosan-derived NPs with redox sensitivity could be a potential mechanism in the therapy of malignancies [104].
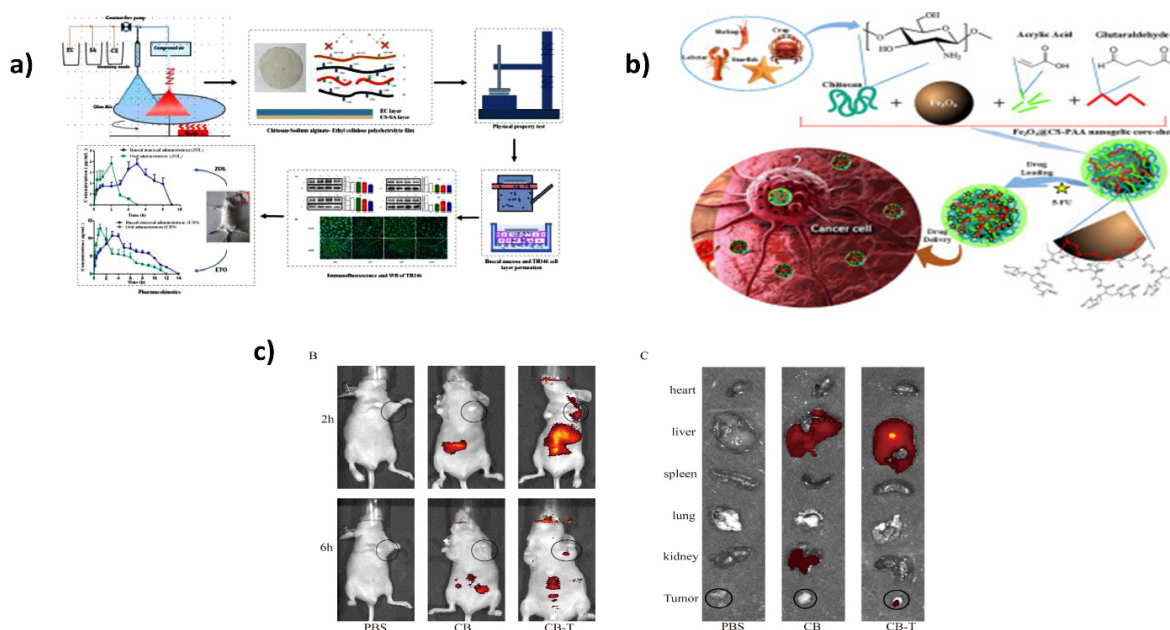
Figure 1. (**a**) Interfacial reaction solvent-drying method for EC-SA-CS polyelectrolyte film via self-made equipment [95]; (**b**) Preparation and characterization of chitosan-based magnetic nanohydrogels for 5-fluorouracil drug administration and a kinetic assessment. Reproduced with permission from [97], copyright Elsevier 2022; (**c**) (B) Tumor-infected animals were given Cy5.5-labeled nanoparticles intravenously. The biodistribution of various compositions in vivo at 2 and 6 h, (C) ex vivo imaging of main organs and tumors. Reproduced with permission from [103], copyright Elsevier 2021.

In addition to the above, several other studies that were carried out to facilitate drug delivery by chitosan-based carriers include aluminum-modified mesoporous silica nanoparticles (H/Al-MSN)/curcumin/chitosan/mesalamine [105]; chitosan/polyvinyl pyrrolidone (PVP)/5-Fluorouracil [106]; quaternized chitosan/thiolated carboxymethyl chitosan [107]; chitosan/aptamer/mesoporous silica nanoparticles/doxorubicin [108]; norborene functionalized chitosan (CsNb)/polyacrylic acid (PAA)/5-Amino salicylic acid [109]; chitosan/pectin/5-Fluorouracil [110]; chitosan/dopamine/inulin aldehyde/indomethacin [111]; chitosan/magnetic alginate/amoxicillin [112]; chitosan/PVP/α-Fe2O3/doxorubicin [113]; and chitosan/mesoporous silica/methotrexate [114].

8. Applications in Gene Delivery

In the recent decade, the applications of RNA-interfering agents in gene therapy have been developed to exponential levels. Nevertheless, the tumor-targeting potential of these small interfering RNAs (siRNAs) is still a bottleneck [115–117]. Cancer progression involves various stages; caspases-linked anti-apoptotic factors inhibit apoptotic protein ex-

pression. One such gene, the survivin gene, is implicated in several physiological processes, such as regulating the cell cycle, cellular protection, and apoptosis suppression; these processes ensure that the cancerous cells survive [118,119]. Chitosan and polyethylene glycol (PEG) are known to aid the synthesis of cationic oligonucleotide nanoparticles [120,121]. Polyethyleneimine (PEI), an efficient gene carrier owing to its proton-sponge effect, functions as a buffer surrounding the endosome and delivers substances into the cytoplasmic space [122]. PEG helps reduce PEI toxicity, facilitates the formation of stable colloids, and prevents the deposition of nanoparticles [123]. The nanoparticles are coated by the chitosan, thus stabilizing them and preventing agglomeration. Hence, Arami et al. fabricated Fe3O4-PEG-LAC-chitosan-PEI nanoparticulate carriers, which were sufficiently cationic to react with siRNA. In vitro, they transferred the survivin siRNA to human breast cancer cells (MCF-7) and human chronic myelogenous leukemia cells (K562) using the nanoparticulate carrier. They found that the Fe3O4-PEG-LAC-chitosan-PEI nanoparticles combined sufficiently with siRNA, their sub-nanomolar size made them suitable gene carriers, and the survivin siRNA therapy was biocompatible and non-toxic to healthy cells [124].

Chitosan has shown potential for protecting siRNA from plasma denaturation and delivery into cancer cells by promoting the deposition of antineoplastic agents and biomolecules in the solid tumor tissues via the enhanced permeability retention (EPR) pathway [125]. Even though chitosan can be endocytosed by a ligand-receptor-mediated mechanism [126], the mono-ligand uptake of NPs is limited due to the saturation of membrane receptors [127]. RNA interference as a gene delivery method is limited by its low ability for targeted therapy and cellular absorption of small interfering RNA (siRNA). Hence, Zheng et al. fabricated chitosan-based dual-ligand nanoparticles (NPs) (GCGA) loaded with siPAK1 (GCGA-siPAK1), as shown in Figure 2a, whereby the targeting activity was influenced by the ligand molecules of glycyrrhetinic acid (GA) and galactose of lactobionic acid (LA). The NP targetability and siPAK1 cellular uptake were enhanced in the hepatocellular carcinoma by the GCGA-siRNA system [128].
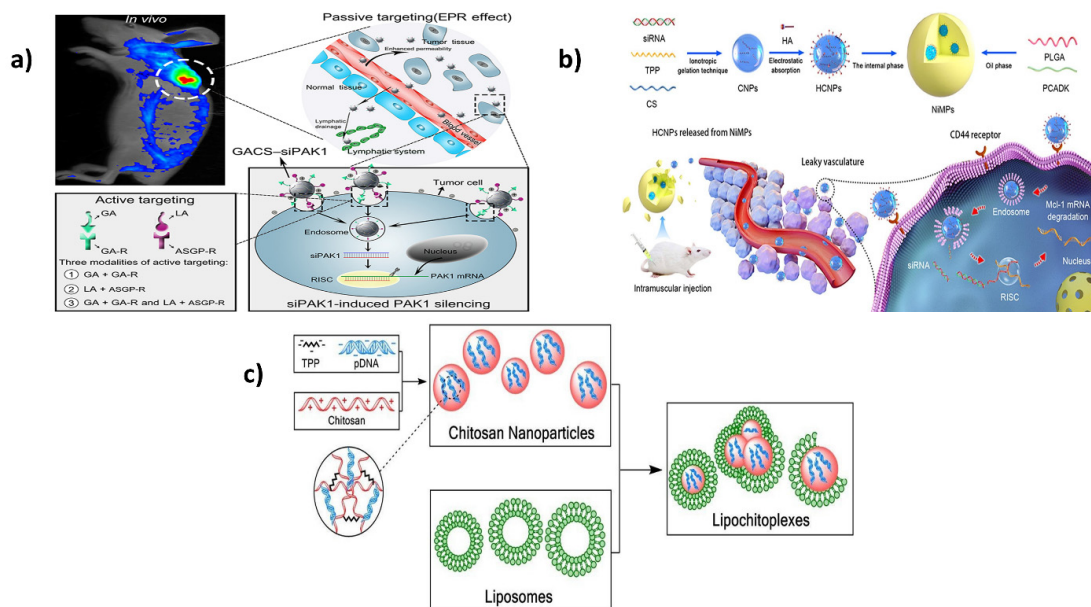
Figure 2. (**a**) Delivery of siRNA via Dual-Targeting Nanoparticle-based Gene Therapy for Hepatocellular Carcinoma [128]; (**b**) A systematic approach for rheumatoid arthritis treatment using PLGA/PCADK hybrid microspheres encapsulating hyaluronic acid–chitosan siRNA nanoparticles. Reproduced with permission from [129], copyright Elsevier 2021; (**c**) Improved gene delivery with lipid-enveloped chitosan-DNA nanoparticles. Reproduced with permission from [130], copyright Elsevier 2018.

In another study, Zhao et al. utilized the cationic chitosan's ability as a siRNA vector modified using a targeting molecule such as hyaluronic acid (HA), which has an affinity toward CD44 receptors expressed on activated macrophages. They developed a sustained-release composite MP system using poly (cyclohexane-1, 4-diylacetone dimethylene ketal) (PCADK)-loaded HCNPs and PLGA-based siRNA therapy for rheumatoid arthritis (as depicted in Figure 2b). The HCNPs were prepared by the ionotropic gelation method as a barrier for nuclease-mediated siRNA degradation and were then loaded as the aqueous phase into 20% PCADK and PLGA MPs, forming an NP-in-MP composite system (NiMPs) without disturbing the pH microenvironment inside the MPs. However, the introduction of HCNPs made the repulsion into attraction because of the surface positive charge on chitosan and changed the siRNA distribution from the periphery into a uniform distribution. In vitro release of siRNA was sustained release of 70% in 15 days. In vivo experiments on rat models revealed that siRNA had a relatively similar concentration in blood for up to 8 days and the pharmacodynamic effects were the same as HCNPs [129].

Chitosan offers the benefit of a biodegradable and highly biocompatible biopolymer when used as a polycationic non-viral vector for gene transfer. Nevertheless, owing to its poor ability to successfully transfect under biological settings, it is of little value as a genetic delivery device without arduous chemical alterations to its composition. To solve this issue, Baghdan et al. created lipochitoplexes, which are liposome-encapsulated chitosan nanoparticles (LCPs), as shown in Figure 2c. The ionotropic gelation process was used to develop chitosan nanoparticles (CsNPs). A polyanionic tripolyphosphate was used for cross-linking the low molecular weight chitosan with a high DD, resulting in the effective trapping of plasmid DNA (pDNA) within the nanoparticles. The chitosan nanoparticles were incubated with anionic liposomes (DPPC/Cholesterol) to make LCPs. In physiological environments, the LCPs provided excellent pDNA protection, lower cytotoxicity, and a twofold improvement in transfection efficiency. In the chorioallantoic membrane model (CAM), the efficacy of the delivery vector was also demonstrated in vivo. The LCPs could transfect the CAM without causing any damage to the nearby vascular capillaries. This unique biocompatible hybrid framework, free of chemical alterations, organic solvents, or harsh manufacturing processes, was deemed an ideal gene delivery mechanism for in vivo studies, revealing new information about non-viral therapeutics [130].

Other such studies related to gene delivery using chitosan are PEGylated chitosan/CRISPR-Cas9 dry powder [131]; carbonized chitosan/zeolite imidazolate nanoparticles/luciferase-expressing plasmid (Pgl3)/splice correction oligonucleotides (SCO) [132]; methyl methacrylate-based chitosan/DNA [133]; cell-penetrating peptide-loaded chitosan-based iron oxide nanoparticles/plasmid pGL3/small interfering RNA/splice correction oligonucleotides [134]; thiolated trimethyl aminobenzyl chitosan/methylated 4-N,N-dimethyl aminobenzyl N,O carboxymethyl chitosan/thiolated trimethyl chitosan/plasmid DNA [135]; alkylamine-modified chitosan/p53 [136]; chitosan nanoparticles/polyethylene glycol/poly lactic acid/nerve growth factor/acteoside/plasmid DNA [137]; chitosan/5-Amino-tetrazole(3-Chloropropyl) trimethoxysilane/Fe3O4 [138]; chitosan/starch polyplexes/plasmid DNA [139]; and chitosan/gelatin/oxidized sucrose/timolol maleate [140].

9. Applications in Protein Delivery

Protein therapies have gained much traction in the medical business to fight diseases such as cancer, digestive problems, and autoimmune conditions. Protein distribution in vitro and in vivo, on the other hand, is hampered by protein degradation and a shorter lifetime. As a carrier system for protein, Rebekah et al. developed magnetic nanoparticles coated with graphene oxide chitosan hybrid (Fe-GO-CS), as shown in Figure 3A. To investigate the integrity and function of the produced nanocarrier, bovine serum albumin (BSA) was used as a protein. After 30 min and 3 h of exposure to Fe-GO-BSA and Fe-GO-CS-BSA solutions in trypsin, the SDS-PAGE examination revealed no significant changes. When relative to the Fe-GO composites, the Fe-GO-CS has a better drug load and release pattern, and the carrier system preserves the peptide from proteolytic action. As a result,

the Fe-GO-CS composite provides a superior nanocarrier that can be used in therapeutic settings [141].

Salivary proteins, such as histatins (HTNs), have been shown to have important physiological activities in dental homeostasis and avoiding periodontal disease. HTNs, on the other hand, are vulnerable to the mouth environment's considerable proteolytic activity. To preserve peptides from hydrolytic enzymes at a normal salivary pH, pH-sensitive chitosan nanoparticles (CNs) have been proposed as possible carriers in a study by Zhu et al. The optimized formulations had a batch-to-batch consistency of 144 ± 6 nm, a polydispersity value of 0.15 ± 0.04, and a zeta potential of 18 ± 4 mV at a maximum pH of 6.3. Cationic polyacrylamide gel electrophoresis was used to examine HTN3 entrapment and release characteristics. HTN3 was successfully entrapped by the CNs, which were swollen exclusively at lower pH to aid HTN3 release. In diluted whole saliva, the stability of HTN3 against proteolysis was examined. Compared to unbound HTN3, HTN3 enclosed in CNs showed a longer lifetime. Biofilm density and microbial vitality were likewise lowered by CNs both in the presence and absence of HTN3. The study's findings showed that CNs are suitable as prospective protein carriers for oral purposes, particularly in the case of the difficulties that emerge under acidic circumstances [142].

Because of their versatility, supramolecular hydrogels are considered attractive drug vehicles for tissue regeneration [143]. Chitosan hydrogels lacking chemical cross-linkers are low in cytotoxicity and offer a high distribution potential, but they have poor mechanical qualities for injectable hydrogels. Jang et al. used click chemistry to create novel chitosan analogs for constructing supramolecular hydrogels with greater structural rigidity under mild circumstances (as depicted in Figure 3B). A sulfur–fluoride exchange process was used to synthesize the chitosan derivatives effectively, and the resulting chitosan-mPEG/Pluronic-F127 (CS-mPEG/F127) bonded with -cyclodextrin (-CD) to produce a supramolecular hydrogel through a host–guest interaction. The proportion of chitosan-mPEG and F127 could influence gelation kinetics, hydrogel characteristics, and bovine serum albumin (BSA) release. Thus, supramolecular hydrogels represent potential long-term tissue regeneration protein carriers [144].

The effective therapy of irritable bowel syndrome can benefit from the targeted administration of bioactive molecules such as proteins to the colonic region. Hence, Cao et al. used a single-step electro-spraying approach to make alginate/chitosan microcapsules (Alg/Chi/IL-1Ra MC) encapsulating IL-1Ra, as shown in Figure 3C. The pH-stimulation of the microcapsule and the in vitro release pattern was evaluated as critical efficacy considerations. The therapeutic efficacy of the Alg/Chi/IL-1Ra microcapsules was assessed using the dextran sodium sulfate (DSS)-induced colitis murine model, and the findings revealed that the Alg/Chi microcapsules shielded IL-1Ra from the hostile conditions of the upper gastrointestinal region. This was due to the microcapsule's pH-sensitive reaction, which enabled the targeted delivery of IL-1Ra in the colon. The Alg/Chi/IL-1Ra microcapsules reduced DSS-induced colitis in mice as measured by DAI, colonic length, colorectal tissue shape, histological injury ratings, and comparative protein concentrations (MPO, TNF-, and IL-1). This study indicated a viable method for oral protein administration, in situ colon release, and the potential use of IL-1Ra in treating autoimmunity and inflammatory illnesses [145].

Injectable hydrogels have long been a popular biomaterials subject. Unfortunately, due to tissue secretions, they are easily distributed during gelatinization in vivo, resulting in controlled-release drug delivery inability. To address this issue, Huang et al. described a new natural polymer-based injectable hydrogel made from aldehyde-modified xanthan (Xan-CHO) and carboxymethyl-modified chitosan (NOCC) that self-crosslinks, as illustrated in Figure 3D). The molar ratio of Xan-CHO and NOCC was adjusted to enhance the physical characteristics. Studies indicated that this composite material had self-healing, anti-enzymatic hydrolysis, biological compatibility, and biodegradability features. The release curve showed that BSA-FITC released in liquids was stable after 10 h. There was an association between this biopolymer and the hosts after integration with a vascular

endothelial growth factor, which expedited the rebuilding of the abdomen wall in rats. As a result, from a carrier perspective, this injectable hydrogel could minimize drug eruption in a range of circumstances and serve as a tissue-building scaffold [146].
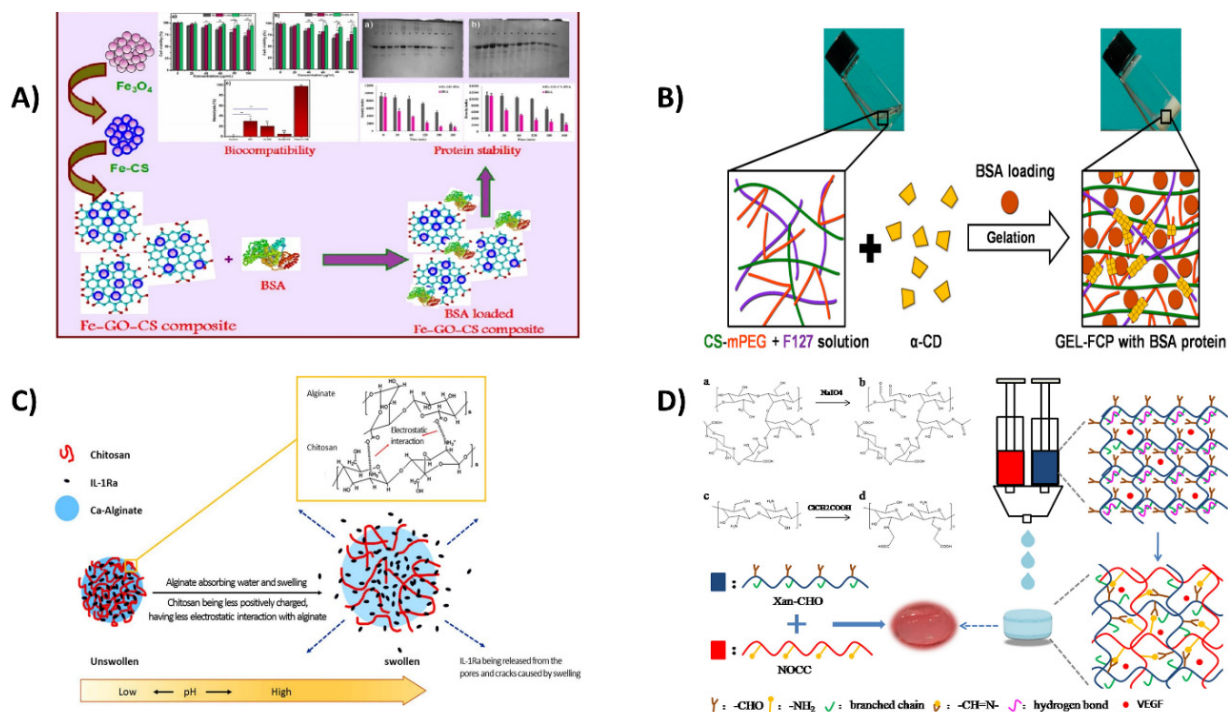
Figure 3. (**A**) A graphene oxide–chitosan combination with magnetic nanoparticles as a protein-delivering vehicle. Reproduced with permission from [141], copyright Elsevier 2021. (**B**) Fabrication of Chitosan–PEG conjugates and its Supramolecular Hydrogels for Protein Delivery Using Sulfur (VI) Fluoride Exchange (SuFEx) [144] (**C**) In situ application of the protein interleukin-1 receptor antagonist (IL-1Ra) for the therapy of dextran sulfate sodium (DSS)-induced colitis in a murine model using alginate/chitosan microcapsules. Reproduced with permission from [145], copyright Elsevier 2019. (**D**) For localized drug delivery, a unique in situ forming hydrogel consisting of xanthan and chitosan re-gelifying in liquids. Reproduced with permission from [146], copyright Elsevier 2018.

Other studies conducted for chitosan-based protein delivery were fluorinated chitosan-chlorine e6/catalase [147]; chitosan/tripolyphosphate nanoparticles/ selenomethionine [148]; chitosan/ multiwalled carbon nanotubes/arginine-glycine-aspartic acid (RGD)/ urokinase [149]; mannose-anchored quaternized chitosan/thiolated carboxymethyl chitosan [107]; glycol chitosan/telechelic difunctional poly(ethylene glycol)/doxorubicin/gemcitabine [150]; chitosan/mesoporous silica/oxidized sodium carboxymethyl cellulose/sodium hyaluronate/ cytarabine/methotrexate [151]; chitosan/poly(N-isopropylacrylamide) (PNIPAAm)/ methotrexate [152]; chitosan/graphene oxide/folic acid [153]; chitosan/Fe_3O_4 nanoparticles/oxaliplatin/irinotecan [154]; and chitosan/acrylic acid [155].

10. Vaccine Delivery

Traditionally, vaccines were considered for large-dose administration, with limited targetability and noticeable immunogenicity. Thus, they necessitated using immunity-modifying adjuvants to improve their specific immunity [156,157]. The vaccine technology has since come a long way, and now nano-vaccines have demonstrated some added advantages such as higher antigenic retention ability, convenient administration, better-targeted delivery, and enhanced bioavailability. Since chitosan has desirable properties, including its high biodegradability, non-toxicity, immunostimulatory activity, targeting potential, and provision for controlled vaccine release, it shows good potential for carrier material in nano-vaccines and their adjuvants. Chitosan-based materials also function as

adjuvating agents in vaccines and impart both immunostimulatory and immunotherapy functions. In addition, chitosan-based nanogels demonstrate improved penetrability and controlled drug release features; additionally, they show antigen-storing ability, antigen presentation, and immunoregulation.

The nanoparticles containing chitosan having a net positive surface charge can improve the adhesiveness of antigenic substances to the nasal mucosa and thus augment its absorption, which is essential for intranasal vaccine administration. To this end, Gao et al. developed chitosan NPs via a gelation method and functionalized the chitosan NPs using mannose by a hybridization technique. Using bovine serum albumin (BSA) as the model antigen, they prepared an intranasal vaccine using an optimization-based design of experiments (DOE). It was found that the mannose-based chitosan NPs (Man-BSA-CS-NPs) demonstrated good modification ability and an average particle size distribution and surface charge of 156 nm and +33.5 mV, respectively. The release of BSA from the systems displayed no irreversible deterioration or agglomeration. Additionally, the fluorescence analysis revealed an excellent binding constant between BSA and CS, indicating that BSA had good stability. In vitro studies also show that the Man-BSA-CS-NPs were non-toxic and biocompatible. Moreover, the Man-modified BSA-FITC-CS-NPs promoted the endocytic uptake and internalization of BSA-FITC when tested in DC2.4 cells. More importantly, the Man-BSA-CS-NPs demonstrated significant immunogenic enhancement of the BSA-specific IgG titer and the highest BSA-specific IgA response in the nasal lavage samples of in vivo mice models. Thus, this study shows how modifying chitosan with sugars and proteins and loading into NPs could be useful in vaccine delivery [158].

Wei et al. evaluated the vaccine delivery potential of a hydrophilic ph-responsive phosphorylated CS (PCS) incorporating ovalbumin (OVA) antigen and tested it in vivo on mice models. PCS solution in the mice formed a dense gel-like OVA network, resulting in enhanced immunity. This was hypothesized to be because of the sustained and controlled release of OVA, giving lengthier immune protection. Moreover, hydrogels' aqueous solubility enabled a convenient and hassle-free vaccine administration. Hence, because of the biocompatibility and non-toxicity of pH-responsive CS, hydrogels could be a potential platform for vaccine delivery [157]. However, their instability in solution and in vivo systems limits their overall applicability. Researchers suggest that modifying chitosan's hydrophilic surface moieties, deacetylation, or reduction in its MW may improve its water solubility. Otherwise, chemical alterations to its structure could be attempted to prevent its in vivo degradation [157].

Zho et al. developed a thermoresponsive hydrogel comprising N-(2-hydroxypropyl)-3-trimethylammonium chitosan chloride (HTCC) and α-β-glycerophosphate (α-β-GP) as the vaccine carrier system for the *C. psittaci* antigen against avian influenza. The intranasal mucosal route of administration of vaccine gave the highest immune response in chickens [159].

Since the positively charged chitosan can easily interact with cellular membranes, contributing to its high biodegradability and formability, Zhang et al. prepared a chitosan-based PLGA nanoparticle vaccine encapsulating the recombinant protein OmpAVac (Vo) (VoNPs) against the *Escherichia coli* K1 caused meningitis in mice. The freeze-dried VoNPs were immunomodulatory in mice even after 180 days of storage [160].

Table 1 focuses on recent investigations on chitosan formulations for delivering active pharmaceutical compounds.

Table 1. Recent studies on chitosan focusing on delivering therapeutic compounds.

Device Type	Model Drug/Drug	Polymer Formulation	Preparation Method	Administration Route	Delivered Site	Effect/Results	References
Solid–lipid nanoparticles	Leflunomide	Chitosan/Folic acid	Layer-by-layer coating	oral	joint	FA-CS-SLNs exhibited sustained release for 168 h and lowered liver toxicity and enhanced joint healing compared to leflunomide suspensions.	[161]
Implants	Ibuprofen	Chitosan/polycaprolactone	Hotmelt extrusion/Fused deposition modeling	-	-	Sustained release for 120 h by diffusion-erosion, 75.3% cell viability.	[162]
Hydrogel-based microneedles	Salvia miltiorrhiza	Carboxymethyl chitosan/oxidized pullulan		Skin	Mucosa	Simple penetration of HFM-1 into infant porcine skin was demonstrated because of its remarkable mechanical characteristics. Drug release was rapid from HFM-1, hence suitable for transdermal delivery.	[163]
Hydrogel	Berberine chloride hydrate	Chitosan/puerarin	Interpenetrating network	Injectable		Increased rheological properties due to dense structure of CS/PUE$_{18}$ hydrogels. Dual anti-inflammatory and antimicrobial activities with pH-dependent drug release	[164]
Thermogel	Dexamethasone	Hexanoyl glycol chitosan		Injectable	Inner ear	Versatile release kinetics with no initial burst release. Excellent residual stability without any ear-related side effects and could deliver high concentrations of the drug to the inner ear.	[165]
Hydrogel	Acyclovir	Chitosan/β-cyclodextrin/methacrylic acid (MAA) and N′N′-methylenebis-acrylamide (MBA)	Free radical polymerization	Oral		Zero-order kinetics of drug release with pH-dependent swelling behavior. After acute oral toxicity studies, no significant behavioral, histopathological, and clinical changes were observed in Wistar rats. Increased bioavailability as compared to acyclovir suspension at a dose of 20 mg/kg in rabbit plasma.	[166]
Hollow capsule	Gemcitabine/curcumin	Chitosan/poly (ethylene glycol dimethacrylate-co-methacrylic acid)	Layer-by-layer method			pH-dependent drug delivery at pHs 5.5 and 7.4. Encapsulation efficiency was above 84%, and release efficiency was 82%. Good cytotoxicity towards HCT-116 colorectal cancer cell lines.	[167]
Nanohybrid	5-fluorouracil	Chitosan/collagen/gold nanoparticles/biotin-quat188-chitosan (Bi-QCS-AuNPs@collagen)	Layer-by-layer assembly	-	-	Bi-QCS-AuNPs@collagen overcame the low drug load capacity of AuNPs from 64.675 to 87.46% as well as excellent anti-inflammatory activity in macrophage cell lines (RAW264.7). Moreover, in comparison to free 5-FU, the nanohybrid improved drug activity by 3.3-fold in HeLa cell lines and 6.2-fold in A549 cell lines, respectively.	[168]
Nanoparticles	Voriconazole	Chitosan	Spray-drying	Topical	Skin	The drug loading in NPs ranged from 75% to 90%. Sustained-release profile in rat skin model and exhibited antifungal activity against *C. albicans.*	[169]
Films	Ciprofloxacin	Chitosan/chitosan-depolymerization products	Casting	-	-	Low acetylated and molecular weight CDP-based films exhibited reduced swelling and ciprofloxacin released in a controlled manner for up to 54% in 24 h in a pH-dependent manner.	[170]

11. Tissue Engineering

A recently blooming field of research for regenerating injured/damaged tissues utilized versatile biomaterials encouraging cell adhesion and proliferation in tissue engineering (TE) [171]. Tissue engineering is a technique for developing biomaterials that can be used to repair, maintain, or regain tissue functionalities or entire organs. Tissue engineering has been a benefit to science. It has the capability of taking the place of traditional treatments, such as xenotransplantation and implanted devices. It is a technique for recovering or regenerating damaged tissues utilizing a combination of scaffolds, cells, and growth regulators. The scaffold components for tissue repair have been developed from various natural polymeric materials. Because of the desirable features, such as good biodegradability, biological activity, and biocompatibility, chitosan has been the most widely recognized biopolymer for constructing tissue frameworks among numerous biopolymers [172]. Table 2 describes the recent studies on chitosan formulations utilized for tissue engineering.

11.1. Bone

Bone tissue engineering (BTE) is a rapidly growing subject of research because it circumvents the limitations in therapeutic bone therapies, such as allogeneic or autologous bone transplantation, and irreversible prostheses' implants [173]. Using scaffolds, biomolecules, and implantable devices, BTE plays a critical role in the healing and regeneration of bone. When the injury is severe and has developed, bone tissue loses its potential to self-heal [174–176]. Nevertheless, this technique causes issues such as cell-specific bioactivity, the formation of massive structures, and a less inter-linked system [177]. As a result, nanoparticles and nanostructured materials are used to resolve this issue [178]. Chitosan has been explored for bone tissue regeneration because of its easy fabrication, chemical adjustments, compatibility with tissues, as well as other biomaterials, and its non-toxic nature.

Chitosan is reported to promote cell growth, suppress inflammatory reactions, and cause wound healing. In the early 2000s, Park et al. fabricated CS scaffolds loaded with platelet-derived growth factor (PDGF) for tissue regeneration in rat calvarial bones. Bernardi et al. showed that CS-derived scaffolds act as an independent stimulant for osteogenic maturation and do not merely act as a cell carrier. Nonetheless, native CS hydrogel has insufficient mechanical strength and a tendency for in vivo degradation. Thus, Zhang et al. incorporated short-chain chitosan (CS) into a semi-interpenetrating composite hydrogel (CG) in a covalently bound tetra-armed poly (ethylene glycol) network, as shown in Figure 4a. Acetylsalicylic acid (ASA) was encapsulated in the network by chain intermeshing and electrostatic attraction and obtained sustained release for more than 14 days and promoted osteogenic differentiation and growth of periodontal ligament stem cells (PDLSC) in a mouse calvarial osteogenic-defect model. This could be due to the expression of monocyte chemoattractant protein-1 on host mesenchymal stem cells and PDLSCs, which led to the stimulation of M2 macrophages and in situ polarization, demonstrating its potential for BTE [179].

Biopolymer-based nanomaterials have lately been used in therapeutic applications such as suture components, therapeutic delivery systems, tissue scaffolds, and inner bone stabilization implant devices. The biofilms formed by polymer-derived implants, on the other hand, are very sensitive to microbiological adherence. Chitosan biopolymer has good flexibility but poor mechanical properties; hence, when combined in composite films or nanoparticles, it leads to increased surface porosity and mechanical properties [180,181]. To this end, Prakash et al. created Chitosan/Polyvinyl alcohol/Graphene oxide/Hydroxyapatite/gold film materials for possible orthopedic applications. The graphene oxide/hydroxyapatite/gold hybrid (GO/HAP/Au) was made using a facile hydrothermal process, and the GO/HAP/Au composite integrated polymer film was made using the gel casting process. The biofilms were revealed to be compatible with murine mesenchymal cells (3.74% RBC lysis) and promoted osteoblast development, as indicated

154

by higher alkaline phosphatase enzymatic activity within the cells. As an outcome of these findings, it appeared that the biocomposite films created have osteogenic capabilities for managing bone-related disorders. High mechanical strength was seen, with tensile strength values ranging from 35.2% to 36.4% for composite films. According to the microbiological investigation, these films had high inhibitory regions against gram-positive and gram-negative microorganisms (*Pseudomonas aeruginosa, Staphylococcus aureus, Streptococcus mutans*, and *Escherichia coli*). As a result, the biocomposite biofilms developed were extremely biocompatible and could be employed for bone tissue regeneration [182].

Immune-modifying biomaterials have rapidly evolved as critical new systems for bone tissue regeneration. Eliciting macrophages to develop into the M2 subtype can lower inflammatory and immunological responses and speed the tissue healing following implants. Two biological compounds, bone morphogenetic protein-2 (BMP-2) and interleukin-4 (IL-4), were loaded and delivered in a controlled way in an inter-penetrable network hydrogel made of graphene oxide (GO)-carboxymethyl chitosan (CMC)/poly (ethylene glycol) diacrylate (PEGDA) to stimulate macrophage differentiation into M2 variety and improve bone growth in a study by Zou et al. (as depicted in Figure 4b). These two components were loaded with GO before being incorporated into a CMC/PEGDA hydrogel for long-term delivery. The hydrogel had improved mechanical rigidity, hardness, and stability. In vitro, the hydrogel containing IL-4 and BMP-2 strongly stimulated macrophage M2-type development and bone-marrow mesenchymal stem-cell bone formation. Moreover, in vivo investigations revealed that 8 weeks after insertion, the implantation of this hydrogel significantly lowered the local inflammatory reaction while increasing bone growth. Overall, the findings implied that IL-4- and BMP-2-loaded hydrogels synergistically impact on bone repair. A system such as this for the initiation and immunomodulatory reaction could be a potential method for further bone immunological management and tissue regeneration [183].

Similarly, Lu et al. used electrospun nanofibers of chitosan (CS ENFs) and modified them with fucoidan (Fu) and a CuS NPs polyelectrolyte complex involving genipin-based cross-linking, as shown in Figure 4c. This CuS–ENF composite provided antibacterial effects via photocatalytic and photothermal activities. Moreover, the composite could effectively promote the osteoblastic cells' alkaline phosphatase activity and the growth of capillary tubes within the endothelium. Thus, this novel CS ENF modification strategy could obtain scaffolds for BTE and antibacterial activity [184].

The foundation for generating nano-hydroxyapatite particles integrated in Chitosan/-carrageenan polyelectrolyte complexes (nHAp/CHI/-CGN) nanostructures with physically cross-linked constituents was presented by Zia and coworkers, as illustrated in Figure 4d. In the SBF investigation, the synthesized hybrid composites were shown to have lattice parameters and tensile characteristics similar to native bone and a rough texture, creating a thick apatite-like covering. It was also cytocompatible, biodegradable, and effective for protein adhesion. The nHAp/CHI/-CGN composites were highlighted as a promising contender for a BTE framework [185].
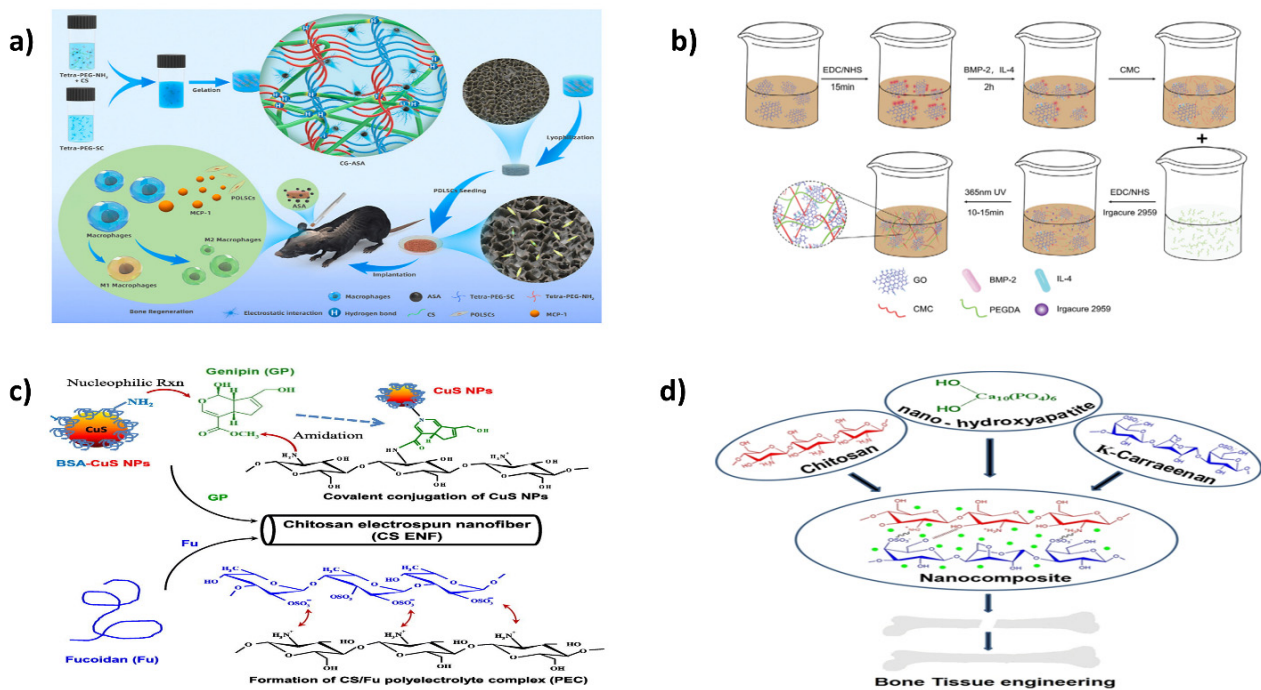
Figure 4. (**a**) Production of a biocompatible composite gel with long-lasting aspirin release for bone tissue regeneration [179]; (**b**) An interpenetrating network hydrogel with a GO-based controlled release mechanism induced M2-type macrophage differentiation for defective bone healing. Reproduced with permission from [183], copyright Wiley Online Library 2021; (**c**) CuS and fucoidan-modified chitosan nanofibers for antimicrobial and bone tissue regeneration. Reproduced with permission from [184], copyright Elsevier 2022; (**d**) Nanocomposite biomaterials for bone regeneration produced from nano-hydroxyapatite impregnated in Chitosan/κ-Carrageenan. Reproduced with permission from [185], copyright Wiley Online Library 2022.

Similarly, other composite scaffolds that researchers developed include chitosan/ decellularized Alstroemeria flower stem [186]; chitosan/gelatin electrospun fibers [187]; chitosan thermo- and pH-responsive hydrogels [182,188]; chitosan/regenerated cellulose nanofibers [189]; copper(II)-chitosan/strontium-substituted hydroxyapatite [190]; chitosan/montmorillonite [191]; chitosan/silver polymeric scaffold [192]; carboxymethyl chitosan/polycaprolactone nanofibers [193]; and chitosan/collagen/hyaluronic acid oligosaccharides [194].

11.2. Cartilage

Chondrocytes create the extracellular matrix (ECM) protein molecules found in cartilages [195]. Articular cartilage provides crucial biomechanical activities to bone structures, including abrasion tolerance, load-carrying, and shock attenuation [196]. Since cartilage tissues are usually devoid of blood vessels, have a complicated structure, have quite a small density of cells, and have significant variability, it is harder to treat them [197]. Furthermore, they work in a rigorous atmosphere. So, when the thickness of the damage exceeds 4 mm, the ability for impulsive self-repair is reduced. Mosaicplasty, autologous chondrocyte injections, and micro-fracture are common therapies for cartilage tissue injuries, although they are not always the same structurally as natural tissue [198]. As a result, bioengineering has emerged as a viable option for osteochondral regeneration.

Given its ability to be employed in various ways, such as fibers, sponges, and hydrogels, chitosan is often utilized in cartilage tissue regeneration [15,199,200]. Chitosan's resemblance to the GAGs present in ECM is also another significant aspect that renders it a desired substance in this domain [201]. Variable electrostatic exchanges with cytokines, receptors, and cell adhesion factors are notable features of GAGs. GAGs can also promote

cartilage chondrogenesis. Chitosan can promote chondrogenesis, cartilage-specific protein production, and binding by electrostatic interactions with oppositely charged GAGs [202]. As a result of chitosan's ability to assist in or encourage the production of cartilage's unique GAGs, chitosan-derived composite scaffolds have now become attractive for osteochondral regeneration [203,204].

In the production of multipurpose microhabitats for cultured cells and tissue construction, bioinspired hydrogels are produced. Several mixtures of chitosan (CH) and hyaluronic acid (HA) derivatives with opposing ions were produced in the investigation by Davachi et al. To improve the communication among these constituents, phenolic moieties were supplemented on the backbones of CH (CHPH) and HA (HAPH) through a carbodiimide-based condensation, and further enzyme-assisted cross-linking in the availability of horseradish peroxidase was used to form a robust microenvironment for cell intercalation and tissue regeneration, as depicted in Figure 5a. The hydrogels' viscoelastic and structural properties revealed that a modest amount of HAPH produces the most remarkable outcomes in the structure. Cellular experiments revealed optimal cell survival and multiplication on the optimal hybrid hydrogel surfaces compared to plain hydrogels. In addition, the composite hydrogels showed better features for developing chondrocyte biomarkers and a greater tendency for MSCs to develop into cartilage-like cells. Altogether, the findings imply that in three-dimensional cartilage tissue regeneration, the optimal composite hydrogel can create an improved biological milieu for chondrocytes [205].

Three-dimensional (3D) printed hydrogel composites containing ceramics have shown promise for cartilage tissue engineering, but their mechanical and biological qualities remain unsatisfactory. In a study by Sadeghi et al. the production of chitosan/alginate-based scaffolds with nano-hydroxyapatite (nHA) using a combination of 3D printing and impregnating processes resulted in a combination, yet new, scaffold architecture for cartilage tissue engineering, as illustrated in Figure 5b. The introduction of nHA raised the Young's modulus of the scaffolds. In addition, the live/dead assay revealed that nHA significantly impacted the ATCD5 cell adhesion and scaffold survival. Moreover, the scaffolds containing nHA embedded in alginate hydrogels improved the cell survival and adhesion. Additionally, the chitosan scaffolds had good antibacterial properties, which were further increased by the nHA-based scaffolds. Overall, the chitosan/HA/alginate composite scaffolds are potential for cartilage tissue engineering, as well as the methodologies developed to generate hybrid scaffolds using 3D printing and impregnation methods, which could be applied to fabricate scaffolds for other applications [206].

For biological purposes, cryogel offers a highly porous architecture with mechanical strength and injectability. Three-dimensional (3D) printing is a form of customized manufacturing. Unfortunately, there is have been limited investigations into cryogel 3D printing. Chen et al. created a 3D-printable chitosan-based cryogel by employing polyfunctional polyurethane nanoparticles as the crosslinking agent, which interacted with chitosan at 4 °C for 4 h to build a rigid pre-cryogel for 3D printing, as shown in Figure 5c. To make 3D-printed chitosan cryogel, the generated pre-cryogel was frozen at 20 °C. The 3D-printed cryogel had features comparable to bulk cryogel, including high compression, elasticity modulus, and 3200 percent water absorption. The cell tests revealed that the 3D-printed chitosan cryogel frameworks offered good mechanical properties for human adipose-tissue adult stem-cell propagation and chondrocyte differentiation. The injectable and shape-recoverable 3D-printed chitosan-based cryogel scaffolds are viable substrates for tailored tissue regeneration and less surgical intervention [207].

Engineering a multiple-layered chitosan-based scaffold for osteochondral injury healing required a novel method. A highly porous, bioresorbable framework with a unique pore size distribution (mean = 160–275 m) was created by Pitrolino et al. using a hybrid of freeze-drying and porogen-leaching techniques. The inclusion of 70-weight percent nano-hydroxyapatite (nHA) in the bone-like layer strengthened it. The scaffolding displayed fast mechanical restoration during compression loads and did not undergo delamination under tensile load capacity. The scaffold allowed human MSCs to adhere and proliferate,

exhibiting adherent cell morphology on the bony layer vs. the spherical cell shape on the chondrocyte layer. In vitro, the unique pore gradients and material constitution favored the osteogenic and chondrogenic development of MSCs in specific layers of the platform. This scaffold offered the ability to rebuild injured bone and cartilage and was an excellent option for noninvasive arthroscopic administration in the clinical setting [208].

When integrated alone without the inclusion of a chemical crosslinker, a new category of composite hydrogels obtained from chitosan (CS)/hyaluronic acid (HA) and silanized-hydroxypropyl methylcellulose (Si-HPMC) (CS/HA/Si-HPMC) have been synthesized and evaluated as injectable hydrogels for cartilage regeneration by Hu et al. (as shown in Figure 5d). The mechanical investigations revealed that, as the amount of Si-HPMC in the hydrogel grew, the swelling ratio and rheological characteristics rose, the compression strength fell, and the decomposition rate accelerated, so that particularly those containing 3.0% (*w/v*) Si-HPMC and 2.5/4.0% (*w/v*) CS/HA were feasible for cartilage tissue regeneration. The rate of regeneration was around 79.5% on the 21st day of the in vitro studies on cartilage ECM and was suitable for repairing joint cartilage tissue [209].
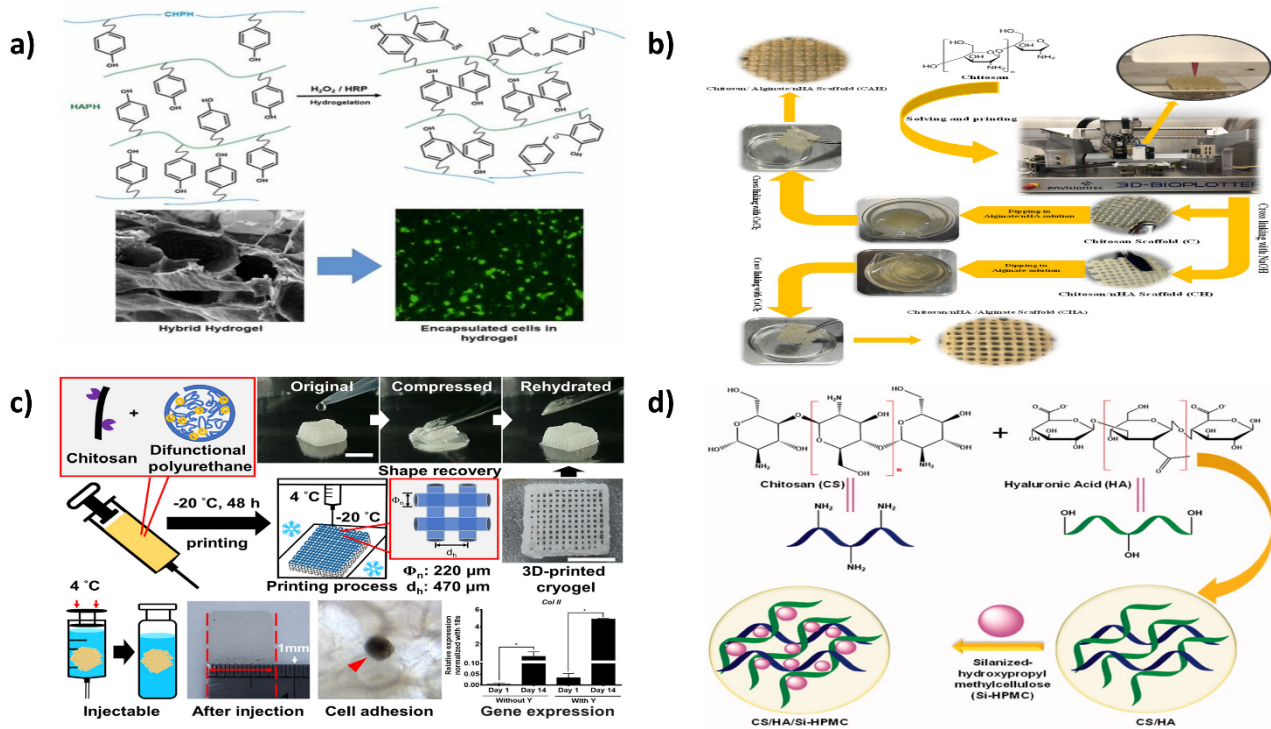
Figure 5. (**a**) Enzymatic synthesizing chitosan/hyaluronic acid hydrogel scaffolds towards cartilage regeneration. Reproduced with permission from [205], copyright Elsevier 2022; (**b**) 3D printing and loading techniques were used to create chitosan/alginate/hydroxyapatite composite scaffolds for prospective cartilage tissue engineering. Reproduced with permission from [206], copyright Elsevier 2022; (**c**) Chitosan cryogel 3D printing as injectable and shape-restorable tissue engineering scaffolds. Reproduced with permission from [207], copyright Elsevier 2022; (**d**) The production steps for the Si-HPMC integrated CS/HA injectable hydrogel are depicted schematically [209].

Other studies for chondral tissue regeneration involve chitosan/xanthan/amniotic fluid stem cells [210], and thiolated chitosan/silk fibroin [211].

11.3. Blood Vessel

Artificial grafts, which allow cells to create viable regenerative tissue, are extensively utilized in vascular tissue engineering [212]. Nevertheless, its usability is frequently restricted due to various host-cell invasions, calcification, or inadequate remodeling. Size incompatibility, supply shortage, and previous arterial disorders are all problems with

vascular autografts. Because the biomimetic implants or patches are proximate with the bloodstream, they must be non-toxic. Inflammatory responses and calcification, as well as post-surgical loss, might result from incompatibility. Biomaterial deterioration must be regulated so that it does not disintegrate too quickly or inadequately. The transplant is prone to form failure if it deteriorates too quickly. Cell growth and incorporation are hampered if it diminishes too gradually. As a result, effectiveness in blood vascular tissue engineering hinges on developing biodegradable polymer grafts, which can sustain cell uptake and multiplication while also undergoing fast remodeling. Based on its porosity and gel-forming capabilities, chitosan would not just be highly biocompatible and degradable but could simply be conveniently tweaked to show desirable qualities. Moreover, chitosan is a glucosamine and an N-acetyl glucosamine biopolymer. Glycosaminoglycans, having a striking resemblance to chitosan, make up the ECM of vasculature tissue. Mixtures of chitosan and other polymeric materials have demonstrated promising improvements in structural rigidity, cell attachment, and growth in this setting [212–214].

Wang et al. made a hybrid scaffold out of gelatin methacryloyl (GelMA) and carboxymethyl chitosan (CMCS), demonstrating its ability to stimulate revascularization. Compared to the pure GelMA scaffold, the composite GelMA/CMCS scaffolds implanted with BMSCs displayed outstanding mechanical characteristics, CD31 induction, and expression of vasculogenic genetic factors. The BMSC function in 3D-printed GelMA/CMCS scaffolds also revealed the potential of bioprinting cells impregnated with GelMA/CMCS hybrid scaffolds. Thus, GelMA/CMCS hybrid scaffolds have the potential to be used in vascular tissue regeneration [215].

Because a discrepancy in mechanical parameters between vascular patches and natural blood vasculature might lead to post-operative failures, vascular patches that mirror the biomechanics of natural blood capillaries should be designed. They created a bioinspired vascular patch by treating a decellularized scaffold (DCS) with a poly (ethylene glycol) (PEG) membrane and altering its surfaces with a heparin–chitosan polyelectrolyte multilayer (PEM). The PEM-functionalized PEG/DCS vascular patches had mechanical properties similar to natural blood vessels. They efficiently repelled platelet attachment, lowered hemolysis, enhanced coagulation time in vitro, and encouraged endothelial cell attachment and development. Additionally, the customized patches preserved the arteries' patency for an extended period (5 months) in vivo [216].

An electrospinning procedure was employed to build a scaffold for blood vessel regeneration using Poly-L-Lactic acid (PLLA) combined with chitosan and collagen in a study by Fiqrianti et al. The conduit's shape, chemical bonding, compressive strength, bursting pressure, hemocompatibility, and cellular viability were all studied using different amounts of chitosan in the mixture. In vitro tests revealed that adding chitosan–collagen to a cell culture could enhance cell survival and hemostasis. The conduit containing 10% PLLA, 0.5 percent chitosan, and 1 percent collagen had optimal results. The compressive modulus was 2.13 MPa, and the burst pressure was 2593 mmHg, both of which were within the biological blood vessel parameters threshold. The vascular graft component met the requirements of high hemocompatibility and lower toxicity with a hemolytic rate of 1.04 percent and a survival rate of 86.2 percent. The findings are encouraging for future research into vascular graft applications [217].

In a study by Soriente et al., they investigated how well the multifunctional chitosan (CS)/Poly (ethylene glycol) diacrylate (PEGDA) related scaffolds might promote revascularization in vitro. The substrates were bioactivated using both organic (BMP-2 peptide) and inorganic (hydroxyapatite nanoparticles) stimuli. In vitro angiogenic assays, focused on cell growth and differentiation, were used to investigate the qualities of the substances regarding physiological response stimulation on human umbilical vein endothelial cells (HUVECs). Their findings showed that the functional signals on the top of the CS/PEGDA scaffolds positively impacted angiogenesis responses, as measured by angiogenic marker production (CD-31) and endothelial tissue development (tube generation). Thus, the

bioactive CS/PEGDA scaffolds could be new inserts for encouraging the angiogenesis of tissue-engineered constructions in the domain of tissue engineering [218].

The grafting failure of medically useful synthetic tissues is caused by defects in the creation of microvascular systems, which bring oxygen and other nutrients to the cells. The vascularization of synthetic tissues can be aided by inflammation and immunomodulatory reactions. Endothelial progenitor cells (EPCs) and RAW264.7 macrophages were used as model cells in a capillary structure made of a gelatin methacrylate-derived cell-laden hydrogel scaffold complexed with interleukin-4 (IL-4)-loaded alginate-chitosan (AC) microspheres. Through electrostatic attachment, the AC microspheres retained and directed the EPCs, allowing for the creation of microvascular connections. The IL-4-loaded microspheres encouraged macrophage polarization into the M2 type, which resulted in a decrease in pro-inflammatory markers and an increase in vasculature [219].

11.4. Corneal

Ocular tissue engineering is a vital branch of bioengineering. The corneal epithelium oversees keeping the cornea clear by pushing ophthalmic fluid into the eyes. Since human corneal epithelial cells cannot renew, visual impairment occurs when they are lost due to aging, injury, or illness. Blindness develops when the body's cells decrease dramatically [220]. According to the World Health Organization, corneal degeneration and cataracts are among the reasons for visual impairment worldwide [221]. Corneal tissue engineering for retinal cell therapy is crucial because of the growing market for, and scarcity of, corneal donations.

The corneal tissue is a non-vascularized tissue that provides visibility. Corneal wounds are frequently repaired with amniotic membrane transplantation, which can be infected and immuno-rejected [222]. In the realm of cornea tissue regeneration, scaffold or membranes created from chitosan, gelatin, genipin, and other polymers are being investigated. Chitosan is popular because of its cytocompatibility and anti-inflammatory properties; however, its scaffolds have limitations, such as low structural rigidity. Polymers are combined with chitosan to improve scaffold qualities, similar to those of existing tissue engineering applications. Cornea tissue supports should have tensile and visual features identical to those of the corneal membrane and the capacity to sustain cells and adhesiveness. Because optical clarity is a critical quality for corneal prostheses, special care must be taken while choosing the material and production procedures. Under surgical treatment, the scaffolds or films should also be malleable and adaptive. The amniotic membranes now employed in clinical practice are not thick enough, disintegrate quickly, and have hygienic storage concerns [223,224].

By integrating chitosan nanoparticles (CSNPs) into chitosan/polycaprolactone (PCL) films, Tayebi et al. created a biodegradable transparent framework for growing corneal endothelium using the solvent casting process. The CSNP/PCL ratio increased, enhancing clarity and surface water sorption. The CSNP/PCL 50/25, which has the lowest WCA, demonstrated similar transparency with human acellular corneal stroma. According to the MTT experiment, the scaffold was non-cytotoxic and enhanced HCEC development. The HCECs were adequately attached to the framework and produced a dense monolayer. From the perspective of transparency and cytocompatibility, the scaffold is appropriate for corneal endothelium repair [225].

Clear, biologically compatible, and in situ formed biomimetic substrates are ideal for ocular bioengineering because they can profoundly fill irregularly shaped corneal stroma abnormalities and facilitate tissue repair. To this end, Feng et al. created a new class of corneal frameworks using oligoethylene glycol (OEG)-based dendronized chitosan (DCs), which have fascinating sol–gel shifts induced by temperatures close to physiological conditions, culminating in very clear, translucent hydrogels. These hydrogels' gelation points can be easily adjusted, and their tensile performance can be significantly increased when introduced into PBS at 37 °C rather than in pure water. In vitro experiments showed that these DC hydrogels have excellent biocompatibility and could enhance keratocyte differentiation and proliferation. In situ-produced DC hydrogels benefitted potential tissue

repair in rabbits' eyes with cornea stromal deficiencies. Given their high biocompatibility and exceptional thermo-responsiveness, these thermo-gelling DCs have a lot of potential as ocular tissue replacements [226].

A hybrid membrane was created using carboxymethyl chitosan (CMCTS), gelatin, and hyaluronic acid in a study by Xu et al. Primary rabbit corneal epithelial cells (CEpCs) were implanted on it, and it was observed to be translucent, biodegradable, and ideal for CEpC adhesion and growth, as well as maintaining CEpC synthesis of epithelial cell-like proteins. The CEpCs/CMCTS membranes were utilized to treat the alkali-induced corneal injury in rabbits, and the membrane had the potential to enhance corneal epithelial restoration dramatically and regain corneal clarity and thickness [227].

There is no appropriate scaffold for transplanting limbal stem cells (LSCs) into the cornea to stimulate corneal regeneration following corneal alkali-induced burns. To this end, Xu et al. created a new alginate-Chitosan hydrogel (ACH) for LSC implantation in situ. Periodate-involved sodium alginate oxidation yielded sodium alginate dialdehyde (SAD), a physiological crosslinker. SAD quickly crosslinked carboxymethyl chitosan via Schiff's base reaction between the accessible aldehyde and amino residues. Self-crosslinking causes the ACH to develop rapidly on the wound surface without requiring any chemical cross-linking components. The in situ hydrogel was found to be remarkably transparent, gelled rapidly, bio-friendly, and noncytotoxic. The stem marker p63 was displayed by LSCs cultivated in vitro, while the differentiated epithelial biomarkers cytokeratin 3 and 12 were not. Moreover, the hydrogel encasing LSCs was proved to dramatically increase the epithelium restoration when applied to an alkali-induced burn site on the corneal region. Altogether, such an innovative in situ hydrogel-LSC grafting approach could be a quick and efficient way to cure corneal wounds [228].

Shahin et al. created a chitosan/gelatin hyaline film containing NHS and EDC crosslinking agents to transplant the corneal epithelial cells. Before crosslinking, the two gelatin and chitosan solutions were uniformly combined in proportions of 20/80, 30/70, 40/60, and 50/50 (Gel/Chi). They were dried in the oven for 24 h. It was found that rising chitosan concentrations enhanced the transparency and cytocompatibility of generated samples, greater water penetration and degradation rate of samples, and dramatically improved cell growth and vitality [229].

Other similar studies include chitosan/polycaprolactone [230]; carboxymethyl chitosan/gelatin/potassium acetate [231]; and chitosan/keratocyte spheroids [232].

11.5. Periodontal

With its biological properties, antibacterial properties, cytocompatibility, and capability to integrate with other substances, chitosan is evaluated as a viable contender for dental purposes. It works just as well as a single element and, in many circumstances, outperforms it when paired with other synthetic or natural components [75]. Chitosan-based materials are employed in a variety of applications, including enamel remineralization and development [233], dentin bonding [234], tooth repair material [235], and surface coatings for dental implants [236].

Meanwhile, periodontal diseases are among the critical challenges in medical research since it causes irreparable erosion of periodontal tissues, resulting in loss of teeth. In the advent of periodontitis, an inflammatory response condition, the hostile oral microenvironment becomes even more unfavorable. As a result, scientists have been looking for a viable biomaterial substitute. Various types and mixtures of chitosan have already been explored and examined; however, very few publications have been published in the last ten years. Many studies focused primarily on chitosan, while others looked at its ability to mix with several other organic and inorganic compounds. In most cases, the resulting material displayed potential dental action [53].

Chitosan, a promising polymer, is now being utilized in dental implant coating. Nevertheless, there is a paucity of studies on coating materials for implants apart from commercially purified titanium. As a result, Alnufaiy et al. studied the impact of chitosan

with two degrees of deacetylation (DDA) as coverings for laser surface microtopographic implants. In the chitosan-functionalized samples, the production of osteogenic biomarkers increased significantly. A high DDA of chitosan aided an enhanced bone mineralization and osteoblast development. As a result, the mixture of laser surfaces and chitosan may improve dental implant recovery and osseointegration procedures [237].

Given its superior biocompatibility, biodegradation by naturally occurring enzymes, suitable physicochemical attributes, and optimum molecular size, chitosan can be employed as a framework for the healing of periodontium (in the therapy of periodontal pockets). Furthermore, pluripotent dental mesenchymal stem cells, including stem cells from human exfoliated deciduous teeth (SHED) and human periodontal ligament cells (HPLCs), can be seeded into chitosan frameworks. Chitosan could be utilized to efficiently regenerate periodontal tissue by stimulating cementoblasts and osteoblasts to produce new tissues. Sukpaita et al. in their study using chitosan/dicarboxylic acid (CS/DA) with seeded HPLCs, found that within 6–12 weeks, significant in vivo bone growth was observed in calvarial-defects mice models [238].

The root canal network is chemo-mechanically debrided, and inflammatory or decaying pulp contaminated by bacteria is removed during root canal therapy. Several studies on the antimicrobial property of chitosan nanoparticles (CSNPs) towards pathogens such as P. gingivali, S. mutans, and E. faecalis have been previously reported. CSNPs could be used with calcium hydroxide as endodontic sealants or for temporary root canal filling. Regenerative endodontic therapies have also used chitosan. Bioactive compounds and growth stimulators can be added to chitosan-derived porous scaffolds. Dentin sialophosphoprotein, alkaline phosphate, and dentin matrix acidic phosphoprotein are odontoblastic indicators that promote the synthesis of secreted signaling chemicals, causing dental pulp stem cells (DPSCs) to proliferate and differentiate into odontoblasts [239].

Similarly, some other studies for dental tissue engineering composed of chitosan-based scaffolds are chitosan/PNIPAAm/graphene oxide [240]; chitosan/Ca-SAPO-34 monometallic or bimetallic nanoparticles [241]; chitosan/calcium [242]; chitosan/nanofluorohydroxyapatite or nanohydroxyapatite [243]; chitosan/gelatin/nanohydroxyapatite [244]; chitosan/PLA-nanofibers [245]; chitosan/collagen/bone morphogenetic protein-7 [246]; chitosan/gelatin [247]; chitosan biguanide/carboxymethyl cellulose [248]; and chitosan/polyurethane nanofibrous membrane/AgNPs [249].

11.6. Miscellaneous

11.6.1. Skin

The skin represents the physical barrier between the surrounding environment and the physiological body [250,251]. Damage to the skin involves conditions such as burns, infections, and acute and chronic disorders such as psoriasis [252–255]. In such instances, TE provides advantages over conventional treatments because of its superior efficiency, fewer chances of donor morbidity, and immuno-compatibility reactions [256]. Additionally, the TE based on biocompatible biomaterials and their composites offer a substitute for fabricating tissue scaffolds that are physiochemically and biologically identical to natural tissues [257,258]. An essential requirement in skin TE is designing novel biopolymeric films or scaffolds resembling the extracellular matrix by combining biological, material chemistry principles and engineering [182], displaying features such as biodegradability, biocompatibility, and material characteristics [259].

Contemporary regenerative therapy is concerned with hypoxia and sepsis. The goal of oxygen-generating biopolymers with antibacterial properties is to address these issues. Oxygen deprivation at the implantation surface causes superoxide radicals, which slow the healing process. In addition, sepsis in the wound leads to a delayed healing process. As a result, antimicrobial and oxygen-producing scaffolds have demonstrated their ability to aid wound healing. The oxygen-releasing, ciprofloxacin-encapsulated collagen-chitosan scaffold used in this work was constructed for long-term oxygen supply. Biochemical oxygen was provided by calcium peroxide (CPO). The oxygenation pattern showed a

consistent diffusion of oxygen together with homogeneous CPO accumulation on the scaffold. Ciprofloxacin was released in a sustained manner. Cell culture experiments showed that the scaffold has good cell adhesion and motility capabilities for the fibroblasts. In the in vivo investigations in the skin, the flip model revealed that wound healing was improved, and necrosis was reduced. Histopathological investigations revealed that tissue structure was preserved, and collagen was deposited. The findings indicated that the suggested CPO-coated ciprofloxacin-based collagen–chitosan scaffold could be a suitable skin tissue regeneration alternative [260].

The tissue regeneration capability of the nanofibrous framework incorporating proteins and polysaccharides appears promising. Hence, Mohamad Pezeshki-Modaress investigated the influence of chitosan in chitosan/gelatin nanofibrous scaffolds created using an improved electrospinning method. The culture of dermal fibroblasts (HDF) on nanofibers in respect of adhesion, shape, and growth was investigated to see how the chitosan concentration affected the bioactivity of the electrospun chitosan/gelatin scaffolds for tissue regeneration. According to morphological observations, HDF cells were adhered to and propagated successfully on extremely porous chitosan/gelatin nanofibrous scaffolds with spindle-like forms and stretching. Electrospun gelatin/chitosan scaffolds in culture media kept their fibrous morphologies for 7 days. The MTS assay was used to measure cell proliferation on electrospun gelatin/chitosan scaffolds, revealing a beneficial influence of chitosan concentration (about 30%) and the nanofibrous pattern on scaffolds' biocompatibility (differentiation and adhesion) [261].

11.6.2. Cardiac Tissue

Injectable biomaterials are a viable therapeutic method for cardiac tissue repair in the treatment of myocardial infarction-related chronic heart failure. Because of the ionized amino acid moieties, chitosan exhibits mucoadhesion, is hemostatic, and is effective in attaching to cellular membranes. Chitosan can also be used to create well-connected scaffolds with enough porosity to ensure cell survival by providing a constant oxygenated blood and nutrient supply [262]. Controlled release of loaded bioactive substances and growth factors becomes another essential aspect of a chitosan-derived scaffold. This makes it an excellent choice for cardiac tissue regeneration. Chitosan is a biocompatible platform that works as an ECM, allowing immobilized angiogenic growth factors to drive endothelial cell migration and proliferation, allowing for the development of a new vasculature to be facilitated [263]. The pig ECM is cross-linked with genipin and chitosan, according to investigations. This aids in maintaining ECM physiological components while also increasing the injected scaffolds' tensile stability. Before employing non-clinical ECM as a scaffold material for tissue engineering, it must be decellularized to minimize the hypersensitivity of the material [262].

11.6.3. Connective Tissue

The 3D printing of the chitosan hydrogel is difficult because of its poor mechanical properties and weak formation capability. To this end, Zhang et al. fabricated acrylate substituted (DS 1.67) maleic chitosan (MCS) and thiol-terminated poly (ethylene glycol) (TPEG) through a step-chain growth photolytic polymerization technique, which helps in overcoming the formidable oxygen inhibitory effect. A strong intermolecular interaction between MCS and TPEG, and as compared to unmodified chitosan hydrogel, the prepared hydrogel showed a 10-fold and 2-fold enhancement in compression strength and gelling rate, respectively. Thus, 3D-printed chitosan hydrogel could be prepared by concurrent extrusion deposition and acrylate-thiol photopolymerization, having good printing efficiency and enhanced stability of the scaffold. The 3D-printed hydrogel demonstrated no cytotoxicity and supported L929 cell growth [264].

So far, only a handful of studies have been undertaken using carboxylated chitosan as a biomaterial for producing porous scaffolds and gels; hence, Yang et al. developed soft chitosan hydrogels in a hybrid composite with recombinant human collagen (RHC-CHI)

through crosslinking-induced gelation method for use as soft-tissue scaffolds for tissue regeneration. They showed tunable mechanical properties by adjusting either the polymer amount or the RHC-to-chitosan ratio. Beyond a specific concentration, increasing chitosan's concentration decreased the hydrogel's tensile strength and started causing degradation. The prepared hydrogels were non-cytotoxic and promoted the adhesion and growth of NIH-3T3 cells. The in vivo tests also revealed that the hydrogels could rapidly infiltrate cells and cause wound closure; thus, they are good candidates for soft-tissue regeneration [265].

Table 2. Recent studies focusing on tissue engineering applications of chitosan formulations.

Device Type	Model Drug/Drug	Polymer Formulation	Preparation Method	Tissue	Effects/Results	Reference
3D-Nanofibrous scaffold	-	Poly(vinyl alcohol)/keratin/chitosan	Layer-by-layer electrospinning	-	5% *w/v* keratin and 2% *w/v* chitosan electrospun with 10% *w/v* PVA showed remarkable properties such as high tensile strength, which doubled with increasing polymer concentration from 10 wt.% to 50 wt.%, swelling ratio (over 100%), porosity (82% to 86%). However, after 4 weeks of incubation, the scaffolds degraded significantly (50–66%).	[266]
Modified halloysite nanotube-based nanocomposite films	-	Chitosan/PVA/PVP	Solution casting	-	The synthesized nanocomposite films demonstrated enhanced thermal and mechanical attributes, uniform size distribution, surface topology, and enzymatic breakdown, with low swelling ratio and hydrophilic properties. In vitro, MTT and AO-EB assay revealed superior cell proliferation and adhesiveness as compared to neat PVA/PVP films ((118.31 $\pm$ 0.68% proliferation by 5 wt.%), and their hemocompatibility with RBCs was low (0.46 $\pm$ 0.05%).	[267]
Membranes	-	Chitosan/collagen/hydroxyapatite	Solvent casting	Bone/cartilage	Micro- and nanoporous membranes had excellent hydroxyapatite dispersion in the matrix. Thermally stable composites due to the incorporation of hydroxyapatite and collagen. No cytotoxicity and the highest adhesion were found in the membrane with 1.5% *w/v* Cs. 0.75% *w/v* collagen and 0.75% *w/v* hydroxyapatite.	[268]
Multilayer scaffold		Chitosan/gelatin/nano-hydroxyapatite	Iterative hierarchical method	Bone/cartilage	Adipose mesenchymal stem cells (ADSCs) differentiated into osteoblasts and chondrocytes similar in morphology to natural tissues, facilitating the expression of both osteogenic genes (OCN, Col I, and Runx2) and chondrogenic genes (ACAN, Sox9, and Col II).	[269]
Electrospun nanofibers	-	Chitosan/polypyrrole/collagen	Electrospinning	Heart/nerve/cardiovascular/skin	10% *w/w* polypyrrole-containing scaffolds exhibited optimum mechanical properties, good cell attachment, growth, and differentiation.	[270]
Composite scaffold		Chitosan/polyvinyl alcohol/cellulose nanocrystals (CNC)/β-Tricalcium Phosphate	Freeze drying	Bone	5% and 10% of CNC-based scaffolds exhibited significant calcium deposition after 72 h of culture.	[271]

Table 2. *Cont.*

Device Type	Model Drug/Drug	Polymer Formulation	Preparation Method	Tissue	Effects/Results	Reference
Hydrogels		Chitosan oxidized quince seed gum/curcumin loaded-halloysite nanotubes	Sonication	-	CS/O-QSG (25:75) exhibited rapid gelation and compression strength, and with 10–30%, CUR-HNTs enhanced cellular growth and proliferation by 150%.	[272]
Hydrogels		Chitosan/mucin/ Montmoril-lonite/hydroxyethyl methacrylate	Freeze drying	-	Good material characteristics such as porosity and water uptake as well as biocompatible with C2C12 and MC3T3E1 cell lines.	[273]
Films		Chitosan/collagen	Dual crosslinking with genipin and tannic acid	Cornea/skin	80% film retention after 2 weeks of incubating with lipase and lysozyme and biocompatible with mouse fibroblast cells.	[274]
Films		Chitosan/silk fibroin	Solvent casting	Bone/adipose/ cartilage/skin	Excellent adhesion, growth, and proliferation of rat bone-marrow-derived mesenchymal stem cells, while promoting osteogenic and adipose differentiation.	[275]
Hydrogels		Chitosan/decellularized annulus fibrosis matrix (DAFM)	Freeze drying	Intervertebral disc	Sustained release of fibroblast growth factors as a stimulus for AFSC growth and expression of ECM factors.	[276]

12. Wound Healing

Apart from its applications in drug delivery and tissue regeneration, some antifungal and antibacterial activity have also been discovered with chitosan and its quaternary derivatives [277,278]. It offers additional benefits compared to other synthetic derivatives, such as its higher killing efficiency, broader antibacterial spectrum, and lower mammalian toxicity [279].

Modifications of chitosan with amino acids have had tremendous advantages for wound healing applications. Several approaches may be carried out for modifying native chitosan with amino acids, including physical and chemical methods, such as like blending, compositing, grafting, cross-linking, etc. Since the amino groups of chitosan have two distinct types of properties, alkaline as well as nucleophilic characteristics, chitosan can form imines and amides and can also lead to the formation of salt derivatives. It has been reported that the functionalization of chitosan with amino acids offers enhanced cell adhesiveness, re-epithelialization potential, rapid angiogenesis, and collagen formation [280].

Chitosan alone has quite limited tissue adhesiveness in a wet environment; hence, catechol-based chitosan was explored because of its ability to form strong covalent interactions between the tissue's thiol or amino group and oxidized catechol moieties. The catechol-functionalized chitosan also showed good anti-infective and tissue adhesive activity. To preserve the anticoagulant effect of chitosan, hydrophobically modified chitosan (hmCS) consisting of alkyl side chains was used as an amphiphilic analog of chitosan. Du et al. developed a hmCS lactate, and hydrocaffeic acid-modified chitosan (CS-HA)-based hydrogel via a two-step procedure, as shown in Figure 6A, which demonstrated good anti-infective activity against *P. aeruginosa* and *S. aureus*. The CS-HA/hmCS hydrogel was non-cytotoxic to 3T3 fibroblast cells and was capable of sutureless wound healing in a rat full-thickness skin model due to the remarkable tissue interfacial adhesiveness of the optimum Gel3, which could maintain the incision structure and promote wound healing [281].

In civil and wartime situations, producing an anti-infective shape-memory hemostasis sponge capable of guiding in situ tissue repair for noncompressible hemorrhages represents a problem. Chitosan has applications in producing hemostats because of its anti-infectivity, biocompatibility, non-toxicity, hemostasis, and so on [282]. However, in situations where severe hemorrhage or microbial infections occur, its hemostatic potential is quite limited [281]. To this end, Du et al. used a combination of 3D-printed microfiber leaching, freeze-drying, and surface-active modifications to create hemostatic chitosan sponges featuring strongly interconnective micro-channels. They showed that the micro-channeled alkylated chitosan

sponge (MACS) could absorb water and blood while also restoring its structure quickly. In potentially deadly, healthy, and heparinized rats and pig hepatic-perforated wound specimens, the MACS provided better pro-coagulant and hemostatic capabilities than the clinically utilized gauze, gelatin sponge, CELOX[TM] (Crewe, UK), and CELOX[TM] gauze. In a rat liver damage model, they showed that it has anti-infective efficacy against *S. aureus* and *E. coli* and promotes liver parenchymal cell migration, vasculature, and tissue incorporation. Therefore, the MACS showed promise as a therapeutic translational tool for treating deadly noncompressible bleeding and promoting healing [283].
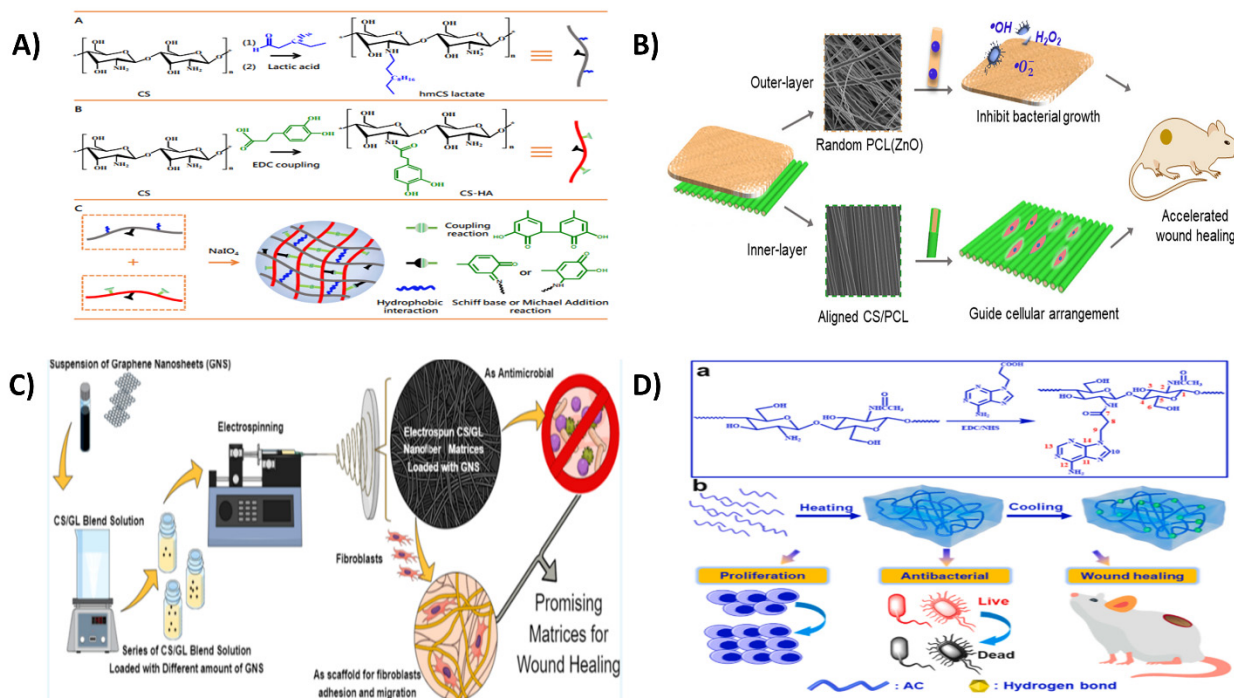
Figure 6. (**A**) Sutureless wound closure with anti-infective and pro-coagulator chitosan-mediated hydrogel tissue adhesives, reproduced with permission from [281], copyright ACS publications 2020; (**B**) Enhanced wound healing with electrospun ZnO-impregnated chitosan/PCL bilayer membranes featuring a spatially tailored structure. Reproduced with permission from [284], copyright Elsevier 2022; (**C**) Graphene-reinforced electrospinning-based chitosan/gelatin nanocomposite scaffolds having antibacterial and wound-healing properties [285]; (**D**) Chitosan-based hydrogels for wound repair that are injectable, self-healing, and antimicrobial. Reproduced with permission from [286], copyright Elsevier 2022.

Similarly, Zhou et al. created a versatile multilayer membrane with electrospun chitosan (CS) and activated ZnO nanoparticles (as illustrated in Figure 6B). The bilayer membrane's external surface was made up of ZnO-loaded poly(-caprolactone) (PCL) fine fibers in an irregularly oriented arrangement, giving it many antimicrobial properties. The internal layer consisted of CS fibers with a core design that might perform as an anti-inflammatory and efficient cell interaction guide. Notably, the composite CS/PCL electrospun membranes containing 1.2 wt. percent ZnO nanoparticles had improved mechanical properties and a clear inhibiting zone against *E. coli* and *S. aureus*, as well as being non-cytotoxic to fibroblast cells. In addition, the bi-layered membranes allowed for the attainment of substantial ZnO nanoparticle bioavailability and coordination with the oriented structural characteristic of CS fibers, which reduced inflammation, encouraged cell motility, and allowed for re-epithelialization in vivo [284].

Ali et al. created electrospun chitosan/gelatin nanofibrous scaffolds that were strengthened with various amounts of graphene nanosheets and could be employed as antimicrobial and wound-healing constructs, as shown in Figure 6C. The different manufactured scaffolds

were fully characterized before being tested for antibacterial activity, cytotoxicity, and cellular migration potential against *Escherichia coli* and *Staphylococcus aureus*. Nanostructures combined with 0.15 percent graphene nanosheets had the smallest width (106 ± 30 nm) and the most significant porosity (90 percent), along with good renewability and swellability. Nevertheless, increasing the number of graphene nanosheets by too great a degree resulted in beaded nanofibers with lower porosity, swelling ability, and degradability. Nanostructures reinforced using 0.15 percent graphene nanosheets, on the other hand, inhibited *E. coli* and *S. aureus* development by 50 and 80 percent, accordingly. When adult fibroblasts were cultivated with either non-reinforced or reinforced nanomaterials, the in vitro cytotoxicity experiments revealed negligible damage. After 24 and 48 h, cell movement was greater in the strengthened nanofibers compared to unmodified nanofibers, which is due mainly to the significant impact of graphene nanosheets on cellular migratory capability. After 48 h, cell migration outcomes for reinforced and unreinforced nanofibers were up to 93.69 and 97 percent, correspondingly [285].

A crucial healthcare concern is developing a cost-effective and readily available substance for better skin tissue regeneration. Hence, Deng et al. created injectable, self-healing adenine-functionalized chitosan (AC) hydrogels meant to expedite the healing process significantly without the need for medicinal agents and were inspired by the notion of wet wound repair, as shown in Figure 6D. In aqueous solutions, various AC derivatives with degrees of substitution (DS) ranging from 0.21 to 0.55 were synthesized, and AC hydrogels were constructed using a facile heating/cooling technique. AC hydrogels showed remarkable self-healing capability, low swelling rates, cytocompatibility, cell proliferation promotion, and hemostatic action. The hydrogels were proved to possess antibacterial properties against gram-negative and gram-positive bacteria, fungus, and bacteria with antibiotic resistance. Furthermore, full-thickness skin lesion model investigations revealed that AC hydrogels could greatly minimize inflammatory cell invasion and speed the wound repair. The hydrogel has the potential to revolutionize the design of multipurpose wound dressings [286].

Similar studies exploring the antibacterial wound healing abilities of chitosan were chitosan-based quaternary ammonium salt/gentamicin sulphate hydrogel films [287]; chitosan/polyvinyl alcohol hydrogel/ZnO nanoparticles [288]; chitosan/pectin/lidocaine hydrogel [289]; quaternized chitosan/Matrigel/polyacrylamide hydrogels [290]; chitosan/carboxymethyl chitosan/AgNPs polyelectrolyte complex [291]; chitosan/PVA/starch electrospun mats [292]; carboxymethyl chitosan/polyurethane/helatin hydrolysate [293]; oxidized chitosan/amidated pectin hydrogel [294]; chitosan/PVA/copper [295]; and chitosan/PVA/HKUST-1 electrospun mats [296].

Table 3 depicts the latest investigations on chitosan formulations for wound healing

Table 3. Recent studies focusing on the wound healing applications of chitosan formulation.

Device Type	Model Drug/Drug	Polymer Formulation	Preparation Method	Wound Site	Effects/Results	References
Hydrogels	-	Gallic acid/chitosan	Discharge plasma technology		Traditional DPPH scavenging experiments revealed remarkable antioxidant characteristics. CS-GA formed hydrogels by cross-linking by undergoing oxidation at a physiological state. High cytocompatibility and hemocompatibility were observed in vivo rat skin-layer defects and liver hemorrhagic models (46.6% collagen fiber growth by the 7th day). CS-GA functions at the wound site without the application of prolonged pressure.	[297]

Table 3. *Cont.*

Device Type	Model Drug/Drug	Polymer Formulation	Preparation Method	Wound Site	Effects/Results	References
Hydrogels		Catechol-modified chitosan/Oyster peptide microspheres/β-sodium glycerophosphate (β-GP)				[298]
Hydrogels	Amoxicillin, tetracycline, cefuroxime, acetylsalicylic acid	Chitosan/genipin		Ulcer wounds/dermal tissue	Synergistic antibacterial-anti-inflammatory wound healing was observed with ASA-based antibiotic combinations with sustained drug release.	[299]
Hydrogels		Carboxymethyl chitosan/oxidized quaternized guar gum OQGG@CMCS			Excellent antibacterial and hemostatic activity, self-healing in *S. aureus* rat model.	[300]
Electrospun mats		Chitosan/poly-ε-caprolactone fibrous mat/polyurethane foam/ethanolic extract of propolis (EEP)	Electrospinning		PCL/CS-PU/EEP bilayered wound dressing exhibited improved biocompatibility and healing potential both in vitro and in vivo.	[301]
Thermosensitive hydrogel-microparticles based hybrid		Chitosan/β-glycerophosphate thermosensitive hydrogel/decellularized amniotic membrane/polylactic acid microparticles			The hybrid oxygen-generating wound dressing material promoted cell adhesion and growth and was non-cytotoxic, and released oxygen for 7 days.	[302]
Bionanocomposite		Carboxymethyl cellulose/tragacanth gum/silver-titanium nanoparticles	Freeze drying		The wound dressing exhibited porosity between 65–79%, which increased with the addition of silver-TiO$_2$. Higher wound dressing weight loss was observed for the highest concentration of AgO/TiO$_2$.	[303]
Hydrogels		Chitosan/lignin/polyvinyl alcohol	Freeze thawing		Lignin-based PVA-chitosan hydrogels had good mechanical strength, protein adsorbing capacity, and wound healing with environmental regulation ability.	[304]
Membrane		Chitosan/hyaluronan/phosphatidyl-choline dihydroquercetin (Ch/HA/PCDQ)			Ch/HA/PCDQ membranes displayed antibacterial, antioxidant, and anti-inflammatory activities as well as showed biocompatibility. Significantly greater wound healing potency was observed in mouse full thickness wound model.	[305]
Nanoparticles-loaded electrospun nanofibers	OH-CATH30 antibacterial peptide	Chitosan/polyvinyl alcohol	Electrospinning	Skin wounds	NP-30-NFs exhibited antibacterial activity against *E.coli* and *S. aureus* and showed wound healing in mouse skin wounds.	[306]

Despite its various advantages, chitosan and chitosan-based formulations do suffer various drawbacks. The variations due to the source and preparation methods of chitosan have a direct influence on their mechanical and biological properties [307]. Moreover, due to its high solubility at an acidic pH, the ability of chitosan to control the release rate and stability of drugs is limited, requiring an additional coating of acid-resistant anionic polymers, such as alginate [308]. In gene delivery applications, the transfection efficiency of chitosan as a non-viral carrier depends on the media pH, degree of acetylation, cell type, molecular weight, etc. Most reports focus on the in vitro gene delivery efficacy, however, extensive research on in vivo models is still scarce [309].

13. Conclusion and Future Perspectives

Chitosan displays remarkable physicochemical attributes and good biocompatibility and links with human proteins, cells, and organs. The terminal amino groups present in its skeleton facilitate the formation of polycations in an acidic medium when the amine groups undergo protonation; this enables interactions with anionic polymers in various shapes and geometry. It is expected that chitosan and chitosan-based derivatives may be used to fabricate tissue repair scaffolds for a plethora of tissues, such as bone, cartilage, skin, cornea, blood vessel, and so on, with suitable properties. Such matrices are beneficial because of their natural resemblance to host tissues and similarities in structure and function to biological molecules.

As humans become more aware of the intricate biological reactions to the presently available biomaterials, as well as with the expanding knowledge about the human anatomy and physiology, organ and tissue damage, disease proliferation, and cellular changes in protein functions during tissue injury, a co-operative endeavor involving polymer chemists, engineering minds, biologists, and physicians could be undertaken for developing novel polymeric biomaterials specially tailored for each application. Currently, chitosan stands as one of the most reliable and convenient biomaterials for various kinds of biomedical applications, mainly due to its accessibility and peculiarities. Nonetheless, added efforts need to be taken to enhance the tissue scaffold for tailored properties for different types of tissues. Along with in vitro studies, the same scaffolds must also be tested in vivo to determine their clinical utility in humans. Several studies have shown that the in vitro benefits of chitosan composites for tissue and wound healing do not translate as expected in the in vivo animal models. A closer look into the reasons and modifications required must be encouraged.

With the remarkable progress of tissue engineering science such as novel stem cell sources, microfluidics' devices, versatile and tailored biomaterials, etc., some challenges remain, such as engineering blood vessels into the tissue scaffolds, the immunogenicity of the scaffolds, and regulatory issues. The 3D printing platform provides the flexibility to print complex structures, such as cells and scaffolds, while also giving good control of pore size and size distribution. Consequently, recent publications depict the utility of chitosan in printing constructs for bone, skin, vascular, and cartilage tissue engineering. However, their practical applications and clinical translation are still being investigated. Recent reports have suggested that chitosan and its quaternized derivative can have immunomodulatory effects by activating the antigen-presenting cells and inducing cytokine production. Hence, their role as vaccine adjuvants could open new paradigms in vaccine formulation delivery.

Although there have been definitive strides in technological advancements, more profound research is warranted for evaluating cell-specific intercommunications, in vivo understanding, and replication of bioactivity, long-term stability, and biocompatibility studies to make chitosan a more widely used biomaterial.

Conflicts of Interest: The authors declare no conflict of interest.

Abbreviations

5	FU-5-fluorouracil
AC	Adenine-functionalized chitosan
ADSCs	Adipose mesenchymal stem cells
BP	QCS-quaternized chitosan-modified black phosphorus nanosheets
BSA	Bovine serum albumin
CMCS	Carboxymethyl chitosan
CMCTS	Carboxymethyl chitosan
CNC	Cellulose nanocrystals
CNs	Chitosan nanoparticles
COS	Chitosan-oligosaccharides
CPO	Calcium peroxide
CS	Chitosan
CS/DA	Chitosan/dicarboxylic acid
CS-HA	Hydrocaffeic acid-modified chitosan
CUR	Curcumin
DAFM	Decellularized annulus fibrosis matrix
DCs	Dendronized chitosans
DD	Degree of deacetylation
DDS	Drug delivery systems
DTX	Docetaxel
EC	Ethylcellulose
ECM	Extracellular matrix
EPCs	Endothelial progenitor cells
F/C	Fucoidan/chitosan
GA	Glycyrrhetinic acid
GelMA	Gelatin methacryloyl
H/Al-MSN	Aluminum-modified mesoporous silica nanoparticles
HA	Hyaluronic acid
hmCS	Hydrophobically modified chitosan
HPLCs	Human periodontal ligament cells
HUVECs	Human umbilical vein endothelial cells
iSur -	pDNA-survivin shRNA-expressing plasmids
LA	Lactobionic acid
MACS	Micro-channeled alkylated chitosan sponge
MCS	Maleic chitosan
MT NPs	p-mercaptobenzoic acid-embedded N, N, N-trimethyl chitosan nanoparticles
MTT	3-(4,5-dimethylthiazol-2-yl)-2,5-diphenyl tetrazolium bromide
nHA	Nano-hydroxyapatite
NP	Nanoparticle
OEG	Oligoethylene glycol
OQGG@CMCS	Carboxymethyl chitosan/oxidized quaternized guar gum
PAA	Polyacrylic acid
PCADK	Poly (cyclohexane-1, 4-diylacetone dimethylene ketal)
PCL	Poly(-caprolactone)
PEC	Polyelectrolyte complex
PEGDA	Poly(ethylene glycol) diacrylate
PEM	Polyelectrolyte multilayer
PTX	Paclitaxel
RHC-CHI	Recombinant human collagen-chitosan
rhIL-2	Recombinant human interleukin-2
ROS	Reactive oxygen species
SA	Sodium alginate
SAD	Sodium alginate dialdehyde
SCO	Splice correction oligonucleotides
SHED	Stem cells from human exfoliated deciduous teeth
Si-HPMC	Silanized-hydroxypropyl methylcellulose
siRNA	Small interfering RNA
TPEG	Thiol-terminated poly(ethylene glycol)

References

1. Mady, F.M.; Ibrahim, S.R.; Abourehab, M.A. Development and evaluation of alginate-gum blend mucoadhesive microspheres for controlled release of metformin hydrochloride. *J. Adv. Biomed. Pharm. Sci.* **2021**, *4*, 111–118. [CrossRef]

2. Rezaei, F.S.; Sharifianjazi, F.; Esmaeilkhanian, A.; Salehi, E. Chitosan films and scaffolds for regenerative medicine applications: A review. *Carbohydr. Polym.* **2021**, *273*, 118631. [CrossRef] [PubMed]

3. Knorr, D. Recovery and utilization of chitin and chitosan in food processing waste management. *Food Technol.* **1991**, *45*, 114–122.

4. Knorr, D.; Teutonico, R.A. Chitosan immobilization and permeabilization of amaranthus tricolor cells. *J. Agric. Food Chem.* **1986**, *34*, 96–97. [CrossRef]

5. Hadwinger, L.A.; Fristensky, B.; Riggleman, R.C.I. *Chitin, Chitosan and Related Enzymes*; Zikakis, J.P., Ed.; Academic Press: New York, NY, USA, 1984; pp. 291–302.

6. Flórez, M.; Guerra-Rodríguez, E.; Cazón, P.; Vázquez, M. Chitosan for food packaging: Recent advances in active and intelligent films. *Food Hydrocoll.* **2022**, *124*, 107328. [CrossRef]

7. Mourya, V.K.; Inamdar, N.N. Chitosan-modifications and applications: Opportunities galore. *React. Funct. Polym.* **2008**, *68*, 1013–1051. [CrossRef]

8. Synowiecki, J.; Abdul, N.A.; Al-Khateeb, Q. Mycelia of *LMIlcor Rouxii* as a source of chitin and chitosan. *Food Chem.* **1997**, *60*, 605–610. [CrossRef]

9. Kohlhoff, M.; Niehues, A.; Wattjes, J.; Bénéteau, J.; Cord-Landwehr, S.; El Gueddari, N.E.; Bernard, F.; Rivera-Rodriguez, G.R.; Moerschbacher, B.M. Chitinosanase: A fungal chitosan hydrolyzing enzyme with a new and unusually specific cleavage pattern. *Carbohydr. Polym.* **2017**, *174*, 1121–1128. [CrossRef]

10. Kaczmarek, M.B.; Struszczyk-Swita, K.; Li, X.; Szczęsna-Antczak, M.; Daroch, M. Enzymatic modifications of chitin, chitosan, and chitooligosaccharides. *Front. Bioeng. Biotechnol.* **2019**, *7*, 243. [CrossRef]

11. Pramanik, S.; Sali, V. Connecting the dots in drug delivery: A tour d'horizon of chitosan-based nanocarriers system. *Int. J. Biol. Macromol.* **2021**, *169*, 103–121. [CrossRef]

12. Zargar, V.; Asghari, M.; Dashti, A. A review on chitin and chitosan polymers: Structure, chemistry, solubility, derivatives, and applications. *ChemBioEng Rev.* **2015**, *2*, 204–226. [CrossRef]

13. Islam, M.S.; Haque, P.; Rashid, T.U.; Khan, M.N.; Mallik, A.K.; Khan, M.N.I.; Khan, M.; Rahman, M.M. Core–shell drug carrier from folate conjugated chitosan obtained from prawn shell for targeted doxorubicin delivery. *J. Mater. Sci. Mater. Med.* **2017**, *28*, 55. [CrossRef]

14. Ali, A.; Ahmed, S. A review on chitosan and its nanocomposites in drug delivery. *Int. J. Biol. Macromol.* **2018**, *109*, 273–286. [CrossRef]

15. Shariatinia, Z.; Jalali, A.M. Chitosan-based hydrogels: Preparation, properties and applications. *Int. J. Biol. Macromol.* **2018**, *115*, 194–220. [CrossRef]

16. Li, J.; Cai, C.; Li, J.; Li, J.; Li, J.; Sun, T.; Wang, L.; Wu, H.; Yu, G. Chitosan-based nanomaterials for drug delivery. *Molecules* **2018**, *23*, 2661. [CrossRef]

17. Taylor, P.; Dutta, P.K.; Ravikumar, M.N.V.; Dutta, J. Chitin and chitosan for versatile applications. *J. Macromol. Sci. Part C* **2002**, *42*, 37–41. [CrossRef]

18. Gorantla, S.; Dabholkar, N.; Sharma, S.; Krishna, V.; Alexander, A.; Singhvi, G. Chitosan-based microneedles as a potential platform for drug delivery through the skin: Trends and regulatory aspects. *Int. J. Biol. Macromol.* **2021**, *184*, 438–453. [CrossRef] [PubMed]

19. Martau, G.A.; Mihai, M.; Vodnar, D.C. The use of chitosan, alginate, and pectin in the biomedical and food sector-biocompatibility, bioadhesiveness, and biodegradability. *Polymers* **2019**, *11*, 1837. [CrossRef]

20. Eivazzadeh-Keihan, R.; Noruzi, E.B.; Mehrban, S.F.; Aliabadi, H.A.M.; Karimi, M.; Mohammadi, A.; Maleki, A.; Mahdavi, M.; Larijani, B.; Shalan, A.E. Review: The latest advances in biomedical applications of chitosan hydrogel as a powerful natural structure with eye-catching biological properties. *J. Mater. Sci.* **2022**, *57*, 3855–3891. [CrossRef]

21. Daraghmeh, N.H.; Chowdhry, B.Z.; Leharne, S.A.; Al Omari, M.M.; Badwan, A.A. Chitin. *Profiles Drug Subst. Excip. Relat. Methodol.* **2011**, *36*, 35–102. [CrossRef] [PubMed]

22. Knidri, H.E.L.; Belaabed, R.; El, R.; Laajeb, A.; Addaou, A.; Lahsini, A. Physicochemical characterization of chitin and chitosan produced from parapenaeus longirostris shrimp shell wastes. *J. Mater. Environ. Sci.* **2017**, *8*, 3648–3653.

23. Hashemi, M.; Nazari, Z.; Noshirvani, N. Synthesis of chitosan based magnetic molecularly imprinted polymers for selective separation and spectrophotometric determination of histamine in tuna fish. *Carbohydr. Polym.* **2017**, *177*, 306–314. [CrossRef] [PubMed]

24. Bonilla, J.; Fortunati, E.; Atarés, L.; Chiralt, A.; Kenny, J.M. Physical, structural and antimicrobial properties of poly vinyl alcohol–chitosan biodegradable films. *Food Hydrocoll.* **2014**, *35*, 463–470. [CrossRef]

25. Shajahan, A.; Shankar, S.; Sathiyaseelan, A.; Narayan, K.S.; Narayanan, V.; Kaviyarasan, V.; Ignacimuthu, S. Comparative studies of chitosan and its nanoparticles for the adsorption efficiency of various dyes. *Int. J. Biol. Macromol.* **2017**, *104*, 1449–1458. [CrossRef] [PubMed]

26. Roy, J.C.; Salaün, F.; Giraud, S.; Ferri, A. Solubility of chitin: Solvents, solution behaviors and their related mechanisms. In *Solubility of Polysaccharides*; IntechOpen: Rijeka, Croatia, 2017; Chapter 7; ISBN 978-953-51-3650-7.

27. Kurita, K.; Kamiya, M.; Nishimura, S.I. Solubilization of a rigid polysaccharide: Controlled partial N-acetylation of chitosan to develop solubility. *Carbohydr. Polym.* **1991**, *16*, 83–92. [CrossRef]

28. Hamedi, H.; Moradi, S.; Hudson, S.M.; Tonelli, A.E. Chitosan based hydrogels and their applications for drug delivery in wound dressings: A review. *Carbohydr. Polym.* **2018**, *199*, 445–460. [CrossRef]

29. Jayakumar, R.; Prabaharan, M.; Nair, S.V.; Tokura, S.; Tamura, H.; Selvamurugan, N. Novel carboxymethyl derivatives of chitin and chitosan materials and their biomedical applications. *Prog. Mater. Sci.* **2010**, *55*, 675–709. [CrossRef]

30. Kubota, N.; Tatsumoto, N.; Sano, T.; Toya, K. A simple preparation of half N-acetylated chitosan highly soluble in water and aqueous organic solvents. *Carbohydr. Res.* **2000**, *324*, 268–274. [CrossRef]

31. Kasaai, M.R.; Arul, J. Intrinsic viscosity—Molecular weight relationship for chitosan. *J. Polym. Sci. B Polym. Phys.* **2000**, *38*, 2591–2598. [CrossRef]

32. Zhai, X.; Li, C.; Ren, D.; Wang, J.; Ma, C.; Abd El-Aty, A.M. The impact of chitooligosaccharides and their derivatives on the in vitro and in vivo antitumor activity: A comprehensive review. *Carbohydr. Polym.* **2021**, *266*, 118132. [CrossRef]

33. Onishi, H.; Machida, Y. Biodegradation and distribution of water-soluble chitosan in mice. *Biomaterials* **1999**, *20*, 175–182. [CrossRef]

34. Rao, S.B.; Sharma, C.P. Use of chitosan as a biomaterial: Studies on its safety and hemostatic potential. *J. Biomed. Mater. Res.* **1997**, *34*, 21–28. [CrossRef]

35. Verheul, R.J.; Amidi, M.; van Steenbergen, M.J.; van Riet, E.; Jiskoot, W.; Hennink, W.E. Influence of the degree of acetylation on the enzymatic degradation and in vitro biological properties of trimethylated chitosans. *Biomaterials* **2009**, *30*, 3129–3135. [CrossRef]

36. Kittur, F.S.; Vishu Kumar, A.B.; Varadaraj, M.C.; Tharanathan, R.N. Chitooligosaccharides—Preparation with the aid of pectinase isozyme from *Aspergillus Niger* and their antibacterial activity. *Carbohydr. Res.* **2005**, *340*, 1239–1245. [CrossRef]

37. Kittur, F.S.; Vishu Kumar, A.B.; Tharanathan, R.N. Low molecular weight Chitosans—Preparation by depolymerization with *Aspergillus Niger* pectinase, and characterization. *Carbohydr. Res.* **2003**, *338*, 1283–1290. [CrossRef]

38. McConnell, E.L.; Murdan, S.; Basit, A.W. An investigation into the digestion of chitosan (noncrosslinked and crosslinked) by human colonic bacteria. *J. Pharm. Sci.* **2008**, *97*, 3820–3829. [CrossRef]

39. Kean, T.; Thanou, M. Biodegradation, biodistribution and toxicity of chitosan. *Adv. Drug Deliv. Rev.* **2010**, *62*, 3–11. [CrossRef]

40. Aspden, T.J.; Mason, J.D.; Jones, N.S.; Lowe, J.; Skaugrud, O.; Illum, L. Chitosan as a nasal delivery system: The effect of chitosan solutions on in vitro and in vivo mucociliary transport rates in human turbinates and volunteers. *J. Pharm. Sci.* **1997**, *86*, 509–513. [CrossRef]

41. Aspden, T.J.; Adler, J.; Davis, S.S.; Skaugrud, Ø.; Illum, L. Chitosan as a nasal delivery system: Evaluation of the effect of chitosan on mucociliary clearance rate in the frog palate model. *Int. J. Pharm.* **1995**, *122*, 69–78. [CrossRef]

42. Dyer, A.M.; Hinchcliffe, M.; Watts, P.; Castile, J.; Jabbal-Gill, I.; Nankervis, R.; Smith, A.; Illum, L. Nasal delivery of insulin using novel chitosan based formulations: A comparative study in two animal models between simple chitosan formulations and chitosan nanoparticles. *Pharm. Res.* **2002**, *19*, 998–1008. [CrossRef]

43. Ribeiro, M.P.; Espiga, A.; Silva, D.; Baptista, P.; Henriques, J.; Ferreira, C.; Silva, J.C.; Borges, J.P.; Pires, E.; Chaves, P.; et al. Development of a new chitosan hydrogel for wound dressing. *Wound Repair Regen.* **2009**, *17*, 817–824. [CrossRef]

44. Carreño-Gómez, B.; Duncan, R. Evaluation of the biological properties of soluble chitosan and chitosan microspheres. *Int. J. Pharm.* **1997**, *148*, 231–240. [CrossRef]

45. Gades, M.D.; Stern, J.S. Chitosan supplementation and fecal fat excretion in men. *Obes. Res.* **2003**, *11*, 683–688. [CrossRef]

46. Tapola, N.S.; Lyyra, M.L.; Kolehmainen, R.M.; Sarkkinen, E.S.; Schauss, A.G. Safety aspects and cholesterol-lowering efficacy of chitosan tablets. *J. Am. Coll. Nutr.* **2008**, *27*, 22–30. [CrossRef]

47. Costa, E.M.; Silva, S.; Costa, M.R.; Pereira, M.; Campos, D.A.; Odila, J.; Madureira, A.R.; Cardelle-Cobas, A.; Tavaria, F.K.; Rodrigues, A.S.; et al. Chitosan mouthwash: Toxicity and in vivo validation. *Carbohydr. Polym.* **2014**, *111*, 385–392. [CrossRef]

48. Ravindranathan, S.; Koppolu, B.P.; Smith, S.G.; Zaharoff, D.A. Effect of chitosan properties on immunoreactivity. *Mar. Drugs* **2016**, *14*, 91. [CrossRef]

49. Baldrick, P. The safety of chitosan as a pharmaceutical excipient. *Regul. Toxicol. Pharmacol.* **2010**, *56*, 290–299. [CrossRef]

50. Dowling, M.B.; Kumar, R.; Keibler, M.A.; Hess, J.R.; Bochicchio, G.V.; Raghavan, S.R. A self-assembling hydrophobically modified chitosan capable of reversible hemostatic action. *Biomaterials* **2011**, *32*, 3351–3357. [CrossRef]

51. Horio, T.; Ishihara, M.; Fujita, M.; Kishimoto, S.; Kanatani, Y.; Ishizuka, T.; Nogami, Y.; Nakamura, S.; Tanaka, Y.; Morimoto, Y.; et al. Effect of photocrosslinkable chitosan hydrogel and its sponges to stop bleeding in a rat liver injury model. *Artif. Organs* **2010**, *34*, 342–347. [CrossRef]

52. Valentine, R.; Athanasiadis, T.; Moratti, S.; Hanton, L.; Robinson, S.; Wormald, P.-J. The efficacy of a novel chitosan gel on hemostasis and wound healing after endoscopic sinus surgery. *Am. J. Rhinol. Allergy* **2010**, *24*, 70–75. [CrossRef]

53. Islam, M.M.; Shahruzzaman, M.; Biswas, S.; Nurus Sakib, M.; Rashid, T.U. Chitosan based bioactive materials in tissue engineering applications—A review. *Bioact. Mater.* **2020**, *5*, 164–183. [CrossRef] [PubMed]

54. Li, Q.; Dunn, E.T.; Grandmaison, E.W.; Goosen, M.F.A. Applications and properties of chitosan. *J. Bioact. Compat. Polym.* **1992**, *7*, 370–397. [CrossRef]

55. Tolaimate, A.; Desbrieres, J.; Rhazi, M.; Alagui, A. Contribution to the preparation of chitins and chitosans with controlled physico-chemical properties. *Polymer* **2003**, *44*, 7939–7952. [CrossRef]

56. Rashid, T.U.; Rahman, M.M.; Kabir, S.; Shamsuddin, S.M.; Khan, M.A. A new approach for the preparation of chitosan from γ-irradiation of prawn shell: Effects of radiation on the characteristics of chitosan. *Polym. Int.* **2012**, *61*, 1302–1308. [CrossRef]

57. Kumari, S.; Rath, P.K. Extraction and characterization of chitin and chitosan from (*Labeo Rohit*) fish scales. *Procedia Mater. Sci.* **2014**, *6*, 482–489. [CrossRef]

58. Methacanon, P.; Prasitsilp, M.; Pothsree, T.; Pattaraarchachai, J. Heterogeneous N-deacetylation of squid chitin in alkaline solution. *Carbohydr. Polym.* **2003**, *52*, 119–123. [CrossRef]

59. Pelletier, A.; Lemire, I.; Sygusch, J.; Chornet, E.; Overend, R.P. Chitin/chitosan transformation by thermo-mechano-chemical treatment including characterization by enzymatic depolymerization. *Biotechnol. Bioeng.* **1990**, *36*, 310–315. [CrossRef]

60. Focher, B.; Beltrame, P.L.; Naggi, A.; Torri, G. Alkaline N-deacetylation of chitin enhanced by flash treatments. reaction kinetics and structure modifications. *Carbohydr. Polym.* **1990**, *12*, 405–418. [CrossRef]

61. Domard, A.; Roberts, G.A.F.; Varum, K.M. Advances in chitin science. *Domard A* **1997**, 410.

62. Lertwattanaseri, T.; Ichikawa, N.; Mizoguchi, T.; Tanaka, Y.; Chirachanchai, S. Microwave technique for efficient deacetylation of chitin nanowhiskers to a chitosan nanoscaffold. *Carbohydr. Res.* **2009**, *344*, 331–335. [CrossRef]

63. Aranaz, I.; Mengibar, M.; Harris, R.; Panos, I.; Miralles, B.; Acosta, N.; Galed, G.; Heras, A. Functional characterization of chitin and chitosan. *Curr. Chem. Biol.* **2012**, *3*, 203–230. [CrossRef]

64. Mima, S.; Miya, M.; Iwamoto, R.; Yoshikawa, S. Highly deacetylated chitosan and its properties. *J. Appl. Polym. Sci.* **1983**, *28*, 1909–1917. [CrossRef]

65. Isa, M.H.M.; Yasir, M.S.; Hasan, A.B.; Fadilah, N.I.M.; Hassan, A.R. The effect of gamma irradiation on chitosan and its application as a plant growth promoter in Chinese kale (*Brassica Alboglabra*). *AIP Conf. Proc.* **2016**, *1704*, 030003. [CrossRef]

66. Dimassi, S.; Tabary, N.; Chai, F.; Blanchemain, N.; Martel, B. Sulfonated and sulfated chitosan derivatives for biomedical applications: A review. *Carbohydr. Polym.* **2018**, *202*, 382–396. [CrossRef]

67. Shariatinia, Z. Carboxymethyl chitosan: Properties and biomedical applications. *Int. J. Biol. Macromol.* **2018**, *120*, 1406–1419. [CrossRef]

68. Qin, Y.; Li, P.; Guo, Z. Cationic chitosan derivatives as potential antifungals: A review of structural optimization and applications. *Carbohydr. Polym.* **2020**, *236*, 116002. [CrossRef]

69. Snyman, D.; Hamman, J.H.; Kotze, J.S.; Rollings, J.E.; Kotzé, A.F. The relationship between the absolute molecular weight and the degree of quaternisation of N-trimethyl chitosan chloride. *Carbohydr. Polym.* **2002**, *50*, 145–150. [CrossRef]

70. Wang, T.; Farajollahi, M.; Choi, Y.S.; Lin, I.-T.; Marshall, J.E.; Thompson, N.M.; Kar-Narayan, S.; Madden, J.D.W.; Smoukov, S.K. Electroactive polymers for sensing. *Interface Focus* **2016**, *6*, 20160026. [CrossRef]

71. Sarmento, B.; Goycoolea, F.M.; Sosnik, A.; das Neves, J. Chitosan and chitosan derivatives for biological applications: Chemistry and functionalization. *Int. J. Carbohydr. Chem.* **2011**, *2011*, 802693. [CrossRef]

72. Zhang, Y.; Qu, X.F.; Zhu, C.L.; Yang, H.J.; Lu, C.H.; Wang, W.L.; Pang, Y.; Yang, C.; Chen, L.J.; Li, X.F. A stable quaternized chitosan-black phosphorus nanocomposite for synergetic disinfection of antibiotic-resistant pathogens. *ACS Appl. Bio. Mater.* **2021**, *4*, 4821–4832. [CrossRef]

73. Yadav, A.V.; Bhise, S.B. Chitosan: A potential biomaterial effective against typhoid. *Curr. Sci.* **2004**, *87*, 1176–1178.

74. Dilamian, M.; Montazer, M.; Masoumi, J. Antimicrobial electrospun membranes of chitosan/poly(ethylene oxide) incorporating poly(hexamethylene biguanide) hydrochloride. *Carbohydr. Polym.* **2013**, *94*, 364–371. [CrossRef]

75. Husain, S.; Al-Samadani, K.H.; Najeeb, S.; Zafar, M.S.; Khurshid, Z.; Zohaib, S.; Qasim, S.B. Chitosan biomaterials for current and potential dental applications. *Materials* **2017**, *10*, 602. [CrossRef]

76. Jeon, Y.-J.; Park, P.-J.; Kim, S.-K. Antimicrobial effect of chitooligosaccharides produced by bioreactor. *Carbohydr. Polym.* **2001**, *44*, 71–76. [CrossRef]

77. Fatima, I.; Rasul, A.; Shah, S.; Saadullah, M.; Islam, N.; Khames, A.; Salawi, A.; Ahmed, M.M.; Almoshari, Y.; Abbas, G.; et al. Novasomes as nano-vesicular carriers to enhance topical delivery of fluconazole: A new approach to treat fungal infections. *Molecules* **2022**, *27*, 2936. [CrossRef]

78. Abourehab, M.A.S.; Khames, A.; Genedy, S.; Mostafa, S.; Khaleel, M.A.; Omar, M.M.; el Sisi, A.M. Sesame oil-based nanostructured lipid carriers of nicergoline, intranasal delivery system for brain targeting of synergistic cerebrovascular protection. *Pharmaceutics* **2021**, *13*, 581. [CrossRef]

79. Abd El-Aziz, E.A.E.D.; Elgayar, S.F.; Mady, F.M.; Abourehab, M.A.S.; Hasan, O.A.; Reda, L.M.; Alaaeldin, E. The potential of optimized liposomes in enhancement of cytotoxicity and apoptosis of encapsulated Egyptian propolis on hep-2 cell line. *Pharmaceutics* **2021**, *13*, 2184. [CrossRef]

80. Ashfaq, M.; Shah, S.; Rasul, A.; Hanif, M.; Khan, H.U.; Khames, A.; Abdelgawad, M.A.; Ghoneim, M.M.; Ali, M.Y.; Abourehab, M.A.S.; et al. Enhancement of the solubility and bioavailability of pitavastatin through a self-nanoemulsifying drug delivery system (SNEDDS). *Pharmaceutics* **2022**, *14*, 482. [CrossRef]

81. Abourehab, M.A.S.; Ahmed, O.A.A.; Balata, G.F.; Almalki, W.H. Self-assembled biodegradable polymeric micelles to improve dapoxetine delivery across the blood–brain barrier. *Int. J. Nanomed.* **2018**, *13*, 3679–3687. [CrossRef]

82. Dong, J.; Tao, L.; Abourehab, M.A.S.; Hussain, Z. Design and development of novel hyaluronate-modified nanoparticles for combo-delivery of curcumin and alendronate: Fabrication, Characterization, and cellular and molecular evidences of enhanced bone regeneration. *Int. J. Biol. Macromol.* **2018**, *116*, 1268–1281. [CrossRef]

83. Zhuo, F.; Abourehab, M.A.S.; Hussain, Z. Hyaluronic acid decorated tacrolimus-loaded nanoparticles: Efficient approach to maximize dermal targeting and anti-dermatitis efficacy. *Carbohydr. Polym.* **2018**, *197*, 478–489. [CrossRef] [PubMed]

84. Dawoud, M.; Abourehab, M.A.S.; Abdou, R. Monoolein cubic nanoparticles as novel carriers for docetaxel. *J. Drug Deliv. Sci. Technol.* **2020**, *56*, 101501. [CrossRef]

85. Huang, G.; Liu, Y.; Chen, L. Chitosan and its derivatives as vehicles for drug delivery. *Drug Deliv.* **2017**, *24*, 108–113. [CrossRef] [PubMed]

86. Pramanik, S.; Mohanto, S.; Manne, R.; Rajendran, R.R.; Deepak, A.; Edapully, S.J.; Patil, T.; Katari, O. Nanoparticle-based drug delivery system: The magic bullet for the treatment of chronic pulmonary diseases. *Mol. Pharm.* **2021**, *18*, 3671–3718. [CrossRef]

87. Abourehab, M.A.S.; Ansari, M.J.; Singh, A.; Hassan, A.; Abdelgawad, M.A.; Shrivastav, P.; Abualsoud, B.M.; Amaral, L.S.; Pramanik, S. Cubosomes as an emerging platform for drug delivery: A review of the state of the art. *J. Mater. Chem. B* **2022**, *10*, 2781–2819. [CrossRef]

88. Abdel Mouez, M.; Zaki, N.M.; Mansour, S.; Geneidi, A.S. Bioavailability enhancement of verapamil HCl via intranasal chitosan microspheres. *Eur. J. Pharm. Sci.* **2014**, *51*, 59–66. [CrossRef]

89. Zhang, Y.; Wei, W.; Lv, P.; Wang, L.; Ma, G. Preparation and evaluation of alginate-chitosan microspheres for oral delivery of insulin. *Eur. J. Pharm. Biopharm.* **2011**, *77*, 11–19. [CrossRef]

90. Wang, Y.; Liu, P.; Du, J.; Sun, Y.; Li, F.; Duan, Y. Targeted SiRNA delivery by anti-HER2 antibody-modified nanoparticles of MPEG-chitosan diblock copolymer. *J. Biomater. Sci. Polym. Ed.* **2013**, *24*, 1219–1232. [CrossRef]

91. Kalsoom Khan, A.; Saba, A.U.; Nawazish, S.; Akhtar, F.; Rashid, R.; Mir, S.; Nasir, B.; Iqbal, F.; Afzal, S.; Pervaiz, F.; et al. Carrageenan based bionanocomposites as drug delivery tool with special emphasis on the influence of ferromagnetic nanoparticles. *Oxid. Med. Cell Longev.* **2017**, *2017*, 8158315. [CrossRef]

92. Saeed, R.M.; Dmour, I.; Taha, M.O. Stable chitosan-based nanoparticles using polyphosphoric acid or hexametaphosphate for tandem ionotropic/covalent crosslinking and subsequent investigation as novel vehicles for drug delivery. *Front. Bioeng. Biotechnol.* **2020**, *8*, 4. [CrossRef]

93. Yu, Z.; Ma, L.; Ye, S.; Li, G.; Zhang, M. Construction of an environmentally friendly octenylsuccinic anhydride modified PH-sensitive chitosan nanoparticle drug delivery system to alleviate inflammation and oxidative stress. *Carbohydr. Polym.* **2020**, *236*, 115972. [CrossRef]

94. Barbosa, A.I.; Costa Lima, S.A.; Reis, S. Application of PH-responsive fucoidan/chitosan nanoparticles to improve oral quercetin delivery. *Molecules* **2019**, *24*, 346. [CrossRef]

95. Wang, S.; Gao, Z.; Liu, L.; Li, M.; Zuo, A.; Guo, J. Preparation, in vitro and in vivo evaluation of chitosan-sodium alginate-ethyl cellulose polyelectrolyte film as a novel buccal mucosal delivery vehicle. *Eur. J. Pharm. Sci.* **2022**, *168*, 106085. [CrossRef]

96. Hussain, Z.; Rahim, M.A.; Jan, N.; Shah, H.; Rawas-Qalaji, M.; Khan, S.; Sohail, M.; Thu, H.E.; Ramli, N.A.; Sarfraz, R.M.; et al. Cell membrane cloaked nanomedicines for bio-imaging and immunotherapy of cancer: Improved pharmacokinetics, cell internalization and anticancer efficacy. *J. Control. Release* **2021**, *335*, 130–157. [CrossRef]

97. Kheiri, K.; Sohrabi, N.; Mohammadi, R.; Amini-Fazl, M.S. Preparation and characterization of magnetic nanohydrogel based on chitosan for 5-fluorouracil drug delivery and kinetic study. *Int. J. Biol. Macromol.* **2022**, *202*, 191–198. [CrossRef]

98. Ahmed, M.M.; Fatima, F.; Anwer, M.K.; Ansari, M.J.; Das, S.S.; Alshahrani, S.M. Development and characterization of ethyl cellulose nanosponges for sustained release of brigatinib for the treatment of non-small cell lung cancer. *J. Polym. Eng.* **2020**, *40*, 823–832. [CrossRef]

99. Ansari, M.J.; Alshetaili, A.; Aldayel, I.A.; Alablan, F.M.; Alsulays, B.; Alshahrani, S.; Alalaiwe, A.; Ansari, M.N.; Ur Rehman, N.; Shakeel, F. Formulation, characterization, in vitro and in vivo evaluations of self-nanoemulsifying drug delivery system of luteolin. *J. Taibah Univ. Sci.* **2020**, *14*, 1386–1401. [CrossRef]

100. Ansari, M.J. Factors affecting preparation and properties of nanoparticles by nanoprecipitation method. *Indo Am. J. Pharm. Sci.* **2017**, *2017*, 4854–4858.

101. Ouerghi, O.; Geesi, M.H.; Ibnouf, E.O.; Ansari, M.J.; Alam, P.; Elsanousi, A.; Kaiba, A.; Riadi, Y. Sol-gel synthesized rutile TiO₂ nanoparticles loaded with cardamom essential oil: Enhanced antibacterial activity. *J. Drug Deliv. Sci. Technol.* **2021**, *64*, 102581. [CrossRef]

102. Ansari, M.J. An overview of techniques for multifold enhancement in solubility of poorly soluble drugs. *Curr. Issues Pharm. Med. Sci.* **2019**, *32*, 203–209. [CrossRef]

103. Zhu, X.; Yu, Z.; Feng, L.; Deng, L.; Fang, Z.; Liu, Z.; Li, Y.; Wu, X.; Qin, L.; Guo, R.; et al. Chitosan-based nanoparticle co-delivery of docetaxel and curcumin ameliorates anti-tumor chemoimmunotherapy in lung cancer. *Carbohydr. Polym.* **2021**, *268*, 118237. [CrossRef]

104. Zhang, L.; Li, Q.; Chen, J.; Tang, C.; Yin, C. Enhanced antitumor efficacy of glutathione-responsive chitosan based nanoparticles through co-delivery of chemotherapeutics, genes, and immune agents. *Carbohydr. Polym.* **2021**, *270*, 118384. [CrossRef]

105. Amiry, F.; Sazegar, M.R.; Mahmoudi, A. Smart polymeric nanocomposite based on protonated aluminosilicate, curcumin, and chitosan for mesalamine drug delivery as an anti-inflammatory nanocarrier. *Microporous Mesoporous Mater.* **2022**, *330*, 111533. [CrossRef]

106. Grant, J.J.; Pillai, S.C.; Perova, T.S.; Hehir, S.; Hinder, S.J.; McAfee, M.; Breen, A. Electrospun fibres of chitosan/PVP for the effective chemotherapeutic drug delivery of 5-fluorouracil. *Chemosensors* **2021**, *9*, 70. [CrossRef]

107. Jin, Z.; Hu, G.; Zhao, K. Mannose-anchored quaternized chitosan/thiolated carboxymethyl chitosan composite NPs as mucoadhesive carrier for drug delivery. *Carbohydr. Polym.* **2022**, *283*, 119174. [CrossRef] [PubMed]

108. Lohiya, G.; Katti, D.S. Carboxylated chitosan-mediated improved efficacy of mesoporous silica nanoparticle-based targeted drug delivery system for breast cancer therapy. *Carbohydr. Polym.* **2022**, *277*, 118822. [CrossRef] [PubMed]

109. Hoang, H.T.; Jo, S.H.; Phan, Q.T.; Park, H.; Park, S.H.; Oh, C.W.; Lim, K.T. Dual PH-/thermo-responsive chitosan-based hydrogels prepared using "click" chemistry for colon-targeted drug delivery applications. *Carbohydr. Polym.* **2021**, *260*, 117812. [CrossRef] [PubMed]

110. Li, D.; Wang, S.; Meng, Y.; Guo, Z.; Cheng, M.; Li, J. Fabrication of self-healing pectin/chitosan hybrid hydrogel via diels-alder reactions for drug delivery with high swelling property, PH-responsiveness, and cytocompatibility. *Carbohydr. Polym.* **2021**, *268*, 118244. [CrossRef]

111. Rahnama, H.; Nouri Khorasani, S.; Aminoroaya, A.; Molavian, M.R.; Allafchian, A.; Khalili, S. Facile preparation of chitosan-dopamine-inulin aldehyde hydrogel for drug delivery application. *Int. J. Biol. Macromol.* **2021**, *185*, 716–724. [CrossRef]

112. Yang, D.; Gao, K.; Bai, Y.; Lei, L.; Jia, T.; Yang, K.; Xue, C. Microfluidic synthesis of chitosan-coated magnetic alginate microparticles for controlled and sustained drug delivery. *Int. J. Biol. Macromol.* **2021**, *182*, 639–647. [CrossRef]

113. Gerami, S.E.; Pourmadadi, M.; Fatoorehchi, H.; Yazdian, F.; Rashedi, H.; Nigjeh, M.N. Preparation of PH-sensitive chitosan/polyvinylpyrrolidone/α-Fe2O3 nanocomposite for drug delivery application: Emphasis on ameliorating restrictions. *Int. J. Biol. Macromol.* **2021**, *173*, 409–420. [CrossRef]

114. Zhang, K.; Gao, J.; Li, S.; Ma, T.; Deng, L.; Kong, Y. Construction of a PH-responsive drug delivery platform based on the hybrid of mesoporous silica and chitosan. *J. Saudi Chem. Soc.* **2021**, *25*, 101174. [CrossRef]

115. Aigner, A. Applications of RNA interference: Current state and prospects for SiRNA-based strategies in vivo. *Appl. Microbiol. Biotechnol.* **2007**, *76*, 9–21. [CrossRef]

116. Debus, H.; Baumhof, P.; Probst, J.; Kissel, T. Delivery of messenger RNA using poly(ethylene imine)-poly(ethylene glycol)-copolymer blends for polyplex formation: Biophysical characterization and in vitro transfection properties. *J. Control. Release* **2010**, *148*, 334–343. [CrossRef]

117. Plianwong, S.; Opanasopit, P.; Ngawhirunpat, T.; Rojanarata, T. Fast, facile and ethidium bromide-free assay based on the use of adsorption indicator for the estimation of polyethylenimine to nucleic acid ratio of complete polyplex assembly for gene delivery. *Talanta* **2013**, *115*, 241–245. [CrossRef]

118. Ghanbari, P.; Mohseni, M.; Tabasinezhad, M.; Yousefi, B.; Saei, A.A.; Sharifi, S.; Rashidi, M.R.; Samadi, N. Inhibition of survivin restores the sensitivity of breast cancer cells to docetaxel and vinblastine. *Appl. Biochem. Biotechnol.* **2014**, *174*, 667–681. [CrossRef]

119. Pennati, M.; Folini, M.; Zaffaroni, N. Targeting survivin in cancer therapy. *Expert Opin. Ther. Targets* **2008**, *12*, 463–476. [CrossRef]

120. Jere, D.; Jiang, H.-L.; Kim, Y.-K.; Arote, R.; Choi, Y.-J.; Yun, C.-H.; Cho, M.-H.; Cho, C.-S. Chitosan-graft-polyethylenimine for Akt1 SiRNA delivery to lung cancer cells. *Int. J. Pharm.* **2009**, *378*, 194–200. [CrossRef]

121. Kami, D.; Takeda, S.; Itakura, Y.; Gojo, S.; Watanabe, M.; Toyoda, M. Application of magnetic nanoparticles to gene delivery. *Int. J. Mol. Sci.* **2011**, *12*, 3705–3722. [CrossRef]

122. Wang, J.; Dou, B.; Bao, Y. Efficient targeted PDNA/SiRNA delivery with folate-low-molecular-weight polyethyleneimine-modified pullulan as non-viral carrier. *Mater. Sci. Eng. C Mater. Biol. Appl.* **2014**, *34*, 98–109. [CrossRef]

123. Singha, K.; Namgung, R.; Kim, W.J. Polymers in small-interfering RNA delivery. *Nucleic Acid Ther.* **2011**, *21*, 133–147. [CrossRef]

124. Arami, S.; Mahdavi, M.; Fathi, M.; Entezami, A.A. Synthesis and characterization of Fe3O4-PEG-LAC-chitosan-PEI nanoparticle as a survivin SiRNA delivery system. *Hum. Exp. Toxicol.* **2016**, *36*, 227–237. [CrossRef]

125. Suarato, G.; Li, W.; Meng, Y. Role of PH-responsiveness in the design of chitosan-based cancer nanotherapeutics: A review. *Biointerphases* **2016**, *11*, 04B201. [CrossRef]

126. van der Meel, R.; Vehmeijer, L.J.C.; Kok, R.J.; Storm, G.; van Gaal, E.V.B. Ligand-targeted particulate nanomedicines undergoing clinical evaluation: Current status. *Adv. Drug Deliv. Rev.* **2013**, *65*, 1284–1298. [CrossRef]

127. Mei, L.; Fu, L.; Shi, K.; Zhang, Q.; Liu, Y.; Tang, J.; Gao, H.; Zhang, Z.; He, Q. Increased tumor targeted delivery using a multistage liposome system functionalized with RGD, TAT and cleavable PEG. *Int. J. Pharm.* **2014**, *468*, 26–38. [CrossRef]

128. Zheng, Q.C.; Jiang, S.; Wu, Y.Z.; Shang, D.; Zhang, Y.; Hu, S.B.; Cheng, X.; Zhang, C.; Sun, P.; Gao, Y.; et al. Dual-targeting nanoparticle-mediated gene therapy strategy for hepatocellular carcinoma by delivering small interfering RNA. *Front. Bioeng. Biotechnol.* **2020**, *8*, 512. [CrossRef]

129. Zhao, M.; Zhu, T.; Chen, J.; Cui, Y.; Zhang, X.; Lee, R.J.; Sun, F.; Li, Y.; Teng, L. PLGA/PCADK composite microspheres containing hyaluronic acid–chitosan SiRNA nanoparticles: A rational design for rheumatoid arthritis therapy. *Int. J. Pharm.* **2021**, *596*, 120204. [CrossRef]

130. Baghdan, E.; Pinnapireddy, S.R.; Strehlow, B.; Engelhardt, K.H.; Schäfer, J.; Bakowsky, U. Lipid coated chitosan-DNA nanoparticles for enhanced gene delivery. *Int. J. Pharm.* **2018**, *535*, 473–479. [CrossRef]

131. Zhang, H.; Zhang, Y.; Williams, R.O., III; Smyth, H.D.C. Development of PEGylated chitosan/CRISPR-Cas9 dry powders for pulmonary delivery via thin-film freeze-drying. *Int. J. Pharm.* **2021**, *605*, 120831. [CrossRef]

132. Abdelhamid, H.N.; Dowaidar, M.; Langel, Ü. Carbonized chitosan encapsulated hierarchical porous zeolitic imidazolate frameworks nanoparticles for gene delivery. *Microporous Mesoporous Mater.* **2020**, *302*, 110200. [CrossRef]

133. Jaiswal, S.; Dutta, P.K.; Kumar, S.; Koh, J.; Pandey, S. Methyl methacrylate modified chitosan: Synthesis, characterization and application in drug and gene delivery. *Carbohydr. Polym.* **2019**, *211*, 109–117. [CrossRef] [PubMed]

134. Dowaidar, M.; Nasser Abdelhamid, H.; Hällbrink, M.; Langel, Ü.; Zou, X. Chitosan enhances gene delivery of oligonucleotide complexes with magnetic nanoparticles–cell-penetrating peptide. *J. Biomater. Appl.* **2018**, *33*, 392–401. [CrossRef] [PubMed]

135. Rahmani, S.; Hakimi, S.; Esmaeily, A.; Samadi, F.Y.; Mortazavian, E.; Nazari, M.; Mohammadi, Z.; Tehrani, N.R.; Tehrani, M.R. Novel chitosan based nanoparticles as gene delivery systems to cancerous and noncancerous cells. *Int. J. Pharm.* **2019**, *560*, 306–314. [CrossRef] [PubMed]

136. Huang, G.; Chen, Q.; Wu, W.; Wang, J.; Chu, P.K.; Bai, H.; Tang, G. Reconstructed chitosan with alkylamine for enhanced gene delivery by promoting endosomal escape. *Carbohydr. Polym.* **2020**, *227*, 115339. [CrossRef] [PubMed]

137. Xue, Y.; Wang, N.; Zeng, Z.; Huang, J.; Xiang, Z.; Guan, Y.-Q. Neuroprotective effect of chitosan nanoparticle gene delivery system grafted with acteoside (ACT) in Parkinson's Disease models. *J. Mater. Sci. Technol.* **2020**, *43*, 197–207. [CrossRef]

138. Iravani Kashkouli, K.; Torkzadeh-Mahani, M.; Mosaddegh, E. Synthesis and characterization of aminotetrazole-functionalized magnetic chitosan nanocomposite as a novel nanocarrier for targeted gene delivery. *Mater. Sci. Eng. C* **2018**, *89*, 166–174. [CrossRef] [PubMed]

139. Yasar, H.; Ho, D.-K.; De Rossi, C.; Herrmann, J.; Gordon, S.; Loretz, B.; Lehr, C.-M. Starch-chitosan polyplexes: A versatile carrier system for anti-infectives and gene delivery. *Polymers* **2018**, *10*, 252. [CrossRef] [PubMed]

140. El-Feky, G.S.; Zayed, G.M.; Elshaier, Y.A.M.M.; Alsharif, F.M. Chitosan-gelatin hydrogel crosslinked with oxidized sucrose for the ocular delivery of timolol maleate. *J. Pharm. Sci.* **2018**, *107*, 3098–3104. [CrossRef] [PubMed]

141. Rebekah, A.; Sivaselvam, S.; Viswanathan, C.; Prabhu, D.; Gautam, R.; Ponpandian, N. Magnetic nanoparticle-decorated graphene oxide-chitosan composite as an efficient nanocarrier for protein delivery. *Colloids Surf. A Physicochem. Eng. Asp.* **2021**, *610*, 125913. [CrossRef]

142. Zhu, Y.; Marin, L.M.; Xiao, Y.; Gillies, E.R.; Siqueira, W.L. Ph-sensitive chitosan nanoparticles for salivary protein delivery. *Nanomaterials* **2021**, *11*, 1028. [CrossRef]

143. Ansari, M.J.; Rajendran, R.R.; Mohanto, S.; Agarwal, U.; Panda, K.; Dhotre, K.; Manne, R.; Deepak, A.; Zafar, A.; Yasir, M.; et al. Poly(N-isopropylacrylamide)-based hydrogels for biomedical applications: A review of the state-of-the-art. *Gels* **2022**, *8*, 454. [CrossRef]

144. Jang, K.J.; Lee, W.S.; Park, S.; Han, J.; Kim, J.E.; Kim, B.M.; Chung, J.H. Sulfur(VI) fluoride exchange (SuFEx)-mediated synthesis of the chitosan-PEG conjugate and its supramolecular hydrogels for protein delivery. *Nanomaterials* **2021**, *11*, 318. [CrossRef]

145. Cao, J.; Cheng, J.; Xi, S.; Qi, X.; Shen, S.; Ge, Y. Alginate/chitosan microcapsules for in-situ delivery of the protein, interleukin-1 receptor antagonist (IL-1Ra), for the treatment of dextran sulfate sodium (DSS)-induced colitis in a mouse model. *Eur. J. Pharm. Biopharm.* **2019**, *137*, 112–121. [CrossRef]

146. Huang, J.; Deng, Y.; Ren, J.; Chen, G.; Wang, G.; Wang, F.; Wu, X. Novel in situ forming hydrogel based on xanthan and chitosan re-gelifying in liquids for local drug delivery. *Carbohydr. Polym.* **2018**, *186*, 54–63. [CrossRef]

147. Zhu, T.; Shi, L.; Ma, C.; Xu, L.; Yang, J.; Zhou, G.; Zhu, X.; Shen, L. Fluorinated chitosan-mediated intracellular catalase delivery for enhanced photodynamic therapy of oral cancer. *Biomater. Sci.* **2021**, *9*, 658–662. [CrossRef]

148. Vozza, G.; Danish, M.; Byrne, H.J.; Frías, J.M.; Ryan, S.M. Application of box-behnken experimental design for the formulation and optimisation of selenomethionine-loaded chitosan nanoparticles coated with zein for oral delivery. *Int. J. Pharm.* **2018**, *551*, 257–269. [CrossRef]

149. Zhang, R.; Luo, S.; Hao, L.-K.; Jiang, Y.-Y.; Gao, Y.; Zhang, N.-N.; Zhang, X.-C.; Song, Y.-M. Preparation and properties of thrombus-targeted urokinase/multi-walled carbon nanotubes (MWCNTs)-chitosan (CS)-RGD drug delivery system. *J. Biomed. Nanotechnol.* **2021**, *17*, 1711–1725. [CrossRef]

150. Huang, T.-H.; Hsu, S.; Chang, S.-W. Molecular interaction mechanisms of glycol chitosan self-healing hydrogel as a drug delivery system for gemcitabine and doxorubicin. *Comput. Struct. Biotechnol. J.* **2022**, *20*, 700–709. [CrossRef]

151. Shao, D.; Gao, Q.; Sheng, Y.; Li, S.; Kong, Y. Construction of a dual-responsive dual-drug delivery platform based on the hybrids of *Mesoporous Silica*, sodium hyaluronate, chitosan and oxidized sodium carboxymethyl cellulose. *Int. J. Biol. Macromol.* **2022**, *202*, 37–45. [CrossRef]

152. Soleimanbeigi, M.; Dousti, F.; Hassanzadeh, F.; Mirian, M.; Varshosaz, J.; Kasesaz, Y.; Rostami, M. Boron phenyl alanine targeted chitosan—PNIPAAm core–shell thermo-responsive nanoparticles: Boosting drug delivery to glioblastoma in BNCT. *Drug Dev. Ind. Pharm.* **2021**, *47*, 1607–1623. [CrossRef]

153. Hosseini, S.M.; Mazinani, S.; Abdouss, M.; Kalhor, H.; Kalantari, K.; Amiri, I.S.; Ramezani, Z. Designing chitosan nanoparticles embedded into graphene oxide as a drug delivery system. *Polym. Bull.* **2022**, *79*, 541–554. [CrossRef]

154. Farmanbar, N.; Mohseni, S.; Darroudi, M. Green synthesis of chitosan-coated magnetic nanoparticles for drug delivery of oxaliplatin and irinotecan against colorectal cancer cells. *Polym. Bull.* **2022**. [CrossRef]

155. Ijaz, H.; Tulain, U.R.; Minhas, M.U.; Mahmood, A.; Sarfraz, R.M.; Erum, A.; Danish, Z. Design and in vitro evaluation of PH-sensitive crosslinked chitosan-grafted acrylic acid copolymer (CS-Co-AA) for targeted drug delivery. *Int. J. Polym. Mater. Polym. Biomater.* **2022**, *71*, 336–348. [CrossRef]

156. Kim, T.-H.; Yun, Y.-P.; Shim, K.-S.; Kim, H.-J.; Kim, S.E.; Park, K.; Song, H.-R. In vitro anti-inflammation and chondrogenic differentiation effects of inclusion nanocomplexes of hyaluronic acid-beta cyclodextrin and simvastatin. *Tissue Eng. Regen. Med.* **2018**, *15*, 263–274. [CrossRef]

157. Wei, J.; Xue, W.; Yu, X.; Qiu, X.; Liu, Z. PH sensitive phosphorylated chitosan hydrogel as vaccine delivery system for intramuscular immunization. *J. Biomater. Appl.* **2017**, *31*, 1358–1369. [CrossRef]

158. Gao, X.; Liu, N.; Wang, Z.; Gao, J.; Zhang, H.; Li, M.; Du, Y.; Gao, X.; Zheng, A. Development and optimization of chitosan nanoparticle-based intranasal vaccine carrier. *Molecules* **2022**, *27*, 204. [CrossRef]

159. Zuo, Z.; Zou, Y.; Li, Q.; Guo, Y.; Zhang, T.; Wu, J.; He, C.; Eko, F.O. Intranasal immunization with inactivated chlamydial elementary bodies formulated in VCG-chitosan nanoparticles induces robust immunity against intranasal chlamydia psittaci challenge. *Sci. Rep.* **2021**, *11*, 10389. [CrossRef]

160. Zhang, J.; Sun, H.; Gao, C.; Wang, Y.; Cheng, X.; Yang, Y.; Gou, Q.; Lei, L.; Chen, Y.; Wang, X.; et al. Development of a chitosan-modified PLGA nanoparticle vaccine for protection against *Escherichia Coli* K1 caused meningitis in mice. *J. Nanobiotechnology* **2021**, *19*, 69. [CrossRef]

161. Zewail, M. Folic acid decorated chitosan-coated solid lipid nanoparticles for the oral treatment of rheumatoid arthritis. *Ther. Deliv.* **2021**, *12*, 297–310. [CrossRef]

162. Yang, Y.; Wu, H.; Fu, Q.; Xie, X.; Song, Y.; Xu, M.; Li, J. 3D-printed polycaprolactone-chitosan based drug delivery implants for personalized administration. *Mater. Des.* **2022**, *214*, 110394. [CrossRef]

163. Wei, H.; Liu, S.; Chu, Y.; Tong, Z.; Yang, M.; Guo, Y.; Chen, T.; Wu, Y.; Sun, H.; Fan, L. Hydrogel-based microneedles of chitosan derivatives for drug delivery. *React. Funct. Polym.* **2022**, *172*, 105200. [CrossRef]

164. Yuan, H.; Li, W.; Song, C.; Huang, R. An injectable supramolecular nanofiber-reinforced chitosan hydrogel with antibacterial and anti-inflammatory properties as potential carriers for drug delivery. *Int. J. Biol. Macromol.* **2022**, *205*, 563–573. [CrossRef]

165. Yu, Y.; Kim, D.H.; Suh, E.Y.; Jeong, S.-H.; Kwon, H.C.; Le, T.P.; Kim, Y.; Shin, S.-A.; Park, Y.-H.; Huh, K.M. Injectable glycol chitosan thermogel formulation for efficient inner ear drug delivery. *Carbohydr. Polym.* **2022**, *278*, 118969. [CrossRef]

166. Malik, N.S.; Ahmad, M.; Alqahtani, M.S.; Mahmood, A.; Barkat, K.; Khan, M.T.; Tulain, U.R.; Rashid, A. β-cyclodextrin chitosan-based hydrogels with tunable PH-responsive properties for controlled release of acyclovir: Design, characterization, safety, and pharmacokinetic evaluation. *Drug Deliv.* **2021**, *28*, 1093–1108. [CrossRef]

167. Kazemi-Andalib, F.; Mohammadikish, M.; Divsalar, A.; Sahebi, U. Hollow microcapsule with PH-sensitive chitosan/polymer shell for in vitro delivery of curcumin and gemcitabine. *Eur. Polym. J.* **2022**, *162*, 110887. [CrossRef]

168. Hongsa, N.; Thinbanmai, T.; Luesakul, U.; Sansanaphongpricha, K.; Muangsin, N. A novel modified chitosan/collagen coated-gold nanoparticles for 5-fluorouracil delivery: Synthesis, characterization, in vitro drug release studies, anti-inflammatory activity and in vitro cytotoxicity assay. *Carbohydr. Polym.* **2022**, *277*, 118858. [CrossRef]

169. Shah, M.K.; Azad, A.K.; Nawaz, A.; Ullah, S.; Latif, M.S.; Rahman, H.; Alsharif, K.F.; Alzahrani, K.J.; El-Kott, A.F.; Albrakati, A.; et al. Formulation development, characterization and antifungal evaluation of chitosan NPs for topical delivery of voriconazole in vitro and ex vivo. *Polymers* **2022**, *14*, 135. [CrossRef]

170. Affes, S.; Aranaz, I.; Acosta, N.; Heras, Á.; Nasri, M.; Maalej, H. Chitosan derivatives-based films as PH-sensitive drug delivery systems with enhanced antioxidant and antibacterial properties. *Int. J. Biol. Macromol.* **2021**, *182*, 730–742. [CrossRef]

171. Asghari, F.; Samiei, M.; Adibkia, K.; Akbarzadeh, A.; Davaran, S. Biodegradable and biocompatible polymers for tissue engineering application: A review. *Artif. Cells Nanomed. Biotechnol.* **2017**, *45*, 185–192. [CrossRef]

172. Jagga, S.; Hasnain, M.S.; Nayak, A.K. Chapter 14—Chitosan-based scaffolds in tissue engineering and regenerative medicine. In *Chitosan in Biomedical Applications*; Hasnain, M.S., Beg, S., Nayak, A.K., Eds.; Academic Press: Cambridge, MA, USA, 2022; pp. 329–354. ISBN 978-0-12-821058-1.

173. Lalwani, G.; Henslee, A.M.; Farshid, B.; Lin, L.; Kasper, F.K.; Qin, Y.-X.; Mikos, A.G.; Sitharaman, B. Two-dimensional nanostructure-reinforced biodegradable polymeric nanocomposites for bone tissue engineering. *Biomacromolecules* **2013**, *14*, 900–909. [CrossRef]

174. Holt, B.D.; Wright, Z.M.; Arnold, A.M.; Sydlik, S.A. Graphene oxide as a scaffold for bone regeneration. *Wiley Interdiscip. Rev. Nanomed. Nanobiotechnol.* **2017**, *9*, e1437. [CrossRef]

175. Morozowich, N.L.; Nichol, J.L.; Allcock, H.R. Investigation of apatite mineralization on antioxidant polyphosphazenes for bone tissue engineering. *Chem. Mater.* **2012**, *24*, 3500–3509. [CrossRef]

176. Balagangadharan, K.; Viji Chandran, S.; Arumugam, B.; Saravanan, S.; Devanand Venkatasubbu, G.; Selvamurugan, N. Chitosan/nano-hydroxyapatite/nano-zirconium dioxide scaffolds with MiR-590-5p for bone regeneration. *Int. J. Biol. Macromol.* **2018**, *111*, 953–958. [CrossRef]

177. Dubey, N.; Bentini, R.; Islam, I.; Cao, T.; Castro Neto, A.H.; Rosa, V. Graphene: A Versatile carbon-based material for bone tissue engineering. *Stem Cells Int.* **2015**, *2015*, 804213. [CrossRef]

178. Hasnain, M.S.; Nayak, A.K. 7—Nanocomposites for improved orthopedic and bone tissue engineering applications. In *Applications of Nanocomposite Materials in Orthopedics*; Inamuddin, A.M.A., Ali, M., Eds.; Woodhead Publishing: Sawston, UK, 2019; pp. 145–177. ISBN 978-0-12-813740-6.

179. Zhang, Y.; Dou, X.; Zhang, L.; Wang, H.; Zhang, T.; Bai, R.; Sun, Q.; Wang, X.; Yu, T.; Wu, D.; et al. Facile Fabrication of a biocompatible composite gel with sustained release of aspirin for bone regeneration. *Bioact. Mater.* **2022**, *11*, 130–139. [CrossRef]

180. Nazeer, M.A.; Yilgör, E.; Yilgör, I. Intercalated chitosan/hydroxyapatite nanocomposites: Promising materials for bone tissue engineering applications. *Carbohydr. Polym.* **2017**, *175*, 38–46. [CrossRef]

181. Pistone, A.; Iannazzo, D.; Celesti, C.; Piperopoulos, E.; Ashok, D.; Cembran, A.; Tricoli, A.; Nisbet, D. Engineering of chitosan-hydroxyapatite-magnetite hierarchical scaffolds for guided bone growth. *Materials* **2019**, *12*, 2321. [CrossRef]

182. Prakash, J.; Prema, D.; Venkataprasanna, K.S.; Balagangadharan, K.; Selvamurugan, N.; Venkatasubbu, G.D. Nanocomposite chitosan film containing graphene oxide/hydroxyapatite/gold for bone tissue engineering. *Int. J. Biol. Macromol.* **2020**, *154*, 62–71. [CrossRef]

183. Zou, M.; Sun, J.; Xiang, Z. Induction of M2-type macrophage differentiation for bone defect repair via an interpenetration network hydrogel with a GO-based controlled release system. *Adv. Healthc. Mater.* **2021**, *10*, 2001502. [CrossRef]

184. Lu, H.-T.; Huang, G.-Y.; Chang, W.-J.; Lu, T.-W.; Huang, T.-W.; Ho, M.-H.; Mi, F.-L. Modification of chitosan nanofibers with CuS and fucoidan for antibacterial and bone tissue engineering applications. *Carbohydr. Polym.* **2022**, *281*, 119035. [CrossRef]

185. Zia, I.; Jolly, R.; Mirza, S.; Rehman, A.; Shakir, M. Nanocomposite materials developed from nano-hydroxyapatite impregnated chitosan/κ-carrageenan for bone tissue engineering. *ChemistrySelect* **2022**, *7*, e202103234. [CrossRef]

186. Esmaeili, J.; Jadbabaee, S.; Far, F.M.; Lukolayeh, M.E.; Kırboğa, K.K.; Rezaei, F.S.; Barati, A. Decellularized alstroemeria flower stem modified with chitosan for tissue engineering purposes: A cellulose/chitosan scaffold. *Int. J. Biol. Macromol.* **2022**, *204*, 321–332. [CrossRef] [PubMed]

187. Ranganathan, S.; Balagangadharan, K.; Selvamurugan, N. Chitosan and gelatin-based electrospun fibers for bone tissue engineering. *Int. J. Biol. Macromol.* **2019**, *133*, 354–364. [CrossRef] [PubMed]

188. Lavanya, K.; Chandran, S.V.; Balagangadharan, K.; Selvamurugan, N. Temperature- and PH-responsive chitosan-based injectable hydrogels for bone tissue engineering. *Mater. Sci. Eng. C* **2020**, *111*, 110862. [CrossRef] [PubMed]

189. Maharjan, B.; Park, J.; Kaliannagounder, V.K.; Awasthi, G.P.; Joshi, M.K.; Park, C.H.; Kim, C.S. Regenerated cellulose nanofiber reinforced chitosan hydrogel scaffolds for bone tissue engineering. *Carbohydr. Polym.* **2021**, *251*, 117023. [CrossRef] [PubMed]

190. Gritsch, L.; Maqbool, M.; Mouriño, V.; Ciraldo, F.E.; Cresswell, M.; Jackson, P.R.; Lovell, C.; Boccaccini, A.R. Chitosan/hydroxyapatite composite bone tissue engineering scaffolds with dual and decoupled therapeutic ion delivery: Copper and strontium. *J. Mater. Chem. B* **2019**, *7*, 6109–6124. [CrossRef]

191. Cui, Z.-K.; Kim, S.; Baljon, J.J.; Wu, B.M.; Aghaloo, T.; Lee, M. Microporous methacrylated glycol chitosan-montmorillonite nanocomposite hydrogel for bone tissue engineering. *Nat. Commun.* **2019**, *10*, 3523. [CrossRef]

192. Vaidhyanathan, B.; Vincent, P.; Vadivel, S.; Karuppiah, P.; AL-Dhabi, N.A.; Sadhasivam, D.R.; Vimalraj, S.; Saravanan, S. Fabrication and investigation of the suitability of chitosan-silver composite scaffolds for bone tissue engineering applications. *Process Biochem.* **2021**, *100*, 178–187. [CrossRef]

193. Sharifi, F.; Atyabi, S.M.; Norouzian, D.; Zandi, M.; Irani, S.; Bakhshi, H. Polycaprolactone/carboxymethyl chitosan nanofibrous scaffolds for bone tissue engineering application. *Int. J. Biol. Macromol.* **2018**, *115*, 243–248. [CrossRef]

194. Li, M.; Jia, W.; Zhang, X.; Weng, H.; Gu, G.; Chen, Z. Hyaluronic acid oligosaccharides modified mineralized collagen and chitosan with enhanced osteoinductive properties for bone tissue engineering. *Carbohydr. Polym.* **2021**, *260*, 117780. [CrossRef]

195. Morille, M.; Van-Thanh, T.; Garric, X.; Cayon, J.; Coudane, J.; Noël, D.; Venier-Julienne, M.-C.; Montero-Menei, C.N. New PLGA–P188–PLGA matrix enhances TGF-B3 release from pharmacologically active microcarriers and promotes chondrogenesis of mesenchymal stem cells. *J. Control. Release* **2013**, *170*, 99–110. [CrossRef]

196. Dash, M.; Chiellini, F.; Ottenbrite, R.M.; Chiellini, E. Chitosan—A versatile semi-synthetic polymer in biomedical applications. *Prog. Polym. Sci.* **2011**, *36*, 981–1014. [CrossRef]

197. Balasundaram, G.; Storey, D.M.; Webster, T.J. Novel nano-rough polymers for cartilage tissue engineering. *Int. J. Nanomed.* **2014**, *9*, 1845–1853. [CrossRef]

198. Kock, L.; Van Donkelaar, C.C.; Ito, K. Tissue engineering of functional articular cartilage: The current status. *Cell Tissue Res.* **2012**, *347*, 613–627. [CrossRef]

199. Muxika, A.; Etxabide, A.; Uranga, J.; Guerrero, P.; de la Caba, K. Chitosan as a bioactive polymer: Processing, properties and applications. *Int. J. Biol. Macromol.* **2017**, *105*, 1358–1368. [CrossRef]

200. Domalik-Pyzik, P.; Chłopek, J.; Pielichowska, K. Chitosan-based hydrogels: Preparation, properties, and applications. In *Cellulose-Based Superabsorbent Hydrogels*; Mondal, I.H., Ed.; Springer International Publishing: Cham, Switzerland, 2019; pp. 1665–1693. ISBN 978-3-319-77830-3.

201. Suh, J.K.; Matthew, H.W. Application of chitosan-based polysaccharide biomaterials in cartilage tissue engineering: A review. *Biomaterials* **2000**, *21*, 2589–2598. [CrossRef]

202. Neves, S.C.; Moreira Teixeira, L.S.; Moroni, L.; Reis, R.L.; Van Blitterswijk, C.A.; Alves, N.M.; Karperien, M.; Mano, J.F. Chitosan/poly(ε-caprolactone) blend scaffolds for cartilage repair. *Biomaterials* **2011**, *32*, 1068–1079. [CrossRef]

203. Shamekhi, M.A.; Mirzadeh, H.; Mahdavi, H.; Rabiee, A.; Mohebbi-Kalhori, D.; Baghaban Eslaminejad, M. Graphene oxide containing chitosan scaffolds for cartilage tissue engineering. *Int. J. Biol. Macromol.* **2019**, *127*, 396–405. [CrossRef]

204. Kashi, M.; Baghbani, F.; Moztarzadeh, F.; Mobasheri, H.; Kowsari, E. Green synthesis of degradable conductive thermosensitive oligopyrrole/chitosan hydrogel intended for cartilage tissue engineering. *Int. J. Biol. Macromol.* **2018**, *107*, 1567–1575. [CrossRef]

205. Davachi, S.M.; Haramshahi, S.M.A.; Akhavirad, S.A.; Bahrami, N.; Hassanzadeh, S.; Ezzatpour, S.; Hassanzadeh, N.; Malekzadeh Kebria, M.; Khanmohammadi, M.; Bagher, Z. Development of chitosan/hyaluronic acid hydrogel scaffolds via enzymatic reaction for cartilage tissue engineering. *Mater. Today Commun.* **2022**, *30*, 103230. [CrossRef]

206. Sadeghianmaryan, A.; Naghieh, S.; Yazdanpanah, Z.; Alizadeh Sardroud, H.; Sharma, N.K.; Wilson, L.D.; Chen, X. Fabrication of chitosan/alginate/hydroxyapatite hybrid scaffolds using 3D printing and impregnating techniques for potential cartilage regeneration. *Int. J. Biol. Macromol.* **2022**, *204*, 62–75. [CrossRef]

207. Chen, T.-C.; Wong, C.-W.; Hsu, S. Three-dimensional printing of chitosan cryogel as injectable and shape recoverable scaffolds. *Carbohydr. Polym.* **2022**, *285*, 119228. [CrossRef]

208. Pitrolino, K.A.; Felfel, R.M.; Pellizzeri, L.M.; MLaren, J.; Popov, A.A.; Sottile, V.; Scotchford, C.A.; Scammell, B.E.; Roberts, G.A.F.; Grant, D.M. Development and in vitro assessment of a bi-layered chitosan-nano-hydroxyapatite osteochondral scaffold. *Carbohydr. Polym.* **2022**, *282*, 119126. [CrossRef]

209. Hu, M.; Yang, J.; Xu, J. Structural and biological investigation of chitosan/hyaluronic acid with silanized-hydroxypropyl methylcellulose as an injectable reinforced interpenetrating network hydrogel for cartilage tissue engineering. *Drug Deliv.* **2021**, *28*, 607–619. [CrossRef]

210. Zuliani, C.C.; Damas, I.I.; Andrade, K.C.; Westin, C.B.; Moraes, Â.M.; Coimbra, I.B. Chondrogenesis of human amniotic fluid stem cells in chitosan-xanthan scaffold for cartilage tissue engineering. *Sci. Rep.* **2021**, *11*, 3063. [CrossRef]

211. Liu, J.; Yang, B.; Li, M.; Li, J.; Wan, Y. Enhanced dual network hydrogels consisting of thiolated chitosan and silk fibroin for cartilage tissue engineering. *Carbohydr. Polym.* **2020**, *227*, 115335. [CrossRef]

212. Fukunishi, T.; Best, C.A.; Sugiura, T.; Shoji, T.; Yi, T.; Udelsman, B.; Ohst, D.; Ong, C.S.; Zhang, H.; Shinoka, T.; et al. Tissue-engineered small diameter arterial vascular grafts from cell-free nanofiber PCL/chitosan scaffolds in a sheep model. *PLoS ONE* **2016**, *11*, e0158555. [CrossRef]

213. Chupa, J.M.; Foster, A.M.; Sumner, S.R.; Madihally, S.V.; Matthew, H.W. Vascular cell responses to polysaccharide materials: In vitro and in vivo evaluations. *Biomaterials* **2000**, *21*, 2315–2322. [CrossRef]

214. Huang, C.; Chen, R.; Ke, Q.; Morsi, Y.; Zhang, K.; Mo, X. Electrospun collagen-chitosan-TPU nanofibrous scaffolds for tissue engineered tubular grafts. *Colloids Surf. B Biointerfaces* **2011**, *82*, 307–315. [CrossRef]

215. Wang, L.; Cao, Y.; Shen, Z.; Li, M.; Zhang, W.; Liu, Y.; Zhang, Y.; Duan, J.; Ma, Z.; Sang, S. 3D printed GelMA/carboxymethyl chitosan composite scaffolds for vasculogenesis. *Int. J. Polym. Mater. Polym. Biomater.* **2022**. [CrossRef]

216. Gao, H.; Hu, P.; Sun, G.; Wang, L.; Tian, Y.; Mo, H.; Liu, C.; Zhang, J.; Shen, J. Decellularized scaffold-based poly(ethylene glycol) biomimetic vascular patches modified with polyelectrolyte multilayer of heparin and chitosan: Preparation and vascular tissue engineering applications in a porcine model. *J. Mater. Chem. B* **2022**, *10*, 1077–1084. [CrossRef] [PubMed]

217. Fiqrianti, I.A.; Widiyanti, P.; Manaf, M.A.; Savira, C.Y.; Cahyani, N.R.; Bella, F.R. Poly-L-Lactic Acid (PLLA)-chitosan-collagen electrospun tube for vascular graft application. *J. Funct. Biomater.* **2018**, *9*, 32. [CrossRef] [PubMed]

218. Soriente, A.; Amodio, S.P.; Fasolino, I.; Raucci, M.G.; Demitri, C.; Engel, E.; Ambrosio, L. Chitosan/PEGDA based scaffolds as bioinspired materials to control in vitro angiogenesis. *Mater. Sci. Eng. C* **2021**, *118*, 111420. [CrossRef]

219. Wang, W.; Liu, Y.; Liu, Z.; Li, S.; Deng, C.; Yang, X.; Deng, Q.; Sun, Y.; Zhang, Y.; Ma, Z.; et al. Evaluation of interleukin-4-loaded sodium alginate–chitosan microspheres for their support of microvascularization in engineered tissues. *ACS Biomater. Sci. Eng.* **2021**, *7*, 4946–4958. [CrossRef]

220. Engelmann, K.; Bednarz, J.; Valtink, M. Prospects for endothelial transplantation. *Exp. Eye Res.* **2004**, *78*, 573–578. [CrossRef]

221. World Health Organization. *Universal Eye Health: A Global Action Plan 2014–2019*; World Health Organization: Geneva, Switzerland, 2013; ISBN 9241506563.

222. Kafle, P.A.; Singh, S.K.; Sarkar, I.; Surin, L. Amniotic membrane transplantation with and without limbal stem cell transplantation in chemical eye injury. *Nepal J. Ophthalmol.* **2015**, *7*, 52–55. [CrossRef]

223. Kreft, M.E.; Dragin, U. Amniotic membrane in tissue engineering and regenerative medicine. *Slov. Med. J.* **2010**, *79*, 707–715.

224. Yousaf, S.; Keshel, S.H.; Farzi, G.A.; Momeni-Moghadam, M.; Ahmadi, E.D.; Asencio, I.O.; Mozafari, M.; Sefat, F. Scaffolds for corneal tissue engineering. In *Handbook of Tissue Engineering Scaffolds: Volume Two*; Elsevier: Amsterdam, Netherlands, 2019; pp. 649–672.

225. Tayebi, T.; Baradaran-Rafii, A.; Hajifathali, A.; Rahimpour, A.; Zali, H.; Shaabani, A.; Niknejad, H. Biofabrication of chitosan/chitosan nanoparticles/polycaprolactone transparent membrane for corneal endothelial tissue engineering. *Sci. Rep.* **2021**, *11*, 7060. [CrossRef]

226. Feng, L.; Liu, R.; Zhang, X.; Li, J.; Zhu, L.; Li, Z.; Li, W.; Zhang, A. Thermo-gelling dendronized chitosans as biomimetic scaffolds for corneal tissue engineering. *ACS Appl. Mater. Interfaces* **2021**, *13*, 49369–49379. [CrossRef]

227. Xu, W.; Wang, Z.; Liu, Y.; Wang, L.; Jiang, Z.; Li, T.; Zhang, W.; Liang, Y. Carboxymethyl chitosan/gelatin/hyaluronic acid blended-membranes as epithelia transplanting scaffold for corneal wound healing. *Carbohydr. Polym.* **2018**, *192*, 240–250. [CrossRef]

228. Xu, W.; Liu, K.; Li, T.; Zhang, W.; Dong, Y.; Lv, J.; Wang, W.; Sun, J.; Li, M.; Wang, M.; et al. An in situ hydrogel based on carboxymethyl chitosan and sodium alginate dialdehyde for corneal wound healing after alkali burn. *J. Biomed. Mater. Res. A* **2019**, *107*, 742–754. [CrossRef]

229. Shahin, A.; Ramazani, S.A.; Mehraji, S.; Eslami, H. Synthesis and characterization of a chitosan/gelatin transparent film crosslinked with a combination of EDC/NHS for corneal epithelial cell culture scaffold with potential application in cornea implantation. *Int. J. Polym. Mater. Polym. Biomater.* **2021**, *71*, 568–578. [CrossRef]

230. Wang, Y.-H.; Young, T.-H.; Wang, T.-J. Investigating the effect of chitosan/polycaprolactone blends in differentiation of corneal endothelial cells and extracellular matrix compositions. *Exp. Eye Res.* **2019**, *185*, 107679. [CrossRef]

231. Li, T.; Liang, Y.; Wang, Z.; Zhang, W.; Wang, L.; Zhou, Q.; Xu, W. Tissue-engineered scaffold based on carboxymethyl chitin or chitosan for corneal epithelial transplantation. *Polym. J.* **2018**, *50*, 511–521. [CrossRef]

232. Chou, S.; Lee, C.; Lai, J. Bioengineered keratocyte spheroids fabricated on chitosan coatings enhance tissue repair in a rabbit corneal stromal defect model. *J. Tissue Eng. Regen. Med.* **2018**, *12*, 316–320. [CrossRef]

233. Moradian-Oldak, J.; Qichao, R. Chitosan-Amelogenin Hydrogel for In Situ Enamel Growth. U.S. Patent Application 14/142,086, 3 July 2014.

234. Gu, L.S.; Cai, X.; Guo, J.M.; Pashley, D.H.; Breschi, L.; Xu, H.H.K.; Wang, X.Y.; Tay, F.R.; Niu, L.N. Chitosan-based extrafibrillar demineralization for dentin bonding. *J. Dent. Res.* **2018**, *98*, 186–193. [CrossRef]

235. Mulder, R.; Grobler, S.; Moodley, D.; Perchyonok, T. Towards bioactive dental restorative materials with chitosan and nanodiamonds: Evaluation and application. *Int. J. Dent. Oral Sci.* **2015**, *2*, 147–154. [CrossRef]

236. Park, K.H.; Kim, S.J.; Hwang, M.J.; Song, H.J.; Park, Y.J. Pulse electrodeposition of hydroxyapatite/chitosan coatings on titanium substrate for dental implant. *Colloid Polym. Sci.* **2017**, *295*, 1843–1849. [CrossRef]

237. Alnufaiy, B.M.; Lambarte, R.N.A.; Alhamdan, K.S. The osteogenetic potential of chitosan coated implant: An in vitro study. *J. Stem Cells Regen. Med.* **2020**, *16*, 44–49. [CrossRef]

238. Sukpaita, T.; Chirachanchai, S.; Suwattanachai, P.; Everts, V.; Pimkhaokham, A.; Ampornaramveth, R.S. In vivo bone regeneration induced by a scaffold of chitosan/dicarboxylic acid seeded with human periodontal ligament cells. *Int. J. Mol. Sci.* **2019**, *20*, 4883. [CrossRef]

239. Fakhri, E.; Eslami, H.; Maroufi, P.; Pakdel, F.; Taghizadeh, S.; Ganbarov, K.; Yousefi, M.; Tanomand, A.; Yousefi, B.; Mahmoudi, S.; et al. Chitosan biomaterials application in dentistry. *Int. J. Biol. Macromol.* **2020**, *162*, 956–974. [CrossRef]

240. Amiryaghoubi, N.; Noroozi Pesyan, N.; Fathi, M.; Omidi, Y. Injectable thermosensitive hybrid hydrogel containing graphene oxide and chitosan as dental pulp stem cells scaffold for bone tissue engineering. *Int. J. Biol. Macromol.* **2020**, *162*, 1338–1357. [CrossRef]

241. Navidi, G.; Allahvirdinesbat, M.; Al-Molki, S.M.M.; Davaran, S.; Panahi, P.N.; Aghazadeh, M.; Akbarzadeh, A.; Eftekhari, A.; Safa, K.D. Design and fabrication of M-SAPO-34/chitosan scaffolds and evaluation of their effects on dental tissue engineering. *Int. J. Biol. Macromol.* **2021**, *187*, 281–295. [CrossRef]

242. Soares, D.G.; Bordini, E.A.F.; Cassiano, F.B.; Bronze-Uhle, E.S.; Pacheco, L.E.; Zabeo, G.; Hebling, J.; Lisboa-Filho, P.N.; Bottino, M.C.; de Souza Costa, C.A. Characterization of novel calcium hydroxide-mediated highly porous chitosan-calcium scaffolds for potential application in dentin tissue engineering. *J. Biomed. Mater. Res. B Appl. Biomater.* **2020**, *108*, 2546–2559. [CrossRef]

243. Tondnevis, F.; Ketabi, M.A.; Fekrazad, R.; Sadeghi, A.; Abolhasani, M.M. Using chitosan besides nano hydroxyapatite and fluorohydroxyapatite boost dental pulp stem cell proliferation. *J. Biomim. Biomater. Biomed. Eng.* **2019**, *42*, 39–50. [CrossRef]

244. Vagropoulou, G.; Trentsiou, M.; Georgopoulou, A.; Papachristou, E.; Prymak, O.; Kritis, A.; Epple, M.; Chatzinikolaidou, M.; Bakopoulou, A.; Koidis, P. Hybrid chitosan/gelatin/nanohydroxyapatite scaffolds promote odontogenic differentiation of dental pulp stem cells and in vitro biomineralization. *Dent. Mater.* **2021**, *37*, e23–e36. [CrossRef]

245. Shen, R.; Xu, W.; Xue, Y.; Chen, L.; Ye, H.; Zhong, E.; Ye, Z.; Gao, J.; Yan, Y. The use of chitosan/PLA nano-fibers by emulsion eletrospinning for periodontal tissue engineering. *Artif. Cells Nanomed. Biotechnol.* **2018**, *46*, 419–430. [CrossRef]

246. Yang, X.; Han, G.; Pang, X.; Fan, M. Chitosan/collagen scaffold containing bone morphogenetic protein-7 DNA supports dental pulp stem cell differentiation in vitro and in vivo. *J. Biomed. Mater. Res. A* **2020**, *108*, 2519–2526. [CrossRef]

247. Bakopoulou, A.; Georgopoulou, A.; Grivas, I.; Bekiari, C.; Prymak, O.; Loza, K.; Epple, M.; Papadopoulos, G.C.; Koidis, P.; Chatzinikolaidou, M. Dental pulp stem cells in chitosan/gelatin scaffolds for enhanced orofacial bone regeneration. *Dent. Mater.* **2019**, *35*, 310–327. [CrossRef]

248. Divband, B.; Aghazadeh, M.; Al-qaim, Z.H.; Samiei, M.; Hussein, F.H.; Shaabani, A.; Shahi, S.; Sedghi, R. Bioactive chitosan biguanidine-based injectable hydrogels as a novel BMP-2 and VEGF carrier for osteogenesis of dental pulp stem cells. *Carbohydr. Polym.* **2021**, *273*, 118589. [CrossRef]

249. Lee, D.; Lee, S.J.; Moon, J.-H.; Kim, J.H.; Heo, D.N.; Bang, J.B.; Lim, H.-N.; Kwon, I.K. Preparation of antibacterial chitosan membranes containing silver nanoparticles for dental barrier membrane applications. *J. Ind. Eng. Chem.* **2018**, *66*, 196–202. [CrossRef]

250. Ansari, M.J.; Ahmed, M.M.; Anwer, M.K.; Jamil, S.; Alalaiwe, A.; Alshetaili, A.S.; Al-Shdefat, R.; Ali, R.; Shakeel, F. Formulation and characterization of fluconazole loaded olive oil nanoemulsions. *Indo Am. J. Pharm. Sci.* **2017**, *4*, 852–860.

251. Ansari, M.J.; Ahmed, M.M.; Anwer, M.K.; Jamil, S.; Al-Shdefat, R.; Ali, B. Solubility and stability enhancement of curcumin through cyclodextrin complexation. *Int. J. Biol. Pharm. Allied Sci.* **2014**, *3*, 2668–2675.

252. Guo, J.L.; Kim, Y.S.; Xie, V.Y.; Smith, B.T.; Watson, E.; Lam, J.; Pearce, H.A.; Engel, P.S.; Mikos, A.G. Modular, tissue-specific, and biodegradable hydrogel cross-linkers for tissue engineering. *Sci. Adv.* **2019**, *5*, eaaw7396. [CrossRef]

253. Ahmed, M.M.; Fatima, F.; Anwer, M.K.; Ibnouf, E.O.; Kalam, M.A.; Alshamsan, A.; Aldawsari, M.F.; Alalaiwe, A.; Ansari, M.J. Formulation and in vitro evaluation of topical nanosponge-based gel containing butenafine for the treatment of fungal skin infection. *Saudi Pharm. J.* **2021**, *29*, 467–477. [CrossRef]

254. Abdel-Kader, M.; Al-Shdefat, R. Evaluation of Antifungal Activity of Olive Oil Based Nanoemulsions Evaluation of Essential Oils for Antimicrobial Activity from Some Moroccan Aromatic Plants Medicinal View Project Isoflavonoids View Project. *Bull. Environ. Pharmacol. Life Sci.* **2016**, *5*, 1–4.

255. Fatima, F.; Aldawsari, M.F.; Ahmed, M.M.; Anwer, M.K.; Naz, M.; Ansari, M.J.; Hamad, A.M.; Zafar, A.; Jafar, M. Green synthesized silver nanoparticles using tridax procumbens for topical application: Excision wound model and histopathological studies. *Pharmaceutics* **2021**, *13*, 1754. [CrossRef]

256. He, Y.; Lu, F. Development of synthetic and natural materials for tissue engineering applications using adipose stem cells. *Stem Cells Int.* **2016**, *2016*, 5786257. [CrossRef]

257. Nagarkar, R.; Patel, J. Polyvinyl alcohol: A comprehensive study. *Acta Sci. Pharm. Sci.* **2019**, *3*, 34–44.

258. Kohane, D.S.; Langer, R. Polymeric biomaterials in tissue engineering. *Pediatr. Res.* **2008**, *63*, 487–491. [CrossRef]

259. Rodríguez-Rodríguez, R.; Espinosa-Andrews, H.; Velasquillo-Martínez, C.; García-Carvajal, Z.Y. Composite hydrogels based on gelatin, chitosan and polyvinyl alcohol to biomedical applications: A review. *Int. J. Polym. Mater. Polym. Biomater.* **2020**, *69*, 1–20. [CrossRef]

260. Tripathi, S.; Singh, B.N.; Divakar, S.; Kumar, G.; Mallick, S.P.; Srivastava, P. Design and evaluation of ciprofloxacin loaded collagen chitosan oxygenating scaffold for skin tissue engineering. *Biomed. Mater.* **2021**, *16*, 25021. [CrossRef]

261. Pezeshki, M.; Mojgan, M.; Sarah, Z. Tailoring the gelatin/chitosan electrospun scaffold for application in skin tissue engineering: An in vitro study. *Prog. Biomater.* **2018**, *7*, 207–218. [CrossRef]

262. Sivashankari, P.R.; Prabaharan, M. Prospects of chitosan-based scaffolds for growth factor release in tissue engineering. *Int. J. Biol. Macromol.* **2016**, *93*, 1382–1389. [CrossRef]

263. Prabaharan, M.; Rodriguez-Perez, M.A.; de Saja, J.A.; Mano, J.F. Preparation and characterization of poly(L-lactic acid)-chitosan hybrid scaffolds with drug release capability. *J. Biomed. Mater. Res. B Appl. Biomater.* **2007**, *81*, 427–434. [CrossRef]

264. Zhang, M.; Wan, T.; Fan, P.; Shi, K.; Chen, X.; Yang, H.; Liu, X.; Xu, W.; Zhou, Y. Photopolymerizable chitosan hydrogels with improved strength and 3D printability. *Int. J. Biol. Macromol.* **2021**, *193*, 109–116. [CrossRef]

265. Yang, Y.; Campbell Ritchie, A.; Everitt, N.M. Recombinant human collagen/chitosan-based soft hydrogels as biomaterials for soft tissue engineering. *Mater. Sci. Eng. C* **2021**, *121*, 111846. [CrossRef]

266. Islam, M.T.; Laing, R.M.; Wilson, C.A.; McConnell, M.; Ali, M.A. Fabrication and characterization of 3-dimensional electrospun poly(vinyl alcohol)/keratin/chitosan nanofibrous scaffold. *Carbohydr. Polym.* **2022**, *275*, 118682. [CrossRef]

267. Kouser, S.; Prabhu, A.; Prashantha, K.; Nagaraja, G.K.; D'souza, J.N.; Meghana Navada, K.; Qurashi, A.; Manasa, D.J. Modified halloysite nanotubes with chitosan incorporated PVA/PVP bionanocomposite films: Thermal, mechanical properties and biocompatibility for tissue engineering. *Colloids Surf. A Physicochem. Eng. Asp.* **2022**, *634*, 127941. [CrossRef]

268. Becerra, J.; Rodriguez, M.; Leal, D.; Noris-Suarez, K.; Gonzalez, G. Chitosan-collagen-hydroxyapatite membranes for tissue engineering. *J. Mater. Sci. Mater. Med.* **2022**, *33*, 18. [CrossRef]

269. Hu, X.; Zheng, S.; Zhang, R.; Wang, Y.; Jiao, Z.; Li, W.; Nie, Y.; Liu, T.; Song, K. Dynamic process enhancement on chitosan/gelatin/nano-hydroxyapatite-bone derived multilayer scaffold for osteochondral tissue repair. *Mater. Sci. Eng. C* **2022**, *133*, 112662. [CrossRef]

270. Zarei, M.; Samimi, A.; Khorram, M.; Abdi, M.M.; Golestaneh, S.I. Fabrication and characterization of conductive polypyr-role/chitosan/collagen electrospun nanofiber scaffold for tissue engineering application. *Int. J. Biol. Macromol.* **2021**, *168*, 175–186. [CrossRef]

271. Ali, A.; Bano, S.; Poojary, S.; Chaudhary, A.; Kumar, D.; Negi, Y.S. Effect of cellulose nanocrystals on chitosan/PVA/nano β-TCP composite scaffold for bone tissue engineering application. *J. Biomater. Sci. Polym. Ed.* **2022**, *33*, 1–19. [CrossRef]

272. Yavari Maroufi, L.; Ghorbani, M. Injectable chitosan-quince seed gum hydrogels encapsulated with curcumin loaded-halloysite nanotubes designed for tissue engineering application. *Int. J. Biol. Macromol.* **2021**, *177*, 485–494. [CrossRef]

273. Barik, D.; Kundu, K.; Dash, M. Montmorillonite stabilized chitosan-co-mucin hydrogel for tissue engineering applications. *RSC Adv.* **2021**, *11*, 30329–30342. [CrossRef]

274. Shah, R.; Stodulka, P.; Skopalova, K.; Saha, P. Dual crosslinked collagen/chitosan film for potential biomedical applications. *Polymers* **2019**, *11*, 94. [CrossRef]

275. Li, D.-W.; He, J.; He, F.-L.; Liu, Y.-L.; Liu, Y.-Y.; Ye, Y.-J.; Deng, X.; Yin, D.-C. Silk fibroin/chitosan thin film promotes osteogenic and adipogenic differentiation of rat bone marrow-derived mesenchymal stem cells. *J. Biomater. Appl.* **2018**, *32*, 1164–1173. [CrossRef]

276. Liu, C.; Jin, Z.; Ge, X.; Zhang, Y.; Xu, H. Decellularized annulus fibrosus matrix/chitosan hybrid hydrogels with basic fibroblast growth factor for annulus fibrosus tissue engineering. *Tissue Eng Part A* **2019**, *25*, 1605–1613. [CrossRef]

277. Fang, S.W.; Li, C.F.; Shih, D.Y.C. Antifungal activity of chitosan and its preservative effect on low-sugar candied kumquat. *J. Food Prot.* **1994**, *57*, 136–140. [CrossRef]

278. Kim, C.H.; Choi, J.W.; Chun, H.J.; Choi, K.S. Synthesis of chitosan derivatives with quaternary ammonium salt and their antibacterial activity. *Polymer. Bull.* **1997**, *38*, 387–393. [CrossRef]

279. Franklin, T.J.; Snow, G.A. *Biochemistry of Antimicrobial Action*; Chapman and Hall: London, UK, 1981; ISBN 9780412224409.

280. Torkaman, S.; Rahmani, H.; Ashori, A.; Najafi, S.H.M. Modification of chitosan using amino acids for wound healing purposes: A review. *Carbohydr. Polym.* **2021**, *258*, 117675. [CrossRef] [PubMed]

281. Du, X.; Liu, Y.; Yan, H.; Rafique, M.; Li, S.; Shan, X.; Wu, L.; Qiao, M.; Kong, D.; Wang, L. Anti-infective and pro-coagulant chitosan-based hydrogel tissue adhesive for sutureless wound closure. *Biomacromolecules* **2020**, *21*, 1243–1253. [CrossRef] [PubMed]

282. Zhao, Y.F.; Zhao, J.Y.; Hu, W.Z.; Ma, K.; Chao, Y.; Sun, P.J.; Fu, X.B.; Zhang, H. Synthetic poly(vinyl alcohol)-chitosan as a new type of highly efficient hemostatic sponge with blood-triggered swelling and high biocompatibility. *J. Mater. Chem. B* **2019**, *7*, 1855–1866. [CrossRef] [PubMed]

283. Du, X.; Wu, L.; Yan, H.; Jiang, Z.; Li, S.; Li, W.; Bai, Y.; Wang, H.; Cheng, Z.; Kong, D.; et al. Microchannelled alkylated chitosan sponge to treat noncompressible hemorrhages and facilitate wound healing. *Nat. Commun.* **2021**, *12*, 4733. [CrossRef] [PubMed]

284. Zhou, F.; Cui, C.; Sun, S.; Wu, S.; Chen, S.; Ma, J.; Li, C.M. Electrospun ZnO-loaded chitosan/PCL bilayer membranes with spatially designed structure for accelerated wound healing. *Carbohydr. Polym.* **2022**, *282*, 119131. [CrossRef] [PubMed]

285. Ali, I.H.; Ouf, A.; Elshishiny, F.; Taskin, M.B.; Song, J.; Dong, M.; Chen, M.; Siam, R.; Mamdouh, W. Antimicrobial and wound-healing activities of graphene-reinforced electrospun chitosan/gelatin nanofibrous nanocomposite scaffolds. *ACS Omega* **2022**, *7*, 1838–1850. [CrossRef]

286. Deng, P.; Yao, L.; Chen, J.; Tang, Z.; Zhou, J. Chitosan-based hydrogels with injectable, self-healing and antibacterial properties for wound healing. *Carbohydr. Polym.* **2022**, *276*, 118718. [CrossRef]

287. Zhang, J.; Tan, W.; Li, Q.; Liu, X.; Guo, Z. Preparation of cross-linked chitosan quaternary ammonium salt hydrogel films loading drug of gentamicin sulfate for antibacterial wound dressing. *Mar. Drugs* **2021**, *19*, 479. [CrossRef]

288. Khorasani, M.T.; Joorabloo, A.; Moghaddam, A.; Shamsi, H.; MansooriMoghadam, Z. Incorporation of ZnO nanoparticles into heparinised polyvinyl alcohol/chitosan hydrogels for wound dressing application. *Int. J. Biol. Macromol.* **2018**, *114*, 1203–1215. [CrossRef]

289. Long, J.; Etxeberria, A.E.; Nand, A.V.; Bunt, C.R.; Ray, S.; Seyfoddin, A. A 3D printed chitosan-pectin hydrogel wound dressing for lidocaine hydrochloride delivery. *Mater. Sci. Eng. C* **2019**, *104*, 109873. [CrossRef]

290. Xue, H.; Hu, L.; Xiong, Y.; Zhu, X.; Wei, C.; Cao, F.; Zhou, W.; Sun, Y.; Endo, Y.; Liu, M.; et al. Quaternized chitosan-matrigel-polyacrylamide hydrogels as wound dressing for wound repair and regeneration. *Carbohydr. Polym.* **2019**, *226*, 115302. [CrossRef]

291. Yang, J.; Chen, Y.; Zhao, L.; Feng, Z.; Peng, K.; Wei, A.; Wang, Y.; Tong, Z.; Cheng, B. Preparation of a chitosan/carboxymethyl chitosan/AgNPs polyelectrolyte composite physical hydrogel with self-healing ability, antibacterial properties, and good biosafety simultaneously, and its application as a wound dressing. *Compos. B Eng.* **2020**, *197*, 108139. [CrossRef]

292. Adeli, H.; Khorasani, M.T.; Parvazinia, M. Wound dressing based on electrospun PVA/chitosan/starch nanofibrous mats: Fabrication, antibacterial and cytocompatibility evaluation and in vitro healing assay. *Int. J. Biol. Macromol.* **2019**, *122*, 238–254. [CrossRef]

293. Zhang, M.; Yang, M.; Woo, M.W.; Li, Y.; Han, W.; Dang, X. High-mechanical strength carboxymethyl chitosan-based hydrogel film for antibacterial wound dressing. *Carbohydr. Polym.* **2021**, *256*, 117590. [CrossRef]

294. Amirian, J.; Zeng, Y.; Shekh, M.I.; Sharma, G.; Stadler, F.J.; Song, J.; Du, B.; Zhu, Y. In-situ crosslinked hydrogel based on amidated pectin/oxidized chitosan as potential wound dressing for skin repairing. *Carbohydr. Polym.* **2021**, *251*, 117005. [CrossRef]

295. Ghasemian Lemraski, E.; Jahangirian, H.; Dashti, M.; Khajehali, E.; Sharafinia, S.; Rafiee-Moghaddam, R.; Webster, T.J. Antimicrobial double-layer wound dressing based on chitosan/polyvinyl alcohol/copper: In vitro and in vivo assessment. *Int. J. Nanomed.* **2021**, *16*, 223–235. [CrossRef]

296. Wang, S.; Yan, F.; Ren, P.; Li, Y.; Wu, Q.; Fang, X.; Chen, F.; Wang, C. Incorporation of metal-organic frameworks into electrospun chitosan/poly (vinyl alcohol) nanofibrous membrane with enhanced antibacterial activity for wound dressing application. *Int. J. Biol. Macromol.* **2020**, *158*, 9–17. [CrossRef]

297. Sun, C.; Zeng, X.; Zheng, S.; Wang, Y.; Li, Z.; Zhang, H.; Nie, L.; Zhang, Y.; Zhao, Y.; Yang, X. Bio-adhesive catechol-modified chitosan wound healing hydrogel dressings through glow discharge plasma technique. *Chem. Eng. J.* **2021**, *427*, 130843. [CrossRef]

298. Zhang, D.; Ouyang, Q.; Hu, Z.; Lu, S.; Quan, W.; Li, P.; Chen, Y.; Li, S. Catechol functionalized chitosan/active peptide microsphere hydrogel for skin wound healing. *Int. J. Biol. Macromol.* **2021**, *173*, 591–606. [CrossRef]

299. Andrade del Olmo, J.; Pérez-Álvarez, L.; Sáez-Martínez, V.; Benito-Cid, S.; Ruiz-Rubio, L.; Pérez-González, R.; Vilas-Vilela, J.L.; Alonso, J.M. Wound healing and antibacterial chitosan-genipin hydrogels with controlled drug delivery for synergistic anti-inflammatory activity. *Int. J. Biol. Macromol.* **2022**, *203*, 679–694. [CrossRef]

300. Yu, X.; Cheng, C.; Peng, X.; Zhang, K.; Yu, X. A self-healing and injectable oxidized quaternized guar gum/carboxymethyl chitosan hydrogel with efficient hemostatic and antibacterial properties for wound dressing. *Colloids Surf. B Biointerfaces* **2022**, *209*, 112207. [CrossRef]

301. Karizmeh, M.S.; Poursamar, S.A.; Kefayat, A.; Farahbakhsh, Z.; Rafienia, M. An in vitro and in vivo study of PCL/chitosan electrospun mat on polyurethane/propolis foam as a bilayer wound dressing. *Mater. Sci. Eng. C* **2022**, *135*, 112667. [CrossRef]

302. Dadkhah Tehrani, F.; Shabani, I.; Shabani, A. A hybrid oxygen-generating wound dressing based on chitosan thermosensitive hydrogel and decellularized amniotic membrane. *Carbohydr. Polym.* **2022**, *281*, 119020. [CrossRef]

303. Liang, H.; Mirinejad, M.S.; Asefnejad, A.; Baharifar, H.; Li, X.; Saber-Samandari, S.; Toghraie, D.; Khandan, A. Fabrication of tragacanthin gum-carboxymethyl chitosan bio-nanocomposite wound dressing with silver-titanium nanoparticles using freeze-drying method. *Mater. Chem. Phys.* **2022**, *279*, 125770. [CrossRef]

304. Zhang, Y.; Jiang, M.; Zhang, Y.; Cao, Q.; Wang, X.; Han, Y.; Sun, G.; Li, Y.; Zhou, J. Novel lignin–chitosan–PVA composite hydrogel for wound dressing. *Mater. Sci. Eng. C* **2019**, *104*, 110002. [CrossRef]

305. Hassan, M.A.; Tamer, T.M.; Valachová, K.; Omer, A.M.; El-Shafeey, M.; Mohy Eldin, M.S.; Šoltés, L. Antioxidant and antibacterial polyelectrolyte wound dressing based on chitosan/hyaluronan/phosphatidylcholine dihydroquercetin. *Int. J. Biol. Macromol.* **2021**, *166*, 18–31. [CrossRef]

306. Zou, P.; Lee, W.-H.; Gao, Z.; Qin, D.; Wang, Y.; Liu, J.; Sun, T.; Gao, Y. Wound dressing from polyvinyl alcohol/chitosan electrospun fiber membrane loaded with OH-CATH30 nanoparticles. *Carbohydr. Polym.* **2020**, *232*, 115786. [CrossRef]

307. Ojeda-Hernández, D.D.; Canales-Aguirre, A.A.; Matias-Guiu, J.; Gomez-Pinedo, U.; Mateos-Díaz, J.C. Potential of chitosan and its derivatives for biomedical applications in the central nervous system. *Front. Bioeng. Biotechnol.* **2020**, *8*, 389. [CrossRef]

308. Ahmed, T.A.; Aljaeid, B.M. Preparation, characterization, and potential application of chitosan, chitosan derivatives, and chitosan metal nanoparticles in pharmaceutical drug delivery. *Drug Des. Dev. Ther.* **2016**, *10*, 483–507. [CrossRef]

309. Morin-Crini, N.; Lichtfouse, E.; Torri, G.; Crini, G.; Applications, G.C. Applications of chitosan in food, pharmaceuticals, medicine, cosmetics, agriculture, textiles, pulp and paper, biotechnology, and environmental chemistry. *Environ. Chem. Lett.* **2019**, *17*, 1667–1692. [CrossRef]

Article

Electrochemical and Ion Transport Studies of Li⁺ Ion-Conducting MC-Based Biopolymer Blend Electrolytes

Elham M. A. Dannoun [1], Shujahadeen B. Aziz [2,3,*], Mohamad A. Brza [4], Sameerah I. Al-Saeedi [5], Muaffaq M. Nofal [6], Kuldeep Mishra [7], Ranjdar M. Abdullah [2], Wrya O. Karim [8] and Jihad M. Hadi [9]

1   Associate Chair of the Department of Mathematics and Science, Woman Campus, Prince Sultan University, P.O. Box 66833, Riyadh 11586, Saudi Arabia
2   Hameed Majid Advanced Polymeric Materials Research Lab., Physics Department, College of Science, University of Sulaimani, Qlyasan Street, Kurdistan Regional Government, Sulaimani 46001, Iraq
3   The Development Center for Research and Training (DCRT), University of Human Development, Sulaimani 46001, Iraq
4   Medical Physics Department, College of Medicals & Applied Science, Charmo University, Chamchamal, Sulaimani 46023, Iraq
5   Department of Chemistry, College of Science, Princess Nourah bint Abdulrahman University, P.O. Box 84428, Riyadh 11671, Saudi Arabia
6   Department of Mathematics and Science, Prince Sultan University, P.O. Box 66833, Riyadh 11586, Saudi Arabia
7   Department of Physics, Jaypee University, Anupshahar 203390, Uttar Pradesh, India
8   Department of Chemistry, College of Science, University of Sulaimani, Qlyasan Street, Kurdistan Regional Government, Sulaimani 46001, Iraq
9   Nursing Department, College of Nursing, University of Human Development, Kurdistan Regional Government, Sulaimani 46001, Iraq
*   Correspondence: shujahadeenaziz@gmail.com

Abstract: A facile methodology system for synthesizing solid polymer electrolytes (SPEs) based on methylcellulose, dextran, lithium perchlorate (as ionic sources), and glycerol (such as a plasticizer) (MC:Dex:LiClO₄:Glycerol) has been implemented. Fourier transform infrared spectroscopy (FTIR) and two imperative electrochemical techniques, including linear sweep voltammetry (LSV) and electrical impedance spectroscopy (EIS), were performed on the films to analyze their structural and electrical properties. The FTIR spectra verify the interactions between the electrolyte components. Following this, a further calculation was performed to determine free ions (FI) and contact ion pairs (CIP) from the deconvolution of the peak associated with the anion. It is verified that the electrolyte containing the highest amount of glycerol plasticizer (MDLG3) has shown a maximum conductivity of 1.45×10^{-3} S cm^{-1}. Moreover, for other transport parameters, the mobility (μ), number density (n), and diffusion coefficient (D) of ions were enhanced effectively. The transference number measurement (TNM) of electrons (t_{el}) was 0.024 and 0.976 corresponding to ions (t_{ion}). One of the prepared samples (MDLG3) had 3.0 V as the voltage stability of the electrolyte.

Keywords: biopolymer blend electrolyte; EIS and FTIR; ion transport parameters; complex permittivity; LSV and TNM measurements

1. Introduction

Due to demand for high-energy consumption, for instance, to power laptops and mobile devices, the usage of energy storage devices is widespread. In order to produce low-cost and safe energy storage systems, the design of high-performance electrochemical devices has been extensively studied [1,2]. It is essential to use polymer electrolytes (PEs) for electrochemical devices because of their common advantages including qualities such as wide electrochemical windows, leakage-free, ability to form thin films, lightweight, flexibility, ease of handling, transparency, good conductivity, and solvent-free feature compared to commercial liquid electrolytes (LEs) [3,4]. In the PEs of the energy storage

devices, the host polymer is often divided into two types: natural and synthetic polymers [5]. Non-biodegradable synthetic polymers deplete petroleum resources and introduce disposal difficulties [6]. As a result, biopolymers may be employed as the host polymer to investigate energy storage devices and minimize plastic waste pollution. These polymers, which derive from natural resources, have distinct advantages over synthetic ones, including low cost, wide compatibility with a wide range of solvents, abundance, and high film formation efficiency [7,8]. In PE investigations, starch, cellulose, chitosan, dextran, and carrageenan are the most- often employed biopolymers [9–13].

The search for novel ion-conducting PEs for lithium-based energy devices continues incessantly [14–17]. To replace the LEs in lithium-ion batteries, PEs that are linked to lithium salts and integrated into neutral or ion-conducting polymers have been suggested [18]. In contrast to manufactured polymers, which are durable, natural biopolymers degrade with time [19]. Cellulose is nature's most abundant organic polymer, making it an excellent source of renewable energy [8]. As a natural polymer, cellulose is seen as a potential replacement for petrochemical polymers [20]. Cyanoacrylate is one of the most often used and lowest-priced types of cellulose. A biodegradable polymer that has excellent film-forming capabilities may be transparent and possesses superior mechanical and electrical properties that can be made from alkali cellulose. Methylcellulose (MC) is one of these cellulose derivatives [6]. By adding dimethyl sulfate or methyl chloride to alkali-based cellulose, a polymer with a 1,4 glycosidic link is created, known as MC [21]. Through a dative connection, ions create a complexation with polymer-host-oxygen-containing functional groups. Ion conduction in MC is facilitated by functional groups possessing lone-pair electrons, including hydroxyl, glycosidic link, and mexthoxy groups [22]. When it comes to film-forming and dissolving qualities, MC is a standout because of its strong mechanical, thermal, and chemical stabilities [23]. Glass transition temperature (Tg) for microcrystalline MC is between 184 and 200 °C, making it an excellent material for high-temperature applications [22]. Leuconostoc mesenteroides bacteria produce dextran, a non-toxic and biodegradable polysaccharide that has lone-pair electrons of heteroatoms, such as oxygen, which is essential for dissolving inorganic salts [13]. The polymer blend approach has been reported to generate a polymer mix host with higher ionic conduction sites [24]. A reduced glass transition temperature and degree of crystallinity may be achieved by mixing polymers [25]. A PE based on lithium salts is able to perform well overall in terms of crucial features, such as electrochemical window stability and ionic conductivity [26]. Various plasticizing agents were identified to further improve the above-mentioned properties. The loading of glycerol provided a conductivity of $(1.32 \pm 0.35) \times 10^{-3}$ S cm^{-1} for the chitosan-PS-LiCF$_3$SO$_3$ system [27].

In this study, glycerol (contains three OH groups) as an eligible plasticizer has been used in an effort to pick up the conductivity of the blended polymer system. It causes weakening of the attraction force between the polymer chains and cations and anions of the salts [4]. The objective of this study is to enhance the conductivity of the prepared SPEs by adding glycerol as more ions are dissociated to increase conductivity. The electrochemical tests indicate the films are convenient for applications.

2. Results and Discussion

2.1. FTIR Results

To study polymer-mix developments, several scientists have turned to FTIR. Intermolecular interactions may be studied using FTIR spectroscopy, which analyzes spectra based on the stretching or bending vibrations of specific bonds. Figure 1 showed the spectra of the electrolytes at the 400 to 4000 cm^{-1}. A wide band of 3353 cm^{-1} was observed in the FTIR spectra for MC: Dext, indicating the presence of OH groups [28,29]. The bands, due to -OH bending and -OH stretching, can be found at 1253–1503 cm^{-1} in a sharp peak and 3703–3149 cm^{-1} in a broad-peak form, respectively, by glycerol loading [30,31]. A peak at 1334 cm^{-1} came from -OH bending. The -CH asymmetrical and -CH symmetrical stretching are found at 3049 to 2849 cm^{-1} [32,33]. As the concentration of glycerol rises,

the intensity of the -CH bands increases, indicating a complicated interplay between the glycerol and MC-Dex-LiClO$_4$ [34]. As glycerol concentrations increase, the position of the electrolyte carboxamide and amine band shifts somewhat to 1749–1519 cm^{-1}. The impact of increasing the content of glycerol on the strength of the interaction between the components of the polymer blend is proved where additional ions are interacting with the oxygen atoms and nitrogen atoms [27]. The range of carboxamide and amine bands can be recognized straightforwardly as reported by Aziz et al. [35] and Shukur et al. [36]. Interestingly, a sharp peak lies between 901 and 1203 cm^{-1} that comes from the C-O stretching, which is in accordance with the findings of the study documented by Mejenom et al. [37]. This band peak widens as the glycerol concentration increases. The insertion of LiClO$_4$ salt into MC: Dex resulted in a significant shift in the strength of the bands, which is fascinating. The changes in the macromolecular arrangement have a direct effect on the intensity of these bands. The spectra of the complexes may show more and less organized structures, which might be the cause of these bands [38].
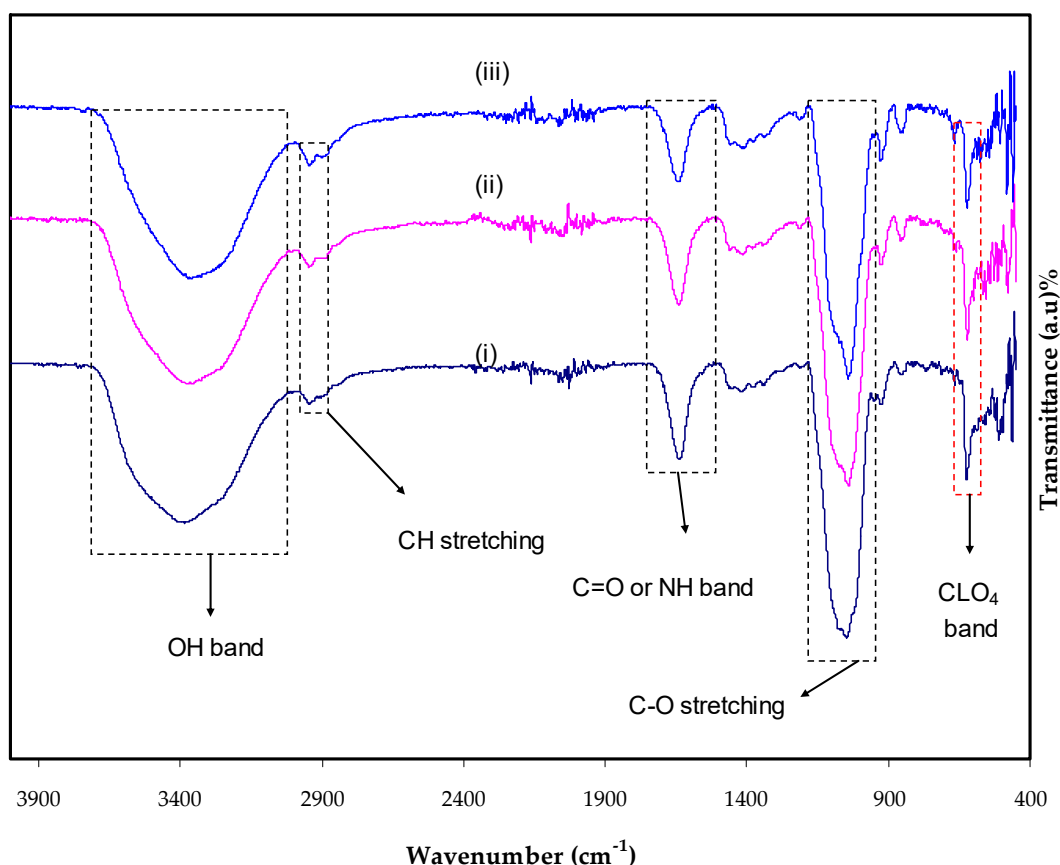
Figure 1. FTIR spectra for (i) MDLG1, (ii) MDLG2, and (iii) MDLG3 in the region 400–4000 cm^{-1}.

Many useful qualities, such as peak resolution, noise removal, and checking for interconnections between deconvolution parameters, are provided by the FTIR deconvolution, which is used in support of the conductivity findings [39]. When using this method, the deconvolution FTIR spectra may be used to determine the ion fraction that conducts electricity. Ramelli et al. noted that FTIR spectra might be deconvoluted, allowing one to isolate existing peaks and modify both intensity and wavenumber [40].

A peak for ClO$_4$ localizes from 650 to 600 cm^{-1} and is regularly utilized in the investigation of ion–ion interactions in the PE and LiClO$_4$ salt addition [41,42]. The ClO$_4$ bands are featured by two peaks extending from 610 to 630 cm^{-1}, which indicates that, at most, two dissimilar sorts of ClO$_4$ anions are present in this material.

Salomon et al. documented that the presence of Li^{+1} is attached to the ClO_4 band located at 610–630 cm^{-1}. CIP ClO_4^{-1} anions were observed at lower than 610 cm^{-1}, while free ClO_4 anions were observed at about 610–630 cm^{-1} [42]. Figure 2a–c show the deconvoluted FTIR spectra for the prepared electrolytes. The free ClO_4 peaks are larger than the peaks of contact-ion pairs, as shown in Figure 2. Glycerol plasticizer helps dissolve $LiClO_4$ salt in the MC: Dex matrix; therefore, this is what happens when the two mixtures are combined.
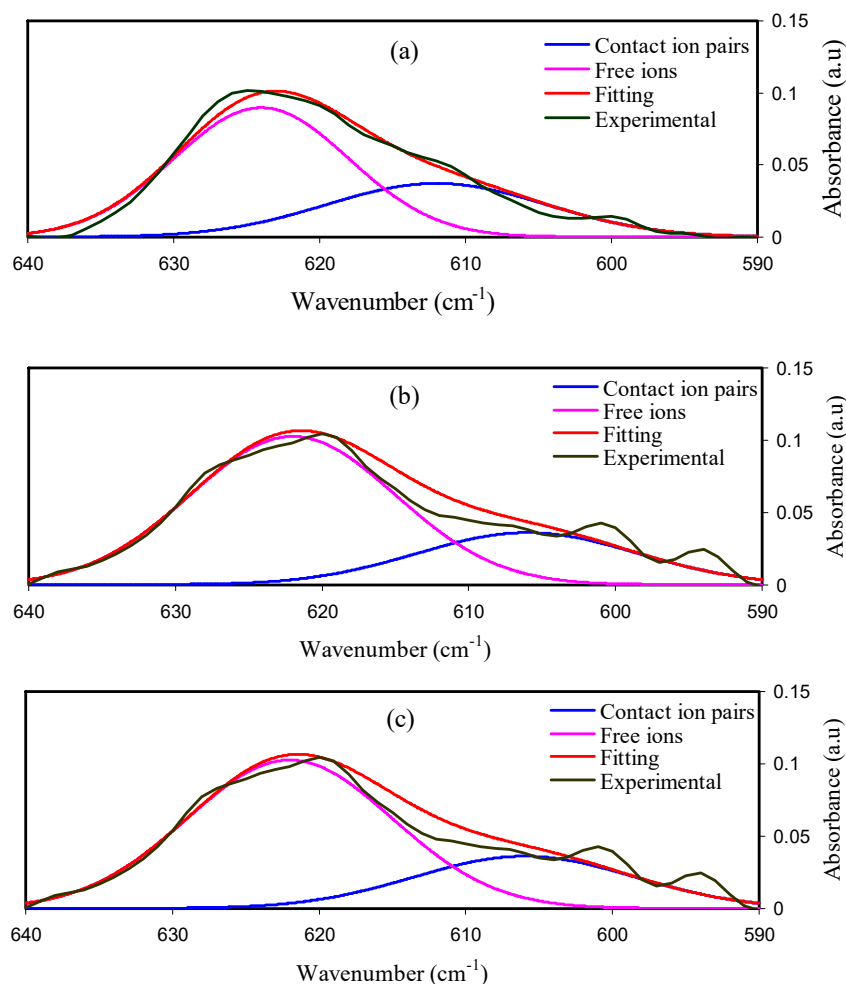
Figure 2. Deconvoluted FTIR spectra for (**a**) MDLG1, (**b**) MDLG2, and (**c**) MDLG3.

The free ions and contact ion pairs were measured using the area of the FTIR bands by the equations below [4]:

$$\text{Percentage of FI (\%)} = \frac{A_f}{A_f + A_c} \times 100\% \tag{1}$$

$$\text{Percentage of CIP (\%)} = \frac{A_c}{A_f + A_c} \times 100\% \tag{2}$$

where A_f is the area of the FIP and A_c is the area of the CIP. The percentages of FI and CIP are shown in Table 1.

Table 1. The percentages of ions.

Sample	FI%	CIP%
MDLG1	65.85%	34.14%
MDLG2	72.58%	27.42%
MDLG3	76.95%	23.05%

The rise in ionic conductivity might also be attributed to the rise in Li^+ ions that dissociate from $LiClO_4$ salts. There is a strong correlation between the conductivity and the proportion of free ions, according to Aniskari and colleagues [43]. The calculation of the number density (n), ionic mobility (μ), and diffusion coefficient (D) for each electrolyte can be calculated from Equations (3)–(5). In these equations, M stands for the molecular weight of glycerol and e is the electron charge, and N_A is the Avogadro's constant. A polymer electrolyte has a total volume of V_{Total}. The calculated values of n, μ, and D are shown in Table 2.

$$n = \frac{M \times N_A}{V_{Total}} \times (freeion\%) \tag{3}$$

$$\mu = \frac{\sigma}{ne} \tag{4}$$

$$D = \frac{\mu kT}{e} \tag{5}$$

Table 2. The n, D, and μ at ambient temperature from FTIR approach.

Glycerol %	n (cm^{-3})	μ (cm^2 V^{-1} s)	D (cm^2 s^{-1})
MDLG1	2.32×10^{22}	4.0×10^{-8}	1.04×10^{-9}
MDLG2	5.92×10^{22}	1.09×10^{-7}	2.83×10^{-9}
MDLG3	1.13×10^{23}	1.10×10^{-7}	2.86×10^{-9}

In Table 2 the D, μ and n values increase as the glycerol increases. The improvement of D and μ can be interpreted according to the increase in polymer chain flexibility upon the addition of the glycerol [1].

The relationship between the ionic conductivity of the electrolyte films and the ionic mobility is well-acknowledged and mathematically stated as follows:

$$\sigma = \sum \eta q \mu \tag{6}$$

where σ denotes the ionic conductivity, η represents the charge carrier density, and q stands for the single charge. From the equation above, it can be observed that the ionic conductivity improves with the increment of the ionic mobility as well as charge carrier density.

2.2. Impedance Study

Figure 3 shows the Cole-Cole plots used to estimate the impedance parameters of the electrolytes used in this study. An appropriate equivalent circuit model, with series connections for the resistor and the capacitor given by bulk resistance (R_b) and the constant phase element (CPE), is shown in the inset figure for each Cole-Cole plot. Ions flow via a resistor, whereas polymer chains remain immobile in a capacitor [44]. Because of the charge buildup and capacitive elements in the electrolytes, there is a spike in the plots created by the diffusion process inside the system [17,45]. This graph also shows how polarization and blocking electrodes in the Pes affect the inclination [46,47].
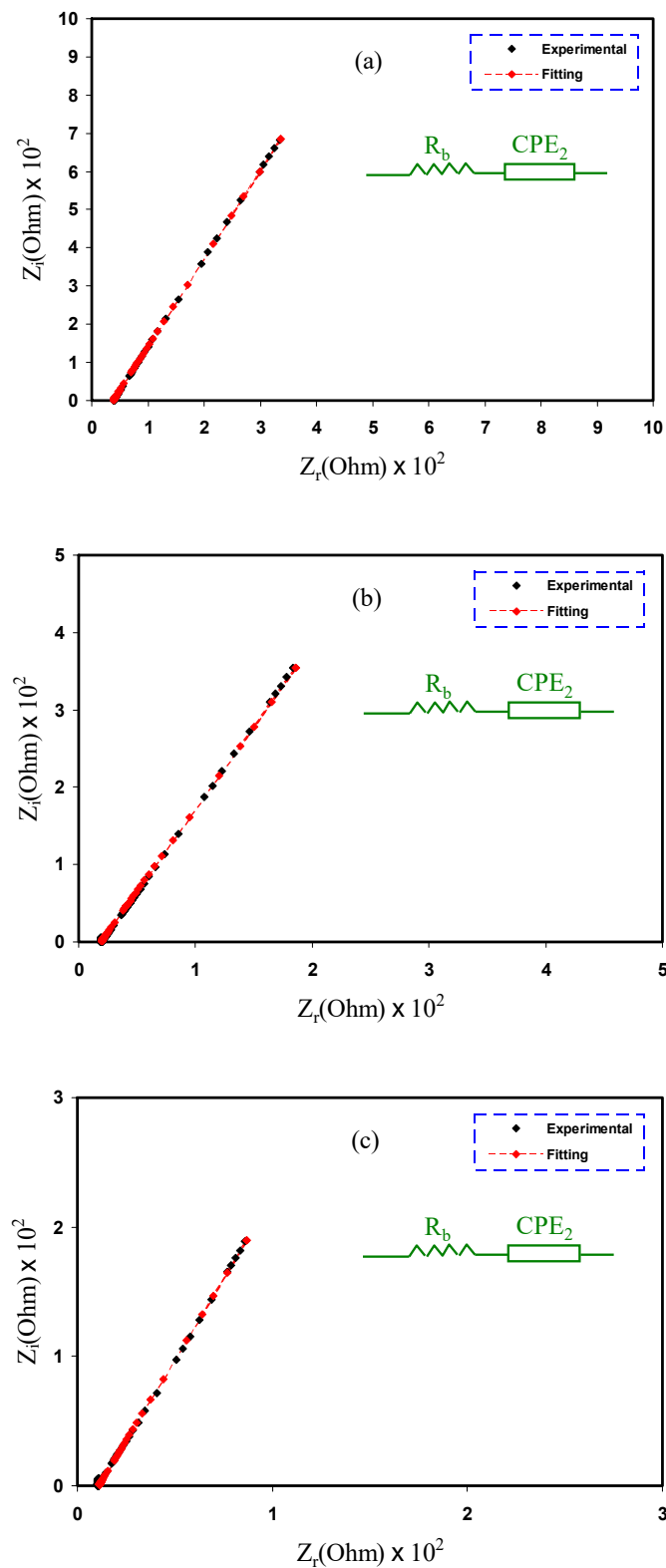
Figure 3. EIS spectra of (**a**) MDLG1, (**b**) MDLG2, and (**c**) MDLG3 electrolytes.

The impedance of *CPE* (Z_{CPE}) is written as follows [48,49]:

$$Z_{CPE} = \frac{1}{C\omega^p}\left[\cos\left(\frac{\pi p}{2}\right) - i\sin\left(\frac{\pi p}{2}\right)\right] \tag{7}$$

where ω denotes the angular frequency, p indicates the deviation of the plot from the axis, and C refers to the capacitance of *CPE* component. The spectra that involve only a spike and R_b are in series with *CPE*, and the real and the imaginary parts of impedance, Z_r and Z_i, are based on the following mathematical relationships.

$$Z_r = R + \frac{\cos\left(\frac{\pi p_2}{2}\right)}{C_2 \omega^{p2}} \tag{8}$$

$$Z_i = \frac{\sin\left(\frac{\pi p_2}{2}\right)}{C_2 \omega^{p2}} \tag{9}$$

The determined R_b and *CPE* for each electrolyte are listed in Table 3. The *CPE* values increase while the R_b values fall when glycerol concentrations increased. There are more ions in a solution, resulting in a higher capacitance value, which results in the greater mobility and dissociation of ions, thereby increasing conductivity [50,51]. The ionic conductivity (σ) measured using Equation (10) and also shown in Table 3 demonstrates this.

$$\sigma_{dc} = \left(\frac{1}{R_b}\right) \times \left(\frac{t}{A}\right) \tag{10}$$

Table 3. EEC fitting parameters for each sample.

Sample	K (F^{-1})	*CPE* (F)	R_b (Ohm)	Conductivity (S cm^{-1})
MDLG1	5.21×10^4	1.92×10^{-5}	3.80×10^1	3.93×10^{-4}
MDLG2	2.45×10^4	4.08×10^{-5}	1.89×10^1	8.16×10^{-4}
MDLG3	1.59×10^4	6.29×10^{-5}	1.10×10^1	1.45×10^{-3}

Here, t refers to the electrolyte's thickness; A denotes the SS electrodes area.

This study demonstrated that the MC:Dex:LiClO$_4$:glycerol combination is more flexible and mobile because of the glycerol [52]. The conductivity of 1.99×10^{-3} S cm^{-1}, achieved by MDLG3, is close to that achieved by Amran et al. [27] and Shukur et al. [30], and they also used glycerol as a plasticizer in their studies. It is also comparable with our previous studies of the biodegradable-blend-polymer electrolytes incorporated with ammonium salts [53,54]. The conductivity that was achieved in this study bodes well for future applications in energy devices [31].

As the samples have only a spike, D, μ, and n are measured by below equations [2]:

D is measured using Equations (11) and (12) [1]:

$$D = D_o \exp\left\{-0.0297[\ln D_o]^2 - 1.4348 \ln D_o - 14.504\right\} \tag{11}$$

where the following is the case.

$$D_o = \left(\frac{4k^2 l^2}{R_b{}^4 \omega_{\min}{}^3}\right) \tag{12}$$

Here, $\omega_{\min}$ and l correspond to the angular frequency that is based on the minimum Z_i and the electrolyte thickness, respectively. μ is measurable from the relationship shown in Equation (13):

$$\mu = \left(\frac{eD}{K_b T}\right) \tag{13}$$

where K_b and T are the Boltzmann constant possess normal meanings.

The conductivity can be measured using Equation (6).

Thus, the number n is measured using Equation (14):

$$n = \left(\frac{\sigma_{dc} K_b T \tau_2}{(e K_2 \varepsilon_o \varepsilon_r A)^2} \right) \tag{14}$$

In Table 4, D, μ, and n increased when glycerol increased. This is caused by increasing the polymer chain's flexibility when the glycerol is loaded [2]. The outcome shows how the concentration of glycerol affects the values of the ion number density, the ionic mobility, and the diffusion coefficient. This increase in D, μ, and n values can cause an increase in conductivity [4]. It is interesting to observe that when glycerol concentration increases, the number of ions (n) tends to increase continuously. Glycerol enhances the dissociation of salts to free ions; thus, n increases correspondingly. Meanwhile, ionic mobility (μ) and diffusion coefficient (D) are observed to follow the same trend of ionic conductivity, as shown in Table 3. The value of the free ion, which gradually increased by adding glycerol to the system, indicates that the ionic conductivity of the present system increased by the increasing the (n) value. These results from EIS and the FTIR deconvolution are in agreement.

Table 4. The values of ion transport parameters of each film from impedance approach.

Sample	D (cm^2 s^{-1})	μ (cm^2 V^{-1} s)	n (cm^{-3})
MDLG1	1.72×10^{-7}	6.71×10^{-6}	3.65×10^{20}
MDLG2	1.88×10^{-7}	7.33×10^{-6}	6.95×10^{20}
MDLG3	2.64×10^{-7}	1.03×10^{-5}	8.80×10^{20}

2.3. Dielectric Properties

According to current research, dielectric material qualities may be defined in multiple ways. There were many ways to increase the accuracy and sensitivity of material characterization [55–59]. Impedance studies at various frequencies have been shown to be a good approach for studying the molecular mobility of dielectric materials [60]. Dielectric studies may be used to examine the conductivity trend. Different amounts of glycerol at ambient temperature affect the dielectric constant (ε') and the dielectric loss (ε''), as observed in Figures 4 and 5, respectively. ε' and ε'' are measured using the equations below [61–63]:

$$\varepsilon' = \left[\frac{Z''}{\omega C_o (Z'^2 + Z''^2)} \right] \tag{15}$$

$$\varepsilon'' = \left[\frac{Z'}{\omega C_o (Z'^2 + Z''^2)} \right] \tag{16}$$

where C_o is the vacuum capacitance, which is equivalent to $\varepsilon_0 A / t$ in which ε_0 is the vacuum permittivity; the angular frequency is denoted by ω ($\omega = 2\pi f$); the frequency is denoted by f.

The conductivity of a polymer electrolyte is determined by its dielectric constant [64]. Real dielectric permittivity (ε') is used to determine the polarization or dipole alignment, which is measured by capacitance. Similarly to ε'', which indicates dielectric loss, conductance reflects the energy needed to align dipoles in a dielectric medium [65]. An important consideration in electrical conductivity testing is the identification of neutral ion pairs produced by the interaction of dissolved ion pairs [59]. In EIS measurements, it was shown that by adding more glycerol, the DC's conductivity significantly increased. ε' and ε'' at low frequencies are higher (Figures 4 and 5), which show variations for the films. Charge carriers or space charge polarization build up at the electrode/electrolyte contact point, causes this phenomenon [60]. Increasing the frequency reduces the dielectric property (bulk property). As a result, ε' and ε'' increase as a result of a decrease in the frequency of

the applied electric field [66]. As a result of the quick reversal of the electric field frequency, there is no new ion diffusion that takes place along its route, and polarization is reduced. Eventually, the peak shrinks to the point where it is no longer frequency dependent [48]. In a comparison to other samples, the system containing 42 wt.% of glycerol had a greater dielectric constant. Dielectric loss (ε'') and constant (ε') are strongly impacted by the conductivity in the system [51,67].
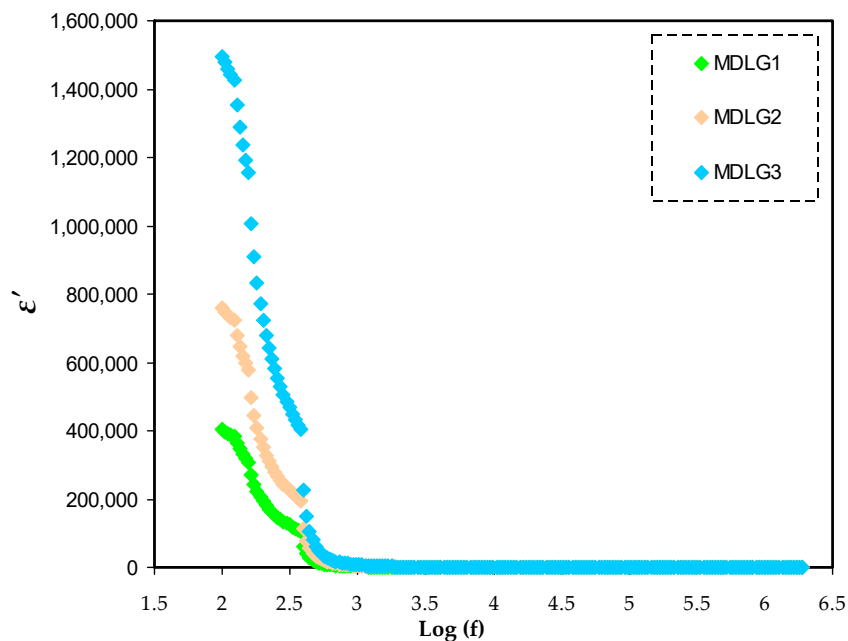
Figure 4. ε' spectra versus frequency for MC:Dex:LiClO$_4$:Glycerol electrolytes.
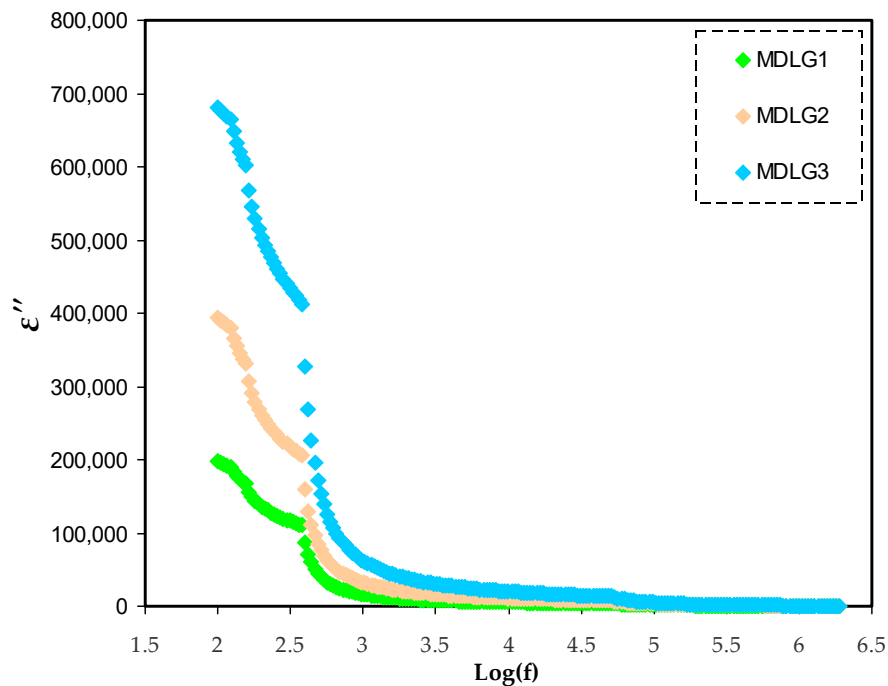
Figure 5. ε'' spectra versus frequency for MC:Dex:LiClO$_4$:Glycerol electrolytes.

It has previously been observed that the dielectric constant (ε') and the density of the charge carriers (n_i) were formulated by the following relationship:

$$n_i = n_o \exp(-U / \varepsilon' K_b T) \tag{17}$$

where U is the dissociation energy.

DC's conductivity, as well as dielectric constant values, can be manipulated successfully [68]. The dielectric constants of polymer electrolytes may be used to determine the conductivity of certain materials and, hence, their electrical properties. A drop in dielectric constant is accompanied with a decrease in capacitance ($\varepsilon' = C/C_o$). The plots show that the ε'' value is higher than the ε', as shown in Figures 4 and 5. DC conduction processes and dielectric polarization processes both have an impact on dielectric loss [51].

2.4. TNM Study

In order to ensure the purely ionic nature of the PE system, the ion transport number (t_{ion}) has been measured for the optimized MC:Dex: LiClO$_4$:Glycerol composition using the DC polarization technique [69]. The curve obtained for the SS | Polymer electrolyte | SS cell (SS: stainless-steel) is shown in Figure 6. An initial current (I_i) of 128 A and the total of ionic and electronic currents were delivered by the cell. Since the SS electrode is ion-blocking in nature, the current declines quickly and is saturated at the residual electronic current (I_e) of 3 μA. The electrolyte system's ionic composition is thought to be responsible for the abrupt reduction in current levels. The t_{ion} and t_{el} values of the electrolyte film, obtained using the Equations (18) and (19), are found to be 0.976 and 0.024, respectively. These results show how ionic the electrolyte system is and how it will protect the electrodes of the energy storage device from each other since it is close to 1, which means it is close to the ideal value of unity. Ions are the key charge carriers in this system of methylcellulose-dextran-LiClO$_4$:Glycerol [70–72]. The result obtained in this study is observed to be high compared to our previous study for methylcellulose-based polymer electrolytes impregnated with potassium iodide [73].
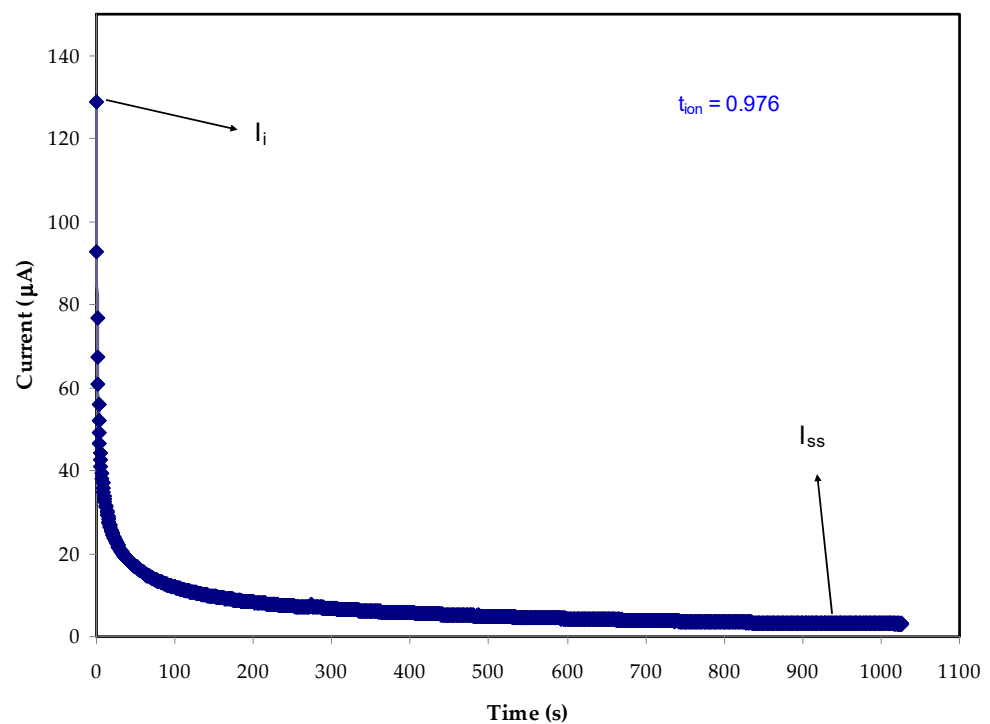
Figure 6. Chronoamperometric profile of for the MDLG3 electrolyte.

Equations (17) and (18) are used to measure t_{ion} and t_{el}.

$$t_{ion} = \frac{I_i - I_{ss}}{I_i} \tag{18}$$

$$t_{el} = 1 - t_{ion} \tag{19}$$

In Equations (18) and (19), the starting and the steady-state current are expressed as I_i and I_{ss}, respectively.

The electrochemical stability window (ESW) is an important parameter for an electrolyte, which determines the working voltage range of the energy storage device. The ESW of the optimized MC:Dextran:40 wt.% LiClO$_4$:48 wt.% Glycerol composition is obtained using linear sweep voltammetry (LSV). The LSV curve, shown in Figure 7, displays a plateau of negligible current without any anodic/cathodic current peak up to ~3 V. The present values increase sharply after the aforementioned potential. A considerable ESW of 3 V is shown, making the electrolyte film acceptable for supercapacitor use. In order for the film to be used in energy storage devices, the stability of the plasticized methylcellulose-dextran-LiClO$_4$ system has been shown to be up to 3 V. The interesting observation in this study is the eligibility of the MDLG3 electrolyte for energy storage device utilization. This is caused by the satisfactory voltage breakdown of the sample at almost 1.0 V [74,75]. The decomposition voltage attained in this study is relatively high compared to our previous studies [76,77]. This could be due to the presence of LiClO$_4$ as an ionic source, which has higher stability than ammonium salts. Moreover, a protic ionic liquid electrolyte was utilized for lithium-ion batteries as documented by Bockenfeld et al. [78]. They demonstrated that the highest potential stability was 2.65 V for their electrolyte that incorporated 0.5 M lithium nitrate (LiNO$_3$) in propylene carbonate-pyrrolidinium nitrate.
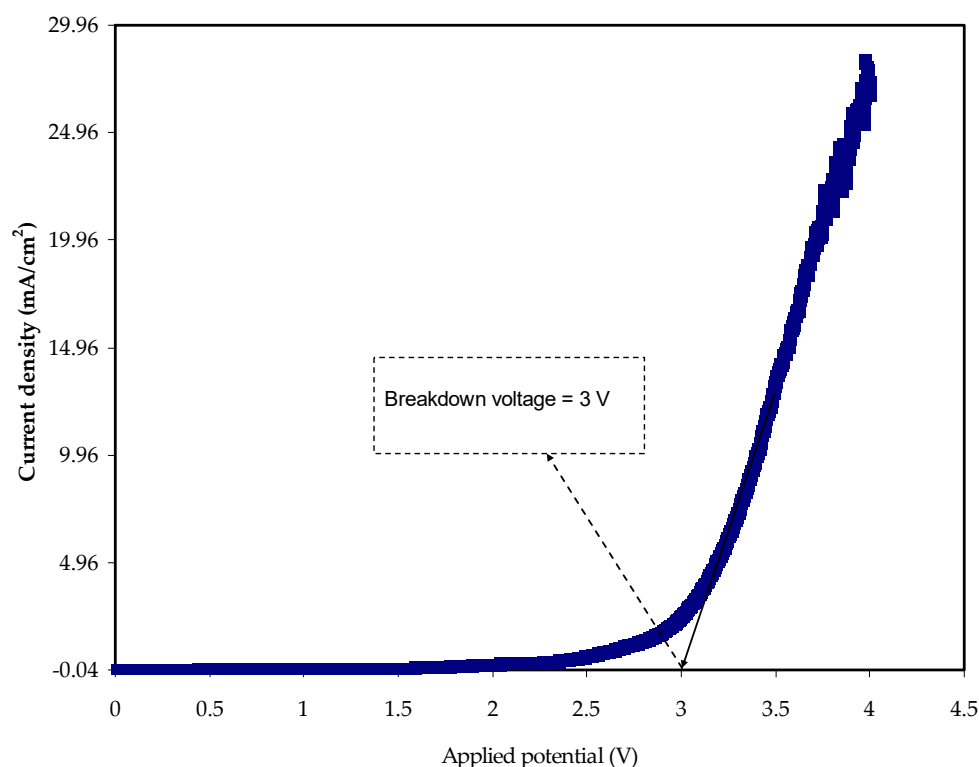
Figure 7. LSV for the MDLG3 film of SPE.

3. Materials and Methods

3.1. Materials

MC polymer ($M_{w\ avg}$ = 10,000–220,000), LiClO$_4$ (M_w = 106.39 g/mol) and glycerol (M_w = 92.09382 g/mol) were purchased from Sigma-Aldrich (Kuala Lumpur, Malaysia).

3.2. Electrolyte Preparation

The synthesis of MC-Dex-blend polymer was performed by stirring and dissolving 40 wt.% of Dex (0.4 g) and 60 wt.% of MC (0.6 g) individually, each in a 1% solution of

30 mL acetic acid, for almost 2 h at room temperature. Then, the two solutions were stirred and blended using a magnetic stirrer for around 4 h until reaching a homogenous-blend solution. Then, with respect to the above solution, 40 wt.% (0.666 g) of LiClO$_4$, MC-Dex-LiClO$_4$ formed. Ultimately, in the step of 14 wt.%, 14, 28, and 42 wt.% of glycerol were added to the MC-Dex-LiClO$_4$ solution followed by continuous stirring until the synthesis of plasticized SPEs was achieved. The labelling of the series of the samples was conducted as follows: MDLG1, MDLG2, and MDLG3 for the MC-Dex-LiClO$_4$ loading 14, 28, and 42 wt.% of glycerol, respectively as shown in Table 5. The casting of the series of sample solutions was carried out in the Petri dishes, followed by leaving them at room temperature to evaporate the solvent gradually. The free solvent sample films were kept in a desiccator.

Table 5. The identification and composition for the MC-Dex-LiClO$_4$–glycerol systems.

Sample Code	MC (g)	Dex (g)	LiClO$_4$ (g)	Glycerol (g)	Glycerol wt.%
MDLG1	0.6	0.4	0.666	0.271	14
MDLG2	0.6	0.4	0.666	0.647	28
MDLG3	0.6	0.4	0.666	1.206	42

3.3. Methods of Characterizations

3.3.1. FTIR and EIS Measurements

The FTIR spectra of the blended polymer systems were acquired using FTIR Spectrophotometer (Malvern Panalytical Ltd., Malvern, UK), ranging from 4000 to 400 cm^{-1} with a resolution of 2 cm^{-1}. The EIS samples spectra were acquired using the EIS (3532-50 LCR HiTESTER (HIOKI), Nagano, Japan) within 50 Hz and 5,000,000 Hz of frequency. The circle film had a geometric circle shape (diameter of 2 cm), which was sandwiched between stainless steel (SS) electrodes using a spring force during electrochemical measurements. The cell was hyphenated with a computer to measure real and imaginary (Z$'$ and Z$''$) parts of the complex impedance spectra (Z*).

3.3.2. TNM and LSV

The ion (t_{ion}) and electron (t_{el}) transference numbers were measured precisely. The cell (SS | MDLG3 | SS) was connected to the UNI-T UT803 multimeter and A&V Instrument DP3003 digital DC power supply. By applying a voltage of 0.2 V to the cell, the polarization of the cell was obtained over a sufficient amount of time at room temperature. To obtain the potential stability of the MDLG3, LSV was used by applying 10 mV s^{-1} within 0.0 and 4.0 V. The cell was the three-electrode type, and the working, counter, and reference electrodes were used by utilizing the Digi-IVY DY2300 potentiostat. The current changes over the mentioned potential were obtained.

4. Conclusions

In this study, SPEs based on MC:Dex:LiClO$_4$ plasticized with glycerol were synthesized by the solution-cast method. The conductivity increased to 1.45×10^{-3} S cm^{-1} due to the doping of glycerol. The FTIR method showed that there was an interaction of LiClO$_4$ and glycerol with the MC and Dex by changing FTIR absorption peaks. The FTIR deconvolution of CLO$_4^-$ anions showed that the free ion percentages increased when glycerol increased, while the percentages of contact ion pairs decreased. Further proof of *DC* conductivity trends was emphasized from the dielectric measurement. The addition of glycerol was effective in increasing the number density (*n*), diffusion coefficient (*D*), and mobility (*μ*). Additionally, the mass transport improvements of the electrolytes originate from the increase in chain flexibility. The values of measured t_{ion} and t_{el} indicate the ion's responsibility for conduction in the polymer-electrolyte system. The stability voltage range of the electrolyte system is satisfactory, meaning that the SPE is eligible for utilization at large scales in electrochemical energy storage devices.

References

1. Hadi, J.M.; Aziz, S.B.; Kadir, M.F.Z.; El-Badry, Y.A.; Ahamad, T.; Hussein, E.E.; Asnawi, A.S.F.M.; Abdullah, R.M.; Alshehri, S.M. Design of plasticized proton conducting Chitosan: Dextran based biopolymer blend electrolytes for EDLC application: Structural, impedance and electrochemical studies. *Arab. J. Chem.* **2021**, *14*, 103394. [CrossRef]

2. Hadi, J.M.; Aziz, S.B.; Brza, M.A.; Kadir, M.F.Z.; Abdulwahid, R.T.; Ali Al-Asbahi, B.; Ahmed Ali Ahmed, A. Structural and energy storage behavior of ion conducting biopolymer blend electrolytes based on methylcellulose: Dextran polymers. *Alex. Eng. J.* **2022**, *61*, 9273–9285. [CrossRef]

3. Alexandre, S.A.; Silva, G.G.; Santamaría, R.; Trigueiro, J.P.C.; Lavall, R.L. A highly adhesive PIL/IL gel polymer electrolyte for use in flexible solid state supercapacitors. *Electrochim. Acta* **2019**, *299*, 789–799. [CrossRef]

4. Brza, M.A.; Aziz, S.B.; Anuar, H.; Ali, F. Structural, Ion Transport Parameter and Electrochemical Properties of Plasticized Polymer Composite Electrolyte Based on PVA: A Novel Approach to Fabricate High Performance EDLC Devices. *Polym. Test.* **2020**, *91*, 106813. [CrossRef]

5. Nyuk, C.M.; Isa, M.I.N.M. Solid biopolymer electrolytes based on carboxymethyl cellulose for use in coin cell proton batteries. *J. Sustain. Sci. Manag.* **2017**, *2017*, 42–48.

6. Salleh, N.S.; Aziz, S.B.; Aspanut, Z.; Kadir, M.F.Z. Electrical impedance and conduction mechanism analysis of biopolymer electrolytes based on methyl cellulose doped with ammonium iodide. *Ionics* **2016**, *22*, 2157–2167. [CrossRef]

7. Hamsan, M.H.; Aziz, S.B.; Shukur, M.F.; Kadir, M.F.Z. Protonic cell performance employing electrolytes based on plasticized methylcellulose-potato starch-NH4NO3. *Ionics* **2019**, *25*, 559–572. [CrossRef]

8. Stepniak, I.; Galinski, M.; Nowacki, K.; Wysokowski, M.; Jakubowska, P.; Bazhenov, V.V.; Leisengang, T.; Ehrlich, H.; Jesionowski, T. A novel chitosan/sponge chitin origin material as a membrane for supercapacitors-preparation and characterization. *RSC Adv.* **2016**, *6*, 4007–4013. [CrossRef]

9. Sudhakar, Y.N.; Selvakumar, M.; Bhat, D.K. Preparation and characterization of phosphoric acid-doped hydroxyethyl cellulose electrolyte for use in supercapacitor. *Mater. Renew. Sustain. Energy* **2015**, *4*, 10. [CrossRef]

10. Hassan, M.F.; Azimi, N.S.N.; Kamarudin, K.H.; Sheng, C.K. Solid polymer electrolytes based on starch-Magnesium Sulphate: Study on morphology and electrical conductivity. *ASM Sci. J.* **2018**, *11*, 17–28.

11. Du, B.W.; Hu, S.Y.; Singh, R.; Tsai, T.T.; Lin, C.C.; Ko, F.H. Eco-friendly and biodegradable biopolymer chitosan/Y2O3 composite materials in flexible organic thin-film transistors. *Materials* **2017**, *10*, 1026. [CrossRef]

12. Moniha, V.; Alagar, M.; Selvasekarapandian, S.; Sundaresan, B.; Hemalatha, R.; Boopathi, G. Synthesis and characterization of bio-polymer electrolyte based on iota-carrageenan with ammonium thiocyanate and its applications. *J. Solid State Electrochem.* **2018**, *22*, 3209–3223. [CrossRef]

13. Hamsan, M.H.; Shukur, M.F.; Aziz, S.B.; Kadir, M.F.Z. Dextran from Leuconostoc mesenteroides-doped ammonium salt-based green polymer electrolyte. *Bull. Mater. Sci.* **2019**, *42*, 57. [CrossRef]

14. Nadirah, B.N.; Ong, C.C.; Saheed, M.S.M.; Yusof, Y.M.; Shukur, M.F. Structural and conductivity studies of polyacrylonitrile/methylcellulose blend based electrolytes embedded with lithium iodide. *Int. J. Hydrogen Energy* **2020**, *45*, 19590–19600. [CrossRef]

15. Salman, Y.A.K.; Abdullah, O.G.; Hanna, R.R.; Aziz, S.B. Conductivity and electrical properties of chitosan-methylcellulose blend biopolymer electrolyte incorporated with lithium tetrafluoroborate. *Int. J. Electrochem. Sci.* **2018**, *13*, 3185–3199. [CrossRef]

16. Simari, C.; Lufrano, E.; Coppola, L.; Nicotera, I. Composite gel polymer electrolytes based on organo-modified nanoclays: Investigation on lithium-ion transport and mechanical properties. *Membranes* **2018**, *8*, 69. [CrossRef]

17. Gohel, K.; Kanchan, D.K. Ionic conductivity and relaxation studies in PVDF-HFP:PMMA-based gel polymer blend electrolyte with LiClO$_4$ salt. *J. Adv. Dielectr.* **2018**, *8*, 1850005. [CrossRef]

18. Porcarelli, L.; Shaplov, A.S.; Salsamendi, M.; Nair, J.R.; Vygodskii, Y.S.; Mecerreyes, D.; Gerbaldi, C. Single-Ion Block Copoly(ionic liquid)s as Electrolytes for All-Solid State Lithium Batteries. *ACS Appl. Mater. Interfaces* **2016**, *8*, 10350–10359. [CrossRef]

19. Mantravadi, R.; Chinnam, P.R.; Dikin, D.A.; Wunder, S.L. High Conductivity, High Strength Solid Electrolytes Formed by in Situ Encapsulation of Ionic Liquids in Nanofibrillar Methyl Cellulose Networks. *ACS Appl. Mater. Interfaces* **2016**, *8*, 13426–13436. [CrossRef]

20. Weng, R.; Chen, L.; Lin, S.; Zhang, H.; Wu, H.; Liu, K.; Cao, S.; Huang, L. Preparation and characterization of antibacterial cellulose/chitosan nanofiltration membranes. *Polymers* **2017**, *9*, 116. [CrossRef] [PubMed]

21. Taghizadeh, M.T.; Seifi-Aghjekohal, P. Sonocatalytic degradation of 2-hydroxyethyl cellulose in the presence of some nanoparticles. *Ultrason. Sonochem.* **2015**, *26*, 265–272. [CrossRef]

22. Shuhaimi, N.E.A.; Teo, L.P.; Majid, S.R.; Arof, A.K. Transport studies of NH4NO3 doped methyl cellulose electrolyte. *Synth. Met.* **2010**, *160*, 1040–1044. [CrossRef]

23. Pinotti, A.; García, M.A.; Martino, M.N.; Zaritzky, N.E. Study on microstructure and physical properties of composite films based on chitosan and methylcellulose. *Food Hydrocoll.* **2007**, *21*, 66–72. [CrossRef]

24. Hamsan, M.H.; Shukur, M.F.; Kadir, M.F.Z. The effect of NH4NO3 towards the conductivity enhancement and electrical behavior in methyl cellulose-starch blend based ionic conductors. *Ionics* **2017**, *23*, 1137–1154. [CrossRef]

25. Kadir, M.; Hamsan, M. Green electrolytes based on dextran-chitosan blend and the effect of NH4SCN as proton provider on the electrical response studies. *Ionics* **2018**, *24*, 2379–2398. [CrossRef]

26. Yang, P.; Liu, L.; Li, L.; Hou, J.; Xu, Y.; Ren, X.; An, M.; Li, N. Gel polymer electrolyte based on polyvinylidenefluoride-co-hexafluoropropylene and ionic liquid for lithium ion battery. *Electrochim. Acta* **2014**, *115*, 454–460. [CrossRef]

27. Amran, N.N.A.; Manan, N.S.A.; Kadir, M.F.Z. The effect of LiCF3SO3 on the complexation with potato starch-chitosan blend polymer electrolytes. *Ionics* **2016**, *22*, 1647–1658. [CrossRef]

28. Vettori, M.H.P.B.; Franchetti, S.M.M.; Contiero, J. Structural characterization of a new dextran with a low degree of branching produced by Leuconostoc mesenteroides FT045B dextransucrase. *Carbohydr. Polym.* **2012**, *88*, 1440–1444. [CrossRef]

29. Dumitra, M.; Meltze, V. Characterization of electron beam irradiated collagen-polyvinylpyrrolidone (PVP) and collagen-dextran (DEX) blends. *Dig. J. Nanomater. Biostruct.* **2011**, *6*, 1793–1803.

30. Shukur, M.F.; Kadir, M.F.Z. Electrical and transport properties of NH4Br-doped cornstarch-based solid biopolymer electrolyte. *Ionics* **2015**, *21*, 111–124. [CrossRef]

31. Aziz, S.B.; Brza, M.A.; Brevik, I.; Hafiz, M.H.; Asnawi, A.S.; Yusof, Y.M.; Abdulwahid, R.T.; Kadir, M.F.Z. Blending and characteristics of electrochemical double-layer capacitor device assembled from plasticized proton ion conducting chitosan:Dextran:NH4PF6 polymer electrolytes. *Polymers* **2020**, *12*, 2103. [CrossRef] [PubMed]

32. Ndruru, S.T.C.L.; Wahyuningrum, D.; Bundjali, B.; Arcana, I.M. Preparation and characterization of biopolymer electrolyte membranes based on liclo4-complexed methyl cellulose as lithium-ion battery separator. *J. Eng. Technol. Sci.* **2020**, *52*, 28–50. [CrossRef]

33. Hafiza, M.N.; Isa, M.I.N. Correlation between structural, ion transport and ionic conductivity of plasticized 2-hydroxyethyl cellulose based solid biopolymer electrolyte. *J. Memb. Sci.* **2020**, *597*, 117176. [CrossRef]

34. Aziz, S.B.; Dannoun, E.M.A.; Murad, A.R.; Mahmoud, K.H.; Brza, M.A.; Nofal, M.M.; Elsayed, K.A.; Abdullah, S.N.; Hadi, J.M.; Kadir, M.F.Z. Influence of scan rate on CV Pattern: Electrical and electrochemical properties of plasticized Methylcellulose: Dextran (MC:Dex) proton conducting polymer electrolytes. *Alex. Eng. J.* **2022**, *61*, 5919–5937. [CrossRef]

35. Aziz, S.B.; Hamsan, M.H.; MNofal, M.; Karim, W.O.; Brevik, I.; Brza, M.; Abdulwahid, R.T.; Al-Zangana, S.; Kadir, M.F.Z. Structural, Impedance and Electrochemical Characteristics of Electrical Double Layer Capacitor Devices Based on Chitosan: Dextran Biopolymer Blend Electrolytes. *Polymers* **2020**, *12*, 1411. [CrossRef]

36. Shukur, M.F.; Azmi, M.S.; Zawawi, S.M.M.; Majid, N.A.; Illias, H.A.; Kadir, M.F.Z. Conductivity studies of biopolymer electrolytes based on chitosan incorporated with NH4Br. *Phys. Scr.* **2013**, *2013*, 014049. [CrossRef]

37. Mejenom, A.A.; Hafiza, M.N.; Isa, M.I.N. X-Ray diffraction and infrared spectroscopic analysis of solid biopolymer electrolytes based on dual blend carboxymethyl cellulose-chitosan doped with ammonium bromide. *ASM Sci. J.* **2018**, *11*, 37–46.

38. Aziz, S.B.; Marif, R.B.; Brza, M.A.; Hassan, A.N.; Ahmad, H.A.; Faidhalla, Y.A.; Kadir MF, Z. Structural, thermal, morphological and optical properties of PEO filled with biosynthesized Ag nanoparticles: New insights to band gap study. *Results Phys.* **2019**, *13*, 102220. [CrossRef]

39. Pistorius, A.M.A.; DeGrip, W.J. Deconvolution as a tool to remove fringes from an FT-IR spectrum. *Vib. Spectrosc.* **2004**, *36*, 89–95. [CrossRef]

40. Ramlli, M.A.; Bashirah, N.A.A.; Isa, M.I.N. Ionic Conductivity and Structural Analysis of 2-hyroxyethyl Cellulose Doped with Glycolic Acid Solid Biopolymer Electrolytes for Solid Proton Battery. In *IOP Conference Series: Materials Science and Engineering*; IOP Publishing: Bristol, UK, 2018; Volume 440, p. 012038. [CrossRef]

41. Xi, J.; Bai, Y.; Qiu, X.; Zhu, W.; Chen, L.; Tang, X. Conductivities and transport properties of microporous molecular sieves doped composite polymer electrolyte used for lithium polymer battery. *New J. Chem.* **2005**, *29*, 1454–1460. [CrossRef]

42. Abarna, S.; Hirankumar, G. Electrical, dielectric and electrochemical studies on new Li ion conducting solid polymer electrolytes based on polyethylene glycol p-tert-octylphenyl ether. *Polym. Sci. Ser. A* **2017**, *59*, 660–668. [CrossRef]

43. Aniskari, N.A.B.; Isa, M.I.N.M. The effect of ionic charge carriers in 2-hydroxyethyl cellulose solid biopolymer electrolytes doped glycolic acid via FTIR-deconvolution technique. *J. Sustain. Sci. Manag.* **2017**, *12*, 71–79.

44. Kumar, M.; Tiwari, T.; Chauhan, J.K.; Srivastava, N. Erratum: UnderstanDing the ion dynamics and relaxation behavior from impedance spectroscopy of NaI doped Zwitterionic polymer system (Materials Research Express (2013) 1 (045003)). *Mater. Res. Express* **2014**, *1*, 045003. [CrossRef]

45. Samsudin, A.S.; Khairul, W.M.; Isa, M.I.N. Characterization on the potential of carboxy methylcellulose for application as proton conducting biopolymer electrolytes. *J. Non. Cryst. Solids* **2012**, *358*, 1104–1112. [CrossRef]

46. Fonseca, C.P.; Cavalcante, F.; Amaral, F.A.; Souza, C.A.Z.; Neves, S. Thermal and conduction properties of a PCL-biodegradable gel polymer electrolyte with LiClO$_4$, LiF$_3$CSO$_3$, and LiBF$_4$ salts. *Int. J. Electrochem. Sci.* **2007**, *2*, 52–63.

47. Misenan, M.; Khiar, A. Conductivity, Dielectric And Modulus Studies of Methylcellulose-NH 4 TF Polymer. *Eurasian J. Biol. Chem. Sci. J.* **2018**, *1*, 59–62.

48. Teo, L.P.; Buraidah, M.H.; Nor, A.F.M.; Majid, S.R. Conductivity and dielectric studies of Li$_2$SnO$_3$. *Ionics* **2012**, *18*, 655–665. [CrossRef]

49. Aziz, S.B.; Marif, R.B.; Brza, M.A.; Hamsan, M.H.; Kadir, M.F.Z. Employing of Trukhan model to estimate ion transport parameters in PVA based solid polymer electrolyte. *Polymers* **2019**, *11*, 1694. [CrossRef]

50. Lee, D.K.; Allcock, H.R. The effects of cations and anions on the ionic conductivity of poly[bis(2-(2-methoxyethoxy)ethoxy) phosphazene] doped with lithium and magnesium salts of trifluoromethanesulfonate and bis(trifluoromethanesulfonyl)imidate. *Solid State Ionics* **2010**, *181*, 1721–1726. [CrossRef]

51. Awasthi, P.; Das, S. Reduced electrode polarization at electrode and analyte interface in impedance spectroscopy using carbon paste and paper. *Rev. Sci. Instrum.* **2019**, *90*, 124103. [CrossRef]

52. Marf, A.S.; Aziz, S.B.; Abdullah, R.M. Plasticized H+ ion-conducting PVA:CS-based polymer blend electrolytes for energy storage EDLC application. *J. Mater. Sci. Mater. Electron.* **2020**, *31*, 18554–18568. [CrossRef]

53. Aziz, S.B.; Ali, F.; Anuar, H.; Ahamad, T.; Kareem, W.O.; Brza, M.A.; Kadir, M.F.Z.; Abu Ali, O.A.; Saleh, D.I.; Asnawi, A.S.F.M.; et al. Structural and electrochemical studies of proton conducting biopolymer blend electrolytes based on MC:Dextran for EDLC device application with high energy density. *Alex. Eng. J.* **2022**, *61*, 3985–3997. [CrossRef]

54. Aziz, S.B.; Hadi, J.M.; Elham, E.M.; Abdulwahid, R.T.; Saeed, S.R.; Marf, A.S.; Karim, W.O.; Kadir, M.F.Z. The study of plasticized amorphous biopolymer blend electrolytes based on polyvinyl alcohol (PVA): Chitosan with high ion conductivity for energy storage electrical double-layer capacitors (EDLC) device application. *Polymers* **2020**, *12*, 1938. [CrossRef]

55. Uğuz, H.; Goyal, A.; Meenpal, T.; Selesnick, I.W.; Baraniuk, R.G.; Kingsbury, N.G.; Haiter Lenin, A.; Mary Vasanthi, S.; Jayasree, T.; Adam, M.; et al. ce pte d M us pt. *J. Phys. Energy* **2020**, *2*, 1–31.

56. Al-Omari, A.N.; Lear, K.L. Dielectric characteristics of spin-coated dielectric films using on-wafer parallel-plate capacitors at microwave frequencies. *IEEE Trans. Dielectr. Electr. Insul.* **2005**, *12*, 1151–1161. [CrossRef]

57. Park, S.J.; Yoon, S.A.N.; Ahn, Y.H. Dielectric constant measurements of thin films and liquids using terahertz metamaterials. *RSC Adv.* **2016**, *6*, 69381–69386. [CrossRef]

58. Anderson, L.; Jacob, M. Microwave characterization of a novel, environmentally friendly, plasma polymerized organic thin film. *Phys. Procedia* **2011**, *14*, 87–90. [CrossRef]

59. Aziz, S.B.; Mamand, S.M.; Saed, S.R.; Abdullah, R.M.; Hussein, S.A. New Method for the Development of Plasmonic Metal-Semiconductor Interface Layer: Polymer Composites with Reduced Energy Band Gap. *J. Nanomater.* **2017**, *2017*, 060803. [CrossRef]

60. Aziz, S.B.; Kadir, M.F.Z.; Hamsan, M.H.; Woo, H.J.; Brza, M.A. Development of Polymer Blends Based on PVA:POZ with Low Dielectric Constant for Microelectronic Applications. *Sci. Rep.* **2019**, *9*, 13163. [CrossRef]

61. Hadi, J.M.; Aziz, S.B.; Saeed, S.R.; Brza, M.A.; Abdulwahid, R.T.; Hamsan, M.H.; Abdullah, R.M.; Kadir, M.F.Z.; Muzakir, S.K. Investigation of ion transport parameters and electrochemical performance of plasticized biocompatible chitosan-based proton conducting polymer composite electrolytes. *Membranes* **2020**, *10*, 363. [CrossRef]

62. Hadi, J.M.; Aziz, S.B.; Mustafa, M.S.; Hamsan, M.H.; Abdulwahid, R.T.; Kadir, M.F.Z.; Ghareeb, H.O. Role of nano-capacitor on dielectric constant enhancement in PEO:NH$_4$SCN:xCeO$_2$ polymer nano-composites: Electrical and electrochemical properties. *J. Mater. Res. Technol.* **2020**, *9*, 9283–9294. [CrossRef]

63. Hadi, J.M.; Aziz, S.B.; Mustafa, M.S.; Brza, M.A.; Hamsan, M.H.; Kadir, M.F.Z.; Ghareeb, H.O.; Hussein, S.A. Electrochemical Impedance study of Proton Conducting Polymer Electrolytes based on PVC Doped with Thiocyanate and Plasticized with Glycerol. *Int. J. Electrochem. Sci.* **2020**, *15*, 4671–4683. [CrossRef]

64. Tamilselvi, P.; Hema, M. Structural, thermal, vibrational, and electrochemical behavior of lithium ion conducting solid polymer electrolyte based on poly(vinyl alcohol)/poly(vinylidene fluoride) blend. *Polym. Sci. Ser. A* **2016**, *58*, 776–784. [CrossRef]

65. Aziz, S.B.; Brza, M.A.; Mohamed, P.A.; Kadir MF, Z.; Hamsan, M.H.; Abdulwahid, R.T.; Woo, H.J. Increase of metallic silver nanoparticles in Chitosan:AgNt based polymer electrolytes incorporated with alumina filler. *Results Phys.* **2019**, *13*, 102326. [CrossRef]

66. Aziz, S.B.; Abdullah, R.M. Crystalline and amorphous phase identification from the tanδ relaxation peaks and impedance plots in polymer blend electrolytes based on [CS:AgNt]x:PEO(x−1) (10 ≤ x ≤ 50). *Electrochim. Acta* **2018**, *285*, 30–46. [CrossRef]

67. Khiar, A.S.A.; Anuar, M.R.S.; Parid, M.A.M. Effect of 1-ethyl-3-methylimidazolium nitrate on the electrical properties of starch/chitosan blend polymer electrolyte. *Mater. Sci. Forum* **2016**, *846*, 510–516. [CrossRef]

68. Aziz, S.B.; Rasheed, M.A.; Abidin, Z.H.Z. Optical and Electrical Characteristics of Silver Ion Conducting Nanocomposite Solid Polymer Electrolytes Based on Chitosan. *J. Electron. Mater.* **2017**, *46*, 6119–6130. [CrossRef]

69. Aziz, S.B.; Asnawi, A.S.F.M.; Abdulwahid, R.T.; Ghareeb, H.O.; Alshehri, S.M.; Ahamad, T.; Hadi, J.M.; Kadir, M.F.Z. Design of potassium ion conducting PVA based polymer electrolyte with improved ion transport properties for EDLC device application. *J. Mater. Res. Technol.* **2021**, *13*, 933–946. [CrossRef]

70. Nofal, M.M.; Aziz, S.B.; Brza, M.A.; Abdullah, S.N.; Dannoun, E.M.A.; Hadi, J.M.; Murad, A.R.; Al-Saeedi, S.I.; Kadir, M.F.Z. Studies of Circuit Design, Structural, Relaxation and Potential Stability of Polymer Blend Electrolyte Membranes Based on PVA:MC Impregnated with NH4I Salt. *Membranes* **2022**, *12*, 284. [CrossRef]

71. Nofal, M.M.; Hadi, J.M.; Aziz, S.B.; Brza, M.A.; Asnawi, A.S.F.M.; Dannoun, E.M.A.; Abdullah, A.M.; Kadir, M.F.Z. A Study of Methylcellulose Based Polymer Electrolyte Impregnated with Potassium Ion Conducting Carrier: Impedance, EEC Modeling, FTIR, Dielectric, and Device Characteristics. *Materials* **2021**, *14*, 4859. [CrossRef]

72. Hadi, J.M.; Aziz, S.B.; Nofal, M.M.; Hussein, S.A.; Hamsan, M.H.; Brza, M.A.; Abdulwahid, R.T.; Kadir, M.F.Z.; Woo, H.J. Electrical, Dielectric Property and Electrochemical Performances of Plasticized Silver Ion-Conducting Chitosan-Based Polymer Nanocomposites. *Membranes* **2020**, *10*, 151. [CrossRef] [PubMed]

73. Aziz, S.B.; Dannoun, E.M.A.; Hamsan, M.H.; Ghareeb, H.O.; Nofal, M.M.; Karim, W.O.; Asnawi, A.S.F.M.; Hadi, J.M.; Kadir, M.F.Z.A. A Polymer Blend Electrolyte Based on CS with Enhanced Ion Transport and Electrochemical Properties for Electrical Double Layer Capacitor Applications. *Polymers* **2021**, *13*, 930. [CrossRef] [PubMed]

74. Shuhaimi, N.E.A.; Alias, N.A.; Majid, S.R.; Arof, A.K. Electrical Double Layer Capacitor With Proton Conducting K-Carrageenan–Chitosan Electrolytes. *Funct. Mater. Lett.* **2009**, *1*, 195–201. [CrossRef]

75. Mazuki, N.; Majeed, A.P.P.A.; Samsudin, A.S. Study on electrochemical properties of CMC-PVA doped NH4Br based solid polymer electrolytes system as application for EDLC. *J. Polym. Res.* **2020**, *27*, 135. [CrossRef]

76. Aziz, S.B.; Nofal, M.M.; Kadir, M.F.Z.; Dannoun, E.M.A.; Brza, M.A.; Hadi, J.M.; Abdullah, R.M. Bio-Based Plasticized PVA Based Polymer Blend Electrolytes for Energy Storage EDLC Devices: Ion Transport Parameters and Electrochemical Properties. *Materials* **2021**, *14*, 1994. [CrossRef]

77. Aziz, S.B.; Nofal, M.M.; Abdulwahid, R.T.; Kadir, M.F.Z.; Hadi, J.M.; Hessien, M.M.; Kareem, W.O.; Dannoun, E.M.A.; Saeed, S.R. Impedance, FTIR and transport properties of plasticized proton conducting biopolymer electrolyte based on chitosan for electrochemical device application. *Results Phys.* **2021**, *29*, 104770. [CrossRef]

78. Böckenfeld, N.; Willeke, M.; Pires, J.; Anouti, M.; Balducci, A. On the Use of Lithium Iron Phosphate in Combination with Protic Ionic Liquid-Based Electrolytes. *J. Electrochem. Soc.* **2013**, *160*, A559–A563. [CrossRef]

Mohammad A. S. Abourehab [1,2,*], Rahul R. Rajendran [3], Anshul Singh [4], Sheersha Pramanik [5,*], Prachi Shrivastav [6,7], Mohammad Javed Ansari [8], Ravi Manne [9], Larissa Souza Amaral [10] and A. Deepak [11]

1   Department of Pharmaceutics, College of Pharmacy, Umm Al Qura University, Makkah 21955, Saudi Arabia
2   Department of Pharmaceutics and Industrial Pharmacy, Faculty of Pharmacy, Minia University, Minia 11566, Egypt
3   Department of Mechanical Engineering and Mechanics, Lehigh University, 19 Memorial Drive West, Bethlehem, PA 18015, USA
4   Department of Chemistry, Baba Mastnath University, Rohtak 124021, Haryana, India
5   Department of Biotechnology, Bhupat and Jyoti Mehta School of Biosciences, Indian Institute of Technology Madras, Chennai 600036, Tamil Nadu, India
6   Department of Pharmaceutics, National Institute of Pharmaceutical Education and Research (NIPER), Sector 67, S.A.S. Nagar, Mohali 160062, Punjab, India
7   Bombay College of Pharmacy, Kolivery Village, Mathuradas Colony, Kalina, Vakola, Santacruz East, Mumbai 400098, Maharashtra, India
8   Department of Pharmaceutics, College of Pharmacy, Prince Sattam Bin Abdulaziz University, Al-Kharj 11942, Saudi Arabia
9   Chemtex Environmental Lab, Quality Control and Assurance Department, 3082 25th Street, Port Arthur, TX 77642, USA
10   Department of Bioengineering, University of São Paulo (USP), Av. Trabalhador São Carlense, 400, São Carlos 13566590, SP, Brazil
11   Saveetha School of Engineering, Saveetha Institute of Medical and Technical Sciences, Chennai 600128, Tamil Nadu, India
*   Correspondence: maabourehab@uqu.edu.sa (M.A.S.A.); sheershopramanik24@gmail.com or bt19d601@smail.iitm.ac.in (S.P.)

Abstract: Biopolymeric nanoparticulate systems hold favorable carrier properties for active delivery. The enhancement in the research interest in alginate formulations in biomedical and pharmaceutical research, owing to its biodegradable, biocompatible, and bioadhesive characteristics, reiterates its future use as an efficient drug delivery matrix. Alginates, obtained from natural sources, are the colloidal polysaccharide group, which are water-soluble, non-toxic, and non-irritant. These are linear copolymeric blocks of α-(1→4)-linked l-guluronic acid (G) and β-(1→4)-linked d-mannuronic acid (M) residues. Owing to the monosaccharide sequencing and the enzymatically governed reactions, alginates are well-known as an essential bio-polymer group for multifarious biomedical implementations. Additionally, alginate's bio-adhesive property makes it significant in the pharmaceutical industry. Alginate has shown immense potential in wound healing and drug delivery applications to date because its gel-forming ability maintains the structural resemblance to the extracellular matrices in tissues and can be altered to perform numerous crucial functions. The initial section of this review will deliver a perception of the extraction source and alginate's remarkable properties. Furthermore, we have aspired to discuss the current literature on alginate utilization as a biopolymeric carrier for drug delivery through numerous administration routes. Finally, the latest investigations on alginate composite utilization in wound healing are addressed.

Keywords: alginate; drug delivery system; formulations; administration route; controlled release; wound healing; extraction methods

1. Introduction

In the past, there had been a hurdle in the investigation to reveal naturally derived polymers with exceptional physicochemical characteristics and a high magnitude of compatibility for applications in drug delivery. Escorted by the advancement in pharmaceutical discovery methods in recent years, several therapeutically active substances have come to notice. Nevertheless, the curative agent's delivery to the intentional site has been a severe hurdle in addressing many ailments. These novel pharmaceuticals need exquisite drug delivery systems (DDSs) that could be employed to improve their pharmacokinetics and pharmacodynamics characteristics, thereby advancing cell/tissue specificity along with their biocompatible properties. Therefore, the blooming of an effective DDS that can transport and administer an active accurately and safely to the desired site of action has to become the "bourne" of scientists.

A drug delivery system (DDS) refers to a system that carries curative substances inside the body to accomplish a required remedial outcome. Two principal classes of DDSs are identified, namely, conventional drug delivery systems and novel drug delivery systems (NDDSs) [1]. The actives are supplied by the conventional method via different routes such as oral, buccal/sublingual, rectal, intravenous, subcutaneous, and intramuscular. The conc. of therapeutic actives is not persistent during the therapy and demands continual dosage management in the conventional route [2]. Hence, this describes the prompt enhancement in the level of the drugs in the blood beyond the toxicity limit after individual administration and later declines to a sub-therapeutic level until the following administration [3]. The enhancement in actives conc. beyond the toxicity limit leads to perniciousness in the body. Moreover, the increase of repeated administration might sum up to the remedial non-compliance upon the sufferer [4].

To surmount the aforementioned limitations of the conventional approach, the progressive approach, NDDS, was prepared and included dosage forms. Consequently, the drug rate is sustained within the therapeutic-efficient level with controlled release of actives in both speed and period. Moreover, the NDDS transports actives to the particular action site with optimal dose and diminished toxic effect in contrast to the traditional drug delivery systems [4,5]. The convenient features of the NDDS (as pictured in Figure 1) encompass actives' controlled release, the capability to utilize different administrative ways, improved active guard and efficiency, the improved substrate solubility showing low solubility, and a novel business market prospective to retrieve pharmaceuticals that have been unsuccessful throughout the traditional drug delivery approaches [1,6,7].
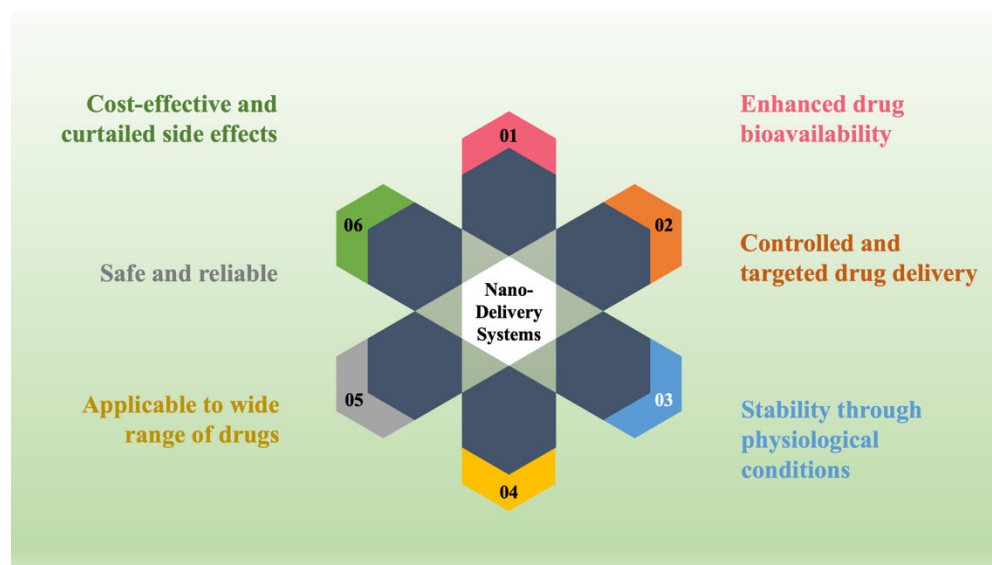
Figure 1. The ideal characteristics of nano delivery systems.

Out of diverse mechanisms of delivery, "controlled drug delivery" and "targeted drug delivery" have been sighted as some of the utmost challenging and fast-progressing investigational areas in the past four years. It provides myriad benefits in contrast to conventional systems, e.g., it improves the absorption rate and biocompatible properties, enhances the actives protection against proteolytic enzyme degradation, cell and tissue-specific active targeting, and helps to regulate active levels within the body, inside the therapeutic level range, over a more prolonged time [8,9]. However, despite the advantages of controlled releases that were formerly persuasive, potential shortcomings, for example, toxicity inside the body, complicated synthetic pathways and the resulting degradation by-products, and operative methods required to explant systems that are non-biodegradable, persist as severe impediments [10,11].

In NDDSs, the active carrier is a base that permits actives to be carried to the intended location, delivering the actives in a controlled manner, thereby enhancing the active bioavailability [12]. Nanoparticles, liposomes, microspheres, polymeric micelles, etc., are some of the significant actives carriers utilized in NDDSs [13–18].

Nonetheless, due to their suitable, variable characteristics, polymeric biomaterials are the most alluring opportunity for delivering drugs in a controlled and directed manner. They can be produced on an industrial scale and readily customized to meet the required applications [19]. But the polymer selection utilized for the drug carrier preparation performs a critical function in the process of actives delivery. The two kinds of polymers that are obtainable in the market are natural and synthetic polymers. Natural polymers (for example, chitosan, alginate, and bacterial cellulose), as well as many synthetic polymers such as poly(lactic-co-glycolic acid) (PLGA), poly-L-lysine (PLL), polycaprolactone (PCL), etc., are used as carriers for drug delivery. These polymers have less toxicity, are biocompatible, and are biodegradable, by which they are degraded via the action of enzymes [20,21]. Therefore, natural polymers, such as polysaccharides, polypeptides, or phospholipids, are generally used to prepare a cornerstone. From all of these, alginate (ALG), an anionic polysaccharide, enticed a growing appreciation for actives delivery with its extraordinary physical and biological characteristics. Among different ALGs, sodium alginate (SA) remains one of the most researched in the pharmaceutical area for applications in drug delivery.

2. The Purview of the Present Review

This review article comprises state of the art ALG-based preparation in the field of actives delivery. The first segment highlights the exceptional ALG characteristics, trailed by its most recent application in carrying therapeutically active substances. The review acknowledges the research field concentrating on pretty substantial advancement in the past period in medicinal delivery employing ALG and its derivatives as a carrier through various administration routes. Lastly, the review addresses the latest trends in the utilization of ALG composites in wound healing applications.

3. Sources of Extraction and Properties of Alginate

ALG, a naturally abundant linear and anionic polysaccharide, is generally obtained from the cell wall of brown seaweed belonging to the class Phaeophyceae [22], including *Ascophyllum nodosum*, *Laminaria hyperborea*, *Laminaria digitata*, *Laminaria japonica*, and *Microcystis pyrifera* [23], and many bacterial strains, including *Acetobacter* and *Pseudomonas* spp. Although it can be created from bacterial origins, it is commercially accessible from algae as SA in its salt form [24]. They are a class of linearly arranged biopolymers comprising 1,4-linked-β-D-mannuronic acid (M-blocks) and 1,4-α-L-guluronic acid (G-blocks) residues ordered in sequences of identical (MM, GG) or heterogeneous (MG) blocks (as portrayed in Figure 2) [25]. Divalent cations, for example, Ba^{2+} and Ca^{2+}, can rapidly construct egg-box systems with G block to build ALG hydrogels via the procedure of gelation [26]. Increasing the molecular weight and G-block length dramatically increases the mechanical properties of ALG. Commercially available ALG has an average molecular

weight varying between 32,000 and 400,000 g/mol. The ALG solutions have a maximum viscosity at pH 3.0–3.5 because of the hydrogen bonding of the carboxylate groups forming the ALG backbone [23].

1,4 α-L-Guluronic acid   1,4 β-D-Mannuronic acid

G-block   M-block   GM-block
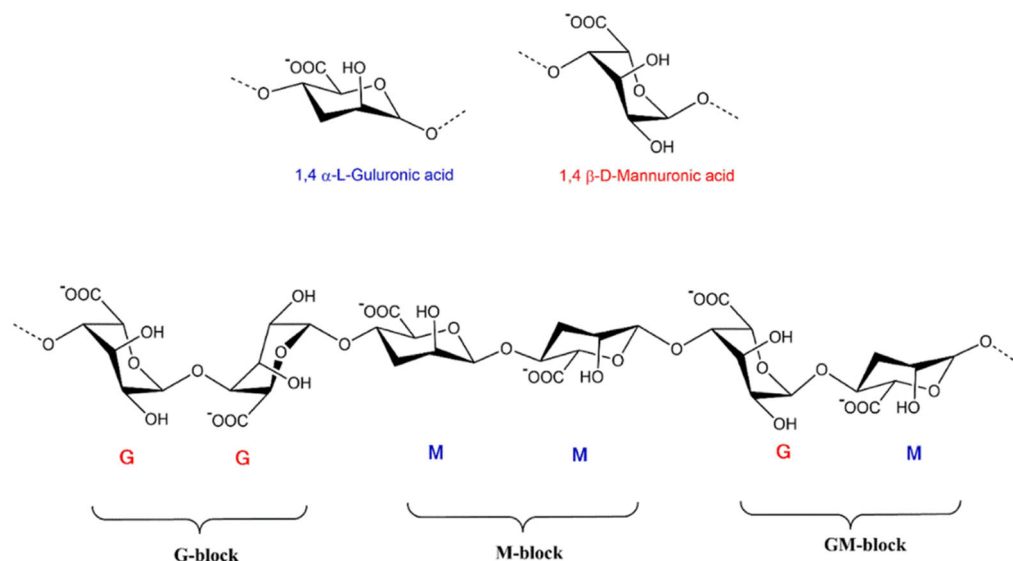
Figure 2. The monomer's conformation and blocks distribution of ALG salt [27].

Recently, a multistage extraction process (from brown seaweeds, as illustrated in Figure 3) is being carried out, which involves acid pretreatment of the seaweed extract, followed by aqueous alkali treatment (mainly sodium hydroxide) in which different salt forms of natural ALG are modified into aqueous-soluble SA [28]. Subsequently, the filtered extract is incorporated with sodium or calcium chloride, and ALG gets precipitated. Then, dilute HCL is added, and salts of ALG get converted to alginic acid; following further purification and modification, a powder form of water-soluble SA is prepared [29].
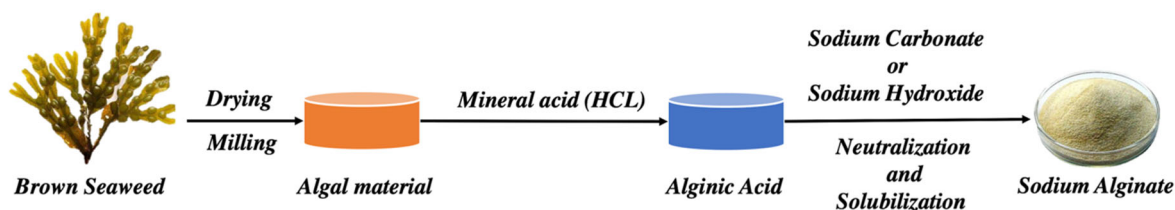
Figure 3. The extraction technique of ALG from brown seaweeds.

The ALG production from bacterial biosynthesis has definite physical characteristics and chemical structures different from the extracted ALG from brown seaweed. The different steps of ALG biosynthesis are (1) synthesis of the precursor substrate, (2) transfer polymerization and cytoplasmic membrane, (3) transport and alteration of the periplasmic membrane, and (4) conveying via the outer membrane [30].

Table 1 denotes the literature survey of various extraction methods of ALG.

Table 1. Various methods for the extraction of ALG.

Seaweed Species	Components Used for Extraction	Extraction Yield (% Dry Weight—d.w.)	Characteristics	References
Sargassum mangarevense and *Turbinaria ornata*	Formaldehyde-acidification-Na$_2$CO$_3$-ethanol	*Sargassum mangarevense* (6.0–12.4% d.w.); *T. ornata* (16.8–21.1% d.w.)	*T. ornata* demonstrated a greater viscosity and yield than *S. mangarevense*. Both the species showed a high M:G ratio (1.25–1.42) compared to the reported literature. No seasonal variation was observed.	[31]
Sargassum vulgare	Formaldehyde-HCl-Na$_2$CO$_3$	16.9%	M/G ratio for *S. vulgaris* low density and *S. vulgaris* high density were higher than most Sargassum species ALG (1.56 and 1.27, respectively). Optimal conditions for extraction of ALG from *S. vulgaris* were 60 °C and 5 h duration. Newtonian activity seen for a solution fraction was 0.7% for SVLV, whereas, it was 0.5%. for the SVHV sample.	[32]
Sargassum turbinarioides Grunow	Formaldehyde-HCl-Na$_2$CO$_3$	10%	M/G ratio was 0.94, $\eta < 1$, M.W. (5.528×10^5 g mol^{-1}), and polydispersity index were low (1.43).	[33]
Laminaria digitata and *Ascophyllum nodosum*	Na$_2$CO$_3$ or NaOH after different acid pre-treatments (H$_2$SO$_4$ and HCl) at different temperatures	28.65 ± 0.92% to 78.02 ± 16.81%	Unrefined extracts produced films with appropriate mechanical characteristics without cationic complexation. The treatment with sodium carbonate resulted in extracts with good plasticizing capacity, while sodium hydroxide extraction guided to polymer chains with enhanced cross-linking ability. Ascophyllum films possessed radical scavenging property.	[34]
Tunisian seaweed (*Cystoseira barbata*)	high-temperature alkaline extraction	9.9%	M/G ratio was 0.59, pseudoplastic flow behavior. The emulsion formed was highly stable at acidic pH and less affected by temperature. CBSA exhibited DPPH radical scavenging activity (74% 33 inhibition at a concentration of 0.5 mg/mL). Excellent hydroxyl-radical scavenging activity, ferric reducing potential, and protection against DNA breakage were observed.	[35]
Macrocystis pyrifera	Ethanol route, HCl route, CaCl$_2$ route	25–33%	Direct polymer precipitation with ethanol gave the best yield. The precipitation step with calcium and cation exchange gave an ALG with poor viscoelastic properties. A pH higher than 3.5 in the acid pre-treatment step amended the ethanol route, thereby preventing the ethanol linkages from being ruptured.	[36]

Table 1. *Cont.*

Seaweed Species	Components Used for Extraction	Extraction Yield (% Dry Weight—d.w.)	Characteristics	References
Sargassum muticum	conventional alkaline extraction and hydrothermal fractionation	5.04–10.09%	EC50 values for DPPH radical scavenging (0.72 and 1.18 g L^{-1} at 190 °C than at 220 °C, respectively) were comparable with synthetic antioxidants. However, at the minimum tested value (0.2 g L^{-1}), the manufactured extracts at 190 °C appeared to be prooxidant. The AAC values that reached the maximum tested concentration at (0.5 g L^{-1}) were similar to those for BHA and BHT.	[37]
Sargassum sp. (SRG) (genus *Sargassum), Turbinaria* sp. (TRB) (genus *Turbinaria), Hormophysa* sp. (RHT) (genus *Hormophysa)*	HCl-Na$_2$CO$_3$-EDTA	SRG 31 RHT 31 TRB 30	M/G ratio by ^{1}H NMR 0.7–1.0, while after hydrolysis was 0.52–1.1. TRG with M/G <1 Gave a softer gel than SRG, while RHT, rich in mannuronic acid, gave the softest gel.	[38]
Sargassum muticum	Formaldehyde-HCl-Na$_2$CO$_3$	13.57 ± 0.13%	Optimum conditions for extraction are 86 °C temperature, 3% alkali, and 93% ethanol for 3 h. M/G was 1.08.	[39]

ALG's biocompatibility, rheological properties [40,41], biodegradability, marginal toxicity, and chemical versatility [42] are prominent, along with its exceptional characteristics in producing stable gel in aqueous conditions and a mild environment by adding multivalent cations, making ALG beneficial for drug delivery [43,44]. Furthermore, ALGs can be readily created into various semi-solid or solid frameworks under a moderate environment due to their exceptional sol/gel transition capability. Hence, ALGs are also frequently utilized as viscosity-enhancing substances and thickening agents in the pharma industry [44].

The percentage of the three sorts of blocks—MM, GG, and MG—specifies the ALG's physical properties. In having a higher percentage of G, ALGs have higher gelling characteristics, while in having a high M content, ALGs have greater viscosity. Determining the M/G ratio is also essential for ALGs, those with a high ratio of M/G produce elastic gels, while those with small M/G ratios produce brittle gels [33,45]. The ALG-based formulation's mechanical characteristics rigorously rely on the count and conc. of G and M units. If G residues beat M, the formulation exhibits higher mechanical rigidity. Thus, by changing the content of G and M, it is possible to modify the elastic modulus [46].

ALG undergoes hydration at low pH, which leads to the development of "acid gels", which are highly viscous. The pH sensitivity of ALG can be attributed to acidic pendant groups that accept or release protons due to intermolecular binding when the pH is changed. As a result, the water molecules enter the ALG matrix and get physically entrapped within them but are still free to migrate. This ability is essential in the formation of ALG gels for cell encapsulation [47]. The ALG's capability to produce two different classes depending on the pH, i.e., acid gel at low pH and ionotropic gel at higher pH, makes it unique compared to neutral molecules [48].

ALG has excellent mucoadhesive characteristics due to the existence of free carboxyl moieties, enabling the biopolymer to attach to mucin via hydrogen bonding as well as electrostatic interaction. On the other hand, ALG solubility is largely dependent on environmental pH and, accordingly, affects their mucoadhesive property since only ionized carboxyl groups are proficient in engaging with tissues of the mucosa. Moreover, soluble ALG assists the penetration of solvent through the polymer matrix, forming a highly

viscous and cohesive gel framework for enhancing the mucoadhesive bond strength. In contrast, excessive and exorbitant ALG matrix hydration in physiological solution could diminish mucoadhesive properties due to the weakening of ALG functional groups accessible for mucosal tissue interactions [49,50].

ALGs can be tailored to fulfill the requirements of either pharmaceutical or biomedical applications. Owing to their high water uptake, sustained release, enhanced porosity, and non-immunogenicity, ALGs have found widespread applications in wound dressings [51]. ALG-based composites offer great utility in bioremediation by removing heavy metals, dyes, antibiotics, and other contaminants from wastewater [52]. Based on the types of cross-linkers and the cross-linking approaches used, materials ranging from small drug substances to macromolecular proteins can be designed as controlled drug delivery systems [53].

Biocompatibility is one more vital factor to be studied as the extraction of ALG obtained from nature is accompanied by the existence of numerous impurities capable of inciting allergic responses. In effect, an immune reaction has been stated in industrial-grade ALG; nonetheless, the multi-stage extraction method for eliminating metallic impurities and polyphenolic substances permits the acquisition of ALG of substantially high purity for use in biomedical applications [54].

ALG's antioxidant and anti-inflammatory actions have also been noticed. It has been reported that ALG oligosaccharides reduce nitric oxide, reactive oxygen species (ROS), and eicosanoids, such as prostaglandin E2 and cyclooxygenase COX-2 production [55–57]. Thus, ALG's exceptional characteristics have unlocked the doorways in its widespread actives delivery applications.

4. Hydrogel Formation Methods

In biomedicine, ALG is commonly utilized in the form of a hydrogel for wound healing, medicament delivery, and tissue regeneration applications. Hydrogels refer to highly cross-linked 3D networks comprising hydrophilic polymers. Because hydrogels are physically comparable to biomacromolecular constituents, they are frequently biocompatible and can be administered into the body by non-invasive administration. Hydrogels are commonly formed from hydrophilic polymers by chemical and/or physical cross-linking; their physicochemical characteristics depend on the type of cross-linking, the density of the cross-linker, and the polymers' chemical composition and molecular weight [58]. We present a review of different methods for cross-linking ALG sequences to generate gels and the effects of these methods on the hydrogel features crucial in the biomedical field.

4.1. Ionic Cross-Linking

Combining an aqueous ALG mixture with ionically cross-linking reagents, particularly divalent cations (i.e., Ca^{2+}), is the most frequent approach to preparing hydrogels. It is thought that divalent cations attach distinctly to the guluronate block polymers of the ALG chains because the guluronate blocks' structure permits a good extent of divalent ion coordination. Acknowledged as the egg-box fashion of cross-linking, the guluronate units of one ALG chain form bonds with the guluronate blocks of neighboring polymer chains, culminating in a gel structure [59]. Calcium chloride ($CaCl_2$) is a commonly utilized ionic cross-linking agent for ALG. Given the high solubility in aqueous solutions, it often drives fast and poorly regulated gelation. One option is to use a phosphate-rich buffer (e.g., sodium hexametaphosphate) to restrict and control gel formation. These phosphate molecules throughout the buffer compete with the ALG's carboxylate groups to interact with calcium cations, thus slowing the gelation process [60].

When utilizing divalent cations, the rate of gelation plays an important role in affecting gel strength and consistency; a higher gelation rate results in more homogenous structures and enhanced mechanical character [61]. The temperature at which gelation occurs impacts the gelation speed and the gels' material performance; the typical reactivity of ionic cross-linkers (e.g., Ca^{2+}) is lowered at lower temperatures and consequently hampers the cross-linking. The cross-linked framework that results has more order, which ame-

liorates mechanical characteristics [46]. Furthermore, determined by the ALGs' chemical composition, the mechanical properties of ionically cross-linked ALG hydrogels might vary dramatically. For instance, ALG hydrogels made from a large concentration of G blocks are stiffer than those made from ALG with a lower number of G blocks [62].

Ionotropically cross-linked ALG hydrogels incorporating S-nitroso-mercaptosuccinic acid (S-nitroso-MSA), a NO donor, and AgNPs produced from green tea were prepared by Urzedo et al. using glycerol as a plasticizer, which enhanced the flexibility of the hydrogel. Rheological analysis revealed that G′ (elastic modulus) > G″ (viscous modulus) at all temperatures, indicating the prevalence of a solid-like gel structure with thermal stability. Relative to control ALG hydrogel, ALG hydrogels with AgNPs had a modest drop in elastic modulus (G′), leading to a lowering of the elastic response of the resulting nanocomposite gels, manifesting that the addition of AgNPs reinforces the hydrogel network while also preventing the creation of cross-linked junctions between ALG chains. As a consequence, the degree of stress required to break the elastic framework may be reduced. Because the ALG hydrogels were physically in the form of gels, the inclusion of MSA and AgNPs had no substantial effect on their rheological properties [63].

Bruchet and Melman demonstrated a reductive cation exchange mechanism for the synthesis of calcium-cross linked hydrogels from iron (III) ALG hydrogels while still maintaining the shape of the initial hydrogel. Hydrogels prepared by the traditional ionic cross-linking method are heterogeneous and difficult to control. They previously reported the selective oxidation of iron (II) cations, which dissolve homogeneously in SA, to iron (III) cations, triggering the formation of hydrogels; the obtained hydrogel films dissolve on electrochemical/photochemical reduction. Patterned films or coatings can be subsequently prepared from the as-prepared hydrogels [64].

Gattás-Asfura et al. studied various 1-methyl-2-diphenylphosphino-terephthalate (MDT) end groups, polar charged groups, polymer size, and material constitution to alter the physical characteristics of the cross-linkers and increase the capability for covalent stabilization of Alg-N3 beads by Staudinger ligation. The breakdown of cross-linkers after bead production was found to be reduced by branched poly(ethylene glycol) (PEG) polymers, albeit this effect was minimized as polymer miscibility was increased. Due to the elevated miscibility and absence of pre-incubation time for the synthesis of covalently stabilized beads, the results suggested that an ALG-based cross-linker gave the most stable and homogenous beads [65].

In another investigation, Awasthi et al. aimed to make a prolonged-release repaglinide encapsulated double cross-linked ALG-pectin bead matrix utilizing Ca^{2+} ions and the bifunctional alkylating agent epichlorohydrin. The dual cross-linked beads showed higher surface smoothness than single-cross-linked ALG beads owing to the higher cross-linking degree. On the other hand, ALG-pectin beads demonstrated a decrease in mucoadhesive strength due to the inability of solvent penetration owing to the rigid matrix [66].

4.2. Covalent Cross-Linking

Covalent cross-linking is being studied extensively to enhance the stability of ALG hydrogels for a variety of biomedical applications, with its carboxylate group being the main site of covalent bonding interactions. The cross-links disintegrate and reorganize in another location, and water is removed from the hydrogel, and the stress applied to it relaxes, resulting in plastic deformation. Although water migration can cause stress relaxation in covalently cross-linked gels, the incapability of dissolving and re-establishing bond formation causes considerable elastic deformity. Covalent cross-linking reagents, on the other hand, could be hazardous, and unreacted compounds may require elimination entirely from gels.

The covalent cross-linking of ALG with variable molecular weight poly(ethylene glycol)-diamines was initially studied with the purpose of generating gels with a diverse extent of mechanical behavior. As the elastic modulus grew steadily with the increase in the crosslinking density or weight fraction of PEG in the gel, it then declined as the molecular

weight between cross-links (Mc) became lower than that of the softer PEG [67]. By exploring the use of various types of cross-linking agents and regulating the cross-linking densities, it was later proved that ALG hydrogels' mechanical characteristics and swelling might be finely controlled. As one may imagine, the chemical constitution of the cross-linking chains has a considerable impact on the swelling ability of the hydrogel. The addition of hydrophilic cross-linking compounds (e.g., PEG) as a supporting macromolecule can rationalize the hydrogel's loss of hydrophilicity due to the cross-linking reaction [68]. Gao et al. employed dual cross-linked methacrylated ALG hydrogel to overcome ionic cross-linked hydrogels' tendency to be prone to aqueous decomposition. The covalent cross-links between the methacrylate groups prevented the fracture of dual cross-linked chains of the hydrogels prepared under UV irradiation [69].

Basu et al. designed a nanocomposite DNA-based hydrogel via the establishment of reversible imine bonds that were crosslinked with oxidized alginate (OA). Storage moduli, yield stress, yield strain, and swift restoration following the withdrawal of cyclic stress were all highest in formulations containing OA with a higher oxidation degree. Owing to the reversibility of the covalent imine linkages generated between the aldehyde groups of OA and the amine groups found in the DNA molecules, the hydrogel preparations displayed self-recovering and shear-thinning capabilities. The improved hydrogel was effective in enhancing simvastatin's prolonged release for more than seven days [70].

In another investigation, Xing et al. reported covalently cross-linked carbohydrate-based ALG/chitosan (CS) hydrogel inserted ALG microspheres encapsulating bovine serum albumin (BSA). The gelation occurred due to the Schiff-base reaction between the amino and aldehyde groups of N-succinyl CS (N-Chi) and OA. Higher content of OAlg in the hydrogels resulted in the creation of stable hydrogels, lowered swelling degree, and higher compression strength [71].

4.3. Photo Crosslinking

Photocross-linking is a novel method of in situ gelation that takes advantage of covalent cross-linking. With suitable chemical precursors, photocrosslinking can be done in mild reaction circumstances, even immediately contacting drugs and cells. ALG hydrogels are transparent and flexible when treated with methacrylate and cross-linked with a laser (argon-ion laser, 514 nm) for 30 s with eosin and triethanolamine treatment [72]. Rouillard et al. employed photocross-linking of methacrylate-modified ALG by the photoinitiator VA-086 in order to get high cell viability scaffolds (>85%) [73]. Bonino et al. monitored the reaction kinetics of methacrylate-modified SA hydrogels cross-linked by UV radiation in the presence of a photoinitiator by in-situ dynamic rheology [74].

In a similar study, Jeon et al. created a bioadhesive with adjustable material characteristics, adhesiveness, and biodegradation rate using a dual crosslinked oxidized methacrylated ALG/8-arm PEG amine (OMA/PEG) hydrogel framework. ALG had been chemically modified by reacting aldehydic groups via oxidation with PEG amino groups, and a proportion of the ALG carboxylate groups was further transformed with 2aminoethyl methacrylate (AEMA) using carbodiimide chemistry to enable photocross-linking of the methacrylate by UV light. When cultivated in the presence of human bone marrow-derived mesenchymal stem cells, the functionalized OMA/PEG hydrogels exhibited cytocompatibility. Furthermore, the adhesiveness of the hydrogels proved to be better than that of commercially available fibrin glue, which can be controlled by altering the oxidation level of ALG and assessed on a pig skin model [75].

4.4. Click Chemistry Reactions

Most of the strategies for preparing covalently cross-linked ALG hydrogels employ hazardous chemicals and catalysts that impact the biocompatibility of the hydrogels [76]. Hence, in recent times, copper-free "click" chemical procedures are effectively used to make hydrogels based on biopolymers without any need for catalysts or activators, with few side reactions, and are suitable for physiological environments even under mild conditions [77].

The most typical example is 1,3-dipolar cycloadditions, a copper (I)-catalyzed reaction of azides with alkynes, which has recently been used to generate biodegradable peptide-modified ALG hydrogels exhibiting usefulness as artificial analogous to extracellular matrix in tissue regeneration [78].

Anugrah et al. prepared novel near-infrared light-sensitive ALG hydrogels via click cross-linking by inverse electron demand Diels–Alder reaction between norbornene-modified ALGs and tetrazine cross-linkers consisting of diselenide bonds. Indocyanine green (ICG) produced reactive oxygen species upon NIR light irradiation that dissolved diselenide linkages in the hydrogel network, causing the gel-sol transition followed by the release of encapsulated DOX [79]. García-Astrain et al. synthesized cross-linked ALG hydrogels by means of Diels–Alder (DA) click chemistry. Furan groups were added to ALG by an amidation reaction using furfuryl amine. The ALG-containing furan was subsequently cross-linked utilising a DA reaction and the polymer poly(propylene oxide)-b-poly(ethylene oxide)-b-poly(propylene oxide). As a bifunctional crosslinking agent, bismaleimide was used. The hydrogels as-prepared displayed rapid pH responsiveness and pulsatory activity between acidic and alkaline conditions, both of which were important characteristics for drug delivery of the model drug vanillin [80]. Coupling DA click chemistry with the thiol–ene reaction, antibacterial SA hydrogels SA/PEG–HHC10 were developed and manufactured by Wang et al. The cysteinyl-terminated antibacterial polypeptide HHC10–CYS (HHC10) was seeded employing the thiol–ene mechanism between the oxy-norbornene group and the thiol group after the hydrogels were made through DA click chemistry with high mechanical properties. The antibiotic hydrogels had a significant antibacterial effect (sterilization rate after 24 h was almost 100%) and excellent biocompatibility [81]. Lückgen et al. rendered the norbornene-tetrazine click cross-linked ALG hydrogels hydrolytically-degradable by oxidation of the backbone with sodium periodate in order to regulate the rheological, physicomechanical, and degradation properties. The produced hydrogels were suitable for cell seeding in 2D and encapsulating in 3D, as evidenced by cell number constancy and excellent viability preservation [82]. In a different study, Pérez-Madrigal et al. fabricated strong ALG/hyaluronic acid (HA) thio-yne click-hydrogel tissue engineering scaffolds which exhibited remarkable mechanical properties (the maximum compressive strength was 1.4 ± 0.55 MPa, with the strain at the break being around 97%; after 7 days, the hydrogels swelled to $198 \pm 5.3\%$) and cytocompatibility [83].

4.5. Thermal Gelling

As a result of their customizable temperature-responsive swelling capabilities, thermo-sensitive hydrogels have recently been intensively explored in various pharmaceutical applications. This allows for pro re nata control of drug delivery from the gels [84]. The most widely used thermo-sensitive gels are poly(N-isopropyl acrylamide) (PNIPAAm) hydrogels, which undergo a reversible phase change in aqueous solutions at body temperature (low critical solution temperature near 32 °C). Notwithstanding the significance of thermo-responsive hydrogels in biomedical pertinence, several ALG-based systems have been documented thus far because ALG is not intrinsically thermo-sensitive. In situ copolymerization of N-isopropyl acrylamide (NIPAAm) with poly(ethylene glycol)-co-poly(-caprolactone) (PEG-co-PCL) macromer by the addition of SA was used to create semi-interpenetrating polymer network (semi-IPN) framework. At a fixed temperature, the swelling capacity of the gels rose with the amount of SA and reduced with a temperature rise. The introduction of SA in semi-IPN structures enhanced the mechanical properties and BSA release from the hydrogels, suggesting that it could be advantageous in drug delivery [85]. Bezerra et al. prepared furosemide-loaded sericin/ALG beads via ionic gelation and then subjected them to thermal or covalent cross-linking using proanthocyanidin as the cross-linker to achieve gastro-resistant sustained release diuretic particles [86].

4.6. Cell Cross-Linking

Whereas a variety of chemical as well as physical ways of forming ALG gels have been documented, the potential of cells to promote gel production has largely been overlooked. Despite the lack of chemical cross-linkers, the ability of cells to attach multiple polymer chains can result in longer, reversible network development when ALG is altered with cell adhesion ligands. Cells introduced into an arginine–glycine–aspartic acid (Arg–Gly–Asp, RGD) functionalized ALG solution produce a uniform dispersion, and this system then forms the cross-linked networks without the use of any extra cross-linking chemicals through specialized receptor–ligand associations [23].

Yu et al. produced peptide-modified ALG microspheres encapsulating human mesenchymal stem cells for delivery into injured myocardium. Cell–ECM interface dynamics have an influence on both cell-matrix adhesion but also cellular processes, including migration, growth, maturation, and cytokine and growth factor signaling. In vitro data reveal that hMSCs adhere to the RGD-functionalized ALG surfaces more firmly than the un-modified ALG. Furthermore, compared to the non-modified cohort, the FGF2 expression level on the RGD-treated surface was considerably higher [87].

Similarly, in a study by Fonseca et al., ALG was modified by partial cross-linking with a matrix metalloproteinase cleavable peptide (proline–valine–glycine–leucine–isoleucine–glycine) by carbodiimide chemistry and co-incorporated into cell-adhesive RGD-ALG hydrogels. Matrix metalloproteinase-2 (MMP-2) function was enhanced in MSC grown in ALG functionalized with MMP-sensitive polypeptide; thus, this approach increased their role as ECM analogs in a more flexible and physiological 3-D cell milieu [88].

Other novel methods for ALG gelation include cryogelation, where growing crystals form interconnecting pores, generating solid materials and expelling swelling agents from gels via freeze-drying [89].

In the non-solvent induced phase separation technique, when the solubility of polymers decreases caused by the presence of a non-solvent, a polymeric solution segregates into polymer-heavy and polymer-lean phases. As an outcome, a lyogel is formed, which can be "hardened" by removing the parent solvent further [90,91].

At normal room temperature, a suspension of metal carbonate or hydroxycarbonate (Ca, Sr, Ba, Zn, Cu, Ni, or Co) is exposed to pressured carbon dioxide (30–50 bar) in a process called carbon dioxide-induced gelation. One of the driving forces behind the establishment of CO_2-induced gelation is to eliminate some of the processes in aerogel manufacture as much as is feasible by merging gelation, solvent exchange, and SC-drying into a single procedure [92].

Another upcoming process of ALG gelation is the so-called carboxylic acid-induced gelation. Gelation was shown to be quick with oxalic, citric, and maleic acids, allowing the formation of gel beads by expelling ALG solution (4% *w/v*) into the relevant acidic solution (0.5 M). These findings demonstrate that the acid and ALG chains have such a strong interaction that gel breakdown was not observed after several washes of carboxylic acid-induced crosslinked gels in an aqueous medium at pH 7 [93,94].

Aerogels are an upcoming class of carriers for therapeutic drug delivery, having low density (0.005–0.50 g/cm^3), high specific surface area (300–1000 m^2/g), and high porosity (upto 99%) [95–97]. Polymers such as starch, cellulose, pectin, ALG, etc., can be used to produce highly adsorption-efficient aerogel microparticles. Lovskaya and Menshutina prepared ALG-based microparticles loaded with three model drugs (loratadine, nimesulide, and ketoprofen) using the supercritical adsorption process. The release rate of drugs in the ALG-based aerogels was found to increase compared to pure drugs [98]. Similarly, Athamneh et al. used aerogel-based microspheres prepared by ALG and ALG-HA hybrids by the emulsion gelation method as carriers for pulmonary drug delivery. These ALG-based microspheres showed an in vitro aerodynamic diameter of 5 μm, indicating the favorable properties of ALG-based microspheres for pulmonary delivery [99,100].

5. ALG Particles Formation Methods

ALG gelation occurs via one of two mechanisms: (1) external gelation, in which cations enter the ALG system from the outside, or (2) internal gelation, in which cations escape the ALG structure. ALG-based particles of a variety of dimensions can be produced and categorized into various categories: (1) macroparticles, such as that of drug or vitamin tablets, may be seen by the naked eye; (2) microparticles vary significantly in size from a few microns to several millimeters; and (3) nanoparticles have a diameter ranging between 1 to 100 nm [101–104]. The most popular method for producing ALG particles is the drop-by-drop expulsion of an ALG solution through a needle in a cationic bath. External gelation is used to create ALG particles with diameters between 500–5000 μm [105–107]. The ALG particle size can be lowered, and particles having a smaller size distribution could be generated using several ways depending on this external gelation process, including coaxial laminar airflow at the nozzle, electrostatic fields, and vibrating nozzles [107–110]. In their study, Patel et al. described a method detailing the impact of ionotropic gelation residence time (IGRT) on the extent of cross-linking of ALG particles with Ca^{2+} ions. They found that to prevent the dissolution of the drug into the bulk cross-linking solution, the IGRT must be kept short which also enhances drug loading [111].

An emulsification–gelation process can also be used to make ALG spheres. Gelled spheres are made by emulsifying an ALG solution in an organic phase, followed by the gelation of the ALG emulsion droplets. External gelating of the ALG emulsion droplets leads to emulsion cracking; however, the spheres aggregate and, as a result, numerous emulsion droplets (W/O/W) are formed [112,113]. Membrane emulsification may yield ALG particles with a quite small size distribution; however, particle production is confined to the micro range (>1 μm), and clogging of the membrane layer, as well as the feasibility of the process scale-up, remains a concern. Mechanical emulsification is the most practical for industry, as it produces ALG particles of all sizes. Nevertheless, the size variation of the ALG particles produced is relatively wide. ALG nanoparticles can be made in various ways, although the majority of them rely on complexation, either through interactions with ions like calcium or negatively charged polyelectrolytes like CS [114] or poly-L-lysine [115]. Complexation is used in other processes as well, such as emulsification, to strengthen nanoparticles. In most cases, complexation will be required as a supplement to obtain the particles. The incorporation of calcium chloride into the ALG solution produces nanoaggregates; generally, the drug is typically added before this step. The size of nanoparticles varies greatly depending on a variety of factors, such as the manufacturing process, preparation parameters, crosslinking reagent, ALG molecular mass, and so on. Because ALG is a negatively charged polyelectrolyte, nanoparticles can range in size from several tens to nanometers, and the zeta potential is generally negative [116].

6. Current Advancements in ALG Formulations in Drug Delivery

A substantial number of therapeutic actives have been unveiled over the past few years. Numerous of them grasp magnificent therapeutic properties; nevertheless, they manifest poor bioavailability and poor pharmacokinetics, causing detrimental systemic impact after the administration [117]. Therefore, DDS has evolved into an essential device to enhance remedial effectiveness by employing delivery carriers (as illustrated in Figure 4) such as microspheres, hydrogels, beads, liposomes, nanoparticles, nanofibers, etc., to deliver drugs [118–120].

Different approaches (as shown in Figure 5) are employed to develop the aforementioned drug delivery devices.

Below are a few vital employments of ALG-mediated systems for enhanced actives delivery through various administration routes.
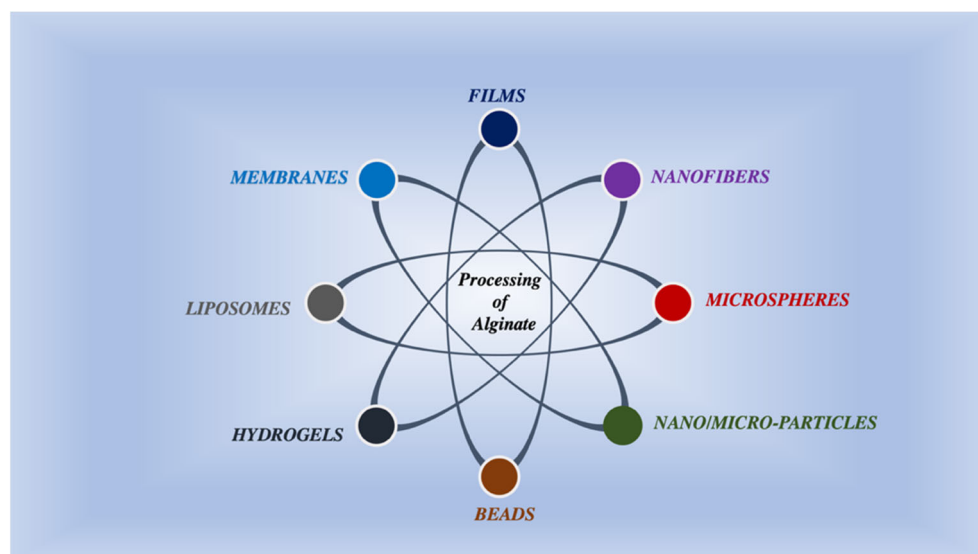
Figure 4. Diagrammatic representation of ALG formulations into diverse forms.
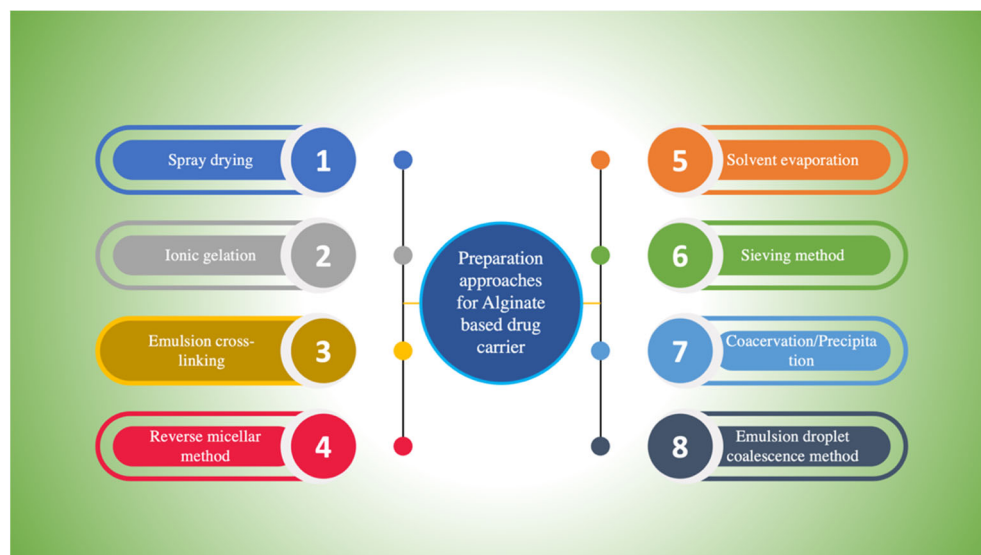
Figure 5. Various approaches for preparing ALG-based particulate carrier matrix.

6.1. Oral Drug Delivery

Oral drug delivery is the first choice route of drug delivery for any therapeutic substance due to its simplicity, patient compliance, cost-effectiveness, easy bulk manufacturing, sustained and controlled release, and generation of immune response in case of vaccination [121–123]. However, some limitations exist, such as variable pH of the gastrointestinal tract (the stomach is highly acidic while the small intestine is alkaline), first-pass metabolism in the liver, the occurrence of hydrolytic enzymes, and an absorption barrier in the liver intestine. This limits the extent of the therapeutic action of many drugs given by the oral route. Nevertheless, due to their non-toxicity, biocompatibility, and biodegradability, ALG hydrogels can be safely administered orally [124].

Recently, Ilgin et al. used SA hydrogels as the carrier for diclofenac sodium to obtain controlled drug delivery at a specific pH. The porous structure made them valuable as a drug delivery system. The researchers prepared SA pH-responsive semi-interpenetrating hydrogels by altering the physical and biological properties of the biocompatible and biodegradable ALG via surface functionalization with the aid of monomers such as HEMA, MAPTAC, and MA. Polyvinyl alcohol (PVA) was employed to provide chemical stability,

and nMBA was the copolymer. The resultant hydrogels were evaluated for their swelling, drug loading, drug release, and antimicrobial activity. PVA and HEMA proved to be good polymeric systems because they enhanced biocompatibility and mechanical properties. Maximum swelling (38 g_{water}/g_{gel}), drug loading (22.8%), and release profiles were observed at pH 7.0, where 95% release of drug was observed at the end of 2 h, as compared to 4.5% at pH 1.5. Antibacterial activity was observed against *E. coli*, *B. subtilis*, and *S. aureus* by the disk diffusion method, and it displayed excellent inhibition of the growth of all three microorganisms. Thus, ALG is confirmed to be a great, intelligent drug release platform for oral drug delivery, providing a controlled release [125].

To obtain colon-specific drug delivery for inflammatory bowel diseases such as Crohn's disease, it is challenging to move through the different pH conditions of the GI tract undisturbed. Hence, Ayub et al. tried to enhance the delivery of Paclitaxel to colonic cancer cells by formulating a self-assembled cysteamine-based disulfide cross-linked biodegradable thiolated SA-derived nanoparticles via a layer-by-layer assembly approach (as shown in Figure 6A). SA was oxidized using sodium periodate before adding cysteamine hydrochloride to alter its backbone. The disulfide bonds prevented the leakage of the drug before it reached its target site. The encapsulation efficiency of P3DL/PAH/PSCCMA was found to be 77.1%, with a cumulative-drug release of 45.1% after 24 h (as displayed in Figure 6B). The nanospheres demonstrated their maximum size at pH 7.0, thus signifying their efficacy in selectively delivering the actives to the colon. The MTT assay revealed the high viability (86.7%) of HT-29 cells (as shown in Figure 6C). More than 70% of the nanospheres were detected in human colon cancer adenocarcinoma HT-29 cells, indicating their high cellular uptake, as displayed in Figure 6D). Stability studies indicated that most nanospheres changed slightly in size and PDI but were stable with negligible differences in zeta potential. Thus, this approach could be employed for colon-targeted drug delivery with minimal toxic effects [126].

In order to furnish controlled drug delivery via the oral route, Cong et al. prepared an ALG hydrogel/CS micelle composite system encapsulating emodin. The research group prepared cross-linked micelles because, unlike conventional polymeric micelles, cross-linked micelles prevent drug leakage and protect them from dissociating quickly. Emodin was chosen as a model drug because it has poor water solubility and undergoes extensive first-pass metabolism. It was loaded onto CS micelles and then mixed with SA hydrogels developed by cross-linking with Ca^{2+} ions and β-GP to form hydrogel/micelle beads. Based on response surface methodology, the optimized biopolymer concentrations were determined. The 1:1 hydrogel/micelle beads showed sustained drug delivery, while the 3:1 ratio provided colon-specific delivery. The morphological, swelling, and degradation studies were carried out. The diameter of micelles increased from 80 nm in aqueous solution to 100–200 nm in the hydrogel, likely due to electrostatic interaction between the amino group of the CS chain and the carboxylate group of the ALG chain. The swelling of micelles was reduced at pH 1.2 due to SA hydrogel, whose swelling ratio is at acidic pH, thus preventing the release and degradation of CS chains. The initial release amount was 28% in SGF, and a final release amount of 85% for 1:1 micelle/hydrogel systems was reported. Thus, this pH-responsive hydrogel/micelle system could be an encouraging candidate for sustained-release or site-targeted actives delivery for unstable or hydrophobic actives [127].

Amphotericin-B is the first-choice drug for many fungal infections, including leishmaniasis. However, it has limited solubility, is susceptible to gastric pH, and its oral bioavailability is low; it is generally administered intravenously [128]. Hence, to overcome this issue, Senna et al. utilized nanostructured lipid carriers (NLC) combined with stimuli-sensitive ALG polymers using a high-pressure homogenization technique with calcium chloride as the cross-linker, providing a dual-benefit of oral drug delivery and protection from gastric pH without structural degradation and promoting drug release at intestinal pH. Nanostructured lipid carriers are systems in which hydrophilic drugs are dispersed in polymeric matrices, forming nanometric droplets, thus enhancing adsorption and preventing enzymatic degradation [129]. AmpB was solubilized by solid lipid glyceryl

214

monostearate (GSM). Studies using the trypan blue exclusion test showed that the NLCs showed low cytotoxicity on Vero cells (ATCC® no. CCL-81™), very high specificity, and their drug release profiles were equivalent to ALG swelling degree profiles, indicating that the drug delivery was primarily due to the polymer's swelling rate. In the responsive pH range, the carboxylic acid groups of ALGs became ionized and acquired a negative charge, resulting in electrostatic repulsion and allowing water molecules to enter. The NLC particles maintained their framework even after rehydration; thus, the aforementioned system proved promising for the delivery of AmpB orally [130].
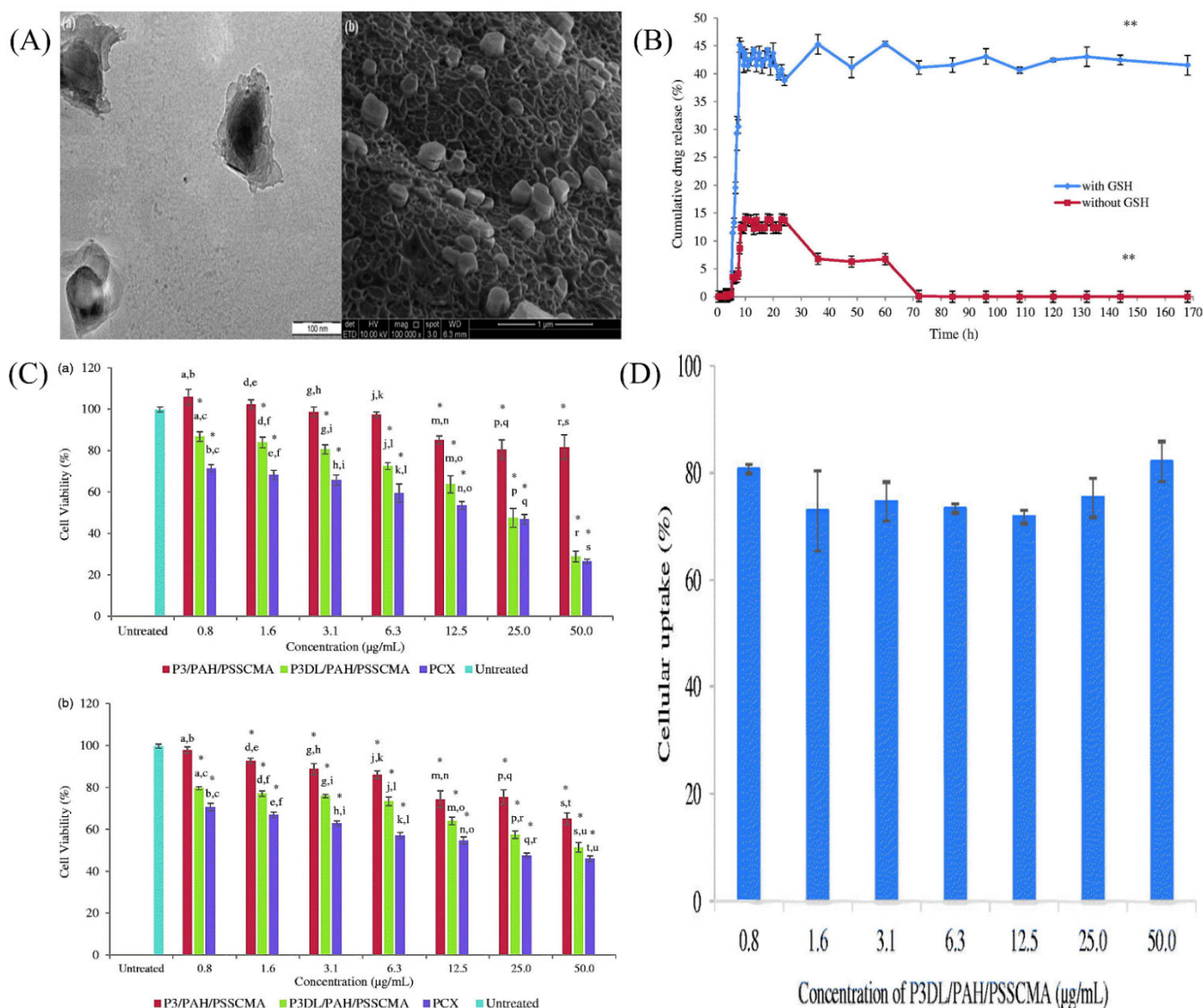
Figure 6. Biocompatible disulfide cross-linked SA derivative nanoparticles for oral colon-targeted drug delivery (**A**) P3DL/PAH/PSSCMA (a) TEM and (b) FeSEM pictures at magnifications of 110,000 and 100,000, respectively. (**B**) For 170 h in a simulated gastrointestinal medium, the cumulative % drug release of P3DL/PAH/PSSCMA was measured. ** means $p < 0.01$. (**C**) The effects of P3/PAH/PSSCMA, P3DL/PAH/PSSCMA, PCX and untreated P3/PAH/PSSCMA on (a) HT-29 and (b) CRL 1790. Data marked with the same letters show significant difference between the samples. * Indicates $p < 0.05$ compared to the untreated samples. (**D**) P3DL/PAH/PSSCMA nanospheres tagged with rhodamine 110 are taken up by HT-29 cells. Reproduced with permission from [126], copyright Taylor & Francis Online, 2019.

Due to its simplicity, non-invasiveness, patient compliance, and economy, oral drug delivery is the most favored route. Particles having a size between 20–100 nm are readily absorbed from the cells while also avoiding renal clearance [131], while particles below 5 nm are quickly cleared via renal clearance. Thus, Thomas et al. prepared ALG-cellulose nanocrystal hybrid nanoparticles by a green method to achieve controlled-drug delivery of the drug rifampicin, an anti-tubercular agent with poor water solubility, which necessitates the search for alternate drug delivery routes. Cellulose nanocrystals (CNCs) were used to improve the mechanical stability, durability, and high diffusion rates due to ALG's highly porous structure. CNCs have been reported to reduce the voids in the gelatin structure [132]. In addition, CNCs have been shown to enhance the ALG bead's mechanical strength and improve drug release [133]. Ionotropic gelation was utilized to synthesize ALG-CNC NPs using water as the only solvent. The optimum nanoparticle preparation was found to be with 1% surfactant and a 1:6 ratio of ALG CNC. The drug entrapment efficiency (EE) was between 43–69%. The ALG-CNC-NPs swelled rapidly at pH 6.8 to 7.4. It showed 15% drug release in 2 h at pH 1.2, while at pH 7.4, almost 100% of the drug was released in 12 h, demonstrating its controlled-release profile. It has a negative zeta potential (-15 to -20 mV) due to free carboxylic groups, thus facilitating penetration into epithelial cells. CNCs and ALG-CNC NP's cytotoxicity was investigated via MTT assay using the L929 fibroblast. It showed 100% cell viability, thus suggesting that these nanoparticles could be a good candidate for drug delivery [134].

The researchers have prepared many formulations and systems to promote actives delivery efficiency via oral routes to beat oral drug delivery limitations. The recent literature includes preparations such as cationic cyclodextrin/ALG/CS nanoflowers/5-fluorouracil [135], hydroxyethylacryl CS/SA hydrogel/paracetamol [136], pH-sensitive nanocomposite using SA/pectin/tannic acid(TA)/silver(Ag)/propranolol [137], Cyperus esculentus starch-ALG/ibuprofen [138], calcium alginate (CA)/SWCNT-GI/curcumin [139], thiol-modified SA microspheres/bovine serum albumin [140], vitamin B12 modified amphiphilic SA nanoparticles/insulin [141], thiolated SA nanoparticles/docetaxel [142], CA beads/cetuximab/octreotide [143], ALG/barium ion/methotrexate [144], CS/CA/liraglutide [145], nano pol cellulose (CMC)/ALG/CS [146].

6.2. Ocular Drug Delivery

Topical instillation in the eye is the most preferred non-invasive administration route of actives for various anterior and posterior segment diseases, for instance, glaucoma, uveitis, cataract, and age-related macular degeneration. It is best-loved due to its comfort in administration and being patient-friendly. Nevertheless, the eye has several protective anatomical barriers that limit drug absorption through this route. The lacrimal fluid drains the drug quickly from the ocular area. Hence, ocular drug delivery has the challenge of maintaining the conc. of the drug at the site of action for the necessary time [147,148]. To enhance the delivery of topical ocular therapeutics, researchers have principally highlighted two methods: (i) to improve the period of residence of the cornea by employing viscosity enhancers, mucoadhesive, particulate, and/or in situ gelling systems; and (ii) to enhance the permeability of the cornea using (a) penetration enhancers, (b) prodrugs, and (c) colloidal systems (like NPs and liposomes) [149].

There is a probability of permanent visual damage or blindness due to retinal diseases such as macular degeneration, uveitis, macular edema, etc., and hence, in such cases, immunosuppressant drugs must be provided on a long-term basis to sustain the functioning of the eye. Encapsulated-cell therapy, however, provides a modern approach with long-lasting delivery of newly synthesized protein-rich drugs, eliminating the need for surgical treatment and is potentially removable by surgery. Some limitations pertaining to ECT use are its poor mechanical strength, inadequate biocompatibility, and lack of termination mechanisms [150]. Hence, Wong et al. synthesized an injectable ALG collagen (CAC) hydrogel with an inducible termination switch as the encapsulation matrix for glial-derived neurotrophic factor for safer ocular delivery. Here, collagen acts to enhance the cell viability

of ALG. The CAC ECT gels were developed by ionotropic gelation employing calcium chloride, where they used a Tet-on-pro-Casp8 switch mechanism for the effective termination of ECT systems. An oral DOX treatment was sufficient for the termination of the gel system. The therapeutic delivery was evaluated in pink-eyed dystrophic RCS/lav rats, a recessive RP model characterized by a progressive loss of photoreceptors and electrophysiological response. The retinal function of rats acquiring GDNF-secreting gels was found to be better than that of the control group. The ECT gel system was mechanically stable, viable, and functional in vivo. Stability studies revealed that following six months of implantation, the system was mechanically stable, strong, and assisted the growth of various types of cells, viz., HEK293 and ARPE-18 cells. Thus, this approach may be utilized to address a range of posterior eye disorders [151].

Nepafenac is a non-steroidal anti-inflammatory agent utilized to address post-surgery pain in the cornea, such as cataracts. Because of its water insolubility, it is only formulated as a suspension, which leads to irritation in the eye, severe lacrimation, and consequently decreased drug's residence time due to rapid drainage into the systemic circulation, limiting the conc. of the drug at the action site [152]. Hence, Shelley et al. utilized the ion-activated in-situ gel formation of ALG with Ca^{2+} ions in the lacrimal fluid to accomplish a sustained release of the actives. HPBCD was the actives solubilizer and permeation enhancer, and the retention time and permeation parameters were observed in the ex-vivo porcine perfusion eye model. The in-situ gel formulation showed a considerably increased diffusion rate and permeation rate than the placebo, with a sustained release of over 24 h with release kinetics following the Korsmeyer-Peppas equation [153].

In another investigation, Nagarwal et al. prepared CS-coated SA-CS nanoparticles for the intra-ocular delivery of 5-FU used for corneal carcinoma. It demonstrated an encapsulation efficiency (almost 27%) and drug loading capacity (around 19%). Moreover, the in-vitro and in-vivo drug-release profiles showed a sustained release (8 h) in contrast to the 5-FU solution and also showed good tolerability when tested by the Draize test on the rabbit eye [154].

Conventional ocular drug dosage forms, for example, solutions, suspensions, and ointments, possess certain disadvantages that cause poor absorption of the drug, such as the sweeping activity of eyelids, tears washing away the drug, impermeable endothelium, and blood barrier. In-situ gelling systems are an effective drug delivery and absorption method since the less viscous solution undergoes gelling in the presence of stimuli such as pH, ionic strength, and temperature. Hence, Noreen et al. developed ALG in situ gelling systems using gum obtained from Terminalia arjuna bark with moxifloxacin HCl as the drug for ophthalmic delivery. It undergoes a sol to gel transition at the pH of tear fluid. The preservative was methylparaben, and the osmolarity was adjusted with sodium chloride. The drug was stable and provided sustained release for 12 h. The ex vivo transcorneal penetration was found to be 4.76 ± 0.27%, and corneal hydration was 78.85 ± 0.19%. No ocular irritation was observed [155]. Thus, the overall results demonstrated the aforementioned system as a promising candidate for ocular drug delivery.

In another investigation, Polat et al. formulated nanofibrous ocular inserts for the therapy of bacterial keratitis incorporating the drug Besifloxacin HCl or BH-hydroxypropyl-beta-cyclodextrin (HP-β-CD) complex comprising PCL/PEG fibrous inserts coated with mucoadhesive polymers such as SA or thiolated sodium alginate (TSA) based on the electrospinning method. The coating with SA and TSA increased the insert's bioadhesion. The preparation demonstrated an initial burst release followed by a slow release for two days, and the thickness and diameter of the inserts were comparable to commercial formulations. Drug loading efficiency was over 90%. Even after seven days of incubation, the inserts did not attain acidic pH values, indicating that the inserts did not cause eye irritation. In vitro studies on ARPE-19 cells on exposure to the ocular inserts demonstrated no cytotoxicity, and their antibacterial activity was comparable to that of commercial formulations. Ex vivo transport research showed that HP-β-CD enhanced solubility and corneal permeability, and

the actives delivery was equivalent to commercial formulations [156]. Hence, the overall results reported that the newly prepared system was suitable for ocular drug delivery.

Different researchers have studied various ALG-based preparations for enhanced ocular delivery of drugs. For example, CS/ALG multilayers/diclofenac [157], CS/ALG/daptomycin [158], CS/ALG/acetamiprid [159], ALG/CS/levofloxacin [160], SA/glycerin/flurbiprofen [161], ALG/peppermint phenolic extract [162], SA/methyl cellulose/sparfloxacin [163], ALG/calcium gluconate(CaG)/tryptophan [164], SA dialdehyde/carboxymethyl CS/limbal stem cells (LSC) [165], SA/methyl cellulose/CMC/carbopol/pilocarpine [166], CS/SA/azelastine [167], SA/butyl methacrylate/lauryl methacrylate/linezolid [168] are few of the current investigations which portrayed excellent ocular actives delivery.

6.3. Pulmonary Drug Delivery

The lungs are an appealing site for the pulmonary administration of actives via diverse DDSs [169,170]. Moreover, the pulmonary route provides numerous benefits over traditional per oral administration, for instance, greater surface area with fast absorption owing to the high vascularization and evasion of the first-pass metabolism [171]. This selectivity enables targeted actives delivery and, therefore, diminishes the side effects [169]. Nevertheless, the pulmonary route is challenging to deliver the actives deep to the alveolar regions of the lung owing to diverse respiratory obstacles, including mechanical, chemical, pathological, and immunological hindrance [172]. The mechanical barrier employs mucociliary clearance to remove particles (having a mean diameter of >6 μm) [173]. When clearance takes place quicker than absorption, in particular of poorly soluble drugs, the availability of actives in the lungs might be restricted. Additionally, under pathologic states like asthma and COPD, excessive mucus is accumulated in the lung, which inhibits the deeper penetration of actives [173,174]. Furthermore, the chemical barrier containing proteolytic enzymes can degrade the breathed materials, which leads to the destruction of functions of actives and/or delivery carriers. Ultimately, the immunological barrier comprising primarily alveolar macrophages assembles the immunological reactions in the intense lung that eradicate all foreign materials with no difference between potential detrimental materials and advantageous ones. Thus, pulmonary bioavailability and systemic bioavailability for actives provided by maximum traditional pulmonary products are less. Therefore, the progress of unique, more effective DDSs is pivotal to alleviating the consequences of these obstacles [175].

The FDA-approved pulmonary dry powder inhalers are predominantly fast-releasing. To obtain sustained delivery to the lungs, Athamneh et al. developed an aerogel microsphere formulation for suitable delivery to the lower pulmonary tract using the ALG-HA hybrid system by the emulsion gelation method followed by drying with supercritical CO_2. Combining these approaches resulted in highly porous Alg-HA microspheres with very low density and a high BET-specific surface area. The addition of HA to Alg successfully reduced the particle agglomeration and enhanced its biodegradation, possibly due to the formation of a hydrogen bond between ALG's carboxylate groups and N-acetyl-glucosamine amide in the hybrid aerogel. In addition, HA was employed to improve the physical characteristics of ALG, such as gelling efficiency and lung tolerance. This led to achieving the desired particle size for pulmonary deposition and improving biodegradability. However, more research using active pharmaceutical ingredients needs to be carried out in this area [100].

Drugs administered to the lungs to treat COPD and cancer suffer from low bioavailability due to distribution to other body tissues, thus requiring multiple dosing and increasing the risk of adverse effects [176]. Mahmoud et al. formulated microparticles based on ALG using the emulsified nano spray-drying process for the pulmonary carrier of roflumilast, a selective inhibitor of the phosphodiesterase-4 enzyme in lung cells. Isopropyl myristate was used as an oil, Tween 80 was used as a surfactant, and calcium beta-glycerophosphate was used as a cross-linking agent. The developed microparticles were assessed based on

encapsulation efficiency, particle size, and in vitro release of actives. The aerodynamic data showed that the actives could be deposited deep into the lungs at the bronchi or bronchial tube (as shown in Figure 7a). The formulation with the spherical-shaped microparticles swelled within 3 h at pH 7.4. Furthermore, it showed a remarkable cytotoxic effect on A-549 tumor cell lines (2.5-fold decrease in IC_{50} compared to the pure drug) (as demonstrated in Figure 7b) and reduced pro-inflammatory cytokines (TNF-alpha, IL-6, and IL-10) in contrast to pure actives (as exhibited in Figure 7c). In addition, CD-based microparticles showed higher sustained bronchodilation on human volunteers than marketed Ventolin®HFA (as shown in Figure 7d). Thus, CD-based microparticles could be a propitious approach for delivering roflumilast in humans [177].
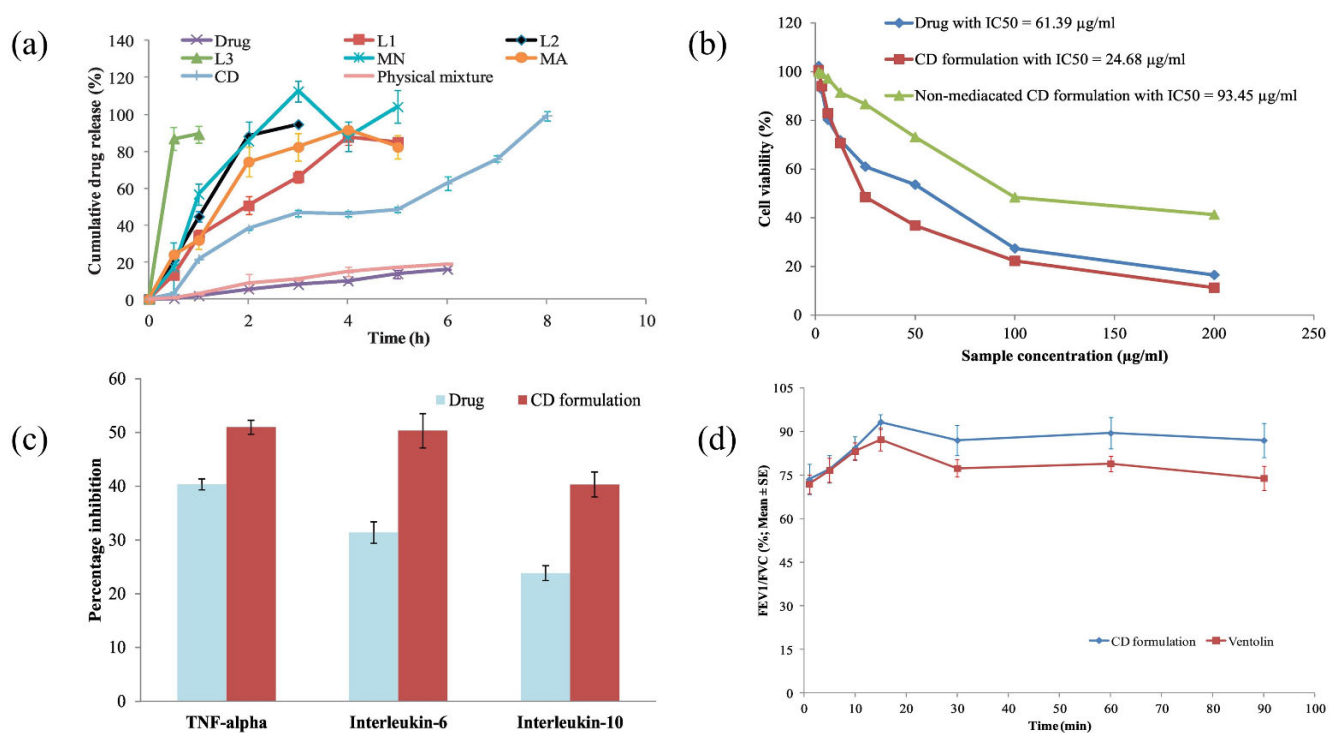
Figure 7. Design and characterization of emulsified spray-dried ALG microparticles as a carrier for the dually acting drug roflumilast (**a**) In an ethanolic phosphate buffer saline solution (30% *v/v*; pH 7.4), release patterns of roflumilast and emulsified spray-dried ALG microparticles were studied. (**b**) The effects of roflumilast, a medicated CD formulation, and a non-medicated CD formulation on the proliferation of A-549 tumor cells. (**c**) TNF-alpha, interleukin-6, and interleukin-10 levels were reduced in A-549 tumor cells by roflumilast and CD formulation. (**d**) FEV1/FVC%—time curve in healthy human volunteers upon inhaling the chosen CD formulation vs. Ventolin® HFA. Reproduced with permission from [177], Copyright Elsevier 2018.

The pulmonary route has also administered anti-cancer drugs to treat lung cancer due to their faster onset of action and evasion of the first-pass metabolism. One of them, cisplatin, shows toxicity in rat liver, lungs, and kidneys, due to which Alsmadi et al. developed CS-ALG nanoporous aerogel carriers loaded with cisplatin for the treatment of lung cancer using an emulsion–gelation method followed by supercritical fluid extraction. The drug exhibited excellent drug loading (76%) while retaining its crystal structure and gave a sustained release of over 6 h. The cisplatin aerogels, thus prepared, decreased the lung toxicity in rats and prevented weight loss [178].

In another investigation, Iglesias et al. prepared ALG aerogel by thermal inkjet technology followed by supercritical drying to encapsulate salbutamol sulfate, which is used to treat asthma attacks and COPD. The current pulmonary drug delivery system suffers from limitations in particle size uniformity and the presence of surfactants. This can

be potentially used for personalized medicine. However, the gel precursor concentrations severely restrict the printable region. The process was highly compatible with the active ingredient (salbutamol sulfate), having a homogenous texture in the nanoporous range. The SS-loaded aerogel was well deposited in the bronchi and bronchioles owing to their nano-particle size. Thus, these aerogels may pave the way for pulmonary drug delivery and personalized medicine, fulfilling the demands of nanostructured, miniaturized, high-resolution product designs [179].

Liposomes, micelles, and polymeric drug particles have been delivered by pulmonary route using biocompatible, biodegradable, and flexible biopolymers such as CS, ALG, gelatin, and other natural polymers. Blends of CS-ALG nanoparticles and microparticles find their applications in controlled drug delivery systems, with calcium chloride often acting as the cross-linking agent. However, researchers have found that using calcium chloride for pulmonary particles induces inflammatory responses. Hence, Alnaief et al. formulated hybrid ALG-CS aerogels via the emulsion-gelation technique without any cross-linking agent. CS solution (2%) was put into the oil phase containing liquid paraffin and 4% surfactant (Span 80 or Span 85), followed by the addition of 1% ALG solution. The resultant hybrid particles were isolated from the oil phase by the process of centrifugation. The pore liquid was replaced with ethanol by a solvent exchange method. The prepared aerogels were later dried with supercritical carbon dioxide. The polymer addition order throughout the gelling procedure and the kind of surfactant employed greatly affected the properties of the hydrogel. Samples prepared using span 85 showed high positive zeta potentials (35.4 ± 5.37 mV), indicating that CS was surrounding the ALG core, whereas those prepared using span 80 showed high negative zeta potentials (-2.15 ± 3.70 to -5.98 ± 5.37 mV), suggesting that ALG was surrounding the CS core. The particle size ranged from 70 nm to 4.17 µm, whereas the aerodynamic diameter ranged from 0.17 to 2.29 µm [180]. Thus, the entire results revealed the developed system is a promising candidate for pulmonary actives delivery.

For the treatment of cystic fibrosis, a potentially life-threatening disease characterized by mutations in the cystic fibrosis transmembrane conductance regulator (CTFR), antibiotics (colistimethane sodium) are generally prescribed. Due to the loss of Cl-channel activity, the lungs become more susceptible to bacterial infections. Of these, Pseudomonas aeroginosa survives the antibiotic treatment and emerges as the predominant infecting organism over time [181–183]. Tobramycin is the drug of choice for such infections that are deteriorating with regular colistimethane sodium. One issue associated with tobramycin therapy is the non-compliance of patients due to twice-daily dosing, which leads to the failure of antibiotic treatment. Another concern is the potential for ototoxicity and nephrotoxicity associated with nearly all aminoglycosides, although there is less evidence of ototoxicity and nephrotoxicity in clinical trials with inhaled tobramycin [184,185]. Hence, Hill et al. developed ALG/CS particles using $CaCl_2$ as the crosslinker. During the optimization studies, increasing the concentration of cations in the formulation resulted in a more significant aggregation of the particles. The optimal formulation was ALG: CS: tobramycin 9:1:1.5, giving high drug loading and narrow size distribution. Tobramycin release was evaluated, depicting a biphasic release with 18.9% of the entrapped drug released within 24 h. In vitro antibacterial studies showed that the drug-loaded optimal formulation showed a dose-dependent activity against P. aeroginosa with a MIC of 6.25 µg/mL, while the unloaded formulation demonstrated no action. Tobramycin alone had a MIC of 1.5 µg/mL, possibly due to the drug diffusion rate. The Zeta potential was found to be 2.16 ± 0.07% mV and the %EE was 44.5%. SLPI conjugation enhanced the mucoadhesive properties [186]. Hence, the prepared system could help deliver drugs via the pulmonary route.

Moreover, investigators have developed various formulations to intensify pulmonary DDSs. For example, SA/CS/Tween 80/rifampicin [187], ALG/poly(N-isopropyl acryl amide (PNIPAAm)/theophylline [188], ALG/ciprofloxacin [189], ALG/CS/lapazine [190], $ALG/CaCO_3$/levofloxacin/DNAse [191], ALG/HA/naproxen [99], ALG/CS/DOX/paclitaxel [192], ALG modified PLGA nanoparticles/amikacin/moxifloxacin [193], ALG

particles encapsulating live Bacille Calmette– Guérin (BCG) and *Mycobacterium indicus pranii* (MIP) [194], CS/ALG/BSA gel/DOX [195] are some of the recent formulations showing excellent delivery of drugs via pulmonary delivery.

6.4. Vaginal Drug Delivery

Lately, the vagina has been considered a potential administration route replacing the parenteral route for actives delivery, bestowed with systemic effects that cannot be favorably administered per os due to the hepatic or GI degradation or to the commencement of adverse consequences in the GI. The significant constraint of such an administration route is described by the physiological elimination mechanisms, which are active in the vagina's lumen and are responsible for an unsatisfactory residence time of the conventional formulated system at the targeted site, following an unsteady actives dissemination onto the mucosa [196]. The vagina, a prominent female reproductive organ, allows for local and systemic actives delivery due to its large surface area and high blood supply. However, it is also associated with variations in the size of the endometrium during menstruation, which may alter the drug absorption properties [197,198].

Vaginal dosage forms should ideally be easy to administer, requiring fewer doses, and patient-compliant. However, it is challenging to formulate small water-soluble drugs through the vaginal route. Hence, Meng et al. prepared spray-dried microparticles (MPs) using thiolated-CS coated SA by the layer-by-layer method for the vaginal delivery of HIV microbicides. They were studied for their cytotoxicity and pre-clinical safety on human vaginal (VK2/E6E7) and endocervical (End1/E6E7) epithelial cell lines and in vivo on female mice. The outcomes showed that TCS-coated Ag-based multilayer microparticles had 20–50 fold more adhesion than native AGMPs [199]. Hence, the developed formulation could be useful for vaginal drug delivery.

Urogenital infections affect about a billion women worldwide. It is caused due to *Escherichia coli* and other enterobacteria commonly found in the vaginal tract. The chances of UTIs are increased in post-menopausal women, which account for 25% of all bacterial infections. Cystitis, the most common UTI, usually affects young women, with *E. coli* being the cause of most diseases. The treatment of UTIs is still a challenge because of frequent recurrence, the association of co-morbidities, and high prevalence. Cefixime, a third-generation cephalosporin, is usually given for such infections. However, its poor water solubility, limited oral bioavailability, and incomplete absorption limit its use. Hence, Maestrelli et al. developed a bioadhesive vaginal dosage form of cefixime that can overcome many drawbacks. They prepared CS-coated CA microspheres using an ionotropic gelation method, and their mean weight, diameter, %EE, and loading capacity were evaluated. All MS batches showed prolonged adhesion greater than 2 h on the excised porcine vaginal mucosa; %EE enhanced with increasing drug concentration. In vitro studies revealed the direct relationship between CFX drug release and % inhibition in *E. coli* metabolic activity [200]. Thus, the overall results demonstrated the developed system as an auspicious candidate for vaginal delivery of actives.

Despite having several benefits, for example, enormous surface area, evasion of the first-pass metabolism, and the ability to optimize drug absorption for systemic effects, it also has certain drawbacks, such as the restoration action on vaginal fluids and its acidic environment (pH 4.0–4.5), which hampers the local delivery of drugs due to low residence time and stability. Hence, Ferreira et al. formulated CA hydrogels based on the earlier formation of polyelectrolyte complexes (PECs) for the vaginal delivery of polymyxin B. First, PECs were formed between ALG and PMX, ensued by cross-linking with calcium chloride. The aforementioned system displayed a pore size of between 100–200 μm and adequate syringability; in vitro tests demonstrated mucoadhesiveness. The drug release was found to be pH-dependent with a sustained release of six days. A burst release was noticed at pH 7.4, and the drug was released by anomalous transport. At pH 4.5, actives release followed the Weibull model and actives transport was through Fick's diffusion [201]. Thus, the formulated system could be suitable for vaginal drug delivery.

Vulvovaginal candidiasis caused by the fungus Candida albicans is generally treated using azole antifungals like fluconazole given orally. However, fluconazole is reported to have severe side effects like nausea, vomiting, diarrhea, and abdominal pain [202,203]. Hence, Darwesh et al. developed vaginal inserts using PEC based on anionic ALG and cationic CS. The mucoadhesion was highest for Na–Alg-based vaginal inserts (pKa 3.21) as compared to carbopol (pKa 5.0) because the mucoadhesion depends on the no. of hydrogen bonds (-OH, -COOH) concerned in the mucoadhesion interaction. The ALG: CS (5:5) PEC revealed controlled release of fluconazole (RE_{6h} ranged from 56.46 $\pm$ 3.42 to 79.38 $\pm$ 3.42%), good mucoadhesion, and therefore suitable vaginal retention. Moreover, it demonstrated excellent antifungal action against Candida albicans both in vitro (MIC for fluconazole vaginal inserts was 31 $\pm$ 0.4 mm and that of fluconazole solution was 22 $\pm$ 0.4 mm) and in vivo (complete healing after seven days in rats) with reduced inflammatory cells [204]. Thus, the overall results depicted that the formulated system could be a promising candidate for vaginal drug delivery.

In another investigation, Soliman et al. developed an in situ thermosensitive bioadhesive gel for the vaginal delivery of sildenafil citrate as a prospective therapy for endometrial thinning caused by the administration of clomiphene citrate for ovulation initiation in women with type II gonadotrophic anovulation. They were developed using various grades of Pluronic® (PF-68 and PF-127) grades, into which mucoadhesive polymers such as SA and hydroxyethylcellulose were incorporated in different concentrations. The thermosensitive gels were developed by the cold method. The acceptable range of $T_{sol-gel}$ of 28–37 °C was achieved by decreasing PF-127 concentration and modulating the addition of PF-68. There was increased gel viscosity and mucoadhesive force when the concentration of Pluronic® was raised, but there was a reduction in drug release rate during in vitro evaluation in a standard semi-permeable cellophane membrane at pH 4.5 using citrate buffer to mimic the vaginal fluid. Due to its rapid swelling property, SA aided the formation of adhesive interaction between ALG and mucosa, which led to increased mucosal retention. The in situ gels substantially enhanced endometrial thickness and uterine blood flow, thus potentially improving conception chances in anovulatory women with clomiphene citrate failure [205].

Researchers also synthesized ALG/CS/P4/Pluronic® F-127/progesterone [206], CS/SA/polycarbophil/metronidazole [207], SA/CS/α,β-glycerophosphate/Bletilla striata/tenofovir [208], SA loaded with anise/fluconazole β-cyclodextrin inclusion complexes [209], CS/ALG/metronidazole [210], HPMC/SA/abacavir [211], dextran/ALG nanofibers/clotrimazole [212], Polaxomer 407/SA/*Lactobacillus crispatus* [213], ALG/CMC/clove essential oil [214], and ALG/CS/metronidazole [215] formulations which enhanced the vaginal drug delivery.

6.5. Nasal Drug Delivery

Nasal actives delivery includes the inhalation of drugs into the extremely vascularized mucosal layer of the nasal epithelium, which ultimately reaches the systemic circulation [216]. The nose has an enormous surface area for actives absorption, quicker onset of action, and evasion of first-pass metabolism [217]. The curative action of the majority of the drugs is impacted owing to the BBB's existence. Therefore, nasal route delivery favors therapeutics straightaway reaching the central nervous system (CNS). Furthermore, nasal delivery of actives shows benefits from brain-targeting, fewer side effects, and easy administration [218].

Rhinosinusitis, inflammation of the nasal cavities characterized by nasal polyp growth, typically extending beyond the nasal valve, is generally treated using nasal corticosteroids since oral ones show systemic side effects. However, its long-term use causes an increase in intraocular pressure and changes in serum cortisol levels. Hence, Dukovski et al. formulated dexamethasone-loaded lipid/ALG nanoparticles dispersed in pectin solution based on an in-situ gelling process that undergoes a sol-gel transformation after contact with the Ca^{2+} ions in the nasal mucosa. The in vitro biocompatibility experiments utilizing colon

carcinoma Caco-2 cell lines suggested no effect on cell viability; however, in-vivo studies are required to confirm this observation [219].

It becomes feasible to administer vaccines in dry powder form during influenza outbreaks due to their ease of transport, patient compliance, and stability. As compared to conventional vaccines, dry powder vaccines provide both humoral and cellular immunity adequately. Thus, Dehghan et al. formulated ALG NPs using the ionotropic gelation method encapsulating whole inactivated influenza viruses and administered them to rabbits, which showed significantly higher IgG titers when short single-stranded cytosine triphosphate and guanine triphosphate-containing synthetic oligodeoxynucleotides (CpG ODN) were used as the adjuvant (as exhibited in Figure 8c,d). ALG NPs released 65.87% of CpG ODN, 35.68% of QS, and 34.00% of influenza antigen within 4 h (as displayed in Figure 8a). In addition, the XTT test demonstrated safety for in-vivo applications (as shown in Figure 8b), making the formulation useful for nasal drug delivery [220].
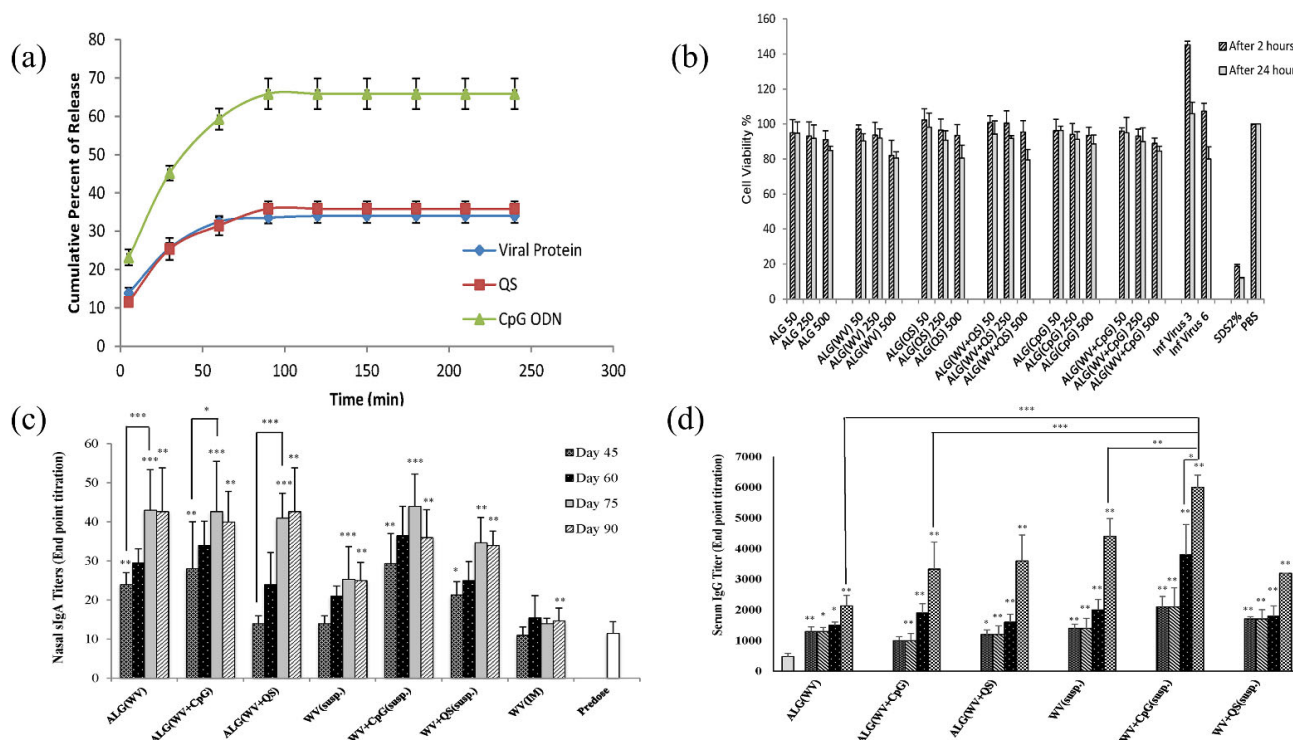
Figure 8. Preparation, characterization, and immunological evaluation of ALG nanoparticles loaded with whole inactivated influenza virus: Dry powder formulation for nasal immunization in rabbits (**a**) % of viral protein, QS, and CpG ODN released in vitro from ALG NPs over four hours. (**b**) After 2- and 24-h exposure with varying concentrations of each formulation, the effect of ALG NPs and influenza virus suspension on cell viability in Calu-6 cell lines (**c**) HAI antibody titers in each vaccination group on day zero (control), day 45 (after prime dose), day 60 (after the second dose), day 75 (after the third dose), and day 90 (after the final booster) (**d**) IgG titers in blood samples taken from each vaccinated cohort on days zero (negative control), 45 (prime dose), 60 (second dose), 75 (third dose), and 90 (after the final booster). * means $p < 0.05$, ** means $p < 0.01$, *** means $p < 0.001$. Reproduced with permission from [220], Copyright Elsevier 2019.

In a different study, Rao et al. formulated the anti-Parkinson drug Ropinirole as a thermoreversible in situ nasal gel. The rationale for the nasal delivery of Parkinson's patients is that it becomes difficult for them to swallow oral solid dosage forms due to muscle rigidity. It was prepared by the cold method using PF 127 and HPMC K4M as the thermoreversible polymer. They observed an astounding five-fold enhancement in the bioavailability of ropinirole in contrast to intravenous drug delivery. Furthermore, in vitro

evaluation of sheep nasal mucosa demonstrated that the in situ gel had a more protective impact on nasal mucosa than the plain drug, which caused mucosal damage [221].

In another investigation, Youssef et al. developed SA nanoparticles for the anti-migraine drug Almotriptan utilizing the w/o/w double emulsion solvent evaporation procedure. It is a water-soluble drug; hence, SLNs were prepared to help pass the drug through the lipophilic BBB. Poloxamer 407 was used as a stabilizer and evaluated for its physicochemical properties by combining various mucoadhesive polymers, for example, SA, sodium CMC, and carbopol. In addition, the gelling temperature, gelling time, viscosity, gel strength, pH, %EE, and in vitro mucoadhesion were evaluated [222]. The overall results demonstrated the prepared formulation to be suitable for nasal drug delivery.

Vaccines typically include adjuvant substances to enhance the humoral or cellular response to an antigen. The most common antigen, aluminum, instigates a Th2 antibody response; hence, aluminum-based vaccines are unsuitable for intracellular pathogens and chronic diseases. Currently, usable vaccines through the intramuscular (i.m.) or subcutaneous (s.c.) routes fail to elicit a mucosal immune response. Nasal immunization, a relatively simple, non-invasive route, can provide mucosal immunity [223–227]. However, an acceptable mucosal immune response depends on the mucociliary clearance, the tolerogenic character of the mucosal epithelium, and the huge size of the antigen. To circumvent this problem, the antigens can be incorporated into mucoadhesive polymeric NPs, extending the duration of antigen residence and conferring protection against enzymes [228,229]. Hence, Mosafer et al. developed SA-coated CS and trimethyl CS nanoparticles incorporated with the PR8 influenza virus for nasal administration. The zeta potential was -29.6 mV. The vaccine was evaluated in BALB/c mice, wherein the PR8-TMC-ALG formulation manifested a more excellent IgG2a/IgG1 ratio than PR8-TMC, PR8-CHT, and PR8-ALG. Thus, ALG-NPs could be used as immunoadjuvants for nasal immunization. The ALG-coated NPs generated an excellent immune reaction compared to uncoated NPs [230].

The recent nasal formulations include SA/Polaxomer 407/gellan gum/timosaponin BII [231], SA in situ gels based on agomelatine (AGM) [232], ALG based magnetic short nanofibres 3D composite hydrogel encapsulating human olfactory mucosa stem cells [233], OA-dopamine conjugate [234], ALG nanoparticles/venlafaxine (VLF-AG-NPs) [235], *Mycobacterium bovis* Bacille Calmette-Guérin (BCG)-loaded microparticles using ALG/CS [236], ALG/CS/attenuated Androctonus australis hector (Aah) venom [237], CS/ALG nanoparticles/SpBMP-9 (growth factor) [238], ALG/trimethyl CS liposomes/lipopeptide subunit vaccine [239], SA microspheres/*Lactobacillus casei* [240].

6.6. Transdermal Drug Delivery

Transdermal drug delivery relates to the delivery of actives via the skin for systemic or local absorption. They are advantageous over the conventional administration routes due to their capability to deliver controlled release of drugs, reducing the first-pass metabolism, less systemic side effects, effective control of drug plasma profile, and patient compliance [241]. However, its applications are limited owing to the extensive skin hindrance, particularly the stratum corneum. Consequently, few actives can penetrate the skin and reach the blood at a therapeutic concentration [242].

Insulin is usually given hypodermically via s.c. injection for the therapy of diabetes mellitus. But it generates biohazardous waste; furthermore, patient compliance is also a challenge, especially in children. Several approaches have come into the picture to resolve the issue, such as inhalational microparticles, oral administration of nanoparticles, and needle-free high-pressure injection systems [243–245]. Among these, transdermal patches have attracted much attention owing to minimal pain and tissue injury [246,247]. In this context, Yu et al. fabricated a dissolving polymer microneedle patch comprising 3-aminophenyl boronic acid-modified ALG (ALG-APBA) and HA that can quickly dissolve in the interstitial fluid of the skin. Alginate was chemically modified by adding 3-aminophenyl boronic acid to form ALG-APBA, and HA was crosslinked to form MNs in the presence of Ca^{2+} ions. The MNs thus prepared were evaluated for their mechanical strength, degradation,

ex vivo skin insertion, stability of insulin, in vivo transdermal delivery to SD rats, and pharmacokinetic and pharmacodynamic activity in SD rats. In addition, the resistance of MNs to static and dynamic forces was calculated, and it was found that no change in the tips was observed even after the addition of 10–100 g weight on the microneedle patch, with no breaks in the needle after the addition of 500 g, demonstrating its excellent mechanical strength. The encapsulated insulin has comparable pharmacological activity to an s.c. injection with the same insulin dose, with RPA and RBA at 90.5 ± 6.8% and 92.9 ± 7.0%, respectively [248]. Overall results made the aforementioned system advantageous for nasal drug delivery.

In a different investigation, Lefnaoui et al. fabricated transdermal films based on ALG-CS PECs for the antiasthmatic drug ketotifen fumarate (KF). Polyethylene glycol was used as a plasticizer, and Span 20, and Tween 80 were utilized as permeability enhancers. The films were prepared by the film casting method and evaluated for their uniformity in weight, thickness, folding endurance, loss of moisture, and absorption of moisture. Furthermore, actives release and permeation through the rat abdomen mounted on the Franz diffusion cell were characterized. The transdermal films made by a 1:1 ratio of CS and ALG yielded smooth, flexible, strong, bioadhesive, biocompatible films. The drug release research showed that the KF was released in a controlled way over a long period (99.88% release after 24 h) to treat asthma, allergic rhinitis, and conjunctivitis [249]. The results revealed that the prepared formulation is favorable for transdermal drug delivery.

In another study, Abebeet et al. developed a self-adhesive hydrogel for strain-responsive transdermal delivery using gallic acid (GA) modified ALG as the mucoadhesive polymer. The model drug, caffeine, was encapsulated in the hydrogels prepared by the one-pot synthesis method. The diffusion kinetics were controlled by Fickian diffusion. The developed hydrogels had a 25% increase in tensile strength and twice the transdermal release of the drug. A powerful adhesion of 100 kPa was reported on a glass substrate. A close to 800% strain was observed, and it was attributed to the free movement and adhesion of ALG and polyacrylic acid. It could withstand body movement as well as skin stretching when tested on human skin. Thus, GA hydrogel seems to be a promising route for strain-controlled TDD [250].

In another investigation, Abnoos et al. prepared a CS-ALG nanocarrier for the transdermal delivery of pirfenidone (PFD) in idiopathic pulmonary fibrosis, a disease characterized by progressive dyspnea and pulmonary function loss [251,252]. CS-SA nanoparticles were developed by the pre-gelation technique, and the drug Pirfenidone, an anti-inflammatory and antifibrotic agent, was encapsulated with 94% efficiency. The prepared nanoparticles were evaluated using SEM, TEM, and DLS. These studies showed that particle morphology was spherical with an average size of 80 nm. FTIR spectra observed the complex formation between CS and ALG. The drug release studies show that PFD had undergone an initial burst release of 12% after 5 h and was later released in a sustained manner for 24 h. Ex vivo studies revealed that skin permeation of PFD was improved by using CS-SA nanoparticles compared to standard PFD solution. The permeation was also observed through fluorescent microscopic images labeled with FITC. SEM studies reveal that the nanoparticles could remain stable for six months [253]. Thus, the results proved that the prepared formulation is useful for transdermal drug delivery.

In another investigation, Anirudhan et al. formulated bio-polymer matrix films acquired from CMC, SA, and PVA to transdermally deliver diltiazem, a calcium channel blocking drug used for cardiac failure. The oral bioavailability of DTZ is only 30–40%. Hence, alternative routes of drug delivery are being explored. Since diltiazem (DTZ) is hydrophilic in nature, a hydrophilic matrix consisting of polyethylene glycol coated vinyl trimethoxy silane-g-CS (PEG@VTMSg-CS) with matrices like Na-ALG, CMC, and PVA was developed. A dispersion of the matrix was prepared to avoid the undesirable effect of shrinkage of the polymer network when the drug is being eluted out of the matrix. The drug release studies were based on Franz diffusion cells. SA films showed more significant swelling than PVA films. The ALG films displayed a thickness value of

0.052 ± 0.01 mm and a water permeation of 0.07 g cm^2/24 h. DTZ permeation was less due to less film thickness. The in vitro skin penetration research of DTZ on rat skin revealed the effectiveness of the films with more than 49% viability in HaCaT and PBMC cell lines with no histological alterations on the skin. The present formulation could deliver 70% of the drug in 24 h [254]. Thus, the overall results demonstrated that the system is promising for transdermal drug delivery.

The currently investigated formulations include ALG/PVA/ciprofloxacin electrospun composite nanofibers [255], SA/propylene glycol/metoclopramide films [256], SA/glucosamine sulphate [257], ALG/maltose composite microneedles/insulin [258], ALG/CS/rabeprazole [259], oleic acid/SA/Na CMC/2,3,5,40-tetrahydroxystilbene 2-O-β-D-glucoside (THSG) [260], SA/CS/piplartine [261], SA/polyvinyl alcohol/quercetin [262], ALG/Hidrox-6/Hydroxytyrosol [263], sodium L-cysteine ALG/isopropyl myristate/ropinirole hydrochloride [264], ALG coated aminated nanodextrin/CS coated folate decorated aminated β-CD nanoparticles/curcumin/5-flurouracil [265] which intensified transdermal drug delivery.

6.7. Mucosal Drug Delivery

In order to evade parenteral routes and beat biological impediments, one more DDS, specifically the mucosal delivery system, appeared in the limelight. Mucus gel layers line the vagina, lungs, and gastrointestinal tract (GIT). GIT represents a complicated condition, including several digestive enzymes and a changeable pH (acidic pH-stomach and basic pH-intestine). Different drugs necessitate being guarded against the circumstances referred to above to evade degradation by proteolytic enzymes. These pharmaceuticals exhibit inadequate permeability in gastric mucosa and also bear the first-pass effect. To preserve the actives of interest facing such conditions, ALG serves as one of the most satisfactory polymers with mucoadhesive characteristics and improved permeation results, and acts as a defensive envelope for such actives through mucosal delivery [266]. Mucoadhesion refers to the capability of materials to bind to the mucosal membrane and offer some retention. Mucoadhesive drug delivery provides various benefits over other routes of administration, for example, faster distribution to the local blood vessels, avoidance of first-pass metabolism, reduced dose frequency, and rapid relief [267]. Thus, the formulated system might be helpful for mucoidal drug delivery.

Oral cancer, one of the most common cancers, is usually treated with surgery and chemotherapy [268], but they have the drawback of alteration of facial morphology followed by surgical procedures. Hence, to provide an alternative approach, Shtenberg et al. formulated a mucoadhesive ALG/liposome paste. DOX-loaded liposomes were prepared, and ALG-fluorescein was synthesized using FITC and ethylenediamine; on homogenization, a cross-linked hybrid paste was formed. It showed the liposome's sustained release from ALG cross-linked paste (release index of 8). Furthermore, in vitro toxicity studies on human cell lines acquired from tongue SCC (CAL 27) showed viability of 15% after 48 h. Thus, polymers released from the liposomes were active and effective. Therefore, this approach could be used for potential oral cancer therapy [269].

Oral mucosal vaccine delivery has the disadvantage of significant enzymatic degradation of the antigen in the GI tract, and these have difficulty in uptaking from the intestine. To overcome this issue, HbsAg-loaded CS nanoparticles with an ALG coating were prepared by Saraf et al., in which lipopolysaccharides acted as an adjuvant. It showed elevated levels of sIgA in intestinal (3.32 mIU/mL) secretions compared to non-ALG coated HB-CNPs (as displayed in Figure 9c). Thus, ALG-coated CS NPs (CNPs) could entrap HbsAg effectively (as shown in Figure 9b). The release profile of protein showed that 84% of the drug was released at 0.5 h. owing to CNPs' loose binding that led to increased desorption at the acidic pH, but 95.5% of the drug was released at 48 h (as displayed in Figure 9a). Coating with ALG stabilized increased the stability of CNPs and provided a sustained release of 51.42% after 48 h. In addition, the ALG-coated NPs adhered better than uncoated NPs. The cell viability of RAW 264.7 cell lines was 70.45%; nevertheless, the cell viability decreased

to 66.45% after 48 h. This time-dependent decrease in cytotoxicity could be due to contact between positively charged nanoparticles and negatively charged membranes. Mucosal M-cell-specific ALG-coated CS nanoparticles elicited a significant immunological response in mice (as demonstrated in Figure 9d). Hence, overall results showed the aforementioned system is favorable for mucosal drug delivery [270].
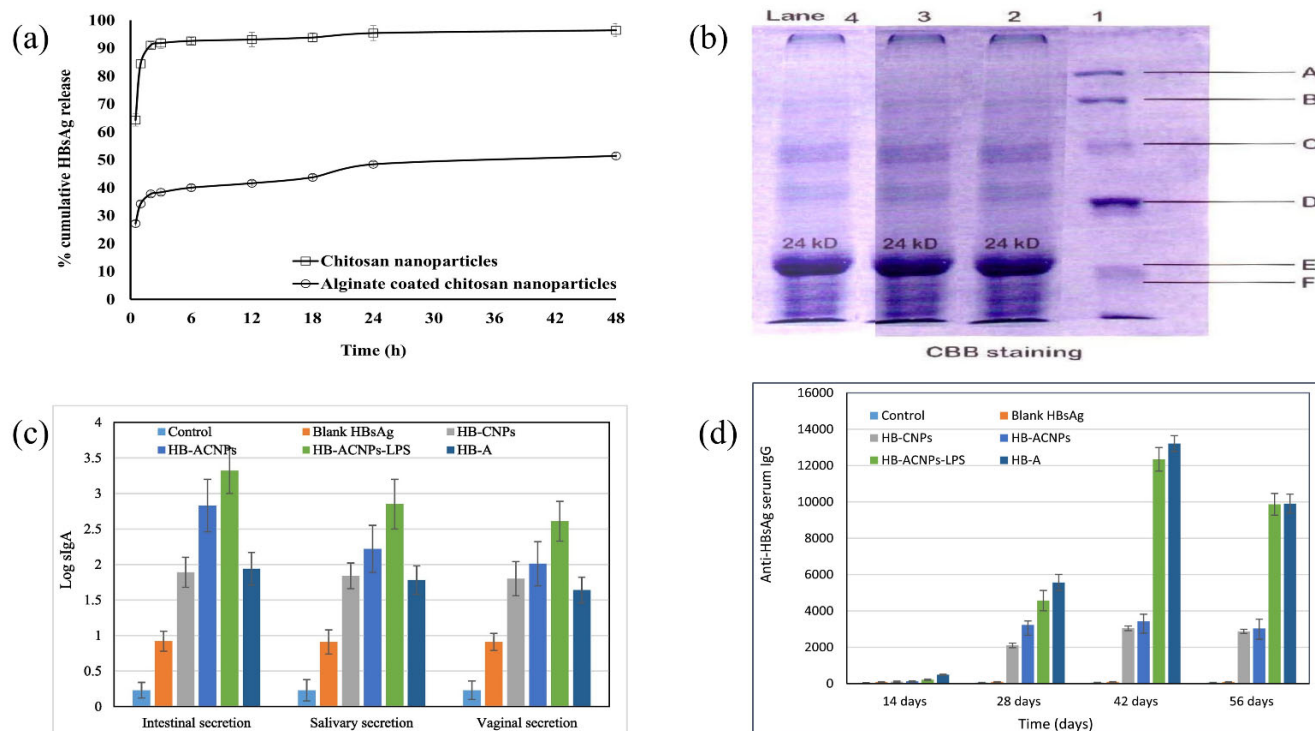
Figure 9. Lipopolysaccharide-derived ALG coated Hepatitis B antigen-loaded CS nanoparticles for oral mucosal immunization (**a**) Release profile of produced nanoparticles in vitro. (**b**) HBsAg release as determined by SDS-PAGE: Lane 1: Molecular weight markers; Lane 2: HBsAg solution; Lane 3: HBsAg loaded CS nanoparticles, Lane 4: HBsAg-loaded ALG coated CS nanoparticles produced from LPS. (**c**) The levels of sIgA in the fluid secretions of mice immunized with different formulations. (**d**) Anti-HBsAg IgG levels in mice inoculated orally with various formulations. Reproduced with permission from [270], Copyright Elsevier, 2020.

In another investigation, Ghumman et al. utilized linseed mucilage-ALG mucoadhesive microspheres loaded with Metformin HCl developed by an ionotropic gelation procedure for mucosal actives delivery. Drug encapsulation efficiency was up to 92% with sustained release for 12 h. The results revealed that an optimized formulation (FM-4) could furnish sustained release for up to 12 h and hold the level of blood glucose by regulating and enhancing the absorption of metformin systemically. Therefore, LSM, a natural emerging mucoadhesive agent, proved to be preferable for controlled release mucoadhesive microspheres designed for oral utilization [271].

In periodontitis, there is inflammation and destruction of tooth tissues, and the pathogen forms a biofilm around the inflamed tissues. Currently, treatment approaches include mechanical removal of the biofilm aided by antibiotics whose systemic side effects limit the effectiveness of treatment. Hence, Kilicarslanet al. used clindamycin phosphate-loaded ALG/CS PEC film to overcome this issue. CS and ALG, being oppositely charged biopolymers, form a PEC by cross-linking with each other. It was observed that increased ALG concentrations in the polymer mixture increased adhesiveness, making it valuable for mucosal drug delivery [272].

In another investigation, Gonçalves et al. developed highly porous ALG/carrageenan aerogel nanoparticles for drug delivery of powdered model drugs quercetin and ketoprofen.

Biopolymer aerogels have low toxicity and are biocompatible, with large surface areas with accessible pores or drug loading. The emulsion gelation method was used to produce the hybrid biopolymer nanoparticles, followed by drying using supercritical CO_2. Pectin and ALG had better interaction, with an increased degree of cross-linking between the two polysaccharides giving NPs of higher specific surface area ($>300 \text{ m}^2 \text{ g}^{-1}$) and lower shrinkage. The drug-loading capacity was $17 \pm 2\%$ for ketotifen and 3.8% for quercetin. The cytotoxicity test using the MTS assay on human carcinoma Caco-2 cell line showed almost 100% cell viability, thus demonstrating the prepared nanoparticles to be highly non-toxic. The drug release from ALG/κ-carrageenan aerogel was quicker than from ALG/pectin [273]. Thus, the developed system was found to be suitable for drug delivery.

In another research, Martín et al. developed effective antifungal mucoadhesive drug delivery systems to treat oral candidiasis using ALG microspheres containing the drug nystatin. Oral candidiasis is caused by the opportunistic pathogen Candida albicans, especially in immunocompromised, diabetic patients undergoing chemotherapy. Nystatin, a polyene antifungal antibiotic, is indicated to treat mucocutaneous fungal infections caused by C. albicans. However, nystatin possesses a huge lactone ring and numerous double bonds, which render it amphiphilic and amphoteric and thus render its formulation difficult. Consequently, it has been formulated as micellar gels, liposomes, intralipids, niosomes, and various other dosage forms [274–276]. Thus, Martin et al. developed nystatin microspheres based on the emulsification/internal gelation procedure with some modifications [277]. Evaluation of particle size, zeta potential, swelling behavior, loading content, encapsulation efficiency, rheology, mucoadhesive force, drug release studies, antimicrobial activity, and in vivo studies were carried out. It was found that the mean size of the microspheres was 85–135 um, and the viscosity was that of a Newtonian fluid. The drug release was in two steps; first, an initial burst release was followed by a more sustained drug release, with about 60% of the drug released in the first 2 h. The prepared microspheres showed marked antifungal activity with a drastic reduction in C. albicans colonies. In vivo research on the buccal mucosa of experimental animals demonstrated that the retained amount, which is 4 to 6 times higher than the MIC, was enough to elicit the therapeutic response [278].

Researchers have also formulated lysozyme mucoadhesive tablets/Ca^{2+} cross-linked ALG with HPMC [279], silybin/nanocrystals-in-microspheres PEC/ALG/CS [280], co-delivery of ketorolac and lidocaine/polymeric wafers/2:1 SA:PVP -25 and 10% glycerol [281], HPMC/SA/nicotine [282], ALG modified with maleimide-PEG/ibuprofen sodium [283], silicone sheet/dexamethasone/ALG [284], ALG/sterculia gum/citicoline [285], ALG/ghatti gum/montmorillonite/flubiprofen [286], pectin/ALG/repaglinide [66], polyacrylamide-g/locust bean gum/ALG/ketoprofen [287], CS/CA/*Lactobacillus casei* [288] for improved mucosal actives delivery.

6.8. Intravenous Drug Delivery

ALG, owing to its biocompatibility and safety in vivo, has been explored for intravenous drug delivery in order to increase the bioavailability of drugs that the conventional oral route cannot deliver.

Hydrophobic medicines can be entrapped in hydrophilic nanoparticles like CA and delivered to their site of action. Curcumin and resveratrol are both polyphenolic molecules found in nature that have anti-cancer properties. Their low water solubility and bioavailability unfortunately limit their therapeutic utility. In a study by Saralkar et al., the emulsification and cross-linking procedures were used to make curcumin and resveratrol-based CA nanoparticles. Particle size, zeta potential, moisture content, physicochemical stability, and %EE were all measured in the nanoparticles. For the combined estimation of curcumin and resveratrol, the UPLC methodology was designed and validated. The in vitro efficiency of ALG nanoformulation on DU145 prostate cancer cells was investigated. Curcumin and resveratrol had entrapment efficiencies of $49.3 \pm 4.3\%$ and $70.99 \pm 6.1\%$, respectively. In 24 h, resveratrol had a greater release than curcumin ($87.6 \pm 7.9\%$ against $16.3 \pm 3.1\%$). Curcumin, both in solution and as nanoparticles, was found to be taken up by cells. Resveratrol

was poorly absorbed by cells. On DU145 cells, the drug-loaded nanoparticles cause cytotoxicity. The drug solution was more hazardous than nanoparticles at high concentrations. The intravenous administration of the ALG nanoformulation was proven to be safe [289].

Over the last 10 years, multifunctional theranostics have created some intriguing novel possibilities for chemotherapy and tumor detection. In a study by Yang et al., the photosensitizer chlorin e6 (Ce6) and the anticancer medication DOX were subsequently adsorbed onto the magnetic mesoporous silica nanoparticles (M-MSNs) to produce a pH-sensitive drug release and for adsorbing P-glycoprotein short hairpin RNA (P-gp shRNA) for preventing multidrug resistance, ALG/CS polyelectrolyte multilayers (PEM) were constructed on the M-MSNs (M-MSN(DOX/Ce6)/PEM/P-gp shRNA). Upon laser illumination, the nanoparticles with a mean diameter of 280 nm showed a pH-responsive drug release profile and increased singlet oxygen formation in tumor cell lines. The delivery mechanism only released 12 percent Ce6 after 30 h at pH 7.4 but >95 percent after 36 h at pH 4.0. In terms of DOX release, roughly 30% of it was released from M-MSN(DOX/Ce6)/PEM nanocomposites in 32 h at physiological pH (7.4), compared to a 46% release of DOX at pH 4.0. The multifunctional nanocomplexes greatly boosted apoptosis in vitro, as demonstrated by the CCK-8 assay and calcein-AM/PI co-staining. Using cancerous Balb/c mice for the animal studies, researchers used a combination of photodynamic treatment and chemotherapy to achieve a synergistic anti-cancer activity in vivo. Additionally, the cores of the bifunctional Fe_3O_4-Au nanoparticles in the multifunctional nanocomplexes allowed dual-modal MR and CT imaging, revealing high uptake into tumor-bearing animals via intravenous injection. This study demonstrates the excellent performance of magnetic mesoporous silica nanocomposites as a multipurpose delivery system for imaging-guided cancer synergistic therapy [290].

For cancer treatment, nanocarrier drug delivery systems (NDDSs) have received more attention than traditional drug delivery methods. The rapid evacuation of activated macrophages from the bloodstream, however, hinders efficacy. In a study by Wang et al., glycyrrhizin (GL) was loaded into ALG nanogel particles (NGPs) to create a versatile delivery mechanism to reduce activated macrophage clearance and improve anticancer activity with GL and DOX combined therapy. GL-ALG NGPs could not only prevent eliciting macrophage immuno-inflammatory responses, but they could also reduce macrophage phagocytosis. DOX/GL-ALG NGPs increased DOX bioavailability by 13.2 times compared to free DOX in the blood. The use of mice with normal immune systems instead of nude mice in the construction of tumor-bearing mice further revealed that NGPs are biocompatible. In vitro and in vivo, GL-mediated ALG NGPs had an exceptional hepatocellular carcinoma targeting effect [291].

Arsenic trioxide (ATO) is efficacious in managing acute promyelocytic leukemia (APL) and late-stage primary hepatic cancer, although it has serious adverse effects. Hence, Lian et al., in order to address these issues, synthesized red blood cell membrane-camouflaged ATO-loaded SA nanoparticles (RBCM-SA-ATO-NPs, RSANs). Ion crosslinking was used to make ATO-loaded SA nanoparticles (SA-ATO-NPs, SANs), wherein RBCM was deposited over the surface to make RSANs. RSANs had a mean particle size of 163.2 nm with an entire shell-core bilayer arrangement and a 14.31 percent encapsulation efficiency. When relative to SANs, a decreased phagocytosis in RAW 264.7 macrophages was observed RSANs by 51%, and the in vitro cumulative release rate was 95% at 84 h, indicating a notable sustained release. Moreover, RSANs were found to have reduced cytotoxicity than natural 293 cells and to have anti-cancer activity on both NB4 and 7721 cells. In vivo investigations also revealed that ATO can induce minor organ damage, whereas RSANs can minimize toxicity and boost anti-tumor efficacy [292].

Curcumin administration by nanocarriers is an appealing strategy for overcoming its limited bioavailability and rapid metabolism in the liver. Karabasz et al. developed AA-Cur, a blood-compatible ALG-curcumin combination that produced colloidally stable micelles of around 200 nm and displayed high cytotoxic effects against mouse cancer cell lines, as previously demonstrated. In their study, they investigated AA-toxicity and

anticancer efficacy in two different animal tumor models. In the first study, C57BL/6 mice were administered with colon cancer MC38-CEA cells subcutaneously. Breast tumor 4T1 cells were administered orthotopically, that is, into the mammary adipose tissue of BALB/c mice in the second study. Investigations of blood biochemistry, histology, morphology, DNA integrity (comet assay), and cytokine screening were used to assess the toxicity of intravenously injected AA-Cur (flow cytometry). The anticancer effects of AA-Cur were determined by comparing the development of colon MC38-CEA- or orthotopically injected breast 4T1 tumor cells in untreated and AA-Cur-treated mice. Four injection dosages of AA-Cur revealed no toxicity, showing that the conjugate is safe to use. The anti-cancer efficacy of AA-Cur was moderate in colon MC38-CEA and breast 4T1 carcinomas [293].

Other applications of ALG in intravenous drug delivery include ALG/deferoxamine conjugates [294], ALG Microparticles/Amphotericin B [295], ALG/poly(amidoamine)/ MC3T3-E1 pre-osteoblasts hybrid hydrogel [296], octanol grafted ALG nanoparticles/ propofol [297], pH-Responsive ALG/CS multilayer coating on Mesoporous Silica Nanoparticles encapsulating DOX [298], ALG-glycyl-prednisolone conjugate nanogel [299].

6.9. Others

The buccal mucosa is an extremely appealing route of actives delivery for actives with low bioavailability, poor gastric stability, and vulnerability to first-pass metabolisms such as proteins and peptides, by carrying the actives straightaway into the bloodstream. The oral mucosa also lacks Langerhan cells, making the oral mucosa tolerant to various allergens [300]. Aphthous stomatitis, a type of inflammation in the intraoral cavity whose causative agent is still unknown, is currently treated symptomatically using corticosteroids. Ambroxol is gaining popularity as an upcoming agent to treat chronic inflammation. Laffleur and Küppers developed a buccal dosage form by anchoring sulfhydryl groups of the amino acid cysteine onto the ALG adhesive backbone, incorporating ambroxol as the antisecretory drug. Mucoadhesive studies show that ALG-SH had an 11.56-fold increase in adhesion time due to the binding of the sulfhydryl group to the cysteine-rich mucus glycoprotein, leading to prolonged residence time in comparison to the weak van der Waals and hydrogen bonding in native polymers. Permeation studies on freshly excised buccal mucosa showed a 1.89-fold increase in permeation of ALG-SH as compared to native ALG. The mechanism of permeation enhancement was by tyrosine kinase inhibition by disulfide bond formation between the sulfhydryl group of the polymer and the cysteine group of the protein. Ambroxol release from ALG-SH showed a 1.4-fold-controlled release compared to native ALG, possibly due to inter and intra-crosslinking formation, thus providing stability. Therefore, sulfhydryl-anchored ALG could be used for the effective therapy of aphthae [301].

Periodontal diseases affect the gums and bones of the teeth due to bacterial infections. The desirable properties of drug delivery systems for periodontal illnesses include low toxicity, biodegradability, and the ability to treat bacterial infections. Hence, Prakash et al. utilized a controlled-release formulation of amoxicillin using PVA/ALG/hydroxyapatite (HAp) films by wet precipitation to treat periodontal infections. SEM studies show HAp NPs were effectively blended and embedded with amoxicillin irrespective of the annealing temperature. The in-vitro analysis, cell viability assay (70%), fluorescent staining, and hemolysis assay provided conclusive evidence for the suitability of this composite film in treatment. It gave a sustained release, with 87% of the actives released by day 10. The swelling ratio was almost 80% for all films annealed at different temperatures. The tensile strength was more significant than the standard PVA/SA patch, and it increased with increasing annealing temperature. The fabricated films exhibit high anti-bacterial action against *Escherichia coli*, *Staphylococcus aureus*, *Enterococcus faecalis*, and *Pseudomonas aeruginosa*. The fabricated films are also highly biocompatible and hemocompatible, as evidenced by in vitro analysis, cell viability studies, fluorescent staining, and hemolysis assay. Annealing at different temperatures ranging from 300, 500, and 700 °C, respectively, gave films that can encapsulate and release the drug at different

extents. HAp also helps in the regeneration of damaged bone segments, in addition to its drug matrix properties. Thus, PVA/SA/HAp/amoxicillin films are good candidates for treating periodontal defects, orthopedic implants, and bone grafting [302].

The sublingual route of vaccine delivery is attracting a lot of attention because of the ease of self-administration of vaccines as well as an abundance of antigen-presenting cells in the sublingual mucosa. In contrast to intravenous and subcutaneous vaccines, sublingual vaccines confer mucosal immunity as well against pathogens like SARS, HIV, and HPV [303]. However, they suffer from a lack of adhesion and absorption through the sublingual epithelium. Hanson et al. prepared a biopolymer platform based on mucoadhesive ALG and CMC polymer wafers loaded with HIV gp14 protein for the delivery via sublingual route and protection of protein vaccines. The wafers were prepared by dissolving ALG:CMC polymers along with NaCl in deionized water. Microstructural analysis of the wafers revealed that CMC wafers had huge pores with thick strands, while the pores of ALG were smaller and smoother. This may be due to CMC being phased out of water during freezing while amorphous ALG chains were more flexible, hence more extensive entanglement. In addition, it was found that wafers with high ALG content showed high mechanical stability as well as protection from impairment owing to lyophilization and exorbitant heat, partly due to their network-forming capability and poor crystallinity. In contrast, a large number of CMC incorporated wafers were extremely mucoadhesive to sublingual mucosa tissue and could endure washing, leading to enhanced protein permeation into the tissue. Compared to liquid gp140 solution, the vaccines produced comparable T-cell and B-cell mediated immune reactions in mice and comparable IgA and IgG levels in blood, vagina, and saliva. The optimum formulation (CMC:ALG ratio of 1:1) could be safely stored and carried without a cold chain while also preserving its immunogenicity following vaccination in mice via a sublingual route. Thus, this novel platform could be used for the potential delivery of sublingual vaccines [304].

ALG-based formulations are presently in the limelight owing to their exceptional characteristics. They are researched meticulously to obtain the utmost benefits of drug delivery (shown in Tables 2 and 3).

Table 2. Recent research on ALG-based formulations for improved actives delivery.

Devices	Model Drug/Drug	Composition	Preparation Technique	Delivery Site	Route of Administration	Key Features	References
Microparticles	Ropinirole hydrochloride	ALG	Spray-drying	Nasal epithelium	Intranasal	Excellent drug loading efficiency, in vitro rapid drug release (>95% in 30 min), negative zeta potential (−39.82 to and 70.07 mV), and no detrimental impact on the nasal mucosa.	[305]
Nanocomplexes	Doxorubicin and Temozolamide	Folic acid-CS-ALG	Complexation	-	-	Spherical diameter between 70–120 nm, Zeta potential ranging from 30–35 mV. In-vitro research on human cervical carcinoma cells and mouse fibroblasts showed more significant cytotoxicity or the dual-drug loaded formulation as compared to single-drug and free-drug formulations.	[306]
Nanoparticles	Insulin	CS-ALG	Self-assembly		Oral	The %EE of ALG-coated and CS-coated NPs were $81.5 \pm 7.4\%$ and $55.2 \pm 7.0\%$, respectively. Effective plasma glucose reduction and prolonged insulin release after oral delivery to diabetic rats.	[307]
Microspheres	Retinoic acid	SA	One-pot method	eye	Intravitreal	Average particle size was 95.7 ± 9.6 μm. Stable and controlled release, no harm to the optic nerve, and physiological function assessed by VEP 5b and ERG b wave.	[308]
Microspheres	Clove essential oil	SA	Modified emulsification		Oral	% Yield of microspheres, loading capacity, encapsulation efficiency, and in vitro release were found to be 72.73%, $0.99 \pm 0.3\%$, $24.77 \pm 7.47\%$, and $48.64 \pm 3.00\%$ after 4 h, respectively. The microspheres showed a controlled in vitro release profile of the clove oil.	[309]

Table 2. *Cont.*

Devices	Model Drug/Drug	Composition	Preparation Technique	Delivery Site	Route of Administration	Key Features	References
Nanoparticles	Amygdalin	CS-ALG	Ionic cross-linking		Mucosal	Zeta potential (-36 ± 0.88 and $+32 \pm 4.8$ mV), mean size (around 119 nm), encapsulation efficiency ($\sim90.3 \pm 0.5\%$), effective swelling, and sustained release characteristics at pH 3.1, 5.0, 7.1, suitable mucoadhesive property in BioFlux system.	[310]
Multiple layer mucoadhesive films	Metformin	Thiolated SA and CMC sodium	Double casting followed by compression	Intrapocket	Mucosal	Homogeneous, thin, and strong films for effortless insertion into the periodontal cavity. Adequate mucoadhesion and sustained release for 12 h.	[311]
Nanoparticles	Naringenin	ALG coated CS	Dual crosslinking using Na_2SO_4 and $CaCl_2$	Small intestine	Oral	Characterization by DLS, SEM, FTE, XRD, and pH-dependent dialysis study demonstrated excellent %EE of 91% and sustained flavonoid release. In vivo studies on rats showed significant anti-diabetic responses after oral delivery.	[312]
Nanoparticles	Miltefosine	ALG	Emulsification-external gelation method	mucosa	Oral	MFS-Alg NPs exhibited an average size of 279.1 ± 56.7 nm, polydispersity index of 0.42 ± 0.15, the zeta potential of -39.7 ± 5.2 mV, and %EE of $81.70 \pm 6.64\%$. It presented no hemolysis or toxicity in G. mellonella larvae. Histopathological and CFU data show that MFS-Alg nanoparticles decreased the fungal load.	[313]
Microspheres	Ciprofloxacin	CS-coated konjac glucomannan/SA/graphene oxide	electrospinning	colon	Oral	The KGM/SA/GO microspheres were evaluated for their swelling rate (290%), drug loading (7.02%) and %EE (19.11%), zeta potential (-10.84. and -10.55 mV), and drug release (52% drug release after 20 h).	[314]

Table 2. *Cont.*

Devices	Model Drug/Drug	Composition	Preparation Technique	Delivery Site	Route of Administration	Key Features	References
Nanoparticles	Curcumin diethyl disuccinate (CDD)	CS-ALG	Emulsification-ionotropic gelation	Human breast cancer	Oral	Encapsulated CDD in CANPs improved the stability and bio accessibility during the digestive stimulation and exhibited higher chemical stability when exposed to UV radiations. Bioavailability was enhanced five-fold. Greater cellular uptake and cytotoxicity in HepG2 cells than free CDD.	[315]
Nanocomposites	Doxorubicin	Fe3O4-SA-PVA-BSA	Co-precipitation/Ionotropic gelation	Cancer cells	Oral	The zeta potential ranged from −48.1 ± 2.3 to −22.4 ± 4.1 mV. The %EE varied between 36.2 ± 0.01 and 96.45 ± 2.12%. In vitro cytotoxicity tests using HepG2 and L02 cells demonstrated that DOX-loaded NPs (Fe3O4-SA-DOX-PVA-BSA) showed more significant cytotoxicity to HepG2 cells and non-toxic to L02 cells as compared to unloaded nanocomposites.	[316]

Table 3. Current approaches in ALG preparation for enhanced drug delivery.

Devices	Model Drug/Drug	Composition	Preparation Method	Delivery Site	Applications	References
Microspheres	Curcumin	ALG	Emulsion-gelation	Mucosa	Parenteral drug delivery	[317]
Layered double hydroxide Nanocomposites	Bovine serum albumin	ALG/CS	Ionic gelation	Intestine	Oral vaccine drug delivery	[318]
Multi-particulates	Dalfampridine	Tamarind seed gum//ALG	Ionotropic gelation	Intestine	Oral drug delivery	[319]
Microspheres	Icariin	CS/SA	Emulsification-internal gelation	Colon	Oral drug delivery	[320]
Nanoparticles	Doxycycline	CS/SA	Coacervation method	Spleen, blood	Oral drug delivery	[321]
Microbeads	Resveratrol	CS/ALG and ALG/sucrose	Ionotropic gelation	Intestine	Oral drug delivery	[322]

Table 3. Cont.

Devices	Model Drug/Drug	Composition	Preparation Method	Delivery Site	Applications	References
Microbeads	Chlorhexidine	CA	Internal gelation	Oral cavity	Periodontal drug delivery	[323]
Microspheres	Omega-3 rich oils (fish liver oil)	ALG/CS	Oil-in-water (o/w) emulsification, gelation, and microencapsulation	Intestine	Oral drug delivery	[324]
PECs/hydrogels	Bevacizumab	ALG	Dispersion	-	Local drug delivery	[325]
Nanoparticles	Lysozyme	Polymethacrylate/ALG	Coacervation	-	Delivery system	[326]
Hydrogels	Deferoxamine	CS/ALG with poly(d,l-lactide-co-glycolide)	Mixing	Intestine	Oral drug delivery	[327]
Hydrogels	5-Fluorouracil	Succinoglycan dialdehyde cross-linked hydrazine functionalized ALG	Ionic cross-linking		pH-controlled drug delivery	[328]
Films	Omeprazole	Hydroxypropyl methyl cellulose (HPMC)/Methyl cellulose (MC)/SA/carrageenan(CA)/metolose(MET)	Film casting	Stomach	Buccal drug delivery	[329]
Floating In situ gel	Celecoxib	SA/PEG	Ionic cross-linking	Site of inflammation/edema	Oral sustained drug delivery	[330]
Hydrogel beads	Ibuprofen	ALG-magnetic nitrocellulose (m-CNC)	Ionic cross-linking	-	Drug delivery	[331]
Hydrogel encapsulated microspheres	5-Fluorouracil	CS/ALG/gelatin	Emulsion cross-linking	-	Drug delivery	[332]
Microspheres entrapped hydrogels	Methotrexate, loaded Calcium Carbonate, and Aspirin	ALG and sodium CMC crosslinked with Ca^{2+} ions	Co-precipitation	-	Drug delivery	[333]
Films	Tamoxifen	ALG/CS	Spray-assisted LbL technique	-	Drug delivery	[334]

7. Recent Advances in ALG Formulations in Wound Healing

Skin represents the largest human organ that functions as a protective barrier against dehydration, pathogens, environmental stresses, etc. [335]. Skin injuries can be acute or chronic and can occur in arterial insufficiency, diabetes mellitus, immunological disorders, and other infections. Rarely does complete re-epithelialization happen in repairing skin defects; hence, increased attention is diverted to preparing wound dressings to promote wound healing and reduce scars while also protecting from microbial infections and dehydration at the wound site [336,337].

Wound dressings play a vital part in wound management as they are applied to a variety of burns and wounds to aid in the repair and renewal of injured tissues, as well as to encourage healing and minimize the infection risk. The optimum wound dressing should decrease the recovery period and discomfort, increase tissue regeneration and recovery, absorb excess exudate from the wounds, encourage healing, and prevent infectious complications. For several decades, scientists have aspired to develop a specialized dressing to treat injuries. Traditionally, dressings are made from plant-based fibers, honey, animal fats, etc. Currently, biopolymeric materials are used as wound dressings as they offer unique properties, such as antibacterial, re-epithelializing, antioxidizing, and anti-inflammatory properties, that significantly promote wound healing [338,339].

Recent developments in wound dressings also enable the release of therapeutic agents to restore skin homeostasis and integrity [336]. Biopolymers are attractive wound healing materials as they can maintain a moist wound bed due to water sorption; they can also absorb any tissue exudates and allow oxygen permeation across the wound [340]. Furthermore, because of the hydrophilic nature and structural features of these wound dressings, a sustained release of the encased bioactive substances could be achieved [341]. Both synthetic and natural polymers are useful for wound dressing, including heparin, CS, HA, dextrans, ALGs, and β-glucans, because of their desirable physical and biochemical properties [338,342].

ALG is a biopolymer widely used for tissue engineering applications, particularly in wound healing [343]. It has been used as a food additive for ages; hence, it is considered a biocompatible polymer. It has found applications in tissue regeneration and bioactive delivery because of its biodegradability and slow dissolution in the biological fluids when cross-linked with exchangeable cations. This rate could be adjusted by controlling the oxidation [344] and reducing ALG's molecular weight [345]. ALG composites are used for wound healing and soft tissue regeneration to strengthen the capacity and material characteristics of native ALG to adapt to different biomedical applications [346–348]. Calcium ions are released when water-insoluble CA encounters wound exudates as a function of calcium ions being replaced by sodium ions in bodily fluids, which can operate to achieve hemostasis. The SA-based fibers absorb a massive amount of exudates and transform into a gel-like substance, which maintains the moist barrier on the wound surface [349,350]. Some recent investigations of ALG composites in wound healing applications have been discussed in Table 4.

Diabetes-induced wounds currently have no effective treatment and thus represent a challenge in wound healing. Reports suggest that bacteria-caused inflammations due to the alkaline pH of ulcer wounds and incomplete blood flow to the wounds due to slow angiogenesis may be responsible for delayed diabetic wound healing. Hence, Wang et al. developed a novel, pH-sensitive CA-based hydrogel loaded with protamine nanoparticles and hyaluronan oligosaccharides (protamine NP/HAO CA hydrogel) by the ionotropic gelation method. The loading efficiency of HAO was $85.4 \pm 6.25\%$, and 44.5% of the drug was released in 8 h at pH 3.0. At pH 8.0, which mimics the diabetic wound state, CA hydrogel swelled by the absorption of water, and a faster drug release of NPs and HAO took place. Compared to plain CA hydrogels, the protamine-loaded ones showed improved antibacterial activity against *E. coli* and *S. aureus*, enhanced adherence to wound tissue sites, and absorption of wound fluid into the hydrogels. Wounds closed with rates of up to 96.8% after 14 days without ulceration and festering at the wound site. Re-epithelialization was

observed, indicated by the formation of fibroblasts and collagen. Moreover, the composite hydrogels reduced inflammation and encouraged angiogenesis [351].

PECs produced from the polysaccharides ALG and CS at defined flow rates, pH, and agitation speeds give rise to slender, stable, and transparent sponges or films possessing excellent swelling ability in physiological medium. Unfortunately, these PECs have inadequate mechanical properties, which may negatively affect their performance in articulated regions such as knees, shoulders, and elbows. To overcome this, Pires et al. fabricated CS-ALG-based wound dressings with the addition of poly (dimethylsiloxane) to improve the flexibility and sorption capacity in contact with biological fluids. The optimum amount of poly(dimethylsiloxane) per gram of PEC was found to be 0.1 g, wherein the formulation exhibited high stability, a tensile strength of 12 MPa, non-hemolysis, and induction of thrombus formation. Moreover, when beta-carotene and thymol were loaded onto the formulations via the supercritical carbon dioxide impregnation/deposition (SSI/D) technique at 45 °C and 250 bar for 14 h, higher bioactive loading capacities were observed using SSI/D and a high depressurization rate (10 bar/min). A substantial amount of Thy and Bc were preserved in the matrix structure with the SSI/SD method, which functioned as a reservoir system. Thus, the combination of ALG, CS, and silicone gel could be a potentially successful wound dressing in the case of less articulated body sites and low extruding wounds [352].

The combination of ALG with proteins holds a lot of promise in enhancing the cellular interactions of ALG and for tailoring the biodegradation of the composite materials in tissue regenerating applications. Elastin, a highly flexible protein abundant in the extracellular matrix, is a good candidate for composites because it renders the tissues elastic enough to withstand continuous cycles of deformation/recovery without rupturing. Hence, Bergonzi et al. fabricated ALG/human elastin-like polypeptide (HELP) hybrid films by the solvent casting method with loaded curcumin to provide antioxidant activity. Strong intermolecular hydrogen bonding between the N-H amide bonds of HELP and the carboxylate group of ALG leads to close network formation due to molecular associations, thus giving higher tensile strength and Young's modulus, which is representative of its higher elasticity. Swelling capacity was higher in HALCur than in ALCur (as shown in Figure 10a). The incorporation of HELP was not only instrumental for obtaining a controlled release of curcumin (as depicted in Figure 10b), which helped in a higher antioxidant effect (as illustrated in Figure 10d), but also in enhancing the cytocompatibility of the final biomaterial, as shown in Figure 10c). With more in vivo studies, it may be possible to design customized bioplatforms for biomedical applications [353].

Full-thickness healing requires extensive healing time, which increases the risks of infections, wound ulcers, necrosis, and even fatal complications. To tackle this, a hybrid hydrogel composed of amine-functionalized fish collagen and OA was prepared by Feng et al. by a simple Schiff base reaction, and antimicrobial peptides bacitracin and Polymyxin B (AC/OSA-PB) were loaded into the hydrogels without the need for catalysts. These hydrogels illustrated modifiable gelation time, stable rheology, and a strain resembling that of human skin. Moreover, they could effectively cause inhibition of *S. aureus* and *E.coli* growth, promoting angiogenesis and cell proliferation in vitro. Similar results were observed in vivo too, with enhanced full-thickness wound healing ability by promoting granular tissue formation and deposition of collagen and accelerating neovascularization and re-epithelialization [354].

In a similar study related to full-thickness wound healing by Chaudhary et al., CA nanoparticles (CA-NPs) were used as hemostatic agents along with antimicrobial AgNPs in a CS-based hydrogel network. Herein, the fresh blood of the subjects was used in the hydrogels to substitute the growth factors required for wound healing. The CA-NPs had mean hydrodynamic sizes of 1037 nm and 120.56 nm, respectively, and a zeta potential of less than −30 mV indicated their negligible electrostatic repulsion tendency. The prepared hydrogels exhibited good spreadability and viscoelasticity. Moreover, they showed bacterial inhibition against both gram-positive and gram-negative strains and also

illustrated remarkable scar-free healing in vivo for up to 15 days by aiding in collagen deposition and acting as a protective sheath against microbial contamination for diabetes-induced wounds. Thus, the proposed composite films could be an exciting wound dressing for patients who have chronic diabetes [355].
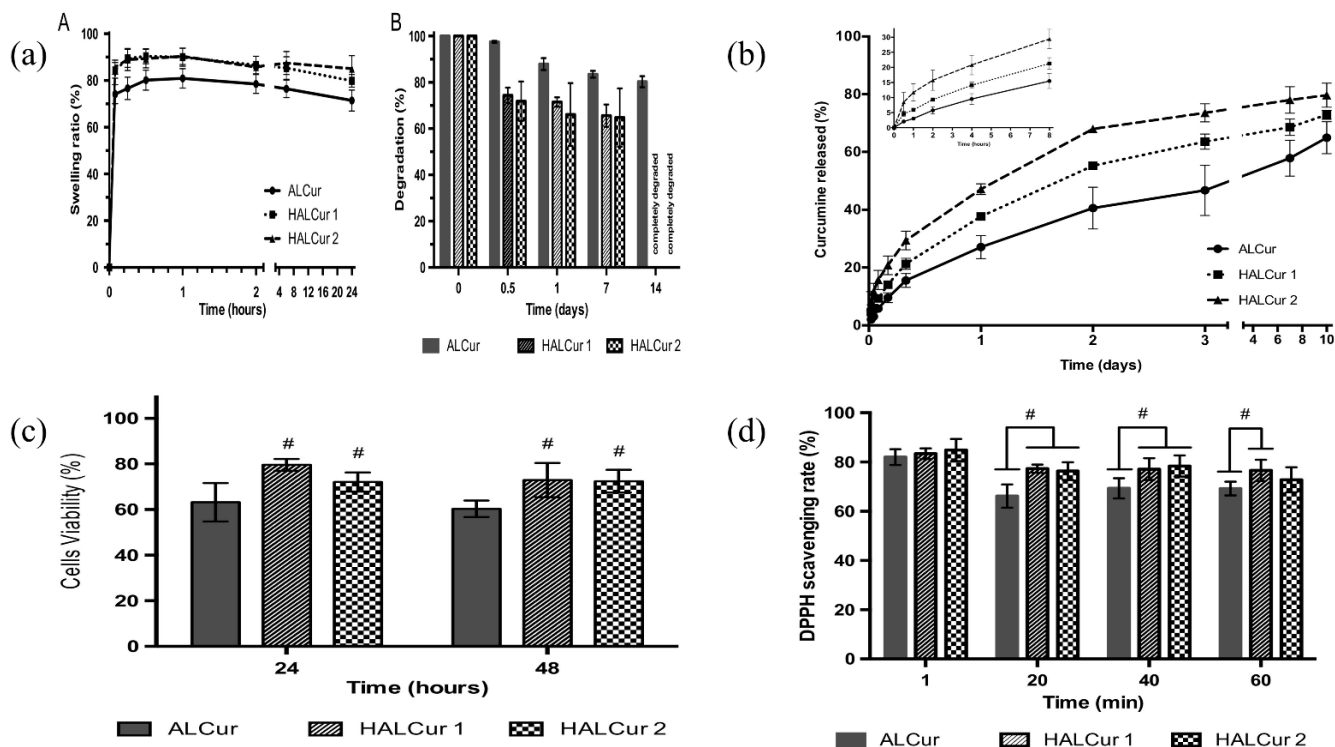
Figure 10. ALG/human elastin-like polypeptide composite films with antioxidant properties for potential wound healing applications. (**a**) swelling (A) and stability (B) graphs of ALCur, HALCur films encapsulating 0.1% curcumin. (**b**) % curcumin release characteristics of ALCur, HALCur films encapsulating 0.1% curcumin. (**c**) Cell viability assay of ALG/HELP composites on human fibroblast cell lines. (**d**) DPPH assay of ALCur and HALCur films indicating antioxidant activities. # p <0.05. Reproduced with permission from [353], copyright Elsevier 2020.

In another study, Sharma et al. loaded rifampicin into ALG-gelatin fibers through a physical cross-linking reaction by the extrusion-gelation method and then embedded it into transdermal films for wound healing applications. The tensile strength of the fibers was between 2.32 ± 0.45 to 14.32 ± 0.98 N/mm^2, and the extensibility was between 15.2 ± 0.98% to 30.54 ± 1.08%. The range of moisture absorption was low (up to 14.68%), which is essential for transdermal films. Other parameters such as the swelling ratio and water vapor transmission rate demonstrated the extensive gelation properties of the polymer and the reduced channel pore size. Antibacterial activities against *E. coli* and *S. aureus* were observed for the transdermal films. In vivo animal studies exhibited close to 83 degrees of contraction of the wound, marginally less than the commercial formulation (91.87 ± 3.72%). The drug release from the films followed sustained release; this could be due to sufficient contact of the wound dressing with the wound layer with hair growth signs evident from the 10th day onwards. Thus, the proposed fiber-in-films could be excellent carriers for drug delivery and wound healing purposes [356].

Other studies where ALG composites showed promising results in wound healing include SA/HA films/sulfadiazine/silver nanoparticles [357], ALG/gelatin fibers/curcumin [358], SA/xanthan gum film/pycnogenol [359], ALG/CS/maltodextrin/pluronic F127/pluronic P123/tween 80/curcumin polymeric micelles [360], SA/pectin/cefazolin nanoparticles [361], CA/ibuprofen hydrogels [362], ALG/cannabidiol [363], SA/polyvinyl

alcohol/curcumin/graphene [364], ALG/polyhexanide/AgNPs [365], ALG/carboxymethyl CS/Kangfuxin sponges [366].

Table 4. Recent investigations of ALG-based composites for wound healing applications.

Type of Wound Dressing Materials	ALG-Based Composite Materials	Applications	References
Nanocomposite hydrogel	ALG/Eudragit	Chronic cutaneous wound healing in diabetic mice	[367]
Hydrogel	ALG/collagen	Drug delivery for skin wounds in trauma patients	[368]
Hydrogel	ALG/Pluronic F127	Drug release-based bleeding wound healing	[369]
Films	ALG	Chronic wound healing	[370]
Hydrogel	ALG/gelatin methacrylate	Wound healing	[371]
Hydrogel	Oxidized ALG	Chronic wound healing in diabetic mice	[372]
Thermoreversible hydrogel	SA/chondroitin sulfate	Drug delivery and diabetic wound healing	[373]
Ion exchange responsive film	ALG/hyaluronate	Drug delivery and skin wound healing	[374]
Films	ALG/pectin	Wound healing for moderate exudates	[375]
Hydrogel	SA/poly(N-isopropyl acrylamide)	Drug delivery and wound healing	[376]
Xerogel	ALG/g-polyethylene glycol methacrylate	Wound healing	[377]
Film	SA/K-carrageenan	Sustained drug release-based topical wound dressing	[378]
Electrospun mat	ALG/polyvinyl alcohol	Wound dressing and real-time evaluation of healing	[379]
Sponges	ALG/CS/HA	Wound healing in full-thickness wounds in rats	[380]

8. Conclusions

ALG emerges as a prospective naturally derived biomaterial in NDDSs due to the biocompatible, degradable characteristics and gel-forming capability of ALG. Controlled and targeted actives delivery via ALG carrier can be accomplished via well-created formulation as well as accurate parameters of synthesis concerned with the process of fabrication. Hence, this article provides an extensive review of the recent advances of ALG and its advancement in actives delivery. The most significant characteristics of ALG encompass safety, biocompatibility, and ease of preparation. Due to its biocompatible, biodegradable, and non-toxic characteristics, it is employed in diverse drug-delivery technologies. A significant challenge that persists is the preparation of environmentally friendly procedures for the NPs formation having a narrow size distribution, high mechanical and chemical stability, and practicality to scale up to the volumes of industrial-scale production. Moreover, it is critical to assess the toxic effects on cells, immune response, and biodegradability of such formulations in drug delivery.

As we look towards the future, the ALG-based composites utilized in pharmaceutical applications are possibly going to develop significantly. Although ALG composites are already used clinically for wound healing, they perform quite a passive function. Forthcoming dressings will probably perform a considerably more active role. One or more bioactives that assist wound healing can be loaded into ALG-based dressings, as such gels have displayed usefulness in preserving local conc. of biological factors (for example, proteins) for a prolonged period. In wound healing, and more usually, actives delivery, accurate control

over the single vs. multiple drugs delivery or drug release in sustained vs. sequential manner in response to exterior environmental modifications is immensely advisable.

Therefore, investigators are required to modernize the ALG-associated composite's advancement, and this review is the origin of advice for forthcoming investigation.

Institutional Review Board Statement: Not applicable.

Informed Consent Statement: Not applicable.

Data Availability Statement: Not applicable.

Conflicts of Interest: The authors declare no conflict of interest.

Abbreviations

5-FU	5-Fluorouracil
AAC	antioxidant activity coefficient
Aah	Androctonus australis hector
AGM	agomelatine
AGMPs	sodium alginate(AG)based microparticles
ALG	Alginate
Alg-APBA	3-aminophenylboronic acid-modified alginate
ALG-CNC NPs	Alginate cellulose nanocrystals nanoparticles
AmpB	Amphotericin B
ARPE-18	Human retinal pigmented epithelium cells
ATO	Arsenic trioxide
BALB/c	Bagg Albino mouse strain
BBSA	Bifurcaria bifurcata
BCG	Bacille Calmette–Guérin
BET	Brunauer–Emmett–Teller
BSA	Bovine serum albumin
CA	Calcium alginate
CAC	composite alginate collagen
CaG	calcium gluconate
CANPs	chitosan/alginate nanoparticles
CBSA	C. barbata sodium alginate
CD	Crohn's disease
CDD	Curcumin diethyl disuccinate
CFX	Cefixime
CMC	carboxymethyl cellulose
CNCs	Cellulose nanocrystals
COPD	Chronic obstructive pulmonary disease

CpG ODN	CpG oligodeoxynucleotides
CS	Chitosan
CTFR	cystic fibrosis transmembrane conductance regulator
DDS	Drug delivery system
DLS	Dynamic light scattering
Dox	Doxorubicin
DPPH	1,1-Diphenyl-2 picrylhydrazyl
DTZ	diltiazem
ECT	Encapsulated-cell therapy
EE	Entrapment efficiency
ERG	electroretinogram
F–ERG	Flash electroretinogram
Fe_3O_4-SA-DOX	Fe_3O_4-sodium alginate–doxorubicin
FITC	fluorescein isothiocyanate
FSSA	*Fucus spiralis* L.
G	4-α-L-guluronic acid
GA	gallic acid
GDNF	glial-derived neurotropic factor
GL	glycyrrhizin
GO	graphene oxide
GSM	glyceryl monostearate
HA	Hyaluronic acid
HaCat	Cultured Human Keratinocyte
HAI	Haemagglutinin inhibition
HAp	hydroxyapatite
HB-CNPs	HbsAg-loaded chitosan nanoparticles
HbsAg	Hepatitis B surface antigen
HEK293	Human Embryonic Kidney cells
HEMA	(Hydroxyethyl)methacrylate
HPBCD	Hydroxypropyl beta cyclodextrin
HPMC	Hydroxypropyl methylcellulose
HP-β-CD	hydroxypropyl-beta-cyclodextrin
i.m.	intramuscular
IL	Interleukins
KF	ketotifen fumarate
KGM	Konjac glucomannan
M	1,4-linked-β-D-mannuronic acid
MA	Methyl acrylate
MAPTAC	Methacryolyl aminopropyl trimethyl ammonium chloride
m-CNC	magnetic cellulose nanocrystal
MFS	Miltefosine
MIC	Minimum inhibitory concentration
MMP-2	Matrix metalloproteinase-2
M-MSNs	magnetic mesoporous silica nanoparticles
MNs	Microneedles
MPs	Microparticles
MTT	3-(4,5-dimethylthiazol-2-yl)-2,5-diphenyl tetrazolium bromide
NLC	nanostructured lipid carriers
nMBA	N, N'-methylenebisacrylamide
OA	Oxidized alginate
PAH	poly(allylamine hydrochloride)
PBMC	Peripheral blood mononuclear cell
PCL	Polycaprolactone
PECs	polyelectrolyte complexes
PEG	Polyethylene glycol
PEG-co-PCL	poly (ethylene glycol)-co-poly(-caprolactone)
PEG@VTMSg-CS	Polyethylene glycol coated vinyl trimethoxy silane-g-chitosan

PEM	polyelectrolyte multilayers
PF	Pluronic
PFD	pirfenidone
P-gp shRNA	P-glycoprotein short hairpin RNA
PGX	Pressurized gas expanded liquid
PLC/PEG	poly(caprolactone)/polyethylene glycol
PLGA	poly (lactic-co-glycolic acid)
PLL	Polylysine
PMX	Polymyxin B
PR8-ALG	PR8 influenza virus sodium alginate
PR8-CHT	PR8 influenza virus chitosan
PR8-TMC-ALG	PR8 influenza virus sodium alginate-coated chitosan and trimethyl chitosan
PSSCMA	poly(4-styrenesulfonic acid-co-maleic acid) sodium salt
RBA	Relative Bioavailability
RCS	Royal College of Surgeons
RPA	Relative Pharmacologic Availability
s.c.	subcutaneous
SA	sodium alginate
SA-ATO-NPs	make ATO-loaded sodium alginate nanoparticles
SCC	squamous cell carcinoma
SD rat	Sprague Dawley rat
SGF	simulated gastric fluid
SH	sulfhydryl
SpBMP-9	Small peptide Bone Morphogenetic Protein 9
SRG	*Sargassum* sp
SS	salbutamol sulfate
SWCNT-GI	single-walled carbon nanotube modified by glucose
TA	Tannic acid
TCS	thiolated-chitosan coated sodium alginate
TEM	Transmission electron microscopy
THSG	2,3,5,40 -tetrahydroxystilbene 2-O-β-D-glucoside
TRB	*Turbinaria* sp
TSA	thiolated sodium alginate
UTI	Urinary tract infection
VEP	visual evoked potential
VLF-AG-NPs	venlafaxine alginate nanoparticles
XRD	X-ray Diffraction

References

1. Jain, K.K. Drug Delivery Systems—An Overview. *Methods Mol. Biol.* **2008**, *437*, 1–50.
2. Ansari, M.J.; Ahmed, M.M.; Anwer, M.K.; Jamil, S.; Alshetaili, A.S.; Ali, R.; Shakeel, F. Formulation and Characterization of Fluconazole Loaded Olive Oil Nanoemulsions. *Indo Am. J. Pharm. Sci.* **2017**, *4*, 852–860.
3. Agrawal, P. Significance of Polymers in Drug Delivery System. *J. Pharmacovigil.* **2015**, *3*, 10–12. [CrossRef]
4. Bhowmik, D.; Gopinath, H.; Kumar, B.P.; Duraivel, S.; Kumar, K.P.S. Controlled Release Drug Delivery Systems. *Pharma Innov. J.* **2012**, *1*, 24–32.
5. Abourehab, M.A.S.; Ansari, M.J.; Singh, A.; Hassan, A.; Abdelgawad, M.A.; Shrivastav, P.; Abualsoud, B.M.; Amaral, L.S.; Pramanik, S. Cubosomes as an Emerging Platform for Drug Delivery: A State-of-the-Art Review. *J. Mater. Chem. B* **2022**, *10*, 2781–2819. [CrossRef]
6. Ansari, M.J. An Overview of Techniques for Multifold Enhancement in Solubility of Poorly Soluble Drugs. *Curr. Issues Pharm. Med. Sci.* **2019**, *32*, 203–209. [CrossRef]
7. Ahmed, M.M.; Fatima, F.; Anwer, M.K.; Ansari, M.J.; Das, S.S.; Alshahrani, S.M. Development and Characterization of Ethyl Cellulose Nanosponges for Sustained Release of Brigatinib for the Treatment of Non-Small Cell Lung Cancer. *J. Polym. Eng.* **2020**, *40*, 823–832. [CrossRef]
8. Grund, S.; Bauer, M.; Fischer, D. Polymers in Drug Delivery-State of the Art and Future Trends. *Adv. Eng. Mater.* **2011**, *13*, 61–87. [CrossRef]
9. Zhuo, F.; Abourehab, M.A.S.; Hussain, Z. Hyaluronic Acid Decorated Tacrolimus-Loaded Nanoparticles: Efficient Approach to Maximize Dermal Targeting and Anti-Dermatitis Efficacy. *Carbohydr. Polym.* **2018**, *197*, 478–489. [CrossRef] [PubMed]
10. Langer, R. Polymeric Delivery Systems for Controlled Drug Release. *Chem. Eng. Commun.* **1980**, *6*, 1–48. [CrossRef]

11. Mady, F.M.; Ibrahim, S.; Abourehab, M. Development and Evaluation of Alginate-Gum Blend Mucoadhesive Microspheres for Controlled Release of Metformin Hydrochloride. *J. Adv. Biomed. Pharm. Sci.* **2021**, *4*, 111–118. [CrossRef]

12. Hussain, Z.; Rahim, M.A.; Jan, N.; Shah, H.; Rawas-Qalaji, M.; Khan, S.; Sohail, M.; Thu, H.E.; Ramli, N.A.; Sarfraz, R.M.; et al. Cell Membrane Cloaked Nanomedicines for Bio-Imaging and Immunotherapy of Cancer: Improved Pharmacokinetics, Cell Internalization and Anticancer Efficacy. *J. Control. Release* **2021**, *335*, 130–157. [CrossRef]

13. Pramanik, S.; Sali, V. Connecting the Dots in Drug Delivery: A Tour d'horizon of Chitosan-Based Nanocarriers System. *Int. J. Biol. Macromol.* **2021**, *169*, 103–121. [CrossRef]

14. Abourehab, M.A.; Ahmed, O.A.; Balata, G.F.; Almalki, W.H. Self-Assembled Biodegradable Polymeric Micelles to Improve Dapoxetine Delivery across the Blood-Brain Barrier. *Int. J. Nanomed.* **2018**, *13*, 3679–3687. [CrossRef]

15. Dong, J.; Tao, L.; Abourehab, M.A.S.; Hussain, Z. Design and Development of Novel Hyaluronate-Modified Nanoparticles for Combo-Delivery of Curcumin and Alendronate: Fabrication, Characterization, and Cellular and Molecular Evidences of Enhanced Bone Regeneration. *Int. J. Biol. Macromol.* **2018**, *116*, 1268–1281. [CrossRef]

16. Fatima, I.; Rasul, A.; Shah, S.; Saadullah, M.; Islam, N.; Khames, A.; Salawi, A.; Ahmed, M.M.; Almoshari, Y.; Abbas, G.; et al. Novasomes as Nano-Vesicular Carriers to Enhance Topical Delivery of Fluconazole: A New Approach to Treat Fungal Infections. *Molecules* **2022**, *27*, 2936. [CrossRef]

17. Ashfaq, M.; Shah, S.; Rasul, A.; Hanif, M.; Khan, H.U.; Khames, A.; Abdelgawad, M.A.; Ghoneim, M.M.; Ali, M.Y.; Abourehab, M.A.S.; et al. Enhancement of the Solubility and Bioavailability of Pitavastatin through a Self-Nanoemulsifying Drug Delivery System (SNEDDS). *Pharmaceutics* **2022**, *14*, 482. [CrossRef]

18. Abdel-Kader, M.; Al-Shdefat, R. Evaluation of Antifungal Activity of Olive Oil Based Nanoemulsions. *Bull. Env. Pharmacol. Life Sci.* **2016**, *5*, 1–4.

19. Tiwari, G.; Tiwari, R.; Bannerjee, S.; Bhati, L.; Pandey, S.; Pandey, P.; Sriwastawa, B. Drug Delivery Systems: An Updated Review. *Int. J. Pharm. Investig.* **2012**, *2*, 2–11. [CrossRef]

20. Hamid Akash, M.S.; Rehman, K.; Chen, S. Natural and Synthetic Polymers as Drug Carriers for Delivery of Therapeutic Proteins. *Polym. Rev.* **2015**, *55*, 371–406. [CrossRef]

21. Pramanik, S.; Shrivastav, P.; Pramanik, S.; Vaidya, G.; Abdelgawad, M.A.; Ghoneim, M.M.; Singh, A.; Abualsoud, B.M.; Amaral, L.S.; Abourehab, M.A.S. Bacterial Cellulose as a Potential Biopolymer in Biomedical Applications: A State-of-the-Art Review. *J. Mater. Chem. B* **2022**, *10*, 3199–3241. [CrossRef]

22. Hay, I.D.; Rehman, Z.U.; Moradali, M.F.; Wang, Y.; Rehm, B.H.A. Microbial Alginate Production, Modification and Its Applications. *Microb. Biotechnol.* **2013**, *6*, 637–650. [CrossRef] [PubMed]

23. Lee, K.Y.; Mooney, D.J. Alginate: Properties and Biomedical Applications. *Prog. Polym. Sci.* **2012**, *37*, 106–126. [CrossRef]

24. Remminghorst, U.; Rehm, B.H.A. Bacterial Alginates: From Biosynthesis to Applications. *Biotechnol. Lett.* **2006**, *28*, 1701–1712. [CrossRef] [PubMed]

25. Sachan, N.; Pushkar, S.; Jha, A.; Bhattcharya, A. Sodium Alginate: The Wonder Polymer for Controlled Drug Delivery. *J. Pharm. Res.* **2009**, *2*, 1191–1199.

26. Tavakoli, J.; Laisak, E.; Gao, M.; Tang, Y. AIEgen Quantitatively Monitoring the Release of Ca2+ during Swelling and Degradation Process in Alginate Hydrogels. *Mater. Sci. Eng. C* **2019**, *104*, 109951. [CrossRef] [PubMed]

27. Abasalizadeh, F.; Moghaddam, S.V.; Alizadeh, E.; akbari, E.; Kashani, E.; Fazljou, S.M.B.; Torbati, M.; Akbarzadeh, A. Alginate-Based Hydrogels as Drug Delivery Vehicles in Cancer Treatment and Their Applications in Wound Dressing and 3D Bioprinting. *J. Biol. Eng.* **2020**, *14*, 8. [CrossRef]

28. Mohammed, A.; Bissoon, R.; Bajnath, E.; Mohammed, K.; Lee, T.; Bissram, M.; John, N.; Jalsa, N.K.; Lee, K.Y.; Ward, K. Multistage Extraction and Purification of Waste Sargassum Natans to Produce Sodium Alginate: An Optimization Approach. *Carbohydr. Polym.* **2018**, *198*, 109–118. [CrossRef] [PubMed]

29. Qin, Y. Alginate Fibres: An Overview of the Production Processes and Applications in Wound Management. *Polym. Int.* **2008**, *57*, 171–180. [CrossRef]

30. Satheeshababu, B.K.; Mohamed, I. Synthesis and Characterization of Sodium Alginate Conjugate and Study of Effect of Conjugation on Drug Release from Matrix Tablet. *Indian J. Pharm. Sci.* **2015**, *77*, 579–585. [CrossRef] [PubMed]

31. Zubia, M.; Payri, C.; Deslandes, E. Alginate, Mannitol, Phenolic Compounds and Biological Activities of Two Range-Extending Brown Algae, Sargassum Mangarevense and Turbinaria Ornata (Phaeophyta: Fucales), from Tahiti (French Polynesia). *J. Appl. Phycol.* **2008**, *20*, 1033–1043. [CrossRef]

32. Torres, M.R.; Sousa, A.P.A.; Silva Filho, E.A.T.; Melo, D.F.; Feitosa, J.P.A.; de Paula, R.C.M.; Lima, M.G.S. Extraction and Physicochemical Characterization of Sargassum Vulgare Alginate from Brazil. *Carbohydr. Res.* **2007**, *342*, 2067–2074. [CrossRef]

33. Fenoradosoa, T.A.; Ali, G.; Delattre, C.; Laroche, C.; Petit, E.; Wadouachi, A.; Michaud, P. Extraction and Characterization of an Alginate from the Brown Seaweed Sargassum Turbinarioides Grunow. *J. Appl. Phycol.* **2010**, *22*, 131–137. [CrossRef]

34. Blanco-Pascual, N.; Montero, M.P.; Gómez-Guillén, M.C. Antioxidant Film Development from Unrefined Extracts of Brown Seaweeds Laminaria Digitata and Ascophyllum Nodosum. *Food Hydrocoll.* **2014**, *37*, 100–110. [CrossRef]

35. Sellimi, S.; Younes, I.; Ayed, H.B.; Maalej, H.; Montero, V.; Rinaudo, M.; Dahia, M.; Mechichi, T.; Hajji, M.; Nasri, M. Structural, Physicochemical and Antioxidant Properties of Sodium Alginate Isolated from a Tunisian Brown Seaweed. *Int. J. Biol. Macromol.* **2015**, *72*, 1358–1367. [CrossRef]

36. Gomez, C.G.; Pérez Lambrecht, M.V.; Lozano, J.E.; Rinaudo, M.; Villar, M.A. Influence of the Extraction-Purification Conditions on Final Properties of Alginates Obtained from Brown Algae (Macrocystis Pyrifera). *Int. J. Biol. Macromol.* **2009**, *44*, 365–371. [CrossRef]

37. González-lópez, N.; Moure, A.; Domínguez, H. Hydrothermal Fractionation of Sargassum Muticum Biomass. *J. Appl. Phycol.* **2012**, *24*, 1569–1578. [CrossRef]

38. Pascaline, M.; Andriamanantoanina, H.; Heyraud, A.; Rinaudo, M. Food Hydrocolloids Structure and Properties of Three Alginates from Madagascar Seacoast Algae. *Food Hydrocoll.* **2013**, *32*, 143–146. [CrossRef]

39. Mazumder, A.; Holdt, S.L.; De Francisci, D.; Alvarado-Morales, M.; Mishra, H.N.; Angelidaki, I. Extraction of Alginate from Sargassum Muticum: Process Optimization and Study of Its Functional Activities. *J. Appl. Phycol.* **2016**, *28*, 3625–3634. [CrossRef]

40. Vauchel, P.; Arhaliass, A.; Legrand, J.; Kaas, R.; Baron, R. Decrease in Dynamic Viscosity and Average Molecular Weight of Alginate from Laminaria Digitata during Alkaline Extraction1. *J. Phycol.* **2008**, *44*, 515–517. [CrossRef]

41. Vauchel, P.; Kaas, R.; Arhaliass, A.; Baron, R.; Legrand, J. A New Process for Extracting Alginates from Laminaria Digitata: Reactive Extrusion. *Food Bioprocess Technol.* **2008**, *1*, 297–300. [CrossRef]

42. Peteiro, C. Alginate Production from Marine Macroalgae, with Emphasis on Kelp Farming. In *Alginates and Their Biomedical Applications*; Rehm, B.H.A., Moradali, M.F., Eds.; Springer: Singapore, 2018; pp. 27–66, ISBN 978-981-10-6910-9.

43. Ching, S.H.; Bansal, N.; Bhandari, B. Alginate Gel Particles–A Review of Production Techniques and Physical Properties. *Crit. Rev. Food Sci. Nutr.* **2017**, *57*, 1133–1152. [CrossRef]

44. Cardoso, M.J.; Costa, R.R.; Mano, J.F. Marine Origin Polysaccharides in Drug Delivery Systems. *Mar. Drugs* **2016**, *14*, 34. [CrossRef]

45. Fertah, M.; Belfkira, A.; montassir Dahmane, E.; Taourirte, M.; Brouillette, F. Extraction and Characterization of Sodium Alginate from Moroccan Laminaria Digitata Brown Seaweed. *Arab. J. Chem.* **2017**, *10*, S3707–S3714. [CrossRef]

46. Augst, A.D.; Kong, H.J.; Mooney, D.J. Alginate Hydrogels as Biomaterials. *Macromol. Biosci.* **2006**, *6*, 623–633. [CrossRef]

47. Jain, D.; Bar-Shalom, D. Alginate Drug Delivery Systems: Application in Context of Pharmaceutical and Biomedical Research. *Drug Dev. Ind. Pharm.* **2014**, *40*, 1576–1584. [CrossRef]

48. Tønnesen, H.H.; Karlsen, J. Alginate in Drug Delivery Systems. *Drug Dev. Ind. Pharm.* **2002**, *28*, 621–630. [CrossRef]

49. Haugstad, K.E.; Håti, A.G.; Nordgård, C.T.; Adl, P.S.; Maurstad, G.; Sletmoen, M.; Draget, K.I.; Dias, R.S.; Stokke, B.T. Direct Determination of Chitosan–Mucin Interactions Using a Single-Molecule Strategy: Comparison to Alginate–Mucin Interactions. *Polymers* **2015**, *7*, 161–185. [CrossRef]

50. Taylor, C.; Pearson, J.P.; Draget, K.I.; Dettmar, P.W.; Smidsrød, O. Rheological Characterisation of Mixed Gels of Mucin and Alginate. *Carbohydr. Polym.* **2005**, *59*, 189–195. [CrossRef]

51. Aderibigbe, B.A.; Buyana, B. Alginate in Wound Dressings. *Pharmaceutics* **2018**, *10*, 42. [CrossRef]

52. Wang, B.; Wan, Y.; Zheng, Y.; Lee, X.; Liu, T.; Yu, Z.; Huang, J.; Ok, Y.S.; Chen, J.; Gao, B.; et al. Technology Alginate-Based Composites for Environmental Applications: A Critical Review. *Crit. Rev. Environ. Sci. Technol.* **2019**, *49*, 318–356. [CrossRef]

53. Pawar, S.N.; Edgar, K.J. Biomaterials Alginate Derivatization: A Review of Chemistry, Properties and Applications. *Biomaterials* **2012**, *33*, 3279–3305. [CrossRef]

54. Spasojevic, M.; Bhujbal, S.; Paredes, G.; de Haan, B.J.; Schouten, A.J.; de Vos, P. Considerations in Binding Diblock Copolymers on Hydrophilic Alginate Beads for Providing an Immunoprotective Membrane. *J. Biomed. Mater. Res. Part. A* **2014**, *102*, 1887–1896. [CrossRef]

55. Zhou, R.; Shi, X.; Gao, Y.; Cai, N.; Jiang, Z.; Xu, X. Anti-Inflammatory Activity of Guluronate Oligosaccharides Obtained by Oxidative Degradation from Alginate in Lipopolysaccharide-Activated Murine Macrophage RAW 264.7 Cells. *J. Agric. Food Chem.* **2015**, *63*, 160–168. [CrossRef]

56. Rocha de Souza, M.C.; Marques, C.T.; Guerra Dore, C.M.; Ferreira da Silva, F.R.; Oliveira Rocha, H.A.; Leite, E.L. Antioxidant Activities of Sulfated Polysaccharides from Brown and Red Seaweeds. *J. Appl. Phycol.* **2007**, *19*, 153–160. [CrossRef]

57. Maciel, D.; Figueira, P.; Xiao, S.; Hu, D.; Shi, X.; Rodrigues, J.; Tomás, H.; Li, Y. Redox-Responsive Alginate Nanogels with Enhanced Anticancer Cytotoxicity. *Biomacromolecules* **2013**, *14*, 3140–3146. [CrossRef] [PubMed]

58. Ansari, M.J.; Rajendran, R.R.; Mohanto, S.; Agarwal, U.; Panda, K.; Dhotre, K.; Manne, R.; Deepak, A.; Zafar, A.; Yasir, M.; et al. Poly(N-Isopropylacrylamide)-Based Hydrogels for Biomedical Applications: A Review of the State-of-the-Art. *Gels* **2022**, *8*, 454. [CrossRef]

59. Grant, G.T.; Morris, E.R.; Rees, D.A.; Smith, P.J.C.; Thom, D. Biological Interactions between Polysaccharides and Divalent Cations: The Egg-Box Model. *FEBS Lett.* **1973**, *32*, 195–198. [CrossRef]

60. Crow, B.B.; Nelson, K.D. Release of Bovine Serum Albumin from a Hydrogel-Cored Biodegradable Polymer Fiber. *Biopolymers* **2006**, *81*, 419–427. [CrossRef] [PubMed]

61. Kuo, C.K.; Ma, P.X. Ionically Crosslinked Alginate Hydrogels as Scaffolds for Tissue Engineering: Part 1. Structure, Gelation Rate and Mechanical Properties. *Biomaterials* **2001**, *22*, 511–521. [CrossRef]

62. Drury, J.L.; Dennis, R.G.; Mooney, D.J. The Tensile Properties of Alginate Hydrogels. *Biomaterials* **2004**, *25*, 3187–3199. [CrossRef] [PubMed]

63. Urzedo, A.L.; Gonçalves, M.C.; Nascimento, M.H.M.; Lombello, C.B.; Nakazato, G.; Seabra, A.B. Cytotoxicity and Antibacterial Activity of Alginate Hydrogel Containing Nitric Oxide Donor and Silver Nanoparticles for Topical Applications. *ACS Biomater. Sci. Eng.* **2020**, *6*, 2117–2134. [CrossRef]

64. Bruchet, M.; Melman, A. Fabrication of Patterned Calcium Cross-Linked Alginate Hydrogel Films and Coatings through Reductive Cation Exchange. *Carbohydr. Polym.* **2015**, *131*, 57–64. [CrossRef] [PubMed]

65. Gattás-Asfura, K.M.; Fraker, C.A.; Stabler, C.L. Covalent Stabilization of Alginate Hydrogel Beads via Staudinger Ligation: Assessment of Poly(Ethylene Glycol) and Alginate Cross-Linkers. *J. Biomed. Mater. Res. A* **2011**, *99*, 47–57. [CrossRef] [PubMed]

66. Awasthi, R.; Kulkarni, G.T.; Ramana, M.V.; de Jesus Andreoli Pinto, T.; Kikuchi, I.S.; Molim Ghisleni, D.D.; de Souza Braga, M.; De Bank, P.; Dua, K. Dual Crosslinked Pectin–Alginate Network as Sustained Release Hydrophilic Matrix for Repaglinide. *Int. J. Biol. Macromol.* **2017**, *97*, 721–732. [CrossRef]

67. Eiselt, P.; Lee, K.Y.; Mooney, D.J. Rigidity of Two-Component Hydrogels Prepared from Alginate and Poly(Ethylene Glycol)-Diamines. *Macromolecules* **1999**, *32*, 5561–5566. [CrossRef]

68. Lee, K.Y.; Rowley, J.A.; Eiselt, P.; Moy, E.M.; Bouhadir, K.H.; Mooney, D.J. Controlling Mechanical and Swelling Properties of Alginate Hydrogels Independently by Cross-Linker Type and Cross-Linking Density. *Macromolecules* **2000**, *33*, 4291–4294. [CrossRef]

69. Gao, Y.; Jin, X. Dual Crosslinked Methacrylated Alginate Hydrogel Micron Fibers and Tissue Constructs for Cell Biology. *Mar. Drugs* **2019**, *17*, 557. [CrossRef] [PubMed]

70. Basu, S.; Pacelli, S.; Paul, A. Self-Healing DNA-Based Injectable Hydrogels with Reversible Covalent Linkages for Controlled Drug Delivery. *Acta Biomater.* **2020**, *105*, 159–169. [CrossRef] [PubMed]

71. Xing, L.; Sun, J.; Tan, H.; Yuan, G.; Li, J.; Jia, Y.; Xiong, D.; Chen, G.; Lai, J.; Ling, Z.; et al. Covalently Polysaccharide-Based Alginate/Chitosan Hydrogel Embedded Alginate Microspheres for BSA Encapsulation and Soft Tissue Engineering. *Int. J. Biol. Macromol.* **2019**, *127*, 340–348. [CrossRef] [PubMed]

72. Smeds, K.A.; Pfister-Serres, A.; Miki, D.; Dastgheib, K.; Inoue, M.; Hatchell, D.L.; Grinstaff, M.W. Photocrosslinkable Polysaccharides for in Situ Hydrogel Formation. *J. Biomed. Mater. Res.* **2001**, *54*, 115–121. [CrossRef]

73. Rouillard, A.D.; Berglund, C.M.; Lee, J.Y.; Polacheck, W.J.; Tsui, Y.; Bonassar, L.J.; Kirby, B.J. Methods for Photocrosslinking Alginate Hydrogel Scaffolds with High Cell Viability. *Tissue Eng.-Part C Methods* **2011**, *17*, 173–179. [CrossRef]

74. Bonino, C.A.; Samorezov, J.E.; Jeon, O.; Alsberg, E.; Khan, S.A. Real-Time in Situ Rheology of Alginate Hydrogel Photocrosslinking. *Soft Matter* **2011**, *7*, 11510–11517. [CrossRef]

75. Jeon, O.; Samorezov, J.E.; Alsberg, E. Single and Dual Crosslinked Oxidized Methacrylated Alginate/PEG Hydrogels for Bioadhesive Applications. *Acta Biomater.* **2014**, *10*, 47–55. [CrossRef] [PubMed]

76. Jeon, O.; Bouhadir, K.H.; Mansour, J.M.; Alsberg, E. Photocrosslinked Alginate Hydrogels with Tunable Biodegradation Rates and Mechanical Properties. *Biomaterials* **2009**, *30*, 2724–2734. [CrossRef] [PubMed]

77. Buono, P.; Duval, A.; Averous, L.; Habibi, Y. Lignin-Based Materials Through Thiol–Maleimide "Click" Polymerization. *ChemSusChem* **2017**, *10*, 984–992. [CrossRef]

78. Jain, E.; Neal, S.; Graf, H.; Tan, X.; Balasubramaniam, R.; Huebsch, N. Copper-Free Azide–Alkyne Cycloaddition for Peptide Modification of Alginate Hydrogels. *ACS Appl. Bio Mater.* **2021**, *4*, 1229–1237. [CrossRef]

79. Anugrah, D.S.B.; Ramesh, K.; Kim, M.; Hyun, K.; Lim, K.T. Near-Infrared Light-Responsive Alginate Hydrogels Based on Diselenide-Containing Cross-Linkage for on Demand Degradation and Drug Release. *Carbohydr. Polym.* **2019**, *223*, 115070. [CrossRef]

80. García-Astrain, C.; Avérous, L. Synthesis and Evaluation of Functional Alginate Hydrogels Based on Click Chemistry for Drug Delivery Applications. *Carbohydr. Polym.* **2018**, *190*, 271–280. [CrossRef]

81. Wang, G.; Zhu, J.; Chen, X.; Dong, H.; Li, Q.; Zeng, L.; Cao, X. Alginate Based Antimicrobial Hydrogels Formed by Integrating Diels-Alder "Click Chemistry" and the Thiol-Ene Reaction. *RSC Adv.* **2018**, *8*, 11036–11042. [CrossRef]

82. Lueckgen, A.; Garske, D.S.; Ellinghaus, A.; Desai, R.M.; Stafford, A.G.; Mooney, D.J.; Duda, G.N.; Cipitria, A. Hydrolytically-Degradable Click-Crosslinked Alginate Hydrogels. *Biomaterials* **2018**, *181*, 189–198. [CrossRef]

83. Pérez-Madrigal, M.M.; Shaw, J.E.; Arno, M.C.; Hoyland, J.A.; Richardson, S.M.; Dove, A.P. Robust Alginate/Hyaluronic Acid Thiol-Yne Click-Hydrogel Scaffolds with Superior Mechanical Performance and Stability for Load-Bearing Soft Tissue Engineering. *Biomater. Sci.* **2020**, *8*, 405–412. [CrossRef]

84. Roy, D.; Cambre, J.N.; Sumerlin, B.S. Future Perspectives and Recent Advances in Stimuli-Responsive Materials. *Prog. Polym. Sci.* **2010**, *35*, 278–301. [CrossRef]

85. Zhao, S.; Cao, M.; Li, H.; Li, L.; Xu, W. Synthesis and Characterization of Thermo-Sensitive Semi-IPN Hydrogels Based on Poly(Ethylene Glycol)-Co-Poly(ε-Caprolactone) Macromer, N-Isopropylacrylamide, and Sodium Alginate. *Carbohydr. Res.* **2010**, *345*, 425–431. [CrossRef]

86. Bezerra, I.C.S.; de Freitas, E.D.; da Silva, M.G.C.; Vieira, M.G.A. Synthesis and Characterization of Furosemide-Loaded Sericin/Alginate Beads Subjected to Thermal or Chemical Cross-Linking for Delayed and Sustained Release. *Polym. Adv. Technol.* **2021**, *32*, 461–473. [CrossRef]

87. Yu, J.; Du, K.T.; Fang, Q.; Gu, Y.; Mihardja, S.S.; Sievers, R.E.; Wu, J.C.; Lee, R.J. The Use of Human Mesenchymal Stem Cells Encapsulated in RGD Modified Alginate Microspheres in the Repair of Myocardial Infarction in the Rat. *Biomaterials* **2010**, *31*, 7012–7020. [CrossRef]

88. Fonseca, K.B.; Bidarra, S.J.; Oliveira, M.J.; Granja, P.L.; Barrias, C.C. Molecularly Designed Alginate Hydrogels Susceptible to Local Proteolysis as Three-Dimensional Cellular Microenvironments. *Acta Biomater.* **2011**, *7*, 1674–1682. [CrossRef]

89. Hua, S.; Ma, H.; Li, X.; Yang, H.; Wang, A. PH-Sensitive Sodium Alginate/Poly(Vinyl Alcohol) Hydrogel Beads Prepared by Combined Ca2+ Crosslinking and Freeze-Thawing Cycles for Controlled Release of Diclofenac Sodium. *Int. J. Biol. Macromol.* **2010**, *46*, 517–523. [CrossRef]

90. Tkalec, G.; Kranvogl, R.; Perva Uzunalić, A.; Knez, Ž.; Novak, Z. Optimisation of Critical Parameters during Alginate Aerogels' Production. *J. Non-Cryst. Solids* **2016**, *443*, 112–117. [CrossRef]

91. Mattiasson, B.; Kumar, A.; Galeaev, I.Y. *Macroporous Polymers: Production Properties and Biotechnological/Biomedical Applications*; CRC Press: Boca Raton, FL, USA, 2009; ISBN 1420084623.

92. Subrahmanyam, R.; Gurikov, P.; Meissner, I.; Smirnova, I. Preparation of Biopolymer Aerogels Using Green Solvents. *J. Vis. Exp.* **2016**, *113*, e54116. [CrossRef]

93. Gurikov, P.; Smirnova, I. Non-Conventional Methods for Gelation of Alginate. *Gels* **2018**, *4*, 14. [CrossRef]

94. Pérez-Madrigal, M.M.; Torras, J.; Casanovas, J.; Häring, M.; Alemán, C.; Díaz, D.D. Paradigm Shift for Preparing Versatile M2+-Free Gels from Unmodified Sodium Alginate. *Biomacromolecules* **2017**, *18*, 2967–2979. [CrossRef] [PubMed]

95. Király, G.; Egu, J.C.; Hargitai, Z.; Kovács, I.; Fábián, I.; Kalmár, J.; Szemán-Nagy, G. Mesoporous Aerogel Microparticles Injected into the Abdominal Cavity of Mice Accumulate in Parathymic Lymph Nodes. *Int. J. Mol. Sci.* **2021**, *22*, 9756. [CrossRef] [PubMed]

96. Vasvári, G.; Kalmár, J.; Veres, P.; Vecsernyés, M.; Bácskay, I.; Fehér, P.; Ujhelyi, Z.; Haimhoffer, Á.; Rusznyák, Á.; Fenyvesi, F.; et al. Matrix Systems for Oral Drug Delivery: Formulations and Drug Release. *Drug Discov. Today Technol.* **2018**, *27*, 71–80. [CrossRef] [PubMed]

97. Veres, P.; Sebők, D.; Dékány, I.; Gurikov, P.; Smirnova, I.; Fábián, I.; Kalmár, J. A Redox Strategy to Tailor the Release Properties of Fe(III)-Alginate Aerogels for Oral Drug Delivery. *Carbohydr. Polym.* **2018**, *188*, 159–167. [CrossRef] [PubMed]

98. Lovskaya, D.; Menshutina, N. Alginate-Based Aerogel Particles as Drug Delivery Systems: Investigation of the Supercritical Adsorption and In Vitro Evaluations. *Materials* **2020**, *13*, 329. [CrossRef]

99. Athamneh, T.; Amin, A.; Benke, E.; Ambrus, R.; Gurikov, P.; Smirnova, I.; Leopold, C.S. Pulmonary Drug Delivery with Aerogels: Engineering of Alginate and Alginate–Hyaluronic Acid Microspheres. *Pharm. Dev. Technol.* **2021**, *26*, 509–521. [CrossRef]

100. Athamneh, T.; Amin, A.; Benke, E.; Ambrus, R.; Leopold, C.S.; Gurikov, P.; Smirnova, I. Alginate and Hybrid Alginate-Hyaluronic Acid Aerogel Microspheres as Potential Carrier for Pulmonary Drug Delivery. *J. Supercrit. Fluids* **2019**, *150*, 49–55. [CrossRef]

101. Sugiura, S.; Oda, T.; Izumida, Y.; Aoyagi, Y. Size Control of Calcium Alginate Beads Containing Living Cells Using Micro-Nozzle Array. *Biomaterials* **2005**, *26*, 3327–3331. [CrossRef]

102. Silva, C.M.; Ribeiro, J.; Vit, I. Alginate Microspheres Prepared by Internal Gelation: Development and Effect on Insulin Stability. *Int. J. Pharm.* **2006**, *311*, 1–10. [CrossRef] [PubMed]

103. Ouerghi, O.; Geesi, M.H.; Ibnouf, E.O.; Ansari, M.J.; Alam, P.; Elsanousi, A.; Kaiba, A.; Riadi, Y. Sol-Gel Synthesized Rutile TiO2 Nanoparticles Loaded with Cardamom Essential Oil: Enhanced Antibacterial Activity. *J. Drug Deliv. Sci. Technol.* **2021**, *64*, 102581. [CrossRef]

104. Ansari, M.J. Factors Affecting Preparation and Properties of Nanoparticles by Nanoprecipitation Method. *Indo Am. J. Pharm. Sci.* **2017**, *4*, 4854–4858.

105. Fundueanu, G.; Nastruzzi, C.; Carpov, A.; Desbrieres, J.; Rinaudo, M. Physico-Chemical Characterization of Ca-Alginate Microparticles Produced with Different Methods. *Biomaterials* **1999**, *20*, 1427–1435. [CrossRef]

106. Seifert, D.B.; Phillips, J.A. Production of Small, Monodispersed Alginate Beads for Cell Immobilization. *Biotechnol. Prog.* **2008**, *13*, 562–568. [CrossRef]

107. Andriola, A.K.; Brun-graeppi, S.; Richard, C.; Bessodes, M.; Scherman, D.; Merten, O. Cell Microcarriers and Microcapsules of Stimuli-Responsive Polymers. *J. Control. Release* **2011**, *149*, 209–224. [CrossRef]

108. Zimmermann, H.; Shirley, S.G.; Zimmermann, U. Alginate-Based Encapsulation of Cells: Past, Present, and Future. *Curr. Diab. Rep.* **2007**, *7*, 314–320. [CrossRef]

109. Reis, C.P.; Neufeld, R.J.; Vilela, S.; Ribeiro, A.J.; Veiga, F. Review and Current Status of Emulsion/Dispersion Technology Using an Internal Gelation Process for the Design of Alginate Particles. *J. Microencapsul.* **2006**, *23*, 245–257. [CrossRef] [PubMed]

110. Shilpa, A.; Agrawal, S.S.; Ray, A.R. Controlled Delivery of Drugs from Alginate Matrix. *J. Macromol. Sci.-Polym. Rev.* **2003**, *43*, 187–221. [CrossRef]

111. Patel, M.A.; AbouGhaly, M.H.H.; Schryer-Praga, J.V.; Chadwick, K. The Effect of Ionotropic Gelation Residence Time on Alginate Cross-Linking and Properties. *Carbohydr. Polym.* **2017**, *155*, 362–371. [CrossRef]

112. Poncelet, D.; Lencki, R.; Beaulieu, C.; Halle, J.P.; Neufeld, R.J.; Fournier, A. Production of Alginate Beads by Emulsification/Internal Gelation. I. Methodology. *Appl. Microbiol. Biotechnol.* **1992**, *38*, 39–45. [CrossRef]

113. Poncelet, D. Production of Alginate Beads by Emulsification/Internal Gelation. *Ann. N. Y. Acad. Sci.* **2001**, *944*, 74–82. [CrossRef] [PubMed]

114. Sæther, H.V.; Holme, H.K.; Maurstad, G.; Smidsrød, O.; Stokke, B.T. Polyelectrolyte Complex Formation Using Alginate and Chitosan. *Carbohydr. Polym.* **2008**, *74*, 813–821. [CrossRef]

115. Rajaonarivony, M.; Vauthier, C.; Couarraze, G.; Puisieux, F.; Couvreur, P. Development of a New Drug Carrier Made from Alginate. *J. Pharm. Sci.* **1993**, *82*, 912–917. [CrossRef]

116. Severino, P.; da Silva, C.F.; Andrade, L.N.; de Lima Oliveira, D.; Campos, J.; Souto, E.B. Alginate Nanoparticles for Drug Delivery and Targeting. *Curr. Pharm. Des.* **2019**, *25*, 1312–1334. [CrossRef]

117. Ansari, M.; Ahmed, M.M.; Fatima; Anwer, M.K.; Jamil, S.; Al-Shdefat, R.; Ali, B. Solubility and Stability Enhancement of Curcumin through Cyclodextrin Complexation. *Int. J. Biol. Pharm. Allied Sci.* **2014**, *3*, 2668–2675.

118. Dawoud, M.; Abourehab, M.A.S.; Abdou, R. Monoolein Cubic Nanoparticles as Novel Carriers for Docetaxel. *J. Drug Deliv. Sci. Technol.* **2020**, *56*, 101501. [CrossRef]

119. El-aziz, E.A.; Elgayar, S.F.; Mady, F.M.; Abourehab, M.A.S.; Hasan, O.A.; Reda, L.M.; Alaaeldin, E. The Potential of Optimized Liposomes in Enhancement of Cytotoxicity and Apoptosis of Encapsulated Egyptian Propolis on Hep-2 Cell Line. *Pharmaceutics* **2021**, *13*, 2184. [CrossRef]

120. Ansari, M.J.; Alshetaili, A.; Aldayel, I.A.; Alablan, F.M.; Alsulays, B.; Alshahrani, S.; Alalaiwe, A.; Ansari, M.N.; Ur Rehman, N.; Shakeel, F. Formulation, Characterization, in Vitro and in Vivo Evaluations of Self-Nanoemulsifying Drug Delivery System of Luteolin. *J. Taibah Univ. Sci.* **2020**, *14*, 1386–1401. [CrossRef]

121. Choi, H.J.; Kim, M.C.; Kang, S.M.; Montemagno, C.D. The Osmotic Stress Response of Split Influenza Vaccine Particles in an Acidic Environment. *Arch. Pharm. Res.* **2014**, *37*, 1607–1616. [CrossRef]

122. Araújo, F.; das Neves, J.; Martins, J.P.; Granja, P.L.; Santos, H.A.; Sarmento, B. Functionalized Materials for Multistage Platforms in the Oral Delivery of Biopharmaceuticals. *Prog. Mater. Sci.* **2017**, *89*, 306–344. [CrossRef]

123. Ansari, M.J. Oral Delivery of Insulin for Treatment of Diabetes: Classical Challenges and Current Opportunities. *J. Med. Sci.* **2015**, *15*, 209–220. [CrossRef]

124. Bowman, K.; Leong, K.W. Chitosan Nanoparticles for Oral Drug and Gene Delivery. *Int. J. Nanomed.* **2006**, *1*, 117–128. [CrossRef]

125. Ilgin, P.; Ozay, H.; Ozay, O. Synthesis and Characterization of PH Responsive Alginate Based-Hydrogels as Oral Drug Delivery Carrier. *J. Polym. Res.* **2020**, *27*, 251.

126. Ayub, A.D.; Chiu, H.I.; Yusuf, S.N.A.M.; Kadir, E.A.; Ngalim, S.H.; Lim, V. Biocompatible Disulphide Cross-Linked Sodium Alginate Derivative Nanoparticles for Oral Colon-Targeted Drug Delivery. *Artif. Cells Nanomed. Biotechnol.* **2019**, *47*, 353–369. [CrossRef] [PubMed]

127. Cong, A.Z.; Shi, Y.; Wang, Y. A Novel Controlled Drug Delivery System Based on Alginate Hydrogel / Chitosan Micelle Composites. *Int. J. Biol. Macromol.* **2017**, *107*, 855–864. [CrossRef] [PubMed]

128. Van De Ven, H.; Paulussen, C.; Feijens, P.B.; Matheeussen, A.; Rombaut, P.; Kayaert, P.; Mooter, G. Van Den PLGA Nanoparticles and Nanosuspensions with Amphotericin B: Potent in Vitro and in Vivo Alternatives to Fungizone and AmBisome. *J. Control. Release* **2012**, *161*, 795–803. [CrossRef]

129. Abourehab, M.A.S.; Khames, A.; Genedy, S.; Mostafa, S.; Khaleel, M.A.; Omar, M.M.; El Sisi, A.M. Sesame Oil-Based Nanostructured Lipid Carriers of Nicergoline, Intranasal Delivery System for Brain Targeting of Synergistic Cerebrovascular Protection. *Pharmaceutics* **2021**, *13*, 581. [CrossRef] [PubMed]

130. Barradas, N.; Cardoso, S.; Castiglione, T.C.; Michael, J.; Gyselle, K.; Holanda, D.; Regina, C.; Mansur, E. Dual Alginate-Lipid Nanocarriers as Oral Delivery Systems for Amphotericin B. *Colloids Surf. B Biointerfaces* **2018**, *166*, 187–194. [CrossRef]

131. Panyam, J.; Labhasetwar, V. Biodegradable Nanoparticles for Drug and Gene Delivery to Cells and Tissue. *Adv. Drug Deliv. Rev.* **2003**, *55*, 329–347. [CrossRef]

132. Ooi, S.Y.; Ahmad, I.; Cairul, M.; Mohd, I. Cellulose Nanocrystals Extracted from Rice Husks as a Reinforcing Material in Gelatin Hydrogels for Use in Controlled Drug Delivery Systems. *Ind. Crop. Prod.* **2015**, *93*, 227–234. [CrossRef]

133. Lin, N.; Huang, J.; Chang, P.R.; Feng, L.; Yu, J. Colloids and Surfaces B: Biointerfaces Effect of Polysaccharide Nanocrystals on Structure, Properties, and Drug Release Kinetics of Alginate-Based Microspheres. *Colloids Surf. B Biointerfaces* **2011**, *85*, 270–279. [CrossRef]

134. Thomas, D.; Latha, M.S.; Thomas, K.K. Journal of Drug Delivery Science and Technology Synthesis and in Vitro Evaluation of Alginate-Cellulose Nanocrystal Hybrid Nanoparticles for the Controlled Oral Delivery of Rifampicin. *J. Drug Deliv. Sci. Technol.* **2018**, *46*, 392–399. [CrossRef]

135. Lakkakula, J.R.; Matshaya, T.; Werner, R.; Krause, M. Cationic Cyclodextrin/Alginate Chitosan Nano Fl Owers as 5- Fl Uorouracil Drug Delivery System. *Mater. Sci. Eng. C* **2017**, *70*, 169–177. [CrossRef] [PubMed]

136. Pitchaya Treenate, P.M. In Vitro Drug Release Profiles of PH-Sensitive Hydroxyethylacryl Chitosan/Sodium Alginate Hydrogels Using Paracetamol as a Soluble Model Drug. *Int J Biol Macromol* **2017**, *99*, 71–78. [CrossRef]

137. Agili, F.A.; Aly, S.F.M. Physicochemical Characterization and Release Properties of Oral Drug Delivery: A PH-Sensitive Nanocomposite Based on Sodium Alginate–Pectin–Tannic Acid–Silver. *Polym. Polym. Compos.* **2019**, *28*, 598–608. [CrossRef]

138. Olayemi, O.J.; Apeji, Y.E.; Isimi, C.Y. Formulation and Evaluation of Cyperus Esculentus (Tiger Nut) Starch-Alginate Microbeads in the Oral Delivery of Ibuprofen. *J. Pharm. Innov.* **2020**, *17*, 366–375. [CrossRef]

139. Chegeni, M.; Rozbahani, Z.S.; Ghasemian, M.; Mehri, M. International Journal of Biological Macromolecules Synthesis and Application of the Calcium Alginate / SWCNT-Gl as a Bio-Nanocomposite for the Curcumin Delivery. *Int. J. Biol. Macromol.* **2020**, *156*, 504–513. [CrossRef]

140. Mao, X.; Li, X.; Zhang, W.; Yuan, L.; Deng, L.; Ge, L.; Mu, C.; Li, D. Development of Microspheres Based on Thiol-Modi Fi Ed Sodium Alginate for Intestinal-Targeted Drug Delivery. *ACS Appl. Bio Mater.* **2019**, *2*, 5810–5818. [CrossRef]

141. Long, L.; Lai, M.; Ke, Z.; Yang, L. Investigation Of Vitamin B 12 -Modi Fi Ed Amphiphilic Sodium Alginate Derivatives For Enhancing The Oral Delivery Ef Fi Cacy Of Peptide Drugs. *Int. J. Nanomed.* **2019**, *14*, 7743–7758. [CrossRef]

142. Chiu, H.I.; Ayub, A.D.; Nur, S.; Mat, A.; Yahaya, N. Docetaxel-Loaded Disulfide Cross-Linked Nanoparticles Derived from Thiolated Sodium Alginate for Colon Cancer Drug Delivery. *Pharmaceutics* **2020**, *12*, 38. [CrossRef]

143. Abdellatif, A.A.H.; Ibrahim, M.A.; Amin, M.A. Cetuximab Conjugated with Octreotide and Entrapped Calcium Alginate-Beads for Targeting Somatostatin Receptors. *Sci. Rep.* **2020**, *10*, 4736. [CrossRef]

144. Kahya, N.; Gölcü, A.; Erim, F.B. Barium Ion Cross-Linked Alginate-Carboxymethyl Cellulose Composites for Controlled Release of Anticancer Drug Methotrexate. *J. Drug Deliv. Sci. Technol.* **2019**, *54*, 101324. [CrossRef]

145. Shamekhi, F.; Tamjid, E.; Khajeh, K. Development of Chitosan Coated Calcium-Alginate Nanocapsules for Oral Delivery of Liraglutide to Diabetic Patients. *Int. J. Biol. Macromol.* **2018**, *120*, 460–467. [CrossRef] [PubMed]

146. Karzar Jeddi, M.; Mahkam, M. Magnetic Nano Carboxymethyl Cellulose-Alginate/Chitosan Hydrogel Beads as Biodegradable Devices for Controlled Drug Delivery. *Int. J. Biol. Macromol.* **2019**, *135*, 829–838. [CrossRef] [PubMed]

147. Urtti, A. Challenges and Obstacles of Ocular Pharmacokinetics and Drug Delivery. *Adv. Drug Deliv. Rev.* **2006**, *58*, 1131–1135. [CrossRef]

148. De, M.; Raviña, M.; Paolicelli, P.; Sanchez, A.; Seijo, B.; Jose, M. Chitosan-Based Nanostructures: A Delivery Platform for Ocular Therapeutics . *Adv. Drug Deliv. Rev.* **2010**, *62*, 100–117. [CrossRef]

149. Rupenthal, I.D.; O'Rourke, M. Ocular Drug Delivery—Eye on Innovation. *Drug Deliv. Transl. Res.* **2016**, *6*, 631–633. [CrossRef]

150. Pedraz, L.; Wahlberg, L.U.; De Vos, P.; Emerich, D. Cell Encapsulation: Technical and Clinical Advances. *Trends Pharmacol. Sci.* **2015**, *36*, 537–546. [CrossRef]

151. Siu, F.; Wong, Y.; Kin, K.; Man, A.; Chu, W.; Pui, B.; Ming, K.; Cheuk, A.; Lo, Y. Biomaterials Injectable Cell-Encapsulating Composite Alginate-Collagen Platform with Inducible Termination Switch for Safer Ocular Drug Delivery. *Biomaterials* **2019**, *201*, 53–67. [CrossRef]

152. Patel, A. Ocular Drug Delivery Systems: An Overview. *World J. Pharmacol.* **2013**, *2*, 47–64. [CrossRef]

153. Shelley, H.; Rodriguez-Galarza, R.M.; Duran, S.H.; Abarca, E.M.; Babu, R.J. In Situ Gel Formulation for Enhanced Ocular Delivery of Nepafenac. *J. Pharm. Sci.* **2018**, *107*, 3089–3097. [CrossRef] [PubMed]

154. Nagarwal, R.C.; Kumar, R.; Pandit, J.K. Chitosan Coated Sodium Alginate-Chitosan Nanoparticles Loaded with 5-FU for Ocular Delivery: In Vitro Characterization and in Vivo Study in Rabbit Eye. *Eur. J. Pharm. Sci.* **2012**, *47*, 678–685. [CrossRef] [PubMed]

155. Noreen, S.; Ghumman, S.A.; Batool, F.; Ijaz, B.; Basharat, M.; Noureen, S.; Kausar, T.; Iqbal, S. Terminalia Arjuna Gum/Alginate in Situ Gel System with Prolonged Retention Time for Ophthalmic Drug Delivery. *Int. J. Biol. Macromol.* **2020**, *152*, 1056–1067. [CrossRef]

156. Polat, H.K.; Pehlivan, S.B.; Özkul, C.; Çalamak, S.; Aytekin, E.; Fırat, A.; Ulubayram, K.; Kocabeyoğlu, S. Development of Besifloxacin HCl Loaded Nanofibrous Ocular Inserts for the Treatment of Bacterial Keratitis: In Vitro, Ex Vivo and in Vivo Evaluation. *Int. J. Pharm.* **2020**, *585*, 119552. [CrossRef] [PubMed]

157. Silva, D.; Pinto, L.F.V.; Bozukova, D.; Santos, L.F.; Serro, A.P.; Saramago, B. Chitosan/Alginate Based Multilayers to Control Drug Release from Ophthalmic Lens. *Colloids Surf. B Biointerfaces* **2016**, *147*, 81–89. [CrossRef] [PubMed]

158. Costa, J.R.; Silva, N.C.; Sarmento, B.; Pintado, M. Potential Chitosan-Coated Alginate Nanoparticles for Ocular Delivery of Daptomycin. *Eur. J. Clin. Microbiol.* **2015**, *34*, 1255–1262. [CrossRef] [PubMed]

159. Kumar, S.; Chauhan, N.; Gopal, M.; Kumar, R. International Journal of Biological Macromolecules Development and Evaluation of Alginate—Chitosan Nanocapsules for Controlled Release of Acetamiprid. *Int. J. Biol. Macromol.* **2015**, *81*, 631–637. [CrossRef]

160. Gupta, H.; Aqil, M.; Khar, R.K.; Ali, A.; Bhatnagar, A. An Alternative in Situ Gel-Formulation of Levofloxacin Eye Drops for Prolong Ocular Retention. *J. Pharm. Bioallied Sci.* **2015**, *7*, 9–14. [CrossRef]

161. Gökçe, E.H.; Okur, N.Ü. Novel Nanostructured Lipid Carrier Based Flurbiprofen Loaded Sodium Alginate Inserts for Ocular Drug Delivery. *Lat. Am. J. Pharm.* **2016**, *35*, 972–979.

162. Mokhtari, S.; Jafari, S.M.; Assadpour, E. Development of a Nutraceutical Nano-Delivery System through Emulsification/Internal Gelation of Alginate. *Food Chem.* **2017**, *229*, 286–295. [CrossRef]

163. Khan, N.; Aqil, M.; Ameeduzzafar; Imam, S.S.; Ali, A. Development and Evaluation of a Novel in Situ Gel of Sparfloxacin for Sustained Ocular Drug Delivery: In Vitro and Ex Vivo Characterization. *Pharm. Dev. Technol.* **2015**, *20*, 662–669. [CrossRef]

164. Reed, K.; Lankford, M. Calcium Gluconatee Mediated In-Situ Gelling of Alginates for Ocular Drug Delivery. *J. Am. Pharm. Assoc.* **2018**, *58*, e49.

165. Xu, W.; Liu, K.; Li, T.; Zhang, W.; Dong, Y.; Lv, J.; Wang, W.; Sun, J.; Li, M.; Wang, M.; et al. An in Situ Hydrogel Based on Carboxymethyl Chitosan and Sodium Alginate Dialdehyde for Corneal Wound Healing after Alkali Burn. *J. Biomed. Mater. Res. Part A* **2019**, *107*, 742–754. [CrossRef]

166. Wafa, H.G.; Essa, E.A.; El-Sisi, A.E.; El Maghraby, G.M. Ocular Films versus Film-Forming Liquid Systems for Enhanced Ocular Drug Delivery. *Drug Deliv. Transl. Res.* **2021**, *11*, 1084–1095. [CrossRef]

167. Shinde, U.A.; Shete, J.N.; Nair, H.A.; Singh, K.H. Design and Characterization of Chitosan-Alginate Microspheres for Ocular Delivery of Azelastine. *Pharm. Dev. Technol.* **2014**, *19*, 813–823. [CrossRef]

168. Sadeghi, A.M.; Farjadian, F.; Alipour, S. Sustained Release of Linezolid in Ocular Insert Based on Lipophilic Modified Structure of Sodium Alginate. *Iran. J. Basic Med. Sci.* **2021**, *24*, 331–340. [CrossRef]

169. Jaafar-Maalej, C.; Elaissari, A.; Fessi, H. Lipid-Based Carriers: Manufacturing and Applications for Pulmonary Route. *Expert Opin. Drug Deliv.* **2012**, *9*, 1111–1127. [CrossRef] [PubMed]

170. Pramanik, S.; Mohanto, S.; Manne, R.; Rajendran, R.R.; Deepak, A.; Edapully, S.J.; Patil, T.; Katari, O. Nanoparticle-Based Drug Delivery System: The Magic Bullet for the Treatment of Chronic Pulmonary Diseases. *Mol. Pharm.* **2021**, *18*, 3671–3718. [CrossRef]

171. Sung, J.C.; Pulliam, B.L.; Edwards, D.A. Nanoparticles for Drug Delivery to the Lungs. *Trends Biotechnol.* **2007**, *25*, 563–570. [CrossRef] [PubMed]

172. Rajendran, R.R.; Kumaran, S.; Banerjee, A.; Berlinski, A. A Hybrid in Vitro in Silico Framework for Albuterol Delivery through an Adult Ventilator Circuit to a Patient-Specific Lung Airway Model. *J. Aerosol Sci.* **2021**, *158*, 105844. [CrossRef]

173. Rajendran, R.R.; Banerjee, A. Mucus Transport and Distribution by Steady Expiration in an Idealized Airway Geometry. *Med. Eng. Phys.* **2019**, *66*, 26–39. [CrossRef]

174. Rajendran, R.R.; Banerjee, A. Effect of Non-Newtonian Dynamics on the Clearance of Mucus From Bifurcating Lung Airway Models. *J. Biomech. Eng.* **2020**, *143*, 021011. [CrossRef]

175. Dolovich, M.B.; Dhand, R. Aerosol Drug Delivery: Developments in Device Design and Clinical Use. *Lancet* **2011**, *377*, 19–25. [CrossRef]

176. Yhee, J.; Im, J.; Nho, R. Advanced Therapeutic Strategies for Chronic Lung Disease Using Nanoparticle-Based Drug Delivery. *J. Clin. Med.* **2016**, *5*, 82. [CrossRef]

177. Mahmoud, A.A.; Elkasabgy, N.A.; Abdelkhalek, A.A. Design and Characterization of Emulsified Spray Dried Alginate Microparticles as a Carrier for the Dually Acting Drug Roflumilast. *Eur. J. Pharm. Sci.* **2018**, *122*, 64–76. [CrossRef]

178. Alsmadi, M.M.; Obaidat, R.M.; Alnaief, M.; Albiss, B.A.; Hailat, N. Development, In Vitro Characterization, and In Vivo Toxicity Evaluation of Chitosan-Alginate Nanoporous Carriers Loaded with Cisplatin for Lung Cancer Treatment. *AAPS PharmSciTech* **2020**, *21*, 191. [CrossRef]

179. López-Iglesias, C.; Casielles, A.M.; Altay, A.; Bettini, R.; Alvarez-Lorenzo, C.; García-González, C.A. From the Printer to the Lungs: Inkjet-Printed Aerogel Particles for Pulmonary Delivery. *Chem. Eng. J.* **2019**, *357*, 559–566. [CrossRef]

180. Alnaief, M.; Obaidat, R.M.; Alsmadi, M.M. Preparation of Hybrid Alginate-Chitosan Aerogel as Potential Carriers for Pulmonary Drug Delivery. *Polymers* **2020**, *12*, 2223. [CrossRef]

181. Dulhanty, A.M.; Riordan, J.R. Mutation of Potential Phosphorylation Sites in the Recombinant R Domain of the Cystic Fibrosis Transmembrane Conductance Regulator Has Significant Effects on Domain Conformation. *Biochem. Biophys. Res. Commun.* **1995**, *206*, 207–214. [CrossRef]

182. Haley, C.L.; Colmer-Hamood, J.A.; Hamood, A.N. Characterization of Biofilm-like Structures Formed by Pseudomonas Aeruginosa in a Synthetic Mucus Medium. *BMC Microbiol.* **2012**, *12*, 181. [CrossRef] [PubMed]

183. May, T.B.; Shinabarger, D.; Maharaj, R.; Kato, J.; Chu, L.; Devault, J.D.; Roychoudhury, S.; Zielinski, N.A.; Berry, A.; Rothmel, R.K.; et al. Alginate Synthesis by Pseudomonas Aeruginosa: A Key Pathogenic Factor in Chronic Pulmonary Infections of Cystic Fibrosis Patients. *Clin. Microbiol. Rev.* **1991**, *4*, 191–206. [CrossRef]

184. Selimoglu, E. Aminoglycoside-Induced Ototoxicity. *Curr. Pharm. Des.* **2007**, *13*, 119–126. [CrossRef] [PubMed]

185. Kumin, G.D. Clinical Nephrotoxicity of Tobramycin and Gentamicin: A Prospective Study. *JAMA* **1980**, *244*, 1808–1810. [CrossRef] [PubMed]

186. Hill, M.; Twigg, M.; Sheridan, E.A.; Hardy, J.G.; Elborn, J.S.; Taggart, C.C.; Scott, C.J.; Migaud, M.E. Alginate/Chitosan Particle-Based Drug Delivery Systems for Pulmonary Applications. *Pharmaceutics* **2019**, *11*, 379. [CrossRef]

187. Scolari, I.R.; Páez, P.L.; Musri, M.M.; Petiti, J.P.; Torres, A.; Granero, G.E. Rifampicin Loaded in Alginate/Chitosan Nanoparticles as a Promising Pulmonary Carrier against Staphylococcus Aureus. *Drug Deliv. Transl. Res.* **2020**, *10*, 1403–1417. [CrossRef] [PubMed]

188. Cheaburu-Yilmaz, C.N.; Lupuşoru, C.E.; Vasile, C. New Alginate/PNIPAAm Matrices for Drug Delivery. *Polymers* **2019**, *11*, 366. [CrossRef] [PubMed]

189. Hariyadi, D.M.; Hendradi, E.; Kurniawan, T.D. Alginate Microspheres Encapsulating Ciprofloxacin HCl: Characteristics, Release and Antibacterial Activity. *Int. J. Pharma Res. Health Sci.* **2019**, *7*, 3020–3027. [CrossRef]

190. Longuinho, M.M.; Leitão, S.G.; Silva, R.S.F.; Silva, P.E.A.; Rossi, A.L.; Finotelli, P. V Lapazine Loaded Alginate/Chitosan Microparticles: Enhancement of Anti-Mycobacterium Activity. *J. Drug Deliv. Sci. Technol.* **2019**, *54*, 101292. [CrossRef]

191. Islan, G.A.; Ruiz, M.E.; Morales, J.F.; Sbaraglini, M.L.; Enrique, A.V.; Burton, G.; Talevi, A.; Bruno-Blanch, L.E.; Castro, G.R. Hybrid Inhalable Microparticles for Dual Controlled Release of Levofloxacin and DNase: Physicochemical Characterization and in Vivo Targeted Delivery to the Lungs. *J. Mater. Chem. B* **2017**, *5*, 3132–3144. [CrossRef]

192. Tao, L.; Jiang, J.; Gao, Y.; Wu, C.; Liu, Y. Biodegradable Alginate-Chitosan Hollow Nanospheres for Codelivery of Doxorubicin and Paclitaxel for the Effect of Human Lung Cancer A549 Cells. *Biomed. Res. Int.* **2018**, *2018*, 4607945. [CrossRef] [PubMed]

193. Abdelghany, S.; Parumasivam, T.; Pang, A.; Roediger, B.; Tang, P.; Jahn, K.; Britton, W.J.; Chan, H.K. Alginate Modified-PLGA Nanoparticles Entrapping Amikacin and Moxifloxacin as a Novel Host-Directed Therapy for Multidrug-Resistant Tuberculosis. *J. Drug Deliv. Sci. Technol.* **2019**, *52*, 642–651. [CrossRef]

194. Nagpal, P.S.; Kesarwani, A.; Sahu, P.; Upadhyay, P. Aerosol Immunization by Alginate Coated Mycobacterium (BCG/MIP) Particles Provide Enhanced Immune Response and Protective Efficacy than Aerosol of Plain Mycobacterium against M.Tb. H37Rv Infection in Mice. *BMC Infect. Dis.* **2019**, *19*, 568. [CrossRef] [PubMed]

195. Shen, H.; Li, F.; Wang, D.; Yang, Z.; Yao, C.; Ye, Y.; Wang, X. Chitosan-Alginate BSA-Gel-Capsules for Local Chemotherapy against Drug-Resistant Breast Cancer. *Drug Des. Devel. Ther.* **2018**, *12*, 921–934. [CrossRef] [PubMed]

196. Srikrishna, S.; Cardozo, L. The Vagina as a Route for Drug Delivery: A Review. *Int. Urogynecol. J. Pelvic Floor Dysfunct.* **2013**, *24*, 537–543. [CrossRef] [PubMed]

197. Vermani, K.; Garg, S. The Scope and Potential of Vaginal Drug Delivery. *Pharm. Sci. Technol. Today* **2000**, *3*, 359–364. [CrossRef]

198. Deshpande, A.A.; Rhodes, C.T.; Danish, M. Intravaginal Drug Delivery. *Drug Dev. Ind. Pharm.* **1992**, *18*, 1225–1279. [CrossRef]

199. Meng, J.; Agrahari, V.; Ezoulin, M.J.; Purohit, S.S.; Zhang, T.; Molteni, A.; Dim, D.; Oyler, N.A.; Youan, B.B.C. Spray-Dried Thiolated Chitosan-Coated Sodium Alginate Multilayer Microparticles for Vaginal HIV Microbicide Delivery. *AAPS J.* **2017**, *19*, 692–702. [CrossRef]

200. Maestrelli, F.; Jug, M.; Cirri, M.; Kosalec, I.; Mura, P. Characterization and Microbiological Evaluation of Chitosan-Alginate Microspheres for Cefixime Vaginal Administration. *Carbohydr. Polym.* **2018**, *192*, 176–183. [CrossRef]

201. Ferreira, N.N.; Perez, T.A.; Pedreiro, L.N.; Prezotti, F.G.; Boni, F.I.; Cardoso, V.M.d.O.; Venâncio, T.; Gremião, M.P.D. A Novel PH-Responsive Hydrogel-Based on Calcium Alginate Engineered by the Previous Formation of Polyelectrolyte Complexes (PECs) Intended to Vaginal Administration. *Drug Dev. Ind. Pharm.* **2017**, *43*, 1656–1668. [CrossRef]

202. Jadhav, K.R.; Kadam, V.J.; Pisal, S.S. Formulation and Evaluation of Lecithin Organogel for Topical Delivery of Fluconazole. *Curr. Drug. Deliv.* **2009**, *6*, 174–183. [CrossRef]

203. Bayomi, M.A. Role of Chitosan on Controlling the Characteristics and Antifungal Activity of Bioadhesive Fluconazole Vaginal Tablets. *Saudi. Pharm. J.* **2017**, *26*, 151–161. [CrossRef]

204. Darwesh, B.; Aldawsari, H.M.; Badr-Eldin, S.M. Optimized Chitosan/Anion Polyelectrolyte Complex Based Inserts for Vaginal Delivery of Fluconazole: In Vitro/in Vivo Evaluation. *Pharmaceutics* **2018**, *10*, 227. [CrossRef]

205. Soliman, G.M.; Fetih, G.; Abbas, A.M. Thermosensitive Bioadhesive Gels for the Vaginal Delivery of Sildenafil Citrate: In Vitro Characterization and Clinical Evaluation in Women Using Clomiphene Citrate for Induction of Ovulation. *Drug. Dev. Ind. Pharm.* **2017**, *43*, 399–408. [CrossRef]

206. Hassan, A.; Soliman, G.; Ali, M.; El-Gindy, G. Mucoadhesive Tablets for the Vaginal Delivery of Progesterone: In Vitro Evaluation and Pharmacokinetics/Pharmacodynamics in Female Rabbits. *Drug. Dev. Ind. Pharm.* **2017**, *44*, 224–232. [CrossRef]

207. Kamel, R.; Abbas, H. A Multi-Microcarrier of Metronidazole-Biopolymers Complexes as a Potential Vaginal Delivery System. *Int. J. Polym. Mater. Polym. Biomater.* **2018**, *67*, 239–246. [CrossRef]

208. Yang, T.-T.; Cheng, Y.-Z.; Qin, M.; Wang, Y.-H.; Yu, H.-L.; Wang, A.-L.; Zhang, W.-F. Thermosensitive Chitosan Hydrogels Containing Polymeric Microspheres for Vaginal Drug Delivery. *Biomed. Res. Int.* **2017**, *2017*, 3564060. [CrossRef]

209. Gafitanu, C.A.; Filip, D.; Cernatescu, C.; Rusu, D.; Tuchilus, C.G.; Macocinschi, D.; Zaltariov, M. Design, Preparation and Evaluation of HPMC-Based PAA or SA Freeze-Dried Scaffolds for Vaginal Delivery of Fluconazole. *Pharm. Res.* **2017**, *34*, 2185–2196. [CrossRef]

210. Cirri, M.; Maestrelli, F.; Scuota, S.; Bazzucchi, V.; Mura, P. Development and Microbiological Evaluation of Chitosan and Chitosan-Alginate Microspheres for Vaginal Administration of Metronidazole. *Int. J. Pharm.* **2021**, *598*, 120375. [CrossRef]

211. Ghosal, K.; Ranjan, A.; Brata, B. A Novel Vaginal Drug Delivery System: Anti-HIV Bioadhesive Film Containing Abacavir. *J. Mater. Sci. Mater. Med.* **2014**, *25*, 1679–1689. [CrossRef]

212. Nematpour, N.; Moradipour, P.; Mahdi, M.; Arkan, E. Materials Science & Engineering C The Application of Nanomaterial Science in the Formulation a Novel Antibiotic: Assessment of the Antifungal Properties of Mucoadhesive Clotrimazole Loaded Nano Fi Ber versus Vaginal Fi Lms. *Mater. Sci. Eng. C* **2020**, *110*, 110635. [CrossRef]

213. Gnaman, K.C.N.G.; Bouttier, S.; Yeo, A.; Any-grah, A.A.S.A.; Geiger, S. Characterization and in Vitro Evaluation of a Vaginal Gel Containing Lactobacillus Crispatus for the Prevention of Gonorrhea. *Int. J. Pharm.* **2020**, *588*, 119733. [CrossRef]

214. da Silva Campelo, M.; Melo, E.O.; Arrais, S.P.; do Nascimento, F.B.S.A.; Gramosa, N.V.; de Aguiar Soares, S.; Ribeiro, M.E.N.P.; da Silva, C.R.; Júnior, H.V.N.; Ricardo, N.M.P.S. Clove Essential Oil Encapsulated on Nanocarrier Based on Polysaccharide: A Strategy for the Treatment of Vaginal Candidiasis. *Colloids Surf. A Physicochem. Eng. Asp.* **2021**, *610*, 125732. [CrossRef]

215. Tentor, F.; Siccardi, G.; Sacco, P.; Demarchi, D.; Marsich, E.; Almdal, K. Long Lasting Mucoadhesive Membrane Based on Alginate and Chitosan for Intravaginal Drug Delivery. *J. Mater. Sci. Mater. Med.* **2020**, *31*, 25. [CrossRef]

216. Kissel, T.; Werner, U. Nasal Delivery of Peptides: An in Vitro Cell Culture Model for the Investigation of Transport and Metabolism in Human Nasal Epithelium. *J. Control. Release* **1998**, *53*, 195–203. [CrossRef]

217. Illum, L. Nasal Drug Delivery-Recent Developments and Future Prospects. *J. Control. Release* **2012**, *161*, 254–263. [CrossRef]

218. Fortuna, A.; Alves, G.; Serralheiro, A.; Sousa, J.; Falcão, A. Intranasal Delivery of Systemic-Acting Drugs: Small-Molecules and Biomacromolecules. *Eur. J. Pharm. Biopharm.* **2014**, *88*, 8–27. [CrossRef] [PubMed]

219. Dukovski, B.J.; Plantić, I.; Čunčić, I.; Krtalić, I.; Juretić, M.; Pepić, I.; Lovrić, J.; Hafner, A. Lipid/Alginate Nanoparticle-Loaded in Situ Gelling System Tailored for Dexamethasone Nasal Delivery. *Int. J. Pharm.* **2017**, *533*, 480–487. [CrossRef] [PubMed]

220. Dehghan, S.; Kheiri, M.T.; Abnous, K.; Eskandari, M.; Tafaghodi, M. Preparation, Characterization and Immunological Evaluation of Alginate Nanoparticles Loaded with Whole Inactivated Influenza Virus: Dry Powder Formulation for Nasal Immunization in Rabbits. *Microb. Pathog.* **2017**, *115*, 74–85. [CrossRef]

221. Rao, M.; Agrawal, D.K.; Shirsath, C. Thermoreversible Mucoadhesive in Situ Nasal Gel for Treatment of Parkinson's Disease. *Drug Dev. Ind. Pharm.* **2017**, *43*, 142–150. [CrossRef]

222. Youssef, N.A.H.A.; Kassem, A.A.; Farid, R.M.; Ismail, F.A.; EL-Massik, M.A.E.; Boraie, N.A. A Novel Nasal Almotriptan Loaded Solid Lipid Nanoparticles in Mucoadhesive in Situ Gel Formulation for Brain Targeting: Preparation, Characterization and in Vivo Evaluation. *Int. J. Pharm.* **2018**, *548*, 609–624. [CrossRef]

223. Amorij, J.P.; Hinrichs, W.L.J.; Frijlink, H.W.; Wilschut, J.C.; Huckriede, A. Needle-Free Influenza Vaccination. *Lancet Infect. Dis.* **2010**, *10*, 699–711. [CrossRef]

224. Saluja, V.; Amorij, J.P.; Van Roosmalen, M.L.; Leenhouts, K.; Huckriede, A.; Hinrichs, W.L.J.; Frijlink, H.W. Intranasal Delivery of Influenza Subunit Vaccine Formulated with GEM Particles as an Adjuvant. *AAPS J.* **2010**, *12*, 109–116. [CrossRef]

225. Amin, M.; Jaafari, M.R.; Tafaghodi, M. Impact of Chitosan Coating of Anionic Liposomes on Clearance Rate, Mucosal and Systemic Immune Responses Following Nasal Administration in Rabbits. *Colloids Surf. B Biointerfaces* **2009**, *74*, 225–229. [CrossRef]

226. Tafaghodi, M.; Jaafari, M.; Sajadi Tabassi, S. Nasal Immunization Studies by Cationic, Fusogenic and Cationic-Fusogenic Liposomes Encapsulated with Tetanus Toxoid. *Curr. Drug Deliv.* **2008**, *5*, 108–113. [CrossRef]

227. Slütter, B.; Hagenaars, N.; Jiskoot, W. Rational Design of Nasal Vaccines. *J. Drug Target.* **2008**, *16*, 1–17. [CrossRef] [PubMed]

228. Köping-Höggård, M.; Sánchez, A.; Alonso, M.J. Nanoparticles as Carriers for Nasal Vaccine Delivery. *Expert Rev. Vaccines* **2005**, *4*, 185–196. [CrossRef]

229. Brayden, D.J.; Baird, A.W. Microparticle Vaccine Approaches to Stimulate Mucosal Immunisation. *Microbes Infect.* **2001**, *3*, 867–876. [CrossRef]

230. Mosafer, J.; Sabbaghi, A.H.; Badiee, A.; Dehghan, S.; Tafaghodi, M. Preparation, Characterization and in Vivo Evaluation of Alginate-Coated Chitosan and Trimethylchitosan Nanoparticles Loaded with PR8 Influenza Virus for Nasal Immunization. *Asian J. Pharm. Sci.* **2019**, *14*, 216–221. [CrossRef]

231. Chen, W.; Li, R.; Zhu, S.; Ma, J.; Pang, L.; Ma, B.; Du, L.; Jin, Y. Nasal Timosaponin BII Dually Sensitive in Situ Hydrogels for the Prevention of Alzheimer's Disease Induced by Lipopolysaccharides. *Int. J. Pharm.* **2020**, *578*, 119115. [CrossRef]

232. Fatouh, A.M.; Elshafeey, A.H.; Abdelbary, A. Agomelatine-Based in Situ Gels for Brain Targeting via the Nasal Route: Statistical Optimization, in Vitro, and in Vivo Evaluation. *Drug Deliv.* **2017**, *24*, 1077–1085. [CrossRef]

233. Karimi, S.; Bagher, Z.; Najmoddin, N.; Simorgh, S.; Pezeshki-Modaress, M. Alginate-Magnetic Short Nanofibers 3D Composite Hydrogel Enhances the Encapsulated Human Olfactory Mucosa Stem Cells Bioactivity for Potential Nerve Regeneration Application. *Int. J. Biol. Macromol.* **2021**, *167*, 796–806. [CrossRef] [PubMed]

234. Trapani, A.; Corbo, F.; Agrimi, G.; Ditaranto, N.; Cioffi, N.; Perna, F.; Quivelli, A.; Stefàno, E.; Lunetti, P.; Muscella, A.; et al. Oxidized Alginate Dopamine Conjugate: In Vitro Characterization for Nose-to-Brain Delivery Application. *Materials* **2021**, *14*, 3495. [CrossRef]

235. Haque, S.; Md, S.; Sahni, J.K.; Ali, J.; Baboota, S. Development and Evaluation of Brain Targeted Intranasal Alginate Nanoparticles for Treatment of Depression. *J. Psychiatr. Res.* **2014**, *48*, 1–12. [CrossRef]

236. Caetano, L.A.; Almeida, A.J.; Gonçalves, L.M.D. Effect of Experimental Parameters on Alginate/Chitosan Microparticles for BCG Encapsulation. *Mar. Drugs* **2016**, *14*, 90. [CrossRef] [PubMed]

237. Amokrane, F.; Mohamed, N.; Laraba-djebari, F. Development and Characterization of a New Carrier for Vaccine Delivery Based on Calcium-Alginate Nanoparticles: Safe Immunoprotective Approach against Scorpion Envenoming. *Vaccine* **2016**, *34*, 2692–2699. [CrossRef]

238. Lauzon, M.-A.; Marcos, B.; Faucheux, N. Characterization of Alginate/Chitosan-Based Nanoparticles and Mathematical Modeling of Their SpBMP-9 Release Inducing Neuronal Differentiation of Human SH-SY5Y Cells. *Carbohydr. Polym.* **2018**, *181*, 801–811. [CrossRef] [PubMed]

239. Zhao, L.; Jin, W.; Cruz, J.G.; Marasini, N.; Khalil, Z.G.; Capon, R.J.; Hussein, W.M.; Skwarczynski, M.; Toth, I. Development of Polyelectrolyte Complexes for the Delivery of Peptide-Based Subunit Vaccines Against Group A Streptococcus. *Bioorg. Med. Chem.* **2020**, *10*, 823. [CrossRef]

240. Rodrigues, F.J.; Omura, M.H.; Cedran, M.F.; Dekker, R.F.H.; Barbosa-dekker, A.M.; Garcia, S. Effect of natural polymers on the survival ofLac tobace Pt Ed illus caseiencapsulated in alginate micr Tospheres. *J. Microencapsul.* **2017**, *34*, 431–439. [CrossRef]

241. Ahmed, M.M.; Fatima, F.; Anwer, M.K.; Ibnouf, E.O.; Kalam, M.A.; Alshamsan, A.; Aldawsari, M.F.; Alalaiwe, A.; Ansari, M.J. Formulation and in Vitro Evaluation of Topical Nanosponge-Based Gel Containing Butenafine for the Treatment of Fungal Skin Infection. *Saudi Pharm. J.* **2021**, *29*, 467–477. [CrossRef]

242. Badri, W.; Eddabra, R.; Fessi, H.; Elaissari, A. Biodegradable Polymer Based Nanoparticles: Dermal and Transdermal Drug Delivery. *J. Colloid Sci. Biotechnol.* **2015**, *3*, 141–149. [CrossRef]

243. Tewes, F.; Gobbo, O.L.; Ehrhardt, C.; Healy, A.M. Amorphous Calcium Carbonate Based-Microparticles for Peptide Pulmonary Delivery. *ACS Appl. Mater. Interfaces* **2016**, *8*, 1164–1175. [CrossRef] [PubMed]

244. Shen, Y.B.; Du, Z.; Tang, C.; Guan, Y.X.; Yao, S.J. Formulation of Insulin-Loaded N-Trimethyl Chitosan Microparticles with Improved Efficacy for Inhalation by Supercritical Fluid Assisted Atomization. *Int. J. Pharm.* **2016**, *505*, 223–233. [CrossRef] [PubMed]

245. Shi, K.; Fang, Y.; Kan, Q.; Zhao, J.; Gan, Y.; Liu, Z. Surface Functional Modification of Self-Assembled Insulin Nanospheres for Improving Intestinal Absorption. *Int. J. Biol. Macromol.* **2015**, *74*, 49–60. [CrossRef] [PubMed]

246. Yan, G.; Warner, K.S.; Zhang, J.; Sharma, S.; Gale, B.K. Evaluation Needle Length and Density of Microneedle Arrays in the Pretreatment of Skin for Transdermal Drug Delivery. *Int. J. Pharm.* **2010**, *391*, 7–12. [CrossRef] [PubMed]

247. Vrdoljak, A.; McGrath, M.G.; Carey, J.B.; Draper, S.J.; Hill, A.V.S.; O'Mahony, C.; Crean, A.M.; Moore, A.C. Coated Microneedle Arrays for Transcutaneous Delivery of Live Virus Vaccines. *J. Control. Release* **2012**, *159*, 34–42. [CrossRef] [PubMed]

248. Yu, W.; Jiang, G.; Zhang, Y.; Liu, D.; Xu, B.; Zhou, J. Polymer Microneedles Fabricated from Alginate and Hyaluronate for Transdermal Delivery of Insulin. *Mater. Sci. Eng. C* **2017**, *80*, 187–196. [CrossRef]

249. Lefnaoui, S.; Moulai-Mostefa, N.; Yahoum, M.M.; Gasmi, S.N. Design of Antihistaminic Transdermal Films Based on Alginate–Chitosan Polyelectrolyte Complexes: Characterization and Permeation Studies. *Drug Dev. Ind. Pharm.* **2018**, *44*, 432–443. [CrossRef]

250. Abebe, M.W.; Appiah-Ntiamoah, R.; Kim, H. Gallic Acid Modified Alginate Self-Adhesive Hydrogel for Strain Responsive Transdermal Delivery. *Int. J. Biol. Macromol.* **2020**, *163*, 147–155. [CrossRef]

251. Sgalla, G.; Biffi, A.; Richeldi, L. Idiopathic Pulmonary Fibrosis: Diagnosis, Epidemiology and Natural History. *Respirology* **2016**, *21*, 427–437. [CrossRef]

252. McLean-Tooke, A.; Moore, I.; Lake, F. Idiopathic and Immune-Related Pulmonary Fibrosis: Diagnostic and Therapeutic Challenges. *Clin. Transl. Immunol.* **2019**, *8*, e1086. [CrossRef]

253. Abnoos, M.; Mohseni, M.; Mousavi, S.A.J.; Ashtari, K.; Ilka, R.; Mehravi, B. Chitosan-Alginate Nano-Carrier for Transdermal Delivery of Pirfenidone in Idiopathic Pulmonary Fibrosis. *Int. J. Biol. Macromol.* **2018**, *118*, 1319–1325. [CrossRef]

254. Anirudhan, T.S.; Nair, A.S.; Ss, G. The Role of Biopolymer Matrix Films Derived from Carboxymethyl Cellulose, Sodium Alginate and Polyvinyl Alcohol on the Sustained Transdermal Release of Diltiazem. *Int. J. Biol. Macromol.* **2017**, *107*, 779–789. [CrossRef] [PubMed]

255. Kataria, K.; Gupta, A.; Rath, G.; Mathur, R.B.; Dhakate, S.R. In Vivo Wound Healing Performance of Drug Loaded Electrospun Composite Nanofibers Transdermal Patch. *Int. J. Pharm.* **2014**, *469*, 102–110. [CrossRef] [PubMed]

256. Aktar, B.; Erdal, M.S.; Sagirli, O.; Güngör, S.; Özsoy, Y. Optimization of Biopolymer Based Transdermal Films of Metoclopramide as an Alternative Delivery Approach. *Polymers* **2014**, *6*, 1350–1365. [CrossRef]

257. El-Houssiny, A.S.; Ward, A.A.; Mostafa, D.M.; Abd-El-Messieh, S.L.; Abdel-Nour, K.N.; Darwish, M.M.; Khalil, W.A. Sodium Alginate Nanoparticles as a New Transdermal Vehicle of Glucosamine Sulfate for Treatment of Osteoarthritis. *Eur. J. Nanomedicine* **2017**, *9*, 105–114. [CrossRef]

258. Zhang, Y.; Jiang, G.; Yu, W.; Liu, D.; Xu, B. Microneedles Fabricated from Alginate and Maltose for Transdermal Delivery of Insulin on Diabetic Rats. *Mater. Sci. Eng. C* **2018**, *85*, 18–26. [CrossRef]

259. Ahmed, T.A.; El-Say, K.M. Development of Alginate-Reinforced Chitosan Nanoparticles Utilizing W/O Nanoemulsification/Internal Crosslinking Technique for Transdermal Delivery of Rabeprazole. *Life Sci.* **2014**, *110*, 35–43. [CrossRef]

260. Lai, W.; Tang, R.; Wong, W. Ionically Crosslinked Complex Gels Loaded with Oleic Acid-Containing Vesicles for Transdermal Drug Delivery. *Pharmaceutics* **2020**, *12*, 725. [CrossRef]

261. Giacone, D.V.; Dartora, V.F.M.C.; De Matos, J.K.R.; Passos, J.S.; Miranda, D.A.G.; De Oliveira, E.A.; Silveira, E.R.; Costa-lotufo, L.V.; Maria-engler, S.S.; Lopes, L.B. International Journal of Biological Macromolecules Effect of Nanoemulsion Modi Fi Cation with Chitosan and Sodium Alginate on the Topical Delivery and Ef Fi Cacy of the Cytotoxic Agent Piplartine in 2D and 3D Skin Cancer Models. *Int. J. Biol. Macromol.* **2020**, *165*, 1055–1065. [CrossRef]

262. Esposito, L.; Barbosa, A.I.; Moniz, T.; Lima, S.C.; Costa, P.; Celia, C.; Reis, S. Design and Characterization of Sodium Alginate and Poly (Vinyl) Alcohol Hydrogels for Enhanced Skin Delivery of Quercetin. *Pharmaceutics* **2020**, *12*, 1149. [CrossRef]

263. Ng, S.F.; Tan, L.S.; Buang, F. Transdermal Anti-Inflammatory Activity of Bilayer Film Containing Olive Compound Hydroxytyrosol: Physical Assessment, in Vivo Dermal Safety and Efficacy Study in Freund's Adjuvant-Induced Arthritic Rat Model. *Drug Dev. Ind. Pharm.* **2017**, *43*, 108–119. [CrossRef] [PubMed]

264. Sadashivaiah, R.; Babu, B.K.S. Role of Sodium L-Cysteine Alginate Conjugate and Isopropyl Myristate to Enhance the Permeation Enhancing Activity of BCS Class III Drug from TDDS.; Optimization by Central Composite Design and in Vivo Pharmacokinetics Study. *Drug Dev. Ind. Pharm.* **2020**, *46*, 1427–1442. [CrossRef]

265. Anirudhan, T.S.; Nair, A.S.; Bino, S.J. Nanoparticle Assisted Solvent Selective Transdermal Combination Therapy of Curcumin and 5-Flurouracil for Efficient Cancer Treatment. *Carbohydr. Polym.* **2017**, *173*, 131–142. [CrossRef]

266. George, M.; Abraham, T.E. Polyionic Hydrocolloids for the Intestinal Delivery of Protein Drugs: Alginate and Chitosan-a Review. *J. Control. Release* **2006**, *114*, 1–14. [CrossRef] [PubMed]

267. Khutoryanskiy, V.V. Advances in Mucoadhesion and Mucoadhesive Polymers. *Macromol. Biosci.* **2011**, *11*, 748–764. [CrossRef]

268. Shah, J.P.; Gil, Z. Current Concepts in Management of Oral Cancer-Surgery. *Oral Oncol.* **2009**, *45*, 394–401. [CrossRef] [PubMed]

269. Shtenberg, Y.; Goldfeder, M.; Prinz, H.; Shainsky, J.; Ghantous, Y.; Abu El-Naaj, I.; Schroeder, A.; Bianco-Peled, H. Mucoadhesive Alginate Pastes with Embedded Liposomes for Local Oral Drug Delivery. *Int. J. Biol. Macromol.* **2018**, *111*, 62–69. [CrossRef]

270. Saraf, S.; Jain, S.; Sahoo, R.N.; Mallick, S. Lipopolysaccharide Derived Alginate Coated Hepatitis B Antigen Loaded Chitosan Nanoparticles for Oral Mucosal Immunization. *Int. J. Biol. Macromol.* **2020**, *154*, 466–476. [CrossRef] [PubMed]

271. Akram, S.; Noreen, S. International Journal of Biological Macromolecules Linum Usitatissimum Seed Mucilage-Alginate Mucoadhesive Microspheres of Metformin HCl: Fabrication, Characterization and Evaluation. *Int. J. Biol. Macromol.* **2020**, *155*, 358–368. [CrossRef]

272. Kilicarslan, M.; Ilhan, M.; Inal, O.; Orhan, K. European Journal of Pharmaceutical Sciences Preparation and Evaluation of Clindamycin Phosphate Loaded Chitosan / Alginate Polyelectrolyte Complex Fi Lm as Mucoadhesive Drug Delivery System for Periodontal Therapy. *Eur. J. Pharm. Sci.* **2018**, *123*, 441–451. [CrossRef] [PubMed]

273. Gonçalves, V.S.S.; Gurikov, P.; Poejo, J.; Matias, A.A.; Heinrich, S.; Duarte, C.M.M.; Smirnova, I. Alginate-Based Hybrid Aerogel Microparticles for Mucosal Drug Delivery. *Eur. J. Pharm. Biopharm.* **2016**, *107*, 160–170. [CrossRef]

274. Kaur, I.P.; Kakkar, S. Topical Delivery of Antifungal Agents. *Expert Opin. Drug Deliv.* **2010**, *7*, 1303–1327. [CrossRef]

275. Pemán, J.; Salavert, M. Epidemiología General de La Enfermedad Fúngica Invasora. *Enferm. Infecc. Y Microbiol. Clínica* **2012**, *30*, 90–98. [CrossRef]

276. Croy, S.R.; Kwon, G.S. The Effects of Pluronic Block Copolymers on the Aggregation State of Nystatin. *J. Control. Release* **2004**, *95*, 161–171. [CrossRef]

277. Martín-Villena, M.J.; Fernández-Campos, F.; Calpena-Campmany, A.C.; Bozal-De Febrer, N.; Ruiz-Martínez, M.A.; Clares-Naveros, B. Novel Microparticulate Systems for the Vaginal Delivery of Nystatin: Development and Characterization. *Carbohydr. Polym.* **2013**, *94*, 1–11. [CrossRef] [PubMed]

278. Martín, M.J.; Calpena, A.C.; Fernández, F.; Mallandrich, M.; Gálvez, P.; Clares, B. Development of Alginate Microspheres as Nystatin Carriers for Oral Mucosa Drug Delivery. *Carbohydr. Polym.* **2015**, *117*, 140–149. [CrossRef]

279. Gennari, C.G.M.; Sperandeo, P.; Polissi, A.; Minghetti, P.; Cilurzo, F. Lysozyme Mucoadhesive Tablets Obtained by Freeze-Drying. *J. Pharm. Sci.* **2019**, *108*, 3667–3674. [CrossRef]

280. Wang, Y.; Li, H.; Wang, L.; Han, J.; Yang, Y.; Fu, T.; Qiao, H.; Wang, Z.; Li, J. Colloids and Surfaces B: Biointerfaces Mucoadhesive Nanocrystal-in-Microspheres with High Drug Loading Capacity for Bioavailability Enhancement of Silybin. *Colloids Surf. B Biointerfaces* **2020**, *198*, 111461. [CrossRef]

281. El-feky, G.S.; Abdulmaguid, R.F.; Zayed, G.M.; Kamel, R.; Abdulmaguid, R.F.; Zayed, G.M.; Kamel, R. Mucosal Co-Delivery of Ketorolac and Lidocaine Using Polymeric Wafers for Dental Application. *Drug Deliv.* **2018**, *25*, 35–42. [CrossRef] [PubMed]

282. Okeke, O.C.; Boateng, J.S. Composite HPMC and Sodium Alginate Based Buccal Formulations for Nicotine Replacement Therapy. *Int. J. Biol. Macromol.* **2016**, *91*, 31–44. [CrossRef]

283. Shtenberg, Y.; Goldfeder, M.; Schroeder, A.; Bianco-Peled, H. *Alginate Modified with Maleimide-Terminated PEG as Drug Carriers with Enhanced Mucoadhesion*; Elsevier Ltd.: Amsterdam, The Netherlands, 2017; Volume 175, ISBN 0014350580.

284. Jang, C.H.; Ahn, S.H.; Kim, G.H. Antifibrotic Effect of Dexamethasone/Alginate-Coated Silicone Sheet in the Abraded Middle Ear Mucosa. *Int. J. Biol. Macromol.* **2016**, *93*, 1612–1619. [CrossRef] [PubMed]

285. Singh, B.; Kumar, A. Rohit Synthesis and Characterization of Alginate and Sterculia Gum Based Hydrogel for Brain Drug Delivery Applications. *Int. J. Biol. Macromol.* **2020**, *148*, 248–257. [CrossRef]

286. Bera, H.; Ippagunta, S.R.; Kumar, S.; Vangala, P. Core-Shell Alginate-Ghatti Gum Modified Montmorillonite Composite Matrices for Stomach-Specific Flurbiprofen Delivery. *Mater. Sci. Eng. C* **2017**, *76*, 715–726. [CrossRef]

287. Boppana, R.; Yadaorao Raut, S.; Krishna Mohan, G.; Sa, B.; Mutalik, S.; Reddy, K.R.; Das, K.K.; Biradar, M.S.; Kulkarni, R.V. Novel PH-Sensitive Interpenetrated Network Polyspheres of Polyacrylamide-g-Locust Bean Gum and Sodium Alginate for Intestinal Targeting of Ketoprofen: In Vitro and in Vivo Evaluation. *Colloids Surf. B Biointerfaces* **2019**, *180*, 362–370. [CrossRef]

288. Ivanovska, T.P.; Mladenovska, K.; Zhivikj, Z.; Pavlova, M.J.; Gjurovski, I.; Ristoski, T.; Petrushevska-Tozi, L. Synbiotic Loaded Chitosan-Ca-Alginate Microparticles Reduces Inflammation in the TNBS Model of Rat Colitis. *Int. J. Pharm.* **2017**, *527*, 126–134. [CrossRef]

289. Saralkar, P.; Dash, A.K. Alginate Nanoparticles Containing Curcumin and Resveratrol: Preparation, Characterization, and In Vitro Evaluation Against DU145 Prostate Cancer Cell Line. *AAPS Pharmscitech* **2017**, *18*, 2814–2823. [CrossRef]

290. Yang, H.; Chen, Y.; Chen, Z.; Geng, Y.; Xie, X.; Shen, X.; Li, T.; Li, S.; Wu, C.; Liu, Y. Chemo-Photodynamic Combined Gene Therapy and Dual-Modal Cancer Imaging Achieved by PH-Responsive Alginate/Chitosan Multilayer-Modified Magnetic Mesoporous Silica Nanocomposites. *Biomater. Sci.* **2017**, *5*, 1001–1013. [CrossRef]

291. Wang, Q.S.; Gao, L.N.; Zhu, X.N.; Zhang, Y.; Zhang, C.N.; Xu, D.; Cui, Y.L. Co-Delivery of Glycyrrhizin and Doxorubicin by Alginate Nanogel Particles Attenuates the Activation of Macrophage and Enhances the Therapeutic Efficacy for Hepatocellular Carcinoma. *Theranostics* **2019**, *9*, 6239–6255. [CrossRef]

292. Lian, Y.; Wang, X.; Guo, P.; Li, Y.; Raza, F.; Su, J.; Qiu, M. Erythrocyte Membrane-Coated Arsenic Trioxide-Loaded Sodium Alginate Nanoparticles for Tumor Therapy. *Pharmaceutics* **2020**, *12*, 21. [CrossRef]

293. Karabasz, A.; Lachowicz, D.; Karewicz, A.; Mezyk-Kopec, R.; Stalińska, K.; Werner, E.; Cierniak, A.; Dyduch, G.; Bereta, J.; Bzowska, M. Analysis of Toxicity and Anticancer Activity of Micelles of Sodium Alginate-Curcumin. *Int. J. Nanomed.* **2019**, *14*, 7249–7262. [CrossRef] [PubMed]

294. Sun, T.; Guo, X.; Zhong, R.; Wang, C.; Liu, H.; Li, H.; Ma, L.; Guan, J.; You, C.; Tian, M. Interactions of Alginate-Deferoxamine Conjugates With Blood Components and Their Antioxidation in the Hemoglobin Oxidation Model. *Front. Bioeng. Biotechnol.* **2020**, *8*, 53. [CrossRef] [PubMed]

295. Alvarez-Berrios, M.P.; Aponte-Reyes, L.M.; Diaz-Figueroa, L.; Vivero-Escoto, J.; Johnston, A.; Sanchez-Rodriguez, D. Preparation and in Vitro Evaluation of Alginate Microparticles Containing Amphotericin B for the Treatment of Candida Infections. *Int. J. Biomater.* **2020**, *2020*, 11–16. [CrossRef] [PubMed]

296. Patil, S.S.; Nune, K.C.; Misra, R.D.K. Alginate/Poly(Amidoamine) Injectable Hybrid Hydrogel for Cell Delivery. *J. Biomater. Appl.* **2018**, *33*, 295–314. [CrossRef] [PubMed]

297. Najafabadi, A.H.; Azodi-Deilami, S.; Abdouss, M.; Payravand, H.; Farzaneh, S. Synthesis and Evaluation of Hydroponically Alginate Nanoparticles as Novel Carrier for Intravenous Delivery of Propofol. *J. Mater. Sci. Mater. Med.* **2015**, *26*, 145. [CrossRef] [PubMed]

298. Feng, W.; Nie, W.; He, C.; Zhou, X.; Chen, L.; Qiu, K.; Wang, W.; Yin, Z. Effect of PH-Responsive Alginate/Chitosan Multilayers Coating on Delivery Efficiency, Cellular Uptake and Biodistribution of Mesoporous Silica Nanoparticles Based Nanocarriers. *ACS Appl. Mater. Interfaces* **2014**, *6*, 8447–8460. [CrossRef] [PubMed]

299. Onishi, H.; Mizuno, K.; Ikeuchi-Takahashi, Y.; Hattori, Y. Targeting Potential of Alginate-Glycyl-Prednisolone Conjugate Nanogel to Inflamed Joints in Rats with Adjuvant-Induced Arthritis. *J. Drug Target.* **2021**, *29*, 892–899. [CrossRef] [PubMed]

300. Sudhakar, Y.; Kuotsu, K.; Bandyopadhyay, A.K. Buccal Bioadhesive Drug Delivery—A Promising Option for Orally Less Efficient Drugs. *J. Control. Release* **2006**, *114*, 15–40. [CrossRef] [PubMed]

301. Laffleur, F.; Küppers, P. Adhesive Alginate for Buccal Delivery in Aphthous Stomatitis. *Carbohydr. Res.* **2019**, *477*, 51–57. [CrossRef]

302. Prakash, J.; Kumar, T.S.; Venkataprasanna, K.S.; Niranjan, R.; Kaushik, M.; Samal, D.B.; Venkatasubbu, G.D. PVA/Alginate/ Hydroxyapatite Films for Controlled Release of Amoxicillin for the Treatment of Periodontal Defects. *Appl. Surf. Sci.* **2019**, *495*, 143543. [CrossRef]

303. Shim, B.-S.; Choi, Y.; Cheon, I.S.; Song, M.K. Sublingual Delivery of Vaccines for the Induction of Mucosal Immunity. *Immune Netw.* **2013**, *13*, 81. [CrossRef]

304. Hanson, S.M.; Singh, S.; Tabet, A.; Sastry, K.J.; Michael Barry, C.W. Mucoadhesive Wafers Composed of Binary Polymer Blends for Sublingual Delivery and Preservation of Protein Vaccines. *J. Control. Release* **2021**, *330*, 427–437. [CrossRef]

305. Hussein, N.; Omer, H.; Ismael, A.; Albed Alhnan, M.; Elhissi, A.; Ahmed, W. Spray-Dried Alginate Microparticles for Potential Intranasal Delivery of Ropinirole Hydrochloride: Development, Characterization and Histopathological Evaluation. *Pharm. Dev. Technol.* **2020**, *25*, 290–299. [CrossRef]

306. Di Martino, A.; Trusova, M.E.; Postnikov, P.S.; Sedlarik, V. Folic Acid-Chitosan-Alginate Nanocomplexes for Multiple Delivery of Chemotherapeutic Agents. *J. Drug Deliv. Sci. Technol.* **2018**, *47*, 67–76. [CrossRef]

307. Chen, T.; Li, S.; Zhu, W.; Liang, Z.; Zeng, Q. Self-Assembly PH-Sensitive Chitosan/Alginate Coated Polyelectrolyte Complexes for Oral Delivery of Insulin. *J. Microencapsul.* **2019**, *36*, 96–107. [CrossRef]

308. Wang, F.; He, S.; Chen, B. Retinoic Acid-Loaded Alginate Microspheres as a Slow Release Drug Delivery Carrier for Intravitreal Treatment. *Biomed. Pharmacother.* **2018**, *97*, 722–728. [CrossRef]

309. Faidi, A.; Lassoued, M.A.; Becheikh, M.E.H.; Touati, M.; Stumbé, J.F.; Farhat, F. Application of Sodium Alginate Extracted from a Tunisian Brown Algae Padina Pavonica for Essential Oil Encapsulation: Microspheres Preparation, Characterization and in Vitro Release Study. *Int. J. Biol. Macromol.* **2019**, *136*, 386–394. [CrossRef] [PubMed]

310. Sohail, R.; Abbas, S.R. Evaluation of Amygdalin-Loaded Alginate-Chitosan Nanoparticles as Biocompatible Drug Delivery Carriers for Anticancerous Efficacy. *Int. J. Biol. Macromol.* **2020**, *153*, 36–45. [CrossRef]

311. Kassem, A.A.; Ahmed, D.; Issa, E.; Kotry, G.S. Thiolated Alginate-Based Multiple Layer Mucoadhesive Films of Metformin Forintra-Pocket Local Delivery: In Vitro Characterization and Clinical Assessment. *Drug Dev. Ind. Pharm.* **2017**, *43*, 120–131. [CrossRef]

312. Maity, S.; Mukhopadhyay, P.; Kundu, P.P.; Chakraborti, A.S. Alginate Coated Chitosan Core-Shell Nanoparticles for Efficient Oral Delivery of Naringenin in Diabetic Animals—An in Vitro and in Vivo Approach. *Carbohydr. Polym.* **2017**, *170*, 124–132. [CrossRef]

313. de Castro Spadari, C.; Lopes, L.B.; Ishida, K. Alginate Nanoparticles as Non-Toxic Delivery System for Miltefosine in the Treatment of Candidiasis and Cryptococcosis. *Int. J. Nanomed.* **2019**, *14*, 5187–5199. [CrossRef]

314. Yuan, Y.; Xu, X.; Gong, J.; Mu, R.; Li, Y.; Wu, C.; Pang, J. Fabrication of Chitosan-Coated Konjac Glucomannan/Sodium Alginate/Graphene Oxide Microspheres with Enhanced Colon-Targeted Delivery. *Int. J. Biol. Macromol.* **2019**, *131*, 209–217. [CrossRef]

315. Sorasitthiyanukarn, F.N.; Muangnoi, C.; Rojsitthisak, P.; Rojsitthisak, P. Chitosan-Alginate Nanoparticles as Effective Oral Carriers to Improve the Stability, Bioavailability, and Cytotoxicity of Curcumin Diethyl Disuccinate. *Carbohydr. Polym.* **2020**, *256*, 117426. [CrossRef]

316. Prabha, G.; Raj, V. Sodium Alginate–Polyvinyl Alcohol–Bovin Serum Albumin Coated Fe_3O_4 Nanoparticles as Anticancer Drug Delivery Vehicle: Doxorubicin Loading and in Vitro Release Study and Cytotoxicity to HepG2 and L02 Cells. *Mater. Sci. Eng. C* **2017**, *79*, 410–422. [CrossRef]

317. Thanh Uyen, N.T.; Abdul Hamid, Z.A.; Thi, L.A.; Ahmad, N.B. Synthesis and Characterization of Curcumin Loaded Alginate Microspheres for Drug Delivery. *J. Drug Deliv. Sci. Technol.* **2020**, *58*, 101796. [CrossRef]

318. Yu, X.; Wen, T.; Cao, P.; Shan, L.; Li, L. Alginate-Chitosan Coated Layered Double Hydroxide Nanocomposites for Enhanced Oral Vaccine Delivery. *J. Colloid Interface Sci.* **2019**, *556*, 258–265. [CrossRef]

319. Doniparthi, J.; B, J.J. Novel Tamarind Seed Gum-Alginate Based Multi-Particulates for Sustained Release of Dalfampridine Using Response Surface Methodology. *Int. J. Biol. Macromol.* **2020**, *144*, 725–741. [CrossRef]

320. Wang, Q.S.; Wang, G.F.; Zhou, J.; Gao, L.N.; Cui, Y.L. Colon Targeted Oral Drug Delivery System Based on Alginate-Chitosan Microspheres Loaded with Icariin in the Treatment of Ulcerative Colitis. *Int. J. Pharm.* **2016**, *515*, 176–185. [CrossRef]

321. Abo El-Ela, F.I.; Hussein, K.H.; El-Banna, H.A.; Gamal, A.; Rouby, S.; Menshawy, A.M.S.; EL-Nahass, E.L.S.; Anwar, S.; Zeinhom, M.M.A.; Salem, H.F.; et al. Treatment of Brucellosis in Guinea Pigs via a Combination of Engineered Novel PH-Responsive Curcumin Niosome Hydrogel and Doxycycline-Loaded Chitosan–Sodium Alginate Nanoparticles: An In Vitro and In Vivo Study. *AAPS PharmSciTech* **2020**, *22*, 12. [CrossRef]

322. Balanč, B.; Trifković, K.; Đorđević, V.; Marković, S.; Pjanović, R.; Nedović, V.; Bugarski, B. Novel Resveratrol Delivery Systems Based on Alginate-Sucrose and Alginate-Chitosan Microbeads Containing Liposomes. *Food Hydrocoll.* **2016**, *61*, 832–842. [CrossRef]

323. Scholz, M.; Reske, T.; Böhmer, F.; Hornung, A.; Grabow, N.; Lang, H. In Vitro Chlorhexidine Release from Alginate Based Microbeads for Periodontal Therapy. *PLoS ONE* **2017**, *12*, e0185562. [CrossRef]

324. Hamed, S.F.; Hashim, A.F.; Abdel Hamid, H.A.; Abd-Elsalam, K.A.; Golonka, I.; Musiał, W.; El-Sherbiny, I.M. Edible Alginate/Chitosan-Based Nanocomposite Microspheres as Delivery Vehicles of Omega-3 Rich Oils. *Carbohydr. Polym.* **2020**, *239*, 116201. [CrossRef] [PubMed]

325. Ferreira, N.N.; Caetano, B.L.; Boni, F.I.; Sousa, F.; Magnani, M.; Sarmento, B.; Ferreira Cury, B.S.; Daflon Gremião, M.P. Alginate-Based Delivery Systems for Bevacizumab Local Therapy: In Vitro Structural Features and Release Properties. *J. Pharm. Sci.* **2019**, *108*, 1559–1568. [CrossRef]

326. Sepúlveda-Rivas, S.; Fritz, H.F.; Valenzuela, C.; Santiviago, C.A.; Morales, J.O. Development of Novel EE/Alginate Polyelectrolyte Complex Nanoparticles for Lysozyme Delivery: Physicochemical Properties and in Vitro Safety. *Pharmaceutics* **2019**, *11*, 103. [CrossRef]

327. Rassu, G.; Salis, A.; Porcu, E.P.; Giunchedi, P.; Roldo, M.; Gavini, E. Composite Chitosan/Alginate Hydrogel for Controlled Release of Deferoxamine: A System to Potentially Treat Iron Dysregulation Diseases. *Carbohydr. Polym.* **2016**, *136*, 1338–1347. [CrossRef] [PubMed]

328. Kim, S.; Jung, S. Biocompatible and Self-Recoverable Succinoglycan Dialdehyde-Crosslinked Alginate Hydrogels for PH-Controlled Drug Delivery. *Carbohydr. Polym.* **2020**, *250*, 116934. [CrossRef]

329. Khan, S.; Boateng, J.S.; Mitchell, J.; Trivedi, V. Formulation, Characterisation and Stabilisation of Buccal Films for Paediatric Drug Delivery of Omeprazole. *AAPS PharmSciTech* **2015**, *16*, 800–810. [CrossRef]

330. Abdul Rasool, B.K.; Khalifa, A.Z.; Abu-Gharbieh, E.; Khan, R. Employment of Alginate Floating in Situ Gel for Controlled Delivery of Celecoxib: Solubilization and Formulation Studies. *Biomed. Res. Int.* **2020**, *2020*, 1879125. [CrossRef]

331. Supramaniam, J.; Adnan, R.; Haida, N.; Kaus, M.; Bushra, R. Magnetic Nanocellulose Alginate Hydrogel Beads as Potential Drug Delivery System. *Int. J. Biol. Macromol.* **2018**, *118*, 640–648. [CrossRef] [PubMed]

332. Chen, X.; Fan, M.; Tan, H.; Ren, B.; Yuan, G.; Jia, Y.; Li, J. Materials Science & Engineering C Magnetic and Self-Healing Chitosan-Alginate Hydrogel Encapsulated Gelatin Microspheres via Covalent Cross-Linking for Drug Delivery. *Mater. Sci. Eng. C* **2019**, *101*, 619–629. [CrossRef]

333. Sheng, Y.; Gao, J.; Yin, Z.-Z.; Kang, J.; Kong, Y. Dual-Drug Delivery System Based on the Hydrogels of Alginate and Sodium Carboxymethyl Cellulose for Colorectal Cancer Treatment. *Carbohydr. Polym.* **2021**, *269*, 118325. [CrossRef] [PubMed]

334. Criado-Gonzalez, M.; Fernandez-Gutierrez, M.; San Roman, J.; Mijangos, C.; Hernández, R. Local and Controlled Release of Tamoxifen from Multi (Layer-by-Layer) Alginate/Chitosan Complex Systems. *Carbohydr. Polym.* **2019**, *206*, 428–434. [CrossRef] [PubMed]

335. Hoque, J.; Haldar, J. Direct Synthesis of Dextran-Based Antibacterial Hydrogels for Extended Release of Biocides and Eradication of Topical Biofilms. *ACS Appl. Mater. Interfaces* **2017**, *9*, 15975–15985. [CrossRef] [PubMed]

336. Kujath, P. Wounds–From Physiology to Wound Dressing: In Reply. *Dtsch. Arztebl. Int.* **2008**, *105*, 239–248. [CrossRef]

337. Fatima, F.; Aldawsari, M.F.; Ahmed, M.M.; Anwer, M.K.; Naz, M.; Ansari, M.J.; Hamad, A.M.; Zafar, A.; Jafar, M. Green Synthesized Silver Nanoparticles Using Tridax Procumbens for Topical Application: Excision Wound Model and Histopathological Studies. *Pharmaceutics* **2021**, *13*, 1754. [CrossRef] [PubMed]

338. Mogoşanu, G.D.; Grumezescu, A.M. Natural and Synthetic Polymers for Wounds and Burns Dressing. *Int. J. Pharm.* **2014**, *463*, 127–136. [CrossRef] [PubMed]

339. Vasconcelos, A.; Cavaco-Paulo, A. Wound Dressings for a Proteolytic-Rich Environment. *Appl. Microbiol. Biotechnol.* **2011**, *90*, 445–460. [CrossRef]

340. Qin, Y. Advanced Wound Dressings. *J. Text. Inst.* **2001**, *92*, 127–138. [CrossRef]

341. Anumolu, S.S.; Menjoge, A.R.; Deshmukh, M.; Gerecke, D.; Stein, S.; Laskin, J.; Sinko, P.J. Doxycycline Hydrogels with Reversible Disulfide Crosslinks for Dermal Wound Healing of Mustard Injuries. *Biomaterials* **2011**, *32*, 1204–1217. [CrossRef] [PubMed]

342. Czaja, W.K.; Young, D.J.; Kawecki, M.; Brown, R.M. The Future Prospects of Microbial Cellulose in Biomedical Applications. *Biomacromolecules* **2007**, *8*, 1–12. [CrossRef] [PubMed]

343. Varaprasad, K.; Jayaramudu, T.; Kanikireddy, V.; Toro, C.; Sadiku, E.R. Alginate-Based Composite Materials for Wound Dressing Application:A Mini Review. *Carbohydr. Polym.* **2020**, *236*, 116025. [CrossRef]

344. Bouhadir, K.H.; Lee, K.Y.; Alsberg, E.; Damm, K.L.; Anderson, K.W.; Mooney, D.J. Degradation of Partially Oxidized Alginate and Its Potential Application for Tissue Engineering. *Biotechnol. Prog.* **2001**, *17*, 945–950. [CrossRef]

345. Kong, H.J.; Kaigler, D.; Kim, K.; Mooney, D.J. Controlling Rigidity and Degradation of Alginate Hydrogels via Molecular Weight Distribution. *Biomacromolecules* **2004**, *5*, 1720–1727. [CrossRef]

346. Gong, X.; Dang, G.; Guo, J.; Liu, Y.; Gong, Y. A Sodium Alginate/Feather Keratin Composite Fiber with Skin-Core Structure as the Carrier for Sustained Drug Release. *Int. J. Biol. Macromol.* **2020**, *155*, 386–392. [CrossRef]

347. Ji, M.; Chen, H.; Yan, Y.; Ding, Z.; Ren, H.; Zhong, Y. Effects of Tricalcium Silicate/Sodium Alginate/Calcium Sulfate Hemihydrate Composite Cements on Osteogenic Performances in Vitro and in Vivo. *J. Biomater. Appl.* **2020**, *34*, 1422–1436. [CrossRef]

348. Choe, G.; Oh, S.; Seok, J.M.; Park, S.A.; Lee, J.Y. Graphene Oxide/Alginate Composites as Novel Bioinks for Three-Dimensional Mesenchymal Stem Cell Printing and Bone Regeneration Applications. *Nanoscale* **2019**, *11*, 23275–23285. [CrossRef]

349. Qin, Y.; Hu, H.; Luo, A. The Conversion of Calcium Alginate Fibers into Alginic Acid Fibers and Sodium Alginate Fibers. *J. Appl. Polym. Sci.* **2006**, *101*, 4216–4221. [CrossRef]

350. Miranda, M.E.S.; Marcolla, C.; Rodrígues, C.A.; Wilhelm, H.M.; Sierakowski, M.R.; Bresolin, T.M.B.; de Freitas, R.A. Chitosan and N-Carboxymethylchitosan: I. The Role of N-Carboxymethylation of Chitosan in the Thermal Stability and Dynamic Mechanical Properties of Its Films. *Polym. Int.* **2006**, *55*, 961–969. [CrossRef]

351. Wang, T.; Zheng, Y.; Shi, Y.; Zhao, L. PH-Responsive Calcium Alginate Hydrogel Laden with Protamine Nanoparticles and Hyaluronan Oligosaccharide Promotes Diabetic Wound Healing by Enhancing Angiogenesis and Antibacterial Activity. *Drug. Deliv. Transl. Res.* **2019**, *9*, 227–239. [CrossRef]

352. Luiza, A.; Pires, R.; De Azevedo, L.; Dias, A.M.A.; De Sousa, H.C.; Moraes, Â.M.; Braga, M.E.M. Materials Science & Engineering C Towards Wound Dressings with Improved Properties: E Ff Ects of Poly (Dimethylsiloxane) on Chitosan-Alginate Fi Lms Loaded with Thymol and Beta- Carotene. *Mater. Sci. Eng. C* **2018**, *93*, 595–605. [CrossRef]

353. Bergonzi, C.; D'Ayala, G.G.; Elviri, L.; Laurienzo, P.; Bandiera, A.; Catanzano, O. Alginate/Human Elastin-like Polypeptide Composite Films with Antioxidant Properties for Potential Wound Healing Application. *Int. J. Biol. Macromol.* **2020**, *164*, 586–596. [CrossRef] [PubMed]

354. Feng, X.; Zhang, X.; Li, S.; Zheng, Y.; Shi, X.; Li, F.; Guo, S.; Yang, J. Preparation of Aminated Fish Scale Collagen and Oxidized Sodium Alginate Hybrid Hydrogel for Enhanced Full-Thickness Wound Healing. *Int. J. Biol. Macromol.* **2020**, *164*, 626–637. [CrossRef]

355. Choudhary, M.; Chhabra, P.; Tyagi, A.; Singh, H. Scar Free Healing of Full Thickness Diabetic Wounds: A Unique Combination of Silver Nanoparticles as Antimicrobial Agent, Calcium Alginate Nanoparticles as Hemostatic Agent, Fresh Blood as Nutrient/Growth Factor Supplier and Chitosan as Base Matrix. *Int. J. Biol. Macromol.* **2021**, *178*, 41–52. [CrossRef]

356. Sharma, A.; Puri, V.; Kumar, P.; Singh, I. Rifampicin-Loaded Alginate-Gelatin Fibers Incorporated within Transdermal Films as a Fiber-in-Film System for Wound Healing Applications. *Membranes* **2021**, *11*, 7. [CrossRef]

357. Fahmy, H.M. Hyaluronic Acid / Na-Alginate Fi Lms as Topical Bioactive Wound Dressings. *Eur. Polym. J.* **2018**, *109*, 101–109. [CrossRef]

358. Sharma, A.; Mittal, A.; Puri, V.; Kumar, P.; Singh, I. Curcumin-Loaded, Alginate–Gelatin Composite Fibers for Wound Healing Applications. *3 Biotech.* **2020**, *10*, 464. [CrossRef]

359. Pagano, C.; Puglia, D.; Luzi, F.; Di Michele, A.; Scuota, S.; Primavilla, S.; Ceccarini, M.R.; Beccari, T.; Iborra, C.A.V.; Ramella, D.; et al. Development and Characterization of Xanthan Gum and Alginate Based Bioadhesive Film for Pycnogenol Topical Use in Wound Treatment. *Pharmaceutics* **2021**, *13*, 324. [CrossRef]

360. Akbar, M.U.; Zia, K.M.; Akash, M.S.H.; Nazir, A.; Zuber, M.; Ibrahim, M. In-Vivo Anti-Diabetic and Wound Healing Potential of Chitosan/Alginate/Maltodextrin/Pluronic-Based Mixed Polymeric Micelles: Curcumin Therapeutic Potential. *Int. J. Biol. Macromol.* **2018**, *120*, 2418–2430. [CrossRef]

361. Shahzad, A.; Khan, A.; Afzal, Z.; Umer, M.F.; Khan, J.; Khan, G.M. Formulation Development and Characterization of Cefazolin Nanoparticles-Loaded Cross-Linked Films of Sodium Alginate and Pectin as Wound Dressings. *Int. J. Biol. Macromol.* **2019**, *124*, 255–269. [CrossRef]

362. anne Johnson, K.; Muzzin, N.; Toufanian, S.; Slick, R.A.; Lawlor, M.W.; Seifried, B.; Moquin, P.; Latulippe, D.; Hoare, T. Drug-Impregnated, Pressurized Gas Expanded Liquid-Processed Alginate Hydrogel Scaffolds for Accelerated Burn Wound Healing. *Acta Biomater.* **2020**, *112*, 101–111. [CrossRef]

363. Jiang, X.; Zhang, Z.; Zuo, J.; Wu, C.; Zha, L.; Xu, Y.; Wang, S.; Shi, J.; Liu, X.H.; Zhang, J.; et al. Novel Cannabidiol−carbamate Hybrids as Selective BuChE Inhibitors: Docking-Based Fragment Reassembly for the Development of Potential Therapeutic Agents against Alzheimer's Disease. *Eur. J. Med. Chem.* **2021**, *223*, 113735. [CrossRef]

364. Rezaei, M.; Nikkhah, M.; Mohammadi, S.; Bahrami, S.H.; Sadeghizadeh, M. Nano-Curcumin/Graphene Platelets Loaded on Sodium Alginate/Polyvinyl Alcohol Fibers as Potential Wound Dressing. *J. Appl. Polym. Sci.* **2021**, *138*, 50884. [CrossRef]

365. Asadi, L.; Mokhtari, J.; Abbasi, M. An Alginate–PHMB–AgNPs Based Wound Dressing Polyamide Nanocomposite with Improved Antibacterial and Hemostatic Properties. *J. Mater. Sci. Mater. Med.* **2021**, *32*, 7. [CrossRef] [PubMed]

366. He, Y.; Zhao, W.; Dong, Z.; Ji, Y.; Li, M.; Hao, Y.; Zhang, D.; Yuan, C.; Deng, J.; Zhao, P.; et al. A Biodegradable Antibacterial Alginate/Carboxymethyl Chitosan/Kangfuxin Sponges for Promoting Blood Coagulation and Full-Thickness Wound Healing. *Int. J. Biol. Macromol.* **2021**, *167*, 182–192. [CrossRef]

367. Fan, Y.; Wu, W.; Lei, Y.; Gaucher, C.; Pei, S.; Zhang, J.; Xia, X. Edaravone-Loaded Alginate-Based Nanocomposite Hydrogel Accelerated Chronic Wound Healing in Diabetic Mice. *Mar Drugs* **2019**, *17*, 285. [CrossRef]

368. Mobaraki, M.; Bizari, D.; Soltani, M.; Khshmohabat, H.; Raahemifar, K.; Amirdehi, M.A. The Effects of Curcumin Nanoparticles Incorporated into Collagen-Alginate Scaffold on Wound Healing of Skin Tissue in Trauma Patients. *Polymers* **2021**, *13*, 4291. [CrossRef] [PubMed]

369. Buyana, B.; Aderibigbe, B.A.; Ndinteh, D.T.; Fonkui, Y.T.; Kumar, P. Alginate-Pluronic Topical Gels Loaded with Thymol, Norfloxacin and ZnO Nanoparticles as Potential Wound Dressings. *J. Drug. Deliv. Sci. Technol.* **2020**, *60*, 101960. [CrossRef]

370. Tan, W.S.; Arulselvan, P.; Ng, S.F.; Taib, C.N.M.; Sarian, M.N.; Fakurazi, S. Healing Effect of Vicenin-2 (VCN-2) on Human Dermal Fibroblast (HDF) and Development VCN-2 Hydrocolloid Film Based on Alginate as Potential Wound Dressing. *Biomed. Res. Int.* **2020**, *2020*, 4730858. [CrossRef]

371. Ansari, S.; Pouraghaei Sevari, S.; Chen, C.; Sarrion, P.; Moshaverinia, A. RGD-Modified Alginate-GelMA Hydrogel Sheet Containing Gingival Mesenchymal Stem Cells: A Unique Platform for Wound Healing and Soft Tissue Regeneration. *ACS Biomater. Sci. Eng.* **2021**, *7*, 3774–3782. [CrossRef] [PubMed]

372. Garcia-Orue, I.; Santos-Vizcaino, E.; Sanchez, P.; Gutierrez, F.B.; Aguirre, J.J.; Hernandez, R.M.; Igartua, M. Bioactive and Degradable Hydrogel Based on Human Platelet-Rich Plasma Fibrin Matrix Combined with Oxidized Alginate in a Diabetic Mice Wound Healing Model. *Mater. Sci. Eng. C* **2022**, *135*, 112695. [CrossRef]

373. Shah, S.A.; Sohail, M.; Khan, S.A.; Kousar, M. Improved Drug Delivery and Accelerated Diabetic Wound Healing by Chondroitin Sulfate Grafted Alginate-Based Thermoreversible Hydrogels. *Mater. Sci. Eng. C* **2021**, *126*, 112169. [CrossRef]

374. Sanchez, M.F.; Guzman, M.L.; Apas, A.L.; del Lujan Alovero, F.; Olivera, M.E. Sustained Dual Release of Ciprofloxacin and Lidocaine from Ionic Exchange Responding Film Based on Alginate and Hyaluronate for Wound Healing. *Eur. J. Pharm. Sci.* **2021**, *161*, 105789. [CrossRef]

375. Chin, C.Y.; Jalil, J.; Ng, P.Y.; Ng, S.F. Development and Formulation of Moringa Oleifera Standardised Leaf Extract Film Dressing for Wound Healing Application. *J. Ethnopharmacol.* **2018**, *212*, 188–199. [CrossRef]

376. Zakerikhoob, M.; Abbasi, S.; Yousefi, G.; Mokhtari, M.; Noorbakhsh, M.S. Curcumin-Incorporated Crosslinked Sodium Alginate-g-Poly (N-Isopropyl Acrylamide) Thermo-Responsive Hydrogel as an in-Situ Forming Injectable Dressing for Wound Healing: In Vitro Characterization and in Vivo Evaluation. *Carbohydr. Polym.* **2021**, *271*, 118434. [CrossRef]

377. Rajalekshmy, G.P.; Rekha, M.R. Strontium Ion Cross-Linked Alginate-g-Poly (PEGMA) Xerogels for Wound Healing Applications: In Vitro Studies. *Carbohydr. Polym.* **2021**, *251*, 117119. [CrossRef]

378. Fahmy, H.M.; Aly, A.A.; Sayed, S.M.; Abou-Okeil, A. -Carrageenan/Na-Alginate Wound Dressing with Sustainable Drug Delivery Properties. *Polym. Adv. Technol.* **2021**, *32*, 1793–1801. [CrossRef]

379. Pakolpakçıl, A.; Osman, B.; Göktalay, G.; Özer, E.T.; Şahan, Y.; Becerir, B.; Karaca, E. Design and in Vivo Evaluation of Alginate-Based PH-Sensing Electrospun Wound Dressing Containing Anthocyanins. *J. Polym. Res.* **2021**, *28*, 50. [CrossRef]

380. Meng, X.; Lu, Y.; Gao, Y.; Cheng, S.; Tian, F.; Xiao, Y.; Li, F. Chitosan/Alginate/Hyaluronic Acid Polyelectrolyte Composite Sponges Crosslinked with Genipin for Wound Dressing Application. *Int. J. Biol. Macromol.* **2021**, *182*, 512–523. [CrossRef] [PubMed]

Article

Valorization of Berries' Agro-Industrial Waste in the Development of Biodegradable Pectin-Based Films for Fresh Salmon (*Salmo salar*) Shelf-Life Monitoring

Janira Romero [1], Rui M. S. Cruz [2,3], Alexandra Díez-Méndez [1] and Irene Albertos [4,*]

[1] Faculty of Sciences and Art, Universidad Católica de Ávila (UCAV), Calle Canteros s/n, 05005 Ávila, Spain
[2] Department of Food Engineering, Institute of Engineering, Campus da Penha, Universidade do Algarve, 8005-139 Faro, Portugal
[3] MED—Mediterranean Institute for Agriculture, Environment and Development and CHANGE—Global Change and Sustainability Institute, Faculty of Sciences and Technology, Campus de Gambelas, Universidade do Algarve, 8005-139 Faro, Portugal
[4] Faculty of Health Sciences, Universidad Católica de Ávila (UCAV), Calle Canteros s/n, 05005 Ávila, Spain
* Correspondence: irene.albertos@ucavila.es

Abstract: The healthy properties of berries are known; however, red fruits are very perishable, generating large losses in production and marketing. Nonetheless, these wastes can be revalued and used. The main objective of this study was the development of biodegradable pectin films with berry agro-industrial waste extracts to monitor salmon shelf-life. The obtained extracts from blueberries, blackberries, and raspberries wastes were evaluated in terms of flavonols, phenols and anthocyanins contents, and antioxidant capacity. Then, pectin films with the extracts of different berries were developed and characterized. The results showed that the blueberry extract film was thicker (0.248 mm), darker (L* = 61.42), and opaquer (17.71%), while the highest density (1.477 g/cm^3) was shown by the raspberry films. The results also showed that blueberries were the best for further application due to their composition in bioactive compounds, antioxidant capacity, and color change at different pHs. The salmon samples wrapped in blueberry films showed lower values of pH and deterioration of fish during storage compared to the control and pectin samples. This study contributes to the valorization of berries agro-industrial waste by the development of eco-friendly films that can be used in the future as intelligent food packaging materials contributing to the extension of food shelf-life as a sustainable packaging alternative.

Keywords: biopolymers; intelligent food packaging; bioactive natural compounds; biodegradable; shelf-life; sustainability

1. Introduction

Food packaging is an essential part of the food sector as it guarantees the quality and safety of products, helps in the transport process, provides stable storage, prevents damage and losses, and ensures greater safety for the consumer [1,2]. Traditionally, the packaging is made from petroleum derivatives; however, they generally contain chemicals considered harmful, such as bisphenol and phthalates [3]. In addition, the long life and resistance of plastics to degradation have generated an accumulation of waste that has a great negative impact on the environment [4]. For this reason, we are currently looking for plastic reduction systems and the development of sustainable alternatives. Some of these alternatives are bio-based polymers, e.g., pectin [1] that can generate biodegradable packaging materials. Likewise, these new materials can be incorporated with different compounds, improving characteristics such as permeability or optical features, which allow the production of smart packaging systems [5].

Intelligent packaging is one type of smart packaging and is defined as one capable of making decisions to increase the shelf-life of the food, inform the consumer, and improve

the quality of the product through various methods such as pH indicators through color changes [6]. The containers with pH indicators may incorporate extracts of various fruits or vegetables that have different properties and allow color changes associated with the variation in the pH of the product. Some of these extracts can be obtained from berries such as blueberries, raspberries, and blackberries, which possess antioxidant capacity thanks to their bioactive compounds, such as phenolic compounds and anthocyanins [7]. Berries are a product with increasing attractiveness, and their consumption has increased in recent years due to their beneficial properties for health such as antioxidants, anticancer substances, vitamins, minerals, fibers, and other essential nutrients [8,9]. However, berries are very perishable products since they have a high water content, which makes them susceptible to mechanical damage, contamination, freezing, or dehydration, generating large losses [10]. These losses generate serious nutritional, economic, and environmental problems [11]. To circumvent these problems, the fruits are normally processed, for example, for obtaining juices, from which numerous by-products can be achieved [12]. Food waste is already a global problem that endangers the long-term food supply chain, with 1.300 million tons being discarded every year [13]. For this reason, the Sustainable Development Goals (SDGs) require, by 2030, a halving of food waste per capita in the supply and consumption chain [13]. More than 1.748 million tons of wasted food correspond to fruits and vegetables [13], so there are already several reviews on the possible applications of these residues. Bayram et al., 2021 [14] studied the possible use of biopolymers, biocomposites, smart packaging, and edible films or coatings. In the processing of fruits and vegetables, by-products consisting of seeds and shells are produced in large quantities, which present a large concentration of bioactive components such as antioxidants, pigments, proteins, essential oils, enzymes, and dietary fibers [13].

The residues resulting from processing, called pomace, also in the case of berries can be reused in the food industry as ingredients or natural additives due to the bioactive compounds [11]. As previously referred to, the waste generated represents a great loss of valuable nutrients. For this reason, the biotransformation of waste is receiving increasing attention since it can be used as a resource to obtain useful products with added value [8]. There are numerous biopolymers used in the development of packaging materials, with poly (lactic acid) (PLA), cellulose, starch, and chitosan being more widely used [15]. PLA is a biodegradable polymer with mechanical properties very similar to those of thermoplastics. Starch is also biodegradable and is a polymer that is easily found; however, it has a strong hydrophilic behavior, making it sensitive to moisture [15]. On the other hand, cellulose is one of the most abundant renewable materials being used as a filler or host polymer in packaging [15]. Chitosan contains antimicrobial properties, so it can be used as a host and antimicrobial agent [15]. As previously referred to, another polymer that can be used in the development of packaging films is pectin, in which plant extracts can be easily added to generate active ingredients [16]. Pectin is a good component thanks to its ability as a gelling and emulsifying agent, generating water-soluble films with low opacity [16]. Essential oils can be added to pectin films, the most common being cinnamon, rosemary, oregano, cloves, thyme, lemon, and orange. Other elements that can be incorporated into pectin are agricultural residues such as banana, orange, and lemon peels among others [16]. Plant extracts rich in phenolic compounds are also added to pectin to increase the antioxidant capacity of the films, although there is less research in this area compared to in essential oils [16].

On the other hand, blueberry residues have multiple uses such as biofuel, biogas, biochar, or biocrude oil production [17]. There are also various uses in food as additives; for example, Rai et al., 2021 [18] observed that blueberry residues produce certain ferments that help to improve intestinal microbiota and intestinal function, corroborating its potential use as a functional food [18–20]. Different studies used blueberry residues to develop smart packaging as films based on different biopolymers such as chitosan, starch, and gelatin [21–27]. However, no subsequent application was carried out as smart packaging on food products such as meat or fish.

Fresh fish is considered key in the diet as it provides 17% of the animal protein ingested [28]. Specifically, salmon (*Salmo salar*) is one of the most consumed products worldwide, representing 93% of production [29]. Its consumption has been increasing thanks to the fact that it contains beneficial components for health such as omega-3 long-chain polyunsaturated fatty acids (LC-PUFA) [28] as well as its color, taste, protein content, vitamins, and antioxidants [30]. However, salmon and other fishery products are very perishable due to their high-water activity, almost neutral pH, and other specific components that favor biochemical, physical, and microbial deterioration during the production chain, specifically the deterioration that begins immediately after capture [28].

To our knowledge, there is little information on the use of residues of other berries such as raspberries and blackberries for the development of smart packaging materials, as well as its comparison with blueberries and their subsequent use in fish products, particularly in salmon. In addition, few studies in the literature reported the use of pectin as a matrix to develop intelligent packaging. For this reason, this study aimed to develop and characterize biodegradable pectin films with the incorporation of blueberry, raspberry, and blackberry waste extracts and to study their effect on fresh salmon shelf-life.

2. Results and Discussion

2.1. Characterization of the Extracts

The results (Table 1) indicated significant differences ($p < 0.05$) in flavonol content among the different extracts. The blueberry extract was the one with the highest flavonols content (13.65 ± 0.01 mg of quercetin equivalents per g of extract), followed by the blackberry extract. Similar results were obtained in other studies [31,32].

Table 1. Characterization of the antioxidant properties of the extracts.

	Total Polyphenols	Total Flavonols	Total Anthocyanins	DPPH	ABTS-TEAC
	(mg GAE/100 g)	(mg of Quercetin Equivalents per g of Extract)	(mg of Malvidin-3-Glucoside per L of Extract)	(% Inhibition)	(µmol Trolox/g ext.)
Raspberry	11.80 ± 0.060 [a]	0.99 ± 0.010 [c]	3.54 ± 0.500 [a]	20.65 ± 1.340 [a]	1.63 ± 0.110 [a]
Blackberry	11.80 ± 0.050 [a]	3.90 ± 0.990 [a]	13.21 ± 2.710 [b]	20.85 ± 1.201 [a]	1.48 ± 0.180 [a]
Blueberry	12.14 ± 0.080 [b]	13.65 ± 0.010 [b]	8.58 ± 0.870 [ab]	34.00 ± 0.282 [b]	2.67 ± 0.135 [b]

The values (mean $\pm$ standard deviation) followed by different lowercase letters in the same column, for each parameter, are significantly different ($p < 0.05$).

Blackberry and blueberry extracts showed the highest level of anthocyanins. The raspberry extract (Table 1) presented the lowest level of anthocyanins compared with the blackberry extract ($p < 0.05$). Different studies reported significant differences between anthocyanins obtained from blackberries and raspberries, being the latter of lower content [32,33]. Sariburun et al., 2010 [32] reported that the content of anthocyanins in extracts using water was more effective as they have a high solubility in water. In a variety of raspberry called "Rubin", anthocyanins obtained from an extract with water were 60.3 ± 0.7 mg GAE/100 g, while in an extract with methanol they were 24.1 ± 0.4 mg GAE/100 g. In the case of the blackberries, extraction with water proved to be more effective, showing values of 54.8 ± 0.8 mg GAE/100 g while with methanol the values were lower (41.3 ± 0.3 mg GAE/100 g) [32]. In short, a higher anthocyanin content was shown in blackberries, as in our study.

Blueberry extract showed the highest content of total polyphenols, differing significantly from raspberry and blackberry extracts, although their levels of polyphenols were also high. Other authors reported a higher polyphenol content in blackberry extract (24.85 ± 0.11 mg g^{-1}) while that of cranberry extract was significantly lower (6.08 ± 0.04 mg g^{-1}) [23] due to the extraction method in water to ensure food and environmental safety. In addition, phenols are an important indicator of antioxidant capacity [23]. In our study, the

highest antioxidant capacity in both methods was obtained in blueberry extract (Table 1), while no significant differences ($p > 0.05$) were observed between the antioxidant capacity of blackberry and raspberry extracts. This shows the expected positive correlation between total polyphenol content and antioxidant capacity. The use of two different methods to measure the antioxidant capacity under different reaction conditions allowed us to establish a more precise view of the antioxidant capacity for the developed films. Gündeşli et al., 2019 [34] reported the highest antioxidant capacity in blackberries, followed by raspberries. Unlike other berries, blueberries have the greatest antioxidant capacity in the early stages of ripening, which is related to the high levels of flavonols and hydroxycinnamic acids in the pre-ripening stage [35].

On the other hand, the antioxidant capacity of raspberries was 40% lower than that of blueberries.

2.2. Characterization of the Developed Films

2.2.1. Thickness, Density, and Hardness

The results for thickness, density, and hardness are presented in Table 2. Significant differences ($p < 0.05$) were obtained in the thicknesses of all films, with the pectin films being thinner while the blueberry films were thicker. In either case, it is shown that the addition of fruit powder significantly increased the thickness of the films compared to the control (pectin). For blueberries, similar values were recorded in the literature in the studies reported by Luchese et al., 2018 [24] and Andretta et al., 2019 [26] in cassava starch films. However, in other studies, Luchese et al., 2018 [25] and Jamróz et al., 2019 [36] obtained significantly lower thickness values, even at higher percentages of blueberry and yerba mate extracts. This decrease in thickness is possibly due to the particle size of the powder, which is within 100–300 μm. In the study by Luchese et al., 2018 [25], a lower thickness was observed in the films made from blueberry powder with smaller particle sizes. On the other hand, similar results to those obtained in the thickness of the films with blackberry extract (0.2 mm) were observed in the studies of Gutiérrez, 2018 [37] and Sganzerla et al., 2021 [38]. However, the films made with raspberry powder were thicker than those reported in Yang et al., 2021 [39], possibly due to differences in powder concentration.

Table 2. Thickness, density, and hardness of the developed films.

	Thickness (mm)	Density (g/cm^3)	Hardness (g Force)
Pectin	0.128 ± 0.009 [a]	1.124 ± 0.023 [a]	495.267 ± 15.482 [a]
Raspberry	0.174 ± 0.044 [b]	1.477 ± 0.035 [b]	863.756 ± 12.142 [b]
Blackberry	0.200 ± 0.008 [c]	1.316 ± 0.015 [c]	882.467 ± 7.688 [c]
Blueberry	0.248 ± 0.009 [d]	1.380 ± 0.007 [d]	763.156 ± 10. 650 [d]

The values (mean ± standard deviation) followed by different superscript letters in the same column, for each parameter, are significantly different ($p < 0.05$).

Table 2 shows also the density in the different films; the film with raspberry extract was the one with the highest value (1.477 g/cm^3) followed by the film with blueberry extract. However, the results obtained were lower than those of Yang et al., 2021 [39], possibly due to the different matrices used. In our study, the films were produced with pectin while Yang et al., 2021 [39] used a matrix comprised of pectin, sodium alginate, and xanthan gum. This could be due to the intermolecular interactions between anthocyanins and the matrix, directly influencing their properties and, therefore, the films that contain them [40], and thus, hydrogen bonds benefit from a regular arrangement of the matrix chain in the film, generating a higher density [41–43].

On the other hand, there was also a trend of increasing hardness from pectin films to the films incorporated with the berries' extracts. The film with the blackberry extracts presented the highest hardness while the film with the raspberry extracts the lowest. Probably, the intermolecular hydrogen bonds were formed between the hydroxyl groups

of the raspberry extract and the matrix, reducing the crosslinking of water and the matrix, thus decreasing the hardness of the film [39].

2.2.2. Color

The color and opacity of the films are shown in Table 3. Significant differences were observed in all the color parameters between the different films, except for the L* parameter, where there were no significant differences ($p > 0.05$) between the film with blackberries and the film with blueberries. However, the pectin film showed the highest luminosity (L*) and hue (h*). It is worth noting a clear tendency h* decrease from pectin film (85.19) to the film with blackberries (26.19). Despite the absence of differences in the L* value between the films with blackberry and blueberry extracts, these presented different results in the other parameters. The film with blackberry extract was more reddish compared will all the other films. This may be due to the different composition of anthocyanins in the different extracts. The trend to the red/purple is the result of the presence of cyanidin, which is purple at neutral pH [23]. The results of the parameters a* and b* coincide with the ones given in the study of Kurek et al., 2018 [23], where the same trend was observed among films developed with blackberries and blueberry extracts. Of the films incorporated with berry extracts, the film with raspberry extract was the one that presented the greatest luminosity. The luminosity of the films with raspberry extract (74.75) was similar (77.76) to the raspberry films (0.5 g/L raspberry films) reported by Yang et al., 2021 [39].

Table 3. Color and opacity of the developed films.

	L*	a*	b*	C*	h*	Opacity (%)
Pectin	91.377 ± 0.437 [c]	1.104 ± 0.164 [a]	13.076 ± 0.712 [a]	13.126 ± 0.721 [a]	85.194 ± 0.549 [d]	11.373 ± 0.193 [a]
Raspberry	74.753 ± 0.563 [b]	23.678 ± 0.225 [c]	14.620 ± 0.351 [c]	28.056 ± 1.071 [b]	31.687 ± 0.462 [b]	13.028 ± 0.106 [b]
Blackberry	61.102 ± 1.722 [a]	28.423 ± 1.111 [d]	13.976 ± 0.378 [b]	31.672 ± 1.159 [d]	26.188 ± 0.355 [a]	16.961 ± 0.299 [c]
Blueberry	61.422 ± 1.378 [a]	16.04 ± 0.537 [b]	25.431 ± 0.191 [d]	30.070 ± 0.344 [c]	57.766 ± 0.862 [c]	17.71 ± 0.190 [d]

The values (mean ± standard deviation) followed by different superscript letters in the same column, for each parameter, indicate significant differences ($p < 0.05$).

2.2.3. Opacity

The protective action against light is an important feature in the packaging of food since UV radiation and light are powerful lipid oxidizers [44]. Regarding opacity, there was a clear trend of increase in the incorporation of extracts (Table 3). The film with blueberry extract showed higher opacity than the film with blackberry extract, followed by the raspberry one.

Conversely, Kurek et al., 2018 [23] reported that blackberry extract films turned out to be opaquer than blueberry extract films.

2.2.4. Color Changes at Different pH

The color parameters were evaluated in solutions with different pHs to determine whether color changes at an environmental pH can be shown. The highest color variability according to pH changes was presented in the films with blueberry and raspberry extracts (Figure 1).

In the case of blueberries, significant differences ($p < 0.05$) were determined in the R value from pH 2 to 12. Yellowish brown hues of pH 2–5 were obtained, turning to a slightly darker brown up to pH 12. However, the film with raspberry extract showed very few color variations at different pHs, apart from some points showing significant differences ($p < 0.05$) in R, G, and B values between pH 2 and 6. In fact, these changes were not noticeable in the visual assessment (Figure 1).
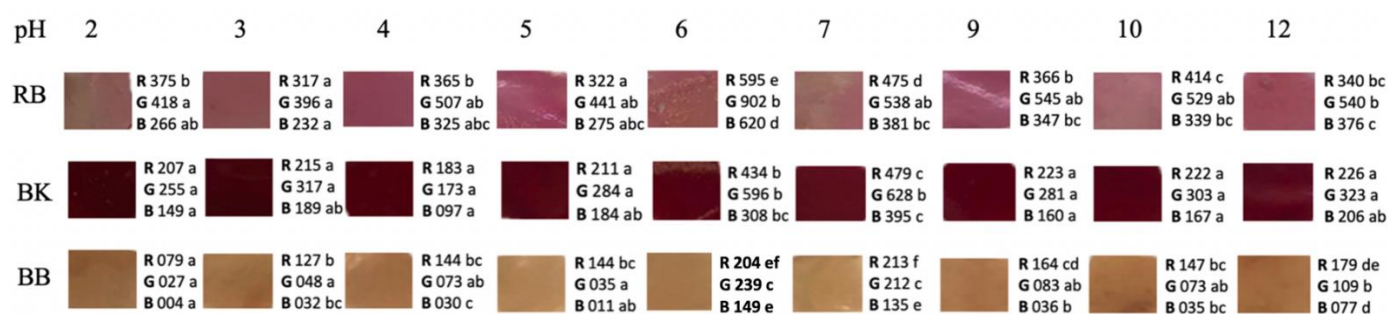
Figure 1. Films color changes at different pH value. RB (Raspberry), BK (Blackberry), and BB (Blueberry). Values followed by different superscript letters in the same row, for each parameter, indicate significant differences (*p* < 0.05).

Other authors such as Kurek et al., 2018 [23] determined color parameters L, a, and b in chitosan films with blueberry and blackberry residue in a pH range of 2–12. Red colors from pH 2 to 4; blue/green at pH 5, 6, and 7; and dark green at pH 10 and 12 were observed for blueberries [23]. Separately, a red color was displayed at pH 2 and 4; violet at pH 5, 6, and 7; and dark blue at pH 10 and 12 for blackberries. In contrast, in a film of carboxymethylcellulose (CMC) and blackberries, the colors obtained in a pH range of 1 to 13 varied from pink in an acid medium to yellowish green in a basic medium [38], possibly due to the influence of the CMC matrix. Luchese et al., 2017 [22] determined the color changes in chitosan films with blueberries, on a pH scale of 2–12, obtaining results like those of Kurek et al., 2018 [23]. In addition, the process of prior blanching of the fruits caused the luminosity values to be lower, obtaining darker films [22]. This procedure was also performed in our study, which is why darker films were obtained such as those of Luchese et al., 2017 [22]. This fact is because in the production of films with unblanched fruits there is a greater degradation of anthocyanins [22]. Andretta et al., 2019 [26] observed in their study with blueberries a color variation from red/orange at acid pH and green/ yellowish at basic pH. Yun et al., 2019 [45] developed films with starch-based blueberries, obtaining colors from pale violet to intense red when exposed to hydrogen chloride. However, in exposure to ammonia, the violet turned blue and then green.

In the case of raspberry, variability was also observed, going from a yellowish rose at pH 2, 3, and 4 to a stronger rose at pH 5 and then to a yellowish rose again in the rest of the pH. In the study of Yang et al., 2021 [39], the color variation was from red to pink from pH 1 to 6, from pink to violet-blue from pH 7 to 10, and green from pH 11 to 13. These colors are because in the acidic media, the red flavylium cation form of the anthocyanins predominates, which changes its structure as the pH becomes basic until it becomes a yellow chalcone [39,40].

Therefore, the films with blueberry extract were selected in our study for the second phase of the study to monitor the shelf-life of salmon fillets due to their higher polyphenol content and second-best in anthocyanin content. In addition, the films were opaquer and showed visible color changes at different pHs.

2.2.5. Biodegradation Properties
Soil

The films showed no changes in their structure after 24 h, although presented some water absorption (from the wet soil). After the seventh day, the films started to show some changes in their structure due to the solubility in water (Figure 2A).
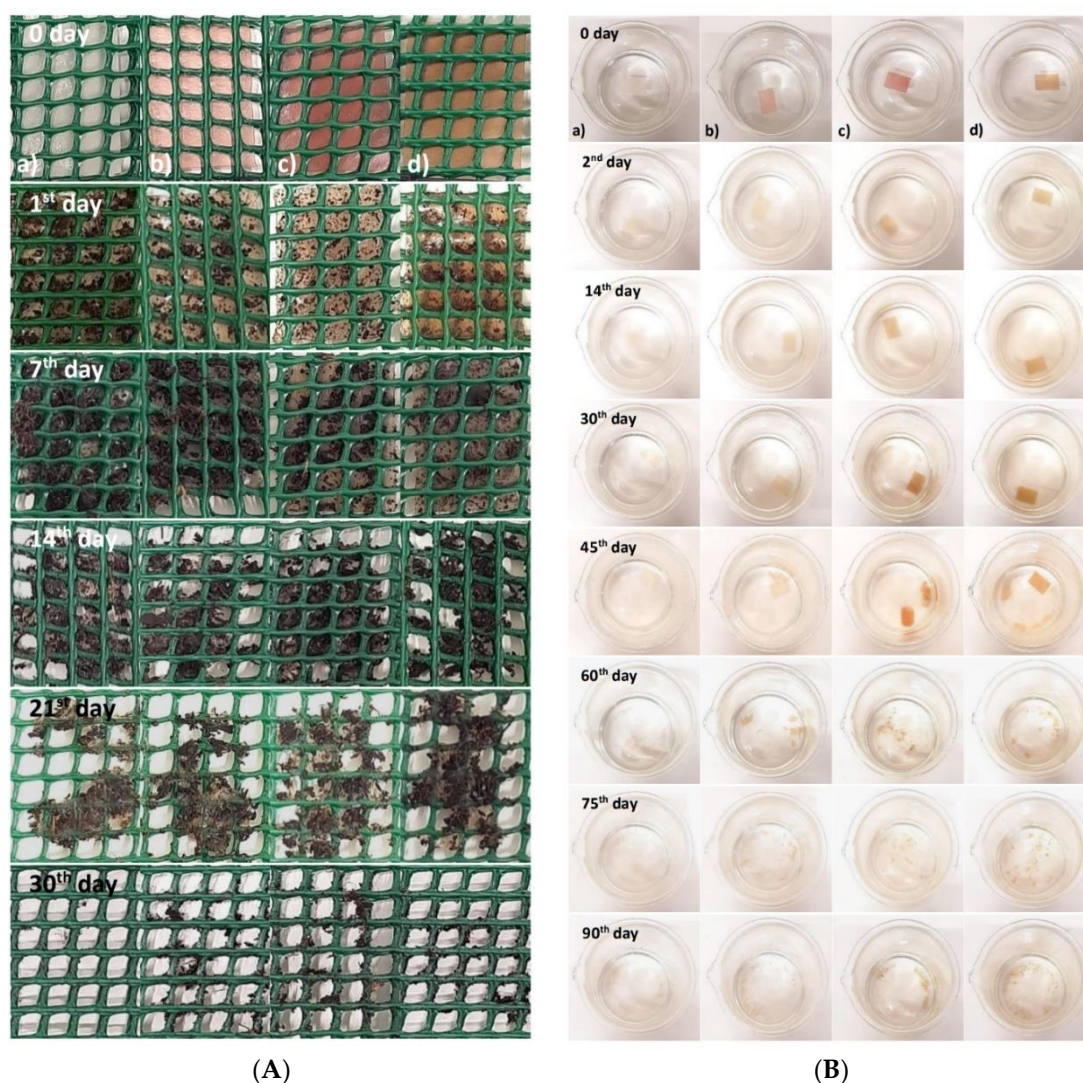
Figure 2. (**A**) Biodegradation test in soil; (**B**) biodegradation test in seawater: (**a**) pectin film (control), (**b**) film with raspberry extract, (**c**) film with blackberry extract, and (**d**) films with blueberry extract.

Moreover, the organic matter and the availability of phosphorus in the soil contribute to a higher load of fungi also responsible for biodegradation [46]. A study in which cassava starch films were developed showed similar results, with signs of biodegradation after 6 days and greater changes in the degradation of the films after 12 days [47].

Norcino et al., 2020 [48] developed pectin-based films with copaiba oil. In this study, the films were practically biodegraded in the soil after 28 days.

In a recent study reported by Ren et al., 2022 [49], pectin-based films also biodegraded significantly after three weeks and were biodegraded completely after five weeks.

The degradation can occur firstly from different physical and biological processes, including wetting/drying, heating/cooling, or freezing/thawing. These processes contribute to the cracking of the polymeric materials. In this study, the initial breakdown of the films occurred due to the presence of water. Then, during the degradation process, the extracellular enzymes from the microorganisms break down the polymer and the depolymerization occurs. Short chains or smaller molecules, such as oligomers, dimers, and monomers, pass the semipermeable outer bacterial membranes and are then converted to carbon dioxide, water, and biomass as the final products of the biodegradation [50,51]. The European Standard EN 13432 [52] indicates 90% as the value for packaging to be considered biodegradable by biological action in 6 months. Thus, it is possible to affirm that the developed films can be considered biodegradable.

Seawater

The films showed several changes during the biodegradation test in seawater (Figure 2B). After the second day, the films with the addition of berry extract kept their initial appearance but showed some loss of color. The results presented by Alvarez-Zeferino et al., 2015 [53] and Pereira et al., 2021 [54] are in agreement with the ones obtained in this study showing low levels of biodegradation in the first days of testing.

On the 30th day, the films' loss of color was more evident, and the seawater in which they were submerged began to show signs of clouding due to the transfer of pigments (i.e., anthocyanins) from the films to the seawater. On the 45th day, it was possible to verify that all films started to be fragmented, and the clouding of the water was also noticeable. On the 60th day, greater changes were observed in the films' structure, as they started to fragment into small pieces and dissolve considerably in the seawater. These changes are related to the swelling of the film, as both the swelling and the solubility of the film can directly affect the water-resistance properties of the film, particularly if it occurs in a humid environment [55,56].

After 90 days, all films lost their initial rectangular shape and were quite fragmented, presenting a "flaky" appearance. Several factors influence the rate of biodegradation of the films, such as the swelling, the movement/agitation of the seawater, the existence of oxygenation, the presence of microorganisms in the seawater, and the ratio volume of seawater/film [53,56,57].

In general, biodegradation in soil was practically obtained in a short period, with an average degradation rate of 3.6% per day while the biodegradation in seawater took more time, showing an average degradation rate of 1% per day. These results are of extreme importance since they quantify and prove the fast degradation of these types of biodegradable materials against plastic or even paper packaging. Paper and plastic degradation are very slow processes, and they can take several years to be fully degraded, depending on the type of plastic or paper and the used conditions [58].

For example, brown newspapers started to degrade by the 10th–12th week of exposure in soil, remaining small pieces of the papers, while plastic bags had thinned off and become transparent [59]. In another study, low-density polyethylene (LDPE) bags were estimated to decompose by 50% after 4.6 years in inland (buried) and 3.4 years in marine environments [60].

2.3. Effect of Films Monitoring Freshness of Salmon Fillets
2.3.1. pH

The results (Table 4) showed a clear upward trend in the pH for both control and pectin treatment over storage. On the other hand, the pH of the fish samples treated with the film with blueberry extract showed a tendency to be maintained until day 4 with a subsequent rise on day 7. In addition, significant differences ($p < 0.05$) were observed among the treatments from day 2.

Table 4. pHs of salmon fillets during storage with different treatments.

	pH			
	Day 1	**Day 2**	**Day 4**	**Day 7**
Control	6.57 ± 0.021 [a B]	6.40 ± 0.030 [c A]	6.97 ± 0.052 [c C]	7.20 ± 0.020 [b D]
Pectin	6.40 ± 0.000 [a C]	6.24 ± 0.011 [b B]	6.97 ± 0.021 [b A]	6.92 ± 0.020 [a D]
Blueberry	6.24 ± 0.010 [a D]	6.00 ± 0.000 [a C]	5.58 ± 0.013 [a B]	6.95 ± 0.000 [a A]

The values followed by different lowercase superscript letters in the same column, for each parameter, are significantly different ($p < 0.05$). The values followed by different capital superscript letters in the same row, for each parameter, are significantly different ($p < 0.05$).

The initial pH values in salmon (pH > 6) for all samples with the different treatments were similar to those reported by Ambrosio et al., 2022 [28]. The increase in pH may be due to the production of ammonia and amines generated by the autolysis of nitrogenous

compounds of bacteria that proliferate the decomposition process [28,61–64]. The films with the blueberry extract prevented the pH increase by avoiding the degradation of proteins and, therefore, the release of alkaline compounds during the first days of storage [65].

Therefore, the results showed a faster degradation in the control samples during the storage time than in the treated samples, especially for the film with the blueberry extract. The films composed of blueberry extract exerted a greater positive effect against deterioration since, being rich in antioxidants, these compounds can migrate to the fish surface, reducing the oxidation reactions [63,66].

2.3.2. Moisture

In the first days of storage, there were no significant differences in the humidity of the samples between each treatment. From the fourth day, it is possible to observe significant differences ($p < 0.05$) between all the treatments (Table 5). A tendency of humidity decrease was also obtained throughout the storage in the treatments compared to the control samples. However, this trend only showed significance in the blueberry treatment. As in our trial, other authors obtained a reduction of humidity in the samples with the different films, possibly due to the absorption of water, which can be beneficial since it can favor the control of microbial growth [65] or due to drip loss.

Table 5. Moisture (%) of salmon fillets during storage with different treatments.

	Moisture (%)			
	Day 1	**Day 2**	**Day 4**	**Day 7**
Control	63. 48 ± 0.011 [a A]	65.29 ± 0.030 [a A]	68.43 ± 0.010 [c A]	67.32 ± 0.010 [b A]
Pectin	63.48 ± 0.020 [a B]	55.72 ± 0.012 [a A]	54.46 ± 0.030 [b A]	51.77± 0.021 [a A]
Blueberry	63.48± 0.000 [a C]	57.96 ± 0.011 [a BC]	44.11 ± 0.000 [a A]	54.28± 0.010 [a B]

The values followed by different lowercase superscript letters in the same column, for each parameter, are significantly different ($p < 0.05$). The values followed by different capital superscript letters in the same row, for each parameter, are significantly different ($p < 0.05$).

2.3.3. Fish Color

For the color analysis, a two-way ANOVA was performed, thus obtaining the global changes regarding the treatment and storage time.

The RGB color model is based on the mixing of red, green, and blue with different intensities to generate a color. Therefore, the color is presented as an RGB triplet. Each of the three colors can vary from zero to the maximum value (in this case 1023). The black color is represented as (000, 000, 000) and the white (1023, 1023, 1023) [67].

The color of fish is one of the most important qualities since it has a great influence on the consumer at the time of purchase [28]. Regarding the color in the salmon samples, significant differences ($p < 0.05$) were observed in all measurement parameters (R, G, and B) between the control samples and the samples with the film with blueberry extract (Figure 3).

The R value (red) obtained the highest values in the pectin treatment and on day 7 of storage. On day 7, the fish samples with a greater reddish color were observed in the samples with blueberry treatment, possibly due to the migration of the compound from the film to the fish. The same was observed in the study of Rico et al., 2020 [65], where color migration occurred from the fennel components to the sample.

On the other hand, authors such as Albertos et al., 2015 [68] obtained a significant decrease in luminosity (L*) in trout (*Trachurus trachurus*), due to the discoloration and reduction of redness during storage, as in our control samples. This reduction of reddish coloration in salmonids may be due to the oxidation of hemoproteins (hemoglobin, and myoglobin), since in their oxidized ferric form they present a brown color [68]. In the treated fish, the reddish color remained better, possibly due to the antioxidant effect of the film.
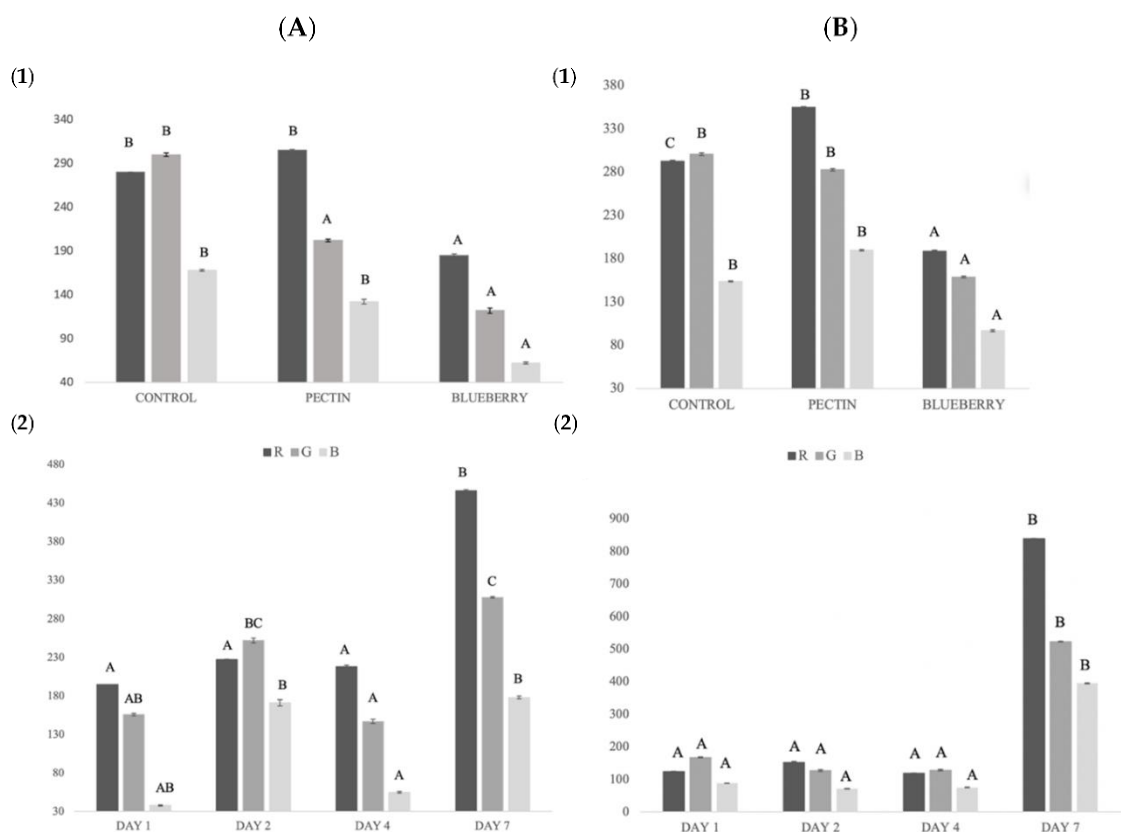
Figure 3. (**A**) Global salmon color changes: (**1**) global color for each treatment; (**2**) global color during storage. (**B**) Global pectin and blueberry film color changes: (**1**) global color for each treatment; (**2**) global color during storage. Different capital letters indicate significant differences ($p < 0.05$).

2.3.4. Film Color

Clear differences were obtained in the treatment with blueberries compared to the treatment with pectin and without any treatment (Figure 3). In the case of G, a small reduction was observed between treatments, although it was not significantly different.

Blueberry film obtained a brownish to more yellowish coloration throughout the storage time. Zhai et al., 2017 [69] showed similar results in a study to control carp freshness using colorimetric films with different anthocyanin concentrations.

The film with the lowest concentration changed from a purple color, going through green, to yellow in a period of about 6 days, while the film with the highest concentration showed no color differences until the third day. In the case of Wu et al., 2019 [70], the color changes were observed at 24 h of storage, going from purple to grayish-blue or brown depending on the anthocyanin concentration of the film.

These results were probably related to the increase of TVB-N (total volatile basic nitrogen). The antioxidant capacity of anthocyanins migrating to fish would inhibit the formation of volatile substances with nitrogen in storage [70], and their effects could vary depending on whether they are in contact with fish. In our case, the film itself simply by being on the surface of the food reduced exposure to oxygen and thus oxidation. In addition, the salmon used in our study has muscle tissue with a reddish coloration due to its high myoglobin content in comparison to Zhai et al., 2017 [69] and Wu et al., 2019 [70], which may affect the color measurement of the films covering the samples.

2.4. Sensorial Analysis

The control samples presented the highest degree of fishy odor established by the panelists (Figure 4), while the lowest value corresponded to the treatment with the film with blueberry extracts. Albertos et al., 2015, 2018 [68,71] performed a sensory analysis in

which similar results were obtained concerning the control of fish odor, rancid odor, and ammonia, which reflects the deterioration of fish meat. In addition, the introduction of red fruit extract prevented the formation of unpleasant odors (fishy smell, rancid smell, and ammonia smell) in the film-covered samples, detecting a slightly fruity aroma. The same happened in the study of Albertos et al., 2018 [71], where an "herbaceous" aroma was found in films incorporated with olive leaf powder.
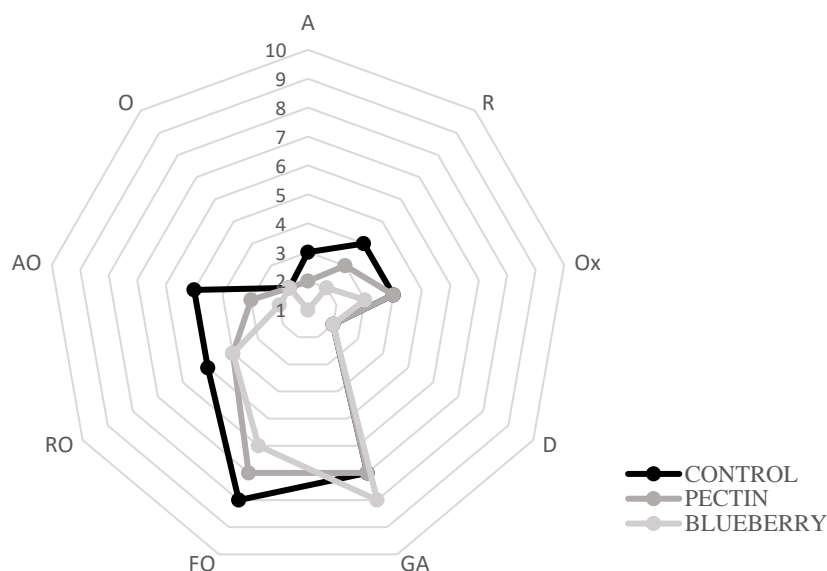

Figure 4. Sensorial analysis on day 2. Aromatic (A), rot (R), oxidation (Ox), dehydration (D), general acceptability (GA), fishy odor (FO), rancid odor (RO), ammonia odor (AO), and others (O).

The control samples showed variability in the different parameters such as fish odor, putrefactive odor, degree of dehydration, ammonia odor ... etc., over storage. On the other hand, in the treatment with the film with the blueberry extract, the values remained constant. This would indicate the effectiveness of films in preserving the fish characteristics.

3. Materials and Methods

3.1. Materials

All the chemicals used in the formulation of films were food-grade quality Panreac products (Panreac Química, Barcelona, Spain). Other reagents were purchased from Sigma-Aldrich (Sigma Aldrich Chemical Co., Steinheim, Germany), and pectin was supplied by Guinama (Guinama S.L.U., Valencia, Spain).

3.2. Raw Materials

Blackberry, raspberry, and blueberry wastes were obtained from Viveros Campiñas (Chañe, Segovia, Spain). Berry wastes were disinfected with sodium hypochlorite (12 °C) for 15 min and immediately dried at room temperature. Afterward, blackberry, raspberry, and blueberry wastes were steamed at 100 °C for 3 min. Then, they were frozen at −83 °C until berry extract preparation.

Gutted salmon (*Salmon salar*) was provided by Gallega de Distribuidores de Alimentación (GADISA) (Ávila, Spain). Fish was captured in the north of Galicia. The salmon was stored at 4 °C and immediately processed.

3.3. Development of Films with Berry Extracts

3.3.1. Preparation of Berry Extracts

Berries wastes were lyophilized (Lyoquest-55, Azbil Telstar Technologies SLU, Terrasa, Spain) and then milled and sieved (100–300 μm) to obtain the residue in powder form.

Berry extracts were then dissolved in distilled water (12.5% *w/v*) for 2 h of stirring at room temperature. After, the suspension was centrifugated at 6000 rpm for 10 min and filtered through Whatman grade number 1 filter paper. The extracts were then stored at −80 °C until use.

3.3.2. Development of the Films

Pectin Films

Low methoxy amidated pectin (3% *w/v*) was dissolved in water and stirred at 80 °C to obtain a homogenous solution. Afterward, glycerol (3%/biopolymer) was added as a plasticizer for 2 h to achieve complete dispersion. The films were obtained by casting 20 mL in 90 mm-diameter Petri dishes and dried at room temperature for 24 h. Before analyses, the films were peeled-off and conditioned in desiccators over a saturated solution of KBr (58% relative humidity) (Figure 5).

Figure 5. Developed films: (**a**) pectin (control); (**b**) raspberry; (**c**) blackberry; and (**d**) blueberry.

Films Incorporated with Berry Extracts

Berry extracts (10% *w/v*) were completely dissolved in water before pectin addition. From this point, the films were prepared as previously referred (Figure 5).

3.4. Characterization of the Antioxidant Properties of the Extracts

3.4.1. Total Phenols (TPs) Content

Total phenols were measured using the Folin–Ciocalteu method [72]. Results were expressed as mg gallic acid equivalents (GAE) per g of extract using a calibration curve with gallic acid (Sigma Aldrich Co., Steinheim, Germany) as the standard (9.8 μM to 70 μM).

3.4.2. Total Flavonols Content

Total flavonols content was analyzed with Neus reagent according to Arnous, Markis, and Kefalas, 2002 [73]. Results were expressed as mg of quercetin equivalents per g of extract.

3.4.3. Total Anthocyanin Content

Total anthocyanin content was determined using the pH differential method [74]. Dilutions were prepared in 50 mL volumetric flasks with buffers pH 1.0 and pH 4.5.

Absorbance was then recorded at 520 nm (Thermo Fisher Scientific, Genesys 150, Madison, WI, USA). Results were expressed as mg of malvidin-3-glucoside per L of extract.

3.4.4. DPPH (1,1-Diphenyl-2-picrylhydrazyl) Radical Scavenging Activity

The effect of antioxidant activity on DPPH was estimated according to the procedure described by Brand-Williams, Cuvelier, and Berset 1995 [75]. Results were expressed as a percentage of the inhibition of DPPH radical.

3.4.5. TEAC (Trolox Equivalent Antioxidant Capacity)

The analysis was carried out according to the method reported by Re et al., 1999 [76]; 100 μL of diluted samples was mixed with 1000 μL of ABTS and working solution in an Eppendorf tube. The decay in absorbance at 734 nm was recorded over 30 min with a spectrophotometer (Thermo Fisher Scientific, Genesys 150, Madison, WI, USA). Trolox was used as the standard (7.5–240 μM). Results were corrected for moisture and expressed as μmol TE 100 g^{-1} d.m.

3.5. Characterization of the Developed Films
3.5.1. Film Thickness and Density

The film thickness was measured using a digital micrometer (Mitutoyo, model IDC 112, Kawasaki, Japan). The results were expressed as the average of 10 replicates of samples taken from different locations on the film surface.

Density was determined from rectangular samples of the developed films with the following dimensions: 30 mm × 20 mm. Then, each film was weighted, and for volume calculation, the thickness of each film was used.

3.5.2. Hardness

The films' hardness (g force) was determined according to the method of Bamdad et al., 2006 [77], with some modifications. Samples were measured in six different areas, using a texturometer (Brookfield, LFRA 1500, Middleborough, MA, USA), a stainless-steel probe with 4 mm diameter (TA44), with a target value of 6 mm of penetration and a test speed of 0.5 mm/s.

3.5.3. Color

Color measurements were performed using a Minolta CR-400 colorimeter (Minolta Inc, Tokyo, Japan) with D65 as illuminant and 10° observer angle. The instrument was calibrated with a white tile standard (L* = 93.97, a* = −0.88 and b* = 1.21). To measure the color of films, a white surface was used as background. The L* parameter (lightness index scale) ranges from 0 (black) to 100 (white). The a* parameter measures the degree of red (+a) or green (−a) color and the b* parameter measures the degree of yellow (+b) or blue (−b) color. Three measurements were taken from each sample, and six samples from each film were tested.

3.5.4. Opacity

The opacity of the samples was calculated based on the method reported by Martins et al., 2010 [78], as the relationship between the opacity of each sample in a black standard (Yb) and the opacity of each sample in a white standard (Yw), as can be seen in Equation (1):

$$\text{Opacity (\%)} = Yb/Yw \times 100 \tag{1}$$

3.5.5. Color Changes at Different pHs

The films were cut into pieces of 2 cm^2 and were immersed in different pH buffers to adjust pH values to 2, 3, 4, 5, 6, 7, 8, 9, 10, and 12. Afterward, the color was determined with a colorimeter on solids PCE-RGB (PCE Ibérica S.L., Albacete, Spain).

3.6. Biodegradation Tests

3.6.1. Soil

The biodegradation test in soil was based on the methodology used by Pereira et al., 2021 [54]. The films were cut (3 cm × 2 cm) and placed inside a perforated polyethylene net (5 cm × 4 cm; mesh opening 4 mm). Then, the films were buried in soil (Eco grow: nitrogen = 80–150 mg L^{-1}; phosphorus = 80–150 mg L^{-1}; potassium = 80–150 mg L^{-1}; organic Matter = >70%; pH = 5.5–6.5; humidity = 50–60%; conductivity = 0.2–1.2 EC) at a distance of 11 cm from the surface in a rectangular vase (71 cm × 26 cm × 25.5 cm) and with a distance of 5 cm between each film. The soil was watered with 500 mL of water every 7 days at 25 °C. The films' appearance was photographed, and the area of biodegradation was measured during the time of the experiment. This test was carried out in triplicate for each sample.

3.6.2. Seawater

The biodegradation test in seawater was based on the methodology used by Pereira et al., 2021 [54]. The films were cut (3 cm × 2 cm) and submerged in 300 mL of seawater (Faro, Portugal, pH = 7.20). The samples were shaken at 150 rpm (Edmund Bühler, KL2 shaker, Tübingen, Germany) and 25 °C. The films' appearance was photographed during the time of the experiment. This test was carried out in triplicate for each sample.

3.7. Monitoring the Shelf-Life of Salmon Fillets

3.7.1. Preparation and Treatments of Salmon Samples

Gutted salmon (*Salmon salar*) was skinned and filleted, then cut into pieces of 5.7 × 2.5 cm (weighing approximately 10 g) and randomly allocated into 3 batches: fish without film (control), pectin film (pectin), and pectin film with blueberry extract. Each fish sample was individually wrapped with 90 mm-diameter films (control, pectin, and blueberry) with the help of tweezers under hygienic conditions. Afterward, all treatments were stored at 4 °C for 7 days. The assay was run in duplicate. All analyses were performed in triplicate.

3.7.2. pH

Each fish sample (10 g) was homogenized in 100 mL of distilled water, and the mixture was filtered. The pH (pH-meter model basic 20, Crison, Barcelona, Spain) of the filtrate was measured at room temperature.

3.7.3. Moisture

The moisture content of each sample was gravimetrically determined [79]: 10 g of fish were prepared until constant weight in an air oven at 100 °C for about 24 h. The moisture was expressed in percentage.

3.7.4. Color Changes

Color changes of films and fish surface without film were measured using a colorimeter on solids PCE-RGB (PCE Ibérica S.L., Albacete, Spain) in the same conditions as previously referred to in Section 3.5.5.

3.7.5. Sensorial Analysis

Samples were subjected to a descriptive test. A trained panel consisting of 10 panelists, formed by 5 men and 5 women, with ages within 25–30, were recruited from the Catholic University of Ávila, for their previous experience in sensory analysis.

In the descriptive test, the panelist scored the following different attributes: fishy (off-odors, putrefaction) odor intensity, aromatic odor intensity, ammonia odor intensity, other odors, drip loss, color without film (oxidation), and general acceptability. The scores ranged between 1 and 10.

3.8. Statistical Analysis

Data were analyzed by a one-way ANOVA. Fisher's LSD (Least Significant Difference) test was applied at a significance level of 0.05 for determining group differences. In the color changes of salmon fillets, a two-way ANOVA (treatment, time) was performed. Kruskal–Wallis test was used to examine differences in the sensorial analysis. The software Statgraphics Centurion XVI was employed for carrying out the statistical analysis.

4. Conclusions

Berries are a source of anthocyanins and can be used as an effective method for controlling the quality and freshness of food as pH indicators. The concentration of anthocyanins in the developed films was a key factor influenced by both the intensity and the rate of color change. The addition of berry extracts to pectin films contributed to changing the films' properties. Moreover, the pectin films' supplement with blueberry extracts not only showed biodegradability properties in soil and seawater but also protected the salmon samples from deterioration due to their anthocyanin content and antioxidant capacity, increasing the salmon's shelf-life. This study contributes to the valorization of berries' agro-industrial waste by the development of eco-friendly films that can be used in the future as food packaging materials to meet the market demands. However, more studies are needed to evaluate different microbiological and quality parameters.

References

1. Alizadeh-Sani, M.; Mohammadian, E.; Rhim, J.-W.; Jafari, S.M. pH-Sensitive (Halochromic) Smart Packaging Films Based on Natural Food Colorants for the Monitoring of Food Quality and Safety. *Trends Food Sci. Technol.* **2020**, *105*, 93–144. [CrossRef]
2. Singh, P.; Wani, A.A.; Langowski, H.C. Introduction: Food Packaging Materials. In *Food Packaging Materials: Testing & Quality Assurance*, 1st ed.; Singh, P., Wani, A.A., Langowski, H.C., Eds.; CRC Press: Boca Ratón, FL, USA, 2017; pp. 1–11. ISBN 978-131-537-439-0.
3. Rhim, J.W.; Park, H.M.; Ha, C.S. Bio-nanocomposites for food packaging applications. *Prog. Polym. Sci.* **2013**, *38*, 1629–1652. [CrossRef]
4. Schmaltz, E.; Melvin, E.C.; Diana, Z.; Gunady, E.F.; Rittschof, D.; Somarelli, J.A.; Virdin, J.; Dunphy-Daly, M.M. Plastic pollution solutions: Emerging technologies to prevent and collect marine plastic pollution. *Environ. Int.* **2020**, *144*, 106067. [CrossRef] [PubMed]
5. Da Rocha, M.; Alemán, A.; Romani, V.P.; López-Caballero, M.E.; Gómez-Guillén, M.C.; Montero, P.; Prentice, C. Effects of agar films incorporated with fish protein hydrolysate or clove essential oil on flounder (*Paralichthys orbignyanus*) fillets shelf-life. *Food Hydrocoll.* **2018**, *81*, 351–363. [CrossRef]
6. Kalpana, S.; Priyadarshini, S.R.; Leena, M.M.; Moses, J.A.; Anandharamakrishnan, C. Intelligent packaging: Trends and applications in food systems. *Trends Food Sci. Technol.* **2019**, *93*, 145–157. [CrossRef]
7. Skrovankova, S.; Sumczynski, D.; Mlcek, J.; Jurikova, T.; Sochor, J. Bioactive compounds and antioxidant activity in different types of berries. *Int. J. Mol. Sci.* **2015**, *16*, 24673–24706. [CrossRef] [PubMed]
8. Pertuzatti, P.B.; Barcia, M.T. Biotransformation in temperate climate fruit: A focus on berries. *A. J. Food Sci. Technol.* **2015**, *3*, 12–17. [CrossRef]
9. Kolman, O.J.; Ivanova, G.V.; Yamskikh, T.N.; Ivanova, A.N. Development of low-waste technologies for agro-processing companies. *IOP Conf. Ser. Earth Environ. Sci.* **2020**, *421*, 022046. [CrossRef]
10. Kumar, S.; Baghel, M.; Yadav, A.; Dhakar, M.K. Postharvest biology and technology of berries. In *Postharvest Biology and Technology of Temperate Fruits*; Mir, S.A., Shah, M.A., Mir, M.M., Eds.; Springer International Publishing AG: Gewerbestrasse, Switzerland, 2018; pp. 349–370. ISBN 978-331-976-842-4.
11. Dueñas, M.; García-Estévez, I. Agricultural and food waste: Analysis, characterization and extraction of bioactive compounds and their possible utilization. *Foods* **2020**, *9*, 817. [CrossRef]

12. Venskutonis, P.R. Berries. In *Valorization of Fruit Processing by-Products*; Galanakis, C.M., Ed.; Academic Press: London, UK, 2020; pp. 95–125. ISBN 978-012-817-106-6.

13. Basri, M.S.M.; Shah, N.N.A.K.; Sulaiman, A.; Tawakkal, I.S.M.A.; Nor, M.Z.M.; Ariffin, S.H.; Ghani, N.H.A.; Salleh, F.S.M. Progress in the Valorization of Fruit and Vegetable Wastes: Active Packaging, Biocomposites, By-Products, and Innovative Technologies Used for Bioactive Compound Extraction. *Polymers* **2021**, *13*, 3503. [CrossRef] [PubMed]

14. Bayram, B.; Ozkan, G.; Kostka, T.; Capanoglu, E.; Esatbeyoglu, T. Valorization and application of fruit and vegetable wastes and by-products for food packaging materials. *Molecules* **2021**, *26*, 4031. [CrossRef]

15. Basri, M.S.M.; Shah, N.N.A.K.; Sulaiman, A.; Tawakkal, I.S.M.A.; Nor, M.Z.M.; Ariffin, S.H.; Ghani, N.H.A.; Salleh, F.S.M. A review on antimicrobial packaging from biodegradable polymer composites. *Polymers* **2022**, *14*, 174. [CrossRef]

16. Nastasi, J.R.; Kontogiorgos, V.; Daygon, V.D.; Fitzgerald, M.A. Pectin-based films and coatings with plant extracts as natural preservatives: A systematic review. *Trends Food Sci. Technol.* **2022**, *120*, 193–211. [CrossRef]

17. Liu, H.; Qin, S.; Sirohi, R.; Ahluwalia, V.; Zhou, Y.; Sindhu, R.; Binod, P.; Singhnia, R.R.; Patel, A.K.; Juneja, A.; et al. Sustainable blueberry waste recycling towards biorefinery strategy and circular bioeconomy: A review. *Bioresour. Technol.* **2021**, *332*, 125181. [CrossRef]

18. Rai, P.; Mehrotra, S.; Priya, S.; Gnansounou, E.; Sharma, S.K. Recent advances in the sustainable design and applications of biodegradable polymers. *Bioresour. Technol.* **2021**, *325*, 124739. [CrossRef]

19. Cheng, Y.; Wu, T.; Chu, X.; Tang, S.; Cao, W.; Liang, F.; Fang, Y.; Pan, S.; Xu, X. Fermented blueberry pomace with antioxidant properties improves fecal microbiota community structure and short chain fatty acids production in an in vitro mode. *LWT-Food Sci. Technol.* **2020**, *125*, 109260. [CrossRef]

20. Kumar, V.; Ahluwalia, V.; Saran, S.; Kumar, J.; Patel, A.K.; Singhania, R.R. Recent developments on solid-state fermentation for production of microbial secondary metabolites: Challenges and solutions. *Bioresour. Technol.* **2021**, *323*, 124566. [CrossRef]

21. de Moraes Crizel, T.; Costa, T.M.H.; de Oliveira Rios, A.; Flôres, S.H. Valorization of food-grade industrial waste in the obtaining active biodegradable films for packaging. *Ind. Crops Prod.* **2016**, *87*, 218–228. [CrossRef]

22. Luchese, C.L.; Sperotto, N.; Spada, J.C.; Tessaro, I.C. Effect of blueberry agro-industrial waste addition to corn starch-based films for the production of a pH-indicator film. *Int. J. Biol. Macromol.* **2017**, *104*, 11–18. [CrossRef]

23. Kurek, M.; Garofulić, I.E.; Bakić, M.T.; Ščetar, M.; Uzelac, V.D.; Galić, K. Development and evaluation of a novel antioxidant and pH indicator film based on chitosan and food waste sources of antioxidants. *Food Hydrocoll.* **2018**, *84*, 238–246. [CrossRef]

24. Luchese, C.L.; Abdalla, V.F.; Spada, J.C.; Tessaro, I.C. Evaluation of blueberry residue incorporated cassava starch film as pH indicator in different simulants and foodstuffs. *Food Hydrocoll.* **2018**, *82*, 209–218. [CrossRef]

25. Luchese, C.L.; Garrido, T.; Spada, J.C.; Tessaro, I.C.; de la Caba, K. Development and characterization of cassava starch films incorporated with blueberry pomace. *Int. J. Biol. Macromol.* **2018**, *106*, 834–839. [CrossRef]

26. Andretta, R.; Luchese, C.L.; Tessaro, I.C.; Spada, J.C. Development and characterization of pH-indicator films based on cassava starch and blueberry residue by thermocompression. *Food Hydrocoll.* **2019**, *93*, 317–324. [CrossRef]

27. Kurek, M.; Hlupić, L.; Garofulić, I.E.; Descours, E.; Ščetar, M.; Galić, K. Comparison of protective supports and antioxidative capacity of two bio-based films with revalorised fruit pomaces extracted from blueberry and red grape skin. *Food Packag. Shelf Life* **2019**, *20*, 100315. [CrossRef]

28. Ambrosio, R.L.; Gogliettino, M.; Agrillo, B.; Proroga, Y.T.R.; Balestrieri, M.; Gratino, L.; Cristiano, D.; Palmieri, G.; Anastasio, A. An Active Peptide-Based Packaging System to Improve the Freshness and Safety of Fish Products: A Case Study. *Foods* **2022**, *11*, 338. [CrossRef]

29. Rollini, M.; Nielsen, T.; Musatti, A.; Limbo, S.; Piergiovanni, L.; Hernandez Munoz, P.; Gavara, R. Antimicrobial performance of two different packaging materials on the microbiological quality of fresh salmon. *Coatings* **2016**, *6*, 6. [CrossRef]

30. Dalsvåg, H.; Cropotova, J.; Jambrak, A.R.; Janči, T.; Španěl, P.; Dryahina, K.; Smith, D.; Rustad, T. Mass Spectrometric Quantification of Volatile Compounds Released by Fresh Atlantic Salmon Stored at 4 °C under Modified Atmosphere Packaging and Vacuum Packaging for up to 16 Days. *ACS Food Sci. Technol.* **2021**, *2*, 400–414. [CrossRef]

31. Bunea, A.; Rugină, D.O.; Pintea, A.M.; Sconţa, Z.; Bunea, C.I.; Socaciu, C. Comparative polyphenolic content and antioxidant activities of some wild and cultivated blueberries from Romania. *Not. Bot. Horti. Agrobot. Cluj-Napoca* **2011**, *39*, 70–76. [CrossRef]

32. Sariburun, E.; Şahin, S.; Demir, C.; Türkben, C.; Uylaşer, V. Phenolic content and antioxidant activity of raspberry and blackberry cultivars. *J. Food Sci.* **2010**, *75*, C328–C335. [CrossRef]

33. Zorzi, M.; Gai, F.; Medana, C.; Aigotti, R.; Morello, S.; Peiretti, P.G. Bioactive compounds and antioxidant capacity of small berries. *Foods* **2020**, *9*, 623. [CrossRef]

34. Gündeşli, M.A.; Korkmaz, N.; Okatan, V. Polyphenol content and antioxidant capacity of berries: A review. *Int. J. Agric. For. Life Sci.* **2019**, *3*, 350–361.

35. Castrejón, A.D.R.; Eichholz, I.; Rohn, S.; Kroh, L.W.; Huyskens-Keil, S. Phenolic profile and antioxidant activity of highbush blueberry (*Vaccinium corymbosum* L.) during fruit maturation and ripening. *Food Chem.* **2008**, *109*, 564–572. [CrossRef]

36. Jamróz, E.; Kulawik, P.; Guzik, P.; Duda, I. The verification of intelligent properties of furcellaran films with plant extracts on the stored fresh Atlantic mackerel during storage at 2 °C. *Food Hydrocoll.* **2019**, *97*, 105211. [CrossRef]

37. Gutiérrez, T.J. Active and intelligent films made from starchy Sources/Blackberry pulp. *J. Polym. Environ.* **2018**, *26*, 2374–2391. [CrossRef]

38. Sganzerla, W.G.; Ribeiro, C.P.P.; Uliana, N.R.; Rodrigues, M.B.C.; da Rosa, C.G.; Ferrareze, J.P.; Veeck, A.P.D.L.; Nunes, M.R. Bioactive and pH-sensitive films based on carboxymethyl cellulose and blackberry (*Morus nigra* L.) anthocyanin-rich extract: A perspective coating material to improve the shelf life of cherry tomato (*Solanum lycopersicum* L. *var. cerasiforme*). *Biocatal. Agric. Biotechnol.* **2021**, *33*, 101989. [CrossRef]

39. Yang, J.; Fan, Y.; Cui, J.; Yang, L.; Su, H.; Yang, P.; Pan, J. Colorimetric films based on pectin/sodium alginate/xanthan gum incorporated with raspberry pomace extract for monitoring protein-rich food freshness. *Int. J. Biol. Macromol.* **2021**, *185*, 959–965. [CrossRef] [PubMed]

40. Yong, H.; Liu, J. Recent advances in the preparation, physical and functional properties, and applications of anthocyanins-based active and intelligent packaging films. *Food Packag. Shelf Life.* **2020**, *26*, 100550. [CrossRef]

41. Wang, S.; Marcone, M.; Barbut, S.; Lim, L.T. The impact of anthocyanin-rich red raspberry extract (ARRE) on the properties of edible soy protein isolate (SPI) films. *J. Food Sci.* **2012**, *77*, C497–C505. [CrossRef]

42. Wang, X.; Yong, H.; Gao, L.; Li, L.; Jin, M.; Liu, J. Preparation and characterization of antioxidant and pH-sensitive films based on chitosan and black soybean seed coat extract. *Food Hydrocoll.* **2019**, *89*, 56–66. [CrossRef]

43. Yong, H.; Wang, X.; Bai, R.; Miao, Z.; Zhang, X.; Liu, J. Development of antioxidant and intelligent pH-sensing packaging films by incorporating purple-fleshed sweet potato extract into chitosan matrix. *Food Hydrocoll.* **2019**, *90*, 216–224. [CrossRef]

44. dos Santos Caetano, K.; Lopes, N.A.; Costa, T.M.H.; Brandelli, A.; Rodrigues, E.; Flôres, S.H.; Cladera-Olivera, F. Characterization of active biodegradable films based on cassava starch and natural compounds. *Food Packag. Shelf Life* **2018**, *16*, 138–147. [CrossRef]

45. Yun, D.; Cai, H.; Liu, Y.; Xiao, L.; Song, J.; Liu, J. Development of active and intelligent films based on cassava starch and Chinese bayberry (*Myrica rubra* Sieb. et Zucc.) anthocyanins. *RSC Adv.* **2019**, *9*, 30905–30916. [CrossRef] [PubMed]

46. Rech, C.R.; da Silva Brabes, K.C.; Bagnara e Silva, B.E.; Bittencourt, P.R.S.; Koschevic, M.T.; da Silveira, T.F.S.; Martines, M.A.U.; Caon, T.; Martelli, S.M. Biodegradation of eugenol-loaded polyhydroxybutyrate films in different soil types. *Case Stud. Chem. Environ. Eng.* **2020**, *2*, 100014. [CrossRef]

47. Jaramillo, M.C.; Gutiérrez, T.J.; Goyanes, S.; Bernal, C.; Famá, L. Biodegradability and plasticizing effect of yerba mate extract on cassava starch edible films. *Carbohydr. Polym.* **2016**, *151*, 150–159. [CrossRef] [PubMed]

48. Norcino, L.B.; Mendes, J.F.; Natarelli, C.V.L.; Manrich, A.; Oliveira, J.E.; Mattoso, L.H.C. Pectin films loaded with copaiba oil nanoemulsions for potential use as bio-based active packaging. *Food Hydrocoll.* **2020**, *106*, 105862. [CrossRef]

49. Ren, W.; Qiang, T.; Chen, L. Recyclable and biodegradable pectin-based film with high mechanical strength. *Food Hydrocoll.* **2020**, *129*, 107643. [CrossRef]

50. Shah, A.A.; Hasan, F.; Hameed, A.; Ahmed, S. Biological degradation of plastics: A comprehensive review. *Biotechnol. Adv.* **2008**, *26*, 246–265. [CrossRef]

51. Folino, A.; Karageorgiou, A.; Calabrò, P.S.; Komilis, D. Biodegradation of wasted bioplastics in natural and industrial environments: A Review. *Sustainability* **2020**, *12*, 6030. [CrossRef]

52. *EN 13432:2000*; Packaging—Requirements for Packaging Recoverable through Composting and Biodegradation—Test. Scheme and Evaluation Criteria for the Final Acceptance of Packaging. European Committee for Standardization: Brussels, Belgium, 2000.

53. Alvarez-Zeferino, J.C.; Beltrán-Villavicencio, M.; Vázquez-Morillas, A. Degradation of plastics in seawater in laboratory. *Open J. Polym. Chem.* **2015**, *05*, 55–62. [CrossRef]

54. Pereira, D.G.M.; Vieira, J.M.; Vicente, A.A.; Cruz, R.M.S. Development and Characterization of Pectin Films with *Salicornia ramosissima*: Biodegradation in Soil and Seawater. *Polymers* **2021**, *13*, 2632. [CrossRef]

55. Nisar, T.; Wang, Z.-C.; Alim, A.; Iqbal, M.; Yang, X.; Sun, L.; Guo, Y. Citrus pectin films enriched with thinned young apple polyphenols for potential use as bio-based active packaging. *CYTA-J. Food* **2019**, *17*, 695–705. [CrossRef]

56. Accinelli, C.; Saccà, M.L.; Mencarelli, M.; Vicari, A. Deterioration of bioplastic carrier bags in the environment and assessment of a new recycling alternative. *Chemosphere* **2012**, *89*, 136–143. [CrossRef]

57. Nakayama, A.; Yamano, N.; Kawasaki, N. Biodegradation in seawater of aliphatic polyesters. *Polym. Degrad. Stab.* **2019**, *166*, 290–299. [CrossRef]

58. Webb, H.K.; Arnott, J.; Crawford, R.; Ivanova, E.P. Plastic degradation and its environmental implications with special reference to poly (ethylene terephthalate). *Polymers* **2013**, *5*, 1–18. [CrossRef]

59. Olaosebikan, O.O.; Alo, M.N.; Ugah, U.I.; Olayemi, A.M. Environmental effect on biodegradability of plastic and paper bags. *IOSR J. Environ. Sci. Toxicol. Food Technol.* **2014**, *8*, 22–29. [CrossRef]

60. Chamas, A.; Moon, H.; Zheng, J.; Qiu, Y.; Tabassum, T.; Jang, J.H.; Abu-Omar, M.; Scott, S.L.; Suh, S. Degradation rates of plastics in the environment. *ACS Sustain. Chem. Eng.* **2020**, *8*, 3494–3511. [CrossRef]

61. Gonzalez-Rodriguez, M.N.; Sanz, J.J.; Santos, J.A.; Otero, A.; Garcia-Lopez, M.L. Bacteriological quality of aquacultured freshwater fish portions in prepackaged trays stored at 3 °C. *J. Food Prot.* **2001**, *64*, 1399–1404. [CrossRef]

62. Qiu, X.; Chen, S.; Liu, G.; Yang, Q. Quality enhancement in the Japanese sea bass (*Lateolabrax japonicas*) fillets stored at 4 °C by chitosan coating incorporated with citric acid or licorice extract. *Food Chem.* **2014**, *162*, 156–160. [CrossRef] [PubMed]

63. Albertos, I.; Martin-Diana, A.B.; Burón, M.; Rico, D. Development of functional bio-based seaweed (*Himanthalia elongata* and *Palmaria palmata*) edible films for extending the shelf-life of fresh fish burgers. *Food Packag. Shelf Life* **2019**, *22*, 100382. [CrossRef]

64. Jiang, G.; Hou, X.; Zeng, X.; Zhang, C.; Wu, H.; Shen, G.; Li, S.; Luo, Q.; Li, M.; Liu, X.; et al. Preparation and characterization of indicator films from carboxymethyl-cellulose/starch and purple sweet potato (*Ipomoea batatas* (L.) Lam) anthocyanins for monitoring fish freshness. *Int. J. Biol. Macromol.* **2020**, *143*, 359–372. [CrossRef]

65. Rico, D.; Albertos, I.; Martinez-Alvarez, O.; Lopez-Caballero, M.E.; Martin-Diana, A.B. Use of sea fennel as a natural ingredient of edible films for extending the shelf life of fresh fish burgers. *Molecules* **2020**, *25*, 5260. [CrossRef]

66. Sahraee, S.; Milani, J.M.; Regenstein, J.M.; Kafil, H.S. Protection of foods against oxidative deterioration using edible films and coatings: A review. *Food Biosci.* **2019**, *32*, 100451. [CrossRef]

67. Santak, V.; Zaplotnik, R.; Milosevic, S.; Klaric, E.; Tarle, Z. Atmospheric pressure plasma jet as an accelerator of tooth bleaching. *Acta Stomatol. Croat.* **2014**, *48*, 268. [CrossRef]

68. Albertos, I.; Jaime, I.; Diez, A.M.; González-Arnáiz, L.; Rico, D. Carob seed peel as natural antioxidant in minced and refrigerated (4 °C) Atlantic horse mackerel (*Trachurus trachurus*). *LWT-Food Sci. Technol.* **2015**, *64*, 650–656. [CrossRef]

69. Zhai, X.; Shi, J.; Zou, X.; Wang, S.; Jiang, C.; Zhang, J.; Huang, X.; Zhang, W.; Holmes, M. Novel colorimetric films based on starch/polyvinyl alcohol incorporated with roselle anthocyanins for fish freshness monitoring. *Food Hydrocoll.* **2017**, *69*, 308–317. [CrossRef]

70. Wu, C.; Sun, J.; Zheng, P.; Kang, X.; Chen, M.; Li, Y.; Ge, Y.; Hu, Y.; Pang, J. Preparation of an intelligent film based on chitosan/oxidized chitin nanocrystals incorporating black rice bran anthocyanins for seafood spoilage monitoring. *Carbohydr. Polym.* **2019**, *222*, 115006. [CrossRef]

71. Albertos, I.; Martín-Diana, A.B.; Jaime, I.; Avena-Bustillos, R.J.; McHugh, T.H.; Takeoka, G.R.; Rico, D. Antioxidant effect of olive leaf powder on fresh Atlantic horse mackerel (*Trachurus trachurus*) minced muscle. *J. Food Process. Preserv.* **2018**, *42*. [CrossRef]

72. Slinkard, K.; Singleton, V.L. Total phenol analysis: Automation and comparison with manual methods. *Am. J. Enol. Vitic.* **1977**, *28*, 49–55.

73. Arnous, A.; Markis, D.; Kefalas, P. Correlation of pigment and flavonol content with antioxidant properties in selected aged regional wines from Greece. *J. Food Compos. Anal.* **2002**, *15*, 655–665. [CrossRef]

74. Lee, J.; Durst, R.W.; Wrolstad, R.E. Determination of total monomeric anthocyanin pigment content of fruit juices, beverages, natural colorants, and wines by the pH differential method: Collaborative study. *J. AOAC Int.* **2005**, *88*, 1269–1278. [CrossRef]

75. Brand-Williams, W.; Cuvelier, M.E.; Berset, C. Use of a free radical method to evaluate antioxidant activity. *LWT-Food Sci. Technol.* **1995**, *28*, 25–30. [CrossRef]

76. Re, R.; Pellegrini, N.; Proteggente, A.; Pannala, A.; Yang, M.; Rice-Evans, C. Antioxidant activity applying an improved ABTS radical cation decolorization assay. *Free Radic. Biol. Med.* **1999**, *26*, 1231–1237. [CrossRef]

77. Bamdad, F.; Goli, A.H.; Kadivar, M. Preparation and Characterization of Proteinous Film from Lentil (*Lens culinaris*). *Food Res. Int.* **2006**, *39*, 106–111. [CrossRef]

78. Martins, J.T.; Cerqueira, M.A.; Souza, B.W.S.; Carmo Avides, M.D.; Vicente, A.A. Shelf-life extension of ricotta cheese using coatings of galactomannans from nonconventional sources incorporating nisin against *Listeria monocytogenes*. *J. Agri. Food Chem.* **2010**, *58*, 1884–1891. [CrossRef]

79. AOAC. *Official Methods of Analysis of AOAC International*, 16th ed.; The Association of Analytical Communities: Arlington, VA, USA, 1995; ISBN 978-093-558-480-6.